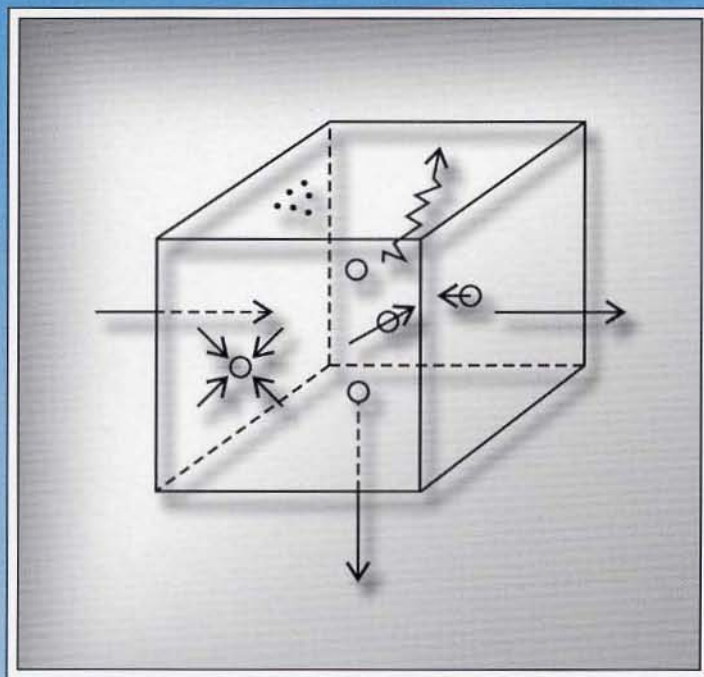


Smoke, Dust, and Haze

Fundamentals of Aerosol Dynamics

SECOND EDITION



Sheldon K. Friedlander

CONTENTS

SMOKE, DUST, AND HAZE

Fundamentals of Aerosol Dynamics

SECOND EDITION

Sheldon K. Friedlander

University of California, Los Angeles

New York • Oxford

OXFORD UNIVERSITY PRESS

2000

Oxford University Press

Oxford New York

Athens Auckland Bangkok Bogotá Buenos Aires Calcutta

Cape Town Chennai Dar es Salaam Delhi Florence Hong Kong Istanbul

Karachi Kuala Lumpur Madrid Melbourne Mexico City Mumbai

Nairobi Paris São Paulo Singapore Taipei Tokyo Toronto Warsaw

and associated companies in

Berlin Ibadan

Copyright © 2000 by Oxford University Press, Inc.

Published by Oxford University Press, Inc.,

198 Madison Avenue, New York, New York, 10016

<http://www.oup-usa.org>

Oxford is a registered trademark of Oxford University Press

All rights reserved. No part of this publication may be reproduced, stored in a retrieval system, or transmitted, in any form or by any means, electronic, mechanical, photocopying, recording, or otherwise, without the prior permission of Oxford University Press.

Library of Congress Cataloging-in-Publication Data

Friedlander, Sheldon K. (Sheldon Kay), 1927–

Smoke, dust, and haze : fundamentals of aerosol dynamics / Sheldon K. Friedlander. – 2nd ed.

p. cm. — (Topics in chemical engineering)

Includes bibliographical references and index.

ISBN 0-19-512999-7

1. Aerosols. 2. Particles. 3. Air-Pollution. I. Title. II. Series.

TD884.5.F76 2000

628.5'32—dc21

00-022537

Printing (last digit): 9 8 7 6 5 4 3 2 1

Printed in the United States of America
on acid-free paper

CONTENTS

Preface xv

Preface to the First Edition xix

Chapter 1 AEROSOL CHARACTERIZATION 1

Parameters Determining Aerosol Behavior 2

Particle Size 3

General 3

Equivalent Particle Diameter 5

Particle Concentration 6

Number Concentration 6

Mass Concentrations 7

Volumetric Concentration 7

Coagulation 8

Size Distribution Function 10

Dimensional Considerations 11

Relationships Among Distribution Functions 11

Averaging of Size Distributions 14

Moments of the Distribution Function 14

Examples of Size Distribution Functions 16

Normal Distributions 17

Power Law Distributions 18

Self-Similar Distribution Functions 18

Chemical Composition 19

Size-Composition Probability Density Function 19

Average Chemical Composition 20

*Distribution of Chemical Composition with Respect to
Particle Size 21*

Aerosol Dynamics: Relation to Characterization	23
Problems	24
References	25

Chapter 2 PARTICLE TRANSPORT PROPERTIES 27

Equation of Diffusion	28
Coefficient of Diffusion	30
Friction Coefficient	33
Agglomerate Diffusion Coefficients	35
Path Length of a Brownian Particle	37
Migration in an External Force Field	38
Electrical Migration	40
<i>General Concepts</i>	40
<i>Field Charging</i>	41
<i>Unipolar Diffusion Charging: Free Molecule Range</i>	42
<i>Unipolar Diffusion Charging: Continuum Range</i>	43
<i>Unipolar Diffusion Charging: Stochastic Theory</i>	46
<i>Bipolar Charging</i>	46
Thermophoresis	50
London-van der Waals Forces	52
Boundary Condition for Particle Diffusion	53
Problems	55
References	56

Chapter 3 CONVECTIVE DIFFUSION: EFFECTS OF FINITE PARTICLE DIAMETER AND EXTERNAL FORCE FIELDS 58

Equation of Convective Diffusion	59
Similitude Considerations for Aerosol Diffusion	60
Concentration Boundary Layer	61
Diffusion to Cylinders at Low Reynolds Numbers: Concentration Boundary Layer Equation	63
Diffusion to Cylinders at Low Reynolds Numbers: Point Particles	64
Diffusion at Low Reynolds Numbers: Similitude Law for Particles of Finite Diameter	66

Low Re Deposition: Comparison of Theory with Experiment	69
Single-Element Particle Capture by Diffusion and Interception at High Reynolds Numbers	73
High Re Deposition: Application to Deposition on Rough Surfaces	76
Diffusion from a Laminar Pipe Flow	78
Diffusion from a Turbulent Pipe Flow	80
Particle Deposition from Rising Bubbles	82
Convective Diffusion in an External Force Field: Electrical Precipitation	84
Thermophoresis: "Dust-Free Space"	87
<i>Vertical Plate</i>	88
<i>Stagnation Flow</i>	89
<i>Effects of Brownian Diffusion on Deposition</i>	90
Problems	90
References	92
Chapter 4 INERTIAL TRANSPORT AND DEPOSITION	94
Particle–Surface Interactions: Low Speeds	95
Particle–Surface Interactions: Rebound	98
Particle Acceleration at Low Reynolds Numbers: Stop Distance	100
Similitude Law for Impaction: Stokesian Particles	102
Impaction of Stokesian Particles on Cylinders and Spheres	104
<i>Introduction</i>	104
<i>Critical Stokes Number for Inviscid Flows</i>	105
<i>Comparison of Experiment and Theory</i>	107
Impaction of Non-Stokesian Particles	108
Deposition from a Rotating Flow: Cyclone Separator	111
Particle Eddy Diffusion Coefficient	113
Turbulent Deposition	115
Aerodynamic Focusing: Aerosol Beams	118
Transition from the Diffusion to Inertial Ranges	121
Problems	122
References	124

Chapter 5 LIGHT SCATTERING 125

- Scattering by Single Particles: General Considerations 126
- Scattering by Particles Small Compared to the Wavelength 128
- Scattering by Large Particles: The Extinction Paradox 130
- Scattering in the Intermediate Size Range: Mie Theory 130
 - General Considerations* 130
 - Angular Scattering* 133
- Scattering by Aerosol Clouds 134
 - General Considerations* 134
 - Extinction Coefficient and Optical Thickness* 136
- Scattering over the Visible Wavelength Range: Aerosol Contributions by Volume 138
- Rayleigh Scattering: Self-Similar Size Distributions 139
- Mie Scattering: Power Law Distributions 141
- Quasi-Elastic Light Scattering 143
- Specific Intensity: Equation of Radiative Transfer 145
- Equation of Radiative Transfer: Formal Solution 146
- Light Transmission Through the Atmosphere: Visibility 148
- Inelastic Scattering: Raman Effect 151
 - Basic Concepts* 151
 - Raman Scattering by Particles* 152
- Problems 154
- References 155

Chapter 6 EXPERIMENTAL METHODS 157

- Sampling 158
- Microscopy 160
- Mass Concentration: Filtration 162
- Total Number Concentration: Condensation Particle Counter 163
- Total Light Scattering and Extinction Coefficients 165
- Size Distribution Function 166
 - Overview* 166
 - Single-Particle Optical Counter* 166

<i>Differential Mobility Analyzer/Electrostatic Classifier</i>	168
<i>Diffusion Battery</i>	170
Mass and Chemical Species Distribution: The Cascade Impactor	171
Aerosol Chemical Analysis	174
<i>Background</i>	174
<i>Multielement Analysis for Source Resolution</i>	175
<i>Single-Particle Chemical Analysis by Mass Spectrometry</i>	177
Summary Classification of Measurement Instruments	178
Monodisperse Aerosol Generators	181
<i>Condensation Generators</i>	181
<i>Atomizing Generators</i>	182
Problems	184
References	186
Chapter 7 COLLISION AND COAGULATION: COALESCING PARTICLES	188
Introduction	188
Collision Frequency Function	189
Brownian Coagulation	190
Brownian Coagulation: Dynamics of Discrete Distribution for an Initially Monodisperse Aerosol	192
Brownian Coagulation: Effect of Particle Force Fields	196
Effect of van der Waals Forces	197
Effect of Coulomb Forces	200
Collision Frequency for Laminar Shear	200
Simultaneous Laminar Shear and Brownian Motion	202
Turbulent Coagulation	204
<i>Dynamics of Turbulence: Kolmogorov Microscale</i>	204
<i>Turbulent Shear Coagulation</i>	206
<i>Turbulent Inertial Coagulation</i>	206
<i>Limitations on the Analysis</i>	207
<i>Comparison of Collision Mechanisms</i>	208
Equation of Coagulation: Continuous Distribution Function	208

Similarity Solution: Coagulation in the Continuum Regime	210
Similarity Solution for Brownian Coagulation	211
Similarity Solution: Coagulation in the Free Molecule Region	215
Time to Reach the Self-Preserving Distribution (SPD)	217
Problems	219
References	220

Chapter 8 DYNAMICS OF AGGLOMERATE FORMATION AND RESTRUCTURING 222

Agglomerate Morphology: Scaling Laws	223
<i>Introduction</i>	223
<i>Autocorrelation Function</i>	223
<i>Prefactor for the Power Law Relationship</i>	226
Computer Simulation of Agglomerate Formation	227
<i>Diffusion-Limited Aggregation</i>	227
<i>Ballistic Aggregation</i>	228
<i>Reaction-Limited Aggregation</i>	228
<i>Coordination Number and Fractal Dimension</i>	229
Langevin Simulations of Agglomeration	230
Smoluchowski Equation: Collision Kernels for Power Law Agglomerates	230
Self-Preserving Agglomerate Size Distributions	233
<i>Time to Reach the Self-Preserving Form</i>	234
Effect of Primary Particle Size on Agglomerate Growth	237
Effect of D_f on Agglomerate Growth	240
Agglomerate Restructuring	242
<i>Thermal Restructuring</i>	242
<i>Restructuring under Tension: Elastic Properties of Chain Aggregates</i>	245
Problems	246
References	247

Chapter 9 THERMODYNAMIC PROPERTIES 249

The Vapor Pressure Curve and the Supersaturated State 249

Saturation Ratio 249

Condensation by Adiabatic Expansion 251

Condensation by Mixing 252

Effect of Solutes on Vapor Pressure 254

Vapor Pressure of a Small Particle 256

The Kelvin Relation 256

Particle Internal Pressure: Laplace's Formula 257

Limit of Applicability of Kelvin Relation 258

Hygroscopic Particle–Vapor Equilibrium 259

Charged Particle–Vapor Equilibria 263

Solid-Particle–Vapor Equilibrium 265

Vapor and Surface Pressures of Crystalline Particles 265

Melting Point Reduction of Small Solid Particles 266

Effect of Particle Size on the Equilibrium of a Heterogeneous Chemical Reaction 266

Molecular Clusters 269

Introduction 269

Equilibrium Size Distribution 270

Problems 273

References 274

Chapter 10 GAS-TO-PARTICLE CONVERSION 275

Condensation by Adiabatic Expansion: The Experiments of C. T. R. Wilson 276

Kinetics of Homogeneous Nucleation 277

Experimental Test of Nucleation Theory 280

Heterogeneous Condensation 283

Growth Laws 284

Transport-Limited Growth 285

Aerosol Phase, Reaction-Limited Growth 286

Dynamics Of Growth: Continuity Relation in v Space 288

Measurement of Growth Rates: Homogeneous Gas-Phase Reactions	290
Simultaneous Homogeneous and Heterogeneous Condensation	293
<i>Theoretical Aspects</i>	293
<i>Oscillating Aerosol Reactors: An Experimental Study</i>	296
Effects of Turbulence on Homogeneous Nucleation	299
<i>Scaling Theory</i>	299
<i>Experimental Tests of Scaling Theory</i>	301
<i>Effect of Splitting the Flow into Multiple Streams</i>	303
Problems	304
References	305
Chapter 11 THE GENERAL DYNAMIC EQUATION FOR THE PARTICLE SIZE DISTRIBUTION FUNCTION	306
General Dynamic Equation for the Discrete Distribution Function	307
Coagulation and Nucleation as Limiting Processes in Gas-to-Particle Conversion	308
General Dynamic Equation for the Continuous Distribution Function	309
The Dynamic Equation for the Number Concentration N_∞	310
The Dynamic Equation for the Volume Fraction	311
Simultaneous Coagulation and Diffusional Growth: Similarity Solution for Continuum Regime	313
Simultaneous Coagulation and Growth: Experimental Results	315
The GDE for Turbulent Flow	318
The GDE for Turbulent Stack Plumes	319
Coagulation and Stirred Settling	321
Coagulation and Deposition by Convective Diffusion	325
Continuously Stirred Tank Reactor	327
Problems	329
References	330

Chapter 12 SYNTHESIS OF SUBMICRON SOLID PARTICLES: AEROSOL REACTORS 331

Aerosol Reactors: Commercial and Pilot Scale **332**

Flame Reactors **332**

Pyrolysis Reactors **334**

Electron-Beam Dry Scrubbing **335**

Evaporation-Condensation Generators **336**

The Collision-Coalescence Mechanism of Primary Particle
Formation **338**

Extension of the Smoluchowski Equation to Colliding,
Coalescing Particles **339**

Rate Equation for Particle Coalescence **340**

General Considerations **340**

Viscous Flow Transport **341**

Transport by Diffusion **341**

*Molecular Dynamic Simulations: Solid-Liquid
Transition* **342**

Solid-State Diffusion Coefficient **343**

Temperature Dependence **343**

Values of D for Lattice Diffusion **345**

High Diffusivity Paths **346**

Estimation of Average Primary Particle Size: Method of
Characteristic Times **346**

Primary Particle Size: Effects of Aerosol Material
Properties **350**

Particle Neck Formation **353**

Particle Crystal Structure **355**

Basic Concepts **355**

Experimental Observations **355**

Problems **356**

References **357**

Chapter 13 ATMOSPHERIC AEROSOL DYNAMICS 359

Atmospheric Aerosol Size Distribution **360**

General Features **360**

Coarse Mode ($d_p > 2.5 \mu\text{m}$) **361**

Accumulation Mode ($0.1 < d_p < 2.5 \mu\text{m}$) **364**

<i>Ultrafine Range ($d_p < 0.1 \mu\text{m}$)</i>	366
<i>Residence Time and Dry Deposition</i>	366
Aerosol Dynamics in Power Plant Plumes	368
Chemical Composition of Urban Aerosols	370
<i>Introduction</i>	370
<i>Chemical Composition of the Fine Aerosol</i>	372
Distributions of Chemical Species with Particle Size	373
<i>Sulfates and Nitrates</i>	374
<i>Primary Submicron Aerosols: PAHs and Elemental Carbon</i>	376
<i>Water</i>	376
Morphological Characteristics of the Submicron Aerosol	378
Common Measures of Air Quality for Particulate Matter: Federal Standards	380
Receptor Modeling: Source Apportionment	380
<i>Basic Concepts</i>	380
<i>Chemical Mass Balance Method</i>	381
<i>Portland Aerosol Characterization Study</i>	382
<i>Relating the CMB to Aerosol Dynamics</i>	385
Statistical Variations of Ambient Aerosol Chemical Components	385
<i>Field Measurements</i>	385
<i>Relation to Aerosol Dynamics</i>	388
Problems	389
References	391
Common Symbols	393
Index	397

PREFACE

The first edition of this book, published in 1977, included an extended discussion of *aerosol dynamics*, the study of the factors that determine the distribution of aerosol properties with respect to particle size. The distributions change with position and time in both natural and industrial processes. The ability to predict and measure changes in the distribution function are of central importance in many applications from air pollution to the commercial synthesis of powdered materials. The aerosol dynamics approach makes it possible to integrate a broad set of topics in aerosol science usually treated in an unconnected manner. These include stochastic processes, aerosol transport, coagulation, formation of agglomerates, classical nucleation theory, and the synthesis of ultrafine solid particles.

I had started writing the first edition after participating in ACHEX, the first large scale atmospheric aerosol characterization experiment which took place in California in the early seventies. K. T. Whitby had shown the power of the new instruments that had been developed for the rapid determination of particle size distributions including the single particle optical counter and electrical mobility analyzer. I realized that this instrumentation provided enough information to warrant a new treatment of aerosol dynamics linked to improved experimental capabilities. (An earlier ground-breaking book on *The Dynamics of Aerocolloidal Systems* had been published in 1971 by G. M. Hidy and J. R. Brock.)

In the approach adopted in my first edition, the derivation and use of the general dynamic equation for the particle size distribution played a central role. This special form of a population balance equation incorporated the Smoluchowski theory of coagulation and gas-to-particle conversion through a Liouville term with a set of special growth laws; coagulation and gas-to-particle conversion are processes that take place within an elemental gas volume. Brownian diffusion and external force fields transport particles across the boundaries of the elemental volume. A major limitation on the formulation was the assumption that the particles were liquid droplets that coalesced instantaneously after collision.

In the second edition, I have sharpened the focus on aerosol dynamics. The field has grown rapidly since its original applications to the atmospheric aerosol for which the assumption of particle sphericity is usually adequate, especially for the accumulation mode. Major advances in the eighties and nineties came about when we learned how to deal with (i) the formation of solid primary particles, the smallest individual particles that compose agglomerates and (ii) the formation of agglomerate structures by collisions. These phenomena, which have important industrial applications, are covered in two new chapters. One chapter describes the extension of classical coagulation theory for coalescing

particles to fractal-like (power law) agglomerates. The other new chapter includes a discussion of the collision-coalescence mechanism that controls primary particle formation in high temperature processes. This phenomenon, first recognized by G. Ulrich, was later incorporated in the general dynamic equation by W. Koch and myself. Also included is an introduction to the fundamentals of aerosol reactors for the synthesis of submicron solid particles. In aerosol reactor design, I have benefited from the work of S. E. Pratsinis (University of Cincinnati and ETH, Zurich) and his students who have pioneered the industrial applications of aerosol dynamics.

Several other chapters have been substantially rewritten to reflect the sharpened focus on aerosol dynamics. For example, the chapter on optical properties has been expanded to include more applications to polydisperse aerosols. It helps support the chapter that follows on experimental methods in which coverage of instrumentation for rapid size distribution measurements has been augmented. Methods for the rapid on-line measurement of aerosol chemical characteristics are discussed in the chapters on optical properties and experimental methods. This chapter has been strongly influenced by the work of the Minnesota group (B. Y. H. Liu, D. Y. H. Pui, P. McMurry, and their colleagues and students) who continue to invent and perfect advanced aerosol instrumentation. Discussions of the effects of turbulence have been substantially expanded in chapters on coagulation and gas-to-particle conversion.

The chapter on atmospheric aerosols in the first edition has been updated and completely rewritten within an aerosol dynamics framework. This important field has implications for the earth's radiation balance and global climate change. J. H. Seinfeld, R. C. Flagan (Caltech), and other members of the aerosol dynamics community are active in this area.

Theory and related experimental measurements are discussed throughout the text. Microcontamination in the semiconductor industry, visibility degradation, manufacture of pyrogenic silica, filtration, and many other applications are used as illustrative examples. The emphasis is on physical explanations of the phenomena of interest, keeping the mathematical analysis to a relatively simple level. Extensive use is made of scaling concepts, dimensional analysis, and similarity theories. These approaches are natural to aerosol dynamics because of the wide range in particle sizes, going from molecules to the stable nuclei of homogeneous nucleation, to primary nanometer and ultrafine solid particles and their aggregates. In keeping with the sharpened focus on dynamics, the book subtitle has been changed to *Fundamentals of Aerosol Dynamics*.

Coupling between chemical kinetics and aerosol dynamics is important for the atmospheric aerosol, the commercial production of fine particles and aerosol emissions from combustion processes. In many cases, the link between the aerosol dynamics and chemical processes can be established in a general way as shown in the text. However the chemical processes must often be treated simultaneously for the specific applications; this is beyond the scope of this book.

Unsolved fundamental problems of great practical importance remain in aerosol dynamics. In addition to the need for rapid chemical measurement methods mentioned above, much more research is required on the effects of turbulence on coagulation and nucleation; the general dynamic equation must be extended to include factors that determine the crystal state of primary particles. We also need to continue efforts to link aerogel formation and aerosol dynamics as initiated by A. A. Lushnikov (Karpov Institute). Experimental and

theoretical research in these and other areas should keep researchers in the aerosol field busy for the next few years.

I have used the notes on which the book is based as a text for a one quarter (ten weeks) course on aerosol science and technology, taken by seniors and graduate students. Most of the students were from chemical engineering with a smaller number from atmospheric sciences, environmental engineering and public health. I cover about eight chapters depending on student interests, in the ten weeks. There is currently an interest in developing undergraduate engineering programs in particle technology. Lectures based on this text could serve as part of a suite of courses in particle technology.

I wish to express my appreciation to B. Scarlett and J. Marijnissen of the Chemical Engineering Department at Delft University (The Netherlands). Several years ago they invited me to offer a series of lectures on aerosol reaction engineering in their comprehensive course on particle technology. Those lectures served as the launching pad for this book. My discussion with the Delft group made me appreciate even more the importance of improving measurement methods in our field.

Much of the research on aerosol science and technology in my Laboratory has been sponsored over the years by EPA, NSF and through the Parsons Chair in Chemical Engineering at UCLA that I hold. For this support, I express my thanks and appreciation.

The preparation of the manuscript which went through countless revisions was accomplished with extraordinary patience by Ms. Phyllis Gilbert. Finally, I thank my wife Marjorie and our children for their forbearance during the course of the writing.

*Los Angeles,
Dana Point, California*

S. K. FRIEDLANDER

PREFACE TO THE FIRST EDITION

Over the last ten years I have taught a course in particulate pollution to seniors and first-year graduate students in environmental and chemical engineering. A course in this field has now become essential to the training of engineers and applied scientists working in the field of air pollution. The subject matter is sufficiently distinctive to require separate coverage; at the same time, it is inadequately treated in most courses in engineering or chemistry. Although there are a few good reference works covering different parts of the field, I have felt the need for a text; this one is based on my own course notes.

There are three main types of practical problems to which the contents of this book can be applied: How are aerosols formed at pollution sources? How can we remove particles from gaseous emissions to prevent them from becoming an air pollution problem? How can we relate air quality to emission sources and thereby devise effective pollution control strategies? The fundamentals of aerosol behavior necessary to deal with these problems are developed in this text. Although fundamentals are stressed, examples of practical problems are included throughout.

The treatment that I have given the subject assumes some background in fluid mechanics and physical chemistry. A student with good preparation in either of these fields should, with diligence, be able to master the fundamentals of the subject. This has been my experience in teaching first-year graduate students with undergraduate majors in almost all branches of engineering, chemistry, and physics.

The first half of the text is concerned primarily with the transport of particles and their optical properties. It is this part of the field that, until recently, had been the most developed. Particle transport theory has application to the design of gas-cleaning devices, such as filters and electrical precipitators, and this is pointed out in the text. However, I have not dealt with the details of equipment design; in most cases, direct application of the theory to design is difficult because of the complexity of gas-cleaning equipment. This leads to the use of methods that are more empirical than otherwise employed in this text. With a good understanding of particle transport, the student will be able to read the specialized works on equipment design intelligently and critically.

Once the student has mastered the concepts of particle transport and optical behavior, he will also find it easy to understand aerosol measurement methods. A chapter on this subject ends the first half of the text on an experimental note; progress in aerosol science is heavily dependent on experimental advances, and it is important to get this across to the student early in his studies. Indeed, throughout the text, theory and experiment are closely linked.

In the second half of the book, the dynamics of the size distribution function are discussed. It is this theory that gives the field of small particle behavior its distinctive theoretical character. The organization of this material is completely new, so far as coverage in book form is concerned. It begins with a chapter on coagulation, and is followed by chapters on thermodynamics and gas-to-particle conversion. Next, the derivation of the general dynamic equation for the size distribution function and its application to emission sources and plumes are discussed. This leads to the final chapter on the relationship of air quality to emission sources for particulate pollution. This chapter is based in part on the preceding theory. However, the power of the theory has not yet been fully exploited, and the next few years should see significant advances.

One of my goals in writing the book was to introduce the use of the equation for the dynamics of the particle size distribution function at the level of advanced undergraduate and introductory graduate instruction. This equation is relatively new in applied science, but has many applications in air and water pollution and the atmospheric sciences.

I have also taken a step toward the linking of aerosol physics and chemistry in the last few chapters. Chemistry enters into the general dynamic equation through the term for gas-to-particle conversion. This turns out to have many important air pollution applications as shown in the last four chapters.

To keep the subject matter to manageable proportions, I have omitted interesting problems of a specialized nature, such as photophoresis and diffusiophoresis, which are seldom of controlling importance in applied problems. Details of the kinetic theory of aerosols have also been omitted. Although of major importance, they usually enter fully developed, so to speak, in applications. Besides, their derivation is covered in other books on aerosol science.

The resuspension of particles from surfaces and the break-up of agglomerates, important practical problems, are not well understood; the methods of calculation are largely empirical and not conveniently subsumed into the broad categories covered in the book.

Before I began writing, I considered the possibility of a general text covering small particle behavior in both gases and liquids. Much of the theory of physical behavior is the same or very similar for both aerosols and hydrosols, almost as much as in the fluid mechanics of air and water. The differences include double layer theory in the case of aqueous solutions and mean free path effects in gases. There are other important, specifically chemical differences.

After some thought, I decided against the general approach. Since I wanted to write a book closely linked to applications, I thought it best to limit it to the air field in which I can claim expertise. Including topics from water pollution would have unduly lengthened the book. However, the students who take my course are often interested in water pollution, and I frequently point out both similarities and differences between the air and water fields.

Special thanks are due C. I. Davidson and P. H. McMurry who served as teaching assistants and helped prepare some of the figures and tables. D. L. Roberts assisted in reviewing the manuscript for clarity and consistency. Professor R. B. Husar of Washington University made a number of useful suggestions on the text.

Pasadena, California
November 1976

S. K. FRIEDLANDER

Aerosol Characterization

SMOKE, DUST, AND HAZE

... of

... ..

1.1 Introduction

Aerosols are suspensions of small particles in a gas. They are formed by the condensation of gaseous particles by the change of temperature and pressure. They are also formed by the mechanical dispersion of solid materials in a gas. The particles are formed in the form of droplets or solid particles, which may be as small as a few micrometers or as large as several millimeters. The particles are formed by the condensation of gaseous particles by the change of temperature and pressure. They are also formed by the mechanical dispersion of solid materials in a gas. The particles are formed in the form of droplets or solid particles, which may be as small as a few micrometers or as large as several millimeters.

The particles which are formed by condensation are called condensation nuclei. They are formed by the condensation of gaseous particles by the change of temperature and pressure. They are also formed by the mechanical dispersion of solid materials in a gas. The particles are formed in the form of droplets or solid particles, which may be as small as a few micrometers or as large as several millimeters. The particles are formed by the condensation of gaseous particles by the change of temperature and pressure. They are also formed by the mechanical dispersion of solid materials in a gas. The particles are formed in the form of droplets or solid particles, which may be as small as a few micrometers or as large as several millimeters.

The particles which are formed by condensation are called condensation nuclei. They are formed by the condensation of gaseous particles by the change of temperature and pressure. They are also formed by the mechanical dispersion of solid materials in a gas. The particles are formed in the form of droplets or solid particles, which may be as small as a few micrometers or as large as several millimeters. The particles are formed by the condensation of gaseous particles by the change of temperature and pressure. They are also formed by the mechanical dispersion of solid materials in a gas. The particles are formed in the form of droplets or solid particles, which may be as small as a few micrometers or as large as several millimeters.

The particles which are formed by condensation are called condensation nuclei. They are formed by the condensation of gaseous particles by the change of temperature and pressure. They are also formed by the mechanical dispersion of solid materials in a gas. The particles are formed in the form of droplets or solid particles, which may be as small as a few micrometers or as large as several millimeters. The particles are formed by the condensation of gaseous particles by the change of temperature and pressure. They are also formed by the mechanical dispersion of solid materials in a gas. The particles are formed in the form of droplets or solid particles, which may be as small as a few micrometers or as large as several millimeters.

And Moses brought forth the people out of the camp to meet with God; and they placed themselves at the foot of the mount.

And mount Sinai smoked in every part, because the Lord had descended upon it in fire; and the smoke thereof ascended as the smoke of the furnace, and the whole mount quaked greatly.

Exodus 19:17,18

Aerosol Characterization

Aerosols are suspensions of small particles in gases. They are formed by the conversion of gases to particles or by the disintegration of liquids or solids. They may also result from the resuspension of powdered material or the breakup of agglomerates. Formation from the gas phase tends to produce much finer particles than do disintegration processes (except when condensation takes place directly on existing particles). Particles formed directly from the gas are usually smaller than $1\ \mu\text{m}$ in diameter ($1\ \text{micron} = 1\ \text{micrometer} = 10^{-4}\ \text{cm}$, designated by the symbol $1\ \mu\text{m}$).

The many words employed to describe particulate systems attest to their ubiquity and to the impression they have made on humans from early times. Smoke, dust, haze, fume, mist, and soot are all terms in common use with somewhat different popular meanings. Thus *dust* usually refers to solid particles produced by disintegration processes, while *smoke* and *fume* particles are generally smaller and formed from the gas phase. *Mists* are composed of liquid droplets. *Soot* usually refers to small carbon particles generated in fuel combustion but is now frequently used to describe very fine solid particles of silica and other inorganic oxides generated intentionally in industrial processes. In this text, however, we will rarely employ these special terms because of the difficulty of exact definition and the complexity of many real systems composed of mixtures of particles. Instead, we employ the generic term *aerosol* to describe all such systems of small particles suspended in air or another gas.

Aerosol science plays a key role in many different fields including (a) atmospheric sciences and air pollution, (b) industrial production of pigments, fillers, and specialty metal powders, (c) fabrication of optical fibers, (d) industrial hygiene, and (e) contamination control in the microelectronics and pharmaceuticals industries. Aerosols present in such applications can usually be considered as desirable or undesirable, but the same basic concepts apply to both types. Specialists in the various applied fields increasingly make use of similar theoretical concepts and experimental techniques in solving aerosol problems. These common approaches are the focus of this book.

Early advances in aerosol science were closely tied to the development of certain fundamental physical concepts. For example, aerosol transport theory is based on Stokes' law including semiempirical corrections made by Millikan in his measurements of the electronic charge. Einstein's theory of the Brownian motion plays a central role in aerosol diffusion which is discussed in the next chapter. The Brownian motion results in coagulation first

explained theoretically by Smoluchowski and discussed at length in the second half of this text. Aerosol optical properties are based on the theories of Rayleigh and Mie for scattering by spherical particles. Aerosol formation by gas-to-particle conversion (nucleation) was first studied quantitatively by C. T. R. Wilson with his cloud chamber at the end of the 19th century.

Modern aerosol scientists have extended these basic theoretical concepts and introduced new ones to describe aerosol behavior more completely. Theoretical advances have been accompanied by major advances in the instrumentation needed to measure aerosol properties. Aerosol science is a broad field, involving many branches of physics and chemistry and even biology. The first few chapters in this text review aerosol transport processes and optical properties. This is necessary to understand aerosol instrumentation, covered next. The rest of the book focuses on *aerosol dynamics*, the study of the factors that determine the *distribution of aerosol properties* with respect to particle size. Distributed aerosol properties of interest include (but are not limited to) the number and mass densities, chemical concentrations and light scattering. Accurate predictions and measurements of changes in the distributions are essential in the applications mentioned above. Moreover, aerosol dynamics provides an integrating framework for the transport and optical properties discussed in the first part of the text. The reader will find a list of basic references to the aerosol literature at the end of this chapter.

PARAMETERS DETERMINING AEROSOL BEHAVIOR

Particle size, concentration, and chemical composition are usually the aerosol properties of most interest. Also important in certain applications are particle charge, crystal structure and optical properties. In industry, particles are collected to recover a desirable product or reduce emissions and occupational exposures. The efficiency of filters, scrubbers and other such devices depends primarily on particle size. As shown in Chapter 3, a minimum is often found when the efficiency of particle removal is plotted as a function of particle size. The efficiency minimum or "window" occurs in the particle size range near a few tenths of a micron for reasons that differ depending on the mechanisms of particle collection. A similar efficiency minimum is observed for particle deposition in the lung as a function of particle size. The explanations for the efficiency minima in the lung and certain types of filters are similar.

The interaction of small particles with light is also a sensitive function of particle size and the optical properties. The light scattered per unit mass of aerosol often passes through a maximum as a function of particle size for incident radiation with wavelengths in the visible range. Atmospheric chemical and physical processes leading to the accumulation of particles in the size range of the light scattering maximum produce the most severe visibility degradation. In the manufacture of titania pigments, the industrial process is operated to produce particles with the maximum surface *hiding power*—that is, ability to scatter visible light per unit mass of material. This occurs usually in the size range around $0.2 \mu\text{m}$.

Particle chemical composition is of toxicological concern, and this is reflected in limits on occupational exposures, air pollution emission standards, and ambient air quality standards. Careful control of aerosol chemical properties is also a central feature in commercial processes such as the fabrication of optical fibers in which a silica aerosol produced by the

oxidation of SiCl_4 is doped with germanium dioxide and deposited in a quartz prefab to serve as the core of the optical fiber.

In the sections that follow, mathematical methods for characterizing aerosol size and chemical properties are discussed. These are primarily of a definitional nature and are needed to provide a common basis for discussing the broad range of aerosol properties and behavior. However, aerosol *characterization* does not provide, directly, information on the mechanisms of aerosol formation, or temporal and spatial changes in the aerosol—that is, *aerosol transport processes* and *aerosol dynamics*. These and related topics are covered in later chapters. Advances in aerosol instrumentation have made it possible to measure many of the most important parameters necessary to characterize aerosols (Chapter 6). However, much remains to be done in developing aerosol instrumentation for research as well as industrial and atmospheric applications.

PARTICLE SIZE

General

With occasional exceptions as noted, particle size refers to diameter in this text. This is usually the case in the modern aerosol literature, but particle radius is also employed from time to time. Both particle volume and area are also used in some applications. The particle diameters of interest in aerosol behavior range from molecular clusters of 10 \AA ($10 \text{ \AA} = 1 \text{ nanometer} = 10^{-9} \text{ meters}$) to cloud droplets and dust particles as large as $100 \mu\text{m}$ (Fig. 1.1). This represents a variation of 10^5 in size and 10^{15} in mass. In air pollution applications, particles larger than $1 \mu\text{m}$ are called *coarse* particles. Submicron particles can be divided (somewhat arbitrarily) into various subranges. The *accumulation mode*, important in air pollution, refers roughly to the range $0.1 < d_p < 2.0 \mu\text{m}$. Particles smaller than 100 nm ($0.1 \mu\text{m}$) are called *ultrafine*. The nanometer (nm) range refers to particles from 10 to 50 down to 1 nm.

For spherical liquid droplets, the diameter (d_p) is an unequivocal measure of particle size. Spherical particles are frequently encountered in polluted atmospheres because of the growth of nuclei by condensation of liquid from the gas phase. For nonspherical particles such as crystal fragments, fibers, or agglomerates, a characteristic size is more difficult to define. In the special case of geometric similarity, particles of different size have the same shape so that a single length parameter serves to characterize any size class. An ellipsoid with fixed ratio of major to minor axes is an example. Sizes of irregular particles such as agglomerates can be defined in terms of an equivalent particle diameter as discussed in the next section.

Particle behavior often depends on the ratio of particle size to some other characteristic length. The mechanisms of heat, mass, and momentum transfer between particle and carrier gas depend on the Knudsen number, $2l_p/d_p$, where l_p is the mean free path of the gas molecules. The mean free path or mean distance traveled by a molecule between successive collisions can be calculated from the kinetic theory of gases. A good approximation for a single-component gas composed of molecules that act like rigid elastic spheres is

$$l_p = 0.707/\pi n_m \sigma^2 \quad (1.1)$$

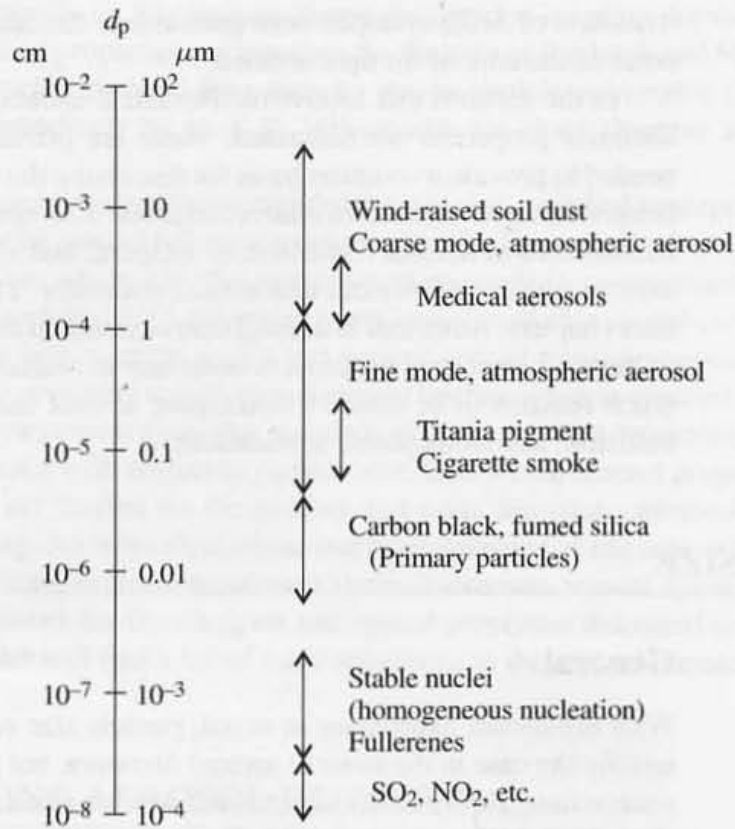


Figure 1.1 Examples of aerosol particle size ranges.

where n_m is the molecular density and σ the molecular diameter. For normal temperatures and pressures, the mean free path in air is about $0.065 \mu\text{m}$. It depends on the pressure and temperature through the ideal gas relationship

$$n_m = p/kT \quad (1.2)$$

where k is Boltzmann's constant and T is the absolute temperature. Because the molecular diameters of low-molecular-weight gases are all of the same order, the mean free path in most gases at standard temperature and pressure is of order 10^{-5} cm.

According to (1.1), the mean free path of a gas is inversely proportional to the molecular density. In a highly rarefied gas, say 0.01 torr, the free path is of order 1 cm. Consider the case of a spherical particle moving at constant velocity through a gas. When the particle diameter is much smaller than the mean free path ($l_p/d_p \gg 1$), molecules bouncing from the surface rarely collide with the mainstream molecules until far from the sphere. Most of the molecules striking the surface of the sphere come from the main body of the gas and are essentially unaffected by the presence of the sphere. The rate of exchange of heat, mass, and momentum between particle and gas can be estimated from molecular collision theory. Appropriately, this range ($l_p/d_p \gg 1$) is known as the free molecular range.

When the particle diameter is much greater than the mean free path ($l_p/d_p \ll 1$), molecules striking the surface are strongly affected by those leaving. The gas behaves as a continuum with a zero velocity boundary condition at the surface when the gas moves

relative to a fixed particle. For continuum flow the drag of a gas on a fixed spherical particle can be calculated from the Navier–Stokes equations of fluid motion. The continuum drag is much larger at the same relative velocity than for gas flow in the free molecule range. Hence, for a particle of given size, decreasing gas pressure while keeping constant relative velocity between particle and gas reduces drag. The transition between the continuum and free molecule ranges takes place continuously, but the transition theory poses formidable difficulties.

Light scattering by small particles depends on the ratio of diameter to the wavelength of the incident light, d_p/λ . For $d_p/\lambda \gg 1$, geometric optics apply and the scattering cross section is proportional to the cross-sectional area of the particle. When $d_p/\lambda \ll 1$, the scattering is calculated from the theory of the oscillation of a dipole in an oscillating electric field. For light in the visible range, λ is of the order of $0.5 \mu\text{m}$ and the transition between the two scattering regimes takes place over the range from 0.05 to $5 \mu\text{m}$. Light scattering in the transition range can be calculated from classical electromagnetic theory, but the computations are complex (Chapter 5).

Equivalent Particle Diameter

For irregular (nonspherical) solid particles, the usual method of particle characterization is to introduce an “equivalent diameter”—that is, the diameter of a spherical particle that would give the same behavior in the experimental system of interest.

The *aerodynamic diameter* is one of the most common equivalent diameters. It can be defined as the diameter of a unit density sphere with the same terminal settling velocity as the particle being measured. The aerodynamic diameter is commonly used to describe the motion of particles in collection devices such as cyclone separators and impactors. However, in shear flows, the motion of irregular particles may not be characterized accurately by the equivalent diameter alone because of the complex rotational and translational motion of irregular particles compared with spheres. That is, the path of the irregular particle may not follow that of a particle of the same aerodynamic diameter. It is of course possible that there may be a sphere of a certain diameter and unit density that deposits at the same point; this could be an average point of deposition because of the effects of turbulence or the stochastic behavior of irregular particles.

Agglomerates of ultrafine solid particles may grow to dimensions of the order of a few microns. The individual particles that compose the agglomerates are called *primary particles*. It is usually assumed that the primary particles are of uniform size, although this is often not a good assumption. The agglomerate structure can sometimes be characterized by the *fractal dimension* (Chapters 2 and 8). The behavior of an agglomerate differs from a sphere of the same mass, and agglomerate structure has significant effects on rates of collision and deposition from gas streams. Agglomerate particle sizes are often measured using an electrical mobility analyzer; the equivalent agglomerate size measured in this way is the *mobility diameter*. The mobility is the ratio of the particle velocity to the force producing the motion. Hence the mobility diameter is the diameter of a sphere with the same mobility as the agglomerate.

In addition to particle motion, other properties can be characterized by an equivalent diameter. For example, light-scattering instruments are often calibrated using spherical

polystyrene latex (PSL) particles. Hence for the given optical configuration of the instrument, a particle that gives the same optical signal would be said to have a diameter equivalent to that of a PSL particle which produces the same signal.

PARTICLE CONCENTRATION

Aerosol concentrations are defined in different ways depending on the application. For example, particle number concentrations (particles per unit volume of gas) are used to characterize clean rooms and atmospheric cloud condensation nuclei; federal air pollution standards both for the atmosphere and for industrial emissions are usually stated in terms of aerosol mass per unit volume of gas. Effects of particles on viscosity depend on the ratio of the volume of particulate matter per unit volume of gas. For aerosols composed of particles all the same size, it is easy to relate the different methods of characterizing the concentration. For aerosols of mixed sizes, concentration measures are easily related only in certain cases as discussed below.

Number Concentration

Particle concentration at a point—expressed as the number of particles per unit volume of gas—is defined in a manner similar to gas density: Let δN be the number of particles in an initially rather large volume δV surrounding the point P in the gas (Fig. 1.2) at a given time. [Excluded from consideration are the molecular clusters that play an important role in the theory of homogeneous nucleation (Chapter 10).] Then the ratio $\delta N/\delta V$ is called the average (number) concentration of the particles within the volume δV . As the volume δV shrinks toward the point P , the average concentration can either increase or decrease depending on the concentration gradient in δV ; in general, however, it will approach a constant value over a range of values of δV in which the gradient is small but many particles are still present (Fig. 1.3). This constant value is the particle concentration at the point P . As the volume continues to shrink, the number of particles becomes so small that the average concentration fluctuates markedly as shown in Fig. 1.3.

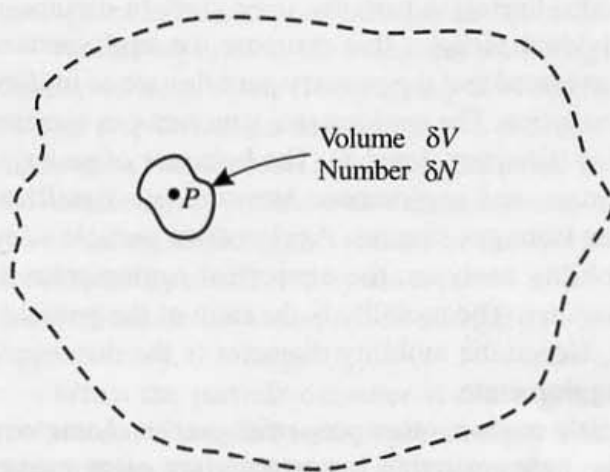


Figure 1.2 The volume δV containing δN particles shrinks toward point P .

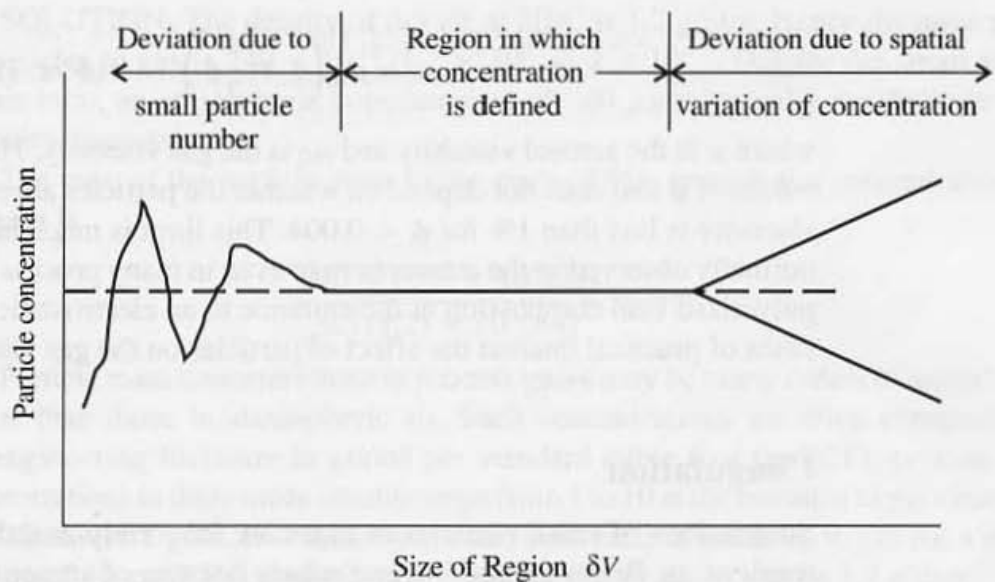


Figure 1.3 Variation of the average particle concentration with size of region. For large values of δV , the average concentration may be larger or smaller than the concentration defined locally, depending on the concentration gradient. For small values of δV , large positive or negative deviations from the average may occur because small numbers of particles are involved.

Clean rooms used in the manufacture of microelectronic devices are maintained at various levels of particle number concentration, depending on product requirements. For example, for a Class 1 clean room, number concentrations of $0.1\text{-}\mu\text{m}$ particles must be kept below 10^3 m^{-3} (Willeke and Baron, 1993, Chapter 34). Particle number concentrations (all sizes) in a polluted urban atmosphere may be of the order of 10^5 per cubic centimeter or higher, while concentrations in less polluted regions are more likely to be 10^4 to 5×10^4 per cubic centimeter.

Mass Concentrations

Aerosol mass concentrations are usually determined by filtering a known volume of gas and weighing the collected particulate matter. The mass concentration, ρ , averaged over the measuring time is found by dividing the measured mass by the volume of gas filtered. Atmospheric aerosol mass concentrations range from about $20\ \mu\text{g}/\text{m}^3$ for unpolluted air to $200\ \mu\text{g}/\text{m}^3$ for polluted air ($1\ \mu\text{g}/\text{m}^3 = 10^{-6}\ \text{g}/\text{m}^3$). Federal standards for atmospheric air and, in some cases, for industrial emissions are expressed in terms of mass concentrations. There is no simple relationship between the mass and number concentrations unless all particles are the same size.

Volumetric Concentration

The viscosity of a suspension of nonsettling spherical particles larger than the mean free path of a gas increases linearly with the *volumetric concentration*, ϕ , expressed as volume fraction of the particles according to a relation first given by Einstein:

$$\mu = \mu_0 \left(1 + \frac{5}{2} \phi \right) \quad (\phi \ll 1) \quad (1.3)$$

where μ is the aerosol viscosity and μ_0 is the gas viscosity. This expression holds for small values of ϕ and does not depend on whether the particles are mixed in size. The increase in viscosity is less than 1% for $\phi < 0.004$. This limit is much higher than the concentrations normally observed in the atmosphere or even in many process gases such as the products of pulverized coal combustion at the entrance to an electrostatic precipitator. Hence in many cases of practical interest the effect of particles on the gas viscosity can be neglected.

Coagulation

Suspensions of small particles in gases are inherently unstable; the particles collide as a result of the Brownian motion and adhere because of attractive forces, the process known as coagulation. The larger particles may settle out or deposit because of inertial effects. The time to reduce the particle concentration to one-tenth its original value by coagulation, $t_{1/10}$, can be calculated from theory (Chapter 7). For coalescing particles with $Kn \ll 1$, $t_{1/10}$ is independent of particle size and volumetric concentration to a first approximation. It is inversely proportional to the initial particle concentration (Table 1.1), and it depends also on gas viscosity and temperature. Table 1.1 can be used to make a rough estimate of the stability with respect to coagulation of an aerosol by comparing $t_{1/10}$ with the residence time. For example, a process gas concentration of 10^9 particles per cubic centimeter would change little during an equipment residence time of a second. For $t_{1/10} = 3.5$ hr, the corresponding concentration is 10^6 per cubic centimeter, the upper limit of the concentration usually observed in polluted urban atmospheres.

TABLE 1.1
Time to Reduce the Concentration of a Monodisperse
Aerosol to One-Tenth the Original Value,
 $N_0(d_p = 0.1 \mu\text{m}, T = 20^\circ\text{C})^a$

$N_0 \text{ cm}^{-3}$	$t_{1/10}$ (approximate)
10^{10}	1.2 sec
10^9	12 sec
10^8	2 min
10^7	20 min
10^6	3.5 hr
10^5	34 hr

^a See also Chapter 7.

Example: At a certain location, the mass concentration of particles in air (20°C and 1 atm) is $240 \mu\text{g}/\text{m}^3$. Determine the corresponding mass ratio of particles to gas. If the local SO_2 concentration is 0.1 ppm on a volume basis, determine the mass ratio of particles to SO_2 .

SOLUTION: The density of dry air at 20°C is 1.2 g/liter. Hence the mass ratio of particles to gas is $240 \times 10^{-6} / 1.2 \times 10^3 = 2 \times 10^{-7}$. Despite the small value of this ratio, an atmospheric concentration of 240 $\mu\text{g}/\text{m}^3$ usually results in severe visibility degradation.

The ratio of the particle mass to the mass of SO_2 present at a concentration of 0.1 ppm is

$$\frac{240 \times 10^{-6} \times 10^6(29)}{0.1(1.2) \times 10^3(64)} = 0.9$$

Particle mass concentrations in process gases may be many orders of magnitude higher than those in atmospheric air. Such concentrations are often expressed in the engineering literature in grains per standard cubic foot (gr/SCF); process gas concentrations in these units usually range from 1 to 10 at the entrance to gas cleaning units. Because $1 \text{ gr/SCF} = 2.288 \text{ g}/\text{m}^3$, the mass ratio of particles to gas for a mass loading of 10 gr/SCF is about 2×10^{-2} , taking the air density to be 1.2 g/liter.

The volumetric concentration, ϕ , of particles at a mass loading of 10 gr/SCF is about 10^{-5} for a particle density of $2.3 \text{ g}/\text{cm}^3$. For such small values of ϕ , the effects of the particles on the viscosity of the gas can be neglected according to (1.4).

Example: An aerosol is composed of particles randomly distributed in space with an average concentration N_∞ particles per unit volume. Let r be the center-to-center distance between two particles that are nearest neighbors. Values of r vary among the particle pairs, that is, there is a distribution of r values. Determine the frequency distribution function for r and calculate the average value of r (Chandrasekhar, 1943).

SOLUTION: Let $p(r)$ be the probability that the nearest neighbor to a particle is a distance r to $r + dr$ away. The separation distance r can take values between zero and infinity. That is, the fraction of the particles with nearest neighbors a distance r apart is

$$df = p(r) dr$$

and

$$\int_0^\infty df = 1 = \int_0^\infty p(r) dr$$

The probability $p(r)$ is equal to the product of the probability that no particles are present in the region interior to r and the probability that a particle is present in the spherical shell between r and $r + dr$. Writing each probability in brackets, we obtain

$$p(r) = \left[1 - \int_0^r p(r) dr \right] [4\pi r^2 N_\infty]$$

Dividing both sides by $4\pi r^2 N_\infty$ and differentiating with respect to r gives

$$\frac{dz}{dr} = -4\pi r^2 z$$

with

$$z = p/4\pi r^2$$

Integrating with the boundary condition that $p(r) \rightarrow 4\pi r^2 N_\infty$, that is, $z \rightarrow 1$ as $r \rightarrow 0$ —we obtain

$$p(r) = \exp(-4\pi r^3 N_\infty/3) 4\pi r^2 N_\infty$$

which satisfies $\int_0^\infty p(r) dr = 1$. The average distance between the particles is given by integrating over all possible values of the distance r separating the particles

$$\begin{aligned} \bar{r} &= \int_0^\infty r p(r) dr \\ &= \int_0^\infty 4\pi r^2 N_\infty \exp(-4\pi r^3 N_\infty/3) dr \\ &= \frac{1}{(4\pi N_\infty/3)^{1/3}} \int_0^\infty e^{-x} x^{1/3} dx \\ &= \Gamma(4/3)/(4\pi N_\infty/3)^{1/3} \\ &= 0.55396 N_\infty^{-1/3} \end{aligned}$$

Except for the constant, the dependence of \bar{r} on $N_\infty^{-1/3}$ could have been predicted on dimensional grounds without the analysis. For a particle concentration of 10^{12} cm^{-3} , the average separation distance is about $0.55 \mu\text{m}$. This result is of interest for evaluating particle interactions—for example, when heat and mass transfer occurs between individual particles and the gas.

SIZE DISTRIBUTION FUNCTION

By taking special precautions, it is possible to generate aerosols composed of particles that are all the same size. These are called *monodisperse* or *homogeneous* aerosols. In most practical cases both at emission sources and in the atmosphere, aerosols are composed of particles of many different sizes. These are called *polydisperse* or *heterodisperse* aerosols.

The most important physical characteristic of polydisperse systems is their particle size distribution. This distribution can take two forms: The first is the *discrete distribution* in which only certain “allowed” particle sizes are considered. Consider a suspension that consists of aggregates of unitary particles formed by coagulation. All particles will then be composed of integral numbers of these unitary particles, and the size distribution can be defined by the quantity n_g , where $g = 1, 2, \dots, k$ represents the number of unitary particles composing the aggregates.

Usually more useful, however, is the concept of the *continuous size distribution*. Let dN be the number of particles per unit volume of gas at a given position in space, represented by \mathbf{r} , and at a given time in the particle diameter range d_p to $d_p + d(d_p)$:

$$dN = n_d(d_p, \mathbf{r}, t)d(d_p) \quad (1.4)$$

This expression defines the particle size distribution function $n_d(d_p, \mathbf{r}, t)$ where the particle diameter may be some equivalent size parameter for nonspherical particles. In theoretical applications, especially coagulation (Chapter 7), it is convenient to introduce a size distribution with particle volume as the size parameter

$$dN = n(v, \mathbf{r}, t) dv \quad (1.5)$$

where dN is the concentration of particles in the size range v to $v + dv$. This distribution is useful because total particle volume is conserved when two particles collide and adhere as in coagulation processes.

Dimensional Considerations

The dimensions of the size distributions defined by (1.4) and (1.5) are given by

$$n_d \equiv L^{-3}l^{-1} \quad (1.6)$$

and

$$n \equiv L^{-3}l^{-3} \quad (1.7)$$

where the symbol \equiv is used to denote “has dimensions of.” The symbols L and l refer to a length dimension for the gas and for the particle size, respectively. Gas volume units are usually m^3 , cm^3 , or ft^3 , and units of particle diameter are microns or nanometers. Although distribution functions can have many different and complex forms (a few examples are discussed later in this chapter), the dimensions of the function are invariant. It should be noted that the length dimensions L and l are not interchangeable. In dimensional analyses of equations involving the size distribution function, both characteristic lengths should be treated independently. Dimensionality plays an important role in the derivation of scaling laws for the distribution function as discussed later in this chapter.

When there is a direct physical interaction between the particulate and gas phases, the two length dimensions become interchangeable. An example is the increase in viscosity of a fluid due to the presence of suspended particles. Equation (1.3) shows the dependence of the aerosol viscosity on the aerosol volumetric concentration, ϕ , which in this case is truly dimensionless (particle volume/gas volume).

Relationships Among Distribution Functions

The two distribution functions n and n_d are not equal but are related as follows: For a spherical particle, the volume and particle diameter are related by the expression

$$v = \frac{\pi d_p^3}{6} \quad (1.8)$$

Hence

$$dv = \frac{\pi d_p^2}{2} d(d_p) \quad (1.8a)$$

Substituting in (1.5), we obtain

$$dN = \frac{\pi d_p^2 n(v) d(d_p)}{2} \quad (1.9)$$

where we have dropped the dependence on position and time. Equating to (1.4) for the same increment of particle diameter, we have

$$n_d(d_p) = \frac{\pi d_p^2 n(v)}{2} \quad (1.10)$$

In a similar way, a particle size distribution function can be defined with surface area as the distributed variable.

In displaying size distribution data, it is often convenient to employ a log scale for d_p which may range over several orders of magnitude. For example, in the meteorological literature it is common to plot $\log n_d$ versus $\log d_p (= \log_{10} d_p)$. This highlights power law relationships between n_d and d_p which appear as straight lines. Another way of presenting the data is in the form $dV/d \log d_p$ versus $\log d_p$, where the cumulative aerosol volumetric concentration is given by $V = \int_0^v n v dv$. The area under curves plotted in this way is proportional to the mass of aerosol over a given size range provided that the particle density is a constant, independent of size. The following relationship holds for the aerosol volume distribution for spherical particles with $v = \pi d_p^3/6$:

$$\frac{dV}{d \log d_p} = \frac{2.3\pi^2 d_p^6 n(v)}{12} \quad (1.11)$$

The mass distribution is related to the volume distribution by

$$\frac{dm}{d \log d_p} = \rho_p \frac{dV}{d \log d_p} \quad (1.11a)$$

where ρ_p is the particle density.

Examples of size distribution functions are shown in Figs. 1.4 and 1.5. Figure 1.4 shows number distributions of commercially produced silica particles in terms of the fraction of particles in the size range around d_p , $dN/N_\infty d(d_p) = n_d(d_p)/N_\infty$, where N_∞ is the total particle concentration. The total particle surface area corresponding to each size distribution is shown. Commercial silica manufactured by the oxidation of SiCl_4 is used as a filler (additive) in rubber. Both coordinate axes in Fig. 1.4 are linear, and the area under each curve should be normalized to unity. A bimodal volume distribution with a minimum near a particle size of $1 \mu\text{m}$ is shown in Fig. 1.5. Distributions of this type are often observed for atmospheric aerosols (Chapter 13); the volume of aerosol material per unit volume of gas above and below a micron is about the same as shown by the area under the curve. Bimodal distributions are also often observed in aerosols from industrial sources as discussed below.

The cumulative number distribution is defined by the expression

$$N(d_p) = \int_0^{d_p} n_d(d_p) d(d_p) \quad (1.12)$$

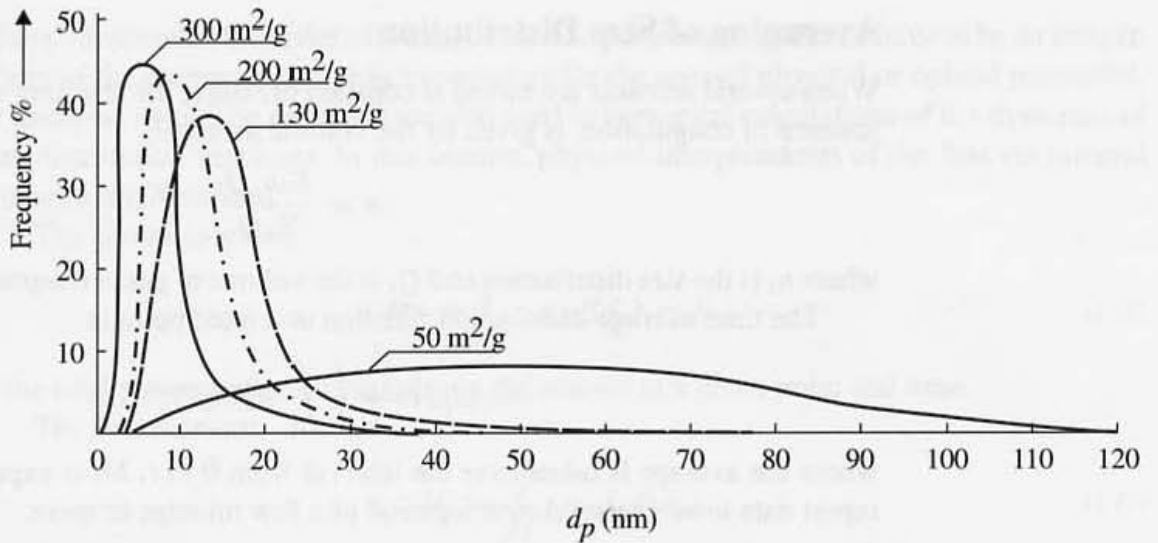


Figure 1.4 Unimodal number distributions for different grades of commercially produced silica particles. The fraction of the particles in the size range between any two diameters, d_{p1} to d_{p2} , is proportional to the area under the curve. Also shown for each distribution is the total particle surface area per gram of material. (After Ettlinger et al., 1991.)

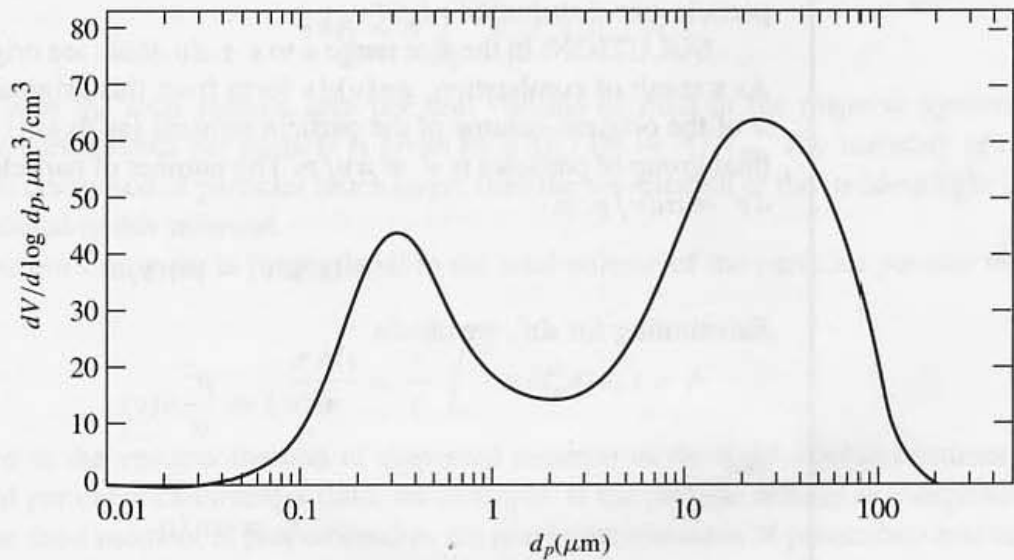


Figure 1.5 Bimodal volume distribution of a type frequently found for atmospheric and combustion aerosols. Such distributions usually result from two different generation processes: The smaller mode is a result of molecular condensation, while the larger one is a result of breakup or redispersion. Unimodal number distributions may conceal bimodal volume distributions.

and is the concentration of particles of diameter less than or equal to d_p . Because $n_d = dN(d_p)/d(d_p)$, the distribution function can be determined by differentiating the cumulative function with respect to d_p . However, the inaccuracies that often accompany differentiation of curves representing experimental data are large.

Averaging of Size Distributions

When several aerosols are mixed at constant pressure, the resulting size distribution, in the absence of coagulation, is given by the volume average:

$$n = \frac{\sum_i n_i Q_i}{\sum_i Q_i} \quad (1.13)$$

where n_i is the size distribution and Q_i is the volume of gas corresponding to the i th aerosol.

The time average distribution function at a fixed point is

$$\bar{n}_d(d_p, \mathbf{r}) = \frac{1}{t} \int_0^t n_d(d_p, \mathbf{r}, t') dt' \quad (1.14)$$

where the average is taken over the interval from 0 to t . Most experimental observations report data time-averaged over a period of a few minutes or more.

Example: During the combustion of pulverized coal, after burn-off of the carbonaceous material, most of the inorganic ash does not volatilize but is left behind as individual particles in the particle size range larger than a few microns (Flagan and Friedlander, 1978). Assume that coal particles in a given size range break up to form p times as many new particles of equal size, where p is independent of particle size. What is the relation of the new size distribution function $n'(v')$ to the original coal particle size distribution $n(v)$?

SOLUTION: In the size range v to $v + dv$, there are originally $n(v)dv$ particles. As a result of combustion, $pn(v)dv$ form from this original group. Only a fraction α of the original volume of the particle remains (as flyash). Thus the volume of the final group of particles is $v' = \alpha v/p$. The number of particles in the new size range, $dv' = \alpha dv/p$, is

$$n'(v')dv' = pn(v)dv$$

Substituting for dv' , we obtain

$$n'(v') = \frac{p^2}{\alpha} n(v)$$

and

$$v' = \alpha v/p$$

MOMENTS OF THE DISTRIBUTION FUNCTION

The general moment of the particle size distribution function can be defined by the expression

$$M_v(\mathbf{r}, t) = \int_0^\infty n_d d_p^v d(d_p) \quad (1.15)$$

where ν represents the order of the moment. The parameter ν does not have to be an integer. Many of the moments appear in expressions for the aerosol physical or optical properties, or transport rates. The moments are also used in numerical calculations of the dynamics of size distribution functions. In this section, physical interpretations of the first six integral moments are discussed.

The *zeroth* moment,

$$M_0 = \int_0^{\infty} n_d d(d_p) = N_{\infty} \quad (1.16)$$

is the total concentration of particles in the aerosol at a given point and time.

The *first* moment,

$$M_1 = \int_0^{\infty} n_d d_p d(d_p) \quad (1.17)$$

when divided by the zeroth moment, gives the number average particle diameter,

$$\bar{d}_p = \frac{\int_0^{\infty} n_d d_p d(d_p)}{\int_0^{\infty} n_d d(d_p)} = \frac{M_1}{M_0} \quad (1.17a)$$

The *second* moment is proportional to the surface area of the particles composing the aerosol:

$$\pi M_2 = \pi \int_0^{\infty} n_d d_p^2 d(d_p) = A \quad (1.18)$$

where A is the total surface area per unit volume of fluid in the disperse system. The average surface area per particle is given by $\pi M_2/M_0 = A/N_{\infty}$. The turbidity of coarse aerosols composed of particles much larger than the wavelength of the incident light is also proportional to this moment.

The *third* moment is proportional to the total volume of the particles per unit volume of gas:

$$\frac{\pi M_3}{6} = \frac{\pi}{6} \int_0^{\infty} n_d d_p^3 d(d_p) = \phi \quad (1.19)$$

where ϕ is the volume fraction of dispersed material in the fluid—cubic centimeters of material per cubic centimeters fluid, for example. If the particle density is independent of size, the third moment is proportional to the mass concentration of particulate matter. The average volume of a particle is defined by

$$\bar{v} = \frac{\phi}{N_{\infty}} = \frac{\pi M_3}{6M_0} \quad (1.20)$$

The *fourth* moment is proportional to the total projected area of the material sedimenting from a stationary fluid. For spherical particles larger than $1 \mu\text{m}$, the terminal settling velocity based on Stokes law and neglecting the buoyant force when the gas density is small is given by

$$c_s = \frac{\rho_p d_p^2 g}{18\mu} \quad (1.21)$$

where ρ_p is the particle density, g is the gravitational constant, and μ is the gas viscosity. Hence the rate at which a horizontal surface is covered by settling particulate matter is given by

$$\int_0^{\infty} \left(\frac{\pi d_p^2}{4} \right) \left(\frac{\rho_p d_p^2 g}{18\mu} \right) n_d(d_p) d(d_p) = \frac{\pi \rho_p g}{72\mu} M_4 \quad (1.22)$$

with cgs units of s^{-1} .

The *fifth* moment is proportional to the mass flux of material sedimenting from a fluid (g/cm^2 sec in cgs units):

$$\int_0^{\infty} n_d c_s \frac{\rho_p \pi d_p^3}{6} d(d_p) = \frac{\pi \rho_p^2 g}{108\mu} M_5 \quad (1.23)$$

The *sixth* moment is proportional to the total light scattering by particles when they are much smaller than the wavelength of the incident light. The scattering efficiency of a small single spherical particle—that is, the fraction of the light incident on the particle that is scattered—is given by

$$K_{\text{scat}} = \frac{8}{3} \left(\frac{\pi d_p}{\lambda} \right)^4 \left| \frac{m^2 - 1}{m^2 + 2} \right|^2 \quad (d_p \ll \lambda) \quad (1.24)$$

where m is the refractive index of the particle, and λ is the wavelength of incident light (Chapter 5). This is known as Rayleigh scattering. Then the total scattering by an aerosol composed of very small particles ($d_p \ll \lambda$) is given by

$$b_{\text{scat}} = \frac{2\pi^5}{3\lambda^4} \left(\frac{m^2 - 1}{m^2 + 2} \right)^2 I \int_0^{\infty} n_d d_p^6 d(d_p) \sim M_6 \quad (1.25)$$

where I is the intensity of the incident light beam. Rayleigh scattering usually does not contribute significantly to light scattering by small particles in the atmosphere. Most of the scattering by atmospheric particles occurs in the size range $d_p \sim \lambda$, for which much more complex scattering laws (Mie theory) must be used (Chapter 5).

Different parts of the particle size distribution function make controlling contributions to the various moments. In a polluted urban atmosphere, the number concentration or zeroth moment is often dominated by the 0.01- to 0.1- μm size range, and the surface area is often dominated by the 0.1- to 1.0- μm range; contributions to the volumetric concentration come from both the 0.1- to 1.0- and 1.0- to 10- μm size ranges (Chapter 13). Moments of fractional order appear in the theory of aerosol convective diffusion (Chapter 3).

EXAMPLES OF SIZE DISTRIBUTION FUNCTIONS

In this section we discuss briefly several size distribution functions that can be used to fit experimental data for aerosols or to estimate average particle size or the effects of aerosols on light scattering. The examples discussed are *normal*, *power-law*, and *self-similar* distributions. Selecting a distribution function depends on the specific application. In some cases, fragmentary information may be available on certain moments or on sections of the

size distribution. Such information can often be used to help select a suitable distribution for interpolation and extrapolation. In all cases, the dimensions of the distribution function must conform to the limitations imposed by the definitions (1.6) and (1.7).

Normal Distributions

The normal or Gaussian distribution is

$$n_d(d_p) = \frac{N_\infty}{(2\pi)^{1/2}\sigma} \exp\left[-(d_p - \bar{d}_p)^2/2\sigma^2\right] \quad (1.26)$$

where

$$\bar{d}_p = \text{arithmetic mean diameter} = \int_0^\infty d_p n_d(d_p) d(d_p)$$

$$\sigma^2 = \text{mean square of the deviation of } d_p \text{ from } \bar{d}_p = \overline{(d_p - \bar{d}_p)^2} = \int_0^\infty (d_p - \bar{d}_p)^2 n_d(d_p) d(d_p)$$

This form is employed in aerosol technology to characterize particles that are nearly monodisperse such as the polystyrene latex spheres used in laboratory studies and in instrument calibration. The value of \bar{d}_p can be calculated using the moment equation (1.15). In integrating, it is necessary to set a lower limit at $d_p \rightarrow 0$ and to assume that the distribution (1.27) can be truncated with negligible particle loss, over the range in which d_p is negative.

Aerosol size distributions often have large standard deviations caused by a long upper "tail" for particles larger than the peak in the distribution. Such distributions can be represented approximately by the lognormal distribution function:

$$n_d(d_p) = \frac{N_\infty}{(2\pi)^{1/2} d_p \ln \sigma_g} \exp\left[-\frac{(\ln d_p - \ln d_{pg})^2}{2 \ln^2 \sigma_g}\right] \quad (1.27)$$

where

$$\ln d_{pg} = \overline{\ln d_p} = \int_0^\infty \ln d_p n_d(d_p) d(d_p) \quad (1.27a)$$

$$\ln^2 \sigma_g = \overline{(\ln d_p - \ln d_{pg})^2} = \text{variance of logs of diameter} \quad (1.27b)$$

$$\sigma_g = \text{geometric standard deviation} \quad (1.27c)$$

The geometric mean diameter, d_{pg} , is defined by (1.27a). The lognormal distribution is thus a normal distribution in which the distributed function is $\log d_p/d_{pg}$, where d_{pg} is a reference size often taken to be d_{pg} . The median is the 50th percentile particle size and the geometric standard deviation σ_g is the ratio of the 50th percentile size (median) to the 16th percentile size, or the ratio of the 84th percentile size to the median. The lognormal distribution is probably the one most frequently utilized in the fitting of aerosol data. For lognormal distributions, the general moment of the size distribution function (1.15) is given by (Hinds, 1982)

$$\ln M_v = v \ln d_{pg} + \frac{v^2}{2} \ln^2 \sigma_g \quad (1.28)$$

The lognormal distribution function can be interpreted physically as the result of a process of breakup of larger particles at rates that are normally distributed with respect to particle size (Aitchison and Brown, 1957). Approximately lognormal distributions also result when the aerosol size distribution is controlled by coagulation (Chapter 7). In this case the value of the standard deviation is determined by the form of the particle collision frequency function. Multimodal aerosols may result when particles from several different types of sources are mixed. Such distributions are often approximated by adding lognormal distributions, each of which corresponds to a mode in the observed distribution and to a particular type of source.

Power Law Distributions

The power law form can be represented by the relation

$$n_d(d_p) = Ad_p^m \quad (1.29)$$

where A is a constant whose dimensions depend on the exponent m which is usually negative. This form is often employed over a limited size range that includes the particle sizes of interest in some particular application. Clearly there must be a lower cutoff in particle size for this function because $n_d(d_p) \rightarrow \infty$ for $d_p \rightarrow 0$ with m negative. The power law form is widely used in meteorological applications to approximate portions of the particle size distribution of the atmospheric aerosol. For $m \approx -4$, (1.29) is called the Junge distribution after the pioneering work of its originator (Junge, 1963).

In the microcontamination field, a power law is used to describe particle size distributions in clean rooms (Cooper, 1993). The cumulative distribution for the power law form is

$$F(d_p) = [A/(m + 1)]d_p^{m+1} \quad (1.30)$$

and in clean room applications, it has been found that $m + 1 \approx -2.2$, that is, $m \approx -3.2$.

Self-Similar Distribution Functions

Size distributions measured at different locations and/or times, either in the atmosphere or in processes gases, can sometimes be scaled by introducing a characteristic particle diameter based on moments of the distribution function. For example, suppose the distribution function depends only on two of its moments, say N_∞ and ϕ , in addition to the particle diameter:

$$n_d(d_p) = f[N_\infty, \phi, d_p] \quad (1.31)$$

The four quantities— n_d , N_∞ , ϕ , and d_p —that appear in (1.31) have two dimensions, L and l , corresponding to the coordinate space and particle size. Thus on dimensional grounds, there are two dimensionless groups that can be formed from these quantities. The groups can be expressed as follows:

$$n_d(d_p) = \frac{N_\infty^{4/3}}{\phi^{1/3}} \psi_d(\eta) \quad (1.32)$$

where

$$\eta = d_p / \bar{d}_p \quad (1.32a)$$

$$\bar{d}_p = [6\phi / \pi N_\infty]^{1/3} \quad (1.32b)$$

The dimensionless function $\psi_d(\eta)$ depends only on the ratio of the particle diameter to the average particle diameter. Hence distribution functions plotted in the form $n_d \phi^{1/3} / N_\infty^{4/3}$ versus η should fall on the same curve for different locations and/or time. Distributions that behave in this way are said to be *self-similar*. The form of $\psi_d(\eta)$ depends on the physicochemical processes that control the particle size distribution. These concepts are discussed in further detail in Chapter 7 for the case of coagulation.

CHEMICAL COMPOSITION

Aerosols are frequently multicomponent, that is, they are composed of many different chemical species. This is often the case for aerosols inadvertently generated in industrial processes such as coal combustion and incineration. The atmospheric aerosol (Chapter 13) is another example. Aerosols intentionally produced in industry are often multicomponent as well. An example is the fabrication of optical fibers in which SiO_2 aerosols produced by the burning of SiCl_4 are doped with optically active agents such as GeO_2 .

A single aerosol particle may be composed of many chemical compounds, and the entire aerosol may consist of mixed particles of differing composition. Two limiting cases are sometimes considered for multicomponent aerosols. If all particles have the same chemical composition, the aerosol is said to be *internally mixed*. If the chemical components are segregated so that the particles are chemically different depending on their sources, the aerosol is said to be *externally mixed*. The two limiting cases can be distinguished by measuring the chemical compositions of the individual particles. Whether the aerosol is internally or externally mixed has important implications for aerosol behavior, including the optical properties of clouds of particles, health effects, and basic physicochemical properties of powdered materials manufactured by aerosol processes.

Size-Composition Probability Density Function

More generally, an infinite number of intermediate cases are possible between the internal and external mixture models. To take into account variations in chemical composition from particle to particle, the particle size distribution function must be generalized, and for that purpose the *size-composition probability density function* has been introduced (Friedlander, 1970). Let dN be the number of particles per unit volume of gas containing molar quantities of each chemical species in the range between n_i and $n_i + dn_i$ with $i = 1, 2, \dots, k$ where k is the total number of chemical species. It is assumed that in each size range v to $v + dv$, the chemical composition of the particles is distributed continuously. Then the size-composition probability density function (p.d.f.), g , is defined by (Friedlander, 1970, 1971):

$$dN = N_\infty g(v, n_1 \dots n_k, \mathbf{r}, t) dv dn_1 \dots dn_k \quad (1.33)$$

This is an example of a *joint* or *simultaneous* distribution function (Cramer, 1955). It is not necessary to include n_1 as one of the independent variables because of the relationship between v and n_i :

$$v = \sum_i n_i \bar{v}_i \quad (1.34)$$

where \bar{v}_i is the partial molar volume of species i . This description is adequate so far as chemical composition is concerned. However, it does not account for structural effects, such as particle surface layers and the morphological characteristics of agglomerates.

Because the integral of dN over all v and n_i is equal to N_∞ , we obtain

$$\int_v \dots \int_{n_k} g(v, n_2 \dots n_k, \mathbf{r}, t) dv dn_2 \dots dn_k = 1 \quad (1.35)$$

Also, the size distribution function can be found from g by integrating over all of the chemical constituents of the aerosol:

$$n(v, \mathbf{r}, t) = N_\infty \int_{n_2} \dots \int_{n_k} g(v, n_2 \dots n_k, \mathbf{r}, t) dn_2 \dots dn_k \quad (1.36)$$

Average Chemical Composition

High-efficiency filtration is the most common method of collecting particulate matter for the determination of chemical composition. Chemical analysis of filter samples provides information on the composition of the aerosol averaged over all particle sizes and over the time interval of sampling. For a constant gas-sampling rate, the mass concentration of species i averaged over particle size and time is related to the size-composition probability density function as follows:

$$\bar{\rho}_i = \frac{M_i}{t} \int_0^t N_\infty \int_0^\infty \left[\int \dots \int g n_i dn_2 \dots dn_i \dots dn_k \right] dv dt' \quad (1.37)$$

where ρ_i is the instantaneous mass concentration of species i per unit volume of gas averaged over particle sizes, and M_i is the molecular weight of species i . The instantaneous concentration of species i in the particulate phase is given by the mass fraction

$$c_i = \rho_i / \rho \quad (1.38)$$

where ρ is the total mass of particulate matter per unit volume of gas. The time averaged value of c_i can in principle be obtained by averaging over the instantaneous values of c_i measured during the sampling period. However, instantaneous values of c_i cannot be obtained in the usual filtration measurements. Instead, the average mass fraction is usually reported as the ratio of the average values of ρ_i and ρ , $\bar{\rho}_i / \bar{\rho}$. As an example, over a certain time period the average concentration of particulate sulfur in the Los Angeles atmosphere was $15 \mu\text{g}/\text{m}^3$, reported as sulfate, and the average total mass of particulate matter was $125 \mu\text{g}/\text{m}^3$. Thus $\bar{c}_{\text{SO}_4} = 0.12$. Information on $\bar{\rho}_i$ and $\bar{\rho}$ is routinely reported for many chemical components of the atmospheric aerosol (EPA, 1996).

Distribution of Chemical Composition with Respect to Particle Size

There are instruments capable of measuring the composition of individual particles (Chapter 6), and eventually it will be possible to determine the size-composition p.d.f. Currently, such measurements are made on a research basis; in practice the average composition of the particles in a discrete size interval is determined by collecting an aerosol sample over a period of several hours using a cascade impactor (Chapter 6) and analyzing the material on each stage chemically. The concentration measured in this way is related to $g(v, n_2, \dots, n_k, \mathbf{r}, t)$ as follows:

$$\overline{\Delta\rho_i} = \frac{M_i}{t} \int_0^t N_\infty \int_{v_1}^{v_2} \left[\int \dots \int g n_i dn_2 \dots dn_i \dots dn_k \right] dv dt' \quad (1.39)$$

where $\overline{\Delta\rho_i}$ is the mass of species i per unit volume of air in the size range v_1 to v_2 . For $v_1 \rightarrow 0$ and $v_2 \rightarrow \infty$, $\overline{\Delta\rho_i}$ becomes the concentration that would be measured by a total filter. The discrete mass distribution can be plotted in the form $\overline{\Delta\rho_i}/\Delta \log d_p$ versus $\log d_p$. An example of distributions of this type is shown in Fig. 1.6 for aerosol emissions from a municipal wastewater sludge incinerator equipped with a cyclone-type scrubber. The area under the histogram between two values of d_p is proportional to the mass of the chemical species (or total mass) in that size range. Figure 1.6a shows the distribution of particle mass as a function of particle size at the inlet and outlet of the scrubber. The mass distribution at the scrubber inlet coming from the incinerator is bimodal. The smaller (in mass) fine mode near $0.2 \mu\text{m}$ probably results from the condensation of gaseous components volatilized during combustion. The coarser mode, greater than 5 to $50 \mu\text{m}$, is probably the residual ash from the sludge feed particles. The size distribution at the scrubber outlet peaks in the size range between 0.2 and $0.5 \mu\text{m}$, indicating that the coarse mode at the scrubber inlet is preferentially removed in the scrubber.

Figure 1.6b shows that the elements cadmium and calcium are distributed with respect to particle size in different ways in the incinerator emission gases at the scrubber inlet. The cadmium forms more volatile compounds in locally reducing atmospheres in the incinerator. These vapors then react to form condensable products, probably oxides and/or sulfates. The resulting particles are very small and grow by coagulation; the cadmium peaks at about $0.2 \mu\text{m}$ and the size distribution is unimodal. The calcium, on the other hand, was bimodal with a small submicron peak, also near $0.2 \mu\text{m}$, and a large coarse mode.

These results illustrate that emissions from combustion facilities tend to be enhanced in certain elements, some toxic, relative to the original composition of the feed. This has been documented both for emissions from incinerators and for coal combustion (Table 1.2). It probably holds for smelting and other high-temperature processes involving multicomponent feedstocks.

Average concentrations for a given size range may give a misleading impression of particulate effects, however. In the case of lung deposition, for example, the local dosage to tissue may depend on the composition of individual particles. The nucleating properties of a particle for the condensation of water and other vapors also depends on the chemical nature of the individual particles.

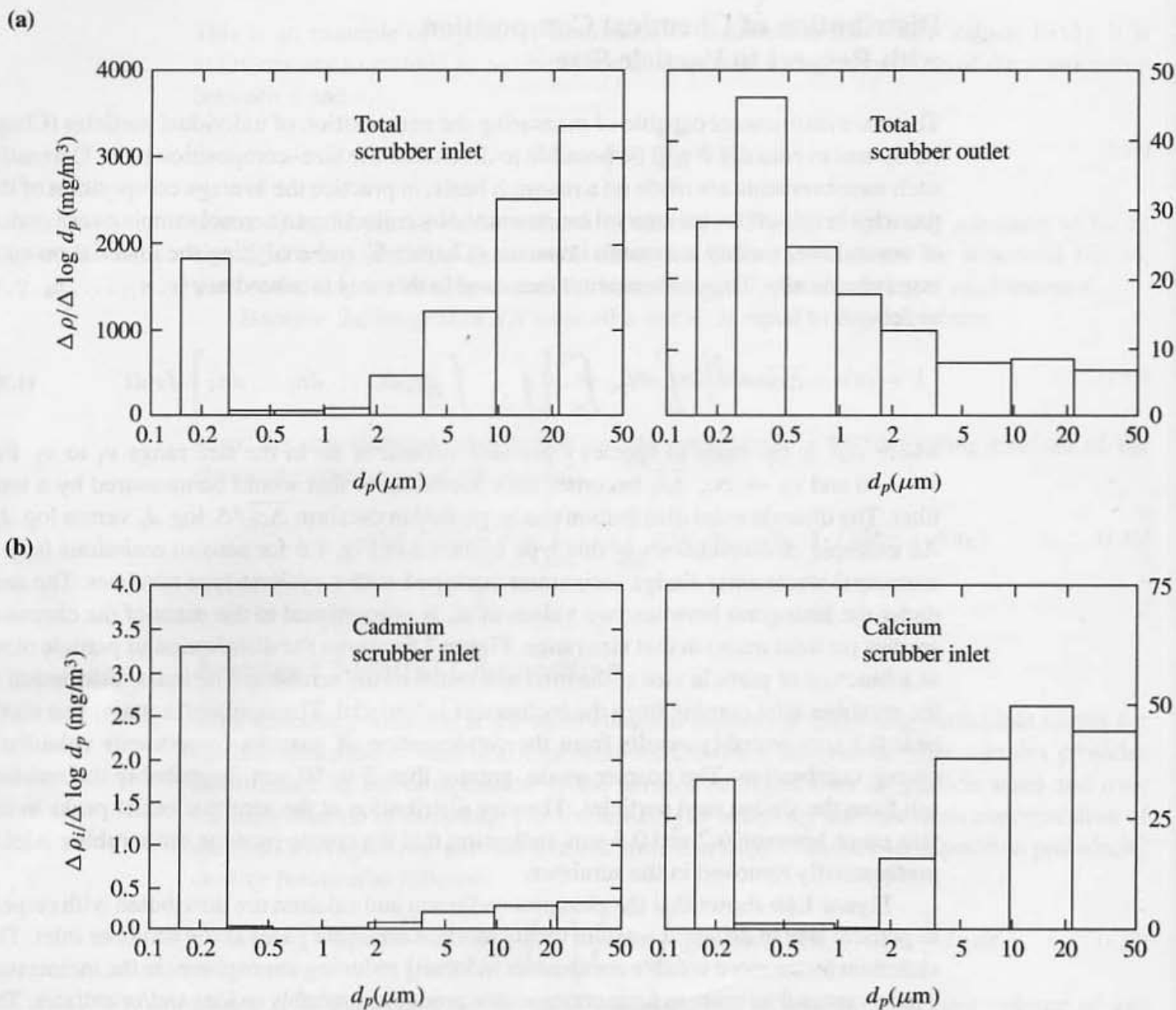


Figure 1.6 (a) Particulate mass as a function of particle size at the inlet and outlet of a scrubber treating emissions from a municipal wastewater sludge incinerator. Note the difference in the scales for the inlet and outlet. The fraction of the mass present as fine particles is much higher in the scrubber outlet gases. Because the data were collected with a cascade impactor, they are represented in a histogram format. (After Bennett and Knapp, 1982.) (b) Chemical species may be distributed with respect to particle size in different ways depending on the physicochemical processes during particle formation and the properties of the chemical components. The figure compares cadmium size distributions in waste incinerator emissions with calcium. Both elements were probably present as oxides and/or sulfates. The cadmium was concentrated in much smaller particles than the calcium. The calcium distribution was bimodal. (After Bennett and Knapp, 1982.)

TABLE 1.2
Elements in Airborne Coal Flyash Particles That Show Pronounced Concentration Trends with Respect to Particle Size (Davison et al., 1974)

Particle Diameter (μm)	Pb	Ti	Sb	Cd	Se	As	Ni	Cr	Zn	S
	$\mu\text{g/g}$									
	wt %									
>11.3	1100	29	17	13	13	680	460	740	8100	8.3
7.3–11.3	1200	40	27	15	11	800	400	290	9000	—
4.7–7.3	1500	62	34	18	16	1000	440	460	6600	7.0
3.3–4.7	1550	67	34	22	16	900	540	470	3800	—
2.1–3.3	1500	65	37	27	19	1200	900	1500	15,000	25.0
1.1–2.1	1600	76	53	35	59	1700	1600	3300	13,000	—
0.65–1.1	—	—	—	—	—	—	—	—	—	48.8

AEROSOL DYNAMICS: RELATION TO CHARACTERIZATION

Aerosol characterization as discussed in this chapter provides a snapshot of the aerosol at a given position and time. The snapshot gives information on particle size and chemical properties that determine many of the effects of aerosols, both desirable and undesirable. However, the size distribution and chemical properties usually change with time and position in industrial process gases or in the atmosphere.

Consider a small volume of gas and associated particles and follow its motion through the system—that is, the atmosphere or an industrial process. The physical and chemical processes shaping the size distribution are summarized in Fig. 1.7. The change in $n(v, \mathbf{r}, t)$ with time can be expressed as the sum of two terms:

$$\frac{dn}{dt} = \left[\frac{dn}{dt} \right]_i + \left[\frac{dn}{dt} \right]_e \quad (1.40)$$

The first term on the right represents processes occurring inside the element including gas-to-particle conversion and coagulation. The second term represents transport across

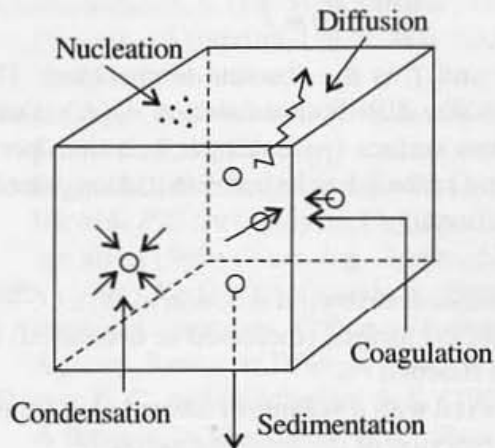


Figure 1.7 Processes shaping the particle size distribution function in a small volume element of gas. Diffusion and sedimentation involve transport across the walls of the element. Coagulation, nucleation, and growth take place within the element.

the boundaries of the element by processes such as diffusion and sedimentation. Transport processes are discussed in the first half of the text; the internal processes, coagulation and gas-to-particle conversion, are covered in the second half. A general dynamic equation for $n(v, \mathbf{r}, t)$ incorporating both internal and external processes is set up and discussed in Chapter 11. By the end of the book, the reader should be able to analyze a problem related to the dynamics of aerosol behavior and identify the principal processes that affect the size distribution function. In some cases, it may be possible to obtain simple solutions, often approximate. In others, numerical methods will be necessary.

PROBLEMS

1.1 Plot the number of molecules as a function of particle size for silica nanoparticles ($d_p < 50$ nm). On the same figure, plot the fraction of the molecules that appear in the surface of the particles. This will require certain assumptions that you should state.

1.2 Derive an expression for the rate at which the particles of a polydisperse aerosol settle on a horizontal plate from a stagnant gas. Dimensions are number per unit time per unit area. Assume that Stokes law holds for the terminal settling velocity, and express your answer in terms of the appropriate moments.

1.3 Let a be the surface area of a spherical particle of diameter d_p . Define an area distribution function n_a for the particles in an aerosol by the relationship

$$dN = n_a(a) da$$

where dN is the number of particles per unit volume of gas with surface area between a and $a + da$. Derive a relationship between $n_a(a)$ and $n_d(d_p)$ in terms of d_p .

1.4 Consider an aerosol composed of very small particles in the size range 10 to 100 nm such as might be produced during a welding process. The average velocity with which particles of mass m collide with a stationary surface exposed to the gas due to the thermal (Brownian) motion is (based on the kinetic theory of gases) given by

$$\bar{c} = \left(\frac{kT}{2\pi m} \right)^{1/2}$$

where k is Boltzmann's constant and T is the absolute temperature. The particles produced during the welding process have a size distribution function $n_d(d_p)$. Derive an expression for the total particle flux across a given surface (particles per unit time per unit area) due to the thermal motion. What is the moment of the particle size distribution, based on particle diameter, to which the particle flux is proportional?

1.5 An aerosol initially has a number distribution function $n_0(d_p)$.

- (a) The volume of the aerosol is changed (increased or decreased) by a factor α . What is the new size distribution function?
- (b) The original aerosol is mixed with a volume of filtered air q times the original volume. What is the distribution function of the resulting aerosol?

- (c) The original aerosol is composed of sea salt droplets that are 3.5% salt by weight. After mixing with equal volumes of dry, filtered air, all of the water evaporates. What is the new distribution function? (Neglect the gas volume of the water evaporated.)
- (d) The original aerosol loses particles from each size range at a rate proportional to the particle surface area. Derive an expression for the distribution function as a function of time and particle diameter. In all cases, express your answer in terms of the initial distribution and any other variables that may be necessary. Define all such variables.

1.6 The size distribution of atmospheric aerosols will sometimes follow a power law of the form

$$n_d(d_p) = \text{const} \frac{\phi}{d_p^4}$$

where ϕ is the volume fraction of dispersed material (volume aerosol per unit volume air). When applicable, this form usually holds for particles ranging in size from about 0.1 to 5 μm . Show that when aerosols that follow this law are mixed, the resulting size distribution obeys a law of the same form. Before mixing, the aerosols have different volume fractions.

1.7 A certain chemical species is adsorbed by the particles of an aerosol. The mass adsorbed is proportional to the surface area of the particle. Derive an expression for the distribution of the species with respect to particle size expressed as mass of the species per unit volume of gas in the size range v to $v + dv$. Express your answer in terms of v and $n(v)$. Define any constants you introduce.

1.8 Verify that the normal and lognormal distribution functions defined in the text in equations (1.26) and (1.27) are dimensionally correct.

1.9 Referring to Fig. 1.6a, plot the collection efficiency of the scrubber as a function of particle diameter. The collection efficiency is the fraction of the mass in a given size range entering the scrubber that is removed in the scrubber.

REFERENCES

- Bennett, R. T., and Knapp, K. T. (1982) *Environ. Sci. Technol.*, **16**, 831.
- Chandrasekhar, S. (1943) Stochastic Problems in Physics and Astronomy in *Reviews of Modern Physics*, **15** (reprinted in N. Wax (Ed.) (1954) *Noise and Stochastic Processes*, Dover, New York).
- Davison, R. L., Natusch, D. F. S., Wallace, J. R., and Evans, C. A., Jr. (1974) *Environ. Sci. Technol.*, **8**, 1107.
- Ettlinger, M., Ferch, H., and Koth, D. (1991) AEROSIL®, Aluminum Oxide C and Titanium Dioxide P25 for Catalysts, Degussa Technical Bulletin Pigments, No. 72, Frankfurt, Germany; see also (1980) *Chem. Ing. Techn.*, **52**, 628.
- EPA (1996) Air Quality Criteria for Particulate Matter, Volume 1, National Center for Environmental Assessment, Office of Research and Development, U.S. Environmental Protection Agency, Research Triangle Park, NC.
- Flagan, R. C., and Friedlander, S. K. (1978) Particle Formation in Pulverized Coal Combustion—A Review, in Shaw, D. T. (Ed.), *Recent Developments in Aerosol Science*, Wiley, New York.

- See also Flagan, R. C., and Seinfeld, J. H. (1988) *Fundamentals of Air Pollution Engineering*, Prentice-Hall, Englewood Cliffs, NJ.
- Forrest, S. R., and Witten, T. A., Jr. (1979) *J. Phys. A: Math., Gen.*, **12**, L109.
- Friedlander, S. K. (1970) *J. Aerosol Sci.*, **1**, 295.
- Friedlander, S. K. (1971) *J. Aerosol Sci.*, **2**, 331.
- Wu, M. K., and Friedlander, S. K. (1993) *J. Colloid and Interface Sci.*, **159**, 246.

Basic Aerosol References

- Davies, C. N. (Ed.) (1966) *Aerosol Science*, Academic Press, New York.
- Fuchs, N. A. (1964) *The Mechanics of Aerosols*, Pergamon, Oxford, republished by Dover, New York (1989). A classic, the first text to treat aerosol phenomena as a scientific discipline.
- Hidy, G. M., and Brock, J. R. (1971) *The Dynamics of Aerocolloidal Systems*, Pergamon, Oxford, UK. Extensive applications of kinetic theory of gases to aerosols.
- Hinds, W. C. (1982) *Aerosol Technology*, Wiley, New York. A comprehensive overview of aerosol behavior including applications to industrial hygiene and inhalation toxicology.
- Junge, C. (1963) *Air Chemistry and Radioactivity*, Academic Press, New York. This classic text established air chemistry as a scientific discipline. It reviews what was known up to the time on the behavior of aerosols and trace gases in the atmosphere.
- Seinfeld, J. H., and Pandis, S. N. (1998) *Atmospheric Chemistry and Physics*, Wiley, New York. Includes a discussion of basic aerosol phenomena with atmospheric applications.
- Williams, M. M. R., and Loyalka, S. K. (1991) *Aerosol Science Theory and Practice with Special Applications to the Nuclear Industry*, Pergamon, Oxford, UK. Emphasis on theory including many detailed derivations.
- Willeke, K., and Baron, P. A. (1993) *Aerosol Measurement*, Van Nostrand Reinhold, New York. A very good overview of aerosol sampling and instrumentation with basic underlying principles.

Mathematics of Distribution Functions

- Aitchison, J., and Brown, J. A. C. (1957) *The Lognormal Distribution Function*, Cambridge University Press, Cambridge, UK.
- Cooper, D. W. (1993) Methods of Size Distribution Data Analysis and Presentation, in Willeke, K., and Baron, P. A. (Eds.), *Aerosol Measurement*, Van Nostrand Reinhold, New York.
- Cramer, H. (1955) *The Elements of Probability Theory*, Wiley, New York. A good introductory discussion of the mathematical properties of distribution functions.

Particle Transport Properties

An understanding of particle transport or movement from one point to another in a gas is basic to the design of gas cleaning equipment and aerosol sampling instruments. The scavenging of particulate matter from the atmosphere by dry and wet deposition processes is also determined by particle transport processes.

The classical problems of particle transport were studied by well-known physicists in the late nineteenth and early twentieth centuries. Stokes, Einstein, and Millikan investigated the motion of small spherical particles under applied forces primarily because of application to (at that time) unsolved problems in physics. They derived relatively simple relationships for spherical particles that can be considered as ideal cases; irregular particles are usually discussed in terms of their deviations from spherical behavior.

In this chapter, we consider Brownian diffusion, sedimentation, migration in an electric field, and thermophoresis. The last term refers to particle movement produced by a temperature gradient in the gas. We consider also the London–van der Waals forces that are important when a particle approaches a surface. The analysis is limited to particle transport in stationary—that is, nonflowing—gases. Transport in flow systems is discussed in the chapters which follow.

The rate of transport of particles across a surface at a point, expressed as number per unit time per unit area, is called the *flux* at the point. Common dimensions for the flux are particles/cm² sec. Expressions for the diffusion flux and diffusion coefficient that apply to submicron particles are derived from first principles in this chapter. The presence of an external force field acting on the particles leads to an additional term in the flux. The transport of particles larger than about a micron is analyzed by solving a momentum balance that incorporates the external force fields.

Aerosol transport processes, including heat, mass, momentum, and charge transfer, take place at two different (but interacting) scales. At the individual particle scale, exchange of mass, heat, momentum, and charge may take place between the particles and the surrounding gas. On a larger scale, clouds of particles move under the influence of concentration, temperature and electric field gradients at rates which depend on the particle size and properties. As explained in this chapter, there may be strong coupling between the two scales because the particle flux is proportional to the product of the large-scale gradient and a coefficient that depends on particle scale transport processes.

As noted by Fuchs and Sutugin (1971), the analysis of particle scale transport is relatively simple in the limiting cases corresponding to very large and very small Knudsen numbers. For small Knudsen numbers (large particles), the transfer processes are described by the equations of diffusion, heat transfer, and fluid mechanics of continuous media. At large Knudsen numbers (small particles) the transfer processes take place in the free molecule regime in which the presence of the particles does not affect the velocity distribution of the molecules moving toward the surface. For molecules moving in the reverse direction from the surface, the distribution function depends on the laws of reflection or evaporation of molecules from the surface of the particle. Intermediate Knudsen number ranges are usually treated by semiempirical interpolation formulas.

EQUATION OF DIFFUSION

Small particles suspended in a fluid exhibit a haphazard dancing motion resulting from the fluctuating forces exerted on them by the surrounding molecules. The motion was reported in 1827 by the botanist Robert Brown, who made the first detailed studies. Brown first observed the phenomenon in aqueous suspensions of pollen and then with particles of mineral origin, showing that the motion was a general property of matter independent of its origin—organic or not. As a result of their random motion, there is a net migration of particles from regions of high to low concentration, a process known as diffusion. An equation that describes the rate of diffusion can be derived in the following way:

A fluid, which is not flowing, contains small particles in Brownian motion. Gradients exist in the concentration of particles, all of which are of the same size. Concentrations are small, however, so that any small flows that accompany diffusion can be neglected. A balance can be carried out on the number of particles in an elemental volume of fluid $\delta x \delta y \delta z$, fixed in space (Fig. 2.1), as follows: The rate at which particles enter the elemental volume across the face $ABCD$ is

$$\left[J_x - \frac{\partial J_x}{\partial x} \frac{\delta x}{2} \right] \delta y \delta z$$

where J_x the flux of particles across the face with c.g.s. units of particles/cm² sec and $\partial J_x / \partial x$ is the gradient of J_x in the x direction at the centroid of the elemental volume. The rate at which particles leave the elemental volume across the opposite face $A'B'C'D'$ is

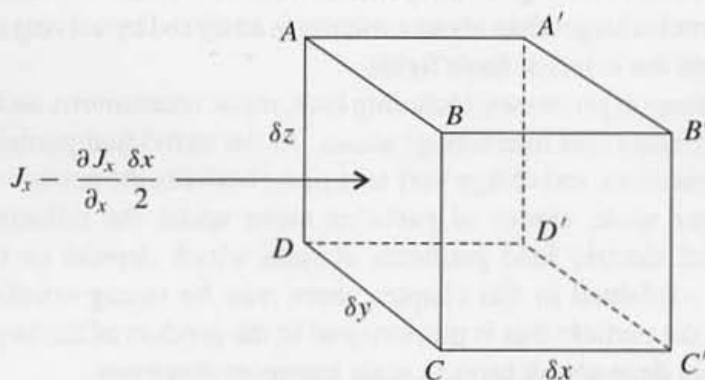


Figure 2.1 An elemental volume of fluid, fixed in space, through which diffusion is occurring in all directions. At the centroid of the element, the particle flux in the x direction is given by J_x . The flux across one face, $ABCD$, is shown.

$$\left[J_x - \frac{\partial J_x}{\partial x} \frac{\delta x}{2} \right] \delta y \delta z$$

The net rate of transport into the element for these two faces is obtained by summing the two previous expressions to give

$$- \delta x \delta y \delta z \frac{\partial J_x}{\partial x}$$

For the $\delta x \delta z$ faces, the corresponding term is

$$- \delta x \delta y \delta z \frac{\partial J_y}{\partial y}$$

and for the $\delta x \delta y$ faces

$$- \delta x \delta y \delta z \frac{\partial J_z}{\partial z}$$

The rate of change of the number of particles in the elemental volume $\delta x \delta y \delta z$ is given by

$$\frac{\partial n}{\partial t} \delta x \delta y \delta z = - \left[\frac{\partial J_x}{\partial x} + \frac{\partial J_y}{\partial y} + \frac{\partial J_z}{\partial z} \right] \delta x \delta y \delta z$$

Dividing both sides by $\delta x \delta y \delta z$, the result is

$$\frac{\partial n}{\partial t} = - \left[\frac{\partial J_x}{\partial x} + \frac{\partial J_y}{\partial y} + \frac{\partial J_z}{\partial z} \right] = - \nabla \cdot \mathbf{J} \quad (2.1)$$

which is the equation of conservation of species in terms of the flux vector, \mathbf{J} , with components J_x, J_y, J_z .

The relationship between the flux and the concentration gradient depends on an experimental observation: A one-dimensional gradient in the particle concentration is set up in a fluid by fixing the concentration at two parallel planes. The fluid is isothermal and stationary. It is observed that the rate at which particles are transported from the high to the low concentration (particles/cm² sec) is proportional to the local concentration gradient, $\partial n / \partial x$:

$$J_x = -D \frac{\partial n}{\partial x} \quad (2.2a)$$

where D , the diffusion coefficient, is a proportionality factor. In general, the diffusion coefficient is a variable depending on the particle size, temperature, and concentration; its concentration dependence can often be neglected.

If the properties of the fluid are the same in all directions, it is said to be isotropic. This is the usual case, and D then has the same value for diffusion in any direction.

$$J_y = -D \frac{\partial n}{\partial y} \quad (2.2b)$$

$$J_z = -D \frac{\partial n}{\partial z} \quad (2.2c)$$

When we substitute in (2.1), the result for constant D is

$$\frac{\partial n}{\partial t} = D \left[\frac{\partial^2 n}{\partial x^2} + \frac{\partial^2 n}{\partial y^2} + \frac{\partial^2 n}{\partial z^2} \right] = D \nabla^2 n \quad (2.3)$$

which is known as Fick's second law of diffusion, the first law being the linear relationship between flux and gradient.

As shown in later sections, the coefficient of diffusion is a function of particle size, with small particles diffusing more rapidly than larger ones. For a polydisperse aerosol, the concentration variable can be set equal to $n_d(d_p, \mathbf{r}, t)d(d_p)$ or $n(v, \mathbf{r}, t) dv$, and both sides of (2.3) can be divided by $d(d_p)$ or dv . Hence the equation of diffusion describes the changes in the particle *size distribution* with time and position as a result of diffusive processes. Solutions to the diffusion equation for many different boundary conditions in the absence of flow have been collected by Carslaw and Jaeger (1959) and Crank (1975).

COEFFICIENT OF DIFFUSION

The coefficient of diffusion, D , with dimensions of square centimeters per second is one of the important transport properties of the particles in an aerosol. An expression for D can be derived as a function of the size of the particle and the properties of the gas.

We consider diffusion in one dimension alone. Suppose that a cloud of fine particles, all the same size, is released over a narrow region around the plane corresponding to $x = 0$. The concentration everywhere else in the gas is zero. With increasing time, the particles diffuse as a result of the Brownian motion. The spread around the plane $x = 0$ is symmetrical (Fig. 2.2) in the absence of an external force field acting on the particles.

The spread of the particles with time can be determined by solving the one-dimensional equation of diffusion,

$$\frac{\partial n}{\partial t} = D \frac{\partial^2 n}{\partial x^2} \quad (2.4)$$

The solution for the concentration distribution is given by the Gaussian form

$$n(x, t) = \frac{N_0}{2(\pi Dt)^{1/2}} \exp\left(\frac{-x^2}{4Dt}\right) \quad (2.5)$$

where N_0 is the number of particles released at $x = 0$ per unit cross-sectional area. The mean square displacement of the particles from $x = 0$ at time t is

$$\overline{x^2} = \frac{1}{N_0} \int_{-\infty}^{\infty} x^2 n(x, t) dx \quad (2.6)$$

When we substitute (2.5) in (2.6), the result is

$$\overline{x^2} = 2Dt \quad (2.7)$$

Thus the mean square displacement of the diffusing particles is proportional to the elapsed time.

An expression for $\overline{x^2}$ can also be derived from a force balance on a particle in Brownian motion, which for one dimension takes the form

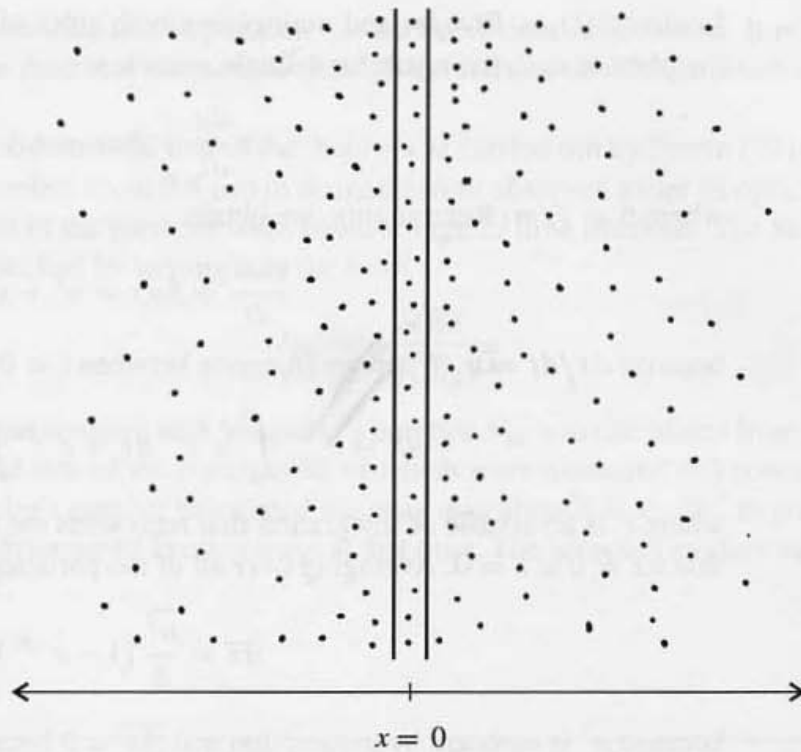


Figure 2.2 The spread of Brownian particles originally concentrated at the differential element around $x = 0$.

$$m \frac{du}{dt} = -fu + F(t) \quad (2.8)$$

where m is the particle mass, u is its velocity, and t is the time. According to (2.8), the force acting on the particle is divided into two parts. The first term on the right is the frictional resistance of the fluid and is assumed to be proportional to the particle velocity. For spherical particles much larger than the gas mean free path, the friction coefficient f based on Stokes law is

$$f = 3\pi\mu d_p \quad (2.9)$$

Other forms for the friction coefficient are discussed in the next section. The term $F(t)$ represents a fluctuating force resulting from the thermal motion of molecules of the ambient fluid. $F(t)$ is assumed to be independent of u and its mean value, $\overline{F}(t)$, over a large number of similar but independent particles vanishes at any given time. Finally, it is assumed that $F(t)$ fluctuates much more rapidly with time than u . Thus over some interval, Δt , u will be practically unchanged while there will be practically no correlation between the values of $F(t)$ at the beginning and end of the interval. These are rather drastic assumptions, but they have been justified by resort to models based on molecular theory (see the review by Green, 1952, p. 151 ff.). The conceptual difficulties attendant upon the use of (2.8) are discussed by Chandrasekhar (1943).

We now consider the group of small particles originally located near the plane $x = 0$ at $t = 0$ (Fig. 2.2). At a later time, these particles have wandered off as a result of the Brownian motion to form a cloud, symmetrical around $x = 0$, as shown in the figure.

Letting $A(t) = F(t)/m$ and multiplying both sides of (2.8) by x , the displacement from the plane $x = 0$, the result for a single particle is

$$x \frac{du}{dt} + \beta ux = xA \quad (2.10)$$

where $\beta = f/m$. Rearranging, we obtain

$$\frac{d ux}{dt} + \beta ux = u^2 + xA \quad (2.10a)$$

because $dx/dt = u$. When we integrate between $t = 0$ and t , the result is

$$ux = e^{-\beta t} \int_0^t u^2 e^{\beta t'} dt' + e^{-\beta t} \int_0^t Ax e^{\beta t'} dt' \quad (2.11)$$

where t' is a variable of integration that represents the time. We have made use of the fact that $ux = 0$ at $t = 0$. Averaging over all of the particles in the field, one finds

$$\overline{ux} = \frac{\overline{u^2}}{\beta} (1 - e^{-\beta t}) \quad (2.12)$$

because $\overline{u^2}$ is constant by assumption and $\overline{Ax} = 0$ because there is no correlation between the instantaneous force and the particle displacement. The following relationships also hold:

$$\overline{ux} = \frac{\overline{x dx}}{dt} = \frac{\overline{dx^2}}{2dt} = \frac{1}{2} \frac{d[\overline{x^2}]}{dt} \quad (2.13)$$

because the derivative of the mean taken over particles with respect to time is equal to the mean of the derivative with respect to time. Equating (2.12) and (2.13) and integrating once more from $t = 0$ to t gives

$$\frac{\overline{x^2}}{2} = \frac{\overline{u^2} t}{\beta} + \frac{\overline{u^2}}{\beta^2} (e^{-\beta t} - 1) \quad (2.14)$$

For $t \gg \beta^{-1}$, this becomes

$$\frac{\overline{x^2}}{2} = \frac{\overline{u^2} t}{\beta} \quad (2.15)$$

We now introduce an important physical assumption, first made by Einstein (1905), that relates the observable Brownian movement of the small particles to the molecular motion of the gas molecules: Because the particles share the molecular-thermal motion of the fluid, the principle of equipartition of energy is assumed to apply to the translational energy of the particles:

$$\frac{m \overline{u^2}}{2} = \frac{kT}{2} \quad (2.16)$$

When we combine the equipartition principle with (2.7) and (2.15), the result is

$$D = \frac{\overline{x^2}}{2t} = \frac{kT}{f} \quad (2.17)$$

This is the Stokes–Einstein expression for the coefficient of diffusion. It relates D to the properties of the fluid and the particle through the friction coefficient discussed in the next section.

A careful experimental test of the theory was carried out by Perrin (1910). Emulsions composed of droplets about $0.4 \mu\text{m}$ in diameter were observed under an optical microscope and the positions of the particles were noted at regular time intervals. The Stokes–Einstein equation was checked by writing it in the form

$$N_{\text{av}} = \frac{2tRT}{3\pi\mu d_p x^2} \quad (2.18)$$

where R is the gas constant and Avogadro's number N_{av} was calculated from the quantities on the right-hand side of the equation all of which were measured or known. The average value of Avogadro's number calculated this way was about 7.0×10^{23} in good agreement with the values determined in other ways at that time. The accepted modern value, however, is 6.023×10^{23} .

FRICITION COEFFICIENT

The friction coefficient is a quantity fundamental to most particle transport processes. The Stokes law form, $f = 3\pi\mu d_p$, holds for a rigid sphere that moves through a fluid at constant velocity with a Reynolds number, $d_p U/\nu$, much less than unity. Here U is the velocity, and ν is the kinematic viscosity. The particle must be many diameters away from any surfaces and much larger than the mean free path of the gas molecules, ℓ_p , which is about $0.065 \mu\text{m}$ at 25°C .

As particle size is decreased to the point where $d_p \sim \ell_p$, the drag for a given velocity becomes less than predicted from Stokes law and continues to decrease with particle size. In the range $d_p \ll \ell_p$, the free molecule range (Chapter 1), an expression for the friction coefficient can be derived from kinetic theory (Epstein, 1924):

$$f = \frac{2}{3} d_p^2 \rho \left(\frac{2\pi kT}{m} \right)^{1/2} \left[1 + \frac{\pi\alpha}{8} \right] \quad (2.19)$$

where ρ is the gas density and m is the molecular mass of the gas molecules.

The accommodation coefficient α represents the fraction of the gas molecules that leave the surface in equilibrium with the surface. The fraction $1 - \alpha$ is specularly reflected such that the velocity normal to the surface is reversed. As in the case of Stokes law, the drag is proportional to the velocity of the spheres. However, for the free molecule range, the friction coefficient is proportional to d_p^2 , whereas in the continuum regime ($d_p \gg \ell_p$), it is proportional to d_p . The coefficient α must, in general, be evaluated experimentally but is usually near 0.9 for momentum transfer (values differ for heat and mass transfer). The friction coefficient calculated from (2.19) is only 1% of that from Stokes law for a 20-\AA particle.

An interpolation formula is often used to cover the entire range of values of the Knudsen number ($2\ell_p/d_p$) from the continuum to the free molecule regimes. It is introduced as a correction to the Stokes friction coefficient:

$$f = \frac{3\pi\mu d_p}{C} \quad (2.20)$$

where the slip correction factor C is given by

$$C = 1 + \frac{2\ell_p}{d_p} \left(A_1 + A_2 \exp\left(\frac{-A_3 d_p}{\ell_p}\right) \right) \quad (2.21)$$

and A_1 , A_2 , and A_3 are constants. The correction factor C is essentially an interpolation formula that shows the proper limiting forms. For $d_p \gg \ell_p$, $C \rightarrow 1$ and f approaches (2.11), whereas for $d_p \ll \ell_p$, f approaches the form of the kinetic theory expression (2.19).

Values of the constants A_1 , A_2 , and A_3 are based on experimental measurements of the drag on small particles. Such measurements were made by Millikan and his co-workers in their oil droplet experiments carried out to determine the electronic charge. A later compilation of experimental data (Davies, 1945) led to the following result: $A_1 = 1.257$, $A_2 = 0.400$, $A_3 = 0.55$. This corresponds to a value of α in (2.19) of 0.84. Values for the diffusion coefficient and settling velocity of spherical particles can be calculated over the entire particle size range using (2.17), (2.20), and (2.21). They are shown in Table 2.1 together with values of the slip correction and Schmidt number discussed in Chapter 3.

As noted above, Stokes' law is derived for the steady-state resistance to the motion of a particle. Why should it apply to the Brownian motion in which the particle is continually accelerated? The explanation is that the acceleration is always very small so that at each

TABLE 2.1
Aerosol Transport Properties:
Spherical Particles in Air at 20°C, 1 atm

d_p (μm)	C	D (cm^2/sec)	Schmidt Number, ν/D	c_s (cm/sec) ($\rho_p = 1\text{g}/\text{cm}^3$)
0.001	216.	5.14×10^{-2}	2.92	
0.002	108.	1.29×10^{-2}	1.16×10^1	
0.005	43.6	2.07×10^{-3}	7.25×10^1	
0.01	22.2	5.24×10^{-4}	2.87×10^2	
0.02	11.4	1.34×10^{-4}	1.12×10^3	
0.05	4.95	2.35×10^{-5}	6.39×10^3	
0.1	2.85	6.75×10^{-6}	2.22×10^4	8.62×10^{-5}
0.2	1.865	2.22×10^{-6}	6.76×10^4	2.26×10^{-4}
0.5	1.326	6.32×10^{-7}	2.32×10^5	1.00×10^{-3}
1.0	1.164	2.77×10^{-7}	5.42×10^5	3.52×10^{-3}
2.0	1.082			1.31×10^{-2}
5.0	1.032			7.80×10^{-2}
10.0	1.016			3.07×10^{-1}
20.0	1.008			1.22
50.0	1.003			7.58
100.0	1.0016			30.3

instant, a quasi-steady state can be assumed to exist.

For nonspherical particles, the drag depends on the orientation of the particle as it moves through the gas. When $d_p \gg \ell_p$, the drag can be calculated by solving the Stokes or “creeping flow” form of the Navier–Stokes equations for bodies of various shapes. In calculating the diffusion coefficient, it is necessary to average over all possible orientations because of the stochastic nature of the Brownian motion. This calculation has been carried out by Perrin (1936) for ellipsoids of revolution. These are bodies generated by rotating an ellipse around one of its axes. We consider an ellipse with semiaxes a and b rotated around the a axis.

For $z = b/a < 1$ (prolate or “cigar-shaped” ellipsoid), the diffusion coefficient is

$$\frac{D}{D_0} = \frac{z^{2/3}}{(1-z^2)^{1/2}} \ln \frac{1+(1-z^2)^{1/2}}{z} \quad (2.22a)$$

and for $z > 1$ (oblate ellipsoid) we obtain

$$\frac{D}{D_0} = \frac{z^{2/3}}{(z^2-1)^{1/2}} \tan^{-1}(z^2-1)^{1/2} \quad (2.22b)$$

where D_0 is the diffusion coefficient of a sphere of the same volume as the ellipsoid. If a_0 is the radius of the sphere, then $a_0 = az^{2/3}$.

The diffusion coefficient of the ellipsoid is always less than that of a sphere of equal volume. However, over the range $10 > z > 0.1$, the coefficient for the ellipsoid is always greater than 60% of the value for the sphere. These results are not directly applicable to the diffusion of particles suspended in a shear field, because all orientations of the particle are no longer equally likely.

AGGLOMERATE DIFFUSION COEFFICIENTS

Consider an aerosol composed of agglomerates of primary particles of radius a_{po} . Any given agglomerate incorporates N_p primary particles and values of N_p vary from agglomerate to agglomerate. The group of agglomerates which have the same number of primary particles N_p constitutes a subset of the total aerosol. This subset may have agglomerates of many different structures. The structure refers to how the primary particles are arranged with respect to each other. It has been found experimentally (Chapter 8) that by averaging over many agglomerates, a power law relationship can often be used to correlate the data:

$$N_p = A \left(\frac{R}{a_{po}} \right)^{D_f} \quad (2.23)$$

where R is the agglomerate radius, a_{po} is the primary particle radius, A is a dimensionless constant of order unity, and the exponent D_f known as the fractal dimension is a measure of the “stringiness” of the agglomerate. For example, $D_f \rightarrow 3$ corresponds to a compact nearly spherical aggregate while $D_f \rightarrow 1$ corresponds to a chainlike structure. For compact agglomerates ($D_f \rightarrow 3$), very little gas flows through the pores of the agglomerate as it

executes its Brownian motion; the diffusion coefficient can be estimated from the Stokes–Einstein relation with the particle radius given by (2.23). The agglomerates become more open and extended as D_f decreases, and some of the gas outside the agglomerate can flow through its pores. This increases the drag and decreases the agglomerate diffusion coefficient for a given value of N_p . Tandon and Rosner (1995) have estimated the drag on agglomerates, hence D , by treating them as porous bodies with spatially nonuniform porosity. They solve the Stokes form of the Navier–Stokes equations outside the agglomerate, and the Brinkman equation for the interior flow field and match the flow fields at the surface. Values of D as a function of N_p calculated in this way for various values of D_f are shown in Fig. 2.3.

The results of Fig. 2.3 apply to the continuum regime in which both the agglomerate and primary particle radius are larger than the mean free path of the gas. In the free molecule regime when the agglomerates are smaller than the mean free path of the gas and $D_f < 2$, most of the primary particles in the agglomerates are exposed to collision with gas molecules. In this case, the agglomerate friction coefficient can be estimated by summing over all of the N_p primary particles composing the agglomerate using the free molecule friction coefficient (2.19).

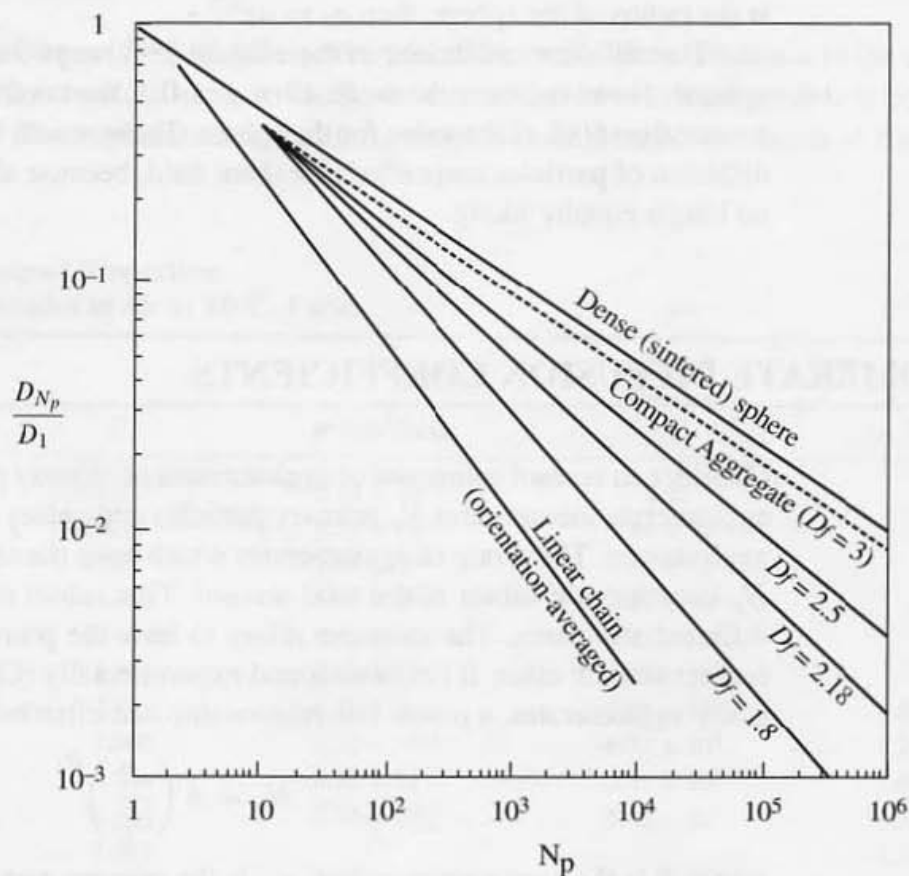


Figure 2.3 Calculated diffusion coefficients for power-law (fractal-like) agglomerates normalized by the Stokes–Einstein diffusion coefficient for a primary particle. The total number of primary particles in the aggregate is N_p , and D_f is the fractal dimension. The results hold for the continuum regime, $a_{po} \gg \ell_p$. (After Tandon and Rosner, 1995.)

PATH LENGTH OF A BROWNIAN PARTICLE

For molecules that behave like rigid elastic spheres, the mean free path is a well-defined quantity that can be calculated from classical kinetic theory (Chapman and Cowling, 1952). Between collisions, the motion of the molecules consists of straight line segments. To estimate the average path length of a particle in Brownian motion in a gas, our first inclination might be to use the mean free path of the particle calculated, for example, from the kinetic theory model for mixtures of rigid elastic spheres. When we make this calculation for 100 Å particles present in vanishing concentrations in air at normal temperature and pressure, it is found that the distance between collisions with gas molecules is only a few angstroms. (Vanishing particle concentration is the proper assumption because the aerosol particle concentrations are generally extremely low compared with that of the gas molecules.) However, the distance calculated in this way does not take into account the tendency of heavy particles (compared with gas molecules) to move in a directed fashion over a distance much larger than the distance between the collisions of a particle with molecules. This effect is known in kinetic theory as the persistence of velocities (Chapman and Cowling, 1952).

A better estimate of the length scale of the particles can be obtained by assuming that the motion of the particles is almost continuous: The change resulting from collision with a molecule of the surrounding gas is so small that the particle motion depends only on the integrated effects of a large number of collisions with molecules. Then one can use the theory of diffusion by continuous movements (Taylor, 1922) to obtain the length scale of the particle motion. Even though the theory was originally developed for application to turbulent diffusion, the mathematical relation between the diffusion coefficient, the length scale of the particle, and r.m.s. velocity holds for any continuous diffusive process. According to the Taylor theory, the particle diffusion coefficient is

$$D = \sqrt{\bar{u}^2} \ell_{pa} \quad (2.24)$$

where \bar{u}^2 is given by the equipartition relation (2.16). The particle length scale, ℓ_{pa} , is defined by the relationship

$$\ell_{pa} = \sqrt{\bar{u}^2} \int_0^\infty R(\theta) d\theta \quad (2.25)$$

where $R(\theta)$ is the Lagrangian velocity correlation coefficient for the particle motion and θ is a time variable for the motion of the particle. Thus the length scale ℓ_{pa} is the distance over which there is significant correlation between the movement of the particle at $\theta = 0$ and some later time. Setting (2.24) equal to the Stokes–Einstein relation (2.17), $\bar{u}^2 = kT/m$ and solving for ℓ_{pa} gives

$$\ell_{pa} = \frac{(mkT)^{1/2}}{f} \quad (2.26)$$

where m is the particle mass.

Path lengths for particle diameters ranging from 10 Å to 1 μm were calculated from (2.26) and are shown in Fig. 2.4 for particles of density 1 g cm⁻³. Particle path length passes through a minimum near 0.2 μm, but is generally of the order of 10 nm. This can

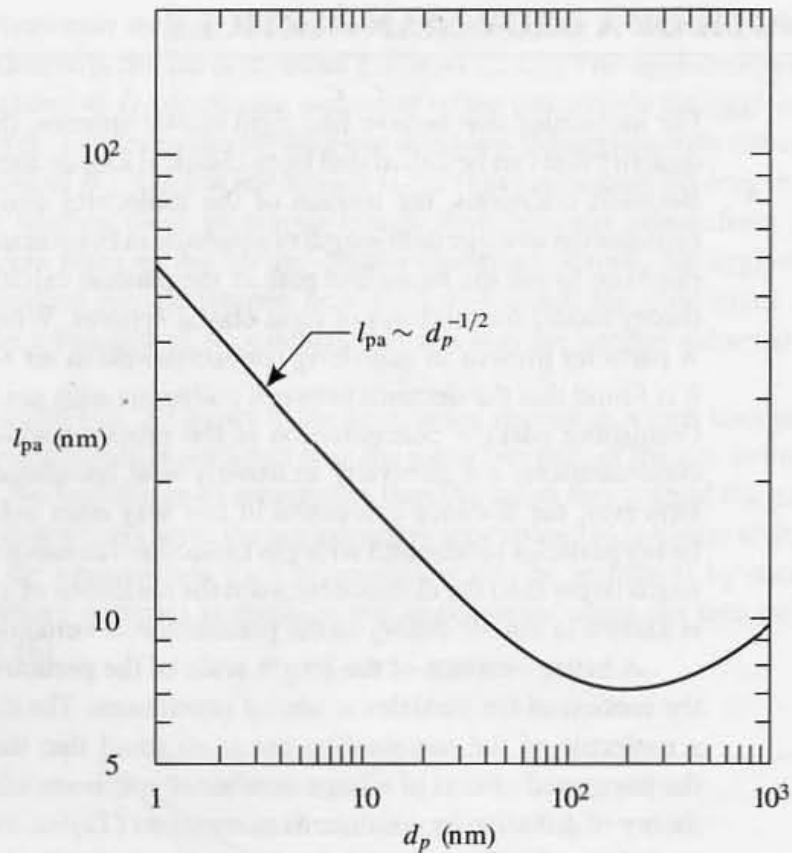


Figure 2.4 Particle path lengths in air at 298 K and 1 atm. The minimum occurs at about $0.2 \mu\text{m}$, significantly larger than the mean free path of the gas. For small values of d_p , we have $\ell_p \sim d_p^{-1/2}$, and for large values we have $\ell_p \sim d_p^{1/2}$.

be compared with the mean free path of gas molecules at NTP which is about ten times greater. Calculations of ℓ_{pa} by Fuchs (1964) and Hidy and Brock (1970) based on a different method of analysis also show a minimum in the path length at about the same particle size, but their values of ℓ_{pa} are about twice the value calculated from the theory of diffusion by continuous movements.

MIGRATION IN AN EXTERNAL FORCE FIELD

The force fields of most interest in particle transport are gravitational, electrical, and thermal, with the last field produced by temperature gradients in the gas. If a balance exists locally in the gas between the force field and the drag on the particle, the two can be equated to give

$$\mathbf{c} = \frac{\mathbf{F}}{f} \quad (2.27)$$

where \mathbf{c} is the migration or drift velocity in the field, \mathbf{F} is the force, and f is the friction coefficient. For the gravitational field,

$$F = \frac{\pi d_p^3}{6} (\rho_p - \rho) g \quad (2.28)$$

where ρ and ρ_p are the gas and particle densities, respectively, and g is the acceleration due to gravity; the migration velocity in this case is called the *terminal settling velocity*:

$$c_s = \frac{\rho_p g d_p^2}{18\mu} C \left[1 - \frac{\rho}{\rho_p} \right] \quad (2.29)$$

Usually ρ/ρ_p can be neglected in this equation. Values of c_s are given in Table 2.1.

The particle flux resulting from simultaneous diffusion and migration in an external force field can be obtained by summing the two effects to give

$$J_x = -D \frac{\partial n}{\partial x} + c_x n \quad (2.30)$$

for the one-dimensional case. In the vector form, we obtain

$$\mathbf{J} = -D \nabla n + c n \quad (2.30a)$$

The same result is obtained from the theory of the Brownian motion taking into account the external force field. When the external force field \mathbf{F} can be derived from the gradient of a potential Φ

$$\mathbf{F} = -\nabla \Phi \quad (2.31)$$

Substituting (2.31) in (2.30a) with the Stokes–Einstein relation (2.17) gives the flux in terms of the potential gradient

$$\mathbf{J} = -D[\nabla n + (\nabla \Phi)n] \quad (2.32)$$

When we substitute (2.32) in (2.1), the equation of conservation of species in the presence of an external force field becomes

$$\frac{\partial n}{\partial t} = \nabla \cdot D \nabla n - \nabla \cdot c n \quad (2.33)$$

Solutions to this equation for constant D and c are given by Carslaw and Jaeger (1959) and Chandrasekhar (1943) for many special applications.

Example: Particles are transported through a thin layer of stationary gas to the surface of a horizontal flat plate. Derive an expression for the deposition rate in the steady state if diffusion and sedimentation are both operative.

SOLUTION. Let z be the distance from the plate measured from the surface. The one-dimensional particle transport rate is given by

$$J = -D \frac{dn}{dz} - c_s n$$

where c_s is given by (2.29). The negative sign appears because the flux, J_z , is positive in the direction of increasing z and c_s is positive. In the steady state, J_z is constant.

When we integrate the first-order linear equation across the gas film with the boundary conditions $n = n_b$ at $z = b$ (the edge of the film) and $n = 0$ at $z = 0$, the result is

$$J = \frac{-c_s n_b}{1 - \exp(-c_s b/D)}$$

For $c_s b \gg D$, $J \rightarrow c_s n_b$, the flux is due to sedimentation alone. For $c_s b \ll D$, it is found that $J \rightarrow -Dn_b/b$, the flux due to diffusion alone, by expanding the exponential in the denominator.

In the sedimentation range, the flux increases with increasing particle size because the larger particles settle more rapidly. In the diffusion range, the flux increases with decreasing particle size because the smaller particles have a larger diffusion coefficient.

As a result, there is a minimum in the deposition flux at an intermediate particle size between the sedimentation and diffusion ranges. The particle size at which the minimum occurs can be found by setting $dJ/[d(d_p)] = 0$. As an approximation, the particle size at the minimum can be estimated by equating the sedimentation and diffusion fluxes and solving for d_p :

$$\frac{Dn_b}{b} = c_s n_b$$

We expect the minimum to occur approximately at the particle diameter for which $c_s b/D = 1$. For $b = 1$ mm, this occurs when $D/c_s = 1$ mm. From Table 2.1, $d_p \approx 0.1 \mu\text{m}$.

ELECTRICAL MIGRATION

General Concepts

The force on a particle carrying i elementary units of charge in an electric field of intensity E is given by

$$F = ieE \quad (2.34)$$

where e is the electronic charge. When the electrical force is balanced by the drag, a steady migration velocity is obtained:

$$c_e = \frac{ieE}{f} \quad (2.35)$$

It is sometimes convenient to employ the electrical mobility,

$$Z = \frac{c_e}{E} = \frac{ie}{f} \quad (2.36)$$

which is the coefficient of proportionality between the migration velocity and the field intensity.

Particle charging can occur by (1) attachment of small ions, (2) static electrification, (3) thermionic charging caused by heating to the point where particles emit ions or electrons, and (4) self-charging due to radioactive decay of particle components (Yeh, 1993). The most common method, small ion attachment, is discussed in this section. Ion attachment depends in a complex way on the ionic atmosphere, the electric field, and the particle size. In gas cleaning by electrostatic precipitation and in certain types of electrical mobility analyzers (Chapter 6), particles are charged by exposure to ions generated in a corona discharge. In industrial electrostatic precipitators, the corona is produced by discharge from a negatively charged wire. Electrons from the corona attach themselves to molecules of oxygen and other electronegative gases to form ions.

Charging by exposure to ions of one sign is called *unipolar charging*. In the atmosphere, both positive and negative ions are generated by cosmic rays and radioactive decay processes. Exposure to mixed ions leads to *bipolar charging* of particles. We consider first unipolar charging under conditions that produce multiply charged particles, then the formation of singly charged ultrafine particles. The section concludes with a discussion of bipolar charging.

Field Charging

When a dielectric or conducting particle is placed in an electric field, the lines of force tend to concentrate in the neighborhood of the particle (Fig. 2.5). Particles become charged by collision with ions moving along lines of force that intersect the particle surface. This process is known as *field charging*. As the particle becomes charged, it tends to repel additional ions of the same sign, and the distribution of electric field and equipotential lines changes. The field distribution can be calculated from electrostatic theory for the region surrounding a charged spherical particle. From the field distribution, the current flow toward the particle at any instant can be calculated. The number of electronic charges accumulated by the particle, n_e , found by integrating the current up to any time t , is

$$i = \left[\frac{\pi e Z_i n_{i\infty} t}{\pi e Z_i n_{i\infty} t + 1} \right] \left[1 + 2 \frac{\epsilon_p - 1}{\epsilon_p + 2} \right] \frac{E d_p^2}{4e} \quad (2.37)$$

Here Z_i is the mobility of the ions, $n_{i\infty}$ is the ion concentration far from the particle, ϵ_p is the dielectric constant of the particle, and t is the time of exposure of the particle to the field.

For sufficiently long times, the charge on the particle approaches a saturation value:

$$i_\infty = \left[1 + 2 \frac{\epsilon_p - 1}{\epsilon_p + 2} \right] \frac{E d_p^2}{4e} \quad (t \rightarrow \infty) \quad (2.38)$$

Under normal operating conditions, the limiting charge is approached after a time small compared with the time of gas treatment in a precipitator. When we combine (2.38) with (2.35), it is found that the migration velocity for field charging increases linearly with particle size when f is given by Stokes law.

The factor $[1 + 2(\epsilon_p - 1)/(\epsilon_p + 2)]$ is a measure of the distortion of the electrostatic field produced by the particle. For $\epsilon_p = 1$, there is no distortion, while for $\epsilon_p \rightarrow \infty$, the factor approaches 3, the value for conducting particles. For the usual dielectric materials, ϵ_p is less than 10, about 2.3 for benzene and 4.3 for quartz.

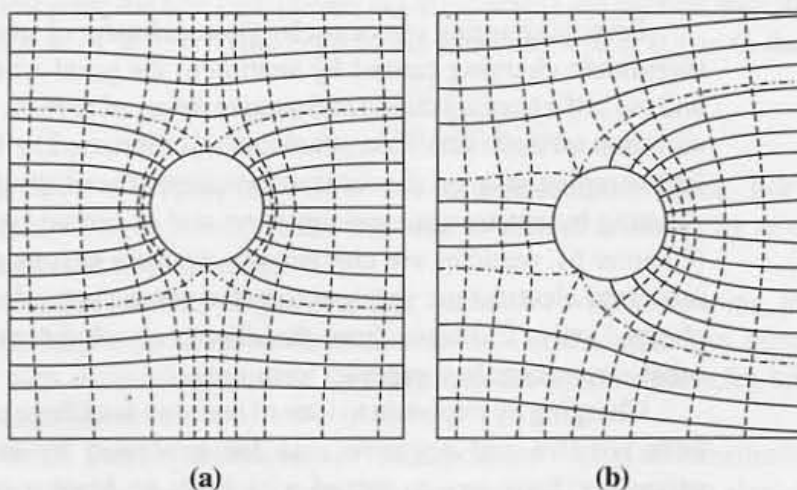


Figure 2.5 Electric force (—) and equipotential (-----) lines around (a) an uncharged conducting sphere in a uniform field and (b) a partially charged conducting sphere in a uniform field. Ions present in the field migrate along the electric force lines: those moving along lines that intersect the surface tend to collide with the sphere. As the particle becomes charged, the field lines become distorted in such a way that the charging process slows (White, 1963).

Unipolar Diffusion Charging: Free Molecule Range

In the previous section, we discussed particle charging by the flow of ions along the lines of force in an electric field. Even in the absence of an applied electric field, particles exposed to an ion cloud become charged. Ion/particle collisions result from the thermal motion of the ions; the particle thermal motion can be neglected by comparison. This mechanism is called *diffusion charging*. Expressions for the particle charge acquired by this mechanism have been derived for the limiting cases of particles much smaller or much larger than the mean free path of the ions. (Ion mean free paths range from about 10 to 60 nm in gases at one atmosphere in the usual applications.) White (1963) derived an expression for the particle charge in the free molecule limit ($d_p \ll$ ion mean free path) based on kinetic theory. He assumed that the ion distribution in the neighborhood of the particle can be approximated by the Boltzmann equilibrium law. For singly charged ions we have

$$n_i = n_{i\infty} \exp \left[\frac{-e\phi}{kT} \right] \quad (2.39)$$

where e is the electronic charge (for negative charging), ϕ is the electrostatic potential in the gas surrounding the particle, and $n_{i\infty}$ is the concentration of ions far from the particle in a region where $\phi = 0$. Because the particle and ion cloud have the same charge, the ion concentration is reduced near the particle/gas interface and then rises to its maximum value $n_{i\infty}$. The potential in the gas is determined by Poisson's equation $\nabla^2\phi = -4\pi\rho$, where ρ is the charge density. The usual practice is to neglect ρ in the region outside the particle but not inside the particle. The result is that for an external point, the effect of a conducting sphere is the same as though the entire charge were concentrated at its center. Hence for the region exterior to the particle we have

$$\phi = \frac{ie^2}{r} \quad (2.40a)$$

where ie is the charge on the particle. Thus the electrostatic potential in the region near the particle surface is

$$\phi_a = \frac{2ie^2}{d_p} \quad (2.40b)$$

With (2.39), this expression determines the ion concentration at the particle surface. The change in the particle charge is given by the rate of collision of ions with the surface of the particle, assuming that every ion that strikes the surface is captured:

$$\frac{di}{dt} = n_{i\infty} \pi d_p^2 \left[\frac{kT}{2\pi m_i} \right]^{1/2} \exp \left[\frac{-2e^2 i}{d_p kT} \right] \quad (2.41)$$

Here m_i is the ionic mass and $[kT/2\pi m_i]^{1/2}$ is the kinetic theory expression for the mean velocity with which ions strike the particle surface. When we integrate with the initial condition $i = 0$ at $t = 0$, the result is

$$i = \frac{d_p kT}{2e^2} \ln \left[1 + \left(\frac{2\pi}{m_i kT} \right)^{1/2} d_p e^2 n_{i\infty} t \right] \quad (2.42)$$

The charge acquired by a particle of given size depends on the $n_{i\infty} t$ product and is independent of the physicochemical properties of the particles. For $t \rightarrow \infty$, i approaches infinity logarithmically. On physical grounds this cannot be true, because there are limits on the charge that a particle can carry. However, for values of $n_{i\infty} t$ encountered in practice ($\sim 10^8$ ion sec cm^3), (2.42) gives results in qualitative agreement with available experimental data.

Unipolar Diffusion Charging: Continuum Range

When the particle diameter is significantly larger than the mean free path of the ions, the charging rate is controlled by continuum diffusion of the ions to the particle surface. This mechanism is likely to be most important for $d_p > 0.1 \mu\text{m}$. Assuming radial symmetry, the flux of ions to a spherical particle is

$$J_i = -D_i \left[\frac{dn_i}{dr} + \frac{d\phi}{dr} n_i \right] \quad (2.43)$$

where D_i is the diffusion coefficient of the ions and n_i and ϕ have been defined above. The particle Brownian motion can be neglected in comparison with ion diffusion. The boundary conditions are $n_i = n_{i\infty}$ for $r \rightarrow \infty$ and $n_i = 0$ at $r = a_p$, the surface of the particle. In the quasi-steady state, the rate of ion transport to the particles is independent of r ; that is, $F_i = 4\pi r^2 J_i(r) = \text{constant}$. Multiplying both sides of (2.43) by $4\pi r^2$ and integrating the resulting linear equation with the boundary conditions stated above gives

$$F_i = \frac{4\pi D_i n_{i\infty}}{\int_{a_p}^{\infty} \frac{1}{r^2} \exp \left[\frac{\phi}{kT} \right] dr} \quad (2.44)$$

Substituting (2.40a) in (2.44) and setting $F_i = di/dt$, the rate of accumulation of charge on the particles is given by

$$\frac{di}{dt} = \frac{4\pi D_i n_{i\infty} i e^2}{kT \left\{ \exp \left[\frac{2ie^2}{d_p kT} \right] - 1 \right\}} \quad (2.45)$$

Integrating with the initial condition $i = 0$ at $t = 0$ gives i as an implicit function of t :

$$\sum_{m=1}^{\infty} \frac{1}{m m!} \left(\frac{2ie^2}{d_p kT} \right)^m = \frac{4\pi D_i e^2 n_{i\infty} t}{kT} \quad (2.46)$$

Calculations by Flagan and Seinfeld (1988) show that (2.46) gives almost the same relationship between i and t as White's equation (2.42) for $0.1 < d_p < 1.0 \mu\text{m}$ and $10^7 < n_{i\infty} t < 10^8 \text{ ion sec cm}^{-3}$. Hence in this range of variables which are of interest in industrial electrostatic precipitation, the simpler explicit equation (2.42) can be used for both free molecule and continuum transport (provided that $i > 1$ as discussed below).

Example: Determine the migration velocity of a conducting $1\text{-}\mu\text{m}$ particle in an electric field with an intensity of 1 kV/cm . The ion concentration is 10^8 cm^{-3} and ion mobility $2(\text{cm/sec})/(\text{V/cm})$. These conditions approximate those in an electrical precipitator.

SOLUTION. The main points of interest are the mixed electrical and mechanical units. Following the customary practice in the field, (2.38) and (2.42) are based on electrostatic (esu) units. Thus when E is expressed in statvolts/cm and the mechanical parameters are expressed in cgs units, the charge ie is in statcoulombs. Moreover,

$$\begin{aligned} 1 \text{ coulomb} &= 3 \times 10^9 \text{ statcoulombs} \\ 300\text{V} &= 1 \text{ statvolt} \end{aligned}$$

The electronic charge is $1.6 \times 10^{-19} \text{ coulomb} = 4.8 \times 10^{-10} \text{ statcoulomb}$. When we substitute in (2.38) for field charging ($d_p = 10^{-4} \text{ cm}$, $E = 3.3 \text{ statvolts/cm}$, $e = 4.8 \times 10^{-10} \text{ statcoulombs}$), it is found that $i = 50$ electronic charges. When we substitute in (2.42) for diffusion charging [$d_p = 10^{-4} \text{ cm}$, $k = 1.38 \times 10^{-16} \text{ ergs/K}$, $T = 300 \text{ K}$, $e = 4.8 \times 10^{-10} \text{ statcoulombs}$, $n_{i\infty} = 10^8 \text{ cc}^{-3}$, and $m_i = 5.3 \times 10^{-23} \text{ g}$ (the mass of an oxygen molecule)], the result is

$$i = 9 \ln[1 + 3.9(10)^3 t] \text{ electronic charges}$$

For $t = 1 \text{ sec}$, $i = 75$ electronic charges.

The migration velocity is given by (2.35). When we substitute $e = 4.8 \times 10^{-10} \text{ statcoulombs}$, $E = 3.33 \text{ statvolts/cm}$, and $f = 3\pi\mu d_p / C$, with the appropriate value for i , it is found that

$$\begin{aligned} c_e &\approx 0.5 \text{ cm/sec for field charging} \\ &\approx 0.8 \text{ cm/sec for diffusion charging} \end{aligned}$$

Field and diffusion charging are of comparable importance in this case. Theories that account for both effects simultaneously have been proposed, requiring numerical computations. Agreement of the calculated charge with some of the limited experimental data is fair (Smith and McDonald, 1975). Adding the charges calculated separately for field and diffusion charging gives somewhat poorer agreement. The total charge calculated by addition is usually less than the measured charge.

Calculated particle migration velocities are shown in Fig. 2.6, based on (2.38) and (2.42) with (2.35). The conditions approximate those in industrial electrostatic precipitation. Field charging is the controlling mechanism for larger particles, whereas diffusion charging controls for smaller particles even in the presence of an applied field. For field charging the migration velocity increases linearly with particle diameter. For diffusion charging the mobility increases as particle diameter decreases because of the form of the slip correction C (2.21). The transition between the mechanisms usually occurs in the 0.1- to 1- μm range. More exact theories for diffusion charging take into account the image forces between ions and particles but require more extensive numerical computations (Marlow and Brock, 1975).

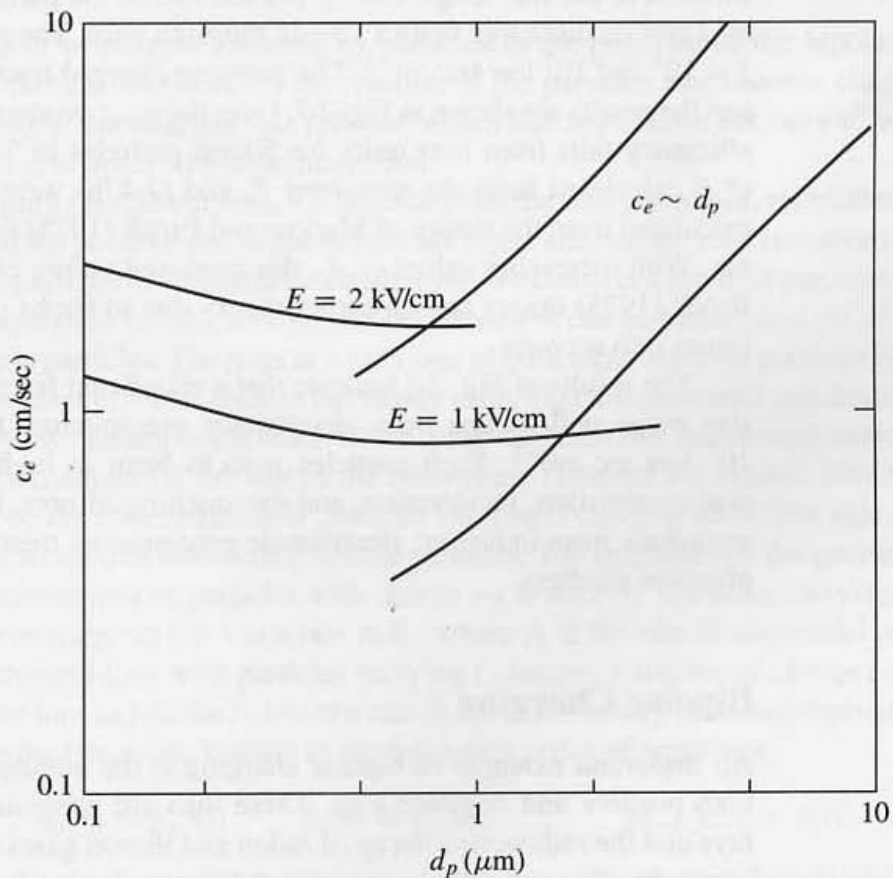


Figure 2.6 Calculated migration velocities for $n_{i\infty t} = 10^8 \text{ sec cm}^{-3}$ and $T = 300 \text{ K}$, based on (2.38) and (2.42). For an electric field intensity of 2 kV/cm, the transition from diffusion to field charging occurs near 0.75 μm under these conditions.

Unipolar Diffusion Charging: Stochastic Theory

For particles smaller than about $0.05 \mu\text{m}$, the diffusion charging theory discussed above breaks down; the calculated number of charges per particle decreases to a value less than unity which is physically unacceptable. Instead, only a fraction of such particles acquire unit charge for values of the $n_{i\infty}t$ product in the range usually of interest in such applications as electrostatic precipitation and aerosol instrumentation ($< 10^8$ ions sec cm^{-3}).

The limiting case of very small particles only a few of which become charged is easiest to treat using a kinetic theory analysis. The rate of successful collisions between ions of unit charge and concentration with uncharged particles of concentration N_0 is

$$-\frac{dN_0}{dt} = \beta N_0 n_{i\infty} \quad (2.47a)$$

where β is the collision frequency function. Integrating from $N_0 = N_0(0)$ at $t = 0$ to $N_0 = N_0(t)$ at $t = t$ gives the fraction charged:

$$f_c = \frac{N_0(t)}{N_0(0)} = 1 - e^{-\beta n_{i\infty} t} \quad (2.47b)$$

Several theoretical models have been proposed for β ; Pui et al. (1988) conducted experiments designed to test them. They generated monodisperse silver and sodium chloride aerosols in the size range 4 to 75 nm and mixed the particles with positive ions produced by a corona discharge from a 25- μm tungsten wire. The $n_{i\infty}t$ product was varied between 3×10^6 and 10^7 ion sec cm^{-3} . The resulting charged fraction of the aerosol was measured and the results are shown in Fig. 2.7. Over the $n_{i\infty}t$ product range investigated, the charging efficiency falls from near unity for 50-nm particles to 5–15% for 5-nm particles. Values of β calculated from the measured f_c and (2.47b) were in good agreement with values calculated from the theory of Marlow and Brock (1975) for particles smaller than about 10 nm. With increasing values of d_p , the measured values of β fall between the Marlow and Brock (1975) theory and an earlier theory due to Fuchs (1963). Both theories take image forces into account.

The results of Fig. 2.7 indicate that a significant fraction of particles in the nanometer size range will escape from electrostatic precipitators for $n_{i\infty}t$ values of the order of 10^7 ion sec cm^{-3} . Such particles tend to form in high-temperature processes such as coal combustion, incineration, and the smelting of ores. Data are lacking on nanoparticle emissions from industrial electrostatic precipitators treating gases from coal-fired power plants or smelters.

Bipolar Charging

An important example of bipolar charging is the atmospheric aerosol that is exposed to both positive and negative ions. These ions are generated in the atmosphere by cosmic rays and the radioactive decay of radon and thoron gases emanating from the soil. Air ion concentrations normally range around 500 per cc at ground level. The ions are believed to consist of singly charged molecules surrounded by a cluster of a few neutral molecules. The ratio of the concentrations of the positive to negative ions is about 1.2; negative ion mobilities are somewhat higher than the positive ion mobilities. Of special interest are

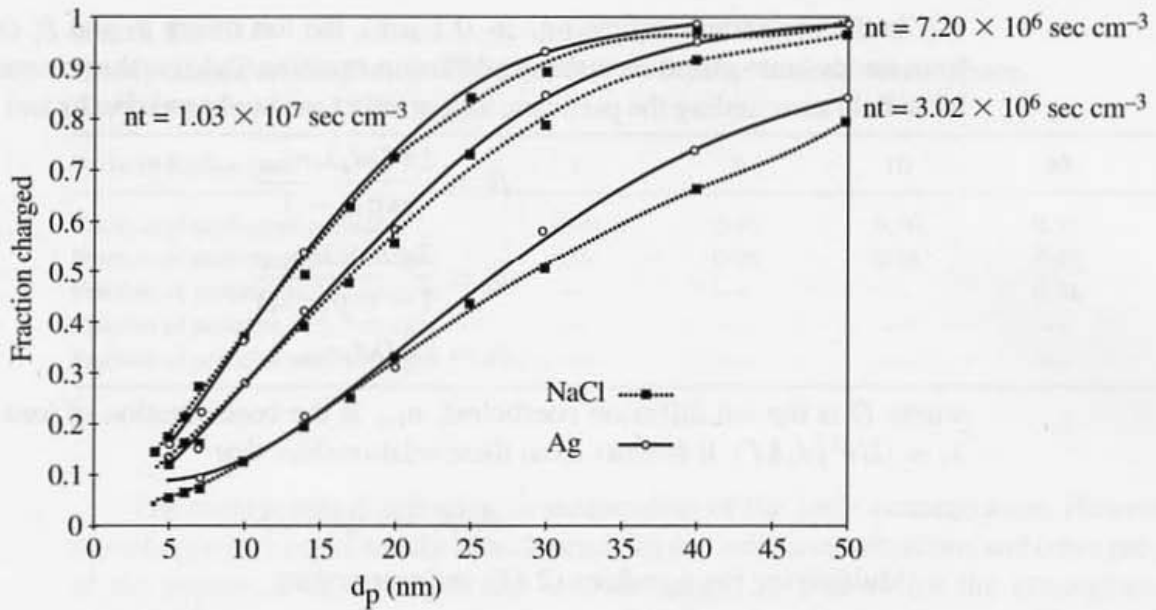


Figure 2.7 Fraction of particles with unit charge after exposure to unipolar air ion sources for various nt products. (Based on Pui et al., 1988.)

(a) the number of charges assumed by particles in the presence of the bipolar ions, as a function of particle size, and (b) the fraction of the particles that become charged. These are calculated in the analysis that follows, which has application not only to atmospheric particles but also to aerosol instrumentation.

To simplify the calculations, it is assumed that the concentrations, mobilities, and other properties of the positive and negative ions are equal and that the concentrations of the ions and charged particles have reached a steady state. We consider a group of particles of uniform size; no coagulation occurs, so a polydisperse aerosol can be treated as a set of uncoupled monodisperse particles. The rates at which ions of both signs attach to particles are assumed to be independent of each other. In the steady state, ions are generated and destroyed at the same rate by attachment to particles. Calculations indicate that ion recombination is not an important mechanism for ion loss in the atmosphere (Bricard and Pradel, 1966).

Let N_i be the concentration of particles carrying i charges, all of like sign, and let N_0 be the concentration of electrically neutral particles. The symmetry of the problem requires that the concentration of particles with charge $-i$ is also N_i . Particles carrying a charge i increase their charge to $i + 1$ at a rate $\beta_i N_i$, where β_i is the rate of successful collisions of positively charged ions with particles carrying i charges. Particles of charge $i + 1$ collide with negative ions to join the i class at a rate $\beta'_i N_{i+1}$. The steady-state assumption is satisfied by equating the two rates, leading to the following series of equations:

$$\beta_0 N_0 = \beta'_1 N_1; \quad \beta_1 N_1 = \beta'_2 N_2; \quad \dots; \quad \beta_{i-1} N_{i-1} = \beta'_i N_i \quad (2.48)$$

where N_i is the steady-state concentration of particles with i charges. Equations (2.48) have the form of the detailed balance relationships that appear in classical equilibrium theory. However, this is not an equilibrium system because the process is driven by the rate that ions are generated by cosmic rays and radon decay.

In the continuum regime ($d_p \gg 0.1 \mu\text{m}$), the ion fluxes β_i and β'_i can be estimated from steady-state solutions to the ion diffusion equation (2.43) in the presence of a Coulomb force field surrounding the particles; image forces are neglected (Fuchs and Sutugin, 1971):

$$\beta_i = \frac{2\pi D d_p \lambda_i n_{i\infty}}{\exp \lambda_i - 1} \quad (2.49a)$$

$$\beta'_i = \frac{2\pi D d_p \lambda_i n_{i\infty}}{1 - \exp(-\lambda_i)} \quad (2.49b)$$

$$\beta_0 = 2\pi D d_p n_{i\infty} \quad (2.49c)$$

where D is the ion diffusion coefficient, $n_{i\infty}$ is the concentration of ions in the gas, and $\lambda_i = |2ie^2/d_p kT|$. It follows from these relationships that

$$\beta_i/\beta'_i = \exp(-\lambda_i) \quad (2.50)$$

Multiplying the equalities (2.48) and rearranging

$$N_i = \frac{\beta_{i-1} \beta_{i-2} \dots \beta_1 \beta_0}{\beta'_i \beta'_{i-1} \dots \beta'_2 \beta'_1} N_0 \quad (2.51a)$$

$$= \frac{\beta_0}{\beta_i} \left(\frac{\beta_i}{\beta'_i} \right) \left(\frac{\beta_{i-1}}{\beta'_{i-1}} \right) \dots \left(\frac{\beta_1}{\beta'_1} \right) N_0 \quad (2.51b)$$

Substituting (2.50) in (2.51b), we obtain

$$N_i = N_0 \frac{\exp \lambda_{i-1}}{\lambda_i} \exp \left(- \sum_1^i \lambda_k \right) \quad (2.52)$$

and substituting for λ_i , we obtain

$$\exp \left[- \sum_1^i \lambda_k \right] = \exp \left(- \frac{2e^2}{d_p kT} \sum_1^i k \right) \quad (2.52a)$$

Noting that $\sum_1^i k = i(i+1)/2$ and substituting in (2.52a) gives

$$\exp \left(- \sum_1^i \lambda_k \right) = \exp \left(- \frac{e^2 i^2}{d_p kT} \right) \exp \left(- \frac{e^2 i}{d_p kT} \right) \quad (2.53a)$$

$$= \exp \left(- \frac{e^2 i^2}{d_p kT} \right) \exp \left(- \frac{\lambda_i}{2} \right) \quad (2.53b)$$

Substituting (2.53b) in (2.52) gives

$$N_i = N_0 \exp(-i^2 e^2/d_p kT) \quad (2.54)$$

Thus, the particle charge distribution is approximated by the Boltzmann equation. This expression holds best for particles larger than about $1 \mu\text{m}$. For smaller particles, the flux terms (2.49) based on continuum transport theory must be modified semiempirically. The results of calculations of the fraction of charged particles are given in Table 2.2. The fraction refers to particles of charge of a given sign.

TABLE 2.2
Steady-State Particle Charge Distribution in a Bipolar Ionized Atmosphere.
 (Fuchs and Sutugin, 1971, p. 45)

Particle Radius (nm)	1	3	10	30	100
Fraction of uncharged particles	0.99	0.95	0.76	0.51	0.29
Fraction of particles with 1 charge	0.01	0.05	0.24	0.45	0.44
Fraction of particles with 2 charges	—	—	—	0.04	0.20
Fraction of particles with 3 charges	—	—	—	—	0.06
Fraction of particles with 4 charges	—	—	—	—	0.01

The steady-state distribution is independent of the ionic concentration. However, the rate of approach to the steady state depends on the ionic concentrations and other properties of the system. The net result can be summarized as follows for the atmosphere. Ions are steadily generated by cosmic rays and radioactive decay processes. These attach to particle surfaces where they are neutralized at a rate equal to their rate of formation. The particle charge distribution is determined by the steady state relationship between particles separated by one charge. In the atmosphere, the equilibration process takes about 30 min. The rate of equilibration can be increased by increasing the ion concentration using a bipolar ion generator. Radioactive ion sources such as ^{85}Kr , are often used in electrical aerosol instrumentation (Chapter 6).

Experimental results for spherical particles and agglomerates are compared with a modified version of the Fuchs theory in Fig. 2.8. For the spherical particles, the charged

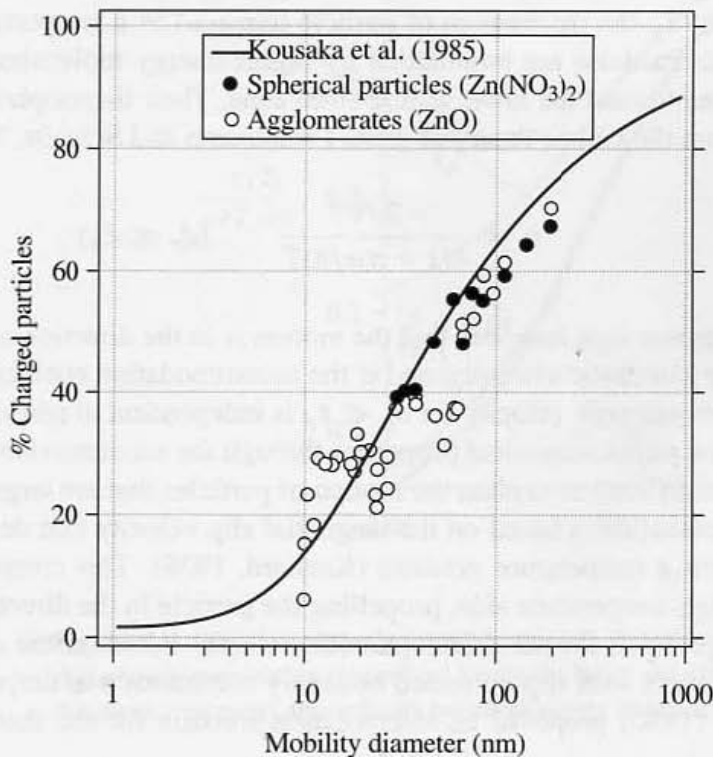


Figure 2.8 Fraction of particles with unit charge after exposure to bipolar ions in a ^{85}Kr charger. The solid line represents Fuchs' theory for spherical particles using the correlation of Kousaka et al. (1985). The theory agrees well with the data for agglomerates and for spherical particles (Matsoukas and Friedlander, 1991).

fraction is in good agreement with the theoretical prediction. The data points for the agglomerates (fractal dimension of about 2.5) are more scattered. Within experimental error, however, the charged fraction for the agglomerates behaves approximately like the charged fraction of spherical particles of the same mobility. The agreement between the two types of particles extends from the free molecule range to the transition regime, and it indicates that diffusion charging of agglomerates can be correlated with their mobility diameter. A more stringent test should involve measurement of the complete distribution of charges.

THERMOPHORESIS

Small particles in a temperature gradient are driven from the high- to low-temperature regions. This effect was first observed in the nineteenth century when it was discovered that a dust-free or dark space surrounded a hot body, suitably illuminated. Particle transport in a temperature gradient has been given the name thermophoresis, which means "being carried by heat." Thermophoresis is closely related to the molecular phenomenon thermal diffusion, transport produced by a temperature gradient in a multicomponent system.

Deposition by thermophoresis causes problems in process applications when hot gases containing small suspended particles flow over cool surfaces. For example, in petroleum refining, hot gases from fluidized beds carry particles produced by catalyst attrition and, perhaps, by condensation. When these gases pass through a heat exchanger, particles deposit on the cold surface, causing scale formation and reduction of the heat transfer coefficient. Thermophoresis finds application in the sampling of small particles from gases. By choosing a proper flow geometry, the particles can be deposited on a surface for subsequent study.

For $d_p \ll \ell_p$ the mechanism of particle transport in a temperature gradient is easy to understand: Particles are bombarded by higher-energy molecules on their "hot" side and thus driven toward the lower temperature zone. Their thermophoretic velocity can be calculated from the kinetic theory of gases (Waldmann and Schmitt, 1966):

$$\mathbf{c}_t = \frac{-3\nu\nabla T}{4(1 + \pi\alpha/8)T} \quad (d_p \ll \ell_p) \quad (2.55)$$

where the negative sign indicates that the motion is in the direction of decreasing temperature, ν is the kinematic viscosity, and α the accommodation coefficient, is usually about 0.9. The thermophoretic velocity for $d_p \ll \ell_p$ is independent of particle size. It depends to some extent on physicochemical properties through the accommodation coefficient α .

It is more difficult to explain the motion of particles that are larger than the mean free path. The explanation is based on the tangential slip velocity that develops at the surface of a particle in a temperature gradient (Kennard, 1938). This creep velocity is directed toward the high-temperature side, propelling the particle in the direction of lower temperature. An expression for the thermophoretic velocity based on the continuum equations of fluid mechanics with slip-corrected boundary conditions was derived by Brock (1962). Talbot et al. (1980) proposed an interpolation formula for the thermophoretic velocity

that approaches (2.55) in the free molecule limit and approaches the Brock equation for $\ell_p/d_p < 0.1$:

$$c_t = \frac{2C_s v \left(\frac{k_g}{k_p} + C_t \frac{2\ell_p}{d_p} \right) C \frac{dT/dz}{T_0}}{\left(1 + 3C_m \frac{2\ell_p}{d_p} \right) \left(1 + 2\frac{k_g}{k_p} + 2C_t \frac{2\ell_p}{d_p} \right)} \quad (2.56)$$

where C is given by (2.21); C_s , C_t , and C_m are dimensionless coefficients that can be calculated from kinetic theory; and k_g and k_p are the thermal conductivities of the gas and particle, respectively. Suggested values for the kinetic theory coefficients are $C_s = 1.17$ for complete thermal accommodation, $C_t = 2.18$, and $C_m = 1.14$. The mean gas temperature in the vicinity of the particle is T_0 .

Values of the dimensionless thermophoretic velocity are shown in Fig. 2.9 as a function of the Knudsen number with k_g/k_p as a parameter. For Knudsen numbers larger than unity, the dependence of the dimensionless thermophoretic velocity on particle size and chemical nature is small. Particle sampling by thermophoresis in this range offers the advantage that particles are not selectively deposited according to size.

Thermophoretic velocities have been measured for single particles suspended in a Millikan-type cell with controlled electrical potential and temperature gradients. Particle diameters are usually larger than about $0.8 \mu\text{m}$, for convenient optical observation.

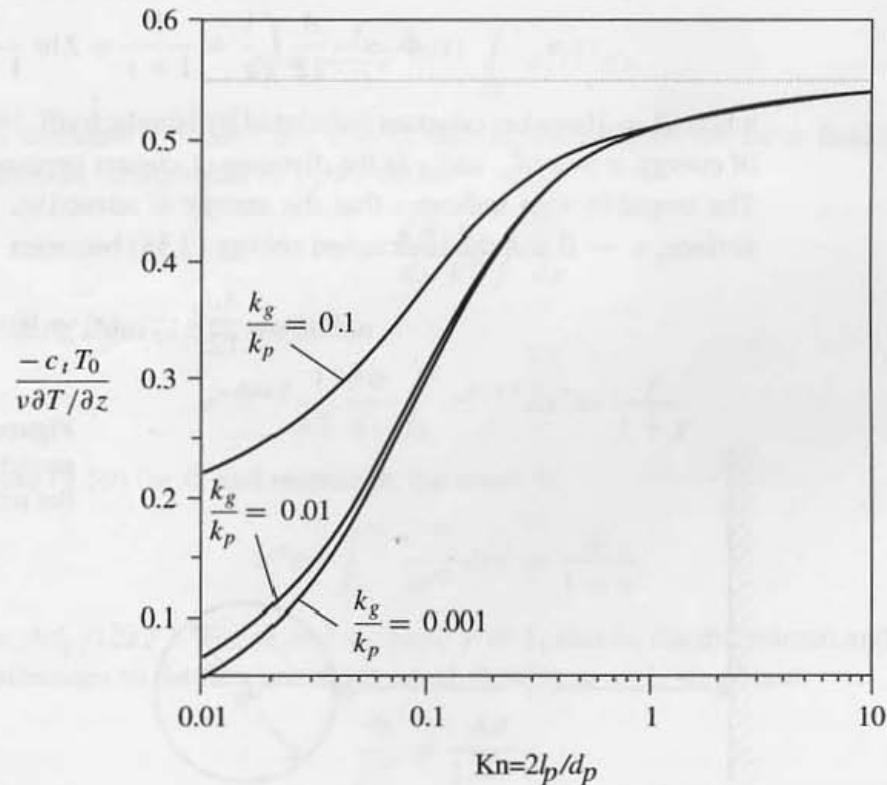


Figure 2.9 Dimensionless thermophoretic velocity calculated from (2.56), an interpolation formula that closely approaches theoretical limits for large and small Kn . For $\text{Kn} > 1$ (particles smaller than the mean free path), the velocity becomes nearly independent of the particle material.

LONDON-VAN DER WAALS FORCES

Gravitational, electrical, and thermophoretic forces act over distances large compared with particle size. London–van der Waals forces, which are attractive in nature, act over shorter distances falling rapidly to zero away from a surface. These are the forces responsible for the effects of surface tension and for deviations from the ideal gas law (Chu, 1967). van der Waals forces result because electrically neutral atoms (or molecules) develop instantaneous dipoles caused by fluctuations in the electron clouds surrounding the nuclei. These instantaneous dipoles induce dipoles in neighboring atoms or molecules. The resulting energy of attraction between the molecules calculated from quantum theory is of the form

$$\Phi = -C/r^6 \quad (2.57)$$

where C , is a constant that depends on the material and r is the distance separating the atoms. For this pair potential energy function, it is possible to derive the van der Waals interaction energies in vacuum (or, approximately, gases at normal pressures) for pairs of bodies of different shapes. As a first approximation, this can be done by summing the energies of interaction of the atoms (or molecules) in one body with the atoms in the other body (Israelachvili, 1992). For a spherical particle in the neighborhood of an infinite mass bounded by a flat surface (Fig. 2.10), the interaction energy is (Chu, 1967, p. 52)

$$\Phi = -\frac{A}{12} \left(\frac{1}{s} + \frac{1}{1+s} + 2 \ln \frac{s}{1+s} \right) \quad (2.58)$$

where A = Hamaker constant (tabulated by Israelachvili, 1992, pp. 186–7) with dimensions of energy, $s = x/d_p$, and x is the distance of closest approach of the particle to the surface. The negative sign indicates that the energy is attractive. As the particle approaches the surface, $x \rightarrow 0$ and the interaction energy (2.58) becomes

$$\Phi = -\frac{Ad_p}{12x} \quad (x \rightarrow 0) \quad (2.59)$$

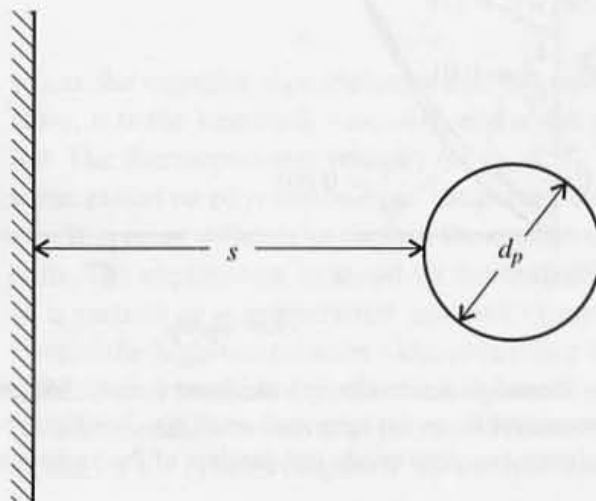


Figure 2.10 Interaction of a spherical particle with a large body bounded by a flat surface.

Thus the energy of attraction becomes infinite as the particle approaches a flat surface. For this reason, it is usually assumed that a surface acts as a perfect sink in the theory of aerosol diffusion; that is, when a particle penetrates to a distance one radius from the surface, the particles adhere. This holds best for submicron particles moving at thermal velocities. Rebound occurs for larger particles moving at high velocities (Chapter 4). This analysis does not take into account the effects of surface roughness of the scale of the particle size or of layers or patches of adsorbed gases or liquids. Such factors may be important in practical applications.

BOUNDARY CONDITION FOR PARTICLE DIFFUSION

We consider particle transport from a gas to a body with a flat bounding surface by Brownian diffusion under the influence of van der Waals forces exerted by the body. The relative contributions of the two mechanisms can be estimated as follows: The total flux normal to the surface is given by the x component of the flux

$$J_x = -D \left[\frac{dn}{dx} + \frac{d\Phi}{dx} \frac{n}{kT} \right] \quad (2.60)$$

The solution for the concentration distribution assuming J_x is constant near the surface is (Spielman and Friedlander, 1974)

$$n = -\frac{J_x}{D} e^{-\Phi/kT} \int_0^x e^{\Phi/kT} dx' \quad (2.61)$$

where n is assumed to vanish for $x = 0$. Setting the ratio of the force field term to the diffusion term in (2.60) equal to γ , we obtain

$$\gamma = \frac{d\Phi}{dx} \frac{n}{kT} \bigg/ \frac{dn}{dx} \quad (2.62)$$

and substituting from (2.61), we obtain

$$e^{-\Phi/kT} \frac{1}{kT} \frac{d\Phi}{dx} \int_0^x e^{\Phi/kT} dx' = \frac{\gamma}{1 + \gamma} \quad (2.63)$$

When we use (2.59) for Φ and rearrange, the result is

$$e^m m^2 \int_m^\infty \frac{e^{-m'}}{m'^2} dm' = \frac{\gamma}{1 + \gamma} \quad (2.64)$$

where $m = Ad_p/12kTx$. For $m = 1$ we have $\gamma \approx 1$; that is, the diffusional and dispersion force contributions to the flux are about equal. Setting $m = 1$, we obtain

$$\frac{\Phi}{kT} = \frac{Ad_p}{12kTx} \quad (2.65)$$

Values of A often range between 10^{-13} and 10^{-12} ergs. For $T = 25^\circ\text{C}$ and taking the smaller value of A , we obtain

$$x = \frac{Ad_p}{12kT} = \frac{10^{-13}d_p}{12(1.38 \times 10^{-16})298} = 0.2d_p \quad (2.66)$$

which satisfies the requirement $x/d_p \rightarrow 0$ on which (2.59) is based. For $d_p = 0.1 \mu\text{m}$ we have $x = 200 \text{ \AA}$; that is, the two flux terms contribute about equally at a location 200 \AA from the surface. As particle size decreases, this distance decreases correspondingly.

Because the dispersion forces are attractive, they tend to increase the rate of particle transport to the surface. When the diffusion path is long compared with the range of operation of the dispersion forces, the attractive effects on diffusion can be neglected (Fig. 2.11). The sink boundary condition is retained, however, and the particle flux can be calculated by solving the diffusion equation in the absence of an external force field with the condition $n = 0$ at a distance $d_p/2$ from the surface. The particle flux is

$$J_x = -D \left[\frac{\partial n}{\partial x} \right]_{x=d_p/2} \quad (2.67)$$

Finally, when d_p is also much smaller than the diffusion path, these conditions become

$$n = 0 \text{ at } x = 0 \quad (\text{on the wall})$$

and the particle flux is

$$J_x = -D \left[\frac{\partial n}{\partial x} \right]_{x=0} \quad (2.68)$$

This is the usual boundary condition for molecular diffusion to surfaces in gases and liquids for a perfectly absorbing surface. Hence the results of experiment and theory for molecular diffusion in the absence of a force field can often be directly applied to particle diffusion. However, the effect of finite particle size is very important when diffusion boundary layers are present as discussed in the next chapter.

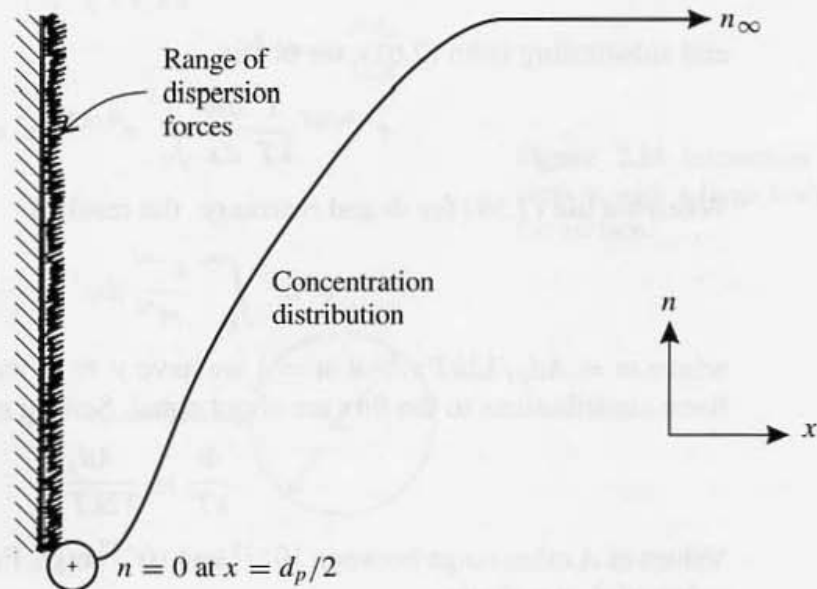


Figure 2.11 Diffusion path or distance from mainstream of the gas is much greater than the range of the dispersion forces.

PROBLEMS

2.1 Show that equation (2.5) in the text,

$$n(x, t) = \frac{N_0}{2(\pi Dt)^{1/2}} \exp\left[\frac{-x^2}{4Dt}\right]$$

satisfies the one-dimensional diffusion equation. Here N_0 is the number of particles released near the plane $x = 0$ at $t = 0$ per unit cross-sectional area perpendicular to x . Show that the total number of particles in the gas per unit cross section parallel to the plane of release is conserved as t increases.

2.2 The first approximation to the coefficient of diffusion for a binary mixture of molecules that act as rigid elastic spheres is given by [Chapman and Cowlong (1952), p. 245]

$$D = \frac{3kT}{2p(d_1 + d_2)^2} \left\{ \frac{kT(m_1 + m_2)}{2\pi m_1 m_2} \right\}^{1/2}$$

where 1 and 2 refer to the components of the mixture, d is the molecular diameter, and m is the mass. Under what circumstances does this expression reduce to kT/f with f the friction coefficient in the free molecule range ($d_p \ll \ell_p$), equation (2.19)?

2.3 Estimate the order of magnitude of the time required for a particle in translational and rotational Brownian motion to turn through an angle of order π around its axis [Landau and Lifshitz (1987), p. 237; Einstein's papers in Furth (1956), p. 33]. The rotational Brownian motion of nonspherical particles results in twinkling when the particles are illuminated from the side.

2.4 The potential energy of an ion (point charge e) in the field of a spherical conducting particle carrying i elementary charges is

$$\phi = \frac{(ie)e}{r} - \frac{e^2 a_p^2}{2r^2 (r^2 - a_p^2)}$$

where r is the radial position with respect to the particle center and a_p is the particle radius. The assumption that the particle is a conductor is usually justified for very small particles. The first term on the right-hand side corresponds to the Coulomb force, and the second term refers to the image force. It is assumed that $i \gg 1$. Show that the charged particle will repel the ion as it is moved from a great distance along a radius toward the center of the particle, until it reaches a distance $\frac{1}{2} a_p i^{-1/2}$ from the particle surface. Near this point, the repulsive force $F_r = -(d\phi/dr)$ exerted by the particle on the ion becomes attractive as the image force takes over. [Based on Problem 9, p. 287 of Jeans (1925), where other problems of this type can be found.]

2.5 Derive an expression relating applied electric field potential, E , and particle diameter for which the charge acquired by field and diffusion charging are equal. Plot particle diameter as a function of E over the range 1 to 10^2 kV/cm for $Nt = 10^7$ ion sec/cm³ at $T = 20^\circ\text{C}$ and 1 atm. The ion mobility is $2.2 \text{ cm}^2/\text{V sec}$, and the dielectric constant of the particles is 8.0.

2.6 In diffusion charging, decreasing particle diameter decreases the charge acquired by a particle for a fixed $n_{i\infty}t$ product. Assume that all particles of a given size acquire the same

charge and estimate d_p for a particle which just acquires unit charge ($i = 1$) under the conditions $n_{i\infty}t = 10^8$ ion sec cm^{-3} when $T = 300$ K and O_2 ions serve as charge carriers.

2.7 An aerosol containing $1\text{-}\mu\text{m}$ particles with a density of 2 g/cm^3 and a thermal conductivity of 3.5×10^{-4} cal/cm sec K flows over a surface. Calculate the minimum temperature gradient at the surface necessary to prevent particle deposition by sedimentation. Neglect diffusion and assume that the air flow is parallel to the surface, which is maintained at 20°C .

REFERENCES

- Bricard, J., and Pradel, J. (1966) Electric Charge and Radioactivity of Naturally Occurring Aerosols, Chapter IV in Davies, C. N. (Ed.), *Aerosol Science*, Academic Press, New York.
- Brock, J. R. (1962) *J. Colloid Sci.*, **17**, 768.
- Carslaw, H. S., and Jaeger, J. C. (1959) *Conduction of Heat in Solids*, Oxford University Press, Oxford, 2nd ed. This work includes a compilation of solutions to the equation of unsteady heat conduction in the absence of flow for many different geometries, initial and boundary conditions. The basic equation is of the same form as the diffusion equation with the thermal diffusivity, $\kappa/\rho C$, in place of the diffusion coefficient. (Here κ , ρ , and C are the thermal conductivity, density, and specific heat of the continuous fluid.) Like D , the thermal diffusivity has cgs. dimensions of cm^2/sec .
- Chandrasekhar, S. (1943) Stochastic Problems in Physics and Astronomy, in *Reviews of Modern Physics*, vol. 15, p. 1. Reprinted in N. Wax (Ed.) (1954) *Noise and Stochastic Processes*, Dover, New York.
- Chapman, S. and, Cowling, T. G. (1952) *Mathematical Theory of Non-Uniform Gases*, Cambridge University Press, 2nd Ed.
- Chu, B. (1967) *Molecular Forces*: Based on the Baker Lectures of Peter J. W. Debye, Wiley-Interscience, New York. This small, concisely written book reviews the origins of the London-van der Waals forces and derives expressions for the interaction energy between bodies under the influence of these forces.
- Crank, J. (1975) *The Mathematics of Diffusion*, Oxford University Press, Oxford.
- Davies, C. N. (1945) *Proc. Phys. Soc.*, **57**, 259.
- Einstein, A. (1905) *Ann. Physik* **17**, 549. This and related articles by Einstein have been translated and reprinted in R. Furth (Ed.) (1956) *Investigations on the Theory of the Brownian Movement*, Dover, New York.
- Epstein, P. S. (1924) *Phys. Rev.*, **23**, 710.
- Flagan, R. C., and Seinfeld, J. H. (1988) *Fundamentals of Air Pollution Engineering*, Prentice-Hall, Englewood Cliffs, NJ.
- Fuchs, N. A. (1963) *Geofis. Pura Appl.*, **56**, 185.
- Fuchs, N. A. (1964) *The Mechanics of Aerosols*, Pergamon, Oxford, UK.
- Fuchs, N. A., and Sutugin, A. G. (1971) High Dispersed Aerosols in Hidy, G. M., and Brock, J. R. (Eds.) *Topics in Current Aerosol Research*, Vol. 2, Pergamon Press, Oxford.
- Green, H. S. (1952) *The Molecular Theory of Fluids*, Interscience, New York.
- Hidy, G. M., and Brock, J. R. (1970) *The Dynamics of Aerocolloidal Systems*, Pergamon, Oxford. An extensive review of the fundamentals of particle transport over a wide range of Knudsen numbers is given in this reference. Values for molecular accommodation coefficients at surfaces collected from various sources are included.
- Israelachvili, J. (1992) *Intermolecular and Surface Forces*, Academic Press, San Diego, CA.

- Jeans, J. H. (1925) *The Mathematical Theory of Electricity and Magnetism*, 5th Ed., Cambridge University Press, Cambridge, UK.
- Kennard, E. H. (1938) *Kinetic Theory of Gases*, McGraw-Hill, New York. A good discussion of the creep velocity at a particle surface resulting from a temperature gradient in the carrier gas is given on pp. 327 ff.
- Kousaka, Y., Okuyama, K., and Adachi, M. (1985) *Aerosol Sci. Technol.*, **4**, 209.
- Landau, L. D., and Lifshitz, E. M. (1987) *Fluid Mechanics*, 2nd ed., Pergamon Press, Oxford, England.
- Marlow, W. H., and Brock, J. R. (1975) *J. Colloid Interface Sci.*, **50**, 32.
- Matsoukas, T., and Friedlander, S. K. (1991) *J. Colloid Interface Sci.*, **146**, 495.
- Perrin, F. (1936) *J. Phys. Radium, Series 7*, **7**, 1.
- Perrin, J. (1910) *Brownian Movement and Molecular Reality*, Taylor and Francis, London.
- Pui, D. Y. H., Fruin, S., and McMurry, P. H. (1988) *Aerosol Sci. Technol.*, **8**, 173.
- Smith, W. B. and McDonald, J. R. (1975) *J. Air Pollut. Control Assoc.*, **25**, 168.
- Spielman, L. A., and Friedlander, S. K. (1974) *J. Colloid Interface Sci.*, **46**, 22.
- Talbot, L., Cheng, R. K., Schefer, R. W., and Willis, D. R. (1980) *J. Fluid Mech.* **101**, 737.
- Tandon, P., and Rosner, D. E. (1995) *Ind. Eng. Chem. Res.*, **34**, 3265.
- Taylor, G. I. (1922) *Proc. London Math. Soc.*, **20**, 196.
- Waldmann, L., and Schmitt, K. H. (1966) Thermophoresis and Diffusiophoresis of Aerosols, Chapter VI in Davies, C. N. (Ed.) *Aerosol Science*, Academic, New York.
- Wax, N. (Ed.) (1954) *Noise and Stochastic Processes*, Dover, New York. A good review of the foundations of the theory of the Brownian movement including applications to communication theory is given in this collection of papers.
- Whitby, K. T., and Liu, B. Y. H. (1966) The Electrical Behavior of Aerosols, Chapter III in Davies, C. N. (Ed.), *Aerosol Science*, Academic, New York.
- White, H. J. (1963) *Industrial Electrostatic Precipitation*, Addison-Wesley, Reading, MA. This highly readable monograph contains much practical operating data as well as discussions of fundamentals.
- Yeh, H. C. (1993) Electrical Techniques, in Willeke, K., and Baron, P. A. (Eds.), *Aerosol Measurement*, Van Nostrand Reinhold, New York.

Convective Diffusion

Effects of Finite Particle Diameter and External Force Fields

Diffusional transport in flowing fluids is called *convective diffusion*. Particle deposition on surfaces by this mechanism is of fundamental importance to the functioning of gas-cleaning equipment, such as scrubbers and filters, as well as aerosol measurement systems, such as the diffusion battery and certain types of filters. Convective diffusion contributes to the scavenging of small atmospheric particles by raindrops, as well as removal by vegetation and other surfaces, and is a significant mechanism of deposition in the lung. The particle size at which convective diffusion is effective depends on velocity and external force fields, but is usually in the submicron range.

The intensity of the Brownian motion increases as particle size decreases (Chapter 2). As a result, the efficiency of collection by diffusion for particles smaller than about $0.5 \mu\text{m}$ increases with decreasing particle size; as shown in this chapter, certain gas-cleaning devices are most efficient for the removal of very small particles.

In what follows, the equation of diffusion derived in Chapter 2 is generalized to take into account the effect of flow. For point particles ($d_p = 0$), rates of convective diffusion can often be predicted from theory or from experiment with aqueous solutions because the Schmidt numbers are of the same order of magnitude. There is an extensive literature on this subject to which the reader is directed. For particle diffusion, there is a difference from the usual theory of convective diffusion because of the special boundary condition: The concentration vanishes at a distance of one particle radius from the surface. This has a very large effect on particle deposition rates and causes considerable difficulty in the mathematical theory. As discussed in this chapter, the theory can be simplified by incorporating the particle radius in the diffusion boundary condition.

Particle diffusion coefficients are small compared with the kinematic viscosity of a gas (large Schmidt numbers), so the region of the gas flow near the surface from which particles are depleted is usually very narrow. This narrow region, the concentration boundary layer, is very important to particle transport and is discussed in detail.

The presence of an external force field has a major effect on particle transport. Important practical examples involving thermophoresis and electrical transport combined with flow and diffusion are reviewed in this chapter.

EQUATION OF CONVECTIVE DIFFUSION

It is sometimes possible to predict rates of deposition by diffusion from flowing fluids by analysis of the equation of convective diffusion. This equation is derived by making a material balance on an elemental volume fixed in space with respect to laboratory coordinates (Fig. 2.1). Through this volume flows a gas carrying small particles in Brownian motion.

The rate at which particles are carried by the flow into the volume element across the face $ABCD$ is given by

$$\delta y \delta z \left[nu - \frac{\delta x}{2} \frac{\partial(nu)}{\partial x} \right]$$

where n is the particle concentration (number per unit volume) and u is the velocity in the x direction. The rate at which particles leave the volume across the opposite face is given by

$$\delta y \delta z \left[nu + \frac{\delta x}{2} \frac{\partial(nu)}{\partial x} \right]$$

The net rate of particle accumulation for the flow in the x direction is given by subtracting the rate leaving from the rate entering:

$$- \delta x \delta y \delta z \frac{\partial nu}{\partial x}$$

Analogous expressions are obtained for the other four faces; summing up for all three pairs, the result for the net accumulation of particles in the volume element is given by

$$- \delta x \delta y \delta z \left[\frac{\partial nu}{\partial x} + \frac{\partial nv}{\partial y} + \frac{\partial nw}{\partial z} \right] = - \delta x \delta y \delta z \nabla \cdot n\mathbf{v}$$

The rate of particle accumulation in the volume $\delta x \delta y \delta z$ taking into account the flow, diffusion, and external force fields (Chapter 2) is obtained by summing the three effects:

$$\frac{\partial n \delta x \delta y \delta z}{\partial t} = - \delta x \delta y \delta z \nabla \cdot n\mathbf{v} + \delta x \delta y \delta z \nabla \cdot (D \nabla n - c\mathbf{n})$$

where D is the coefficient of diffusion and c is the particle migration velocity resulting from the external force field. Dividing both sides by the volume $\delta x \delta y \delta z$ and noting that $\nabla \cdot \mathbf{v} = 0$ for an incompressible fluid, the equation becomes

$$\frac{\partial n}{\partial t} + \mathbf{v} \cdot \nabla n = D \nabla^2 n - \nabla \cdot c\mathbf{n} \quad (3.1)$$

when the diffusion coefficient is constant. As in Chapter 2, this result holds both for monodisperse and polydisperse aerosols. In the polydisperse case, n is the size distribution function, and both D and c depend on particle size. Coagulation and growth or evaporation are not taken into account; these are discussed in later chapters.

Values of D and c are determined by the factors discussed in Chapter 2. The new quantity entering (3.1) is the gas velocity distribution, \mathbf{v} , which is determined by the fluid mechanical regime. In some cases, \mathbf{v} is obtained by solving the equations of fluid motion (Navier–Stokes equations) for which an extensive literature is available (Landau

and Lifshitz, 1987; Schlichting, 1979). In many cases, such as atmospheric transport and in complex gas-cleaning devices, experimental data may be necessary for the gas velocity distribution. In this chapter, velocity distributions are introduced without derivation but with reference to the literature. In all cases, it is assumed that particle concentration has no effect on the velocity distribution. This is true for the low aerosol concentrations usually considered.

There is an extensive literature on solutions to (3.1) for various geometries and flow regimes. Many results are given by Levich (1962). Results for heat transfer, such as those discussed by Schlichting (1979) for boundary layer flows, are applicable to mass transfer or diffusion if the diffusion coefficient, D , is substituted for the coefficient of thermal diffusivity, $\kappa/\rho C_p$, where κ is the thermal conductivity, ρ is the gas density, and C_p is the heat capacity of the gas. The results are directly applicable to aerosols for "point" particles, that is, $d_p = 0$.

SIMILITUDE CONSIDERATIONS FOR AEROSOL DIFFUSION

Consider the flow of an incompressible gas, infinite in extent, over a body of a given shape placed at a given orientation to the flow. This is called an *external* flow. Bodies of a given shape are said to be geometrically similar when they can be obtained from one another by changing the linear dimensions in the same ratio. Hence, it suffices to fix one characteristic length, L , to specify the dimensions of the body. This would most conveniently be the diameter for a cylinder or sphere, but any dimension will do for a body of arbitrary shape. Similar considerations apply for *internal* flows through pipes or ducts.

For an external flow, it is assumed that the fluid has a uniform velocity, U , except in the region disturbed by the body. If the concentration in the mainstream of the fluid is n_∞ , a dimensionless concentration can be defined as follows:

$$n_1 = \frac{n}{n_\infty} \quad (3.2)$$

Limiting consideration to the steady state, the equation of convective diffusion in the absence of an external force field can be expressed in dimensionless form as follows

$$\mathbf{v}_1 \cdot \nabla_1 n_1 = \frac{1}{\text{Pe}} \nabla_1^2 n_1 \quad (3.3)$$

where $\mathbf{v}_1 = \mathbf{v}/U$ and $\nabla_1 = L\nabla$. The dimensionless group LU/D is known as the Péclet number (Pe) for mass transfer.

In many cases, the velocity field can be assumed to be independent of the diffusional field. The steady isothermal flow of a viscous fluid, such as air, in a system of given geometry depends only on the Reynolds number when the velocity is small compared with the speed of sound.

The boundary condition for particle diffusion differs from the condition for molecular diffusion because of the finite diameter of the particle. For certain classes of problems, such as flows around cylinders and spheres, the particle concentration is assumed to vanish at one particle radius from the surface:

$$n = 0 \quad \text{at} \quad \frac{\alpha}{L} = \frac{a_p}{L} = R \quad (3.4)$$

where α is a coordinate measured from the surface of the body. The dimensionless ratio $R = a_p/L$ is known as the interception parameter; particles within a distance a_p of the surface would be intercepted even if diffusional effects were absent.

Hence the dimensionless concentration distribution can be expressed in the following way:

$$n_1 = f_1\left(\frac{r}{L}, \text{Re}, \text{Pe}, R\right) \quad (3.5)$$

Two convective diffusion regimes are similar if the Reynolds, Péclet, and interception numbers are the same.

The local rate of particle transfer by diffusion to the surface of the body is

$$J = -D \left(\frac{\partial n}{\partial \alpha} \right)_{\alpha=\alpha_p} = -\frac{Dn_\infty}{L} \left(\frac{\partial n_1}{\partial \alpha} \right)_{\alpha_1=R} \quad (3.6)$$

Setting the local mass transfer coefficient $k = J/n_\infty$ and rearranging, the result is

$$\frac{kL}{D} = f_2(\text{Re}, \text{Pe}, R) \quad (3.7)$$

The particle transfer coefficient k has dimensions of velocity and is often called the deposition velocity. At a given location on the collector surface the dimensionless group kL/D , known as the Sherwood number, is a function of the Reynolds, Péclet, and interception numbers. Rates of particle deposition measured in one fluid over a range of values of Pe , Re , and R can be used to predict deposition rates from another fluid at the same values of the dimensionless groups. In some cases, it is convenient to work with the Schmidt number $\text{Sc} = \nu/D = \text{Pe}/\text{Re}$ in place of Pe as one of the three groups, because Sc depends only on the nature of the fluid and the suspended particles.

For $R \rightarrow 0$ ("point" particles), theories of particle and molecular diffusion are equivalent. Schmidt numbers for particle diffusion are much larger than unity, often of the same order of magnitude as for molecular diffusion in liquids. The principle of dimensional similitude tells us that the results of diffusion experiments with liquids can be used to predict rates of diffusion of point particles in gases, at the same Reynolds number.

For certain flow regimes, it is possible to reduce the number of dimensionless groups necessary to characterize a system by properly combining them. This further simplifies data collection and interpretation in several cases of considerable practical importance as shown in the sections that follow.

CONCENTRATION BOUNDARY LAYER

Flow normal to a right circular cylinder is the basic model for the theory of aerosol filtration by fibrous and cloth filters, and of particle collection by pipes and rods in a flow (Fig. 3.1). The aerosol concentration at large distances from the surface is uniform; at one particle radius from the surface, the concentration vanishes.

Referring to the nondimensional equation of convective diffusion (3.3), it is of interest to examine the conditions under which the diffusion term, on the one hand, or convection, on the other, is the controlling mode of transport. The Péclet number, dU/D , for flow around a cylinder of diameter d is a measure of the relative importance of the two terms. For $Pe \ll 1$, transport by the flow can be neglected, and the deposition rate can be determined approximately by solving the equation of diffusion in a nonflowing fluid with appropriate boundary conditions (Carslaw and Jaeger, 1959; Crank, 1975).

When the Péclet number is large, the physical situation is quite different. The mainstream flow then carries most of the particles past the cylinder. In the immediate neighborhood of the cylinder, the diffusional process is important since the cylinder acts as a particle sink. Thus at high Pe , there are two different transport regions: Away from the immediate vicinity of the cylinder, convective transport by the bulk flow predominates and carries the particles further downstream. Near the surface, the concentration drops sharply from its value in the mainstream to zero at one particle radius from the surface (Fig. 3.1). The region over which the particle concentration falls from its value in the main flow to zero near the surface is known as the *concentration (or diffusion) boundary layer*. It is in many ways analogous to the velocity boundary layer that forms around the cylinder at high Reynolds numbers, with the Péclet number serving as a criterion similar to the Reynolds number. The role of the concentration boundary layer is fundamental to understanding and predicting the rate of transport of Brownian particles to surfaces. The usefulness of this concept is not limited to flows around cylinders. It applies to flows around other bodies such as spheres and wedges and to flows inside channels under certain conditions as well. Concentration boundary layers may develop in either low- or high-speed flows around collecting objects. Both cases are discussed in the sections that follow.

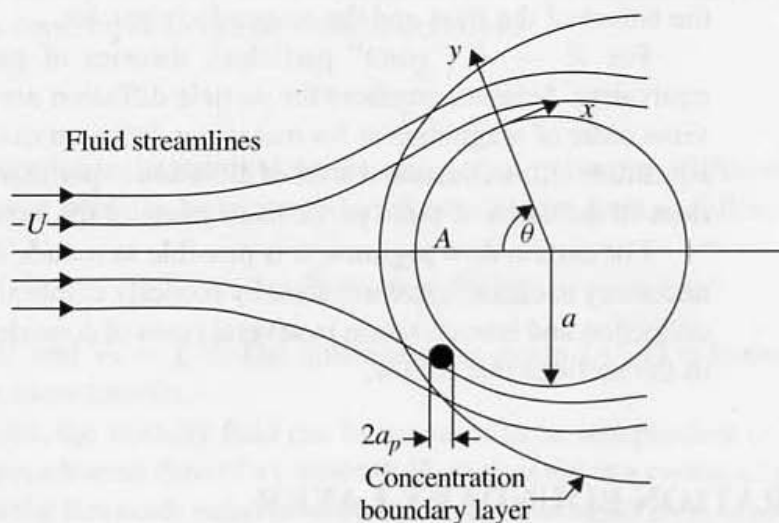


Figure 3.1 Schematic diagram showing concentration boundary layer surrounding a cylinder (or sphere) placed in a flow carrying diffusing small particles. Curvilinear coordinate x , taken parallel to the surface, is measured from the forward stagnation point A . Particle concentration rises from zero at $r = a + a_p$ almost to the mainstream concentration (for example, to 99% of the mainstream value) at the edge of the boundary layer.

DIFFUSION TO CYLINDERS AT LOW REYNOLDS NUMBERS: CONCENTRATION BOUNDARY LAYER EQUATION

We consider first the case of a single cylinder set normal to a low-Reynolds-number aerosol flow (Fig. 3.1). This configuration is of central importance to the functioning of high-efficiency fibrous filters for gas cleaning. Fibrous filters are highly porous mats of fine fibers usually containing less than 10% solid material. The spacing between the individual fibers is much greater than the diameters of the particles filtered. In the absence of electrical effects, small particles are collected by diffusion to the fibers; larger particles are removed by inertial deposition. When the fiber diameter is much larger than the mean free path of the air, continuum theory applies to the gas flow over the fibers. The equation of convective diffusion for the steady state takes the following form in cylindrical coordinates:

$$v_{\theta} \frac{\partial n}{r \partial \theta} + v_r \frac{\partial n}{\partial r} = D \left[\frac{\partial^2 n}{\partial r^2} + \frac{1}{r} \frac{\partial n}{\partial r} + \frac{\partial^2 n}{r^2 \partial \theta^2} \right] \quad (3.8)$$

where v_{θ} and v_r are the tangential and radial components of the velocity. For particles of radius, a_p diffusing to a cylinder of radius, a , the boundary conditions are

$$\begin{aligned} \text{at } r = a + a_p, \quad n &= 0 \\ r = \infty \quad n &= n_{\infty} \end{aligned} \quad (3.8a)$$

For fiber diameters smaller than 10 μm and air velocities less than 10 cm/sec, the Reynolds number is much less than unity. For isolated cylinders, the stream function for the air flow can be approximated by

$$\psi = AUa \sin \theta \left[\frac{r}{a} \left(2 \ln \frac{r}{a} - 1 \right) + \frac{a}{r} \right] \quad (3.9)$$

where to a close approximation $A = [2(2 - \ln \text{Re})]^{-1}$ (Rosenhead, 1963, p. 180). More approximate relations ("cell models") are usually used to take into account interactions among the fibers in developing correlations for filtration.

Even though the Reynolds number is small, there are many practical situations in which $\text{Pe} = \text{Re} \cdot \text{Sc}$ is large because the Schmidt number, Sc , for aerosols is very large. For $\text{Pe} \gg 1$, two important simplifications can be made in the equation of convective diffusion. First, diffusion in the tangential direction can be neglected in comparison with convective transport:

$$D \frac{\partial^2 n}{r^2 \partial \theta^2} \ll \frac{v_{\theta} \partial n}{r \partial \theta}$$

In addition, a concentration boundary layer develops over the surface of the cylinder with its thinnest portion near the forward stagnation point. When the thickness of the concentration boundary layer is much less than the radius of the cylinder, the equation of convective diffusion simplifies to the familiar form for rectangular coordinates (Schlichting, 1979, Chapter XII):

$$u \frac{\partial n}{\partial x} + v \frac{\partial n}{\partial y} = D \frac{\partial^2 n}{\partial y^2} \quad (3.10)$$

where x and y are orthogonal curvilinear coordinates. The x coordinate is taken parallel to the surface of the cylinder and measured from the forward stagnation point. The y axis is perpendicular to x and measured from the surface. The velocity components u and v correspond to the coordinates x and y (Fig. 3.1). When the concentration boundary layer is thin, most of it falls within a region where the stream function (3.9) can be approximated by the first term in its expansion with respect to y :

$$\psi = 2AaU \left(\frac{y}{a}\right)^2 \sin\left(\frac{x}{a}\right) \quad (3.11)$$

The components of the velocity are related to the stream function as follows:

$$u = \frac{\partial\psi}{\partial y}, \quad v = -\frac{\partial\psi}{\partial x} \quad (3.12)$$

Substituting ψ from (3.11) gives

$$u = 4AU \left(\frac{y}{a}\right) \sin\left(\frac{x}{a}\right) \quad (3.13a)$$

$$v = -2AU \left(\frac{y}{a}\right)^2 \cos\left(\frac{x}{a}\right) \quad (3.13b)$$

DIFFUSION TO CYLINDERS AT LOW REYNOLDS NUMBERS: POINT PARTICLES

For the diffusion of point particles ($R \rightarrow 0$), the appropriate boundary conditions on (3.10) are

$$\text{at } y = 0, \quad n = 0 \quad (3.14a)$$

$$y = \infty, \quad n = n_\infty \quad (3.14b)$$

The concentration boundary condition $n = n_\infty$ is set at $y = \infty$, even though the boundary layer form of the equation of convective diffusion (3.10) is valid only near the surface of the cylinder. This can be justified by noting that the concentration approaches n_∞ very near the surface for high Pe .

If x and ψ are taken as independent variables instead of x and y , (3.26) can be transformed into the following equation:

$$\left(\frac{\partial n}{\partial x}\right)_\psi = D \left[\frac{\partial}{\partial \psi} \left(u \frac{\partial n}{\partial \psi} \right) \right]_x \quad (3.15)$$

The x component of the velocity is

$$u = \frac{\partial\psi}{\partial y} = \left(\frac{8AU}{a}\right)^{1/2} \sin^{1/2} x_1 \psi^{1/2} \quad (3.16)$$

where $x_1 = x/a$. Substitution in (3.15) gives

$$\frac{\partial n}{\partial \chi} = \frac{D}{aAU} \frac{\partial}{\partial \psi_1} \left(\psi_1^{1/2} \frac{\partial n}{\partial \psi_1} \right) \quad (3.17)$$

where

$$\chi = \int \sin^{1/2} x_1 dx_1 \quad \text{and} \quad \psi_1 = \frac{\psi}{2AaU}$$

The boundary conditions in the transformed coordinates become

$$\begin{aligned} \text{at } \psi_1 = 0 \text{ (surface of cylinder), } & n = 0 \\ \psi_1 = \infty, & n = n_\infty \end{aligned} \quad (3.18)$$

By inspection of (3.17), we assume as a trial solution that n is a function only of the variable $\xi = \psi_1/\chi^{2/3}$. This assumption must be checked by substitution of the expressions

$$\frac{\partial n}{\partial \chi} = -\frac{2}{3} \frac{\xi}{\chi} \frac{dn}{d\xi} \quad (3.19a)$$

and

$$\frac{\partial n}{\partial \psi_1} = \frac{1}{\chi^{2/3}} \frac{dn}{d\xi} \quad (3.19b)$$

in (3.17). The result of the substitution is an ordinary differential equation:

$$-\frac{APe}{3} \xi \frac{dn}{d\xi} = \frac{d}{d\xi} \left(\xi^{1/2} \frac{dn}{d\xi} \right) \quad (3.20)$$

with the boundary condition $n = 0$ at $\xi = 0$ and $n = n_\infty$ at $\xi \rightarrow \infty$. This supports the assumption that n is a function only of the variable ξ . Integration of (3.20) gives

$$n = \frac{n_\infty \int_0^{\xi^{1/2}} \exp(-\frac{2}{9} APe z^3) dz}{\int_0^\infty \exp(-\frac{2}{9} APe z^3) dz} \quad (3.21)$$

where $Pe = dU/D$ with d the diameter of the cylinder. The integral in the denominator can be expressed in terms of a gamma function, Γ , as

$$\left(\frac{9}{2}\right)^{1/3} \frac{1}{3} \Gamma\left(\frac{1}{3}\right) (APe)^{-1/3} = 1.45 (APe)^{-1/3} \quad (3.22)$$

The rate of diffusional deposition per unit length of cylinder is

$$2D \int_0^\pi \left(\frac{\partial n}{\partial y_1} \right)_{y_1=0} dx_1 = k_{av} \pi dn_\infty \quad (3.23)$$

which defines the average mass transfer coefficient, k_{av} , for the cylinder. The concentration gradient at the surface is obtained by differentiating (3.21) with respect to y . The result is

$$\left(\frac{\partial n}{\partial y_1} \right)_{y_1=0} = \frac{(APe)^{1/3} n_\infty \sin^{1/2} x_1}{1.45 \chi^{1/3}} \quad (3.24)$$

Substituting in (3.23) and evaluating the integral with respect to x_1 gives (Natanson, 1957)

$$\frac{k_{av} d}{D} = 1.17 (APe)^{1/3} \quad (3.25)$$

The concentration gradient at the surface can be expressed in terms of an effective boundary layer thickness, δ_c , as follows:

$$\left(\frac{\partial n}{\partial y}\right)_{y=0} = \frac{n_\infty}{\delta_c} \quad (3.26)$$

substitute (3.24), the result is

$$\frac{\delta_c}{d} \sim (A\text{Pe})^{-1/3} \quad (3.27)$$

with a proportionality constant of order unity near the forward stagnation point. Hence the thickness of the concentration boundary layer is inversely proportional to $\text{Pe}^{1/3}$; large Péclet numbers lead to thin concentration boundary layers as discussed in the previous section.

The theoretical expression (3.25) is in good agreement with data for diffusion in aqueous solutions over the high Pe range of interest in aerosol deposition. Recalling that $\text{Pe} = \text{Sc} \cdot \text{Re}$, (3.25) can be rearranged to give

$$\frac{k_{\text{av}}d}{D} \bigg/ \left(\frac{v}{D}\right)^{1/3} = 1.17(A\text{Re})^{1/3} \quad (3.28)$$

for this low-Reynolds-number case. At higher Reynolds numbers, a different functional form is found for the Reynolds number dependence, but the general relationship

$$\frac{k_{\text{av}}d}{D} \bigg/ \left(\frac{v}{D}\right)^{1/3} = f(\text{Re}) \quad (3.29)$$

holds over a wide range of Reynolds numbers. The form of the function is shown in Fig. 3.2 over both low- and high-Reynolds-number ranges.

The efficiency of removal, η_R , is defined as the fraction of the particles collected from the fluid volume swept by the cylinder:

$$\eta_R = \frac{k_{\text{av}}\pi dn_\infty}{n_\infty Ud} = 3.68A^{1/3}\text{Pe}^{-2/3} \quad (3.30)$$

Because A is a relatively slowly varying function of Reynolds number, the efficiency varies approximately as $d^{-2/3}$, which means that fine fibers are more efficient aerosol collectors than coarse ones. Because $\text{Pe} = dU/D$, $\eta_R \sim d_p^{-2/3}$ and $d_p^{-4/3}$ for the continuum and free molecule ranges, respectively. Hence small particles are more efficiently removed by diffusion than larger particles in the range $d_p < 0.5 \mu\text{m}$. The use of single filter fiber collection efficiencies to test this theory is discussed in a later section.

DIFFUSION AT LOW REYNOLDS NUMBERS: SIMILITUDE LAW FOR PARTICLES OF FINITE DIAMETER

For particles of finite diameter, the interception effect becomes important. A useful similitude law that takes both diffusion and interception into account can be derived as follows (Friedlander, 1967): It is assumed that the concentration boundary layer is thin and falls

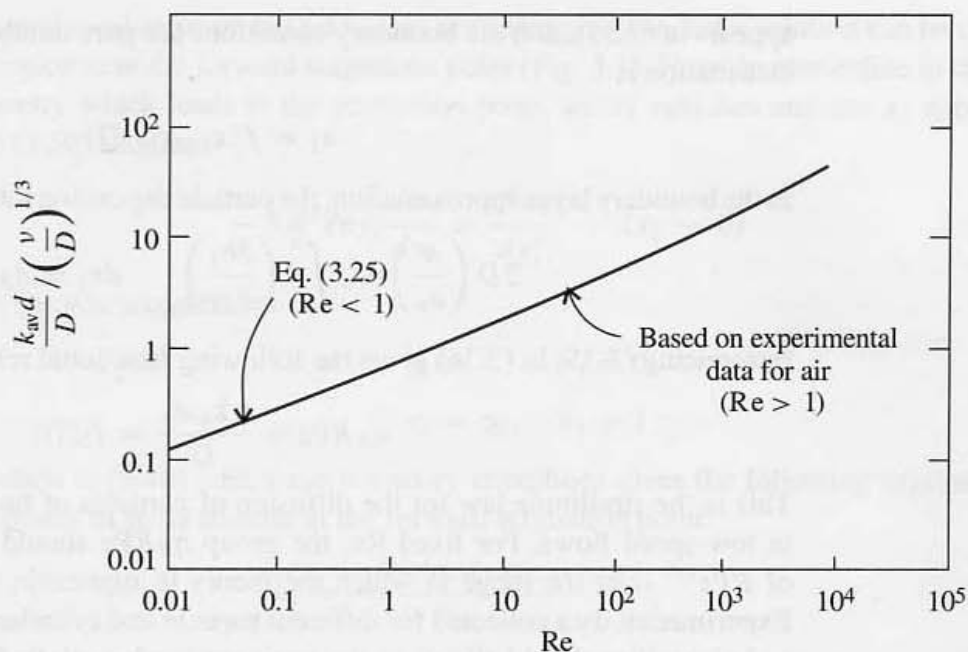


Figure 3.2 Diffusion of point particles ($R \rightarrow 0$) to single cylinders placed normal to an air flow. The theoretical curve for low Reynolds numbers is in good agreement with experimental data for diffusion in aqueous solution (Dobry and Finn, 1956). The curve for high Reynolds numbers is based on data for heat transfer to air (Schlichting, 1979, p. 311) corrected by dividing the Nusselt number by $(v/D)^{1/3}$. This is equivalent to assuming that laminar boundary layer theory is applicable.

within the region where the velocity distribution function is given by (3.13a,b). Substituting (3.13a,b) in (3.10) gives the following equation for convective diffusion:

$$4 \frac{y}{a} \sin \left(\frac{x}{a} \right) \frac{\partial n}{\partial x} - 2 \left(\frac{y}{a} \right)^2 \cos \left(\frac{x}{a} \right) \frac{\partial n}{\partial y} = \frac{D}{AU} \frac{\partial^2 n}{\partial y^2} \quad (3.31)$$

We now introduce the following dimensionless variables:

$$n_1 = \frac{n}{n_\infty}, \quad y_1 = \frac{y}{a_p}, \quad x_1 = \frac{x}{a} \quad (3.32)$$

where a_p is the particle radius and a is the cylinder radius. Note that the curvilinear coordinates normal and parallel to the cylinder surface are nondimensionalized by different characteristic lengths. Then (3.31) becomes

$$4 y_1 \sin x_1 \frac{\partial n_1}{\partial x_1} - 2 y_1^2 \cos x_1 \frac{\partial n_1}{\partial y_1} = \left(\frac{Da^2}{AU a_p^3} \right) \frac{\partial^2 n_1}{\partial y_1^2} \quad (3.33)$$

with boundary conditions

$$\begin{aligned} \text{at } y_1 = 1, \quad n_1 &= 0 \\ y_1 = \infty, \quad n_1 &= 1 \end{aligned}$$

Taking $R = a_p/a$, only one dimensionless group that we take for convenience to be

$$\Pi = R(PeA)^{1/3} \sim (Da^2/AU a_p^3)^{-1/3} \quad (3.34)$$

appears in (3.33), and the boundary conditions are pure numbers. Hence the concentration distribution is

$$n_1 = f(x_1, y_1, \Pi) \quad (3.35)$$

In the boundary layer approximation, the particle deposition rate per unit length of cylinder is

$$2D \left(\frac{a}{a_p} \right) n_\infty \int_0^\pi \left(\frac{\partial n_1}{\partial y_1} \right)_{y_1=1} dx_1 = \eta_R n_\infty dU \quad (3.36)$$

Introducing (3.35) in (3.36) gives the following functional relationship:

$$\eta_R RPe = \frac{\pi k_{av} d_p}{D} = f_2(\Pi) \quad (3.37)$$

This is the similitude law for the diffusion of particles of finite diameter but with $R < 1$ in low-speed flows. For fixed Re , the group $\eta_R RPe$ should be a single-valued function of $RPe^{1/3}$ over the range in which the theory is applicable ($Pe \gg 1$, $Re < 1$, $R \ll 1$). Experimental data collected for different particle and cylinder diameters and gas velocities and viscosities should all fall on the same curve when plotted in the form of (3.37).

In the limiting case, $R \rightarrow 0$, η_R is independent of the interception parameter R . By inspection of (3.37), this result is obtained if the function f_2 is linear in its argument $f_2 \sim \Pi$ such that

$$\eta_R = C_1 \pi A^{1/3} Pe^{-2/3} \quad (3.38)$$

The constant $C_1 \pi = 3.68$ according to (3.25). In the limiting case $Pe \rightarrow \infty$, particles follow the fluid and deposit when a streamline passes within one radius of the surface. This effect is called *direct interception*. The efficiency is obtained by integrating (3.13b) for the normal velocity component over the front half of the cylinder surface:

$$\eta_R = \frac{\int_0^{\pi/2} v_{y=a_p} dx}{Ua} = 2AR^2 \quad (3.39)$$

A result of this form can be obtained from (3.37) by noting that for $Pe \rightarrow \infty$, η_R is independent of Pe . Then the function f_2 must be proportional to the cube of its argument, Π (3.34).

Equations (3.38) and (3.39) are the limiting laws for the ranges in which diffusion and direct interception control, respectively. They show that for fixed velocity and fiber diameter, the efficiency at first decreases as d_p increases because of the decrease in the diffusion coefficient (3.38); further increases in d_p lead to an increase in η_R as $R = d_p/d$ increases in (3.39). The result is a minimum in the plot of efficiency as a function of particle diameter. In the particle size range above the minimum, interception eventually gives way to impaction and/or sedimentation as dominant mechanisms of particle deposition.

The dimensionless group $\Pi = R(PeA)^{1/3}$ is proportional to the ratio of the particle diameter to the concentration boundary layer thickness given by (3.27)

$$d_p/\delta_c \sim R(PeA)^{1/3}$$

So long as this ratio is small, deposition is controlled by diffusion. For particles large compared with the diffusion boundary layer thickness, interception controls.

An analytical solution to (3.33) does not seem possible, but a solution can be obtained for the region near the forward stagnation point (Fig. 3.1). Near the streamline in the plane of symmetry which leads to the stagnation point, $\sin x_1$ vanishes and $\cos x_1$ approaches unity so (3.50) becomes

$$-AR^3Pe y_1^2 \frac{dn_1}{dy_1} = \frac{d^2 n_1}{dy_1^2} \quad (x_1 \rightarrow 0) \quad (3.40)$$

with the boundary conditions

$$\begin{aligned} \text{at } y_1 = 1, \quad n_1 &= 0 \\ y_1 = \infty, \quad n_1 &= 1 \end{aligned} \quad (3.40a)$$

The solution to (3.40) with these boundary conditions gives the following expression for the coefficient of mass transfer at the forward stagnation point:

$$k_0 = \frac{-D(dn/dy)_{y_1=1}}{n_\infty} \quad (3.41a)$$

$$= \frac{(D/a_p)e^{-AR^3Pe/3}}{\int_1^\infty \exp(-AR^3Pe z^3/3) dz} \quad (3.41b)$$

Although this result applies only at $x_1 = 0$, the deposition rate is greatest at this point and illustrates the general functional dependence on Pe and Re over the entire cylinder.

LOW RE DEPOSITION: COMPARISON OF THEORY WITH EXPERIMENT

Figure 3.3 shows the deposition of 1.305- μm particles on an 8.7- μm fiber as a function of time. The deposition process was probably dominated by direct interception. Although these photos are instructive, a direct experimental test of the theory of particle deposition for aerosol flow around single cylinders is difficult. However, the theory has been used to correlate filtration data for an effective single-fiber removal efficiency, which can be determined by measuring the fraction of particles collected in a bed of fibers. The link between theory and experiment can be made as follows. In a regular array of fibers with uniform diameter, d , and a fraction solids, α , let the average concentration of particles of size, d_p , at a distance, z , from the filter entrance be N (Fig. 3.4). For a single fiber, the removal efficiency is defined as

$$\eta_R = \frac{b}{d} \quad (3.42)$$

where b is the width that corresponds to a region of flow completely cleared of all particles by the cylinder. In a differential distance, dz , in the flow direction, there are $\alpha dz/(\pi d^2/4)$ fibers per unit width normal to the flow direction; the removal over this distance by each fiber is

$$-dN \bigg/ \frac{\alpha dz}{\pi d^2/4} = bN = (\eta_R d)N \quad (3.43)$$

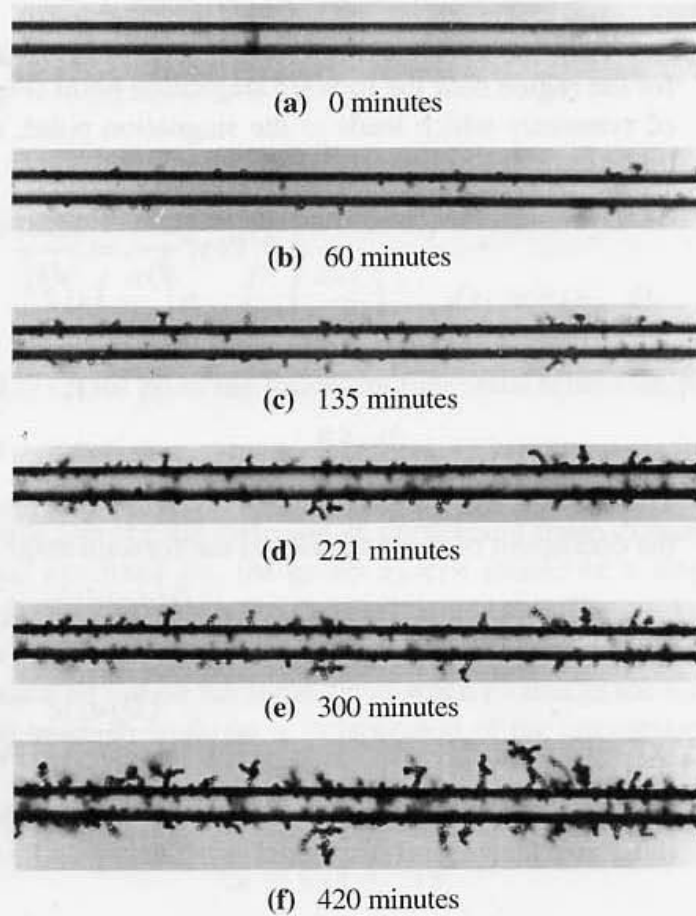


Figure 3.3 Deposits of 1.3- μm polystyrene latex particles on an 8.7- μm glass fiber mounted normal to an aerosol flow and exposed for increasing periods of time. The air velocity was 13.8 cm/sec, and the particle concentration was about 1000 cm^{-3} . Photos by C. E. Billings (1966). The principal mechanism of deposition was probably direct interception. Fractal-like structures develop as the particles deposit.

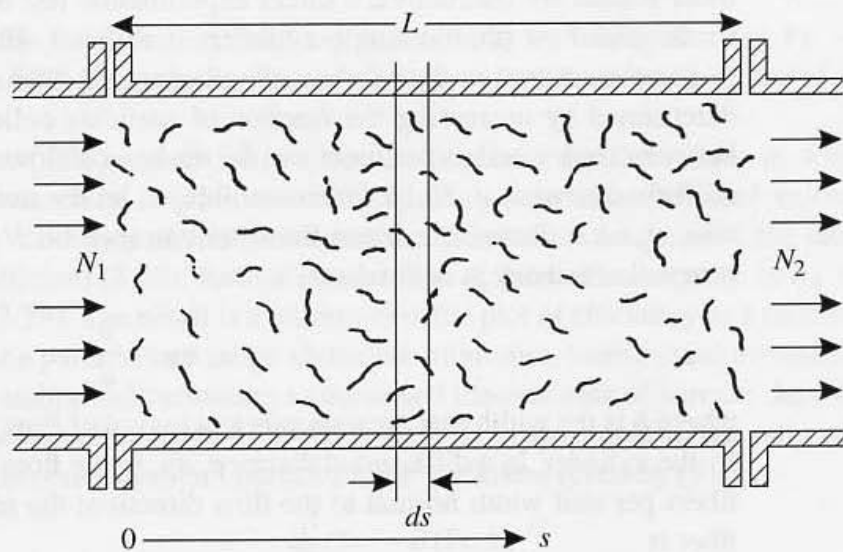


Figure 3.4 Schematic diagram of fibrous filter.

Rearranging and integrating from $z = 0$ to $z = L$, the thickness of the filter is given by

$$\eta_R = \frac{\pi d}{4\alpha L} \ln \frac{N_1}{N_2} \quad (3.44)$$

Because the fiber diameters are usually not all equal and the fibers are arranged in a more or less random fashion, η_R should be interpreted as an effective fiber efficiency that can be calculated from (3.44) and based on an average diameter, \bar{d} , usually the arithmetic average. In an experimental determination of η_R , the practice is to measure N_1 and N_2 , the inlet and outlet concentration of a monodisperse aerosol passed through the filter. The average fiber diameter, \bar{d} , can be determined by microscopic examination.

Chen (1955) and Wong et al. (1956) measured single-fiber efficiencies in experiments with fiber mats and monodisperse liquid aerosols. The filter mats used by both sets of investigators were composed of glass fibers, distributed in size. The data extrapolated to zero fraction solids have been recalculated and plotted in Fig. 3.5 in the form based on the similitude analysis (3.37). The data of Chen covered the ranges $62 < Pe < 2.8 \times 10^4$, $0.06 < R < 0.29$, $1.4 \times 10^{-3} < Re < 7.7 \times 10^{-2}$, and $5.2 \times 10^{-4} < Stk < 0.37$. The Stokes number, $Stk = mU/af$, where m is the particle mass, is a measure of the strength of the inertial effects and must be small for the diffusion-interception theory to apply. For this data set, the analysis was satisfactory for $Stk < 0.37$.

Most of the data fell in the range $10^{-3} < Re < 10^{-1}$, and theoretical curves for the forward stagnation point (3.41b) are shown for the limiting values of the Reynolds number. Rough agreement between experiment and theory is evident. One would expect the experimental data, based on the average deposition over the fiber surface, to fall somewhat below the theoretical curves for the forward stagnation point. This is true over the whole range for Chen's data but not for those of Wong et al.

In later studies, Lee and Liu (1982a,b) used submicron DOP aerosols and dacron fiber filters with $0.035 < d_p < 1.3 \mu\text{m}$, $1 < U < 30 \text{ cm/sec}$ and fiber diameters of 11.0 and 12.9 μm . The dependence of η_R on α was studied systematically, and the data were correlated using the similarity transformation (3.37). As expected from theory, η_R passes through a minimum with increasing particle diameter corresponding to the transition from the diffusional regime (3.38) to removal by direct interception (3.39) (Fig. 3.6). They proposed the following correlation for the single-fiber collection efficiency:

$$\eta_R = 1.6 \frac{Pe^{-2/3}}{(1-\alpha)^{2/3} K^{1/3}} + 0.6 \frac{R^2}{K(1+R)} \quad (3.45)$$

where $K(\alpha) = -\frac{1}{2} \ln \alpha - \frac{3}{4} + \alpha - \frac{1}{4} \alpha^2$ and α is the fraction solids. This has the expected limiting forms for the dependence on Pe and R given by (3.38) and (3.39).

The success of the analysis in correlating experimental data for clean filters offers convincing support for the theory of convective diffusion of particles of finite diameter to surfaces. As particles accumulate in the filter, both the efficiency of removal and the pressure drop increase, and the analysis no longer holds. Some data on this effect are available in the literature. Care must be taken in the practical application of these results because of pinhole leaks in the filters or leaks around the frames.

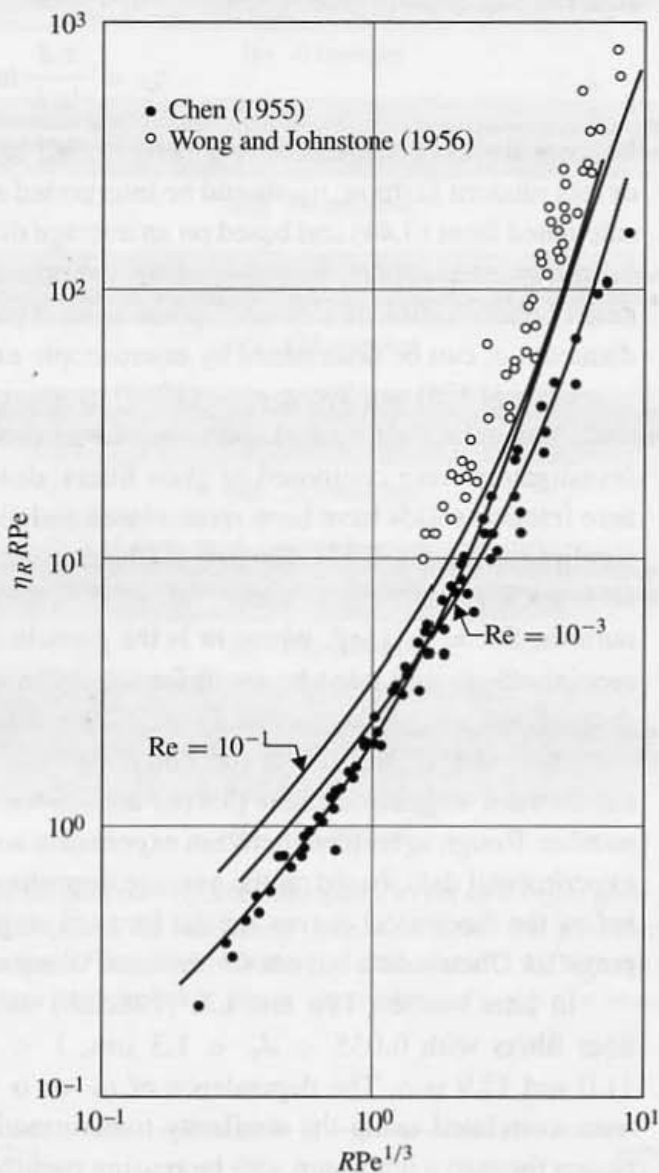


Figure 3.5 Comparison of experimentally observed deposition rates on glass fiber mats for diocetylphthalate (Chen, 1955) and sulfuric acid (Wong et al., 1956) aerosols with theory for the forward stagnation point of single cylinders (Friedlander, 1967). The theoretical curves for $Re = 10^{-1}$ and 10^{-3} were calculated from (3.41b). For all data points the Stokes number was less than 0.5. Agreement with the data of Chen is particularly good. Theory for the forward stagnation point should fall higher than the experimental transfer rates, which are averaged over the fiber surface. The heavy line is an approximate best fit with the correct limiting behavior. The figure supports the use of the similarity transformation (3.37). Similar results have been reported by Lee and Liu (1982a,b). The lower portion of the curve corresponds to the range in which diffusion is controlling and the upper portion corresponds to the direct interception range.

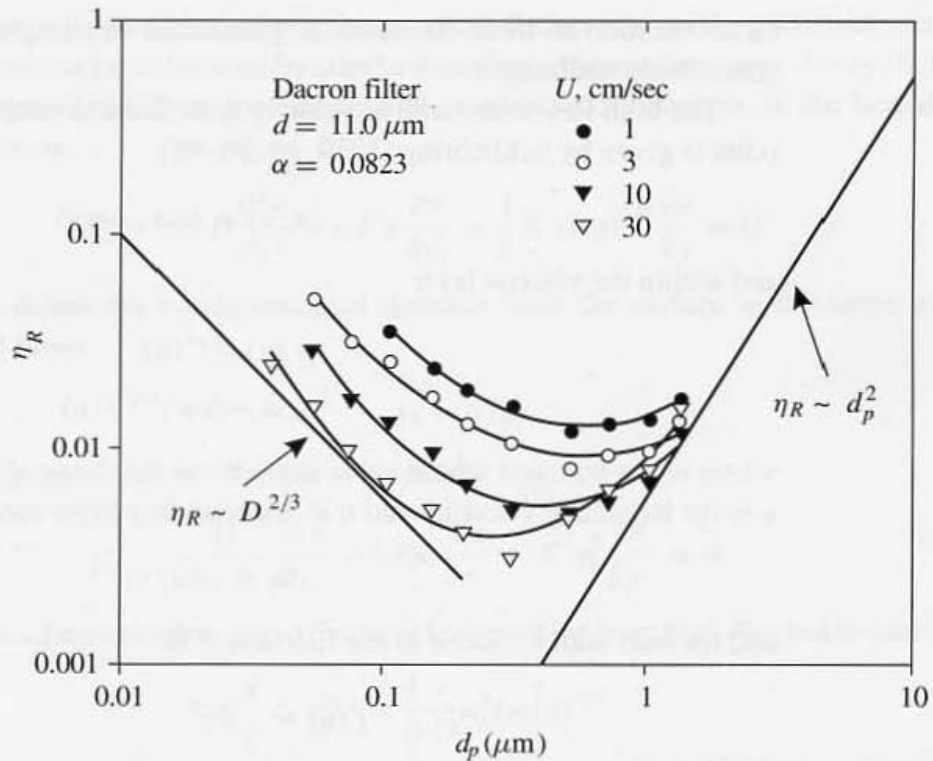


Figure 3.6 Efficiency minimum for single fiber removal efficiency for particles of finite diameter. For very small particles, diffusion controls according to (3.38) and $\eta_R \sim D^{2/3}$. The different curves result from the effects of velocity. In the interception range according to (3.39), $\eta_R \sim d_p^2$, and is practically independent of gas velocity (data of Lee and Liu, 1982a).

SINGLE-ELEMENT PARTICLE CAPTURE BY DIFFUSION AND INTERCEPTION AT HIGH REYNOLDS NUMBERS

An analysis similar to the one for particle deposition from low-speed flows can be made for high Reynolds number flows around blunt objects such as cylinders and spheres (de la Mora and Friedlander, 1982). In this case, an aerodynamic boundary layer develops around the object. Within the aerodynamic boundary layer, a thin concentration boundary layer lies near the surface. The analysis takes into account both diffusion and direct interception—that is, the finite diameter of the particles. The results are important for particle deposition to either (a) cylinders with diameters much larger than those that compose high-efficiency filters, such as coarse wire filters or meshes, or (b) heat exchanger tubes perpendicular to an aerosol flow. Another important application is to deposition from the atmosphere (*dry deposition*) to the Earth's surface which is aerodynamically rough (Monin and Yaglom, 1971). The individual roughness elements such as grass blades and gravel can be treated as collecting elements as discussed in the following section and Chapter 13.

For simplicity we choose a two-dimensional geometry corresponding to the flow normal to a bluff body of arbitrary shape. The origin of coordinates is taken at the stagnation point, and the y axis is normal to the surface at every point, y being zero at the surface.

Generalization to three-dimensional geometries is straightforward, and leaves the main conclusions unchanged.

The high Reynolds number velocity field in the inviscid region close to the stagnation point is given by Schlichting (1979, pp. 96–98)

$$(u, v) = (\omega x, -\omega y) \quad (3.46)$$

and within the viscous layer

$$u = \omega x f'(\eta) \quad (3.47a)$$

$$v = -(v\omega)^{1/2} f(\eta) \quad (3.47b)$$

where ω is a constant whose value depends on the shape of the object (ribbon or cylinder), v is the kinematic viscosity and η is the boundary layer coordinate

$$\eta = y(\omega/v)^{1/2} \quad (3.48)$$

and the near wall behavior of the function f is

$$f(\eta) = \frac{1}{2}\beta\eta^2 \quad (3.49a)$$

$$\eta \ll 1$$

$$f'(\eta) = \beta\eta \quad (3.49b)$$

with

$$\beta = f''(0) = 1.2326 \quad (3.50)$$

Therefore, sufficiently close to the stagnation point

$$u = \omega x \beta \eta \quad (3.51a)$$

$$v = -\frac{1}{2}(v\omega)^{1/2} \beta \eta^2 \quad (3.51b)$$

In the region close to the wall, provided the flow has not separated and before transition to turbulence, (3.51a) and (3.51b) can be generalized away from the stagnation point as follows

$$u = \omega a K(x_1) \eta \quad (3.52a)$$

$$v = -\frac{1}{2}(v\omega)^{1/2} K'(x_1) \eta^2 \quad (3.52b)$$

where we have nondimensionalized x with the obstacle characteristic length a as in the analysis for low-speed flows

$$x_1 = x/a \quad (3.53)$$

and also

$$K' = \frac{dK}{dx_1} \quad (3.54)$$

For large Reynolds numbers, the function K depends on the particular shape of the obstacle and can be calculated by standard methods of boundary layer theory (Schlichting, 1979, Chapter IX). Then, the equation of convective diffusion is, in the boundary layer approximation,

$$-D \frac{\partial^2 n}{\partial y^2} + \omega K \eta \frac{\partial n}{\partial x_1} - \frac{1}{2} K' (v\omega)^{1/2} \frac{\partial n}{\partial y} = 0 \quad (3.55)$$

When we define the nondimensional distance from the surface in the same way as for low-speed flows

$$y_1 = y/a_p \quad (3.56)$$

(3.55) becomes

$$\frac{\Pi^{-3}}{3} \frac{\partial^2 n}{\partial y_1^2} - 2Ky_1 \frac{\partial n}{\partial x_1} + K'y_1^2 \frac{\partial n}{\partial y_1} = 0 \quad (3.57)$$

where Π is a dimensionless group for particle deposition from high-Reynolds-number flows:

$$\Pi^3 = \frac{1}{6} \frac{v}{D} a_p^3 (\omega/v)^{3/2} \quad (3.58)$$

This equation must be solved with the diffusion-interception boundary conditions

$$n = n_\infty \quad \text{for } y_1 \rightarrow \infty \quad (3.59a)$$

$$n = 0 \quad \text{at } y_1 = 1 \quad (3.59b)$$

The solution for any given obstacle [$K(x_1)$ fixed] is

$$n/n_\infty = F(x_1, y_1, \Pi) \quad (3.60)$$

and by (3.36) and (3.37)

$$\eta_R RPe = \frac{k_{av} a_p}{D} = F_2(\Pi) \quad (3.61)$$

where η_R is the removal efficiency for a single cylinder. Also, the Reynolds number in this case is

$$Re \sim \omega a^2 / \nu \quad (3.62)$$

Substitution in (3.58) gives

$$\Pi \sim RPe^{1/3} Re^{1/6} \quad (3.63)$$

where $R = a_p/a$. The parameter Π is related to the corresponding low-Reynolds-number parameter

$$\Pi_{Re < 1} = R(PeA)^{1/3} \quad (3.64)$$

through the weakly varying function of the Reynolds number $Re^{1/6}/A$:

$$\Pi_{Re \gg 1} / \Pi_{Re < 1} \sim Re^{1/6} / A \quad (3.65)$$

As in the case of low-Reynolds-number flows (3.34), the corresponding dimensionless group for high Reynolds numbers (velocity boundary layers) is related to the ratio of the particle diameter to the concentration boundary layer thickness

$$d_p/\delta_c \sim RPe^{1/3}Re^{1/6}$$

For $d_p/\delta_c \ll 1$, deposition is diffusion controlled; for $d_p/\delta_c \gg 1$, interception controls. Approximate expressions for the removal efficiencies of single cylinders and spheres based on this analysis have been given by Parnas and Friedlander (1984). For cylinders

$$\eta_R = 1.88Re^{1/6}Pe^{-2/3} + 0.80R^2Re^{1/2} \quad (3.66)$$

and for spheres

$$\eta_R = 2.40Re^{1/6}Pe^{-2/3} + 1.10R^2Re^{1/2} \quad (3.67)$$

The recommended range of application is $10^2 < Re < 10^4$, and Stokes numbers less than the critical values for impaction, 1/8 and 1/12 for cylinders and spheres, respectively (Chapter 4).

HIGH RE DEPOSITION: APPLICATION TO DEPOSITION ON ROUGH SURFACES

The results of the high-Reynolds-number analysis discussed in the previous section have not been directly tested for flows over single cylinders. However, they have been applied to the substantial body of experimental data from wind tunnel experiments on the deposition of particles from gases to rough surfaces composed of grass blades, gravel, and similar roughness elements. The data were collected for application to atmospheric dry deposition. Much of the area available for mass transport to the walls covered with closely packed roughness elements is not near the bottom surface that anchors the roughness elements, but at the protrusions themselves. Because the convective motion is much more intense around them than further down in the roughness layer, a large fraction of the transfer of matter (gas molecules or particles) would be expected to occur at the roughness elements. Accordingly, they may be viewed as mass "sinks" volumetrically distributed within the flow field, and the transport process can be modeled as in gas filtration discussed in previous sections. With this idea in mind, de la Mora and Friedlander (1982) correlated the data of Chamberlain (1966) on particle deposition from flows over the blades composing an artificial grass using (3.61) and plotting $k_{av}a_p/D$ versus $RPe^{1/3}Re^{1/6}$ as shown in Fig. 3.7. The measured deposition velocity v_d was used in place of k_{av} .

In applying the analysis of the previous section, it was necessary to assume a value for the coefficient ω that appears in (3.46) for the inviscid flow on an individual roughness element:

$$\omega = bU_\infty/a \quad (3.68)$$

where the dimensionless constant b depends on the body geometry, U_∞ is the free stream velocity, and a is a characteristic length of the collector. In Fig. 3.7, $b = 2$, corresponding

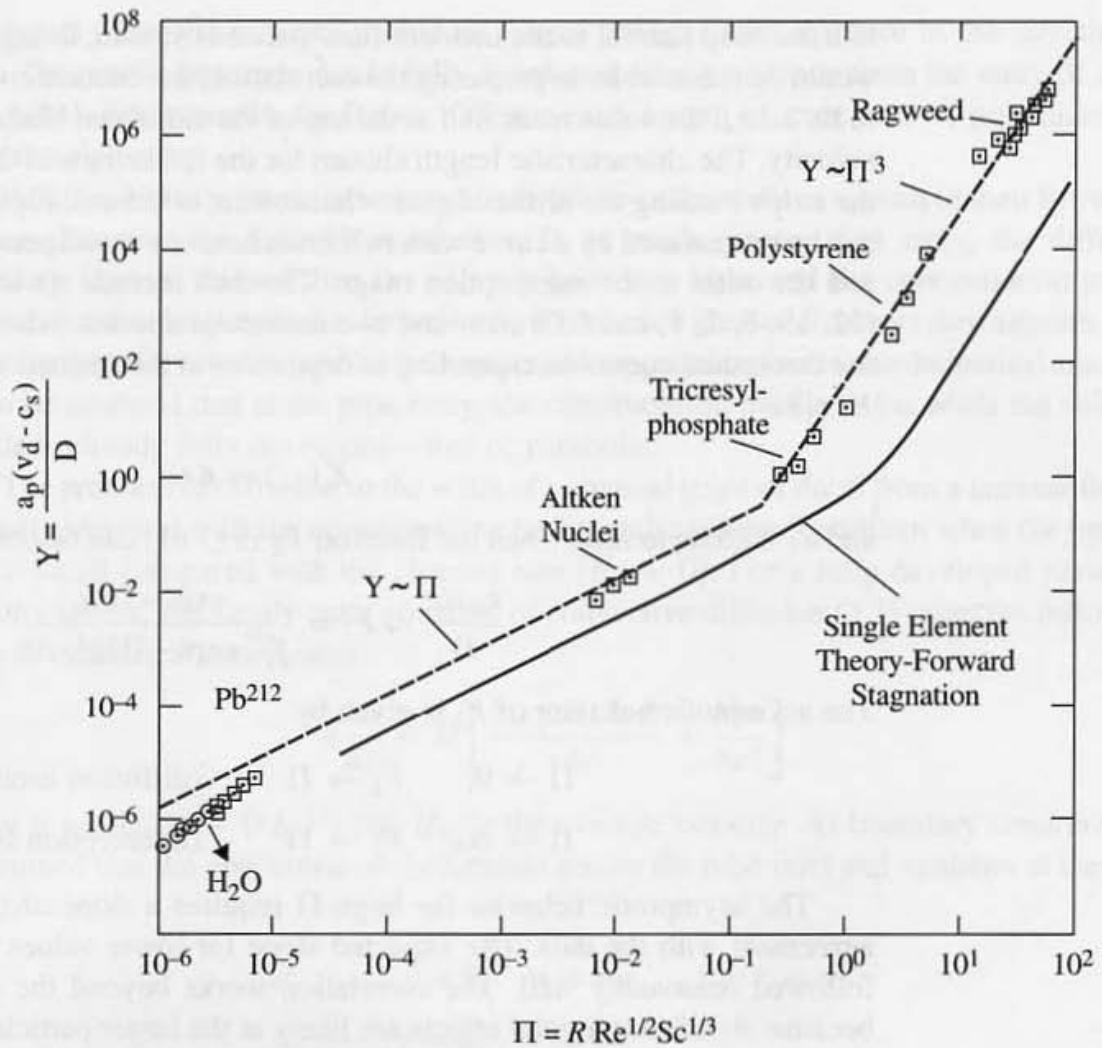


Figure 3.7 Nondimensional particle deposition velocity to artificial grass as a function of the deposition parameter (3.63). Data from Chamberlain (1966), corrected for gravitational settling. Two broken lines (---) with slopes 3 and 1 (corresponding to the interception and diffusion asymptotic regions) are drawn through the data. The solid line (—) shows the single element collection efficiency at the stagnation point of an infinite strip normal to the unseparated potential flow. The data fall significantly higher than the theory for the single element perhaps because of the effects of the neighboring blades present in the wind tunnel measurements. (After de la Mora and Friedlander, 1982.)

This figure supports the hypothesis that deposition to rough surfaces (including atmospheric dry deposition) is a filtration-type process with the roughness elements serving as particle collectors. The measurements were made with roughness elements composed of artificial (teflon) grass blades of the same size and shape. Data for roughness elements of other types including gravel have been correlated in a similar manner by Schack et al. (1985).

to a flat strip normal to the incident (unseparated) stream, though any value of order unity would be reasonable. In preparing the correlation, the characteristic velocity U_∞ was taken to be $2.3u_*$, the value measured at the top of the simulated blades, where u_* is the friction velocity. The characteristic length chosen for the collector was the transverse dimension of the strips forming the artificial grass elements, $a = 0.5$ cm. Figure 3.7 shows that the data can be represented by a curve with two branches, one corresponding to the diffusion range and the other to the interception range. The data include six different particle diameters (32, 19, 5, 2, 1, and $0.08 \mu\text{m}$) and two molecular species. Also shown for comparison is the theoretical curve corresponding to deposition at the stagnation point where the function $K(x_1)$ is

$$K(x_1) = \beta x_1 \quad (3.69)$$

and x_1 is close to zero. Then the function F_2 in (3.61) can be obtained analytically to yield

$$\frac{k_{av} a_p}{D} = F_2 = \frac{\exp(-\Pi^3)}{\int_1^\infty \exp(-\Pi^3 \xi^3) d\xi} \quad (3.70)$$

The asymptotic behavior of F_2 is given by

$$\Pi \rightarrow 0, \quad F_2 \rightarrow \Pi \quad (\text{diffusion limit}) \quad (3.71a)$$

$$\Pi \rightarrow \infty, \quad F_2 \rightarrow \Pi^3 \quad (\text{interception limit}) \quad (3.71b)$$

The asymptotic behavior for large Π requires a slope of three on a log-log plot, in agreement with the data. The expected slope for lower values of Π is unity; this is also followed reasonably well. The correlation works beyond the expected limit of validity because significant inertial effects are likely at the larger particle sizes.

As in the case of low-Reynolds-number flows, the individual element removal efficiency passes through a minimum as particle size increases from the small submicron range to the micron sizes. However, for dry deposition from the atmosphere, collecting objects (grass blades, other vegetation, rocks, etc.) come in various sizes and shapes; this probably results in a broad minimum with respect to particle size compared to the case for uniform collectors.

DIFFUSION FROM A LAMINAR PIPE FLOW

In this section and the next, we discuss particle deposition by diffusion from laminar and turbulent flows through a smooth-walled pipe. The particle diameter is assumed to be much smaller than the tube diameter (or viscous sublayer thickness for turbulent flow), so the interception parameter that was important in the previous discussions does not play a role.

When a gas enters a smooth pipe from a large reservoir through a well-faired entry, a laminar boundary layer forms along the walls. The velocity profile in the main body of the flow remains flat. The velocity boundary layer thickens with distance downstream from the entry until it eventually fills the pipe. If the Reynolds number based on pipe diameter is less than 2100, the pipe boundary layer remains laminar. The flow is said to be fully

developed when the velocity profile no longer changes with distance in the direction of flow. The profile becomes nearly fully developed after a distance from the entry of about $0.04d(\text{Re})$. For example, for $\text{Re} = 1000$ the entry length extends over 40 pipe diameters from the pipe entry.

Small particles present in the gas stream diffuse to the walls as a result of their Brownian motion. Because the Schmidt number, ν/D , is much greater than unity, the diffusion boundary layer is thinner than the velocity boundary layer and the concentration profile tends to remain flat perpendicular to the flow for much greater distances downstream from the entry than the velocity profile. As a reasonable approximation for mathematical analysis, it can be assumed that at the pipe entry, the concentration profile is flat while the velocity profile is already fully developed—that is, parabolic.

The problem of diffusion to the walls of a channel (pipe or duct) from a laminar flow is formally identical with the corresponding heat transfer (Graetz) problem when the particle size is small compared with the channel size ($R \rightarrow 0$). For a fully developed parabolic velocity profile, the steady-state equation of convective diffusion (3.1) takes the following form in cylindrical coordinates:

$$u \frac{\partial n}{\partial x} = D \left[\frac{\partial(r(\partial n/\partial r))}{r \partial r} + \frac{\partial^2 n}{\partial x^2} \right] \quad (3.72)$$

where $u = 2U_{\text{av}}[1 - (r/a)^2]$ and U_{av} is the average velocity. As boundary conditions, it is assumed that the concentration is constant across the tube inlet and vanishes at the pipe wall, $r = a$:

$$\begin{aligned} \text{at } x = 0, \quad n = n_1 \quad \text{for } r < a \\ r = a, \quad n = 0 \end{aligned} \quad (3.73)$$

When $\text{Pe} > 100$, diffusion in the axial direction can be neglected. Solutions to this expression with these boundary conditions have been given by many investigators, and the analysis will not be repeated here. For short distances from the tube inlet, a concentration boundary layer develops for the particle distribution. An analytical solution to the equation of convective diffusion gives the following expression for the fraction of the particles passing through a tube of length L without depositing:

$$P = \frac{n_2}{n_1} = 1 - 2.56\Pi^{2/3} + 1.2\Pi + 0.1767\Pi^{4/3} + \dots \quad (3.74)$$

with $\Pi = \pi DL/Q < 0.02$ where Q is the volumetric flow of air through the tube. At long distances from the tube inlet, the fraction penetrating is obtained by solving (3.72) using separation of variables:

$$\begin{aligned} P = \frac{n_2}{n_1} = 0.819 \exp(-3.66\Pi) + 0.0975 \exp(22.3\Pi) \\ + 0.0325 \exp(-57.0\Pi) + \dots \end{aligned} \quad (3.75)$$

for $\Pi > 0.02$. Original references for these results and the corresponding expressions for flow between flat plates are given by Cheng (1993).

These results can be applied to deposition in sampling tubes and to the design of the diffusion battery, a device used to measure the particle size of submicron aerosols. The

battery may consist of a bundle of capillary tubes, or of a set of closely spaced, parallel flat plates, through which the aerosol passes in laminar flow. The particle concentrations entering and leaving the diffusion battery are measured with a condensation particle counter. From the measured value of the reduction in concentration, the value of Π can be determined from (3.74) or (3.75) or their equivalent for flat plates. The value of D , hence d_p , can be calculated because x , a , and U are known for the system. For polydisperse aerosols, the usual case, the method yields an average particle diameter that depends on the particle size distribution. The theory also has application to efficiency calculations for certain classes of filters (Spurny et al., 1969) composed of a sheet of polymeric material penetrated by many small cylindrical pores.

DIFFUSION FROM A TURBULENT PIPE FLOW

When the pipe Reynolds number is greater than about 2100, the velocity boundary layer that forms in the entry region eventually turns turbulent as the gas passes down the pipe. The velocity profile becomes fully developed; that is, the shape of the distribution ceases to change at about 25 to 50 pipe diameters from the entry. Small particles in such a flow are transported by turbulent and Brownian diffusion to the wall. In the sampling of atmospheric air through long pipes, wall losses result from turbulent diffusion. Accumulated layers of particles will affect heat transfer between the gas and pipe walls.

In analyzing turbulent transport, it is convenient to divide the pipe flow into three different zones along a distance perpendicular to the wall (Fig. 3.8). The core of the pipe is a highly turbulent region in which molecular diffusion is negligible compared with transport by the turbulent eddies. Closer to the wall there is a transition region where both molecular and eddy diffusion are important. Next to the wall itself, there is a thin sublayer in which the transfer of *momentum* is dominated by viscous forces, and the effect of weak turbulent fluctuations can be neglected. This applies also to heat and mass transfer for gases; the Schmidt and Prandtl number are near unity, which means that heat and mass are transported at about the same rates as momentum.

The situation is quite different for particle diffusion. In this case, $\nu/D \gg 1$ and even weak fluctuations in the viscous sublayer contribute significantly to transport. Consider a turbulent pipe flow. In the regions near the wall, the curvature can be neglected and the instantaneous particle flux can be written as follows:

$$J_y = -D \frac{\partial n}{\partial y} + nv \quad (3.76)$$

where y is the distance measured normal to the surface and v is the velocity in the y direction.

In analyzing turbulent pipe flows, it is assumed that the velocity and the concentration can be separated into mean and fluctuating components:

$$v = \bar{v} + v' \quad (\text{because } \bar{v}' = 0) \quad (3.77a)$$

and

$$n = \bar{n} + n' \quad (3.77b)$$

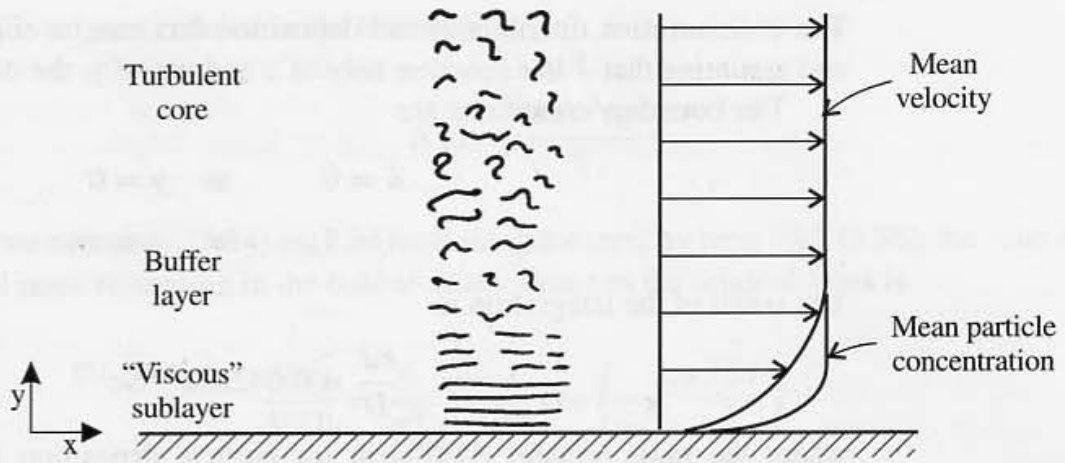


Figure 3.8 Schematic diagram showing the structure of turbulent pipe flow. For convenience, the flow is divided into three regions. Most of the pipe is filled with the turbulent core, with the velocity rising rapidly over the viscous sublayer. The concentration drops more sharply than the velocity because $D \ll \nu$ and turbulent diffusion brings the particles close to the wall before Brownian diffusion can act effectively.

where the bar and prime refer to the mean and fluctuating quantities, respectively. Substituting in (3.76) and taking the time average gives

$$\bar{J} = -D \frac{\partial \bar{n}}{\partial y} + \overline{n'v'} \quad (3.78)$$

The eddy diffusion coefficient, ϵ , is defined by

$$\overline{n'v'} = -\epsilon \frac{\partial \bar{n}}{\partial y} \quad (3.79)$$

Based on experimental data for diffusion controlled electrochemical reactions in aqueous solution, the following expression was proposed by Lin et al. (1953) for the eddy diffusion coefficient in the viscous sublayer:

$$\epsilon = \nu \left(\frac{y^+}{14.5} \right)^3 \quad (3.80)$$

where $y^+ = [yU(f/2)^{1/2}]/\nu$, with U the average velocity, f the Fanning friction factor, and ν the kinematic viscosity. This expression for ϵ holds when $y^+ < 5$. A similar form was found by analyzing the results of a variety of measurements by other investigators (Monin and Yaglom, 1971).

Substituting (3.79) in (3.78), the general expression for the diffusion flux is

$$\bar{J} = -(D + \epsilon) \frac{\partial \bar{n}}{\partial y} \quad (3.81)$$

For particle diffusion, $\nu/D \gg 1$. Compared with momentum transfer, particles penetrate closer to the wall by turbulent diffusion before Brownian diffusion becomes important. The particle concentration, which vanishes at the wall, rises rapidly practically reaching the mainstream concentration, \bar{n}_∞ , within the viscous sublayer in which ϵ is given by (3.80).

The concentration distribution and deposition flux can be obtained by integrating (3.81) and assuming that \bar{J} is a function only of x and not of y , the distance from the surface.

The boundary conditions are

$$\bar{n} = 0 \quad \text{at } y = 0 \quad (3.81a)$$

$$\bar{n} = \bar{n}_\infty \quad \text{at } y = \infty \quad (3.81b)$$

The result of the integration is

$$\frac{kd}{D} = 0.042\text{Re}f^{1/2}\text{Sc}^{1/3} \quad (3.82)$$

where the mass transfer coefficient (or particle deposition velocity) is defined by the relationship $k = -(D/\bar{n}_\infty)(\partial\bar{n}/\partial y)_{y=0}$. This result holds for a *smooth-walled* tube. Higher values would be expected for rough surfaces—for example, when particle layers have already accumulated. This will be important in electrostatic precipitation as discussed below.

PARTICLE DEPOSITION FROM RISING BUBBLES

When an aerosol bubble rises through a liquid, submicron particles diffuse to the gas/liquid interface where they deposit. However, this is usually not a very effective way of gas cleaning for several reasons as explained in the following discussion. Bubbles smaller than about 0.01 cm behave like rigid spheres and follow Stokes law as they rise with Reynolds numbers less than 1. Larger bubbles remain spherical but the resistance to their motion is higher than predicted by Stokes law. As the Reynolds numbers increase to about 500, corresponding to bubble diameters of about 1 mm, the bubbles begin to deform, acquiring the shape of an oblate ellipsoid. The path of bubble rise ceases to be rectilinear and becomes spiral. The resistance law for spherical-bubble rise follows that of a solid sphere; under normal circumstances, bubble surfaces become contaminated by substances dissolved in the liquid which migrate to the high free energy interface. The presence of contaminants tends to stabilize the interface, preventing relative motion and suppressing internal circulation in the bubble. For a noncirculating bubble, the rate of aerosol deposition can be calculated from well-known solutions to the diffusion equation with spherical symmetry:

$$\frac{\partial n}{\partial t} = \frac{\partial Dr^2 \frac{\partial n}{\partial r}}{r^2 \partial r} \quad (3.83)$$

The aerosol concentration in the bubble at the time $t = 0$ is uniform and has the value $n = n_0$. For $t > 0$, $n = 0$ at the bubble surface $r = a$. The appropriate solution to the diffusion equation is (Carslaw and Jaeger, 1959)

$$n(r, t) = \frac{2an_0}{\pi r} \sum_{p=1}^{\infty} \frac{(-1)^{p+1}}{p} \exp\left(-p^2 \frac{\pi^2 Dt}{a^2}\right) \sin \frac{p\pi r}{a} \quad (3.84)$$

The total number of particles in the bubble at time t is obtained by integrating over r :

$$N(t) = \int_0^a n 4\pi r^3 dr \quad (3.85)$$

while the original number in the bubble is

$$N(0) = \frac{4\pi a^3 n_0}{3} \quad (3.86)$$

When we substitute (3.84) in (3.85) and integrate term by term with (3.86), the ratio of the aerosol mass remaining in the bubble at any time t to the original mass is

$$\frac{N(t)}{N(0)} = \frac{6}{\pi^2} \sum_{p=1}^{\infty} \frac{1}{p^2} \exp\left(-p^2 \frac{\pi^2 Dt}{a^2}\right) \quad (3.87)$$

The time for the concentration to fall to $1/e$ of its original value is $\tau_d = 0.05a^2/D$. The center and average concentrations for bubbles are shown in Fig. 3.9.

If special precautions are taken to avoid contamination of the bubble surface, particle deposition by diffusion to the water surface is enhanced by internal circulation. The internal flow can be calculated for very low bubble Reynolds numbers in the creeping flow approximation (Lamb, 1953). A solution has been obtained to the equation of convective

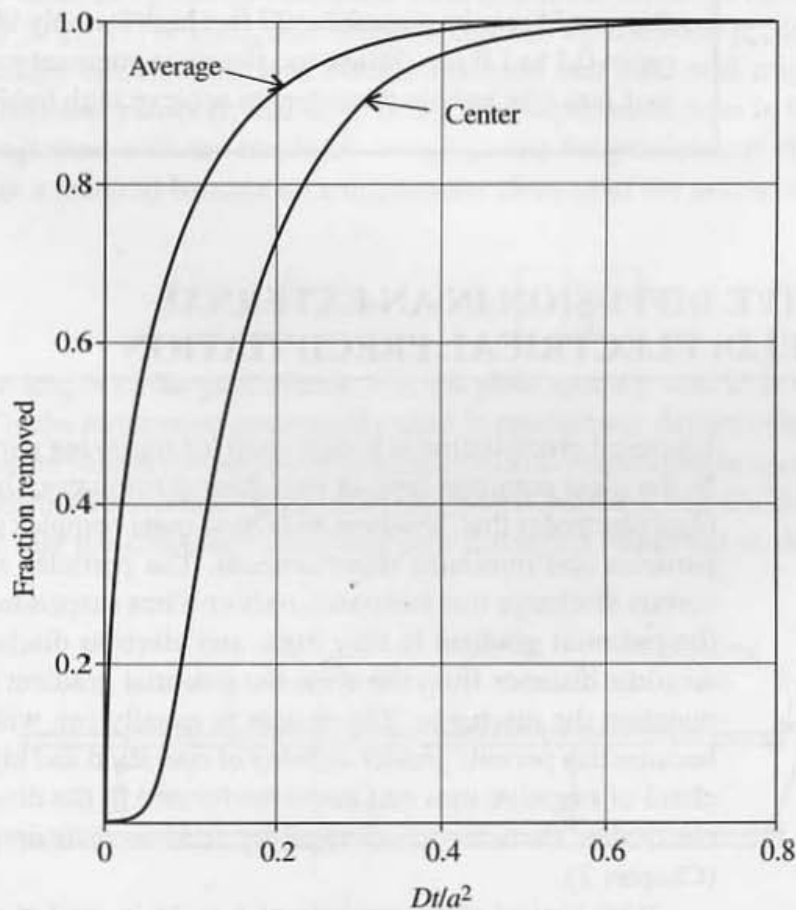


Figure 3.9 Fraction of particles removed from a bubble at center and on average. Initial particle number in bubble $N(0)$, bubble surface concentration zero. Case of noncirculating bubble (3.87).

diffusion in which the streamlines for the internal circulation correspond to surfaces of constant concentration inside the bubble. In this way, the equation of convective diffusion is reduced to a form similar to the unsteady diffusion equation without flow. The solution for the residual number of particles in the bubble is (Kronig and Brink, 1950)

$$\frac{N(t)}{N(0)} = \frac{3}{8} \sum_{p=1}^{\infty} A_p^2 \exp\left(-\mu_p \frac{16Dt}{a^2}\right) \quad (3.88)$$

where $\mu_1 = 1.678$, $\mu_2 = 9.83$, and $A_1 = 1.32$, $A_2 = 0.73$. The time for the aerosol concentration in the bubble to fall to $1/e$ of its original value is $\tau'_d = 0.022a^2/D$ —that is, 40% of the value for the case of the noncirculating bubble.

Example: A 1-mm bubble carrying submicron aerosol particles rises through a column of water at 25°C. How high must the column be to remove 90% of the 0.1- μm particles? The velocity of rise of a 1-mm bubble that behaves like a rigid sphere is about 10 cm/sec. Assume the aerosol in the bubble is initially uniformly mixed.

SOLUTION: From Fig. 3.9, $Dt/a^2 = 0.18$ for 90% removal. Hence $t = 0.18(25 \times 10^{-4})/6.75 \times 10^{-6} = 67$ sec. With a bubble rise velocity of 10 cm/sec, this would require a scrubber 22 feet high for only 90% removal; particles in the size range 0.1 to 1.0 μm diffuse too slowly in stagnant gases even over distances as small as 1 mm (the bubble diameter) to achieve high bubbler removal efficiencies.

CONVECTIVE DIFFUSION IN AN EXTERNAL FORCE FIELD: ELECTRICAL PRECIPITATION

Electrical precipitation is widely used for removing particles from power plant stack gases. In the most common type of industrial precipitator, the dusty gas flows between parallel plate electrodes that, however, may have quite complex geometries to help trap the deposited particles and minimize reentrainment. The particles are charged by ions generated in a corona discharge that surrounds rods or wires suspended between the plates. Near the wire, the potential gradient is very high, and electron discharge and gas ionization take place. At some distance from the wire, the potential gradient drops below the value necessary to maintain the discharge. The system is usually run with the discharge electrode negative, because this permits greater stability of operation and higher voltage before breakdown. The cloud of negative ions and electrons formed in the discharge moves toward the collecting electrodes. Particles are charged by field or diffusion charging depending on their size (Chapter 2).

With typical plate spacings of 6 to 15 in. and gas velocities of 3 to 10 ft/sec, corresponding to Reynolds numbers of 10^4 and greater, precipitator flows are turbulent. The instantaneous particle flux in the direction normal to the collecting plate is

$$J = -D \frac{\partial n}{\partial y} + vn - c_e n \quad (3.89)$$

where c_e is a positive quantity for migration toward the plate. Taking the time average and substituting (3.79) gives

$$\bar{J} = -(D + \epsilon) \frac{\partial \bar{n}}{\partial y} - c_e \bar{n} \quad (3.90)$$

The electrical migration velocity, assumed constant to simplify the analysis, actually varies because it depends on the field strength, which is a function of position, and on the charging time (Chapter 2). We next assume that \bar{n} increases from zero on the collector surface to \bar{n}_∞ , the mainstream concentration, over a narrow region near the surface. For a given value of x in the direction of flow, the flux \bar{J} can be assumed constant over the wall region, and (3.90) can be integrated to give

$$\bar{J}(x) = \frac{-c_e \bar{n}_\infty}{1 - \exp \left\{ -c_e \int_0^\infty dy / (D + \epsilon) \right\}} \quad (3.91)$$

The particle flux is negative for deposition on the surface. The integral $v_d = [\int_0^\infty dy / (D + \epsilon)]$ represents a particle migration velocity resulting from combined Brownian and turbulent diffusion. The value of v_d can be calculated from (3.82) for turbulent flow over a smooth surface. For $v_d \gg c_e$, $|\bar{J}| = v_d \bar{n}_\infty$ and diffusion controls the transport process. In electrical precipitator design calculations, it is usually assumed that electrical migration is much faster than diffusional transport; that is, $c_e \gg v_d$. The exponential term in the denominator can then be neglected with the result $|\bar{J}| = c_e \bar{n}_\infty$, and the precipitator efficiency can be calculated from a material balance on a differential element of the precipitator (Fig. 3.10). The result is

$$\frac{(\bar{n}_{\infty 1} - \bar{n}_{\infty 2})}{\bar{n}_{\infty 1}} = 1 - \exp \left[\frac{-2c_e L}{Ub} \right] \quad (3.92)$$

where L is the length of the precipitator, b is the plate spacing, and U is the average gas velocity. This is the expression customarily used in precipitator design calculations.

The migration velocity passes through a minimum corresponding to a particle size in the transition region between diffusion and field charging (Chapter 2, Fig. 6). By differentiating (3.92), we see that the efficiency must also pass through a minimum at the same particle

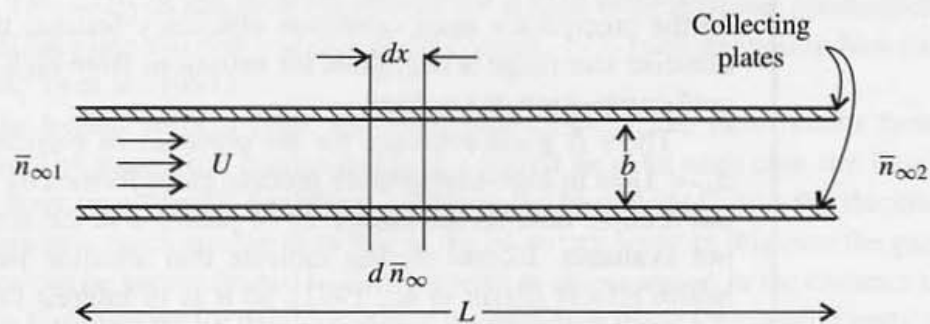


Figure 3.10 Material balance on an element of precipitator $-Ubd\bar{n}_\infty = 2\bar{n}_\infty c_e dx$.

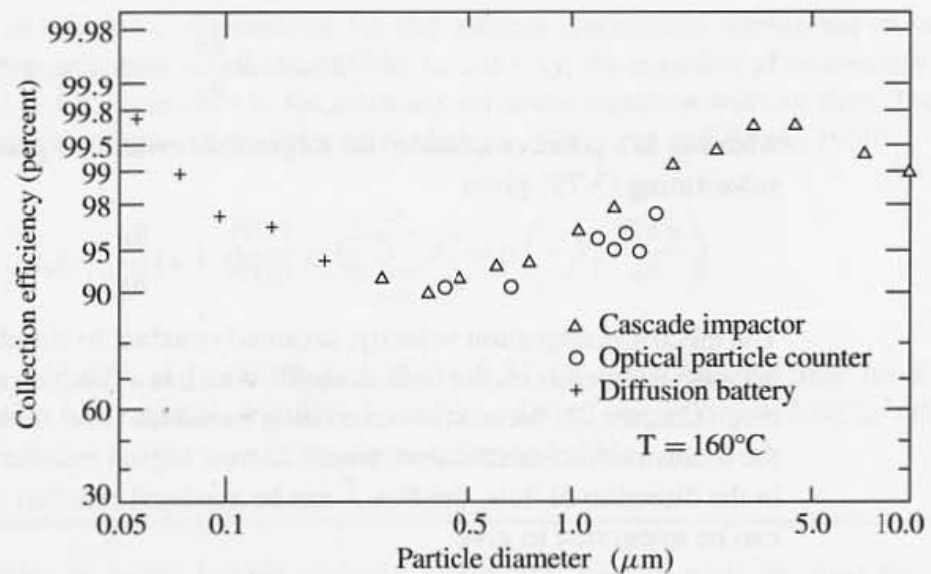


Figure 3.11 Efficiency as a function of particle size for a pilot-scale electrical precipitator treating a side stream of flue gas from a utility boiler burning a low-sulfur coal (McCain et al., 1975). The minimum near $0.5 \mu\text{m}$ probably results from the transition from diffusion to field charging. The decrease in efficiency for particles larger than $3 \mu\text{m}$ may result from reentrainment.

diameter. Indeed, a minimum has been observed experimentally in studies with a plant-scale precipitator (Fig. 3.11), in the particle size range corresponding to the minimum in the migration velocity.

In practice, it is not possible to make accurate calculations of c_e from first principles because of the complexity of the interaction between the particles and the corona discharge. The mechanical and electrical behavior of the deposited dust layer are also difficult to characterize. Thus theory provides guidelines for precipitator design but in practice, design is based to a great extent on empiricism.

Example: For particles smaller than about 50 nm ($0.05 \mu\text{m}$) the fraction of charged particles decreases sharply (Chapter 2). Discuss the effect of the fall-off in particle charging on precipitator collection efficiency.

SOLUTION: The reduction in charging efficiency will have a negligible effect on the precipitator *mass* collection efficiency because the mass of particles in the ultrafine size range is negligible for emissions from high-temperature processes like coal combustion or smelting.

There is good evidence for the presence of particles in the size range $0.1 < d_p < 1 \mu\text{m}$ in high-temperature process gases formed by gas-to-particle conversion, but reliable data on the emissions of particles in the size range below 100 nm are not available. Recent studies indicate that ultrafine particles may cause adverse health effects (Ferri et al., 1992), so it is of interest to estimate their penetration through electrostatic precipitators to see whether field studies of emissions from such installations are warranted.

If electrostatic forces fail for uncharged ultrafine particles, there are at least two other possible removal mechanisms. Ultrafine particles can diffuse to the collecting plates or can coagulate with charged coarser particles that then deposit. Coagulation is discussed in Chapter 7. The other mechanism, diffusional transport, appears with electrostatic precipitation in the combined flux expression (3.91), which, for $v_d \gg c_e$, reduces to $|J| = v_d \bar{n}_\infty$.

Estimating the diffusional deposition velocity v_d for precipitator flows is very difficult. Given the complex structure of the plates and the accumulated dust load, it is reasonable to assume that the flow is completely rough, aerodynamically (Monin and Yaglom, 1971). Then the particle transport process is of the type studied in the wind tunnel experiments of Chamberlain (1966) for application to dry deposition from the atmosphere and also discussed earlier in this chapter. Suppose the aerodynamics for the flow between a given set of plates is equivalent to flow over the natural and artificial grass blades used in Chamberlain's experiments discussed above. In these experiments, the measured deposition velocities for $0.08 \mu\text{m}$ (80 nm) particles fall in the range 0.02 to 0.08 cm/sec for friction velocities in the range 35 to 140 cm/sec. These values are significantly smaller than electrical migration velocities which generally fall in the range 1 to 10 cm/sec for charged particles in electrical precipitators. Because the collection efficiency for ultrafine particles may be significantly less than that of the charged particles, we conclude that field measurements of nanoparticle emissions from electrostatic precipitators are warranted.

THERMOPHORESIS: "DUST-FREE SPACE"

When a heated body such as a horizontal cylinder or a vertical plate is placed in a chamber containing an aerosol and suitably illuminated, a region apparently free of particles appears around the body (Watson, 1936). This "dust-free space" develops as a result of the balance between the gas flow carrying particles toward the surface and the thermophoretic force driving particles away. The thickness of the dust-free space can be estimated by equating the drag force carrying the particles toward the wall to the thermophoretic force in the opposite direction. This analysis has been carried out for at least three different geometries, namely the vertical flat plate and horizontal cylinder (Zernik, 1957) and stagnation flow (Stratmann et al., 1988; Ye et al., 1991).

For the heated vertical plate and horizontal cylinder, the flow results from natural convection. The stagnation configuration is a forced flow. In each case the flow is of the boundary layer type. Simple analytical solutions can be obtained when the thickness of the dust-free space is much smaller than that of the boundary layer. In this case the gas velocity distribution can be approximated by the first term in an expansion in the distance normal to the surface. Expressions for the thickness of the dust-free space for a heated vertical surface and a plane stagnation flow are derived below.

Vertical Plate

It is assumed that the vertical plate is mounted in a large (effectively infinite) volume of air containing small particles. The plate is heated, and a layer of warm air near the surface rises. The air velocity component parallel to the surface increases from zero at the surface to a maximum value and then falls to zero, the value far from the plate.

An important dimensionless parameter for this type of flow is the Grashof number

$$G = \frac{gL^3(T_w - T_\infty)}{\nu^2 T_\infty} \quad (3.93)$$

where g is the gravitational constant, L is the length of the plate, and T_w and T_∞ refer to the temperature at the wall and at large distances from the wall, respectively. For air over the range $10^4 < G < 10^8$, the flow is of the laminar boundary layer type. At higher values of G the flow becomes turbulent, and for lower values the layer becomes too thick for boundary layer theory to apply.

A mathematical analysis has been carried out for the laminar boundary layer on a vertical flat plate with gas properties independent of temperature, and the results have been verified experimentally (Schlichting, 1979, pp. 315 ff). The temperature gradient at the wall is

$$\left(\frac{\partial T}{\partial y}\right)_0 = -0.508(T_w - T_\infty)Cx^{-1/4} \quad (3.94)$$

where

x = distance from the bottom of the plate

$$C = \left[\frac{g(T_w - T_\infty)}{4\nu^2 T_\infty}\right]^{1/4}$$

The velocity component normal to the plate, v_{fy} , is directed toward the surface. Near the surface, this component can be represented by the first term in its expansion:

$$v_{fy} = -0.338\nu C^3 y^2 x^{-3/4} + 0(y^3) \quad (3.95)$$

where the negative sign indicates that the flow is toward the plate. The distance y is measured normal to the surface of the plate. Neglecting diffusion and particle inertia, we can equate the thermophoretic force on the particles to the Stokes drag to find the locus of the surface over which the particle velocity normal to the surface vanishes—that is, the dust-free space (Zernik, 1957):

$$f(v_y - v_{fy}) = -\nu f \frac{K}{T} \left(\frac{\partial T}{\partial y}\right)_{y=0} \quad (3.96)$$

where $\partial T/\partial y$ is evaluated at the surface. The particle velocity vanishes at the edge of the dust-free space. When we substitute (3.95) for v_{fy} and (3.94) for $(\partial T/\partial y)_{y=0}$, the locus of the dust-free space found by setting $v_y = 0$ is given by

$$\delta_{df} = 1.23 \left(\frac{T_\infty - T_w}{T_w}\right)^{1/2} \frac{x^{1/4}}{C} K^{1/2} \quad (3.97)$$

The thickness of the dust-free space increases with distance from the bottom edge of the vertical plate. The value of K can be obtained from (2.56).

Stagnation Flow

It was proposed by the author (Stratmann et al., 1988) that thermophoresis could be used to suppress particle deposition on wafers during clean room operations in the microelectronics industry. To estimate the effect of an applied temperature gradient on particle deposition, the flow of filtered air over the surface of a horizontal wafer can be approximated by a stagnation flow (Fig. 3.12). For both the plane and axially symmetric stagnation flows, the gas velocity component normal to the surface and the temperature fields depend only on the distance from the surface. In the absence of natural convection, the gas velocity normal to the surface in the neighborhood of the plane stagnation flow is

$$v_f = -0.6163 \sqrt{\frac{a^3}{\nu}} y^2 \quad (3.98)$$

The temperature gradient at the wall is (Schlichting, 1979, p. 291)

$$\left(\frac{dT}{dy} \right)_{y=0} = -0.495 \sqrt{\frac{a}{\nu}} (T_w - T_\infty) \quad (3.99)$$

for air (Prandtl number = 0.7). For plane flow over an infinite ribbon normal to the flow, $a = U/R$, where U is the gas velocity normal to the surface, far from the surface, and R is the half-width of the ribbon. Equating the drag force on the particle to the thermophoretic force (neglecting particle acceleration)

$$\delta_{df} = 0.9 \left(\frac{\nu}{a} \right)^{1/2} K^{1/2} \left[\frac{(T_w - T_\infty)}{T_w} \right]^{1/2} \quad (3.100)$$

Thus δ_{df} is proportional to the square root of the thermophoretic coefficient, the temperature

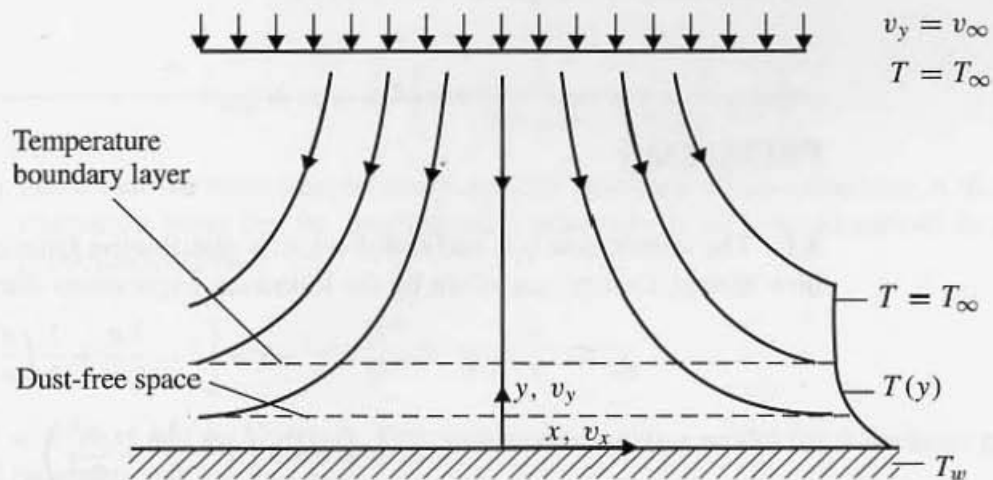


Figure 3.12 Temperature and velocity distribution in plane stagnation flow showing the thickness of the dust-free space and the boundary layer. (After Stratmann et al., 1988.)

difference, and the square root of the gas viscosity. It is inversely proportional to the square root of the gas velocity.

Values of δ_{df} based on the first term of the expansion of the velocity near the surface compare well with numerically computed values based on the complete velocity and temperature distributions. Calculations of δ_{df} for alumina and copper particles ($0.5 < d_p < 2 \mu\text{m}$) indicate that for temperature differences as small as 10°C the dust-free space would be thick enough to prevent particle deposition.

Effects of Brownian Diffusion on Deposition

So far, the analysis has not taken into account the effects of the Brownian motion which allows diffusive leakage through the "dust free space" to the heated surface. This effect has also been studied in some detail in connection with wafer contamination (Friedlander et al., 1988; Ye et al. 1991). The equation for simultaneous convection, diffusion, thermophoresis and sedimentation for the one-dimensional stagnation flow configuration is

$$v \frac{dn}{dy} = D \frac{d^2n}{dy^2} + \frac{d(c_s + c_t)n}{dy} \quad (3.101)$$

where c_s and c_t refer to the sedimentation and thermophoretic velocities, respectively. The results of a numerical solution for an axisymmetric flow around a wafer are compared with experimental data for latex particles in Fig. 3.13. For a given velocity and surface temperature, there exists a particle size range in which there is negligible deposition. For example, for a 10°C temperature difference, this "clean zone" extends between 0.03 and $1.0 \mu\text{m}$. Particles smaller than $0.03 \mu\text{m}$ can diffuse through the thermophoretic barrier. Particles larger than about $1.0 \mu\text{m}$ can penetrate by gravitational sedimentation. As the surface temperature is increased, the width of the clean zone broadens.

Finally, we wish to note that thermophoresis is the controlling mechanism of particle transport in the fabrication of optical fibers by the modified chemical vapor deposition process. In this application, submicron silica particles and associated trace amounts of dopant aerosol oxides are deposited on the inside of a quartz tube. Experiment and theory are discussed by Simpkins et al. (1979).

PROBLEMS

3.1 The stream function and radial velocity distribution function for a low-Reynolds-number flow around a sphere are given by the following expressions due to Stokes:

$$\psi = -\frac{U}{2} a^2 r^2 \sin^2 \theta \left[1 - \frac{3a}{2r} + \frac{1}{2} \left(\frac{a}{r} \right)^3 \right]$$

$$u_r = U \cos \theta \left(1 - \frac{3a}{2r} + \frac{a^3}{2r^3} \right)$$

- (a) Show that the efficiency of particle removal by direct interception for a droplet falling at low Reynolds numbers through an aerosol is given by

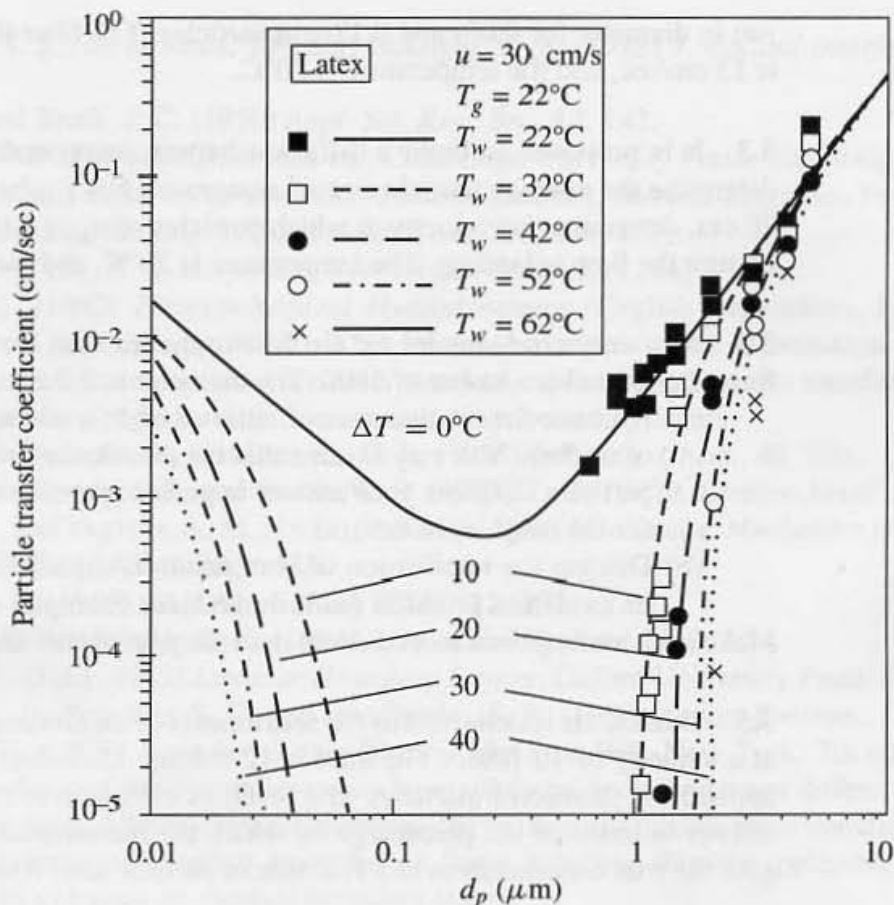


Figure 3.13 Comparison of experiment and theory for the deposition of monodisperse latex particles on a free-standing wafer 4 in. in diameter. The air mainstream velocity normal to the wafer was 30 cm/sec, typical of microelectronics clean room operations. The diffusion equation was solved numerically using calculated velocity and temperature distributions. The curves show that a small increase in surface temperature effectively suppresses deposition over a wide intermediate particle size range. Larger particles deposit by sedimentation; smaller ones break through the thermal barrier by Brownian diffusion. (After Ye et al., 1991.)

$$\eta_{DI} = (1 + R)^2 \left[1 - \frac{3}{2(1 + R)} + \frac{1}{2(1 + R)^3} \right]$$

(b) Show that the mass transfer coefficient for particles of finite diameter at the forward stagnation point (in the concentration boundary layer approximation) is given by (Friedlander, 1967)

$$\frac{k_0 d}{D} = \frac{2e^{-\beta}}{R \int_1^\infty e^{-\beta z^3} dz}$$

where $\beta = R^3 Pe/4$ and $Pe = dU/D$. This system represents a model for diffusional collection by small raindrops and fog droplets.

3.2 Estimate the collection efficiency of a filter mat ($\alpha = 0.0057$) composed of glass fibers 4

μm in diameter for 0.08- and 0.17- μm particles. The filter thickness is 0.8 cm, the air velocity is 13 cm/sec, and the temperature is 20°C.

3.3 It is proposed to build a diffusion battery composed of a bundle of capillary tubes to determine the average particle size of an aerosol. For a tube diameter of 1 mm and a length of 20 cm, determine the velocity at which particles of $d_p = 0.05 \mu\text{m}$ are 90% removed. Check to be sure the flow is laminar. The temperature is 20°C, and the gas is air.

3.4 As a very crude model for air flow in the trachea, assume fully developed laminar pipe flow at a Reynolds number of 1000. The diameter is 2.0 cm.

(a) Estimate the relative rates of removal of SO_2 and sulfuric acid droplets per unit length of trachea. You may assume that the mucous layer is a perfect sink for SO_2 as well as particles. Express your answer in percent per centimeter as a function of particle size for the range $d_p < 0.5 \mu\text{m}$.

(b) Discuss the implication of your result in explaining the effects of sulfur dioxide and its oxidation products (sulfuric acid, for example) on the lung.

Make such assumptions as you deem necessary, but state all assumptions clearly.

3.5 Outside air is delivered to the instruments of an air monitoring station through a 2-in. duct at a velocity of 10 ft/sec. The duct is 12 ft long. Calculate the correction factor that must be applied for submicron particles as a result of diffusion to the walls of the duct. Express your answer in terms of the percentage by which the measured concentration must be multiplied to give the true concentration as a function of particle size. Assume $T = 20^\circ\text{C}$.

3.6 For the particle size range of Fig. 2.6, Chapter 2 and $E = 2 \text{ kV/cm}$, determine the collection efficiency of a plate-type electrical precipitator, taking into account diffusional transport. The plate spacing is 12 in., and the plate length in the direction of flow is 5 ft. Make your calculations for velocities of 3 and 10 ft/sec, and plot efficiency as a function of particle diameter. Assume flat collecting plates and a fully developed turbulent flow.

REFERENCES

- Billings, C. E. (1966) *Effects of Particle Accumulation in Aerosol Filtration*, PhD thesis in Environmental Health Engineering, California Institute of Technology.
- Carslaw, H. S., and Jaeger, J. C. (1959) *Conduction of Heat in Solids*, 2nd ed., Oxford University Press, London.
- Chamberlain, A. C. (1966) *Proc. R. Soc.*, **A296**, 45.
- Chen, C. Y. (1955) *Chem. Rev.*, **55**, 595; also Filtration of Aerosols by Fibrous Media, Annual Report Engineering Experimental Station, University of Illinois, January 30, 1954.
- Cheng, Y. S. (1993) "Condensation Detection and Diffusion Size Separation Techniques," in Willeke, K., and Baron, P. A. (Eds.), *Aerosol Measurement*, Van Nostrand Reinhold, New York.
- Crank, J. (1975) *The Mathematics of Diffusion*, 2nd ed., Oxford University Press, Oxford.
- de la Mora, J.F., and Friedlander, S. K. (1982) *Int. J. Heat Mass Transfer*, **25**, 1725.
- Dobry, R., and Finn, R. K. (1956) *Ind. Eng. Chem.*, **48**, 1540.
- Ferin, J., Oberdörster, G., and Penney, D. P. (1992) *Am. J. Respir. Cell Mol. Biol.*, **6**, 535.
- Friedlander, S. K. (1967) *J. Colloid Interface Sci.*, **23**, 157.

- Friedlander, S. K., de la Mora, J.F., and Gokoglu, S. A. (1988) *J. Colloid Interface Sci.*, **125**, 351.
- Kronig R., and Brink, J. C. (1950) *Appl. Sci. Res., Sec. A2*, 142.
- Lamb, H. (1953) *Hydrodynamics*, 6th ed., Cambridge University Press, Cambridge.
- Landau, L. D., and Lifshitz, E. M. (1987) *Fluid Mechanics*, 2nd ed., Pergamon Press, Oxford.
- Lee, K. W., and Liu, B. Y. H. (1982a) *Aerosol Sci. Technol.*, **1**, 35.
- Lee, K. W., and Liu, B. Y. H. (1982b) *Aerosol Sci. Technol.*, **1**, 147.
- Levich, V. G. (1962) *Physicochemical Hydrodynamics* (English translation), Prentice-Hall, Englewood Cliffs, NJ, pp. 80–85. This reference contains much information on diffusion in aqueous solutions. Included are derivations of expressions for mass transfer coefficients for different flow regimes with thin concentration boundary layers.
- Lin, C. S., Moulton, R. W., and Putnam, G. L. (1953) *Ind. Eng. Chem.*, **45**, 640.
- McCain, J. D., Gooch, J. P., and Smith, W. B. (1975) *J. Air Pollut. Control Assoc.*, **25**, 117.
- Monin, A. S., and Yaglom, A. M. (1971) *Statistical Fluid Mechanics: Mechanics of Turbulence*, vol. 1, MIT Press, Cambridge, MA.
- Natanson, G. L. (1957) *Dokl Akad. Nauk SSSR*, **112**, 100.
- Parnas, R., and Friedlander, S. K. (1984) *Aerosol Sci. Technol.*, **3**, 3.
- Rosenhead, L. (Ed.) (1963) *Laminar Boundary Layers*, Oxford University Press, Oxford, UK.
- Schack, D. J., Jr., Pratsinis, S. E., and Friedlander, S. K. (1985) *Atmos. Environ.*, **19**, 953.
- Schlichting, H. (1979) *Boundary Layer Theory*, McGraw-Hill, New York, 7th ed. This is the classical collection of velocity boundary layer solutions, including many different geometries and flow regimes. The velocity distributions can be used to calculate mass transfer coefficients using concentration boundary layer theory. Some solutions directly applicable to diffusion are given in a chapter on thermal boundary layers.
- Simpkins, P. G., Greenberg-Kosinski, S., and McChesney, J. B. (1979) *J. Appl. Phys.*, **50**, 5676.
- Spurny, K. R., Lodge, J. P., Jr., Frank, E. R., and Sheesley, D. C. (1969) *Environ. Sci. Tech.*, **3**, 453.
- Stratmann, F., Friedlander, S., Fissan, H., and Papperger, A. (1988) *Aerosol Sci. Technol.*, **9**, 115.
- Watson, H. H. (1936) *Trans. Faraday Soc.*, **32**, 1073.
- Wong, J. B., Ranz, W. E., and Johnstone, H. F., (1956) *J. Appl. Phys.*, **27**, 161; also Technical Report 11, Engineering Experimental Station, University of Illinois, October 31, 1953.
- Ye, Y., Pui, D. Y. H., Liu, B. Y. H., Opiolka, S., Blumhorst, S., and Fissan, H. (1991) *J. Aerosol Sci.*, **22**, 63.
- Zernik, W. (1957) *Br. J. Appl. Phys.*, **8**, 117.

Inertial Transport and Deposition

Suspended particles may not be able to follow the motion of an accelerating gas because of their inertia. This effect is most important for particles larger than $1 \mu\text{m}$. It may lead to particle deposition on surfaces, a process known as *inertial deposition*. Inertial deposition is often the controlling mechanism for the removal of larger particles in gas-cleaning devices, such as filters, scrubbers, and cyclone separators. In filters, inertial deposition occurs when the gas flows around the individual fibers or grains composing the filter. The particles that cannot follow the air stream impact on the collecting element. In scrubbers, the collecting elements are water droplets, whereas in cyclone separators, it is the rotating gas stream that deposits the particles on the wall. In each case, it is the acceleration of the gas that leads to deposition. Inertial effects also play a role in atmospheric processes such as rain scavenging and deposition on vegetation and man-made structures.

Unlike diffusion, which is a stochastic process, particle motion in the inertial range is deterministic, except for the very important case of turbulent transport. The calculation of inertial deposition rates is usually based either on a force balance on a particle or on a direct analysis of the equations of fluid motion in the case of colliding spheres. Few simple, exact solutions of the fundamental equations are available, and it is usually necessary to resort to dimensional analysis and/or numerical computations. For a detailed review of earlier experimental and theoretical studies of the behavior of particles in the inertial range, the reader is referred to Fuchs (1964).

Particle transport and deposition from turbulent flows by inertial forces are not well understood and has been the subject of considerable experimental and theoretical study. Correlations for rates of particle deposition from turbulent pipe flow are discussed in this chapter. The concentrations are assumed to be sufficiently small to neglect the effects of the particles on the turbulence. Inertial effects can also be used to focus beams of aerosol particles. This effect can be produced for submicron and even ultrafine particles as described at the end of the chapter.

For particles smaller than about $1 \mu\text{m}$, diffusion becomes increasingly important and the methods of calculation of Chapter 3 become applicable. Rigorous theoretical treatment of the particle size range in which both diffusion and inertial effects are important is difficult.

PARTICLE-SURFACE INTERACTIONS: LOW SPEEDS

As two surfaces approach each other, the fluid between them must be displaced. First, we consider the case of two plane parallel circular disks of radius a approaching each other along their common axis (Fig. 4.1). The disks are immersed in a fluid in which the pressure is p_0 . Without loss of generality, it is possible to assume that one of the disks is fixed and that the other is in relative motion. The motion is sufficiently slow to neglect the inertial and unsteady terms in the equations of fluid motion.

The flow is axisymmetric, and for low velocities the pressure gradient across the gap in the z direction, $\partial p/\partial z$, can be neglected. Hence the pressure is a function only of r . The applicable equations are the r component of the equation of motion

$$\mu \left(\frac{\partial^2 v_r}{\partial r^2} + \frac{1}{r} \frac{\partial v_r}{\partial r} - \frac{v_r}{r^2} + \frac{\partial^2 v_r}{\partial z^2} \right) = \frac{dp}{dr} \quad (4.1)$$

and the continuity relation

$$\frac{1}{r} \frac{\partial r v_r}{\partial r} + \frac{\partial v_z}{\partial z} = 0 \quad (4.2)$$

with the boundary conditions

$$\begin{aligned} \text{at } z = 0 \quad v_r = v_z = 0 \\ z = h \quad v_r = 0, v_z = -U \\ r = a \quad p = p_0 \end{aligned} \quad (4.2a)$$

where h is the distance between the disks and p_0 is the pressure in the external region.

We now make the following “educated guesses” for the forms of the velocity and pressure distributions:

$$v_r = rZ(z) \quad (4.3)$$

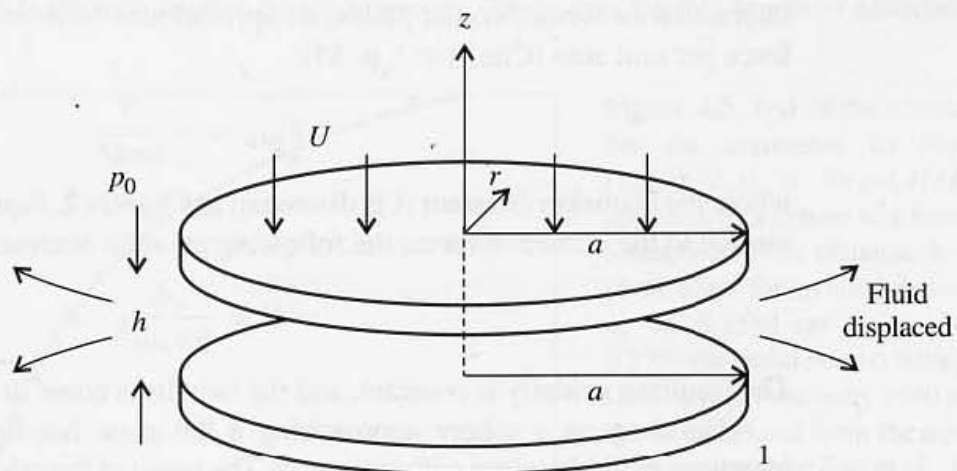


Figure 4.1 Outward radial flow between two flat disks of radius a . Bottom disk is fixed, and top advances with velocity U , which can change slowly with time.

$$\frac{dp}{dr} = Br \quad (4.4)$$

where B is a constant. These assumed forms are tested by substitution in the equation of fluid motion (4.1):

$$\mu \frac{d^2 Z}{dz^2} = B \quad (4.5)$$

When we integrate with the boundary conditions (4.2a) to obtain $Z(z)$, the following expression is found for the radial velocity:

$$v_r = \frac{1}{2\mu} \frac{dp}{dr} z(z-h) \quad (4.6)$$

If the continuity relation (4.2) is integrated with respect to z across the gap between the disks, making use of the boundary conditions on v_z , the result is

$$U = \frac{1}{r} \frac{d}{dr} \int_0^h r v_r dz = -\frac{h^3}{12\mu r} \frac{d}{dr} \left(r \frac{dp}{dr} \right) \quad (4.7)$$

When we integrate twice and remember that U is not a function of r , the result for the variation of the pressure with radial position is

$$p = p_0 + \frac{3\mu U}{h^3} (a^2 - r^2) \quad (4.8)$$

which is consistent with the assumption (4.4) for the pressure distribution. The drag force on the moving disk is calculated by integrating the pressure difference inside and outside the gap over the surface:

$$F = \int_0^a (p - p_0) 2\pi r dr = \frac{3\pi\mu U a^4}{2h^3} \quad (4.9)$$

which is the result obtained by Reynolds in 1886. (See Landau and Lifshitz, 1987, p. 67.) The resistance becomes infinitely great as the disks approach each other.

How, then, can two flat surfaces ever approach close enough to stick? In part, the explanation lies in the London-van der Waals forces that are attractive in nature. For the interaction between two flat plates, an approximate form can be derived for the attractive force per unit area (Chu, 1967, p. 55):

$$F_{vdw} = -\frac{A}{6\pi h^3} \quad (4.10)$$

where the Hamaker constant A is discussed in Chapter 2. Equating the resistance to the disk motion to the attractive force, the following result is obtained for the velocity:

$$U = \frac{A}{9\pi\mu a^2} \quad (4.11)$$

The resulting velocity is constant, and the two disks come in contact in a finite time period.

The drag on a sphere approaching a flat plate has been computed by solving the equations of fluid motion without inertia. The result of the calculation (which is considerably more complex than for the case of the two disks given above) can be expressed in the form

$$F = 3\pi\mu d_p U G \left(\frac{h}{d_p} \right) \quad (4.12)$$

TABLE 4.1
Stokes Law Correction for Motion
Perpendicular to a Flat Plane
(Happel and Brenner, 1965)

$(h + a_p)/a_p$	G
1	∞
1.128	9.25
1.543	3.04
2.35	1.837
3.76	1.413
6.13	1.221
10.07	1.125
∞	1

where the drag has dimensions of force and h is the minimum separation between sphere and plate. The dimensionless function $G(h/d_p)$, which acts as a correction factor for Stokes law is shown in Table 4.1. As the sphere approaches the surface, the drag increases to an infinite value on contact. To test the theory, experiments have been carried out with nylon spheres falling through silicone oil. Good agreement between theory and experiment was found up to distances close to the wall (Fig. 4.2).

For $h/d_p \ll 1$, the drag on a sphere approaches the form (Charles and Mason, 1960)

$$F = \frac{3 \pi \mu d_p^2 U}{2 h} \quad (4.13)$$

In the case of a gas, when the particle arrives at a point of the order of a mean free path from the surface, the continuum theory on which the calculation of resistance is based no longer applies. van der Waals forces contribute to adhesion, provided that the rebound effects discussed in the next section do not intervene. There are also thin layers of adsorbed liquids

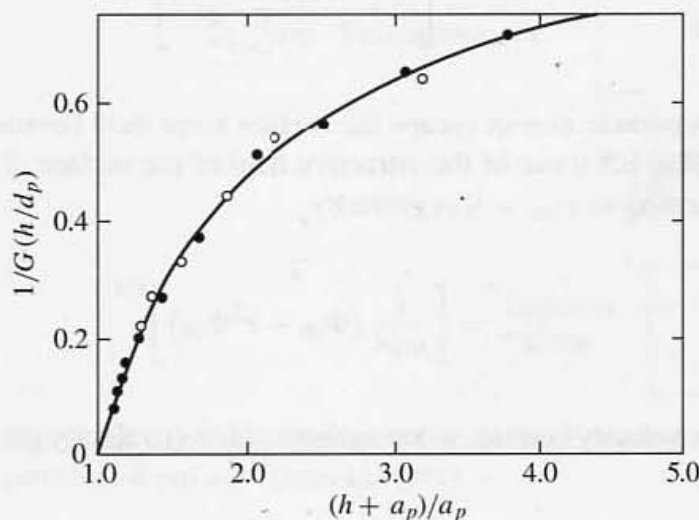


Figure 4.2 Test of theoretical relation for the correction to Stokes law $[1/G(h/d_p)] = 3\pi\mu d_p U/F$ for the approach of a sphere to a fixed plate as a function of the distance, h , from the plate. Data for nylon spheres of radii $a_p = 0.1588$ cm (open points) and 0.2769 cm (solid points) falling through silicone oil of viscosity 1040 poise. The line is calculated from the equations of fluid motion (MacKay et al., 1963).

present on most solid surfaces unless special precautions are taken. These layers help trap small particles when they hit a surface.

PARTICLE-SURFACE INTERACTIONS: REBOUND

At low impact velocities, particles striking a surface adhere, but as the velocity increases, rebound may occur. For simplicity, we consider the case of a spherical particle moving normal to the surface of a semi-infinite target through a vacuum (Dahneke, 1971). In this way, fluid mechanical effects are eliminated. Bounce occurs when the kinetic energy of the rebounding particles is sufficient to escape attractive forces at the surface. Let $v_{1\infty}$ be the particle approach velocity at large distances from the surface (away from the immediate neighborhood of the attractive forces), and let $\Phi_1(z)$ be the potential energy function for the particle surface interaction where z is the distance normal to the surface. The kinetic energy of the particle near the surface just before contact is given by $mv_{1\infty}^2/2 + \Phi_{10}$, and the velocity of rebound v_{20} just after impact is given by

$$\frac{mv_{20}^2}{2} = e^2 \left(\frac{mv_{1\infty}^2}{2} + \Phi_{10} \right) \quad (4.14)$$

where $\Phi_{10} = \Phi_1(0)$ and e is the coefficient of restitution. The velocity at large distances from the surface away from the interfacial force field, $v_{2\infty}$, is given by

$$\frac{mv_{2\infty}^2}{2} + \Phi_{20} = \frac{mv_{20}^2}{2} \quad (4.15)$$

When we substitute, the result for $v_{2\infty}$ is

$$\frac{v_{2\infty}}{v_{1\infty}} = \left[e^2 - \frac{\Phi_{20} - e^2\Phi_{10}}{mv_{1\infty}^2/2} \right]^{1/2} \quad (4.16)$$

When $v_{2\infty} = 0$, a particle cannot escape the surface force field because all of the rebound energy is required to lift it out of the attractive field of the surface. The critical approach velocity corresponding to $v_{2\infty} = 0$ is given by

$$v_{1\infty}^* = \left[\frac{2}{me^2} (\Phi_{20} - e^2\Phi_{10}) \right]^{1/2} \quad (4.17)$$

Particles of higher velocity bounce, whereas those of lower velocity stick. For $\Phi_{10} = \Phi_{20} = \Phi_0$, this becomes

$$v_{1\infty}^* = \left[\frac{2\Phi_0}{m} \left(\frac{1-e^2}{e^2} \right) \right]^{1/2} \quad (4.18)$$

The coefficient of restitution depends on the mechanical properties of the particle and surface. For perfectly elastic collisions, $e = 1$ and the particle energy is conserved after collision. Deviations from unity result from dissipative processes, including internal friction, that lead to the generation of heat and the radiation of compressive waves into the surface material.

Studies of particle-surface interactions in a vacuum can be carried out by means of the particle beam apparatus (Dahneke, 1975). Particle beams are set up by expanding an aerosol through a nozzle or capillary into a vacuum chamber. Because of their inertia, the particles tend to continue in their original direction through the chamber where the gas is pumped off. A well-defined particle beam can be extracted into a second low-pressure chamber through a small collimating hole. The beam can then be directed against a target to study the rebound process (Fig. 4.3).

In his experiments, Dahneke studied the bouncing of polystyrene latex spheres about 1 μm in diameter from polished quartz and other surfaces. Using a laser light source, he measured the velocities of the incident and reflected particles. The velocity of the incident particles was controlled by means of a deceleration chamber.

The coefficient of restitution was found from (4.16) by measuring $v_{2\infty}/v_{1\infty}$ for very large values of $v_{1\infty}$. Figure 4.4 shows the experimental data for 1.27- μm polystyrene latex particles and a polished quartz surface. Shown also is the curve representing (4.16) with $e = 0.960$ and $\Phi_{20} = \Phi_{10}$ chosen to give the best agreement between theory and experiment. Values of Φ_0 determined in this way were several hundred times higher than values calculated from van der Waals force theory. The value of the critical impact velocity, $v_{1\infty}^*$, was estimated to be 120 cm/sec by extrapolation to $v_{2\infty}/v_{1\infty} = 0$.

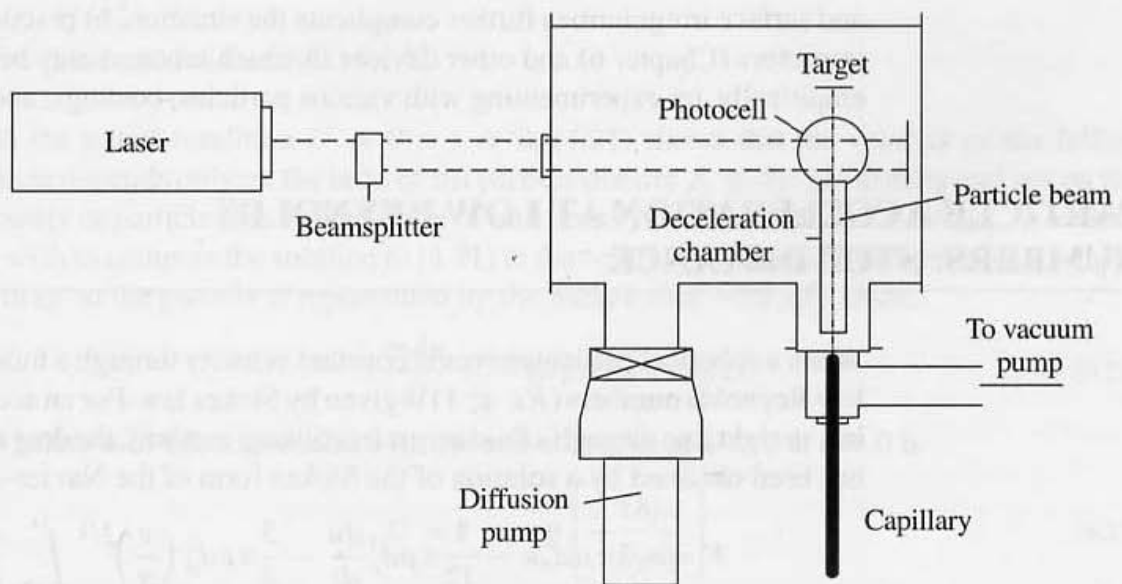


Figure 4.3 Schematic diagram of particle beam apparatus used for studying the bouncing of small particles off surfaces (Dahneke, 1975).

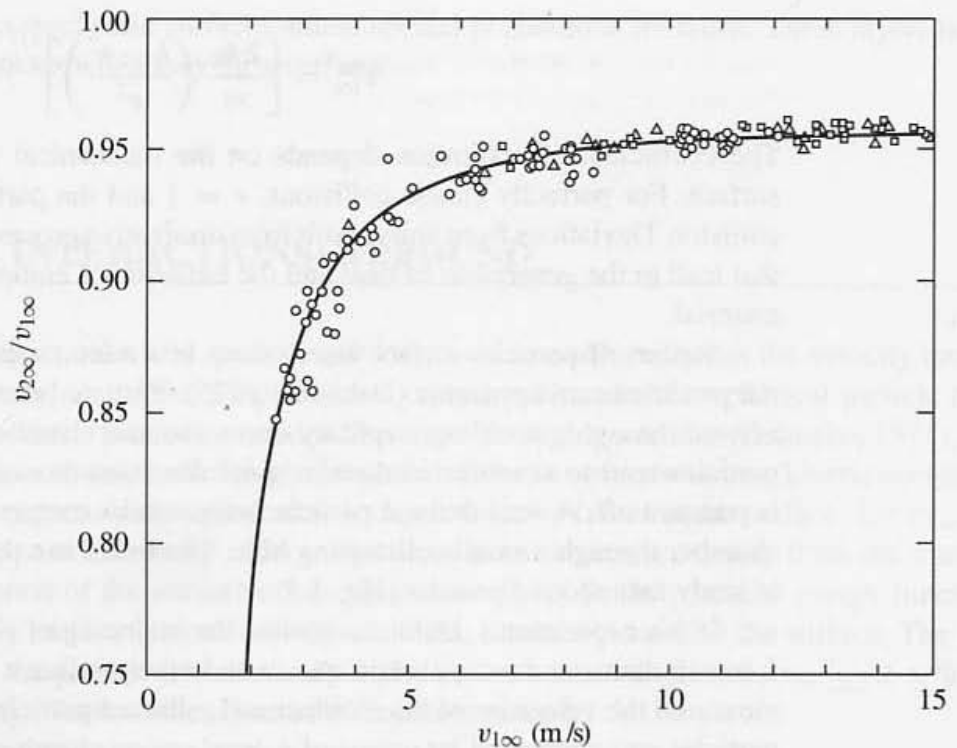


Figure 4.4 Ratio of reflected to incident velocities for 1.27- μm polystyrene latex particles bouncing from polished quartz surfaces. The curve is (4.16) with the value of the coefficient of restitution $e = 0.960$ obtained by extrapolation to very large values of $v_{1\infty}$ (Dahneke, 1975).

A complete model for particle–surface interaction would include both (a) fluid mechanical effects as the particle approaches the surface and (b) elastic and surface forces. The fluid mechanical calculations would take into account free molecule effects as the particle comes to within one mean free path of the surface. The presence of thin films of liquids and surface irregularities further complicate the situation. In practice, the design of cascade impactors (Chapter 6) and other devices in which rebound may be important is carried out empirically, by experimenting with various particles, coatings, and collecting surfaces.

PARTICLE ACCELERATION AT LOW REYNOLDS NUMBERS: STOP DISTANCE

When a spherical particle moves at constant velocity through a fluid at rest, the drag force at low Reynolds numbers ($Re \ll 1$) is given by Stokes law. For an accelerating sphere moving in a straight line through a fluid at rest (rectilinear motion), the drag at low Reynolds numbers has been obtained by a solution of the Stokes form of the Navier–Stokes equations

$$F = -3\pi\mu d_p u - \frac{1}{12}\pi\rho d_p^3 \frac{du}{dt} - \frac{3}{2}\pi\rho d_p^2 \left(\frac{v}{\pi}\right)^{1/2} \int_{-\infty}^t \frac{du}{dt'} \frac{dt'}{(t-t')^{1/2}} \quad (4.19)$$

where ρ is the density of the fluid (Basset, 1910; Landau and Lifshitz, 1987, p. 91). The first term on the right-hand side is equivalent to the Stokes drag. The second and third terms

arise from the particle acceleration, du/dt . The second term represents the resistance of an inviscid fluid to an accelerating sphere. It is equivalent to adding $\pi\rho d_p^3/12$ to the mass of the particle—that is, one-half the mass of an equal volume of fluid. The integral term, the last on the right-hand side, depends on the past history of the sphere.

Numerical calculations of the rectilinear motion of particles in gases can easily be made using (4.19). However, this analysis is not applicable to curvilinear motion usually encountered in practical applications. To deal with particle deposition from gases flowing around obstacles such as cylinders and spheres, the drag law (4.19) is usually simplified by keeping only the Stokes term $3\pi\mu d_p u$ and neglecting the added mass and integral terms. This approximation can be tested in at least two ways. First, calculations based on the approximation for curvilinear motion can be compared with experiment; the important cases of impaction on cylinders and spheres are discussed later in the chapter. Second, an exact calculation based on (4.19) can be compared with the approximate calculation for rectilinear motion. Calculations of this type have been made for a spherical particle released from rest in a gravitational field (Clift et al., 1978, p. 288). The force balance on a spherical particle in a gravitational field is given by

$$m \frac{du}{dt} = F_D + mg \tag{4.20}$$

Substituting F_D from (4.19) and rewriting (4.20) in dimensionless form gives

$$\left(\frac{2\gamma + 1}{9}\right) \frac{dU}{d\theta} = 1 - U - \frac{1}{\pi^{1/2}} \int_0^\tau \frac{dU}{d\theta'} \frac{d\theta'}{(\theta - \theta')^{1/2}} \tag{4.21}$$

where

- $U = u/u_{ts}$
- $u_{ts} =$ terminal settling velocity
- $\gamma = \rho_p/\rho$
- $\theta = vt/a_p^2$
- $\nu =$ kinematic viscosity

With the initial condition $U = 0$ at $t = 0$, (4.21) shows that the velocity of the falling particle depends only on the ratio of the particle density ρ_p to the gas density and not on the viscosity or particle size. For particles of unit density in air at 20°C and 1 atm, $\rho_p/\rho = 830$. We wish to compare the solution to (4.21) to the solution of the simplified problem in which the drag on the particle is represented by the Stokes term $-3\pi\mu d_p$ alone:

$$\frac{mdu}{dt} = -3\pi\mu d_p u + mg \tag{4.22}$$

The solution to this expression with the initial condition $u = 0$ at $t = 0$ is

$$U = 1 - \exp\left[-\frac{18\mu t}{\rho_p d_p^2}\right] \tag{4.23}$$

For $\gamma \approx 10^3$, the deviation of (4.23) from the exact solution to (4.21) is very small for $u < 0.9u_{ts}$ but increases as u approaches u_{ts} . The exact calculation indicates that more

time is needed to reach $u_{t,s}$ than the simplified theory in which the history and added mass terms are neglected.

Example: Show that when a particle is projected into a stationary fluid with a velocity u_0 , it will travel a finite distance before coming to rest as $t \rightarrow \infty$.

SOLUTION: The distance can be calculated approximately by integration of the simplified force balance on the particle:

$$m \frac{du}{dt} = -fu$$

with the initial condition $u = u_0$ to give

$$u = \frac{dx}{dt} = u_0 e^{-t/\tau}$$

Integrating once more with $x = 0$ at $t = 0$ gives

$$x = u_0 \tau (1 - e^{-t/\tau})$$

for the velocity and displacement, respectively. The characteristic time $\tau = \rho_p d_p^2 / 18\mu$. As $t/\tau \rightarrow \infty$, the distance that the particle penetrates, or stop distance, is given by

$$s = \frac{\rho_p d_p^2 u_0}{18\mu}$$

The dimensionless ratio of the stop distance to a characteristic length such as the diameter of a filter element (fiber or grain) or the viscous sublayer thickness is called the *Stokes number*, *Stk*. As shown in the sections that follow, the Stokes number plays an important role in the analysis of inertial deposition. Fuchs (1964, p. 73) has calculated values of the stop distance numerically for particles in air, keeping the integral term but not the added mass term. He reported stop distances appreciably larger than values calculated from the last equation and discusses uncertainties associated with such calculations.

SIMILITUDE LAW FOR IMPACTION: STOKESIAN PARTICLES

When an aerosol flows over an object in its path, the gas velocity decreases as it approaches the surface. Both tangential and normal components of the gas velocity vanish at the surface of a fixed solid body. The particles, however, are unable to follow the gas motion because of their inertia; if they come within one particle radius of the surface, they can adhere depending on the interaction between the attraction and rebound energies discussed in previous sections. An idealized version of the situation is shown in Fig. 4.5. At large

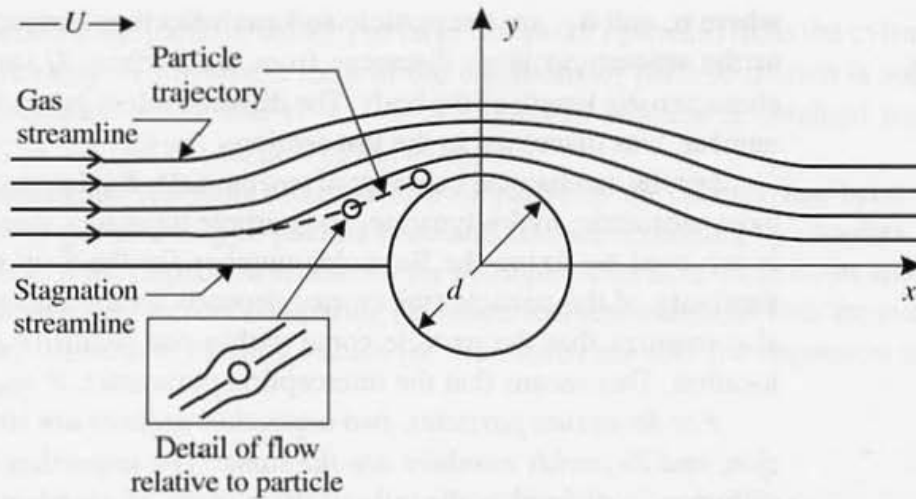


Figure 4.5 Impaction of a small spherical particle on a cylinder placed normal to the flow. The particle is unable to follow the fluid streamline because of its inertia. The drag on the particle is calculated by assuming that it is located in a uniform flow with velocity at infinity equal to the local fluid velocity (see detail). Fore-and-aft symmetry of the streamline exists for low-Reynolds-number flows and for an inviscid flow, but the shapes of the streamlines differ.

distances from the collector, the gas velocity is uniform and the particle velocity is equal to that of the gas.

When the particles are much smaller than the collector, and in sufficiently low concentration, the flow fields for the particle and collector can be uncoupled. For the gas flow field around the collector, the velocity distribution is determined by the Reynolds number based on collector diameter, independent of the presence of the particles. The particle is assumed to be located in a flow with a velocity at infinity equal to the *local* velocity for the undisturbed gas flow around the collector; the drag on the particle is determined by the local relative velocity between particle and gas.

When the Reynolds number for the particle motion is small, a force balance can be written on the particle assuming Stokes law holds for the drag. For the x direction we have

$$m \frac{du}{dt} = -f(u - u_f) \quad (4.24)$$

and for the vector velocity we have

$$m \frac{d\mathbf{u}}{dt} = -f(\mathbf{u} - \mathbf{u}_f) \quad (4.25)$$

Here \mathbf{u} is the particle velocity, \mathbf{u}_f is the local fluid velocity, and f is the Stokes friction coefficient. We call particles that obey this equation of motion *Stokesian particles*. The use of (4.25) is equivalent to employing (4.19), neglecting the acceleration terms containing the gas density. Because (4.19) was derived for rectilinear motion, the extension to flows with velocity gradients and curved streamlines adds further uncertainty to this approximate method.

In dimensionless form, the equation of particle motion can be written

$$\text{Stk} \frac{d\mathbf{u}_1}{d\theta} = -(\mathbf{u}_1 - \mathbf{u}_{f1}) \quad (4.26)$$

where \mathbf{u} , and \mathbf{u}_f , are the particle and gas velocities, respectively, normalized with respect to the velocity at large distances from the surface, U , and $\theta = tU/L$, where L is the characteristic length of the body. The dimensionless group $\text{Stk} = \rho_p d_p^2 U / 18\mu L$, the Stokes number, was discussed in the last section.

For the mechanical behavior of two particle–fluid systems to be similar, it is necessary to have geometric, hydrodynamic, and particle trajectory similarity. Hydrodynamic similarity is achieved by fixing the Reynolds number for the flow around the collector. By (4.26), similarity of the particle trajectories depends on the Stokes number. Trajectory similarity also requires that the particle come within one radius of the surface at the same relative location. This means that the interception parameter, $R = d_p/L$, must also be preserved.

For Stokesian particles, two impaction regimes are similar when the Stokes, interception, and Reynolds numbers are the same. The impaction efficiency, η_R , as in the case of diffusion, is defined as the ratio of the volume of gas cleared of particles by the collecting element to the total volume swept out by the collector. (Refer to Fig. 4.5 for the case of the cylinder.) If all particles coming within one radius of the collector adhere, then we obtain

$$\eta_R = f(\text{Stk}, R, \text{Re}) \quad (4.27)$$

As the particle approaches a surface, the use of Stokes law for the force acting on the particle becomes an increasingly poor approximation. Mean free path effects, van der Waals forces, and hydrodynamic interactions between particle and surface complicate the situation. The importance of these effects is difficult to judge because reliable calculations and good experimental data are lacking.

IMPACTION OF STOKESIAN PARTICLES ON CYLINDERS AND SPHERES

Introduction

Flow around single cylinders is the elementary model for the fibrous filter and is the geometry of interest for deposition on pipes, wires, and other such objects in an air flow (Chapter 3). The flow patterns at low and high Reynolds numbers differ significantly, and this affects impaction efficiencies. For $\text{Re} > 100$, the velocity distribution outside the velocity boundary layer can be approximated by inviscid flow theory. This approximates the velocity distribution best over the front end of the cylinder which controls the impaction efficiency. The components of the velocity in the direction of the mainstream flow, x , and normal to the main flow, y , are

$$u_{f1} = 1 + \frac{y_1^2 - x_1^2}{(x_1^2 + y_1^2)^2} \quad (4.28a)$$

$$v_{f1} = -\frac{2x_1 y_1}{(x_1^2 + y_1^2)^2} \quad (4.28b)$$

where $x_1 = x/a$ and $y_1 = y/a$. Both x and y are measured from the axis of the cylinder. Numerical calculations for the impaction of Stokesian particles have been carried out for the velocity distribution given by (4.28a) and (4.28b). In making the calculations on cylinders,

it is assumed that the particle velocity at large distances upstream from the cylinder is equal to the air velocity. A linearized form of the equations of particle motion is solved for the region between $x_1 = -1$ and $x_1 = -5$. A numerical solution is obtained for the region between $x_1 = -5$ and the surface of the cylinder.

The analogous problem of impaction of particles on spheres has been studied for application to gas cleaning in packed beds and aerosol scrubbing by droplets. Numerical computations of the impaction efficiency for point particles in inviscid flows around spheres have also been made. Before comparing the numerical computations with the available data, we consider theoretical limiting values for the Stokes number for impaction on cylinders and spheres.

Critical Stokes Number for Inviscid Flows

By analyzing the motion of a small particle in the region near the stagnation point, it can be shown that for an inviscid flow, theory predicts that impaction does not occur until a critical Stokes number is reached. For an inviscid flow, the first term in an expansion of the velocity along the streamline in the plane of symmetry which leads to the stagnation point is

$$u_f = -bU(x_1 + 1) \quad (4.29)$$

where the dimensionless constant b depends on the shape of the body and the dimensionless coordinate $x_1 = x/a$ is negative (Fig. 4.5). For a Stokesian particle, the equation of motion along the stagnation streamline takes the form

$$\text{Stk} \frac{d^2 x'_1}{d\theta^2} + \frac{dx'_1}{d\theta} + bx'_1 = 0 \quad (4.30)$$

where $x'_1 = x_1 + 1$ and $\theta = tU/a$. The solution to this equation is

$$x'_1 = A_1 e^{\lambda_1 \theta} + A_2 e^{\lambda_2 \theta} \quad (4.31)$$

where A_1 and A_2 are integration constants and λ_1 and λ_2 are the roots of the characteristic equation

$$\text{Stk}\lambda^2 + \lambda + b = 0 \quad (4.32)$$

and are given by

$$\lambda_{1,2} = -\frac{1}{2\text{Stk}} \left[1 \pm (1 - 4b\text{Stk})^{1/2} \right] \quad (4.33)$$

From (4.31), the velocity can be determined as a function of x_1 in the region near the stagnation point where the linear approximation (4.29) holds. For $\text{Stk} > \text{Stk}_{\text{crit}} = 1/4b$, the roots are complex conjugates and the u versus x diagram has a focal or spiral point at the stagnation point (Fig. 4.6a). The first intersection of the spiral with the u axis corresponds to the finite velocity at the stagnation point. The rest of the spiral has no physical significance, because the particle cannot pass the surface of the collector.

For $\text{Stk} < 1/4b$, the roots are real and both are negative. The u versus x diagram has a nodal point that corresponds to zero particle velocity at the forward stagnation point and zero impaction efficiency (Fig. 4.6b). For $\text{Stk} = 1/4b$, the roots are equal and the system

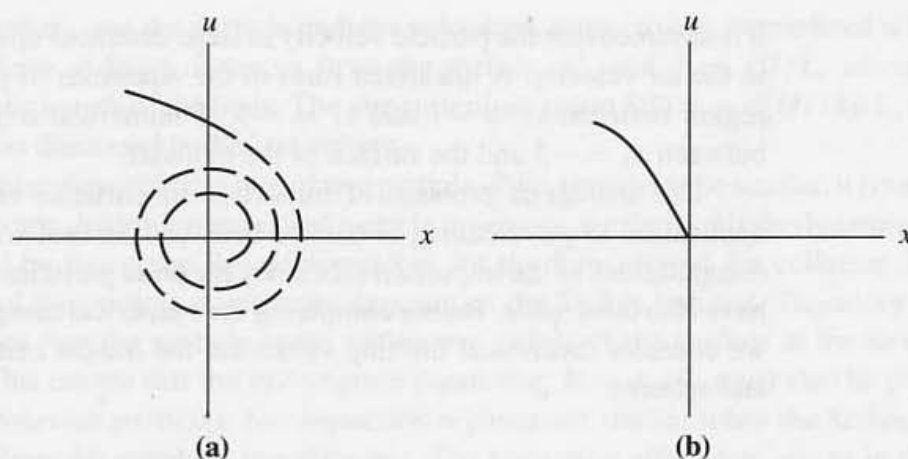


Figure 4.6 (a) Spiral point corresponding to $Stk > Stk_{crit}$. The particle velocity at the surface ($x = 0$) is positive, and the impaction efficiency is nonvanishing. Only the solid portion of the curve is physically meaningful. (b) Nodal point corresponding to $Stk > Stk_{crit}$. Particle velocity vanishes at the surface and the impaction efficiency is zero.

again has a node as its singularity. Thus $Stk = 1/4b$ represents a lower limit below which the impaction efficiency vanishes. For inviscid flow around cylinders, $b = 2$ and $Stk_{crit} = 1/8$, whereas for a sphere, $b = 3$ and $Stk_{crit} = 1/12$, based on the radius of the collector.

This analysis provides a lower anchor point for curves of impaction efficiency as a function of Stokes number. It applies also to non-Stokesian particles, discussed in the next section, because the point of vanishing efficiency corresponds to zero relative velocity between particle and gas. Hence Stokes law can be used to approximate the particle motion near the stagnation point. This is one of the few impaction problems for which an analytical solution is possible.

The analysis neglects boundary layer effects and is probably best applied when the particle diameter is larger than, or of the order of, the boundary layer thickness. The change in the drag law as the particle approaches the surface is also not taken into account. Hence the criterion provides only a rough estimate of the range in which the impaction efficiency becomes small.

For most real (viscous) flows, $u_f \sim (x_1 + 1)^2$ in the region near the stagnation point because of the no-slip boundary condition and the continuity relation. In this case, (4.29) does not apply, the equation of particle motion cannot be put into the form of (4.30), and the analysis developed above is not valid. Instead, numerical calculations for the viscous flow regime ($u_f \sim (x_1 + 1)^2$) indicate that the collection efficiency is finite for all nonzero values of Stk , vanishing for $Stk \rightarrow 0$ (Ingham et al., 1990).

Example: In certain types of heat exchangers, a gas flows normal to a bank of tubes carrying fluid at a different temperature, and heat transfer occurs at the interface. Fouling of the outside surface of the tubes by particles depositing from the flow reduces the heat transfer rate. If the tubes are 1 in. (outside diameter) and the gas velocity is 10 ft/sec, estimate the diameter of the largest particle ($\rho_p = 2 \text{ g/cm}^3$) that can be permitted in the gas stream *without* deposition by impaction on the

tubes. Assume the gas has the properties of air at 100°C ($\nu = 0.33 \text{ cm}^2/\text{sec}$, $\mu = 2.18(10^{-4}) \text{ g/cm sec}$).

SOLUTION: To analyze the problem, consider particle deposition on a single cylinder placed normal to an aerosol flow. The Reynolds number for the flow, based on the cylinder diameter, is 2320, which is sufficiently large to use the potential flow approximation for the stagnation region. We know that the critical Stokes number for the cylinder is

$$\frac{\rho_p d_p^2 U}{18\mu a} = \frac{1}{8}$$

When we substitute and solve for d_p , the result is $d_p \approx 10 \mu\text{m}$. Particles smaller than this will not deposit by impaction on the tubes according to calculations based on potential flow theory. In reality, there may be a small contribution by impaction due to boundary layer effects and direct interception. Diffusion may also contribute to deposition.

Comparison of Experiment and Theory

Experimental studies have been made of the impaction of nearly monodisperse sulfuric acid particles in the size range $0.3 < d_p < 1.4 \mu\text{m}$ on a wire $77 \mu\text{m}$ in diameter over a Reynolds number range 62 to 500 (Ranz and Wong, 1952; Wong and Johnstone, 1953). In Fig. 4.7, these data are compared with numerical computations based on inviscid flow theory for point particles (Brun et al., 1955). Agreement between measured and calculated values is fair. The experimental results fall somewhat below the calculated values for $0.8 < \text{Stk} < 3$. At values of Stk above about 3, the data fall above theory. Data were not taken at sufficiently small values of Stk to test the theoretical value ($\text{Stk}_{\text{crit}} = 1/8$) at which the efficiency is expected to vanish. The results of these measurements are not directly applicable to high-efficiency fibrous filters, which usually operate at much lower Reynolds numbers based on the fiber diameter.

Hahner et al. (1994) studied the deposition of monodisperse droplets ($0.9 < d_p < 15 \mu\text{m}$) on steel spheres a few millimeters in diameter at air velocities ranging from 7 to 28 m/sec. Studies were made with single spheres and multiple sphere arrays. Experimental results for single spheres are compared with theory in Fig. 4.8. Two different theoretical calculations were made, one based on inviscid flow theory and the other for a boundary layer flow at a Reynolds number of 500. Calculated collection efficiencies were about the same for both cases. For $\text{Stk} > 0.5$, there is good agreement between experiment and theory. The experimental measurements were made over a wide range of Reynolds numbers, 1400 to 17,000, based on sphere diameter. Hence the inviscid flow field, which does not vary with Reynolds number, describes the velocity distribution sufficiently well over the forward region of the sphere where most of the deposition occurs. For $\text{Stk} < 0.2$, theory falls below the experimental results; significant deposition occurred at values of $\text{Stk} < 1/12$, the critical cutoff value for impaction on spheres.

The results for arrays of solid spheres are applicable to particle removal by impaction in packed beds. However, care must be taken in extrapolating the results for individual solid

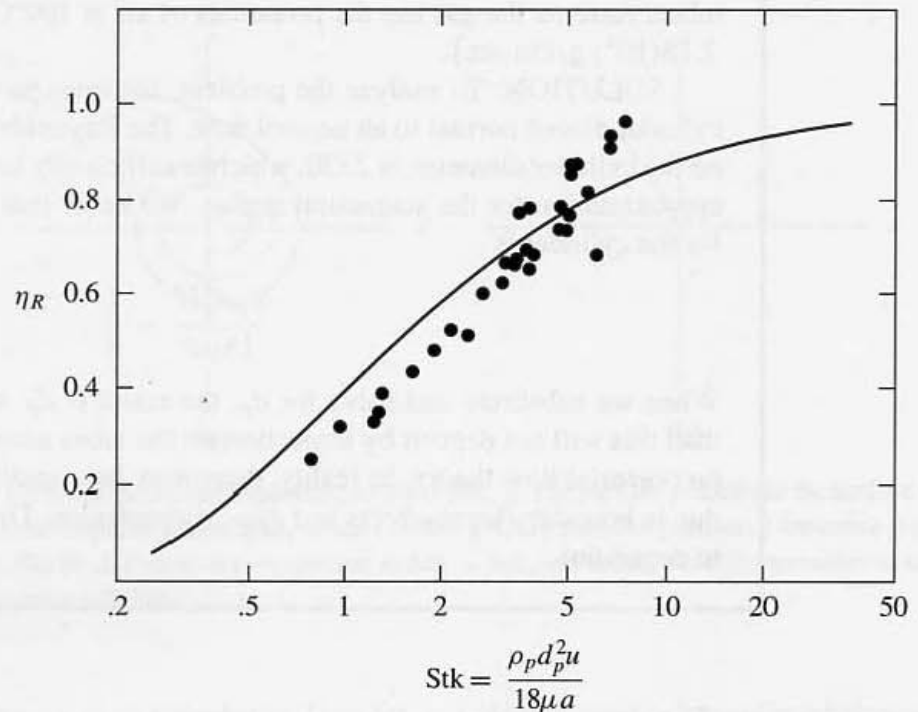


Figure 4.7 Comparison of theory and experiment for impaction on single cylinders. Theoretical calculations are by Brun et al. (1955) for point particles in an inviscid flow, and the data are those of Wong and Johnstone (1953) for $100 < \text{Re} < 330$.

spheres to falling water drops which begin to oscillate once a critical diameter is reached. Single-drop studies in wind tunnels and fall chambers show that such oscillations become noticeable for drop diameters greater than 1 mm ($\text{Re} > 300$) in response to the unsteadiness of the air flow (Pruppacher and Klett, 1997, p. 400). These oscillations and other types of secondary motion (Clift et al., 1978, p. 185) may in turn affect the efficiency of collection by impaction.

IMPACTION OF NON-STOKESIAN PARTICLES

In previous sections, we have considered the case of small particles that follow Stokes law in their motion with respect to the local gas velocity all along their trajectories. For high-velocity flows around a collector, particles with high inertia retain their velocities as they approach the surface, and the Reynolds number for their motion may be too large for the Stokes law approximation to hold. The approach taken previously must then be modified to account for the change in the form of the drag law. Interest in such phenomena was originally stimulated by the problem of the icing of airplane wings caused by deposition of cloud and rain drops on the leading edge of the wing. The problem continues to be troubling, contributing to fatal accidents—especially for propeller planes and helicopters, which fly more slowly and at lower altitudes than jets.

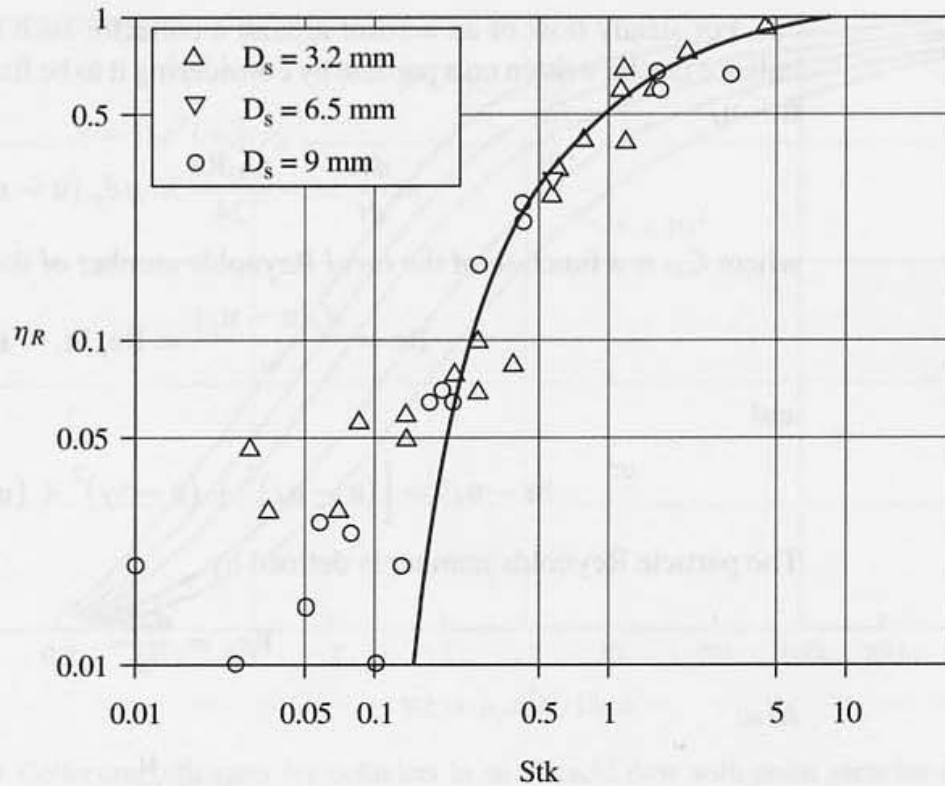


Figure 4.8 Comparison of experiment and theory for impaction of monodisperse droplets on single solid spheres (after Hahner et al., 1994). Points correspond to different collector diameters. The numerical simulations were for a Reynolds number of 500 based on sphere diameter. The two cases considered, potential flow and boundary layer flow, gave similar results. Both agree well with experiment for $Stk > 0.2$. However, the experimental results indicate that measurable deposition occurs at values of $Stk < Stk_{crit} = 1/12$.

Derivation of a modified equation of motion for the particle that accounts approximately for the non-Stokesian motion of the particles is based on the general expression for the drag on a fixed spherical particle in a gas of uniform velocity, U (Brun et al., 1955):

$$F = \frac{\rho \pi d_p^2}{8} C_D U^2 \quad (4.34)$$

This expression defines the drag coefficient, C_D , which by dimensional analysis is a function of the Reynolds number based on particle diameter and gas velocity. For $Re \ll 1$, Stokes law is applicable, and $C_D = 24/Re$. Rewriting (4.34) to include the Stokes form, we obtain

$$F = \frac{C_D Re}{24} (3\pi \mu d_p U) \quad (4.35)$$

In general, it is necessary to use the results of experiments and semiempirical correlations to relate the drag coefficient to the Reynolds number. The expression

$$C_D = \frac{24}{Re} (1 + 0.158 Re^{2/3}) \quad (4.36)$$

agrees well with experiment for $Re < 1000$.

For steady flow of an aerosol around a collector such as a cylinder or sphere, a force balance can be written on a particle by considering it to be fixed in a uniform flow of velocity $\mathbf{u} - \mathbf{u}_f$:

$$m \frac{d\mathbf{u}}{dt} = -\frac{C_D \text{Re}}{24} 3\pi \mu d_p (\mathbf{u} - \mathbf{u}_f) \quad (4.37)$$

where C_D is a function of the *local* Reynolds number of the particle:

$$\text{Re} = \frac{d_p |\mathbf{u} - \mathbf{u}_f|}{\nu} = \text{Re}_p |\mathbf{u}_1 - \mathbf{u}_{f1}| \quad (4.38)$$

and

$$|\mathbf{u} - \mathbf{u}_f| = \left[(u - u_f)^2 + (v - v_f)^2 + (w - w_f)^2 \right]^{1/2} \quad (4.38a)$$

The particle Reynolds number is defined by

$$\text{Re}_p = \frac{d_p U}{\nu} \quad (4.38b)$$

Also

$$\mathbf{u}_1 = \frac{\mathbf{u}}{U} \quad (4.38c)$$

$$\mathbf{u}_{f1} = \frac{\mathbf{u}_f}{U} \quad (4.38d)$$

where U is the gas velocity at large distances from the collector.

As in the case of Stokesian particles, the contribution of particle acceleration to the drag has been neglected. Clearly, (4.37) is on shaky ground from a theoretical point of view. Its application should be tested experimentally, but a rigorous validation has never been carried out. In nondimensional form, (4.37) can be written as follows:

$$\frac{d\mathbf{u}_1}{d\theta} = -\frac{C_D \text{Re}_p}{24} \frac{1}{\text{Stk}} |\mathbf{u}_1 - \mathbf{u}_{f1}| (\mathbf{u}_1 - \mathbf{u}_{f1}) \quad (4.39)$$

where $\theta = tU/a$ and $\text{Stk} = \rho_p d_p^2 U / 18 \mu a$. The gas velocity, \mathbf{u}_{f1} is a function of the Reynolds number based on the collector diameter. The drag coefficient is a function of $\text{Re}_p |\mathbf{u}_1 - \mathbf{u}_{f1}|$. Hence the trajectory of a non-Stokesian point particle is determined by Re , Stk , and Re_p ; one more dimensionless group, Re_p , appears in the theory than in Stokesian particle theory.

Impaction efficiencies for inviscid flows around single elements of various shapes have been determined by solving (4.39) numerically. The case that has received most study is that of impaction on right circular cylinders placed normal to the air flow. Results of numerical calculations are shown in Fig. 4.9. Original applications were to the icing of airplane wings and to the measurement of droplet size in clouds. Because the drop size was not known, a new dimensionless group $P = \text{Re}_p^2 / \text{Stk} = 18 \rho^2 U a / \mu \rho_p$, independent of drop size, was introduced. This new group is formed by combining the two groups on which the efficiency depends in the inviscid flow range. According to the rules of dimensional analysis, this is permissible, but the efficiency is still determined by two groups, which for convenience are chosen to be Stk and P . If the collection efficiency is known, the particle size can be

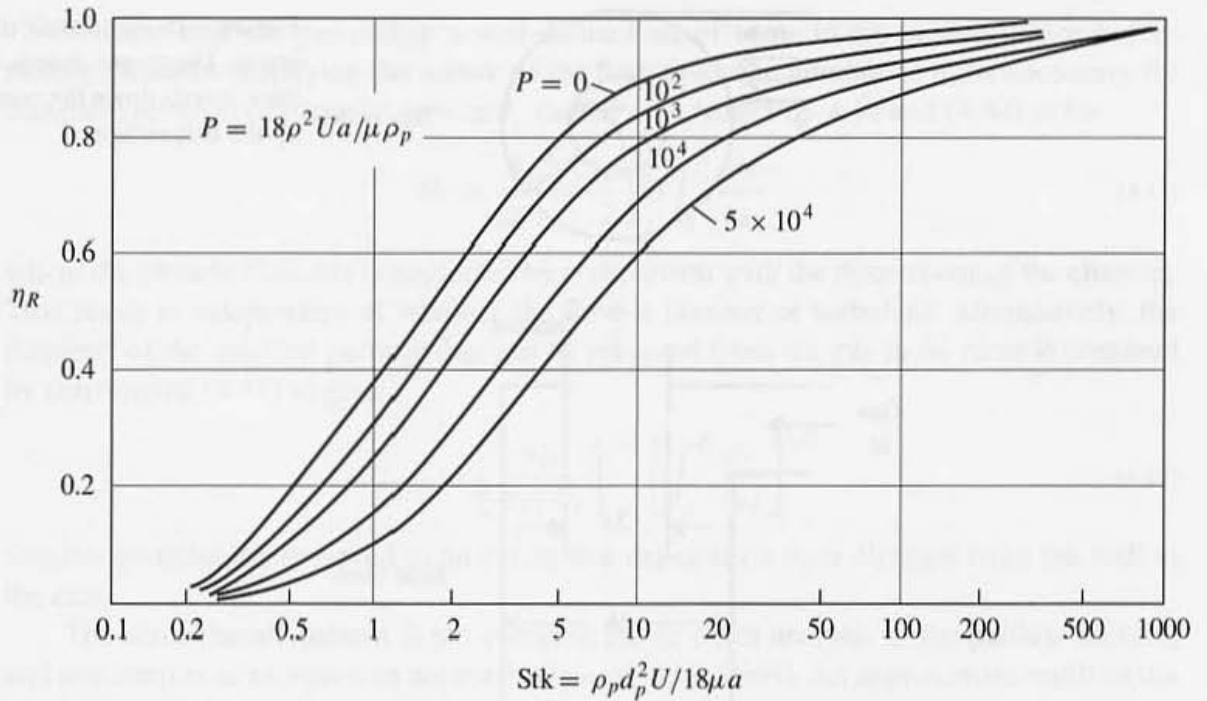


Figure 4.9 Collection efficiency for cylinders in an inviscid flow with point particles (Brun et al., 1955). The rate of deposition, particles per unit time per unit length of cylinder, is $2\eta_R n_\infty U a$, where n_∞ is the particle concentration in the mainstream. The dimensionless group $P = \text{Re}_p^2 / \text{Stk} = 18\rho^2 U a / \mu \rho_p$ is independent of size and is of use in sampling cloud droplets. The magnitude of P is a measure of the deviation from Stokes law for the forces acting on the particle. For $P = 0$, Stokes law holds for the drag on the particle.

determined from Fig. 4.9. More often, the curves are used to determine collection efficiency at known values of Stk and P .

DEPOSITION FROM A ROTATING FLOW: CYCLONE SEPARATOR

Cyclone separators (Fig. 4.10) are frequently used for the removal of particles larger than a few micrometers from process gases. The dusty gas enters the annular space between the wall and the exit tube through a tangential inlet. The gas acquires a rotating motion, descends along the outer wall, and then rises, still rotating, to pass out the exit tube. Particles move to the outer wall as a result of centrifugal forces. They fall from the slowly moving wall layer into a hopper at the bottom. Cyclones are inexpensive and can be constructed in local sheet-metal shops. They have no moving parts and require little maintenance. They are often used for preliminary cleaning of the coarse fraction before the gases pass to more efficient devices, such as electrostatic precipitators. A common application is in the removal of flyash from gases from pulverized coal combustion.

An approximate analysis of the particle motion and cyclone performance can be carried out by setting up a force balance for Stokesian particles in the radial direction:

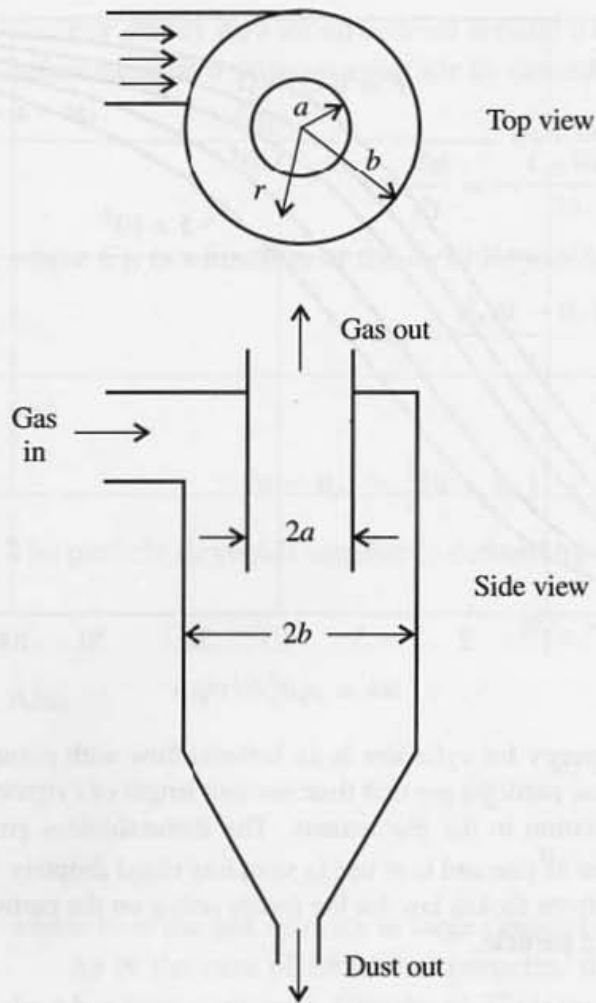


Figure 4.10 Schematic diagram of cyclone separator. Dusty gas enters through the tangential inlet, spirals down the conical section, and moves up the exit section.

$$F_r = m \left[\frac{d^2r}{dt^2} - r \left(\frac{d\theta}{dt} \right)^2 \right] = -3\pi\mu d_p (v_r - v_{rf}) \quad (4.40)$$

where r and θ and the axis of the cyclone separator represent a set of cylindrical coordinates. For small particles, the acceleration term d^2r/dt^2 can be neglected; only the second term on the left-hand side—the “centrifugal force” term—is retained. When we neglect also the radial component of the gas velocity, v_{rf} , the result is

$$v_r = \frac{dr}{dt} = \frac{mr}{3\pi\mu d_p} \left(\frac{d\theta}{dt} \right)^2 \quad (4.41)$$

The particle trajectory is determined by rearranging (4.41):

$$\frac{dr}{d\theta} = \frac{mv_\theta}{3\pi\mu d_p} \quad (4.42)$$

For the motion in the θ direction, it is assumed that the particle and gas velocities are equal, $v_\theta = v_{\theta f}$. It is thus possible to solve (4.42) for the particle trajectories, if the gas velocity distribution, $v_{\theta f}$, is known.

Assume that the gas makes a well-defined set of turns in the annular space before exiting. Without specifying the nature of the flow field, the number of turns necessary for complete removal of particles of size d_p can be seen from Fig. 4.10 and (4.42) to be

$$N_t = \frac{\theta}{2\pi} = \frac{3\mu d_p}{2m} \int_a^b \frac{dr}{v_{\theta f}} \quad (4.43)$$

where the particle diameter is neglected by comparison with the dimensions of the channel. This result is independent of whether the flow is laminar or turbulent. Alternatively, the diameter of the smallest particle that can be removed from the gas in N_t turns is obtained by rearranging (4.43) to give

$$d_{p \min} = \left[\frac{9\mu}{\pi \rho_p N_t} \right]^{1/2} \left[\int_a^b \frac{dr}{v_{\theta f}} \right]^{1/2} \quad (4.44)$$

Smaller particles are removed to an extent that depends on their distance from the wall at the entry.

The aerodynamic pattern is too complex for an exact analysis of the particle motion, and semiempirical expressions are used for $v_{\theta f}$ (Fuchs, 1964). An approximate result of the integration of (4.44) often used in design applications has the form

$$d_{p \min} \sim \left[\frac{\mu(b-a)}{\rho_p N_t U} \right]^{1/2} \quad (4.45)$$

where U is the average velocity of the gas in the inlet tube. The number of turns, N_t , is usually determined empirically. For fixed gas velocity, performance improves as the diameter of the cyclone is reduced, because the distance the particle must move for collection decreases. It is likely the radial gas velocity components, associated with eddies, are also reduced in the smaller diameter cyclones.

PARTICLE EDDY DIFFUSION COEFFICIENT

Small particles in a turbulent gas diffuse from one point to another as a result of the eddy motion. The eddy diffusion coefficient of the particles will in general differ from that of the carrier gas. An expression for the particle eddy diffusivity can be derived for a Stokesian particle, neglecting the Brownian motion. In carrying out the analysis, it is assumed that the turbulence is homogeneous and that there is no *mean* gas velocity. The statistical properties of the system do not change with time. Essentially what we have is a stationary, uniform turbulence in a large box. This is an approximate representation of the core of a turbulent pipe flow, if we move with the mean velocity of the flow.

The analysis is similar to that used in Chapter 2 to derive the Stokes–Einstein relation for the diffusion coefficient. Again we consider only the one-dimensional problem. Particles originally present in the differential thickness around $x = 0$ (Chapter 2) spread through the fluid as a result of the turbulent eddies. If the particles are much smaller than the size of the eddies, the equation of particle motion for Stokesian particles, based on (4.24) (see associated discussion), is

$$m \frac{du}{dt} = -f(u - u_f)$$

where u_f is the local velocity of the turbulent gas. The distance traveled by a particle in time t is obtained by integrating (4.24):

$$x + \frac{u - u_0}{\beta} = \int_0^t u_f(t') dt' \quad (4.46)$$

where $\beta = f/m$. Multiplying the left-hand side by $(1/\beta)(du/dt) + u$ and the right-hand side by u_f , which is permissible by (4.24), we obtain

$$\frac{x}{\beta} \frac{du}{dt} + xu + \frac{(u - u_0)}{\beta^2} \frac{du}{dt} + \frac{u^2 - u_0 u}{\beta} = \int_0^t u_f(t) u_f(t') dt' \quad (4.47)$$

We now average each term in (4.47) over all of the particles originally in the element around $x = 0$. On a term-by-term basis,

$$\frac{\overline{x du}}{dt} = \frac{d \overline{xu}}{dt} - \overline{u^2} \quad (4.48)$$

The particle eddy diffusion coefficient is given by

$$\epsilon_p = \overline{xu} = \frac{1}{2} \frac{d \overline{x^2}}{dt} \quad (4.49)$$

and does not change with time after a sufficiently long interval from the start of the diffusion process. Hence

$$\frac{d \overline{xu}}{dt} = 0 \quad (t \rightarrow \infty) \quad (4.50)$$

Because the statistical properties of the system do not change with time,

$$\frac{\overline{u du}}{dt} = \frac{1}{2} \frac{d \overline{u^2}}{dt} = 0 \quad (4.51)$$

After long periods of time, there is no correlation between the particle acceleration and its initial velocity:

$$\frac{\overline{u_0 du}}{dt} = 0 \quad (t \rightarrow \infty) \quad (4.52)$$

or between its velocity and its initial velocity:

$$\overline{u_0 u} = 0 \quad (t \rightarrow \infty) \quad (4.53)$$

Averaging (4.47) over the particles and substituting (4.46) through (4.53) gives

$$\epsilon_p = \overline{u_f^2} \int_0^{t \rightarrow \infty} R(t') dt' \quad (4.54)$$

The coefficient of correlation, R , between gas velocities *in the neighborhood of the particle* at two different times, t_1 and t_2 , is defined by the relation

$$\overline{u_f(t_1) u_f(t_2)} = \overline{u_f^2} R(t_2 - t_1) \quad (4.55)$$

where $\overline{u_f^2}$ is the mean square gas velocity averaged over the particle trajectory. The value of the correlation coefficient is near unity when t_2 is near t_1 and then becomes very small as the interval $t_2 - t_1$ increases. The integral in (4.54), which has the dimensions of a time, is assumed to approach a limit rapidly.

By (4.54), the particle eddy diffusivity is proportional to the mean square fluid velocity multiplied by the time scale $\int_0^{t \rightarrow \infty} R(t') dt'$. This expression is of the same form as the Taylor eddy diffusion coefficient for the turbulent fluid (Goldstein, 1938, p. 217). However, the correlation coefficient in (4.54) applies to the gas velocities *over the path of the particle*. Heavy particles move slowly and cannot follow the fluid eddies that surge around them. Thus the time scale that should be employed in (4.54) ranges between the Lagrangian scale for small particles that follow the gas and the Eulerian time scale for heavy particles that remain almost fixed (Friedlander, 1957).

Some attempts have been made to determine these time scales. In one set of experiments with a homogeneous grid-generated turbulence, the ratio of the Lagrangian to the Eulerian scales was reported to be three (Snyder and Lumley, 1971). Thus the ratio of the eddy diffusivity of a particle that is too heavy to follow the gas motion to the eddy diffusivity of the gas would be 1/3. What is meant by a *heavy* particle in this context? One measure is the ratio of the characteristic particle time $\rho_p d_p^2 / 18\mu$ to the smallest time scale of the fluid motion $(\nu/\epsilon_d)^{1/2}$, where ν is the kinematic viscosity of the gas and ϵ_d is the turbulent energy dissipation (cm^2/s^3). For a heavy particle, this ratio would be much greater than unity.

Numerical simulation of the eddy diffusion of particles in the turbulent core of a pipe flow indicates that for particles smaller than about $170 \mu\text{m}$, particle and gas eddy diffusion coefficients are about the same (Uijttewaal, 1995). The studies were made for three Reynolds numbers 5500, 18,300, and 42,000 with particles of about unit density and a pipe diameter of 5 cm. Hence for the usual ranges of interest in aerosol dynamics, particle and gas eddy diffusion coefficients can be assumed equal in the turbulent core. However, the viscous sublayer near the wall of a turbulent pipe flow alters the situation as discussed in the next section.

TURBULENT DEPOSITION

When a turbulent gas carrying particles with aerodynamic diameter larger than about $1 \mu\text{m}$ flows parallel to a surface, particles deposit because of the fluctuating velocity components normal to the surface. Particles are unable to follow the eddy motion and are projected to the wall through the relatively quiescent fluid near the surface. The net rate of deposition depends on the relative rates of transport and reentrainment. The first experimental measurements (Friedlander and Johnstone, 1957) were made with turbulent flows through vertical tubes whose smooth walls were coated with an adhesive film to permit measurement of the deposition rate alone. The data were correlated by introducing a particle transfer coefficient $k = |\bar{J}|/\bar{n}_\infty$, where \bar{J} is the particle flux at a given point on the pipe wall and \bar{n}_∞ is the average particle concentration in the mainstream of the fluid at that cross section. The transfer coefficient has the dimensions of a velocity and is sometimes called the deposition velocity.

Data for the deposition of spherical $0.8\text{-}\mu\text{m}$ iron particles in an 0.58-cm smooth-walled tube with a well-faired entry are shown in Fig. 4.11 as a function of distance from the entry.

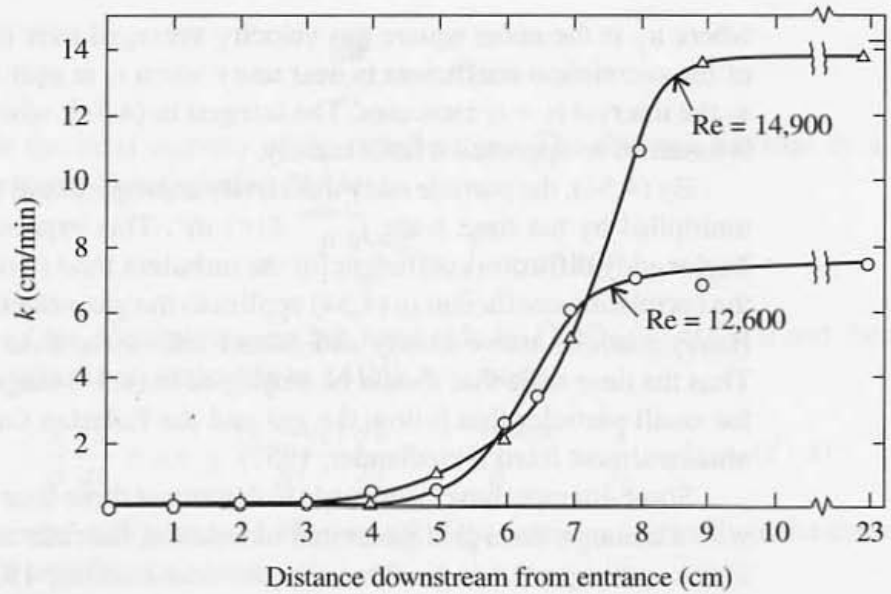


Figure 4.11 Deposition of $0.8 \mu\text{m}$ iron particles near the entrance of an 0.58 cm tube. The Reynolds numbers shown are for the tube flow. Near the tube entrance, the flow is laminar, and no deposition takes place. In the transition region, the boundary layer turns turbulent, and deposition increases until it reaches the value corresponding to fully developed turbulent pipe flow (Friedlander and Johnstone, 1957).

When the Reynolds number based on tube diameter is greater than 2100, the boundary layer becomes turbulent at some distance from the inlet. The transition usually occurs at a Reynolds number, based on distance from the entrance, Re_x , of between 10^5 and 10^6 , depending on the roughness of the wall and the level of turbulence in the mainstream. As shown in Fig. 4.11, the deposition rate tends to follow the development of the turbulent boundary layer. No deposition occurs until Re_x is about 10^5 ; the rate of deposition then approaches a constant value at $Re_x = 2 \times 10^5$ in the region of fully developed turbulence.

On dimensional grounds, the deposition velocity at a given pipe Reynolds number can be assumed to be a function of the friction velocity, u_* , kinematic viscosity, ν , and the particle relaxation time, m/f :

$$k = f(u_*, \nu, m/f) \quad (4.56)$$

Both k and u_* have dimensions of velocity while ν and m/f have dimensions of $(\text{length})^2/\text{time}$ and time, respectively. Effects related to the finite particle diameter such as direct interception and lift are neglected as a first approximation. Because there are four variables and two dimensions, two dimensionless groups can be constructed:

$$k^+ = \frac{k}{u_*} = f\left[\frac{mu_*^2}{fv}\right] \quad (4.57)$$

The dimensionless group that appears on the right-hand side is the ratio of the particle stop distance, mu_*/f , to the characteristic turbulence length, ν/u_* . The stop distance so defined is based on the friction velocity, u_* , which is approximately equal to the rms. fluctuating velocity component normal to the wall in the turbulent core. The dimensionless stop distance

$S^+ = mu_*^2/fv$ can also be interpreted as a dimensionless relaxation time τ^+ , where m/f is a characteristic time for particle motion and v/u_*^2 is a characteristic time for the turbulent fluctuations. Hence $S^+ = \tau^+$. The viscous sublayer is the region near a smooth wall where momentum transport is dominated by the viscous forces, which are large compared with eddy diffusion of momentum. Following the usual practice and taking the sublayer thickness to extend to $y^+ = 5$, particles with a stop distance $S^+ < 5$ would not reach the wall if the sublayer were truly stagnant.

However, the experiments of Friedlander and Johnstone (1957) (Fig. 4.12a) and later measurements by Liu and Agarwal (1974) (Fig. 4.12b) and others clearly demonstrated that particle deposition took place at values of $S^+ < 5$. The data show that particles penetrate the viscous sublayer and deposit even though their stop distance based on the r.m.s. fluctuating velocity in the core is insufficient to propel the particles through a completely stagnant

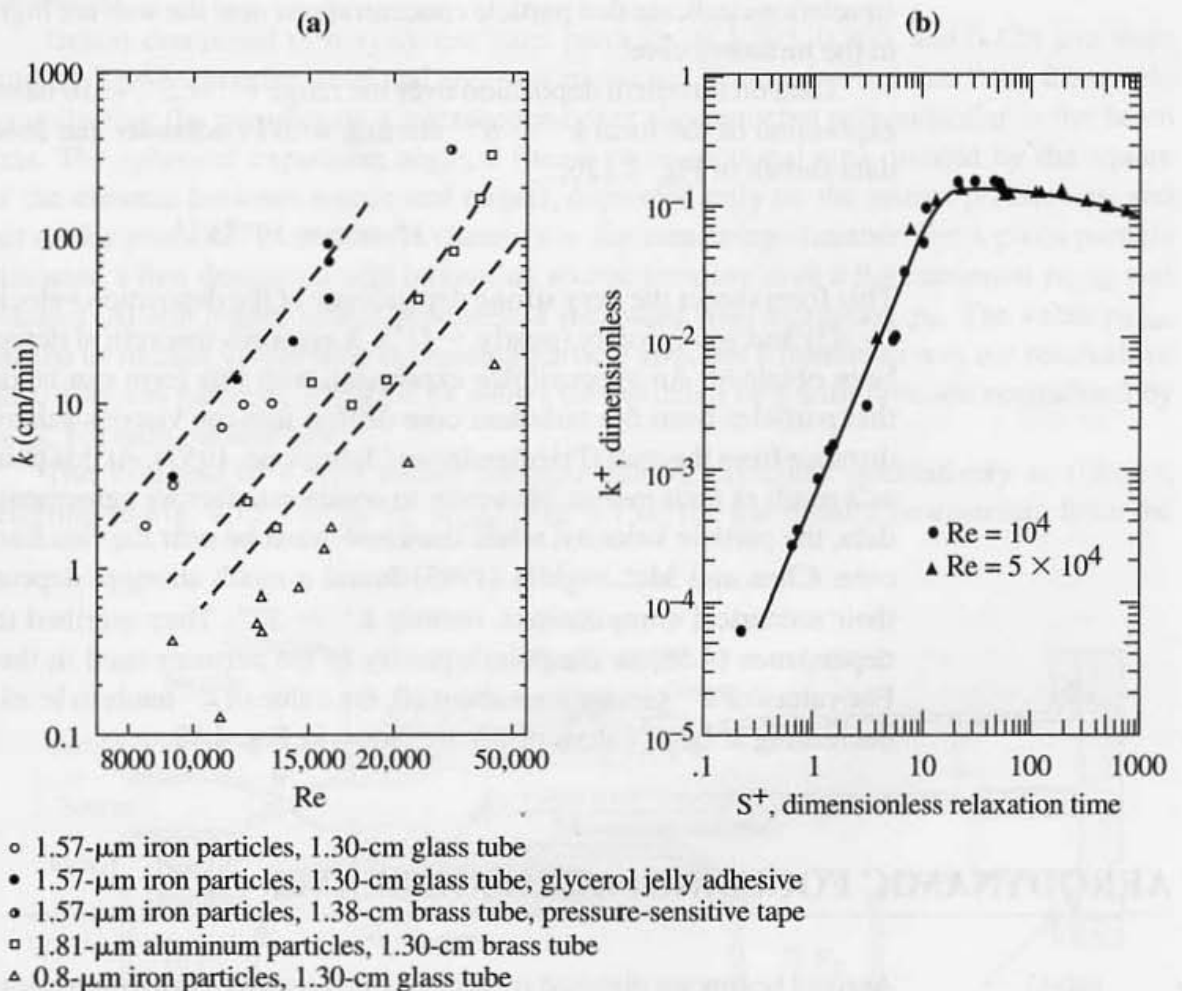


Figure 4.12 (a) Deposition of iron and aluminum particles in glass and brass tubes of different sizes with coatings of various types. A goal of this set of experiments was to vary the electrical and surface characteristics of the system. The dashed curves are theoretical calculations (Friedlander and Johnstone, 1957). (b) Deposition of monodisperse olive oil droplets with particle diameters ranging from 1.4 to 21 μm in a 1/2" glass pipe at two different Reynolds numbers. (After Liu and Agarwal, 1974.)

viscous sublayer. Over the limited Reynolds number range of the measurements, there was relatively little dependence of k^+ on the Reynolds number.

There are at least two ways that particles from the turbulent core can penetrate the viscous sublayer and deposit, even though $S^+ = \tau^+ < 5$: "Hot" particles with velocities larger than the rms fluctuating velocity and correspondingly higher stop distances may shoot through the sublayer to the wall. Alternatively, as noted by Friedlander and Johnstone (1957) in this context, the viscous sublayer is not truly stagnant. Weak gas velocity fluctuations bring the particles sufficiently close to the wall for their inertia to carry them to the surface.

Evidence for both mechanisms based on numerical computations has been reported by Chen and McLaughlin (1995). They found a bimodal distribution in the impact velocities of particles striking the wall for $\tau^+ = 10$. They associated the peak velocities of $0.3u_*$ and $10^{-3}u_*$ with particles projected from the core and particles transported by eddy diffusion, respectively. Chen and McLaughlin (1995) and other investigators also report that numerical simulations indicate that particle concentrations near the wall are higher than concentrations in the turbulent core.

Data on turbulent deposition over the range $\tau^+ = S^+ < 10$ have been correlated by an expression of the form $k^+ \sim S^{+2}$ starting with Friedlander and Johnstone (1957). For the data shown in Fig. 4.12b,

$$k^+ \approx 6 \times 10^{-4} S^{+2} \quad (4.58)$$

This form shows the very strong dependence of the deposition velocity on particle diameter ($\sim d_p^4$) and gas velocity (nearly $\sim U^5$). A rigorous theoretical derivation of (4.58) has not been obtained. An approximate expression with this form can be derived if it is assumed that particles from the turbulent core diffuse into the viscous sublayer to a point one stop distance from the wall (Friedlander and Johnstone, 1957). At this point, the particles deposit as a result of their inertia. However, to obtain satisfactory agreement with the experimental data, the particle velocity, when launched, must be near the rms fluctuating velocity in the core. Chen and McLaughlin (1995) found a much stronger dependence of k^+ on S^+ in their numerical computations, namely $k^+ \sim S^{+4}$. They ascribed the lower values of the dependence (4.58) to the polydispersity of the aerosols used in the experimental studies. For values of τ^+ greater than about 10, the value of k^+ tends to level off at about 0.1 before decreasing at large values of τ^+ , as shown in Fig. 4.12.

AERODYNAMIC FOCUSING: AEROSOL BEAMS

Aerosol beams are directed streams of small particles in a low pressure gas. They are formed when an aerosol expands from a high-pressure reservoir through a nozzle into a low-pressure chamber. Aerosol beams were discussed early in this chapter in connection with studies of particle rebound from surfaces. Such beams are also used to introduce particles into mass spectrometers for single-particle chemical analysis (Chapter 6). The characteristics of the aerosol beam depend on particle size, nozzle configuration (converging or capillary), and skimmer arrangements.

In experiments with a converging nozzle, Israel and Friedlander (1967) showed that the aerosol beam could be focused over a very narrow region. A schematic diagram of their converging nozzle is shown in Fig. 4.13. The diameter of the nozzle was about 1 cm at the entrance and then decreased rapidly to 0.5 mm. The last millimeter of the nozzle formed a cone with a cone angle of $6.5^\circ \pm 0.5^\circ$, and the throat diameter was $157 \pm 1 \mu$. The throat had a sharp edge with inhomogeneities due to glass splinters of less than 15μ . The skimmer consisted of a cone with a rather flat top about 1.3 mm in diameter with an orifice 400μ in diameter. The distance between nozzle and skimmer was 570μ , so that all the particles in the jet entered the measuring chamber, whereas only a small portion of the air passed through the skimmer. The purpose of the skimmer was to separate the air from the air-particle beam to achieve a better vacuum in the measuring chamber. Source pressures ranged from 15 to 200 torr, and downstream chamber pressures ranged from 5×10^{-4} to 5×10^{-2} torr. The pressure ratio p/p_0 (nozzle chamber pressure to source pressure) was always less than 0.53, the critical pressure ratio for air, so the gas reached sonic velocity at the throat.

Beams composed of polystyrene latex particles of 1.305, 0.365, and 0.126μ m were studied. The beam cross-sectional area was measured 28 mm downstream from the nozzle by collecting the particles on a microscope cover slip mounted perpendicular to the beam axis. The spherical expansion angle, δ (beam cross-sectional area divided by the square of the distance between nozzle and target), depended only on the source pressure p_0 and not on the pressures in the nozzle chamber or the measuring chamber. For a given particle diameter, δ first decreased with increasing source pressure until a flat minimum $p_{0\min}$ was reached. At still higher source pressures, δ increased with increasing p_0 . The value $p_{0\min}$ shifted to smaller values with decreasing particle size, but a minimum was not reached for the $0.126\text{-}\mu$ m particles. Figure 4.14 shows the variation of δ with pressure normalized by $p_{0\min}$ for each particle size.

The variation of δ with source pressure can be explained qualitatively as follows, referring to Fig. 4.15. For $p_0 \ll p_{0\min}$ (Fig. 4.15a) the gas density downstream from the

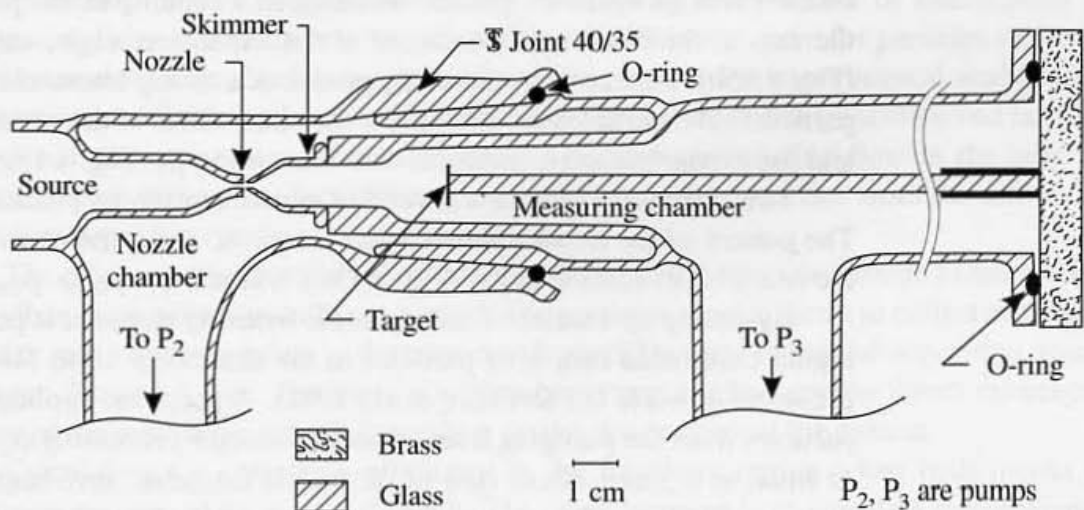


Figure 4.13 Converging nozzle used for the generation and study of aerosol beams (Israel and Friedlander, 1967).

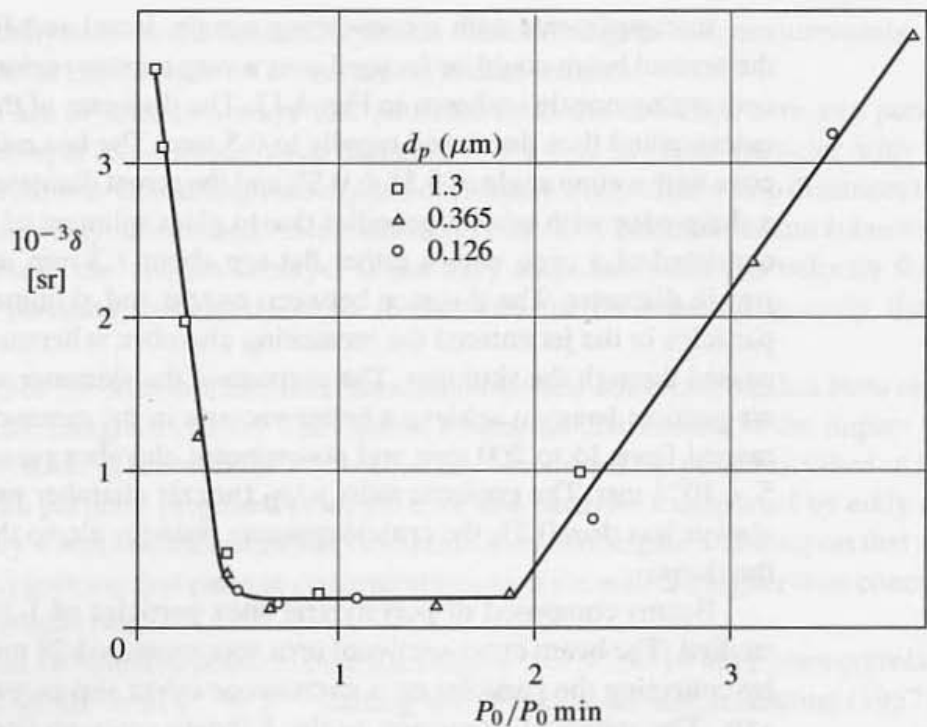


Figure 4.14 Dependence of the beam expansion angle δ on the reduced source pressure $p_0/p_{0\min}$ for the converging nozzle. $p_{0\min}$ ($0.126 \mu\text{m}$) = 29 mm; $p_{0\min}$ ($0.365 \mu\text{m}$) = 51 mm; $p_{0\min}$ ($1.3 \mu\text{m}$) = 330 mmHg.

throat is very low, and there is little drag on the particles, whose size is of the order of, or less than, the mean free path of the gas. Therefore, the particles travel downstream from the throat along rectilinear extensions of the trajectories established in the nozzle. With increasing pressure p_0 —that is, increasing air density in the jet—the influence of the air on the particles becomes greater, resulting in a bending of the particle trajectories toward the axis of the beam and a decrease of the expansion angle, until a minimum is reached (Fig. 4.15b). Further increase of p_0 produces a strong interaction between the jet and the particles. The particles tend to follow the streamlines of the air in the vicinity of the throat and the expansion angle increases with increasing p_0 (Fig. 4.15c).

This qualitative picture was verified experimentally by blocking part of the nozzle inlet. The pattern of the deposit showed that for $p_0 \ll p_{0\min}$ the particle paths crossed between the nozzle inlet and the target (Fig. 4.15a), whereas for $p_0 \gg p_{0\min}$ crossing did not occur.

By setting up a series of aerodynamic focusing stages, it is possible to produce narrow, highly collimated beams of particles in the size range 10 to 500 nm with aerosol source pressures down to 0.1 torr (Liu et al., 1995). A proposed application is to the sampling of particles from the pumping lines of semiconductor processing equipment. Beam diameters as small as 0.3 mm, about 10% of the nozzle diameter, have been obtained at downstream distances of 50 cm. By using a series of aerodynamic focusing stages upstream of an aerosol size spectrometer, considerable gains in instrument resolution can be achieved (de la Mora, 1996).

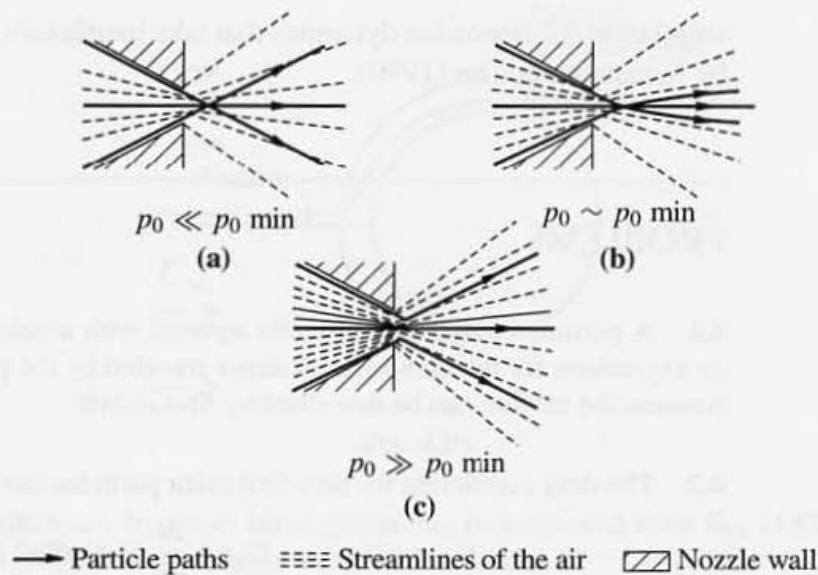


Figure 4.15 Schematic diagram of particle trajectories downstream from the exit of the converging nozzle. (a) Large particles follow their initial motion and their paths cross, producing a divergent beam. (b) Intermediate size particles bend toward the axis under the influence of the gas, producing a focused beam. (c) Very small particles follow the gas motion, producing a divergent beam.

TRANSITION FROM THE DIFFUSION TO INERTIAL RANGES

In the last two chapters, we have considered particle deposition from certain internal and external flows. At a fixed gas velocity, in the absence of an external force field, Brownian diffusion controls the deposition of the small particles. The single-fiber collection efficiency (Chapter 3) passes through a minimum with increasing particle size as interception becomes important; for still larger particles, inertial effects are dominant. For particles larger than a micrometer, the efficiency increases with increasing size because of interception and impaction. Often the result is a "window" in the efficiency curve for particles in the 0.1- to 1.0- μm size range. Such a minimum has been observed in experimental studies of the performance of filters as shown in Chapter 3. Similar behavior has been observed in studies of aerosol deposition at a bifurcation under conditions simulating flow in the lung. For turbulent pipe flow, a similar minimum accompanying the transition from the diffusion to turbulent deposition regimes would be expected.

The often expressed intuitive belief that small particles are more difficult to remove from a gas than large ones is usually not correct. The particles most difficult to collect are those in the size range corresponding to the transition from diffusional to inertial deposition, usually between 0.1 and 1 μm . The transition may be strongly influenced by direct interception (finite particle diameter effect) depending on the dimensions of the system.

Calculating the collection efficiency in the transition region when both inertia and diffusion are important is very difficult. The usual practice is to calculate the efficiencies separately for each effect and then add them to produce a composite curve of efficiency as a function of particle size. More complete analyses are possible such as computer

simulations of Brownian dynamics that take inertia into account. These are briefly reviewed by Konstandopoulos (1990).

PROBLEMS

4.1 A particle is injected vertically upward with a velocity u_0 into a stationary gas. Derive an expression for the maximum distance traveled by the particle against the gravitational field. Assume the motion can be described by Stokes law.

4.2 The drag coefficient for non-Stokesian particles can be represented by the expression

$$C_D = \frac{24}{\text{Re}} (1 + \alpha \text{Re}^{2/3})$$

for $\text{Re} < 1000$ with $\alpha = 0.158$. Show that the stop distance for such particles is given by

$$s = \frac{d_p \alpha^{-2/3} \rho}{6\rho_p} \left[\text{Re}_0^{2/3} \alpha^{1/2} + \arctan \left(\text{Re}_0^{-2/3} \alpha^{-1/2} \right) - \frac{\pi}{2} \right]$$

where Re_0 is the initial value of the Reynolds number (Serafini, 1954; Fuchs, 1964, p. 79).

4.3 A duct 4 ft in diameter with a 90° bend has been designed to carry particles in the range $1 < d_p < 20 \mu\text{m}$, which adhere when they strike the wall. Before construction, it is proposed to carry out bench scale experiments to determine the particle deposition rate in the bend. The model is to be built to 1/10 scale, and the same aerosol will be used as in the full-scale system. Show that it is not possible to maintain both Stokes and Reynolds number similarity in the full-scale and model systems. If Stokes similarity is to be preserved, calculate the Reynolds number ratio for the model to full-scale systems. Why is it more important to preserve Stokes than Reynolds similarity in such experiments?

4.4 An aerosol with particles in the micron size range flows around a smooth solid sphere a few millimeters in diameter. At sufficiently high Reynolds numbers, a laminar boundary layer develops over the sphere from the stagnation point up to an angle of about 110° at which separation takes place. The removal of particles by direct interception can be calculated from the velocity distribution over the forward surface of the sphere, up to 90° from the forward stagnation point (Fig. 4.P4).

The thickness of the boundary layer at 90° from the forward stagnation point is given approximately by

$$\frac{\delta}{d} \approx \frac{3.4}{\sqrt{\text{Re}}}$$

where

$$\text{Re} = dU_\infty/\nu$$

$$d = \text{diameter of the sphere}$$

$$U_\infty = \text{uniform approach velocity at large distances from the sphere}$$

$$\nu = \text{kinematic viscosity}$$

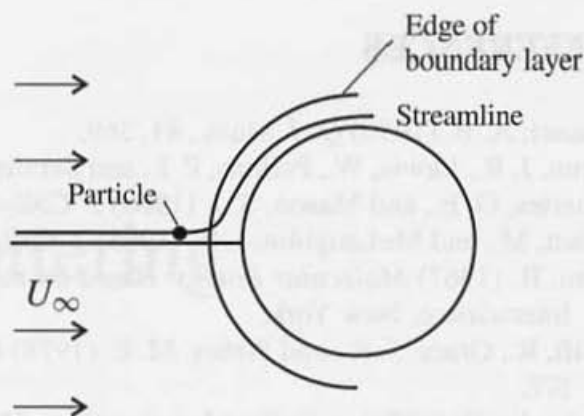


Fig. 4.P4

The removal efficiency by direct interception can be estimated from Eq. (4.67) of Chapter 3, which is based on the boundary layer velocity distribution:

$$\eta_R = 1.10R^2\text{Re}^{1/2}$$

- Calculate the ratio of the particle diameter to the boundary layer thickness at 90° from the stagnation point.
- Calculate η_R for spheres of diameter 3.2 mm for the case $\text{Stk}_{\text{crit}} = 1/12$, the value at which η_R for impaction vanishes for an inviscid flow. Take $d_p = 5 \mu\text{m}$ and $\rho_p = 0.965$. Compare your results with the data shown in Fig. 4.8. Can removal by interception contribute significantly to the efficiencies observed for particle removal at $\text{Stk} < 1/12$?

4.5 An aerosol is to be filtered by passing it through a bed loosely packed with a granular material 1 cm in diameter. Assuming that the bed-packing elements are approximately spherical in shape, *estimate* the minimum size of the particles that can be collected by impaction for an air velocity of 2 ft/sec. The kinematic viscosity of the air is $0.15 \text{ cm}^2/\text{sec}$, and the viscosity is $1.8 \times 10^{-4} \text{ g/cm sec}$. Aerosol particle density is 2 g/cm^3 . Discuss your assumptions.

4.6 Fibrous deep bed filters can be modeled as a collection of single cylindrical fibers set normal to the flow of an aerosol. The removal efficiency for the single fibers can be estimated from theory if the gas velocity distribution around the fibers (cylinders) is known.

- Sketch the form of the single fiber collection efficiency, η_R , as a function of *gas velocity*, V , for a fixed particle diameter, say $0.5 \mu\text{m}$. Plot $\log \eta_R$ vs. $\log V$. Explain the shape of your plot for low, intermediate, and high velocities in terms of the mechanisms of particle transport from the gas to the filter fibers.
- Suppose the particle size is reduced to $0.1 \mu\text{m}$. Show another curve on the figure for this particle size and explain the reasons for the shift in the efficiency for the various ranges of gas velocity.

4.7 Air at 20°C and 1 atm flows through a 6-in. vertical duct at a velocity of 20 ft/sec. Plot the transfer coefficient (cm/sec), k , for deposition on the wall as a function of particle size over the range $10 \mu\text{m} > d_p > 0.01 \mu\text{m}$. Assume that the surface of the duct is smooth and that it acts as a perfect sink for particles. Particle density is 2 g/cm^3 . Show two branches for the curve: diffusion-controlled deposition for submicron particles (Chapter 3) and inertia-controlled turbulent deposition for the larger particles.

REFERENCES

- Basset, A. B. (1910) *Q. J. Math.*, **41**, 369.
- Brun, J. R., Lewis, W., Perkins, P. J., and Serafini, J. S. (1955) NACA Report 1215.
- Charles, G. E., and Mason, S. J. (1960) *J. Colloid Sci.*, **15**, 236.
- Chen, M., and McLaughlin, J. B. (1995) *J. Colloid Interface Sci.*, **169**, 437.
- Chu, B. (1967) *Molecular Forces: Based on the Baker Lectures of Peter J. W. Debye*, Wiley-Interscience, New York.
- Clift, R., Grace, J. R., and Weber, M. E. (1978) *Bubbles, Drops and Particles*, Academic Press, NY.
- Dahneke, B. (1971) *J. Colloid Interface Sci.*, **37**, 342.
- Dahneke, B. (1975) *J. Colloid Interface Sci.*, **51**, 58.
- de la Mora, J. F. (1996) *Chem. Eng. Commun.*, **151**, 101.
- Friedlander, S. K. (1957) *AICHE J.*, **3**, 381.
- Friedlander, S. K., and Johnstone, H. F. (1957), *Ind. Eng. Chem.*, **49**, 1151.
- Fuchs, N. A. (1964) *Mechanics of Aerosols*, Pergamon, New York. This reference contains a thorough review of the literature on the behavior of aerosols in the inertial range through the 1950s. It lists 886 references. Both theory and experiment are covered.
- Goldstein, S. (Ed.) (1938) *Modern Developments in Fluid Dynamics*, Vol. 1, Oxford University Press, Oxford.
- Hahner, F., Dau, G., and Ebert, F. (1994), *Chem. Eng. Technol.*, **17**, 88.
- Happel, J., and Brenner, H. (1965) *Low Reynolds Number Hydrodynamics with Special Applications to Particulate Media*, Prentice-Hall, Englewood Cliffs, NJ.
- Ingham, D. B., Hildyard, L. T., and Hildyard, M. L. (1990) *J. Aerosol Sci.*, **21**, 935.
- Israel, G. W., and Friedlander, S. K. (1967) *J. Colloid Interface Sci.*, **24**, 330.
- Konstandopoulos, A. G. (1990) *J. Aerosol Sci.*, **21**, 983.
- Landau, L. D., and Lifshitz, E. M. (1987) *Fluid Mechanics*, 2nd ed., Pergamon Press, Oxford.
- Liu, B. Y. H., and Agarwal, J. K. (1974) *J. Aerosol Sci.*, **5**, 145.
- Liu, P., Ziemann, P., Kittelson, D. B., and McMurry, P. H. (1995) *Aerosol Sci. Technol.*, **22**, 314.
- MacKay, G. D. M., Suzuki, M., and Mason, S. G. (1963) *J. Colloid Sci.*, **18**, 103.
- Pruppacher, H. R., and Klett, J. D. (1997) *Microphysics of Clouds and Precipitation*, 2nd ed., Kluwer Academic Publishers, Dordrecht, Holland.
- Ranz, W. E., and Wong, J. B. (1952) *Ind. Eng. Chem.*, **44**, 1371.
- Serafini, J. S. (1954) NACA Report 1159.
- Snyder, W. H., and Lumley, J. L. (1971) *J. Fluid Mech.*, **48**, 47.
- Uijtewaal, W. (1995) Particle Motion in Turbulent Pipe Flow, MEAH-128 TU Delft Lab for Aero- and Hydrodynamics.
- Wong, J. B., and Johnstone, H. F. (1953) Collection of Aerosols by Fiber Mats, Technical Report 11, Engineering Experimental Station, University of Illinois.

Light Scattering

Aerosol light scattering plays a major role in the design of aerosol measurement systems (discussed in the next chapter) and radiation transfer through the atmosphere. There are also technological applications in combustion and production of powdered materials. This chapter provides an introduction to the subject.

In broad outline, the problem of light scattering by clouds of small particles can be formulated as follows: Scattering by an individual particle depends on its size, refractive index and shape, and the wavelength of the incident light. There is an extensive literature on the optical properties of single particles (van de Hulst, 1957; Kerker, 1969; Bohren and Huffman, 1983) to which we refer without derivation. The total light scattered from a collimated light beam is obtained by summing the scattering over particles of all sizes and refractive indices, subject to certain limitations discussed in this chapter. In practice, light sources and sinks are distributed in space in a complex way; the radiation intensity at any point is determined by the arrangement of the sources and sinks, the spatial distribution of the aerosol, and its size distribution and composition. In laboratory studies, it is possible to control these variables; and for certain relatively simple configurations (e.g., single scattering and collimated light sources), good agreement can be obtained between theory and experiment. Applications to industrial process gases and to radiation transfer through planetary atmospheres are more complicated. They can sometimes be analyzed using the equation of radiative transfer; an application to atmospheric visibility is discussed.

Central to many applications is the integration of an optical parameter, such as the total or angular scattering, over the particle size distribution. The optical thickness (turbidity) of an aerosol is an important case. Several examples are discussed for different forms of the size distribution functions. In the inverse problem not discussed in this text, the particle size distribution can sometimes be estimated from scattering measurements (Bayvel and Jones, 1981). Most of the phenomena discussed in this chapter involve elastic light scattering in which the frequency of the scattered light is equal to that of the incident beam. At the end of the chapter, we discuss examples in which the frequency of the scattered light is different from that of the incident beam, including quasi-elastic light scattering and inelastic scattering (the Raman effect). Quasi-elastic light scattering refers to weak displacements of the frequency of the scattered beam from the incident wavelength. Applications are to the measurement of the size of very small particles. Raman scattering is potentially important

for on-line measurement of aerosol chemical components. A summary diagram based on simple quantum mechanical concepts illustrates various scattering processes.

SCATTERING BY SINGLE PARTICLES: GENERAL CONSIDERATIONS

When aerosol particles interact with light, two different types of processes can occur. The energy received can be reradiated by the particle in the same wavelength. The reradiation may take place in all directions but usually with different intensities in different directions. This process is called *scattering*. Alternatively, the radiant energy can be transformed into other forms of energy, such as (a) heat and (b) energy of chemical reaction. This process is called *absorption*. In the visible range, light attenuation by absorption predominates for black smokes, whereas scattering controls for water droplets. The next few sections focus on elastic scattering and absorption.

It is convenient to analyze the light attenuation process by considering a single particle of arbitrary size and shape, irradiated by a plane electromagnetic wave (Fig. 5.1). The effect of the disturbance produced by the particle is to diminish the amplitude of the plane wave. At a distance large compared with the particle diameter and the wavelength, the scattered energy appears as a spherical wave, centered on the particle and possessing a phase different from the incident beam. The total energy lost by the plane wave, the extinction energy, is equal to the scattered energy in the spherical wave plus the energy of absorption.

In many applications, the most important characteristic of the scattered wave is its intensity, I , expressed in cgs units as erg/cm² sec. At large distances from the origin, the energy flowing through a spherical surface element is $Ir^2 \sin \theta d\theta d\phi$. This energy flows radially and depends on θ and ϕ but not on r . It is proportional to the intensity of the incident beam I_0 and can be expressed as follows:

$$Ir^2 \sin \theta d\theta d\phi = I_0 \left(\frac{\lambda}{2\pi} \right)^2 F(\theta, \phi, \lambda) \sin \theta d\theta d\phi \quad (5.1)$$

or

$$I = \frac{I_0 F(\theta, \phi, \lambda)}{(2\pi r/\lambda)^2} \quad (5.2)$$

The wavelength of the incident beam, λ , is introduced in the denominator to make the scattering function, $F(\theta, \phi, \lambda)$, dimensionless. In general, $F(\theta, \phi, \lambda)$ depends on the wavelength of the incident beam and on the size, shape, and optical properties of the particles but not on r . For spherical particles, there is no ϕ dependence. The relative values of F can be plotted in a polar diagram as a function of θ for a plane in the direction of the incident beam. A plot of this type is called the *scattering diagram* for the particle.

The scattering function can be determined from theory for certain important special cases as discussed in the following sections. The performance of optical single-particle counters (Chapter 6) depends on the variation of the scattering function with angular position, and much effort has been devoted to the design of such detectors.

The intensity function, by itself, is not sufficient to characterize the scattered light. Needed also are the polarization and phase of the scattered light, which are discussed in the

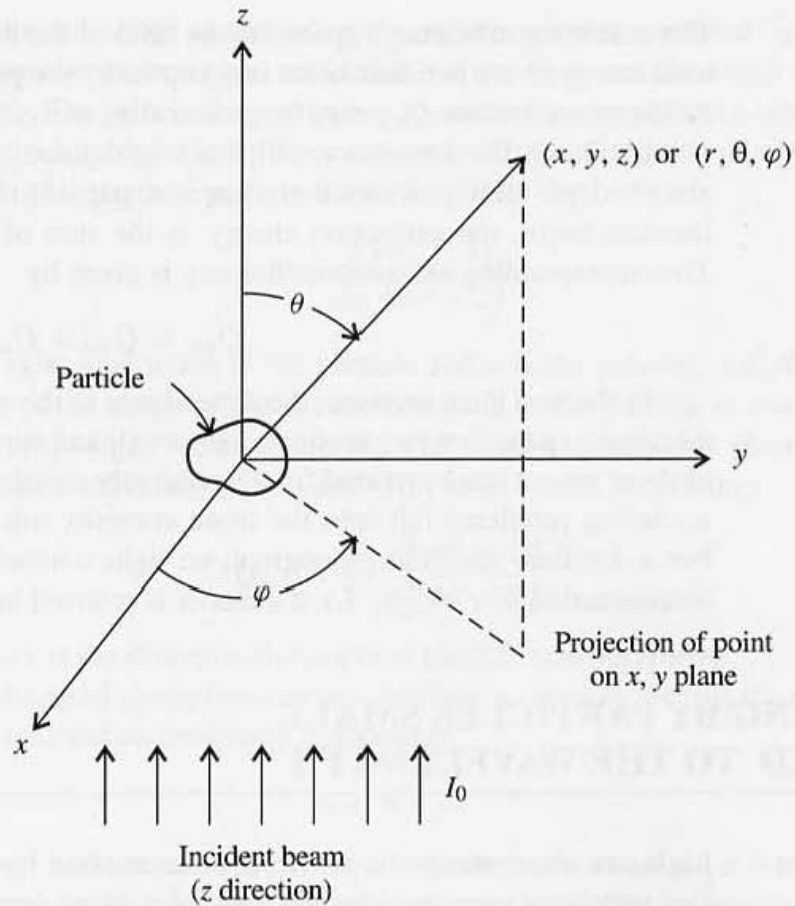


Fig. 5.1 The direction of scattering at any r is characterized by the scattering angle, θ , measured relative to the direction of the incident beam, and the azimuth angle, ϕ .

standard references on the subject. For many applications including atmospheric scattering and optical instrument design, the parameters of most interest are the intensity function and related quantities, defined as follows: Let the total energy scattered in all directions by the particle be equal to the energy of the incident beam falling on the area C_{sca} :

$$\begin{aligned} C_{\text{sca}} &= \frac{1}{I_0} \int_0^{2\pi} \int_0^\pi I r^2 \sin \theta \, d\theta \, d\phi \\ &= \frac{1}{(2\pi/\lambda)^2} \int_0^{2\pi} \int_0^\pi F(\theta, \phi, \lambda) \sin \theta \, d\theta \, d\phi \end{aligned} \quad (5.3)$$

This defines the *scattering cross section* C_{sca} , which has the dimension of area but is not in general equal to the particle cross-sectional area. Indeed it is customary to define the *scattering efficiency*

$$Q_{\text{sca}} = C_{\text{sca}}/s_g \quad (5.4)$$

where s_g is the geometric cross section. Combining (5.3) and (5.4), we obtain

$$Q_{\text{sca}} = \frac{\int_0^{2\pi} \int_0^\pi F(\theta, \phi, \lambda) \, d\theta \, d\phi}{(2\pi/\lambda)^2 s_g} \quad (5.5)$$

The scattering efficiency represents the ratio of the energy scattered by the particle to the total energy in the incident beam intercepted by the geometric cross section of the particle. As discussed below, Q_{sca} may be greater than unity.

Similarly, the absorption efficiency is defined as the fraction of the incident beam absorbed per unit cross-sectional area of particle. The total energy removed from the incident beam, the extinction energy, is the sum of the energy scattered and absorbed. The corresponding extinction efficiency is given by

$$Q_{\text{ext}} = Q_{\text{sca}} + Q_{\text{abs}} \quad (5.6)$$

In the next three sections, the dependence of the scattering efficiency on particle size is discussed; in the first two sections, very small and very large particles are considered. Both of these ranges can be treated from a relatively simple point of view. However, many light-scattering problems fall into the more complex intermediate size range discussed later. For a detailed, readable monograph on light scattering by single particles, stressing the determination of $F(\theta, \phi, \lambda)$, the reader is referred to van de Hulst (1957).

SCATTERING BY PARTICLES SMALL COMPARED TO THE WAVELENGTH

Light, an electromagnetic wave, is characterized by electric and magnetic field vectors. For simplicity, we consider the case of a plane wave, linearly polarized, incident on a small spherical particle. The wavelength of light in the visible range is about $0.5 \mu\text{m}$. For particles much smaller than the wavelength, the local electric field produced by the wave is approximately uniform at any instant. This applied electric field induces a dipole in the particle. Because the electric field oscillates, the induced dipole oscillates; and according to classical theory, the dipole radiates in all directions. This type of scattering is called *Rayleigh scattering*.

The dipole moment, \mathbf{p} , induced in the particle is proportional to the instantaneous electric field vector:

$$\mathbf{p} = \alpha \mathbf{E} \quad (5.7)$$

This expression defines the polarizability, α , which has the dimensions of a volume and which is a scalar for an isotropic spherical particle. From the energy of the electric field produced by the oscillating dipole, an expression can be derived for the intensity of the scattered radiation:

$$I = \frac{(1 + \cos^2 \theta) k^4 \alpha^2}{2r^2} I_0 \quad (5.8)$$

where the wave number $k = 2\pi/\lambda$. The scattering is symmetrical with respect to the direction of the incident beam with equal maxima in the forward and backward directions and the minimum at right angles (Fig. 5.4 for $x < 0.6$).

Because the intensity of the scattered light varies inversely with the fourth power of the wavelength, blue light (short wavelength) is scattered preferentially to red. This strong dependence leads to the blue of the sky (in the absence of aerosol particles) and

contributes to the red of the sunset when the red-enriched transmitted light is observed. In polluted atmospheres, however, molecular scattering is usually small compared with aerosol scattering. The principal contribution to scattering comes from a larger particle size range in which the Rayleigh theory does not apply. This is discussed in a later section.

For an isotropic spherical particle, it can be shown that

$$\alpha = \frac{3(m^2 - 1)}{4\pi(m^2 + 2)}v \quad (5.9)$$

where m is the refractive index of the particle and v is the volume, $\pi d_p^3/6$. This result is valid regardless of the shape of the scatterer so long as the particle is much smaller than the wavelength of the light. When scattering without absorption takes place, the efficiency factor is obtained by substituting (5.9) and (5.8) in (5.5) and integrating:

$$Q_{\text{sca}} = \frac{8}{3}x^4 \left\{ \frac{m^2 - 1}{m^2 + 2} \right\}^2 \quad (5.10)$$

where $x = \pi d_p/\lambda$ is the dimensionless optical particle size parameter.

Both scattering and absorption can be taken into account by writing the refractive index as the sum of a real and an imaginary component:

$$m = n - in' \quad (5.11)$$

where $n^2 + n'^2 = \epsilon$ and $nn' = \lambda\sigma/c$, where ϵ is the dielectric constant, σ is the conductivity, λ is the wavelength in vacuum, and c is the velocity of light. The imaginary term gives rise to absorption; it vanishes for nonconducting particles ($\sigma = 0$). Both ϵ and σ depend on λ , approaching their static values at low frequencies. For metals in the optical frequency range, both n and n' are of order unity. The scattering efficiency of small spherical absorbing particles is given by (van de Hulst, 1957)

$$Q_{\text{sca}} = \frac{8}{3}x^4 \text{Re} \left\{ \frac{m^2 - 1}{m^2 + 2} \right\}^2 \quad (5.12)$$

where Re indicates that the real part of the expression is taken. The absorption efficiency is

$$Q_{\text{abs}} = -4x \text{Im} \left\{ \frac{m^2 - 1}{m^2 + 2} \right\} \quad (5.13)$$

where Im indicates that the imaginary part is taken. For very small particles of absorbing material, the particle extinction coefficient varies only with the first power of x and the total extinction per particle obtained by multiplying Q_{abs} by the cross section is proportional to the particle volume.

For scattering alone, an expansion of the efficiency factor in x based on Mie theory discussed below gives

$$Q_{\text{ext}} = \frac{8}{3}x^4 \left(\frac{m^2 - 1}{m^2 + 2} \right)^2 \left[1 + \frac{6(m^2 - 1)}{5(m^2 + 2)}x^2 + \dots \right] \quad (5.14)$$

When $m = 1.5$ corresponding to certain organic liquids and many metallic salts, the second term in the second bracket is less than 0.1 for $x < 0.53$. Thus the Rayleigh form can be

used with an error of less than 10% for green light ($\lambda = 0.5 \mu\text{m}$) when $d_p < 0.084 \mu\text{m}$ and $m = 1.5$.

SCATTERING BY LARGE PARTICLES: THE EXTINCTION PARADOX

For particles much larger than the wavelength of the incident light ($x \gg 1$), the scattering efficiency approaches 2. That is, a large particle removes from the beam *twice* the amount of light intercepted by its geometric cross-sectional area. What is the explanation for this paradox?

For light interacting with a large particle, the incident beam can be considered to consist of a set of separate light rays. Of those rays passing within an area defined by the geometric cross section of the sphere, some will be reflected at the particle surface and others refracted. The refracted rays may emerge, possibly after several internal reflections. Any of the incident beam that does not emerge is lost by absorption within the particle. Hence all of the energy incident on the particle surface is removed from the beam by scattering or absorption, accounting for an efficiency factor of unity.

There is, however, another source of scattering from the incident beam. The portion of the beam not intercepted by the sphere forms a plane wave front from which a region corresponding to the cross-sectional area of the sphere is missing. This is equivalent to the effect produced by a circular obstacle placed normal to the beam. The result, according to classical optical principles, is a diffraction pattern *within the shadow area* at large distances from the obstacle. The appearance of light within the shadow area is the reason why diffraction is sometimes likened to the bending of light rays around an obstacle.

The intensity distribution within the diffraction pattern depends on the shape of the perimeter and size of the particle relative to the wavelength of the light. It is independent of the composition, refractive index, or reflective nature of the surface. The total amount of energy that appears in the diffraction pattern is equal to the energy in the beam intercepted by the geometric cross section of the particle. Hence the total efficiency factor based on the cross-sectional area is equal to 2.

The use of the factor 2 for the efficiency requires that all scattered light be counted including that at small angles to the direction of the beam. In general, the observation must be made at a large distance from the particle compared with the particle size. As van de Hulst points out, a flower pot in a window blocks only the sunlight falling on it, and not twice that amount, from entering a room; a meteorite of the same size in space between a star and a telescope on Earth will remove twice the amount of starlight falling on it. Because the distance of the detector from a scattering aerosol particle is large compared with the particle diameter, $Q_{\text{sca}} \rightarrow 2.0$ for $x \gg 1$.

SCATTERING IN THE INTERMEDIATE SIZE RANGE: MIE THEORY

General Considerations

Rayleigh scattering for $x \ll 1$ and the large particle extinction law for $x \gg 1$ provide useful limiting relationships for the efficiency factor. Frequently the range $x \sim 1$ is important.

Atmospheric visibility, for example, is limited by particles whose size is of the same order as the wavelength of light in the optical range, from 0.1 to 1 μm in diameter (McCartney, 1976). In this range, the theory of Rayleigh is no longer applicable because the field is not uniform over the entire particle volume. Such particles are still too small for large particle scattering theory to be applicable. As a result, it is necessary to make use of a much more complicated theory due to Mie, which treats the general problem of scattering and absorption of a plane wave by a homogeneous sphere. Expressions for the scattering and extinction are obtained by solving Maxwell's equations for the regions inside and outside the sphere with suitable boundary conditions. It is found that the efficiency factors are functions of x and m alone. This represents a general scaling relationship for light scattering by isotropic spheres. Scattering efficiency calculations must be carried out numerically, and the results for many cases have been tabulated. The theory, sources of detailed calculations and their interpretation are discussed by van de Hulst (1957) and Kerker (1969). Useful computer programs are given by Barber and Hill (1990).

For water, $m = 1.33$, whereas for organic liquids it is often approximately 1.5. The scattering efficiency for these two values of m are shown in Fig. 5.2 as a function of the dimensionless particle diameter x . For $x \rightarrow 0$, the theory of Rayleigh is applicable.

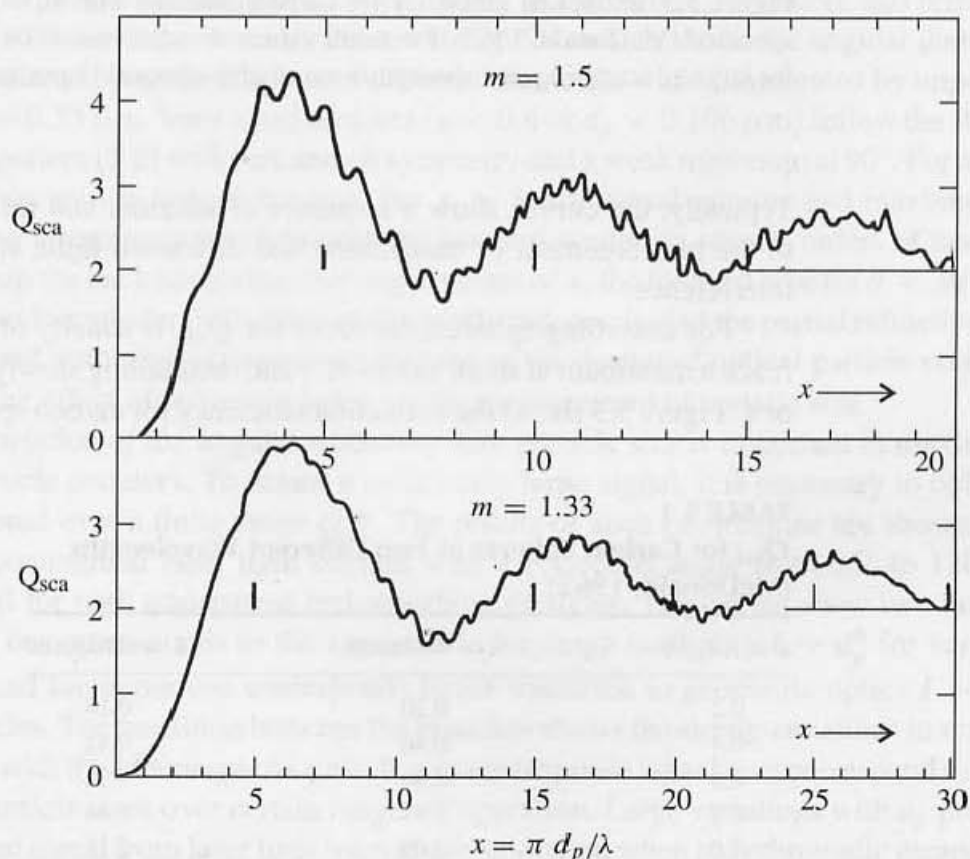


Figure 5.2 Extinction curves calculated from the theory of Mie for $m = 1.5$ and $m = 1.33$ (van de Hulst, 1957). The curves show a sequence of maxima and minima of diminishing amplitude, typical of nonabsorbing spheres with $1 < m < 2$. Indeed, by taking the abscissa of the curve for $m = 1.5$ to be $2x(m - 1)$, all extinction curves for the range $1 < m < 2$ are reduced to approximately the same curve.

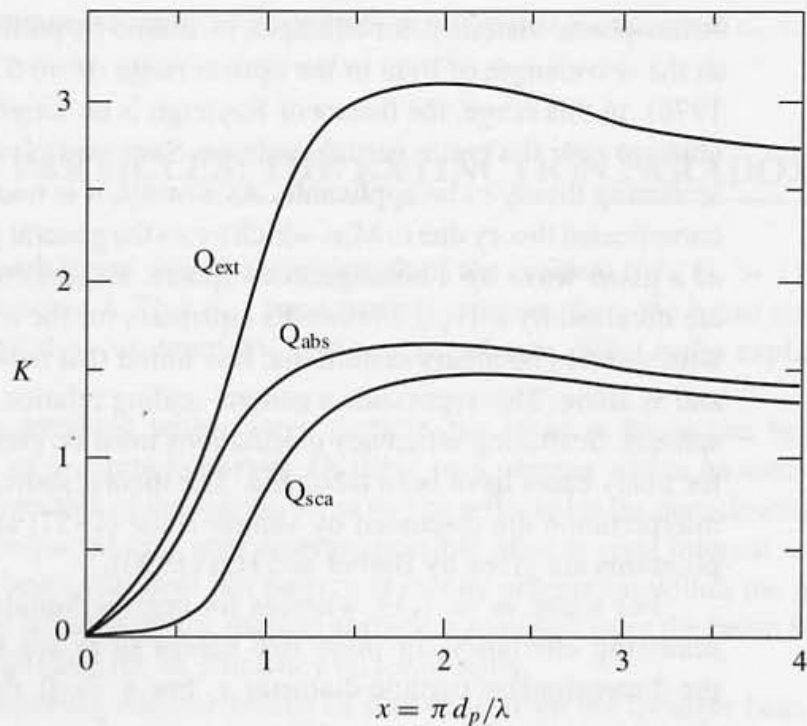


Figure 5.3 Extinction efficiency for carbon particles with $m = 2.00(1 - 0.33i)$, temperature not specified (McDonald, 1962). For small values of x , the extinction is due primarily to absorption; but for large x , scattering and absorption are of almost equal importance.

Typically, the curves show a sequence of maxima and minima: The maxima correspond to the reinforcement of transmitted and diffracted light, while the minima correspond to interference.

For absorbing spheres, the curve for Q_{ext} is usually of simpler form, rising rapidly to reach a maximum at small values of x and then falling slowly to approach two at large values of x . Figure 5.3 shows the extinction efficiency for carbon spheres. For such particles, nearly

TABLE 5.1
 Q_{ext} for Carbon Spheres at Two Different Wavelengths
(McDonald, 1962)

$x = \pi d_p/\lambda$	$\lambda = 0.436\mu\text{m}$	$\lambda = 0.623\mu\text{m}$
0.2	0.20	0.18
0.4	0.46	0.42
0.6	0.86	0.82
0.8	1.45	1.44
1.0	2.09	2.17
1.5	2.82	2.94
2.0	3.00	3.09
4.0	2.68	2.68
8.0	2.46	2.46

all of the scattering is due to diffraction, while almost all of the geometrically incident light is absorbed. The refractive index for absorbing spheres usually varies with wavelength, and this results in the variation of Q_{ext} as well. As shown in Table 5.1, however, the variation over the visible spectrum is not great.

Angular Scattering

Mie scattering by single particles irradiated by conventional laser sources is sufficiently strong to be detected at high signal-to-noise ratios for particles larger than about $0.1 \mu\text{m}$. The noise results from Rayleigh scattering by the gas molecules and from the instrument electronics. The signal depends in a complex way on the angle of the detector with respect to the scattering particle, as well as on the particle size and refractive index.

The angular dependence of the light scattering can be calculated from Mie theory. For values of x approaching unity and small values of m (< 2.0), an asymmetry favoring forward scattering appears. For very large values of m corresponding to opaque or reflecting particles, there is an asymmetry toward back scattering. For $x \gg 1$, forward scattering increases still more strongly (Fig. 5.4), showing very rapid changes for small increases in the scattering angle θ . The scattered light in the $x \gg 1$ limit can be considered to consist of three components interpreted according to classical theory as diffraction, reflection, and refraction.

Some of these features are illustrated in Fig. 5.4, which shows the angular distribution of light scattered by water droplets of different diameters when illuminated by unpolarized light of $\lambda = 0.55 \mu\text{m}$. Very small droplets ($x < 0.6$ or $d_p < 0.106 \mu\text{m}$) follow the Rayleigh scattering pattern (5.8) with fore and aft symmetry and a weak minimum at 90° . For $x > 0.6$, the minimum moves toward the rear. For $x > 3$, additional minima and maxima appear and a strong asymmetry develops with the forward scattering several orders of magnitude stronger than the back scattering. For larger values of x , the forward lobe for $\theta < 30^\circ$ results mainly from Fraunhofer diffraction and is nearly independent of the partial refractive index. Thus forward scattering is sometimes favored in the design of optical particle counters to eliminate the effect of refractive index on the measurement of particle size.

The variation of the angular scattering with particle size is important in the design of optical particle counters. To obtain a sufficiently large signal, it is necessary to collect the light scattered over a finite range of θ . The results of such calculations are shown in Fig. 5.5 for a commercial laser light counter with a collection angle from 35° to 120° from the forward for both transparent and absorbing particles. The curves show two branches: The lower one corresponds to the approach to Rayleigh scattering $I \sim d_p^6$ for very small particles, and the upper one corresponds to the transition to geometric optics $I \sim d_p^2$ for large particles. The transition between the branches shows the strong variations in scattering associated with the Mie range. As a result, a given response signal may correspond to several different particle sizes over certain ranges of operation. Large variations with d_p present in the scattered signal from laser light sources are smoothed when polychromatic incandescent sources with multiple wavelengths are used as shown in Chapter 6.

Scattering cross sections have been measured for liquid suspensions of transparent, irregular particles graded in size by sedimentation (Hodkinson, 1966). The shapes of the curves of the scattering cross sections were simpler than those of spherical particles, but

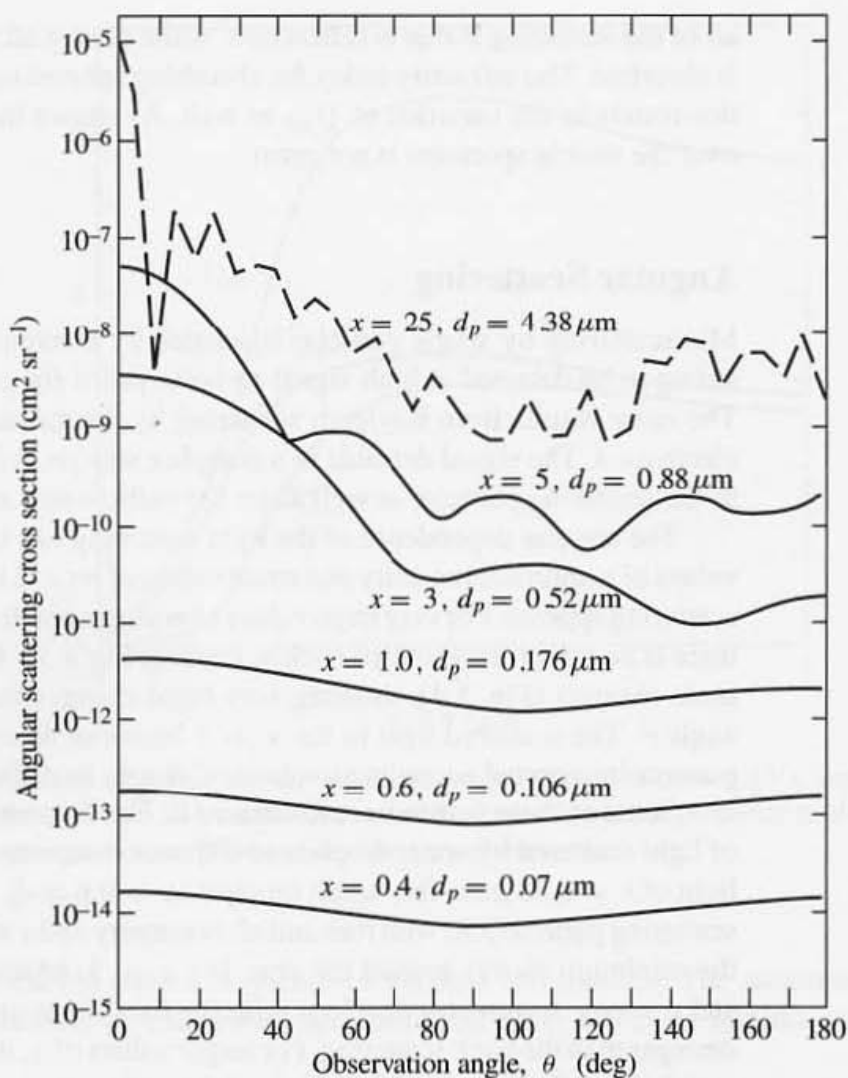


Figure 5.4 Angular scattering for water droplets illuminated by unpolarized light. The results hold for light in the visible range; the indicated values of d_p correspond to $\lambda = 0.55 \mu\text{m}$ (after McCartney, 1976). Very small droplets ($x < 0.6$) show the Rayleigh scattering pattern (5.8) with fore and aft symmetry and a weak minimum at right angles. Larger particles display strong variations with θ associated with scattering in the Mie range.

theoretical predictions have not been made except for very small particles to which the Rayleigh theory is applicable.

SCATTERING BY AEROSOL CLOUDS

General Considerations

We consider the case of an aerosol illuminated by a collimated light source of a given wavelength. The experimental arrangement is shown schematically in Fig. 5.6. A photometer of this type installed in a smoke stack or duct would be suitable for measuring the attenuation

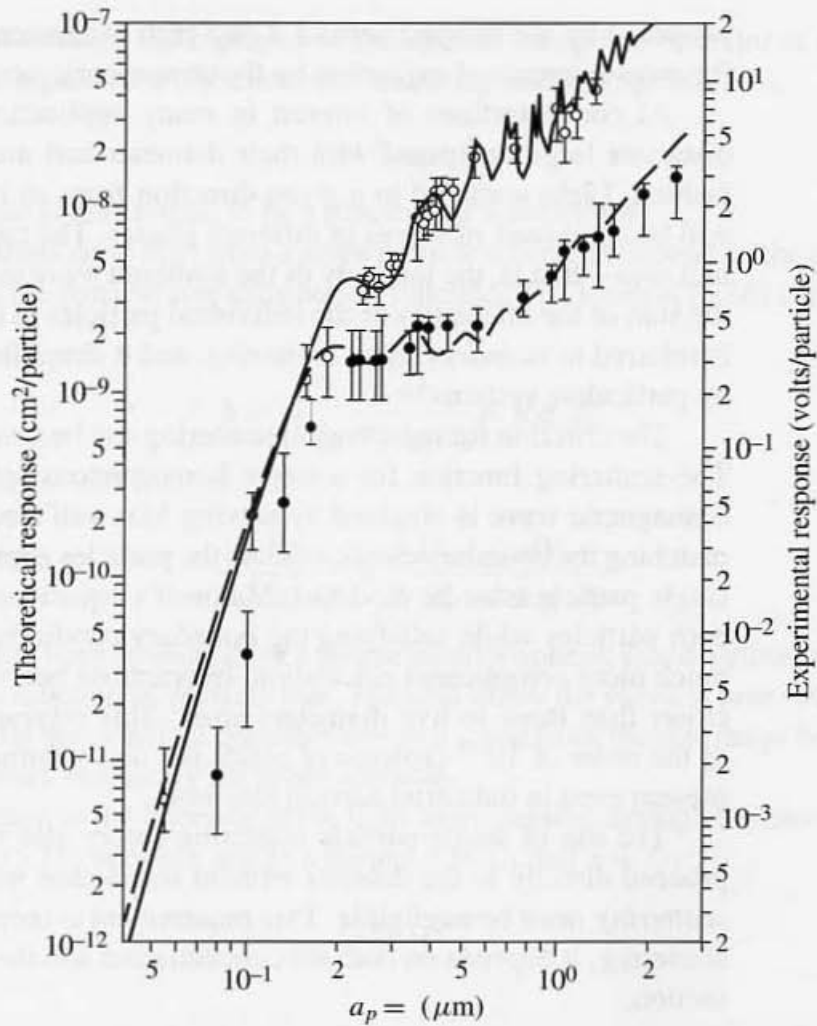


Figure 5.5 Variation of light scattering over the angle from 35° to 120° from the forward direction for a He-Ne laser light source ($\lambda = 0.633 \mu\text{m}$). Particles were latex ($m = 1.588$) and nigrosin dye ($m = 1.67 - 0.26i$). The lower branch shows the approach to the Rayleigh scattering range (response $\sim d_p^6$), and the upper branch shows the approach to geometric optics (response $\sim d_p^2$) (Garvey and Pinnick, 1983).

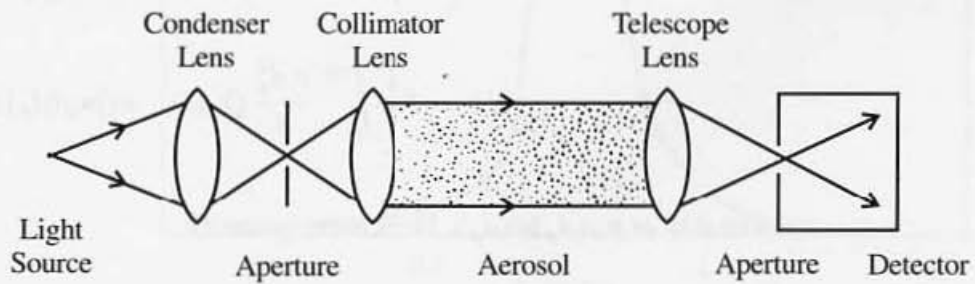


Figure 5.6 Schematic diagram of an apparatus for the measurement of the extinction produced by a cloud of small particles. The goal is to measure only transmitted light and not light scattered by the particles. In practice, light of decreased intensity from the source is measured together with a certain amount of light scattered at small angles from the forward direction by the particles. (After Hodkinson, 1966.)

produced by the flowing aerosol. Long path instruments of this kind have also been used for measurements of extinction by the atmospheric aerosol.

At concentrations of interest in many applications, the particles are separated by distances large compared with their diameter and are distributed in space in a random fashion. Light scattered in a given direction from an incident beam by different particles will be composed of waves of different phases. The total energy of the scattered wave per unit area—that is, the intensity of the scattered wave in a given direction—will be equal to the sum of the intensities of the individual particles in that direction. This type of behavior is referred to as *independent scattering*, and it simplifies calculation of the total scattering by particulate systems.

The criterion for independent scattering can be clarified by referring to the last section. The scattering function for a single homogeneous sphere interacting with a plane electromagnetic wave is obtained by solving Maxwell's equations for the gas and sphere and matching the boundary conditions. As the particles approach each other, the solution for the single particle must be modified. Maxwell's equations must be solved inside and outside both particles while satisfying the boundary conditions at the particle surfaces. This is a much more complicated calculation. Interactions become important when the particles are closer than three to five diameters apart. This corresponds to volumetric concentrations of the order of 10^{-2} (volume of solids per unit volume of gas), much higher than usually present even in industrial aerosol reactors.

The use of single-particle scattering theory also requires that the scattered radiation proceed directly to the detector without interaction with other particles. That is, *multiple scattering* must be negligible. This requirement is more stringent than that of independent scattering; it depends on both the concentration and the path length as discussed in the next section.

Extinction Coefficient and Optical Thickness

If there are dN particles in the size range d_p to $d_p + d(d_p)$ per unit volume of air, this corresponds to a total particle cross-sectional area of $(\pi d_p^2/4)dNdz$ over the light path length, dz , per unit area normal to the beam. The attenuation of light over this length is given by the relation

$$-dI = I \left[\int_0^\infty \frac{\pi d_p^2}{4} Q_{\text{ext}}(x, m) n_d(d_p) d(d_p) \right] dz \quad (5.15)$$

where $dN = n_d(d_p)d(d_p)$. Hence the quantity

$$b = -\frac{dI}{I dz} = \int_0^\infty \frac{\pi d_p^2}{4} Q_{\text{ext}}(x, m) n_d(d_p) d(d_p) \quad (5.16)$$

represents the fraction of the incident light scattered and absorbed by the particle cloud per unit length of path. It is called the *extinction coefficient* (sometimes the *attenuation*

coefficient or turbidity), and it plays a central role in the optical behavior of aerosol clouds. In terms of the separate contributions for scattering and absorption (5.6),

$$b = b_{\text{sca}} + b_{\text{abs}} \quad (5.17)$$

where each term is understood to be a function of wavelength.

The contributions to $b(\lambda)$ from a given particle size range depend on the extinction cross section and on the particle size distribution function. The integral (5.16) can be rearranged as follows:

$$b = \int_{-\infty}^{\infty} \frac{db}{d \log d_p} d \log d_p \quad (5.18)$$

where

$$\frac{db}{d \log d_p} = \frac{3}{2} \frac{Q_{\text{ext}}}{d_p} \frac{dV}{d \log d_p} \quad (4.18a)$$

This function has been evaluated for a measured atmospheric size distribution and is shown in Fig. 5.7 as a function of particle size. The area under the curve is proportional to b . The figure shows that the principal contributions to b come from the size range between 0.1 and 3 μm . This occurs frequently for urban aerosols.

The reduction in the intensity of the light beam passing through the aerosol is obtained by integrating (5.16) between any two points, $z = L_1$ and $z = L_2$:

$$I_2 = I_1 e^{-\tau} \quad (5.19)$$

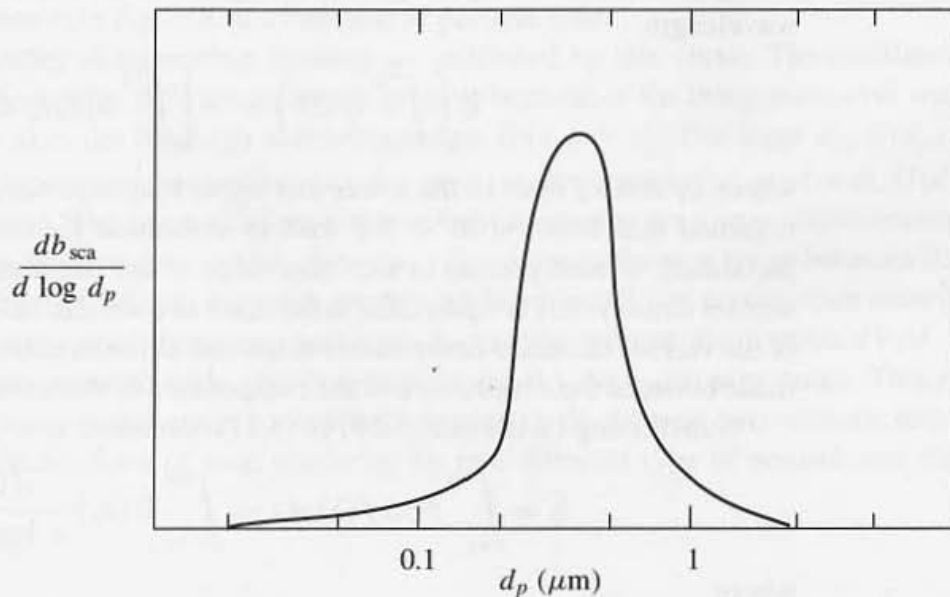


Figure 5.7 Contributions to the scattering coefficient as a function of particle size for the Pasadena, CA, aerosol (August 1969) based on the calculations of Ensor et al. (1972). The curve was calculated from the measured particle size distribution assuming $m = 1.5$. Largest contributions to light scattering came from the 0.2- to 0.5- μm size range for calculations made over the wavelength range $0.365 \mu\text{m} < \lambda < 0.675 \mu\text{m}$.

where the optical thickness, $\tau = \int_{L_1}^{L_2} b \, dz$, is a dimensionless quantity; b has been kept under the integral sign to show that it can vary with position, as a result of spatial variation in the aerosol concentration. Equation (5.19) is a form of Lambert's law. Limitations on the use of (5.19) resulting from multiple scattering are usually stated in terms of τ (van de Hulst, 1957). For $\tau < 0.1$ the assumption of single scattering is acceptable, while for $0.1 < \tau < 0.3$ it may be necessary to correct for double scattering. For $\tau > 0.3$, multiple scattering must be taken into account. The problem of multiple scattering for Rayleigh gases was solved by Chandrasekhar (1960). For particles in the Mie range, approximate methods for the calculation of multiparticle scattering are available (Bayvel and Jones, 1981). For a polluted urban region where aerosol scattering dominates, the value of b_{sca} is of the order of 10^{-3} m^{-1} . Taking $\tau < 0.1$ as the criterion for single scattering, the maximum distance for the passage of a beam in which single scattering dominates is $0.1(10)^3$ or 100 m.

SCATTERING OVER THE VISIBLE WAVELENGTH RANGE: AEROSOL CONTRIBUTIONS BY VOLUME

In many cases of practical interest, the incident light—solar radiation for example—is distributed with respect to wavelength. The contribution to the integrated intensity I from the wavelength range λ to $\lambda + d\lambda$ is

$$dI = I_\lambda \, d\lambda \quad (5.20)$$

where I_λ is the intensity distribution function. The loss in intensity over the visible range, taking into account only single scattering, is determined by integrating (5.20) over the wavelength:

$$d \left(\int_{\lambda_1}^{\lambda_2} I_\lambda \, d\lambda \right) = - \left[\int_{\lambda_1}^{\lambda_2} b(\lambda) I_\lambda \, d\lambda \right] dz \quad (5.21)$$

where λ_1 and λ_2 refer to the lower and upper ranges of the visible spectrum and b is now regarded as a function of λ . We wish to determine the intensity loss resulting from the particulate volume present in each size range of the size distribution function. For constant aerosol density, this is equivalent to the mass in each size range. Knowing the contributions of the various chemical components to the mass in each size range, a quantitative link can be made between the extinction and the components of the aerosol, as discussed in Chapter 13.

Substituting (5.18) and (5.19) in (5.21), the result is

$$\bar{b} = \int_{\lambda_1}^{\lambda_2} b(\lambda) f(\lambda) \, d\lambda = \int_{-\infty}^{\infty} G(d_p) \frac{dV}{d \log d_p} \, d \log d_p \quad (5.22)$$

where

$$G(d_p) = \frac{3}{2d_p} \int_{\lambda_1}^{\lambda_2} Q_{\text{ext}}(x, m) f(\lambda) \, d\lambda \quad (5.22a)$$

$f(\lambda) \, d\lambda$ is the fraction of the incident radiation in the range λ to $\lambda + d\lambda$, and $f(\lambda)$ has been normalized with respect to the total intensity in the range between λ_1 and λ_2 . The quantity

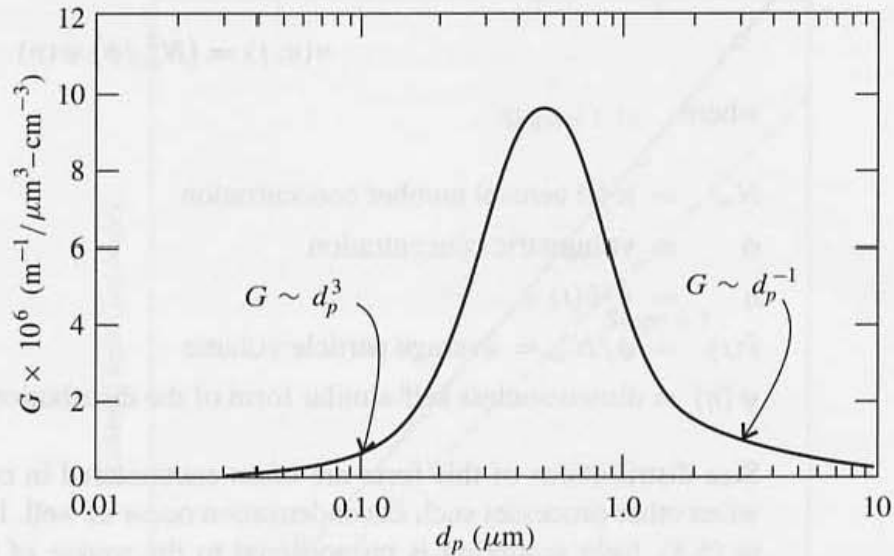


Figure 5.8 Light scattering per unit volume of aerosol material as a function of particle size, integrated over all wavelengths for a refractive index, $m = 1.5$. The incident radiation is assumed to have the standard distribution of solar radiation at sea level (Bolz and Tuve 1970). The limits of integration on wavelength were 0.36 to 0.680 μm . The limits of visible light are approximately 0.350 to 0.700 μm . The curve is independent of the particle size distribution.

$G(d_p)$ represents the extinction over all wavelengths between λ_1 and λ_2 per unit volume of aerosol in the size range between d_p and $d_p + d(d_p)$. It is independent of the particle size distribution function. For a refractive index, $m = 1.5$, $G(d_p)$ has been evaluated for the standard distribution of solar radiation at sea level, using Mie scattering functions. The result is shown in Fig. 5.8 as a function of particle size.

A number of interesting features are exhibited by this curve: The oscillations of the Mie functions (Fig. 5.3) are no longer present because of the integration over wavelength. For $d_p \rightarrow 0$ in the Rayleigh scattering range, $G(d_p) \sim d_p^3$. For large d_p , $G(d_p)$ vanishes because Q_{sca} approaches a constant value (two) at all wavelengths; as a result, $G(d_p) \sim d_p^{-1}$ for $d_p \rightarrow \infty$. The most efficient size for light scattering on a mass basis corresponds to the peak in this function, which, for $m = 1.5$, occurs in the size range between 0.5 and 0.6 μm . Particles of 0.1- μm diameter, on the one hand, and 3 μm on the other contribute only one-tenth the scattering on an equal mass basis. The volume distribution $dV/d \log d_p$ of atmospheric aerosols often shows a peak in the 0.1- to 3- μm size range. This reinforces the importance of this range to total light scattering. In the next two sections, examples are given of calculations of total scattering by two different type of aerosol size distribution functions.

RAYLEIGH SCATTERING: SELF-SIMILAR SIZE DISTRIBUTIONS

An important class of self-similar particle size distributions $n(v, t)$ can be represented by an equation of the form (Chapters 1 and 7):

$$n(v, t) = (N_\infty^2 / \phi) \psi(\eta) \quad (5.23)$$

where

N_∞ = total aerosol number concentration

ϕ = volumetric concentration

η = $v/\bar{v}(t)$

$\bar{v}(t)$ = ϕ/N_∞ = average particle volume

$\psi(\eta)$ = dimensionless self-similar form of the distribution function

Size distributions of this form are often encountered in coagulating aerosols, sometimes when other processes such as condensation occur as well. In the Rayleigh range, according to (5.8), light scattering is proportional to the square of the particle volume; when two particles of the same size combine to form a larger one, the total light scattered doubles. This is true so long as the two original particles are separated by a distance much greater than the wavelength of the incident light. In this case, the two particles scatter independently and out of phase, and the energy of the scattered light is the sum of the energies scattered separately by the two particles. When the two particles are combined and still much smaller than the wavelength of the light, the electric field scattered will be the sum of the two electric fields in phase. As a result, double the amplitude of the single particle or four times the energy of a single particle will be scattered. Hence the light scattered by a coagulating small particle aerosol increases with time.

For self-similar particle size distributions, the average particle size can be determined directly by measuring the extinction. Total scattering in the Rayleigh range is

$$b_{\text{sca}} = B \int_0^\infty n(v) v^2 dv \quad (5.24)$$

where

$$B = \frac{24\pi^3}{\lambda^4} \left| \frac{m^2 - 1}{m^2 + 2} \right|^2$$

Substituting the self-similar form for the size distribution function, (5.23), we obtain

$$b_{\text{sca}} = B\phi\bar{v} \int_0^\infty \psi(\eta) \eta^2 d\eta \quad (5.24a)$$

The integral in (5.24a) is a constant that depends on the form of the size distribution function. For the special case of coagulating, coalescing aerosols composed of spherical particles, the integral is 2.01 (Chapter 7) and

$$b_{\text{sca}} = 2.01 B\phi\bar{v} \quad (5.25)$$

Hence for a coagulating aerosol with constant ϕ , the scattered light intensity is proportional to the instantaneous mean particle volume, $\bar{v} = \phi/N$. Thus by measuring the extinction, the average particle volume \bar{v} can be determined for this special case. No arbitrary constants appear in the analysis.

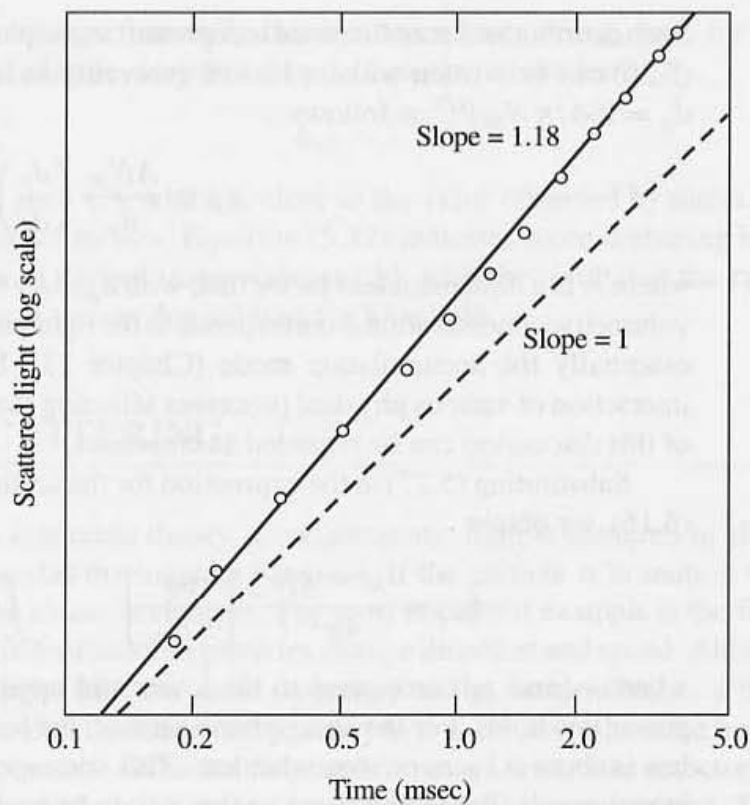


Figure 5.9 Increase, with time, of light scattered by coagulating lead particles generated by the decomposition of tetramethyl lead. The light source was an argon laser (Graham and Homer, 1973). As coagulation takes place, the total light scattering increases although N_{∞} decreases and ϕ stays constant. This figure applies to free molecule aerosols.

Light scattering by a coagulating aerosol in the Rayleigh size range was measured by Graham and Homer (1973). The aerosol was generated by passing a shock wave through argon containing tetramethyl lead (TML). The TML decomposes behind the shock to form a supersaturated lead vapor that nucleates and produces small lead droplets that subsequently coagulate. The rate of coagulation was followed by measuring light scattered perpendicular to the incident argon laser beam (Fig. 5.9). The slope in logarithmic coordinates is very close to the theoretical value of $6/5$ (Chapter 7).

If there are many particles larger than the Rayleigh range, calculations based on (5.25) underestimate particle size. The measured scattering by the larger particles will generally be less than the value calculated, assuming that the particles were in the Rayleigh range.

MIE SCATTERING: POWER LAW DISTRIBUTIONS

Aerosol size distributions can sometimes be represented by a power law relationship in the size subrange $0.1 < d_p < 3 \mu\text{m}$, where most of the contribution to light scattering occurs:

$$n_d(d_p) \sim d_p^{-p} \quad (5.26)$$

Such distributions are often used to represent atmospheric and clean room aerosols. Equation (5.26) can be written without loss of generality in terms of the average particle diameter $\bar{d}_p = [6\phi/\pi N_\infty]^{1/3}$ as follows:

$$n_d = \frac{AN_\infty}{\bar{d}_p} \left(\frac{d_p}{\bar{d}_p} \right)^{-p} \quad (5.27)$$

where A is a dimensionless factor that, with \bar{d}_p , may be a function of time and position. The volumetric concentration ϕ corresponds to the light-scattering subrange ($0.1 < d_p < 3 \mu\text{m}$), essentially the accumulation mode (Chapter 13). Equation (5.27) may result from the interaction of various physical processes affecting the size distribution, but for the purposes of this discussion can be regarded as empirical.

Substituting (5.27) in the expression for the scattering part of the extinction coefficient, (5.16), we obtain

$$b_{\text{sca}} = \frac{\lambda^{3-p} AN_\infty}{4\pi^{2-p}} \left[\frac{6\phi}{\pi N_\infty} \right]^{(p-1)/3} \int_{x_1}^{x_2} Q_{\text{sca}}(x, m) x^{2-p} dx \quad (5.28)$$

where x_1 and x_2 correspond to the lower and upper limits, respectively, over which the power law holds. For the atmospheric aerosol, the lower limit of applicability of the power law is about $0.1 \mu\text{m}$ or somewhat less. This corresponds to $x_1 < 1$, and for this range Q_{sca} is very small (Rayleigh range) so that x_1 can be replaced by zero. The contribution to the integral for large values of x is also small because p is usually greater than 3 or 4 and Q_{sca} approaches a constant, 2. Hence the upper limit x_2 can be set equal to infinity as a good approximation. The result is

$$\begin{aligned} b_{\text{sca}} &= \frac{\lambda^{3-p} AN_\infty}{4\pi^{2-p}} \left[\frac{6\phi}{\pi N_\infty} \right]^{(p-1)/3} \int_0^\infty Q_{\text{sca}}(x, m) x^{2-p} dx \\ &= AA_1 \lambda^{3-p} N_\infty^{(4-p)/3} \phi^{(p-1)/3} \end{aligned} \quad (5.29)$$

where A_1 is a constant defined by this expression. Thus if the distribution obeys a power law (5.26) and (5.27), the order, p , can be determined by measuring the wavelength dependence of the extinction coefficient. Moreover, for the power law distribution, the wavelength dependence of b_{sca} is independent of the shape of the extinction curve, provided that it satisfies the asymptotic limiting relationships discussed above.

Experimentally, it is sometimes found that

$$b_{\text{sca}} = A_2 \phi \quad (5.30)$$

where A_2 is a constant. This corresponds to $p = 4$ and constant A ; by (5.27) we obtain

$$n_d = \frac{6A\phi}{\pi d_p^4} \quad (5.31)$$

a power law form that often holds approximately for the light-scattering subrange of the atmospheric aerosol. However, (5.31) cannot extend to infinitely large particle diameters because the aerosol volumetric concentration becomes logarithmically infinite. Equation (5.30) holds better when the value of ϕ corresponds to the subrange $0.1 < d_p < 1 \mu\text{m}$ rather than the total volumetric concentration. The constants, of course, differ.

It is also found experimentally that the dependence of b_{sca} on λ for the atmospheric aerosol can sometimes be represented by an equation of the form

$$b_{\text{sca}} \sim \lambda^{-1.3} \quad (5.32)$$

corresponding to $p = 4.3$, which is close to the value observed by direct measurement of the size distribution function. Equation (5.32) indicates more scattering in the blue (short wavelength) than in the red (long wavelength), with the result that the range of vision in hazy atmospheres is greater for red than for blue light.

QUASI-ELASTIC LIGHT SCATTERING

In classical light-scattering theory, monochromatic light is scattered in all directions with the same frequency as the incident beam ω_0 . If the particle is in motion with respect to a fixed observer, the situation changes. The most important example is the Brownian motion (Chapter 2) in which submicron particles change direction and speed. Although the moving particle scatters light with the same frequency as the incident beam, a fixed observer or detector will see a slightly different frequency $\omega = \omega_0 + \Delta\omega$, where the frequency shift $\Delta\omega$ is an optical Doppler shift. If the emitting particle moves toward the detector, the light it emits appears more blue-shifted; if it moves away it appears more red-shifted. The Doppler shift depends only on the particle velocity and not on its material or optical properties. Particles of a given size have a Maxwellian velocity distribution determined by the equipartition principle and the absolute temperature (Chapter 2).

The Doppler shift is very small compared with the main frequency. To a close approximation, it is given by

$$\Delta\omega = \frac{v}{c}\omega_0 \quad (5.33)$$

where v is the particle velocity with respect to the detector and c is the velocity of light. Because the mean thermal speed of a $0.1\text{-}\mu\text{m}$ particle is of the order of 10 cm/sec , it is clear that the Doppler shift is very small. For this reason it can be neglected in the classical light-scattering studies discussed above. However, with suitable instrumentation, it is possible to detect the shift averaged over the particles and determine the particle size in this way. The phenomenon is called *quasi-elastic light scattering* (QELS); the frequency shift is so small that the scattering is nearly elastic (Berne and Pecora, 1976; Dahneke, 1983). QELS, also known as photon correlation spectroscopy or dynamic light scattering, can be used to measure the size of monodisperse particles in the size range from 0.01 to a few tenths of a micron. The method is widely used for small particles and large molecules suspended in aqueous solutions. It has also been applied in a few cases to aerosols (Dahneke, 1983).

In a QELS system, a laser beam is passed through a cloud of Brownian particles. Light is scattered into the detector that is set at an angle θ with respect to the incident beam. The scattering volume is defined by the intersection between the incident and the detector collection solid angles. The instantaneous intensity of the scattered light along a given path $I(t)$ can be written as the sum of the average intensity, \bar{I} , and a fluctuating intensity, $I'(t)$

$$I(t) = \bar{I} + I'(t) \quad (5.34)$$

The time-averaged scattered intensity \bar{I} is the basis of conventional light-scattering techniques used for aerosol measurements.

The intensity fluctuations due to the Brownian motion take place on a time scale much faster than conventional photometers or the human eye can detect. The variation in the fluctuating scattered light intensity with time resembles a noise signal that can be analyzed in terms of its correlation function with respect to time. The usual practice is to measure the polarized intensity time correlation function that is related to the diffusion coefficient for monodisperse particles as follows

$$G(\xi) = \overline{I(t)I(t+\xi)} = A [1 + \beta|\alpha^2 N_\infty g(\xi)|^2] \quad (5.35)$$

where

A = baseline constant

β = instrument constant

α = molar polarizability of the particles

$g(\xi)$ = normalized autocorrelation function for the translational Brownian motion

N_∞ = average particle concentration

For monodisperse particles

$$g(\xi) = \exp(-q^2 \xi D) \quad (5.36)$$

where D = particle diffusion coefficient and $q = (4\pi/\lambda) \sin(\theta/2)$. The autocorrelation function $g(\xi)$ is the parameter sought, and from it the diffusion coefficient, hence particle diameter can be obtained. The procedures have been worked out in most detail for application to hydrosols and high-molecular-weight polymeric solutions (Dahneke, 1983).

Rearranging (5.35) gives the autocorrelation function in terms of the experimentally measured variable $G(\xi)$:

$$\alpha^2 N_\infty g(\xi) = \frac{1}{\sqrt{A\beta}} [G(\xi) - A]^{1/2} \quad (5.37)$$

Various methods are used to determine the diffusion coefficient. For example after subtraction of the baseline constant, A , $G(\xi)$ may be fitted to an exponential function to permit calculation of the decay constant $q^2 D$, hence particle size from the value of D .

For polydisperse aerosols, the simple expression (5.36) for the autocorrelation function must be averaged over the particle size distribution function. In the Rayleigh scattering range

$$N_\infty g(\xi) = \int_0^\infty n_d(d_p) d_p^6 \exp(-q^2 \xi D) d(d_p) \quad (5.38)$$

There is no general exact method for extracting size distribution functions $n_d(d_p)$ from (5.38) and the experimentally measured function $G(\xi)$ when the form of $n_d(d_p)$ is not known. In the method of cumulants, the one most commonly used to estimate hydrosol size distributions from this integral, the logarithm of the autocorrelation function $g(\xi)$ is expanded in ξ :

$$\ln g(\xi) = K_1 \xi - K_2 \frac{\xi^2}{2} + \dots \quad (5.39)$$

The coefficients of ξ are moments of the size distribution function known as *cumulants*. In practice, only the first two cumulants can be accurately determined from the experimental data:

$$K_1 = q^2 \bar{D} \quad (5.40a)$$

and

$$K_2 = q^4 \overline{(D - \bar{D})^2} \quad (5.40b)$$

Here the averaging is weighted by d_p^6 as in (5.38). For a free molecule aerosol we have $D \sim d_p^{-2}$ (Chapter 2), so \bar{D} is proportional to the fourth moment of the particle size distribution. This heavily weights the upper end of the distribution function. If the form of the distribution function is known, the cumulants can be used to evaluate the parameters of the distribution. For example, if the size distribution is self-preserving (Chapter 7), any moment can be used to estimate the complete distribution.

SPECIFIC INTENSITY: EQUATION OF RADIATIVE TRANSFER

In the general case of aerosol/light interactions in the atmosphere or within a confined space, the light is neither unidirectional nor monochromatic; each volume element is penetrated in all directions by radiation. This requires a more careful definition of the intensity of radiation than used before. For the analysis of this case, an arbitrarily oriented small area, $d\sigma$, is chosen with a normal \mathbf{n} (Fig. 5.10). At an angle θ to the normal we draw a line S , the axis of an elementary cone of solid angle $d\omega$. If through every point of the boundary of the area $d\sigma$ a line is drawn parallel to the nearest generator of the cone $d\omega$, the result is a truncated semi-infinite cone $d\Omega$, similar to the cone $d\omega$. Its cross-sectional area, perpendicular to S at the point P , will be $d\sigma \cos \theta$.

Let dE be the total quantity of energy passing in time dt through the area $d\sigma$ inside cone $d\Omega$ in the wavelength interval λ to $\lambda + d\lambda$. For small $d\sigma$ and $d\omega$, the energy passing through $d\sigma$ inside $d\Omega$ will be proportional to $d\sigma d\omega$.

The specific intensity of radiation or simply the intensity, I_λ , is defined by the relation

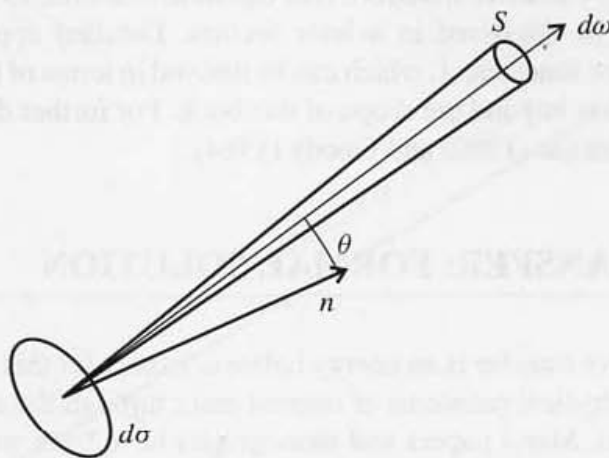


Figure 5.10 Geometric factors determining specific intensity of radiation.

$$I_\lambda = \frac{dE}{d\sigma \cos \theta dt d\omega d\lambda} \quad (5.41)$$

The intensity is, in general, a function of the position in space of the point P , the direction \mathbf{s} , time t , and wavelength λ :

$$I_\lambda = I_\lambda(P, \mathbf{s}, t, \lambda) \quad (5.42)$$

If I_λ is not a function of direction, the intensity field is said to be *isotropic*. If I_λ is not a function of position the field is said to be *homogeneous*. The total intensity of radiation is $I = \int_0^\infty I_\lambda d\lambda$. In the rest of this chapter, we suppress the suffix λ to simplify the notation.

Now consider the radiant energy traversing the length, ds , along the direction in which the intensity is defined; a change in the intensity results from the combination of the effects of extinction (absorption and scattering) and emission:

$$dI(P, s) = dI(\text{extinction}) + dI(\text{emission}) \quad (5.43)$$

The loss by extinction can be written as before in terms of the extinction coefficient, b :

$$dI(\text{extinction}) = -bI ds \quad (5.44)$$

Emission by excited dissociated atoms and molecules in the air is usually small in the visible compared with solar radiation. Thermal radiation is important in the far infrared but not in the visible. Hence consistent with the assumptions adopted in this chapter, gaseous emissions can be neglected in the usual air pollution applications.

In an aerosol, however, a *virtual emission* exists because of rescattering in the \mathbf{s} direction of radiation scattered from the surrounding volumes. The gain by emission is written in the form of a source term:

$$dI(\text{emission}) = bJ ds \quad (5.45)$$

This equation defines the source function, J .

Hence the energy balance over the path length, ds , takes the form

$$-\frac{dI}{b ds} = I - J \quad (5.46)$$

which is the *equation of radiative transfer*. This equation is useful, as it stands, in defining atmospheric visibility as discussed in a later section. Detailed applications require an expression for the source function, J , which can be derived in terms of the optical properties of the particles, but this is beyond the scope of this book. For further discussion, the reader is referred to Chandrasekhar (1960) and Goody (1964).

EQUATION OF RADIATIVE TRANSFER: FORMAL SOLUTION

The equation of radiative transfer is an energy balance; except for this concept, its physical content is slight. The physical problems of interest enter through the extinction coefficient and the source function. Many papers and monographs have been written on its solution

for different boundary conditions and spatial variations of the optical path (Chandrasekhar, 1960; Goody, 1964). Some simple solutions are discussed in this and the next section. Most of the applications have been to planetary atmospheres and astrophysical problems rather than to configurations of industrial interest or small scale pollution problems.

The formal solution of the equation of transfer is obtained by integration along a given path from the point $s = 0$ (Fig. 5.11):

$$I(s) = I(0)e^{-\tau(s, 0)} + \int_0^s J(s')e^{-\tau(s, s')}b ds' \quad (5.47)$$

where $\tau(s, s')$ is the optical thickness of the medium between the points s and s' :

$$\tau(s, s') = \int_{s'}^s b ds \quad (5.48)$$

The source function $J(s')$ over the interval 0 to s must be known to evaluate the integral in (5.47).

The interpretation of (5.47) is interesting: The intensity at s is equal to the sum of two terms. The first term on the right-hand side corresponds to Lambert's law (5.19), often used for the attenuation of a light beam by a scattering medium. The second term represents the contributions to the intensity at s from each intervening radiating element between 0 and s , attenuated according to the optical thickness correction factor. In the absence of external light sources and if secondary scattering by the surrounding aerosol can be neglected, the source function J becomes zero. This is the situation for configuration of a properly designed transmissometer, which is used to measure the attenuation of a light beam through the smoke flowing through a stack and in other industrial applications.

When the medium extends to $-\infty$ in the s direction and there are no sources along s , it may be convenient not to stop the integration at the point 0 but to continue it indefinitely:

$$I(s) = \int_{-\infty}^s J(s')e^{-\tau(s, s')}b ds' \quad (5.49)$$

Thus the intensity observed at s is the result of scattering by all of the particles along the line of sight.

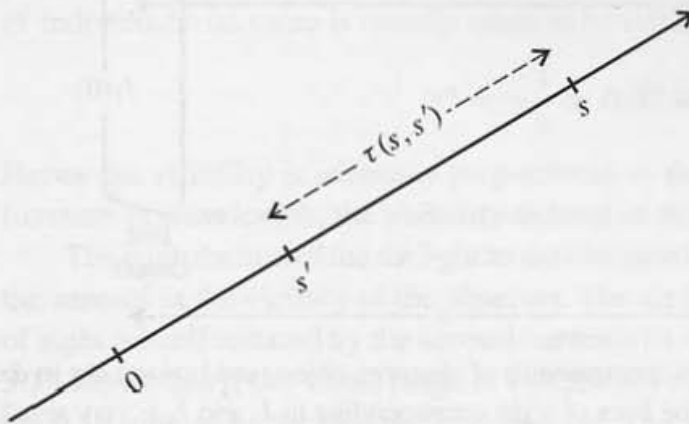


Figure 5.11 Path of integration along the s vector. Light at point 0 reaches any point s attenuated according to Lambert's law. In addition, light is scattered toward s by particles between 0 and s such as those at the point s' .

LIGHT TRANSMISSION THROUGH THE ATMOSPHERE: VISIBILITY

An important and interesting application of the theory of radiative transfer is to the definition of atmospheric visibility. The terms “visibility” and “visual range” may be used interchangeably to signify the distance at which it is just possible to distinguish a dark object against the horizon. As pointed out by Middleton (1952), “the problem, then, is to establish usable theoretical relationships between light, eye, target, and atmosphere that will permit the calculation of the visual range at any time; and to provide means of measuring the necessary parameters quickly and accurately enough.” This can be accomplished by solving the equation of radiative transfer, subject to a set of assumptions concerning human response to the obscuration of objects.

Most of the information that we obtain through our sense of vision depends on our perception of differences in intensity or of color among the various parts of the field of view. An object is recognized because its color or brightness differs from its surroundings, and also because of the variations of brightness or color over its surface. The shapes of objects are recognized by the observation of such variations.

Differences in intensity are particularly important and are the principal basis for the classical theory of visibility (Steffens, 1956): An isolated object on the ground such as a building is viewed from a distance along a horizontal line of sight (Fig. 5.12). The intensity contrast between the test object and the adjacent horizon sky is defined by the expression

$$C = \frac{I_1 - I_2}{I_2} \quad (5.50)$$

where I_2 is the intensity of the background and I_1 is the intensity of the test object, both measured at the same distance from the observer.

Expressions for the intensity can be obtained by integrating the equation of radiative transfer (5.46) over the horizontal distance from the test object to the point of observation. If b and J are not functions of s , the integration gives

$$I(s) = I(0)e^{-bs} + J[1 - e^{-bs}] \quad (5.51)$$

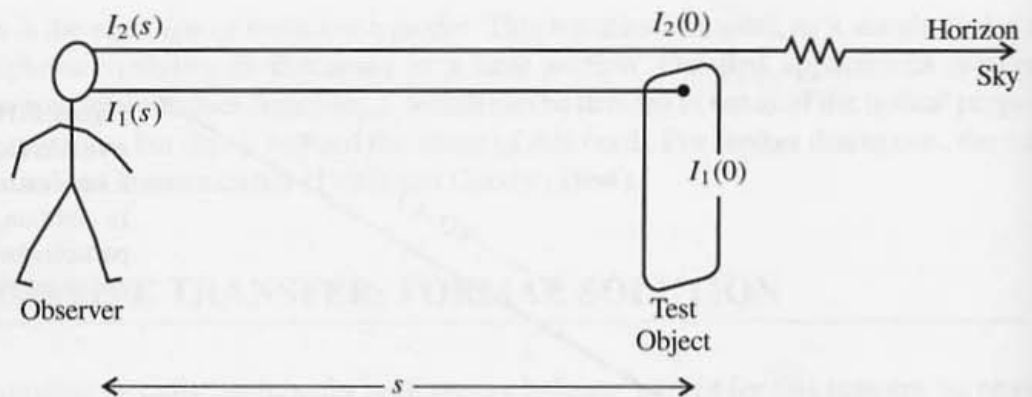


Figure 5.12 Relative arrangements of observer, object, and horizon sky in definition of the visibility. The angle between the lines of sight corresponding to I_1 and I_2 is very small.

where $s = 0$ corresponds to the location of the test object. Rewriting (5.50) as

$$C = \frac{I_2(0) [I_1(s) - I_2(s)]}{I_2(s) I_2(0)} \tag{5.52}$$

and substituting (5.51) for $[I_1(s) - I_2(s)]$ gives with (5.50)

$$C = \frac{I_2(0) [I_1(0) - I_2(0)] e^{-bs}}{I_2(s) I_2(0)} = \frac{I_2(0)}{I_2(s)} C(0) e^{-bs} \tag{5.53}$$

where $C(0)$ is the contrast at the test object.

In viewing the horizon sky, the observer sees the virtual emission, J , resulting from the light from the sun and surroundings scattered in the direction of the observer by the atmosphere. This is sometimes referred to as the air light or the skylight. By assumption, the air light is not a function of s . Suppose that 2 refers to the line of sight in the direction of the horizon sky. The intensity at any plane normal to this sightline is equal to the virtual emission or air light J ; that is, $I_2(s) = I_2(0) = J = \text{constant}$ and (5.53) becomes

$$C = C(0) e^{-bs} \tag{5.54}$$

If the test object is perfectly black, then $I_1(0) = 0$, $C(0) = -1$, and

$$C = -e^{-bs} \tag{5.55}$$

The minus sign in this expression results because the test object is darker than the background.

The visual range or, more commonly, the visibility is defined as the distance at which the test object is just distinguishable from background. Hence the minimum contrast that the eye can distinguish must now be introduced into the analysis. This contrast is denoted by C^* and the corresponding visibility $s = s^*$. For a black object at $s = s^*$,

$$C^* = -\exp(-bs^*) \tag{5.56}$$

or

$$s^* = -\frac{1}{b} \ln(-C^*) \tag{5.57}$$

The parameter C^* is sometimes called the threshold contrast or “psychophysical constant” because it depends on human perception. Based on data averaged over responses of a group of individuals, its value is usually taken to be 0.02:

$$s^* = -\frac{1}{b} \ln 0.02 = \frac{3.912}{b} \tag{5.58}$$

Hence the visibility is inversely proportional to the extinction coefficient. Because b is a function of wavelength, the visibility defined in this way also depends on wavelength.

The contribution of the air light to the obscuration of distant objects comes mostly from the aerosol in the vicinity of the observer. The air light from more distant parts of the line of sight is itself reduced by the aerosol between its region of origin and the observer. Figure 5.13 shows that if the visual range is 1 mile, half of the obscuration would be produced by the 0.18 mile of aerosol nearest the observer. The strong weighting of the aerosol near the

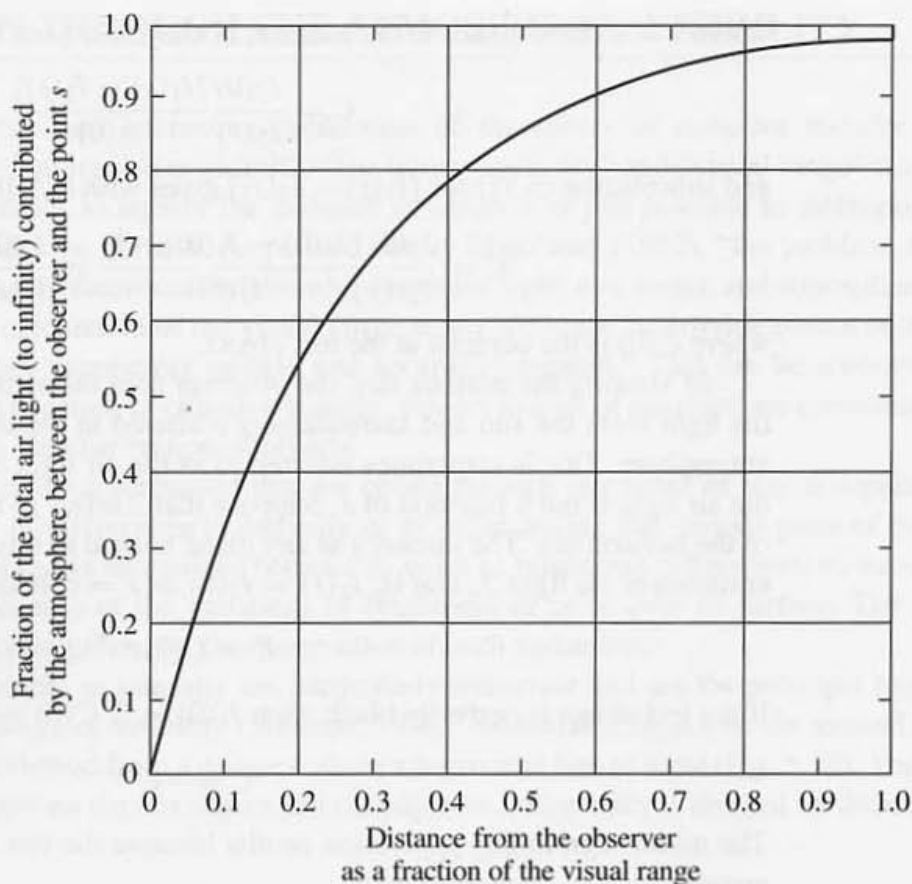


Figure 5.13 Fraction of the total air light (to infinity) contributed by the portion of the atmosphere between the observer and the point s from the observer. The air light that obscures distant objects arises mostly from the aerosol in the immediate vicinity of the observer (for a uniform atmosphere). (See Problem 6.) (After Steffens, 1956.)

observer is one reason why the idealized theoretical analysis discussed above works as well as it does. As long as the aerosol is fairly uniform in the neighborhood of the observer, the conditions beyond have little influence.

The total atmospheric extinction is the sum of contributions for the aerosol, molecular scattering, and, perhaps, some gas absorption at certain wavelengths characteristic of strong absorbers such as NO_2 :

$$b = b_{\text{aerosol}} + b_{\text{molecular}} \quad (5.59)$$

Molecular scattering coefficients for air have been tabulated (Table 5.2). For $\lambda = 0.5 \mu\text{m}$, the visibility calculated from (5.58) is about 220 km or 130 mi. Hence the visibilities of a few miles or less, often observed in urban areas when the humidity is low, are due primarily to aerosol extinction. In some cases, however, there may be a contribution by NO_2 absorption.

TABLE 5.2
Rayleigh Scattering Coefficient for Air at 0°C and
1 atm^a (Penndorf, 1957)

$\lambda(\mu\text{m})$	$b_{\text{scat}} \times 10^8$ (cm^{-1})
0.2	954.2
0.25	338.2
0.3	152.5
0.35	79.29
0.4	45.40
0.45	27.89
0.5	18.10
0.55	12.26
0.6	8.604
0.65	6.217
0.7	4.605
0.75	3.484
0.8	2.684

^aTo correct for the temperature, $b_T = b_{T=0^\circ\text{C}}(273/T \text{ K})$ at 1 atm. This approximate formula does not take into account the variation of refractive index with temperature.

INELASTIC SCATTERING: RAMAN EFFECT

Basic Concepts

The previous discussions were limited to scattering processes in which the wavelengths of the incident and scattered light are equal (or nearly equal), that is, elastic scattering. Light may be scattered at a wavelength different from the incident beam, inelastic scattering, as a result of quantum mechanical effects. This phenomenon, known as Raman scattering, is illustrated in Fig. 5.14, which summarizes absorption and the various scattering processes discussed in this chapter. Two vibrational quantum states present in a scattering molecule are shown: the ground state $V = 0$ and the $V = 1$ energy state. The energy of the incident beam is assumed to be several times larger than the energy difference between the two states. Photons from the incident beam may raise the molecule from state 0 or 1 to a virtual state that does not correspond to any allowed state. Three outcomes are possible. The molecule may return to its original state (0 or 1) by emission of a photon with the same energy as the incident beam, equivalent to elastic scattering. Alternatively, the molecule originally in state 0 may drop to state 1 by emitting a photon of less energy than the incident beam (Stokes emission). Finally the molecule originally in state 1 may fall to state 0 by emitting a photon of higher energy than the incident beam (anti-Stokes emission). Thus the Stokes lines appear at lower frequencies and the less intense anti-Stokes lines at higher frequencies

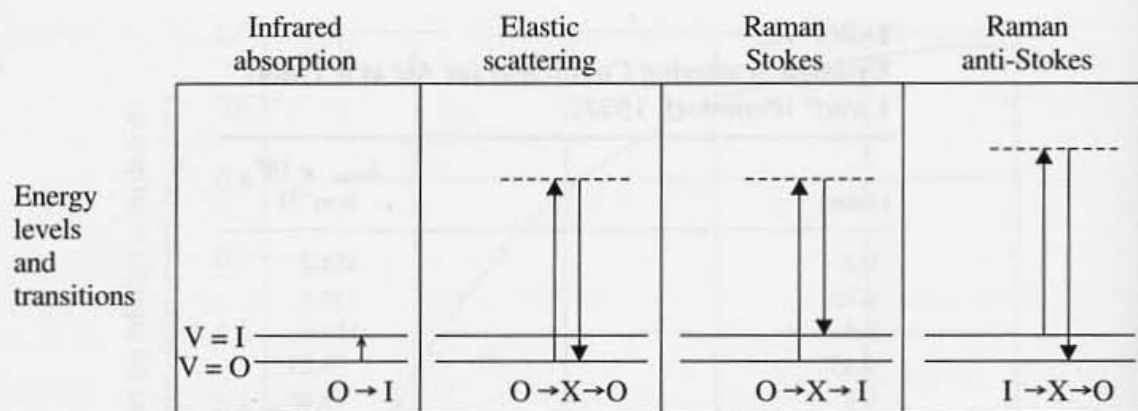


Figure 5.14 Schematic diagram illustrating infrared absorption and elastic and inelastic (Raman) scattering by a molecule with two vibrational quantum states, the ground state $\nu = 0$ and the $\nu = 1$ energy level. In infrared absorption, the incident photon has the same frequency as the molecular vibration. In elastic and inelastic scattering, the incident photon has a much higher frequency, seven times that of the vibrational quantum state in this diagram. Scattered photons are of two types: the lower (“Stokes”) or higher (“anti-Stokes”) frequencies ($7\nu \pm \nu$). The photon frequency difference before and after scattering is equal to the molecular vibrational frequency. (After Colthup et al., 1990, p. 61.)

than that of the incident beam. The intensity of the Raman scattering is usually several orders of magnitude smaller than that of elastic scattering.

Raman spectra have a number of features that simplify their interpretation: (1) The Raman shift or difference between the frequencies of the incident and scattered light is independent of the frequency of the incident light; (2) to a first approximation, the Raman shift is independent of the state (gas, liquid, or solid) of the scattering medium; (3) the energy corresponding to the Raman shift frequency, $h\nu_R$, is equal to the difference between the energies of two stationary states of the scattering molecules; precise information on this energy difference can be obtained from the absorption and emission spectra of the scattering material.

Raman Scattering by Particles

There are few methods suitable for on-line chemical analysis of aerosol particles. Raman spectroscopy offers the possibility of identifying the chemical species in aerosol particles because the spectrum is specific to the molecular structure of the material, especially to the vibrational and rotational modes of the molecules. Raman spectra have been obtained for individual micron-sized particles placed on surfaces, levitated optically or by an electrodynamic balance, or by monodisperse aerosols suspended in a flowing gas. A few measurements have also been made for chemically mixed and polydisperse aerosols. The Raman spectrum of a spherical particle differs from that of the bulk material because of morphology-dependent resonances that result when the Raman scattered photons undergo Mie scattering in the particle. Methods have been developed for calculating the modified spectra (McNulty et al., 1980).

Both measurements and calculations based on Raman theory indicate that the scattering intensity is approximately proportional to the particle volume (or mass) over certain

refractive index ranges and values of $\pi d_p/\lambda > 0.2$. Calculations (Fig. 5.15) show this holds best for scattering in the forward direction. Figure 5.16 shows experimental measurements of the ratio of the Raman intensity of monodisperse and polydisperse diethylsebacate aerosols to that of the nitrogen carrier gas peak as a function of aerosol mass loading for aerosols with various size distributions. Mass mean diameters ranged from 0.4 to 1.8 μm , and the mass loadings ranged from 0.4 to 13 g/m^3 . The figure shows that the Raman signal is approximately independent of the size distribution over this range and is proportional to the total mass concentration. Neither the theoretical calculations nor the experimental measurements show a strong effect of the morphology-dependent resonances on the relationship of the scattering intensity to particle volume for spherical particles.

The mass loadings in these studies were high, with the lowest approximately 0.4 g/m^3 . These concentrations fall in the range of some industrial and therapeutic aerosols but are several orders of magnitude higher than atmospheric aerosol concentrations. Buehler et al. (1991) also found an approximate dependence of scattering on particle volume for large suspended single droplets ($25 < d_p < 66 \mu\text{m}$). These results suggest that at sufficiently high mass loadings it may be possible to monitor the mass concentration of Raman active

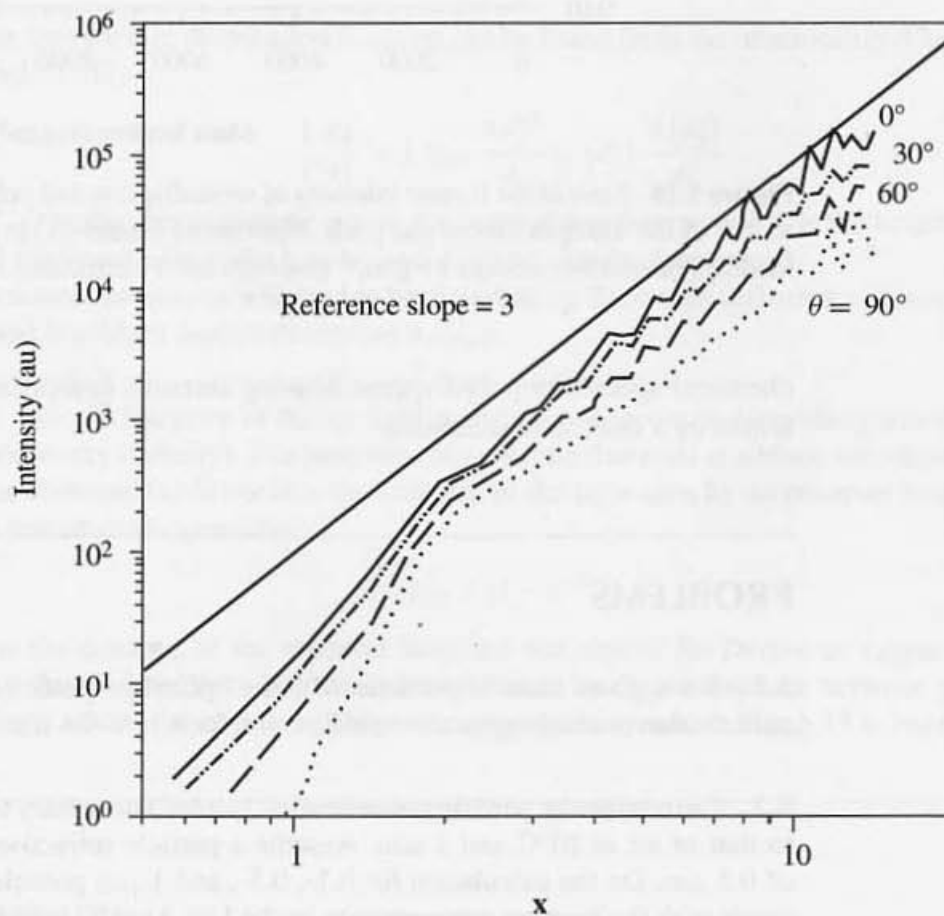


Figure 5.15 Calculated values of the intensity of Raman scattering at various values of the scattering angle for $m = 1.5$. The intensity is approximately proportional to the particle volume for $x > 2$ (Stowers and Friedlander, 1998).

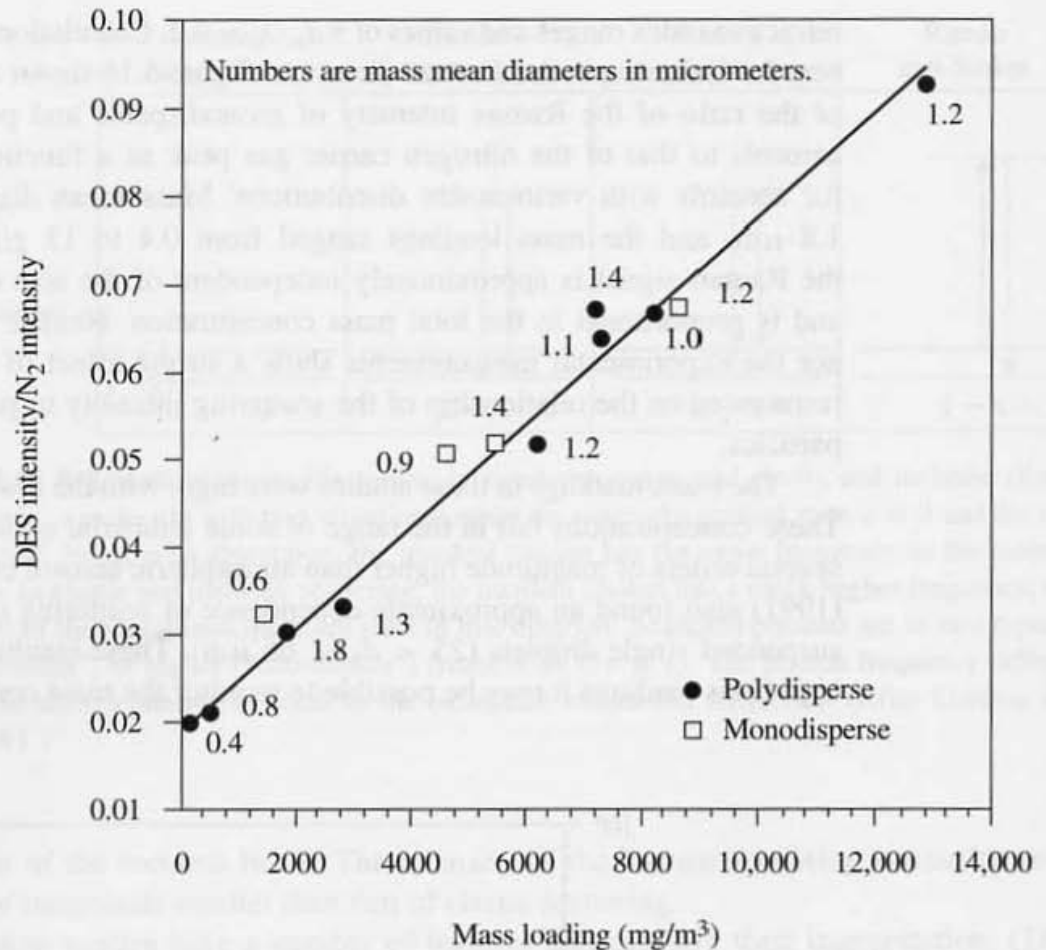


Figure 5.16 Ratio of the Raman intensity of monodisperse and polydisperse diethylsebacate aerosols to that of the nitrogen carrier gas peak. Mass mean diameters ranged from 0.4 to 1.8 μm , and mass loadings ranged from 0.4 to 13 g/m^3 (Stowers and Friedlander, 1998).

chemical species in polydisperse flowing aerosols composed of particles larger than a few tenths of a micron in diameter.

PROBLEMS

5.1 For a given mass of particles with the optical properties of carbon spheres, determine the particle size producing maximum extinction for $\lambda = 0.436 \mu\text{m}$. Assume monodisperse particles.

5.2 Determine the particle concentration ($\mu\text{g}/\text{m}^3$) necessary to scatter an amount of light equal to that of air at 20°C and 1 atm. Assume a particle refractive index of 1.5 and a wavelength of 0.5 μm . Do the calculation for 0.1-, 0.5-, and 1- μm particles of unit density. Compare your result with the average concentration in the Los Angeles atmosphere, about 100 $\mu\text{g}/\text{m}^3$.

5.3 The California visibility standard requires that the visibility be greater than 10 miles on days when the relative humidity is less than 70%. Consider a day when the visibility controlling

aerosol is composed of material with a refractive index of 1.5. Estimate the aerosol concentration in the atmosphere that would correspond to the visibility standard. Assume (1) the density of the spherical particles is 1 g/cm^3 ; (2) the aerosol is monodisperse with a particle size, $d_p = 0.5 \text{ }\mu\text{m}$; and (3) the wavelength of interest is $0.5 \text{ }\mu\text{m}$. Express your answer in micrograms of aerosol per cubic meter of air.

5.4 The extinction of light by an aerosol composed of spherical particles depends on its optical properties and size distribution. Consider the distribution function $n_d(d_p) \sim d_p^{-4}$, often observed at least approximately. Suppose these particles are composed of an organic liquid ($m = 1.5$), on the one hand, or of carbon, on the other. This might correspond to a photochemical aerosol ($m = 1.5$) and a soot aerosol generated by a diesel source or other combustion processes. Calculate the ratio $b_{\text{carbon}}/b_{1.5}$ for fixed size distribution.

5.5 It is possible, in principle, to determine the size distribution of particles of known optical properties by measurement of the light scattered by a settling aerosol. In this method, the intensity of the light transmitted by the aerosol in a small cell, I , is recorded as a function of time. The aerosol is initially uniform spatially, and there is no convection.

The light scattered from a horizontal beam at a given level in the cell remains constant until the largest particles in the aerosol have had time to fall from the top of the cell through the beam. The scattering will then decrease as successively smaller particles are removed from the path of the beam.

Show that the size distribution function can be found from the relationship (Gumprecht and Sliepcevic, 1953)

$$-\frac{1}{I} \frac{dI}{dt} = L Q_{\text{sca}} \frac{\pi d_p^{*2}}{4} n_d(d_p^*) \frac{d(d_p^*)}{dt}$$

where d_p^* is the maximum particle size in the beam at any time, t , and L is the length of the light path (cell thickness). Describe how d_p^* and $d(d_p^*)/dt$ can be determined.

In practice, the system will tend to be disturbed by Brownian diffusion and convection, and this method is seldom used to determine $n_d(d_p)$.

5.6 Let J be the intensity of the air light seen by an observer looking along a horizontal path to the horizon sky (infinity). The path falls close to one that ends at a black test object a distance s from the observer. (a) Show that the intensity of the light seen by an observer looking toward the black test object is given by

$$I(s) = J (1 - e^{-bs})$$

where s is the distance of the observer from the test object. (b) Derive an expression for the fraction of the total air light (to infinity) contributed by the atmosphere between the observer and the point s from the observer. This is the expression on which Fig. 5.13 is based (Steffens, 1956).

REFERENCES

- Barber, P. W., and Hill, S. C. (1990) *Light Scattering by Particles: Computational Methods*, World Scientific, Singapore.

- Bayvel, L. P., and Jones, A. R. (1981) *Electromagnetic Scattering and Its Applications*, Applied Science Publishers, Essex, England.
- Berne, B. J., and Pecora, R. (1976) *Dynamic Light Scattering*, Wiley-Interscience, New York.
- Bohren, C. F., and Huffman, D. R. (1983) *Absorption and Scattering of Light by Small Particles*, Wiley, New York.
- Bolz, R. E., and Tuve, G. E. (Eds.) (1970) *Handbook of Tables for Applied Engineering Science*, Chemical Rubber Company, Cleveland, OH, p. 159.
- Buehler, M. F., Allen, T., and Davis, E. J. (1991) *J. Colloid Interface Sci.*, **146**, 79.
- Chandrasekhar, S. (1960) *Radiative Transfer*, Dover, New York. This is the classic reference on the equation of radiative transfer and its solutions.
- Colthup, N. B., Daly, L. H., and Wibberly, S. E. (1990) *Introduction to Infrared and Raman Spectroscopy*, 3rd ed., Academic Press, San Diego.
- Dahneke, B. E. (1983) (Ed.) *Measurement of Suspended Particles by Quasi-Elastic Light Scattering*, Wiley-Interscience, New York.
- Ensor, D. S., Charlson, R. J., Ahlquist, N. C., Whitby, K. T., Husar, R. B., and Liu, B. Y. H. (1972) *J. Colloid Interface Sci.*, **39**, 242; also in Hidy, G. M. (Ed.) (1972) *Aerosols and Atmospheric Chemistry*, Academic, New York.
- Garvey, D. M., and Pinnick, R. G. (1983) *Aerosol Sci. Technol.*, **2**, 477.
- Goody, R. M. (1964) *Atmospheric Radiation: I. Theoretical Basis*, Oxford University Press, Oxford. This monograph includes application of the theory of small particle scattering and the equation of radiative transfer to Earth's atmosphere.
- Graham, S. C., and Homer, J. B. (1973) *Faraday Symp.*, **7**, 85.
- Gumprecht, R. D., and Slipecevic, C. M. (1953) *J. Phys. Chem.*, **57**, 95.
- Hodkinson, J. R. (1966) The Optical Measurement of Aerosols, in Davies, C. N. (Ed.), *Aerosol Science*, Academic, New York.
- Kerker, M. (1969) *The Scattering of Light and Other Electromagnetic Radiation*, Academic, New York. This includes a very good discussion of Mie theory with helpful physical insights as well as references to related experimental studies.
- McCartney, E. J. (1976) *Optics of the Atmosphere*, Wiley, New York.
- McDonald, J. E. (1962) *J. Appl. Meteor.*, **1**, 391.
- McNulty, P. J., Chew, H. W., and Kerker, M. (1980) in Marlow, W. W. (Ed.) *Aerosol Microphysics I: Particle Interaction*, Springer, p. 89.
- Middleton, W. E. K. (1952) *Vision Through the Atmosphere*, University of Toronto Press.
- Penndorf, R. B. (1957) *J. Opt. Soc. Am.*, **47**, 176.
- Steffens, C. (1956) Visibility and Air Pollution, in Magill, P. L., Holden, F. R., and Ackley, C. (Eds.), *Air Pollution Handbook*, McGraw-Hill, New York.
- Stowers, M. A., and Friedlander, S. K. (1998) Paper presented at the AIChE Meeting in Miami, November 15–20.
- van de Hulst, H. C. (1957) *Light Scattering by Small Particles*, Wiley, New York. This is a good place to turn for detailed information on elastic light scattering by single elements, including spheres and other bodies of simple shapes. It is primarily a theoretical work but includes several chapters on practical applications.

Experimental Methods

The design of many of the instruments used for measuring aerosol properties depends on the particle transport and optical properties discussed in the previous chapters. The principal applications of measurement systems are to atmospheric measurements, the monitoring of air pollution, the testing of gas cleaning equipment such as filters and scrubbers, and the monitoring of process streams including stack gases. Theory provides useful guidelines for instrument design, but it is rarely possible to predict instrument performance from first principles. It is almost always necessary to calibrate the instruments using aerosols of known properties.

A comprehensive review of measurement methods is beyond the scope of this book. Excellent reviews of aerosol instrumentation have appeared in recent years (Spurny, 1986; Pui and Liu, 1988; Willeke and Baron, 1993; ACGIH, 1995). A practical guide to aerosol chemical analysis is given in the book edited by Lodge (1989). Much information on the sampling and analysis of the atmospheric aerosol can be found in the EPA (1996) Air Quality Criteria Document for particulate matter. The measurement methods discussed in this chapter provide information on a broad spectrum of physical and chemical properties. The discussion starts with basic sampling methods and microscopy, goes on to integral measurement methods including mass and number concentrations and total light scattering, and finally to instruments that provide more detailed information on size distribution and chemical properties. Instruments with different sensing systems will, in general, have different response times, and the aerosol properties measured by each only partially overlap. A summary classification scheme in this chapter permits comparison of the various instruments according to the type of information they provide and helps identify gaps in aerosol instrumentation.

For example, many methods are available for the chemical analysis of deposited aerosol particles. Individual particles can be analyzed as well as heavier deposits. A serious gap in aerosol instrumentation is the lack of instruments for on-line measurement of aerosol chemical constituents without removing them from the gas. Very large amounts of information on multicomponent, polydisperse aerosols would be generated by an instrument capable of continuously sizing and chemically analyzing each particle individually, thereby permitting the determination of the size–composition probability density function, g (Chapter 1). From this function, in principle, many of the chemical

and physical properties of aerosols can be obtained by integration. Progress has been made in the development of such a system based on mass spectrometry as described in this chapter.

Aerosol measurements require various levels of interference with the system under study. Least invasive are *in situ* measurements made without removing a sample from a flowing aerosol stream, usually by optical techniques. On-line analysis involves the continuous removal of a sample stream from a flowing aerosol. The sample stream then passes to an instrument where the desired measurement is made without collection, usually with a short time lag with respect to the main flow. Still more invasive techniques involve deposition of particles on collecting surfaces either by introducing the surface directly into the flow stream or by removing a sample and collecting the particles. Particle collection on surfaces followed by redispersal and physical or chemical analysis is usually considered to be an undesirable practice; irreversible changes in the collected material make it difficult to relate results of such measurements to the original flowing aerosol.

The instrument or group of instruments selected for a particular application depend on several factors. Most important, of course, is the type of information sought. Other factors include cost, portability, and reliability under the conditions of operation. Process and stack gas monitoring pose particularly difficult demands because of extreme conditions of temperature and humidity. In the case of measurement systems designed for routine monitoring, the maintenance required is an important factor.

Much effort and ingenuity have gone into the development of generators capable of producing monodisperse aerosols, and several are discussed at the end of this chapter. These are used for the testing of gas-cleaning equipment, the calibration of size measurement devices, and basic studies of aerosol behavior.

SAMPLING

Optical methods can, in some cases, be used to measure aerosol characteristics in the original gas stream without withdrawing a sample. In most cases, however, it is necessary to sample from a flowing gas through a tube into an instrument, such as those discussed in the following sections.

Care must be taken in the design of the sampling system to ensure that a representative sample is obtained. The sampling stream intake should be designed to minimize preferential withdrawal of particles with respect to size. Deposition on the inside walls of the sampling tube and subsequent reentrainment must be minimized or taken into account. Precautions are also necessary to prevent condensation and other gas-to-particle conversion processes (Chapter 10). This problem is particularly acute in the sampling of hot, high relative humidity stack gases.

When there is a velocity difference between the gas stream and the gas entering the sampling probe, preferential withdrawal of particles with respect to size takes place. In analyzing the performance of a sampling probe oriented in the direction of the flow, it is assumed that the flow is uniform both in the mainstream of the gas and in the entrance to the probe. On dimensional grounds, for the particle size range $d_p > 1 \mu\text{m}$, the ratio of the

concentration in the sample, n_s , to that in the mainstream, n_m , depends on the velocity ratio, U_m/U_s , and on the Stokes number:

$$\frac{n_s}{n_m} = f\left(\frac{U_m}{U_s}, \text{Stk}\right) \quad (6.1)$$

where s and m refer to the sampling and mainstreams, respectively. The goal of the sampling procedure is to ensure that $n_s = n_m$.

The dependence of n_s/n_m on the velocity ratio is shown in Fig. 6.1 for particles of varying size. To explain the shapes of these curves, we consider the case of fixed sampling velocity. For low mainstream velocities ($U_m/U_s \rightarrow 0$), the sample tends to be representative ($n_s \approx n_m$). The sampling orifice acts as a point sink, and the streamlines of the flow are practically straight (Fig. 6.2a). As a result, inertial effects can be neglected. The n_s/n_m ratio initially decreases as mainstream velocity increases because inertial effects carry the particles around the sampling orifice (Fig. 6.2b). Further increase in the mainstream velocity leads to an upturn in n_s/n_m , which approaches unity for $U_s = U_m$ (Fig. 6.2c). Sampling at the same velocity as that of the gas is known as *isokinetic sampling*. At higher mainstream velocities, particles are preferentially carried into the sampling tube (Fig. 6.2d).

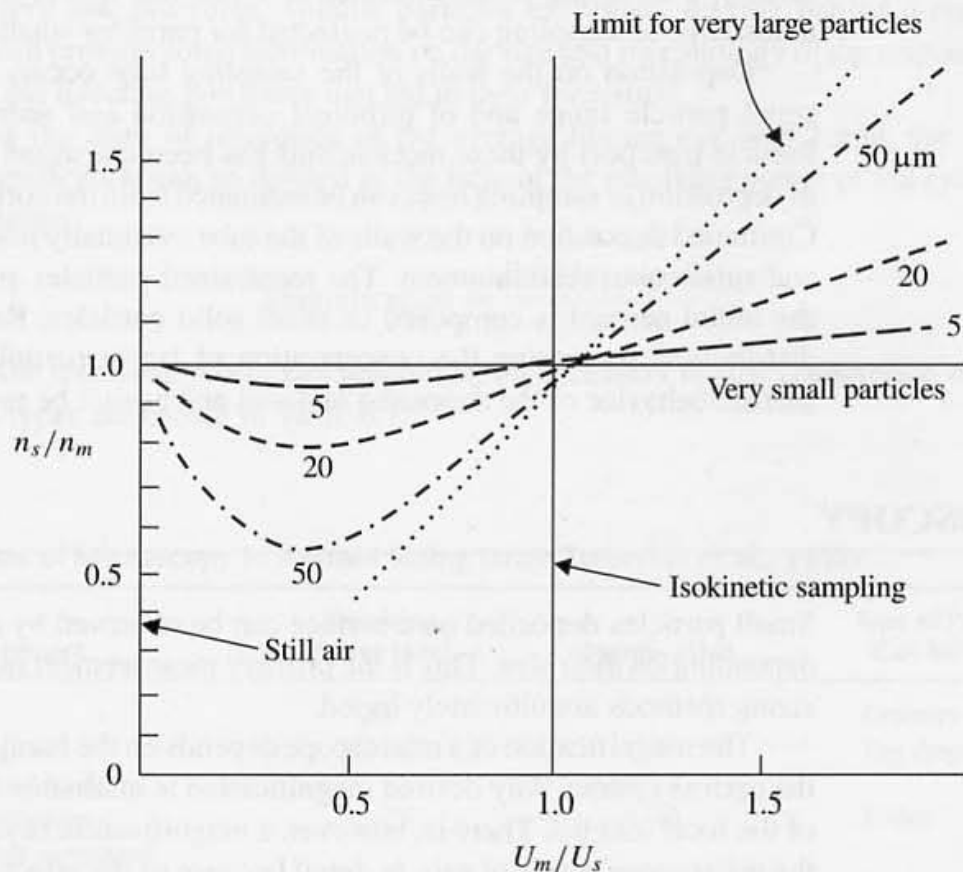


Figure 6.1 Effect of velocity ratio on concentration ratio for a sampling tube oriented in the direction of the mainstream flow. The curves are approximate representations of the data of various experimenters for unit density particles of diameters (in μm) as indicated. The displacement of the point $n_s/n_m = 1$ from $U_m/U_s = 1$ results from the finite particle diameter. The curves apply to a nozzle of 1- to 2-cm-diameter sampling at about 5 m/sec (May, 1967).

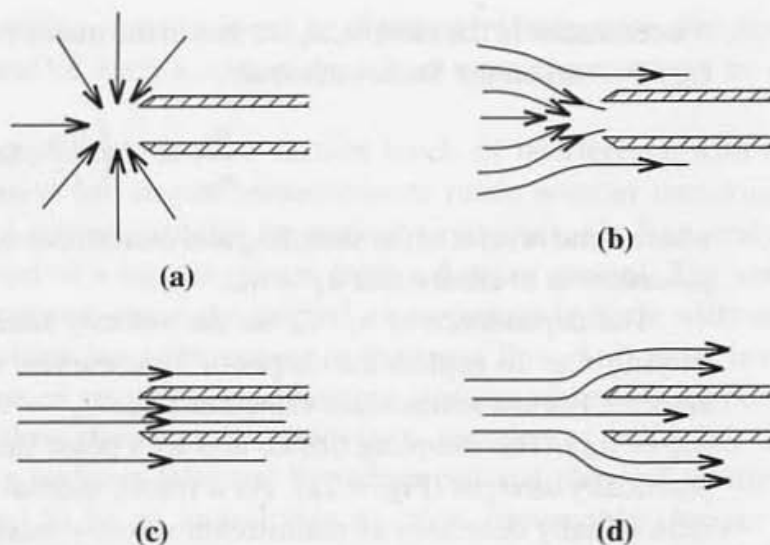


Figure 6.2 Patterns of gas flow at the entrance to a sampling probe for different ratios of sampling to gas velocities.

Because the effect is inertial, it increases for larger particles. For particles of unit density, a sampling probe diameter of 1 cm, and a velocity of 500 cm/sec, the effect of nonisokinetic sampling can be neglected for particles smaller than 5 μm .

Deposition on the walls of the sampling tube occurs as a result of diffusion in the small particle range and of turbulent deposition and sedimentation for larger particles. Particle transport by these mechanisms has been discussed in previous chapters, and rates of deposition in sampling lines can be estimated from the correlations for flow through tubes. Continued deposition on the walls of the tube eventually leads to the formation of a deposit and subsequent reentrainment. The reentrained particles are likely to be agglomerates, if the initial aerosol is composed of small solid particles. Reentrainment modifies the size distribution, increasing the concentration of larger particles. The effect depends on the surface behavior of the deposited material and cannot be predicted from theory.

MICROSCOPY

Small particles deposited on a surface can be observed by optical or electron microscopy, depending on their size. This is the primary measurement method upon which most aerosol sizing methods are ultimately based.

The magnification of a microscope depends on the focal lengths of the lenses making up the optical system. Any desired magnification is attainable in principle by proper selection of the focal lengths. There is, however, a magnification beyond which the image formed in the microscope does not gain *in detail* because of the effects of diffraction. Thus the image of a point object produced by an ideal lens (all aberrations corrected) is not a point but a diffraction pattern consisting of a circular disk surrounded by alternating dark and light rings of diminishing intensity.

Sizing of a particle observed under a microscope depends on our ability to distinguish one edge of the particle from the other on the opposite side. The ability of a microscope to size in this way is measured by its *resolving power*, the closest distance to which two

objects under observation can approach and still be recognized as separate. By definition, the resolving power or limit of resolution of the instrument is the radius of the central disk of the diffraction pattern. From diffraction theory, this is given by

$$\ell_{\text{res}} = \frac{0.61\lambda}{m \sin \theta} \quad (6.2)$$

where λ is the wavelength of the light, m is the refractive index of the medium in which the object is located, and θ is the half-angle of the light rays coming from the object. To maximize the resolution, λ should be small, and m and θ should be large. The refractive index can be increased by immersing the object under observation in an oil ($m \approx 1.5$) instead of air ($m = 1$). The highest numerical aperture, $m \sin \theta$, attainable in this way is about 1.4. Thus when we take $\lambda = 0.5 \mu\text{m}$, the best resolution achievable with the optical microscope is about $0.2 \mu\text{m}$.

A significant improvement in resolving power over the oil immersion optical microscope is possible using the much shorter wavelengths associated with high-speed electron beams. Both electric and magnetic fields can be used as lenses for electrons so the elements of a microscope are available. The normal magnification ranges from 1400 to 200,000, permitting measurements down to a few angstroms. Electron microscopes are operated at pressures of 10^{-5} to 10^{-4} torr to avoid scattering of the electron beam by gas molecules. At these very low pressures, volatile particles evaporate, leaving behind a residue that, however, can provide some information on the size and morphology of the original particle, as well as the dynamic processes that led to their formation.

Taking the limit of resolution of the average human eye as 0.2 mm, the maximum useful magnification can be defined as the ratio of the resolving power of the eye to that of the microscope:

$$\text{Magnification} = \frac{0.033m \sin \theta}{\lambda} \quad (6.3)$$

Values of the resolving power and magnification necessary for the observation of particles of various types are shown in Table 6.1.

TABLE 6.1
Applications of Microscopy to Aerosol Sizing (after Zworykin et al., 1945)

Type of Instrument	Resolving Power (μm)	Magnification	Type of Particle That Can be Observed
Eye	200	1	Ordinary objects
Magnifying glass	25–100	2–8	Fog droplets
Low-power compound optical microscope	10–25	8–20	Pollen
Medium-power compound optical microscope	1–20	20–200	Aireborne soil dust
High-power compound optical microscope	0.25	800	Titania pigment, cigarette smoke
High-power compound optical microscope using ultraviolet light	0.10	2000	Surface area peak in urban aerosols
Electron microscope	angstroms	1400–200,000	Nanoparticles

Particles can be deposited on surfaces for optical or electron microscopy using a number of different devices including thermal and electrical precipitators, filters, and cascade impactors. The preparation of samples for microscopy including the use of these devices is reviewed by Silverman et al. (1971). For detailed information on the size and morphological characteristics of particulate matter, there is no substitute for microscopy, provided that sampling and observation do not modify the particle physically and/or chemically. However, for routine monitoring and for studies of aerosol dynamics, it is usually more convenient to use calibrated continuous, automatic counters of the types described in this chapter. A catalog of photomicrographs of particles of different origins, showing the remarkable variations in size and shape, has been published (McCrone et al., 1973).

MASS CONCENTRATION: FILTRATION

The mass concentration is the most commonly measured aerosol property:

$$\rho = \int_0^{\infty} \rho_p n(v) v \, dv \quad (6.4)$$

where ρ_p , the density of the aerosol material, can be a function of particle size. When the density varies among particles in the same size range, ρ_p must be taken to be the average in the size range. Mass concentrations are often determined by filtering the gas at a known flow rate and weighing the filter before and after filtration under conditions of controlled humidity. Samples are also collected by filtration for chemical analysis.

Many different types of filters are available commercially. They can be broadly classified into two types with, however, some overlap. *Fibrous filters* are composed of mats of fibers that may be made of cellulose, quartz, glass, polymeric materials, or metals. *Porous membrane filters* are usually composed of thin films of polymeric materials 0.05 to 0.2 mm thick sufficiently porous for air to flow through under pressure. Pore size is controlled in the manufacturing process and ranges from 0.02 to 10 μm . A significant fraction of the particles may be caught on the upstream surface of the filter, but some particles may also penetrate and be caught inside the pores of the medium as well.

The use of the term "membrane" for these filters is somewhat misleading. Membranes are normally used to separate the components of a gas mixture which have different permeabilities through the membrane material. The permeabilities, in turn, can be related to the solubilities and diffusion coefficients in the membrane which differ for different gases. However, for a membrane filter, the gas passes through the pores of the film by a macroscopic flow process, driven by the pressure gradient. No gas separation takes place. The principal mechanisms of particle deposition for both fibrous and membrane filters are the diffusion and impaction of particles of finite diameter. Settling and electrostatic effects may contribute to removal.

Quartz fiber filters 8 in. \times 10 in. are used routinely to monitor compliance with the U.S. ambient air quality standard for particulate matter. The EPA requires filters with < 1% penetration of 0.3- μm dioctyl phthalate particles and low alkalinity, both provided by quartz and Teflon membrane filters (Appel, 1993; this reference cites publications on air sampling methodologies prescribed by EPA). Teflon membrane filters have a relatively high pressure

drop, especially as particles accumulate, and are normally used at lower gas flow rates. The weights of quartz, Teflon, and glass filters are less sensitive to changes in relative humidity than the more hygroscopic cellulose and cellulose ester filters. Filter efficiencies are often reported for 0.3- μm particles, because these fall in the size range corresponding to the minimum in the efficiency curve (Chapter 3). Hence particles of other sizes would, in general, be expected to be collected more efficiently.

TOTAL NUMBER CONCENTRATION: CONDENSATION PARTICLE COUNTER

Most of the particle analyzers measure properties averaged over large numbers of particles, but a few provide information on single particles. The condensation particle counter (CPC) is used to measure the total number concentration of particles in the size range from a few nanometers to 1 μm . The aerosol is introduced into the instrument where it is saturated with a vapor such as water or an alcohol. A supersaturated state is produced, and the vapor condenses on the particles to form droplets in the size range from 5 to 15 μm . The systems differ according to (a) the condensable vapor, (b) the method of producing supersaturation and (c) the detection scheme. The lower limit of particle size detection, generally between 3 and 10 nm, results from the enhanced vapor pressure above small particles (Kelvin effect, Chapter 9) and nonuniformities in concentrations of the condensable vapor.

In the Pollak counter (Fig. 6.3), the aerosol is introduced into a vertical tube about 60 cm long and 2 to 3 cm in diameter, lined with a wetted, porous ceramic material. The tube is sealed at the top and bottom by electrically heated glass plates. The tube is fitted with a light source at the top and with a detector, a photomultiplier tube, at the bottom. The tube is flushed several times with aerosol, usually room or atmospheric air, to replace the contents. A fixed quantity of filtered particle-free air is then introduced into the tube under pressure. A period of 50 sec is allowed for the air to become saturated and to equilibrate thermally. After reading the photo cell current, I_0 , to obtain a measure of the initial extinction, the exit valve is opened and the pressure released. The gas expands adiabatically, reaching a supersaturated state in a range below that at which homogeneous nucleation takes place. Condensation takes place on the particles that grow into the light-scattering range. The growth process takes place in a nearly uniform gas mixture, and the process is diffusion-limited. As a result, even if the original aerosol is polydisperse, the particles tend to grow into droplets, all of which are of about the same size (Chapter 10). The new photo cell current, I , is read, and the droplet concentration, which is equal to the original particle concentration, is obtained from the ratio $(I_0 - I)/I_0$.

The instrument can be calibrated by allowing the droplets to settle on a slide. The concentration is determined by counting the deposited droplets corresponding to each value of $(I_0 - I)/I_0$. Commercial instruments of this type are usually factory-calibrated by comparison with a counter built and operating according to the original specifications of Pollak and his coworkers (Pollak and Metnieks, 1957).

The expansion-type CPC is cyclic in operation, and this may pose a problem in measuring concentrations from steady flow devices such as the electrical mobility analyzer and diffusion battery discussed later. Continuous-flow CPCs have been developed in

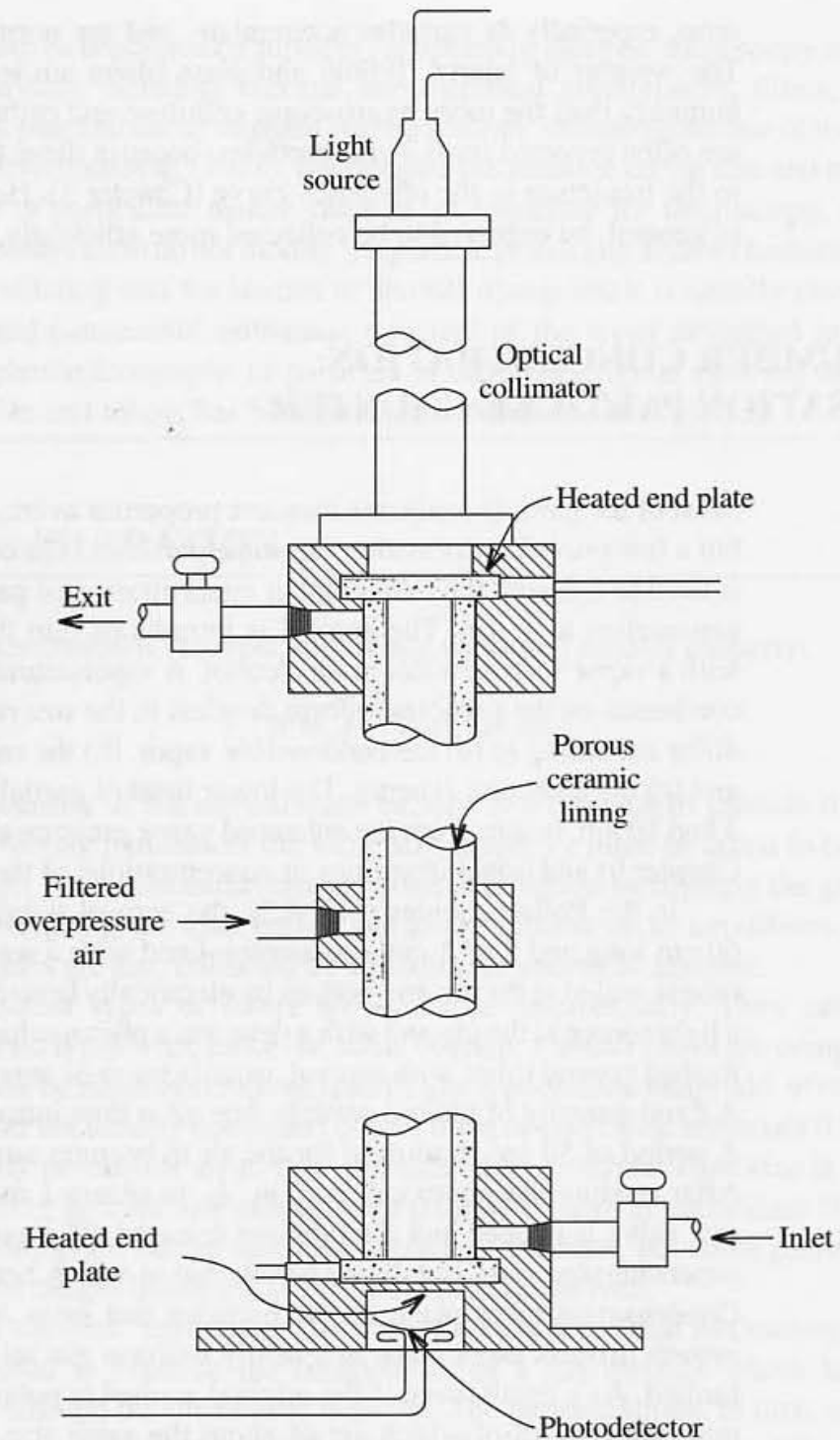


Figure 6.3 Schematic diagram of condensation particle counter.

which supersaturation is produced by conduction/convection cooling instead of adiabatic expansion (Cheng, 1993). This allows for steady-state operation. The aerosol is first saturated with a condensable vapor by passing it over a liquid reservoir, usually butanol, maintained at a suitable temperature, say 35°C. At a flow rate of 300 cc/min, the aerosol then passes to a condenser tube maintained at 10°C. The vapor concentration and saturation ratio are at a maximum at the center of the tube and decrease radially to the wall. The counting efficiency for particles smaller than about 10 nm decreases because smaller particles do

not nucleate in the regions of low supersaturation. After passing through the condenser, the droplet cloud passes to a photodetector that is operated as a single-particle counter for particle concentrations less than $10^3/\text{cc}$ and as a photometer at higher concentrations.

TOTAL LIGHT SCATTERING AND EXTINCTION COEFFICIENTS

A variety of instruments have been designed for the measurement of light extinction by clouds of small particles. *Transmissometers* are available commercially for stack installation and for use with other process gases containing relatively high concentrations of particles. The principle of the transmissometer is discussed in Chapter 5. The design and calibration of an in-stack instrument is described by Conner and Hodkinson (1967). Instruments have been designed for the measurement of atmospheric extinction usually over a long path (Middleton, 1952). When absorption by the particles can be neglected, the extinction results from scattering, and measurements of scattering can be used as a substitute for extinction. This assumption is probably acceptable for marine hazes and, perhaps, for photochemical aerosols such as those in Los Angeles where concentrations of absorbing particles are usually low. Aerosol absorption may be more important in regions where carbon and soot concentrations are relatively high.

A schematic diagram of a compact instrument designed for the measurement of the scattering coefficient of the atmospheric aerosol (Chapter 5) is shown in Fig. 6.4. This device is known as an *integrating nephelometer*, because it integrates the scattering over almost all angles along the axis of the detector to give the scattering coefficient.

Important features of the instrument include a light source whose radiation intensity follows a cosine law, together with a specially designed light collection system for defining the shape of the scattering volume. The measurement volume is small compared to the scale over which b_{sca} changes in the atmosphere. Hence the instrument gives a local light-scattering coefficient that, for a uniform atmosphere, is inversely related to the visibility

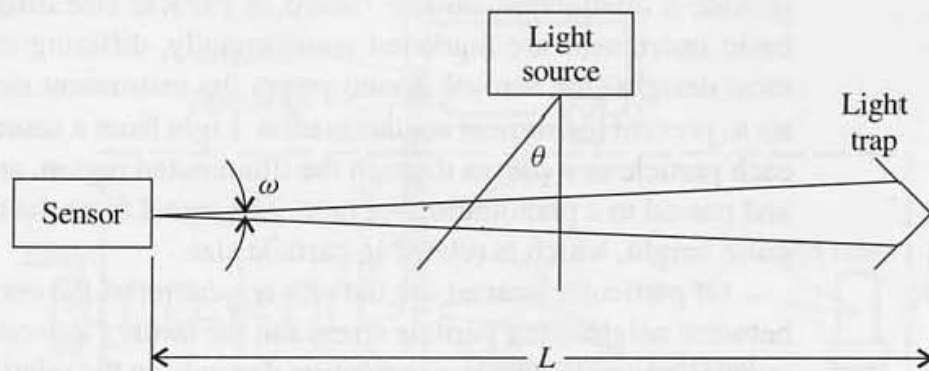


Figure 6.4 Principle of the integrating nephelometer. The sensor detects the light scattered by the particles present in the region defined by the solid angle ω . The light source has the special property that its intensity in any direction θ is given by $I_0 \cos \theta$. When the sensor and light trap are sufficiently far apart, it can be shown (Middleton, 1952) that for this special light source the sensor signal is proportional to the integral of the scattered light. By proper calibration, the quantity b_{sca} can be obtained. Commercial instruments are about 6 ft long and 7 in. in diameter.

or visual range (Chapter 5). The local value of b_{sca} measured in this way can be related to the properties of the aerosol, including the size distribution and chemical composition, also measured locally. The use of the integrating nephelometer in atmospheric measurements is discussed by Butcher and Charlson (1972).

SIZE DISTRIBUTION FUNCTION

Overview

The measurement of particle size distributions is a distinguishing feature of aerosol instrumentation. The particle size range of interest is so wide—from a few nanometers to tens of micrometers—that no single instrument is available that can cover the entire range. As a result, in characterizing polydisperse aerosols, it is usually necessary to use several instruments simultaneously. These instruments are based on different physical principles, and it is found that the match of the experimental results in the region of instrument overlap is often imperfect.

In this section, we briefly review three types of instruments, the optical particle counter, electrical aerosol classifier, and diffusion battery. These systems are based on very different physical characteristics of the aerosols. The optical counters respond to signals from individual particles. The electrical analyzers depend on the measurement of a current carried by a stream of charged aerosol particles. The diffusion battery also depends on the behavior of particle clouds. The system often used to cover the size range from about 10 nm to 10 μm is a combination of (a) the electrical analyzer up to about 0.2 μm and (b) the optical particle counter over the rest of the range.

Single-Particle Optical Counter

For particles larger than a few tenths of a micrometer, single-particle optical counters can provide a continuous, on-line record of particle size distributions. Many versions of the basic instrument are marketed commercially, differing chiefly in the optical system. In most designs, the aerosol stream enters the instrument surrounded by a sheath of filtered air to prevent instrument contamination. Light from a source of illumination is scattered by each particle as it passes through the illuminated region, and the scattered light is collected and passed to a photomultiplier tube. The signal from the tube is classified as a function of pulse height, which is related to particle size.

Of particular interest are the *size resolution* of the counter, or its ability to distinguish between neighboring particle sizes, and the *limit of detection*, or smallest size to which the counter responds. The size resolution depends on the relationship between pulse height and particle size, the *response curve*. For particles of given optical properties, this relationship is determined by the geometry of the illumination and light collection systems. Particle shape and refractive index also influence the relationship.

For air pollution monitoring, it would be desirable to have detectors whose response is a single-valued function of particle size (volume) and not of shape or refractive index, because these parameters may vary from particle to particle. Practical measurement systems fall far

short of this ideal. In some commercial instruments, local minima occur in the response curve, which means that the pulse height versus size relationship is not unique (Mercer, 1973). In other cases, the response is very sensitive to refractive index.

The characteristics of a modified commercial instrument with an ellipsoidal mirror light collector have been studied by Husar (1974); we describe this system as an example (Fig. 6.5). The light source is a filament lamp, and in the sensing volume, the light beam is 1.5 mm wide and 1 mm high. The sensing volume is located at one of the focal points of the ellipsoidal mirror collector. Light scattered from the sensing volume in the range between 35 and 100° is reflected by the mirror into the other focal point at which the photomultiplier tube is located.

Response curves calculated from Mie theory are compared with an experimentally measured curve for polystyrene latex particles in Fig. 6.6. For both calculated and measured curves, pulse height increases in a fairly smooth way with particle diameter. No local minima, local maxima, or size-independent ranges are present. For nonabsorbing spheres over the ranges of refractive index studied, the error in the indicated size is always less than 30% if the polystyrene latex calibration is used. The response curve for a counter with a laser light source is given in Chapter 5. Examples of other response functions are given by Gebhart (1993).

The limit of detection of an optical particle counter depends on instrument noise, Rayleigh scattering by the air molecules, and stray light resulting from imperfect optics. For commercial counters with an incandescent light source, the limit of resolution is about 0.3 μm . Instruments with laser light sources can go down to about 70 nm.

Difficulties are encountered in using optical counters with aerosols from mixed sources because the refractive index varies from particle to particle in an unknown way. The usual

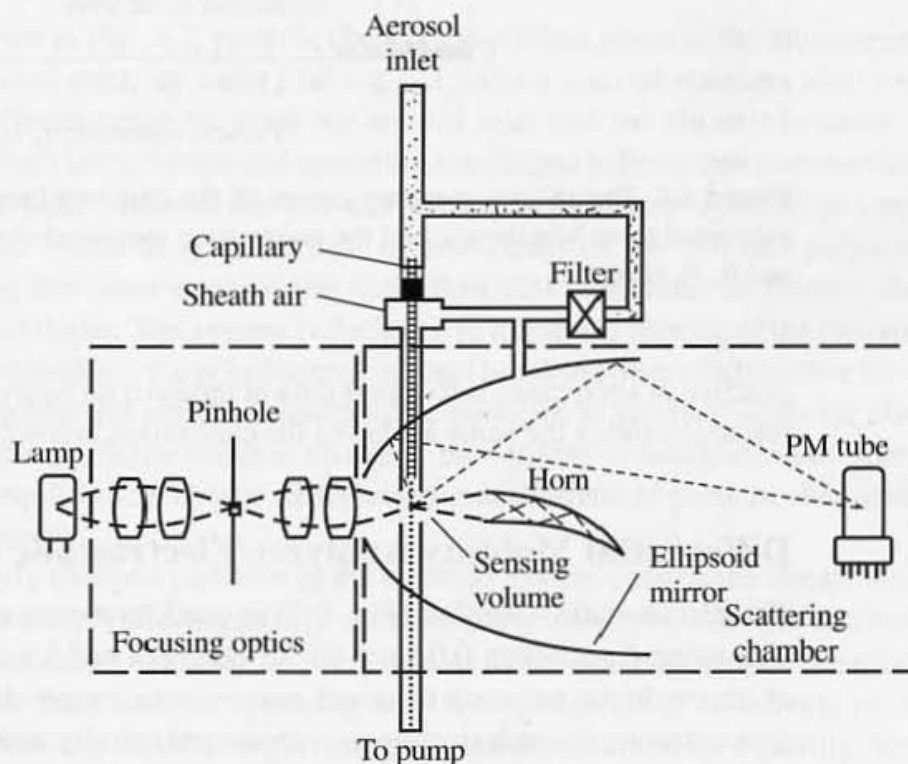


Figure 6.5 Schematic diagram of the ellipsoidal mirror optical counter (Husar, 1974).

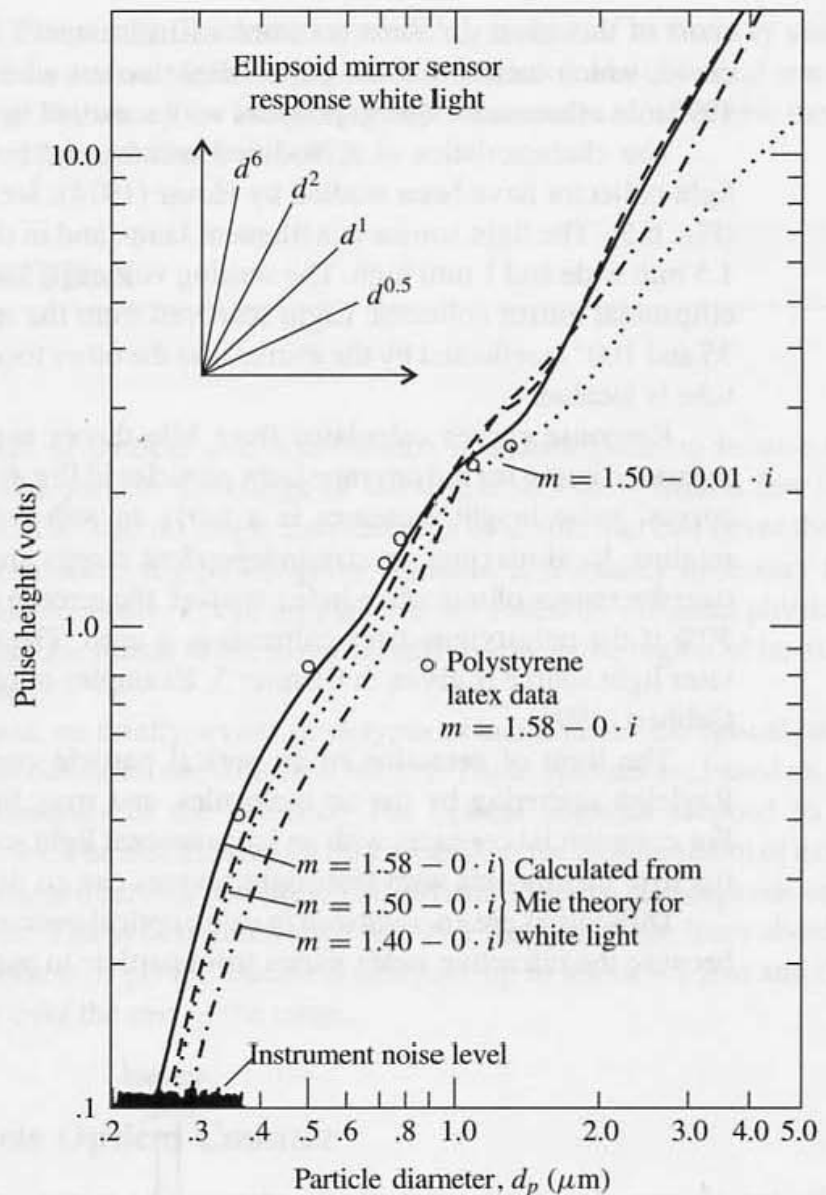


Figure 6.6 The relative response curves of the ellipsoidal mirror optical counter. The lines were calculated from Mie theory, and the points were measured experimentally. (Courtesy S. L. Heisle and R. B. Husar.)

practice in such cases is to report data in terms of an equivalent diameter for particles with a refractive index the same as that of the calibration aerosol—for example, polystyrene latex.

Differential Mobility Analyzer/Electrostatic Classifier

The electrostatic classifier (Fig. 6.7) is used to measure particle size distributions in the size range from about $0.01 \mu\text{m}$ to $0.5 \mu\text{m}$ (Pui and Liu, 1988). The classifier is operated at atmospheric pressure to select narrow size ranges from a polydisperse aerosol. The concentration in each size range is measured usually with a condensation particle counter, and in this way the particle size distribution can be determined.

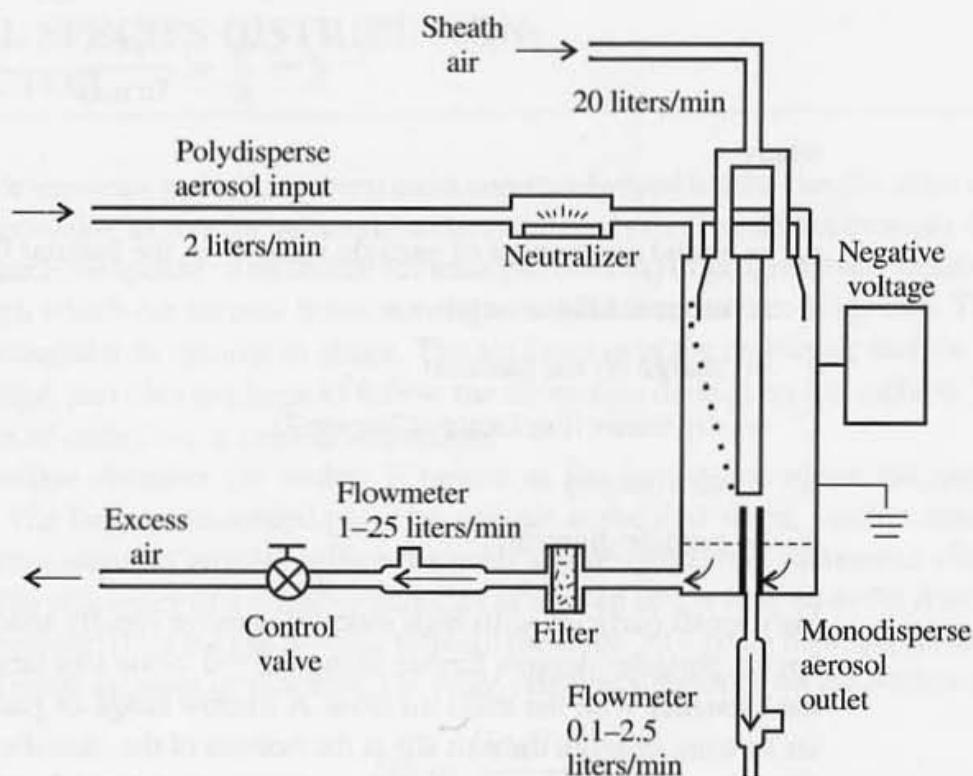


Figure 6.7 Electrostatic classifier. Devices of this type can be used to generate nearly monodisperse aerosols in the ultrafine range or to measure size distributions by suitably scanning the applied potential. The dotted line near the central rod is the trajectory of a particle that is withdrawn as product. (After Pui and Liu, 1988.)

As shown in Fig. 6.7, particle classification takes place in the annular region between a stainless steel outer cylinder (3.9-cm I.D.) and a coaxial stainless steel center rod (1.9-cm O.D.). The distance between the aerosol inlet and the slit exit is about 44 cm for the system shown. (Dimensions and operating conditions refer to one commercial instrument.) The electric field between the rod and the grounded outer cylinder is varied from 0 to about 11,000 V/cm. A small stream (2 liters/min) of the original polydisperse aerosol passes along the outer edge of the main flow (20 liters/min) of filtered sheath air, next to the outer cylinder. The system is designed to minimize mixing of the two streams. Before entering the classifier, the polydisperse aerosol is passed over a radioactive Kr-85 source that generates bipolar gas ions that attach to the particles to produce a bipolar charged aerosol. Not all of the particles become charged; the system is designed such that the particles acquire an equilibrium charge distribution independent of particle chemical composition and morphology.

Positively charged particles in the lamellar stream outside the sheath air move toward the negative rod, while negatively charged particles deposit on the surface of the outer cylinder. The radial velocity of the particles is determined by the balance between the electric force field and the opposing drag force, neglecting the effects of diffusion. The electrical mobility, Z , of a singly charged particle obtained by equating the electric field and drag forces is given by (Chapter 2)

$$Z = \frac{v_r}{E} = \frac{eC}{3\pi\mu d_p} \quad (6.5)$$

where

v_r = radial component of particle velocity in the annular flow region

E = electric field strength

e = charge on the electron

C = slip correction factor (Chapter 2)

μ = air viscosity

d_p = particle diameter

Very small particles with high mobilities move rapidly toward the center rod and deposit. Larger particles deposit further along the rod while still larger ones pass out the bottom of the classifier with the main air flow. A narrow range of particle sizes is removed with the air flowing through the exit slit at the bottom of the classifier. The particle concentration in this stream can be measured with a condensation particle counter.

To measure the distribution of particle mobilities, the applied potential between the rod and tube is systematically varied and the particle concentrations are measured. The size distribution of the inlet aerosol can be calculated from the distribution of particle mobilities using (6.5) and the Boltzmann distribution (Chapter 2) or an equivalent relationship.

Diffusion Battery

The diffusion battery consists of banks of tubes, channels, or screens through which a submicron aerosol passes at a constant flow rate. Particles deposit on the surface of the battery elements, and the decay in total number concentration along the flow path is measured, usually with a condensation particle counter. The equations of convective diffusion (Chapter 3) can be solved for the rate of deposition as a function of the particle diffusion coefficient. Because the diffusion coefficient is a monotonic function of particle size (Chapter 2), the measured and theoretical deposition curves can be compared to determine the size for a monodisperse aerosol.

For a polydisperse aerosol, the number of particles deposited up to any point in the system can be calculated from the theory for monodisperse aerosols and then integrating over the initial size distribution, which is the quantity sought. The experimental measurements made with the condensation nuclei counter gives the number concentration of the polydisperse aerosol as a function of the distance from the inlet to the diffusion battery. The recovery of the size distribution function from the measured decay in particle concentration can be accomplished in an approximate way. Various numerical schemes based on plausible approximations have been developed to accomplish the inversion (Cheng, 1993). The lower detection limit for the diffusion battery is 2 to 5 nm. Systems are not difficult to build for specific applications or can be purchased commercially.

**MASS AND CHEMICAL SPECIES DISTRIBUTION:
THE CASCADE IMPACTOR**

The cascade impactor is the instrument most commonly used for the classification of aerosol particles according to size for subsequent chemical analysis. The device consists of a series of stages, each composed of an orifice (or multiple orifices) of progressively decreasing gap size through which the aerosol flows normal to a collecting surface (Fig. 6.8). The orifice may be rectangular or circular in shape. The air flows over the collecting surface and on to the next stage; particles too large to follow the air motion deposit on the surface. The basic mechanism of collection is inertial impaction.

The orifice diameter (or width) is largest at the first stage, where the gas velocity is lowest. The largest suspended particles deposit at the first stage; smaller ones pass on to succeeding stages of smaller orifice diameter and progressively increasing efficiency of removal. The efficiency of a stage for particles of a given size is defined as the fraction of the particles removed from the gas flowing through the stage. At a given flow rate, in the absence of particle reentrainment or rebound, the stage efficiency depends on the Stokes number,

$$Stk = \frac{C\rho_p U d_p^2}{18\mu d} \tag{6.6}$$

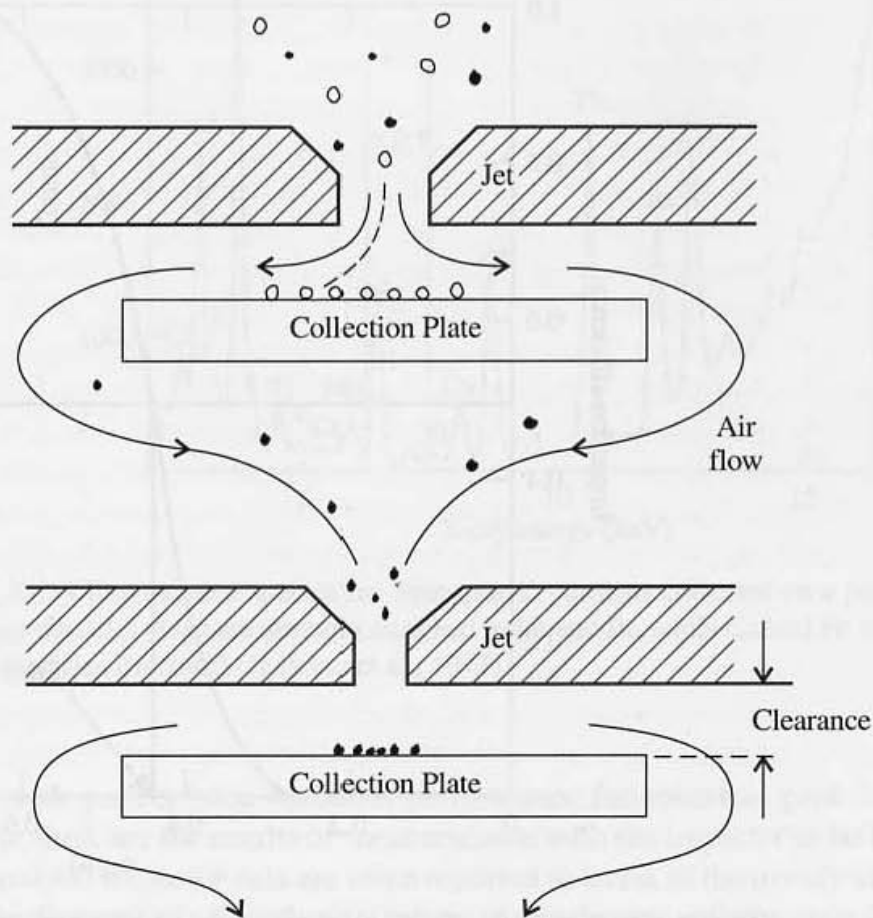


Figure 6.8 Schematic diagram showing two stages of a cascade impactor. The last stage of a multistage impactor is often followed by a filter.

where U is the average velocity through the jet, d is the jet width or diameter, and C is the slip correction factor (Chapter 2). Ideally, the efficiency curve should be a step function corresponding to a given Stokes parameter. All larger particles would be caught at the stage whereas all smaller particles would pass. In practice, the efficiency curve is S-shaped as shown in Fig. 6.9. A stage is usually characterized by the diameter corresponding to 50% efficiency:

$$d_p^* = \left[\frac{18\mu d \text{Stk}^*}{C\rho_p U} \right]^{1/2} \quad (6.7)$$

where the asterisk refers to the value at 50% efficiency. For round jets, $\text{Stk}^* \approx 0.2$ for values of the ratio of clearance (see Fig. 6.8) to diameter (Fig. 6.10) over the range between 1 and 10. For rectangular jets, $\text{Stk}^* \approx 0.66$ for clearance to jet width ratios of 1 to 5. Reynolds number similarity (Chapter 4) has not been investigated in detail. It is usually ignored, and this is supported by the data of Ranz and Wong (1952) over a limited range. It is good practice to calibrate each stage of an instrument, whether commercial or laboratory-constructed, using monodisperse aerosols.

In the case of a complex aerosol (such as atmospheric particulate matter) the size, shape, and density vary among particles that deposit on the same impactor stage. This is true even

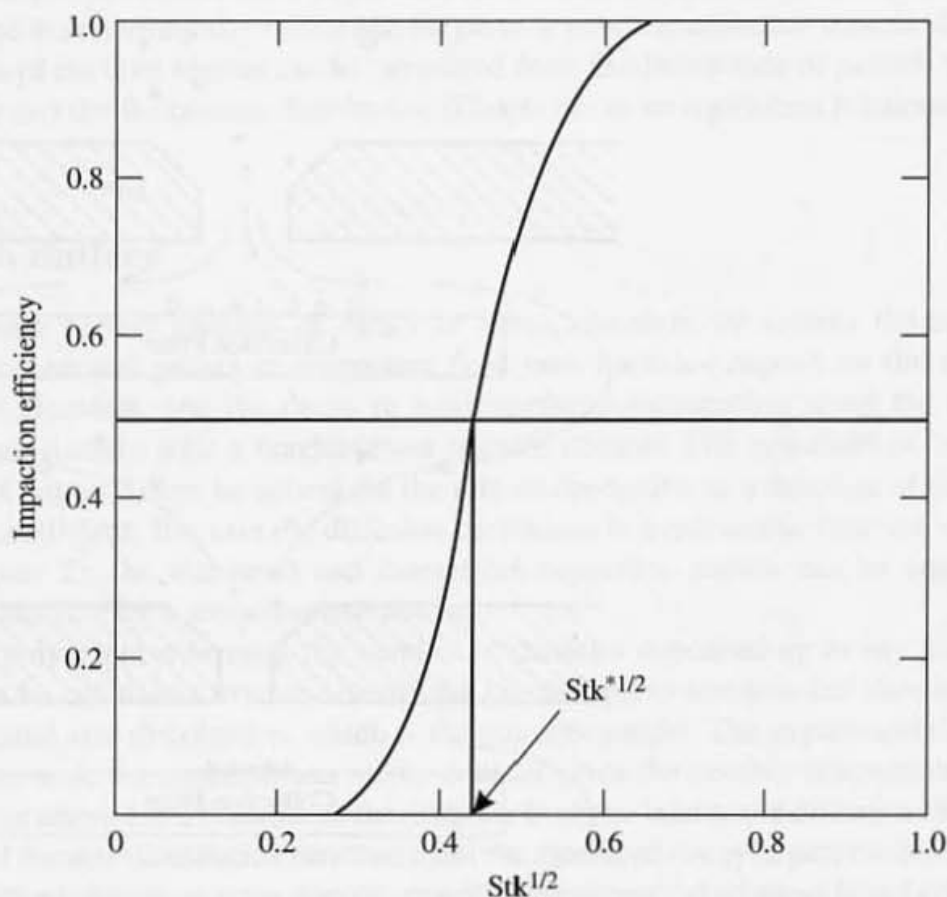


Figure 6.9 Schematic diagram of jet impactor efficiency showing Stk^* corresponding to 50% impaction efficiency. For round jets, the lower tail of the efficiency curve may not exist (Marple and Liu, 1974).

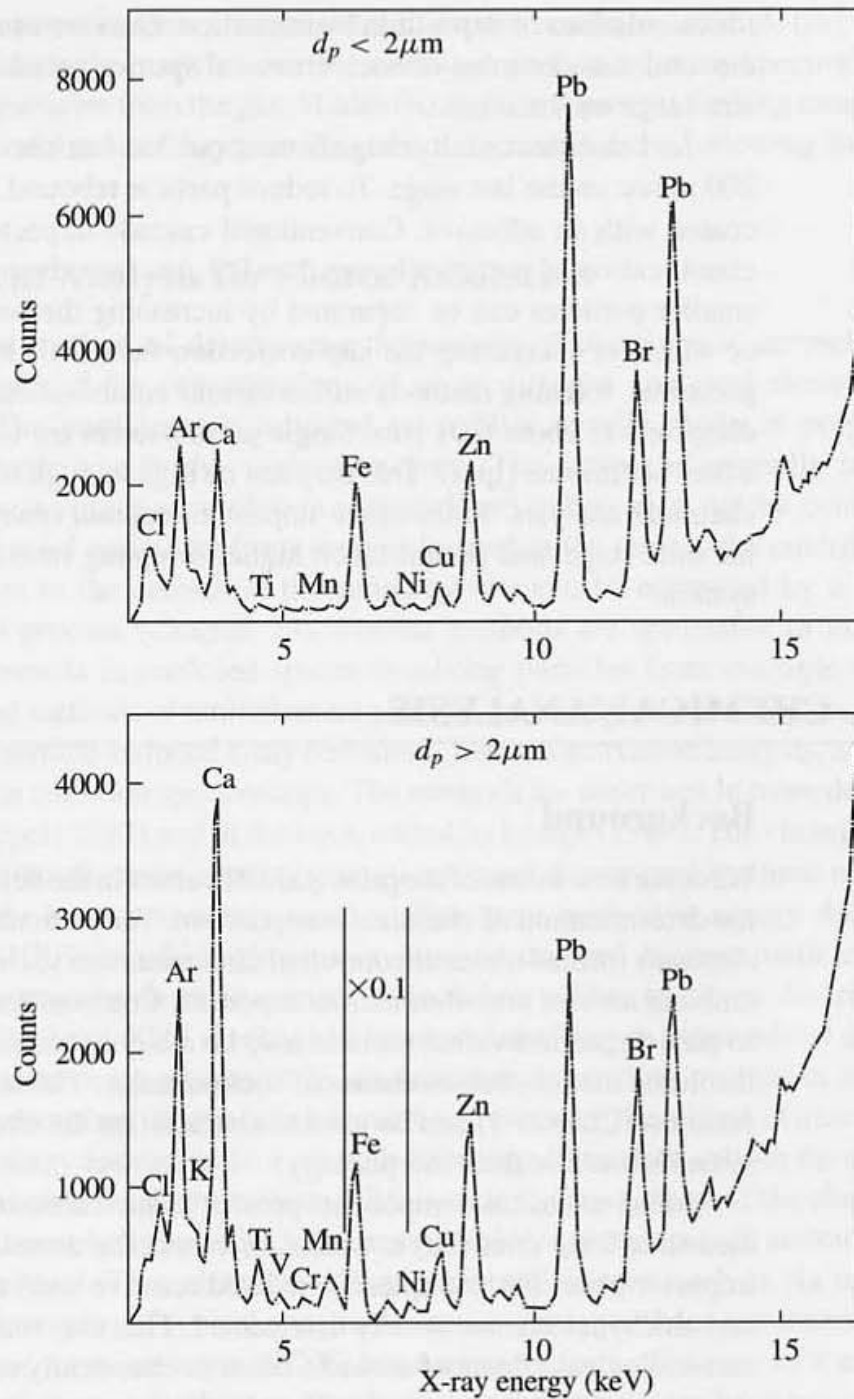


Figure 6.10 X-ray fluorescence spectra for atmospheric particles collected on a pair of membrane filters. The fine particles (**top**) are strongly enriched in Pb and Br, while Ca and Fe are found mostly in the coarse particles (**bottom**) (Jaklevic et al., 1977).

for a stage with perfect (step function) performance for spherical particles of constant density. How, then, are the results of measurements with the impactor to be interpreted for complex aerosols? Impactor data are often reported in terms of the *aerodynamic diameter*, defined as the diameter of a hypothetical sphere of unit density with the same Stokes number (or settling velocity) as the particle in question. Particles of different size, shape, and density may have the same aerodynamic diameter. The aerodynamic diameter is particularly useful

for calculations of deposition by impaction. Data are usually shown in histogram form with the total mass or mass of each chemical species on each stage plotted against the particle size range on the stage.

Jet velocities usually range from about 3 to 4 m/sec on the first stage to between 100 and 200 m/sec on the last stage. To reduce particle rebound, the collection surfaces are usually coated with an adhesive. Conventional cascade impactors are usually satisfactory for the classification of particles larger than $0.3 \mu\text{m}$ (aerodynamic diameter). According to (6.7), smaller particles can be separated by increasing the velocity, decreasing orifice diameter or width, or increasing the slip correction factor, C , by operating the impactor at lower pressures. Existing methods utilize various combinations of these methods to reduce cutoff diameters to about $0.01 \mu\text{m}$. Single jet impactors are usually designed to operate at about a liter per minute (lpm). This may not be high enough to accumulate sufficient material for chemical analysis. Multiorifice impactors contain many jets at each stage, up to 2000 at the final stage, and permit much higher sampling rates, about 30 lpm for one commercial system.

AEROSOL CHEMICAL ANALYSIS

Background

We come now to one of the principal difficulties in the field of aerosol measurements, namely, the determination of chemical composition. The difficulties stem from a number of factors. Aerosols formed under uncontrolled circumstances such as many industrial emissions or the ambient aerosol are often multicomponent. Compositions differ significantly from particle to particle; an individual particle may be a highly concentrated solution droplet containing insoluble matter such as chains of soot particles. The size composition probability density function (Chapter 1) can be used to characterize the chemicals and size properties of such systems (but not their morphology).

Many chemical components present in such aerosols are relatively stable; they can be measured long after (days, weeks, or more) the aerosol has been collected on a filter or impactor plate, for example. Short-lived reactive and/or volatile species such as peroxides and aldehydes are not usually determined. This may make it difficult to evaluate the health and ecological effects of aerosols because chemically reactive chemical species tend to be the most active biochemically. The chemical components present in the particles collected on a filter or impactor plate may react with each other when they are in close proximity. Particle deposits in filters or on surfaces may also react with molecular components of the gases flowing over them. Chemical reactions between the gas and aerosol may not affect measurements of metallic elements but may modify chemical speciation (compound form) on the collector surface. All of these factors must be taken into account in selecting sampling and measurement methods for aerosol chemical properties.

Aerosol chemical analysis can be conducted in several different modes including (but not limited to) the following: (i) Single particles deposited on a suitable substrate can be analyzed by microanalytical techniques (Hopke, 1985; Spurny, 1986; Fletcher and Small, 1993). (ii) Multielement analysis is used routinely to measure the composition of macroscopic quantities of particulate matter collected on a filter or impactor stage. Between

10 and 30 or more elements are measured in source resolution studies. (iii) The chemical composition of single particles can be measured on line by mass spectrometry without removing the particles from the gas. Modes (ii) and (iii) represent limiting cases with respect to the type of information they provide and are discussed in the following subsections.

Multielement Analysis for Source Resolution

A widely used method of determining the sources of atmospheric aerosols depends on the measurement of the concentrations of many different chemical elements present in the aerosol. The particles are collected on a filter usually made of polycarbonate or polytetrafluoroethylene in the nucleopore form. The sample is normally taken at a site far from a single strong air pollution source. From information on the concentrations of elements in aerosol emissions from sources located in the region, the contributions of the various sources to the aerosol at the sampling site can be estimated by a mathematical deconvolution process (Chapter 13). Similar methods are applicable to indoor aerosols or to other aerosols in enclosed spaces involving particles from multiple sources. Four frequently used methods of multielement analysis are briefly discussed in this section: x-ray fluorescence, particle-induced x-ray emissions, neutron activation analysis, and inductively coupled plasma emission spectroscopy. The methods are described in more detail by Hopke (1985) and Appel (1993) and in the book edited by Lodge (1989). The chemical compound form in which the elements appear (speciation) is not determined by these methods.

Perhaps the most commonly used multielement method is energy dispersive x-ray fluorescence (XRF) in which photons (x rays) or charged nuclear particles are used to induce x-ray emissions from an aerosol collected on a filter of a type described earlier in this chapter. The basic XRF mechanism involves knocking an inner orbital electron out of the atom by an incoming photon or by nuclear particles such as protons or alpha rays. An outer-shell electron then fills the inner electron vacancy with the release of the excess binding energy. This energy appears as an x ray with an energy dependent only on the energies of the two orbitals involved in the transition. XRF is used to detect many of the chemical species of interest in atmospheric particles but is not suitable for elements with atomic numbers less than 12 (aluminum). Thus elements of environmental interest such as Na and Mg cannot be detected. Examples of typical spectra for atmospheric particles are shown in Fig. 6.10. Particle-induced x-ray emission (PIXE) has a more uniform efficiency of x-ray production as a function of atomic number, so a wide range of elements can be measured in a single bombardment. PIXE has a relatively high sensitivity but requires a proton accelerator.

In instrument neutron activation analysis (INAA) a small fraction of the stable atomic nuclei present in the sample are made radioactive by irradiation with neutrons or other particles. By measuring the resulting radioactivity, the original elements present can be determined. Reactor or thermal neutrons are usually used. The method does not work well for certain key elements of environmental interest including silicon, sulfur, and lead. Table 6.2 shows INAA detection limits for various elements and typical concentrations of these elements in urban air. In atmospheric samples, the limit of detectability for a particular element depends on the quantities of the other elements in the filter matrix. The table is based on a total air sample of 17 m³ actually used in the measurements. The tabulated results show that all elements listed could be detected in this air volume with the exception

TABLE 6.2
Detection Limit for Neutron Activation Analysis Compared
with Ambient Air Concentrations (Olmez, 1989)

Element	Minimum Detection Limits (ng)	Typical Urban Concentration (ng/m ³)	Element	Minimum Detection Limits (ng)	Typical Urban Concentration (ng/m ³)
Na	70	400	Cu	850	25
Mg	9000	650	Zn	85	360
Al	700	1700	Ga	14	3
S	1.7×10^5	7200	As	5	15
Cl	140	180	Se	2	6
K	700	600	Br	10	200
Ca	2700	1600	Sr	140	9
Sc	0.03	0.5	Ag	3	0.3
Ti	1900	100	Cd	100	4
V	17	100	In	0.2	0.1
Cr	5	30	Sb	2	20
Mn	3	50	I	35	10
Fe	100	1600	Cs	0.9	0.2
Co	0.5	1.4	Ba	170	30

of S, Ti, Cu, Sr, and Cd. A serious disadvantage of INAA is the need for access to a nuclear reactor and other specialized equipment and technical personnel.

The inductively coupled plasma (ICP) method utilizes emission spectroscopy for the simultaneous analysis of a large number of elements. The argon plasma is generated inside an induction coil energized by a high-frequency alternating current. The aerosol sample is first digested in concentrated nitric acid and then diluted and sprayed into the plasma. Highly excited atoms of the aerosol material produce the emission spectrum. ICP response is linear in the component concentrations over several orders of magnitude. The method is inherently destructive of the sample in contrast with XRF and INAA. The detection limit, however, may not be sufficient for certain elements of importance in source resolution.

In addition to multielement analysis, source resolution requires data on various carbon containing components and sulfate, nitrate, and ammonium ions. The total carbon and classes of organic compounds can be measured by thermogravimetric techniques in which carbon-containing compounds are oxidized to CO₂ at different temperatures (Grosjean et al., 1994). The compounds coming off at each temperature are related to their volatility, which tends to correspond to their molecular weights. A wide variety of methods are used to measure individual organic chemical components. For example, high-pressure liquid chromatography in combination with UV fluorescence is used to measure polycyclic aromatic hydrocarbons. Inorganic water-soluble ions—especially sulfate, nitrate, and ammonia—are usually measured by ion chromatography.

Most of the chemical species analyzed in studies of collected aerosol particles are relatively stable; they are usually measured long after (days, weeks, or more) the aerosol has been collected. Hence short-lived and/or volatile species such as peroxides and aldehydes are generally not reported. This poses a problem in evaluating the health and ecological effects of aerosols because the short-lived, reactive chemical species are likely to be the most active biochemically.

Single-Particle Chemical Analysis by Mass Spectrometry

While the application of analytical techniques to collected aerosol material is relatively advanced, on-line methods for the measurement of aerosol chemical properties represent a serious gap in existing aerosol instrumentation. In this context, on-line refers to the ability to measure chemical constituents while the particles are airborne without depositing them on a surface before chemical analysis. The two systems that have been investigated in most detail in this regard are particle analysis by mass spectrometry (PAMS), an inherently destructive technique, and Raman scattering (Chapter 5), which may be destructive or nondestructive. The PAMS technique is further along in its development. There are two different measurement modes. The first is an integral mode in which the ion signals from individual particles accumulate to produce a DC signal related to the total mass concentration of the chemical component in the air. Most of the studies with PAMS, however, have involved the analysis of single particles larger than a few tenths of a micron in diameter.

PAMS systems have three main components: (1) a specially designed interface or inlet through which the aerosol is transferred from the exterior gas into (2) the ion source region of the mass spectrometer where the particles are volatilized and ionized and (3) the mass analyzer in which the ions are separated according to mass and the ion currents for different masses are measured. Several alternatives are available for each of these components. Much current research in this field is directed toward selecting components for optimal performance. A schematic diagram of the system is shown in Fig. 6.11. The earliest instrument to incorporate these elements used a quadrupole mass spectrometer and a heated rhenium filament for ionization (Sinha et al., 1982); more recent systems have used time-of-flight mass spectrometry and laser volatilization and ionization (Prather et al., 1994; Weiss et al., 1997).

The interface between the exterior aerosol and the ion source is usually a specially designed and calibrated aerosol beam (Chapter 4) with an associated skimmer arrangement. In the aerosol beam generator, the gas is expanded through a nozzle to near sonic velocity. Because the particles have high inertia compared with the gas, they cannot follow the gas motion and, instead, attain a velocity that depends on their diameter. Using particles of known diameter, the dependence of particle velocity on diameter can be determined. By measuring the time of transit of the particles between two HeNe laser beams, the particle velocity, hence its diameter, can be determined (Sinha, 1984). The particles can then be volatilized and ionized by a high-energy (for example, excimer) laser beam triggered by the HeNe laser. The burst of ions produced from each particle is characteristic of the amount and type of material composing the particles.

As a result of the complex aerodynamics of the particle beam and associated skimmers, the size distribution of the particles that reach the ion source differs significantly from that in the gas samples from outside the system. To relate the measured chemical compositions to the outside aerosol, it is necessary to correct for this effect. This can be accomplished in principle by determining the efficiency of transmission of particles from the exterior into the chamber. It is also possible to use data for particle size distributions measured outside the spectrometer to characterize the external aerosol. Because the particle size distribution measured with an optical particle counter does not correspond to the aerodynamic diameter, there will be some difficulties of interpretation.

Spectra for two different particles in the air of a laboratory in the Netherlands are

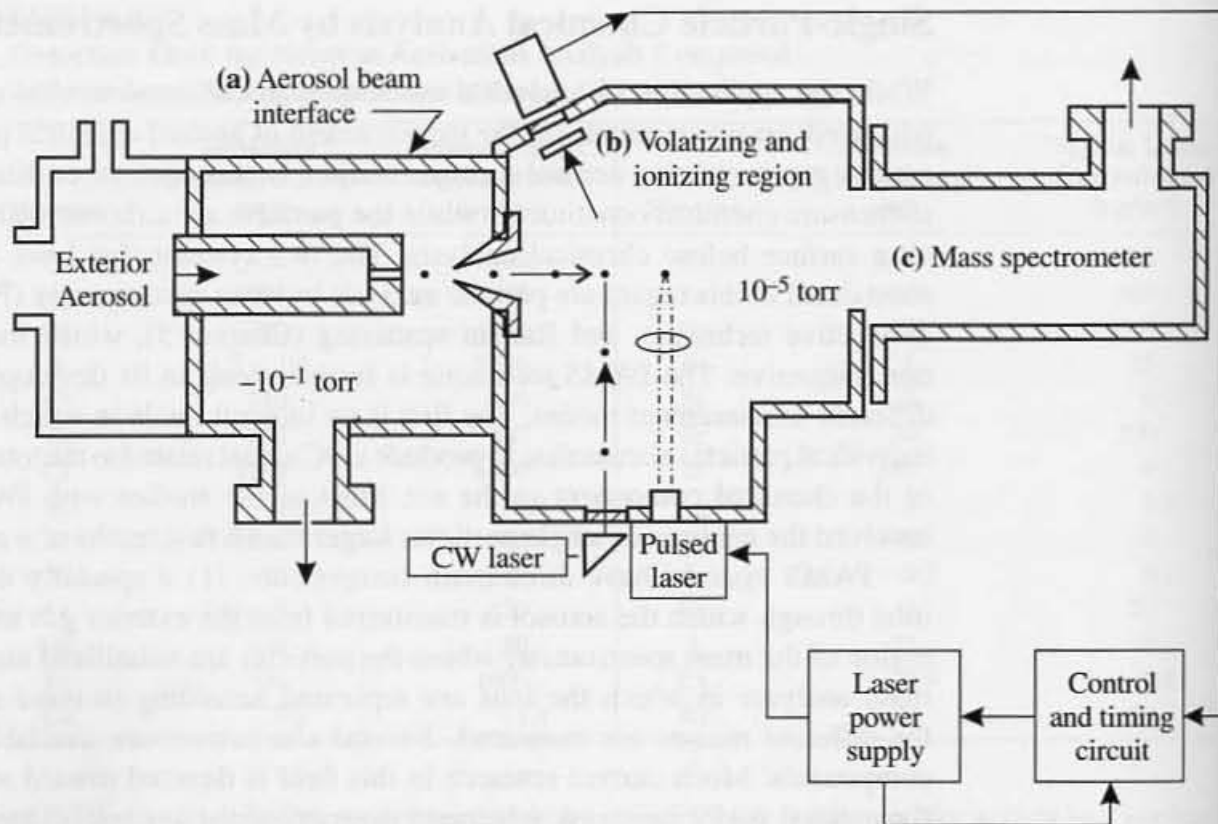


Figure 6.11 Schematic diagram of the system components for particle analysis by mass spectrometry. (a) Interface with external aerosol. Particles are introduced from the exterior through an aerosol beam with associated skimmers into (b) volatilizing and ionizing region. The arrival of each particle at the detector location is sensed by a laser that energizes a more powerful laser which focuses on the incoming particle to generate ions that pass to the (c) mass spectrometer, which may be of various types including quadrupole or time-of-flight. (From Sinha et al. 1983.)

shown in Fig. 6.12. The upper spectrum is the one most commonly observed and shows high sodium and potassium peaks. These indicate a marine aerosol origin probably from air over the North Sea about 20 km to the west. The lower spectrum shows low sodium and potassium and high calcium compound peaks. This particle probably comes from building materials such as plaster and concrete. The PAMS Technique has also been applied to the analysis of bacterial cells (Sinha et al., 1985). Remarkably similar spectra were observed for three different types of bacteria but with significant differences in the relative intensities for certain peaks.

SUMMARY CLASSIFICATION OF MEASUREMENT INSTRUMENTS

Aerosol measurement instruments can be conveniently classified according to the type and quantity of information they provide about aerosol properties. The physical principles on which the instruments are based are of secondary importance in this classification scheme, and indeed the instruments can be considered "black boxes." This approach makes it possible

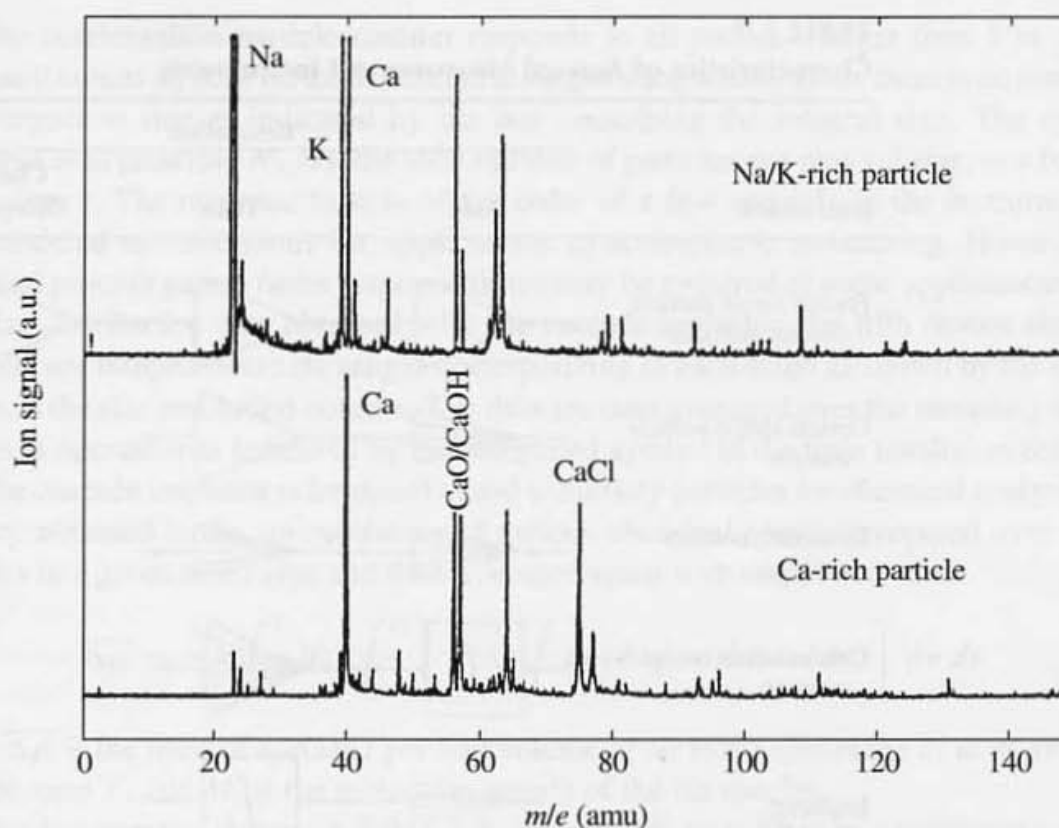


Figure 6.12 Mass spectra for two particles measured using time-of-flight mass spectrometry in a laboratory at the Technical University of Delft in The Netherlands (Weiss et al., 1997). The top spectrum probably comes from a particle of marine origin and the bottom from a local source with construction material components.

to see how far measurement technology has advanced and indicates gaps in instrumentation and likely future developments.

In Table 6.3, instruments discussed in previous sections are classified in terms of their performance characteristics. The second column shows whether the instrument classifies the particles according to size and also how fine the size resolution is. The third column shows the time response behavior of the system—that is, whether the instrument responds to single particles or to short- or long-term time averages. The fourth column indicates whether single particles are analyzed chemically or the average composition of collections of particles is determined.

The first device listed, the “single-particle counteranalyzer” (SPCA), chemically sizes and analyzes each particle, thereby permitting the determination of g . The SPCA, operating perfectly, would classify the particles according to size, identifying each class separately with no “lumping” of classes. This perfect classification is represented by the open sector shown in the size column. As an example, a single class is shown passing to the time resolution column; because the counter responds to the individual particles, the time resolution is also perfect as indicated by the open sector in the time column. Complete chemical analysis of a single-time class is indicated by the open sector in the chemical composition column.

The PAMS system provides some of the information necessary for the evaluation of g , but current instruments have significant limitations. Most require that the particles be larger

TABLE 6.3
Characteristics of Aerosol Measurement Instruments

Instrument	Resolution			Quantity Measured (Integrand $\times N_{\infty}^{-1}$)
	Size	Time	Chemical Composition	
Perfect single particle counter analyzer				g
Optical single particle counter				$\int_{V_1}^{V_2} \int g \, dn_i \, dv$
Electrical mobility analyzer				$\int_{V_1}^{V_2} \int g \, dn_i \, dv$
Condensation nuclei counter				$\int g \, dv \, dn_i = 1$
Impactor				$\int_{V_1}^{V_2} \int g \, dn_i \, dv$
Impactor chemical analyzer				$\int_{V_1}^{V_2} \int g n_j \, dn_i \, dv$
Whole sample chemical analyzer				$\int \int g n_i a n_i \, dn_j \, dv$

Key:

Resolution at single particle level

Discretizing process

Averaging process

than a few tenths of a micron in diameter to furnish enough mass for measurement. Particles may be too refractory for volatilization. In other cases, volatilization and ionization may change the chemical speciation of the aerosol components.

The other devices listed in the table measure certain integral functions of g as shown in the last column. The first few devices have a relatively fast time response. However, the single-particle optical counter lumps the data over small but discrete size ranges. This lumping of size classes is represented by the striated pattern shown in the size sector. Optical counters currently available are limited to particles larger than about a tenth of a micrometer in diameter. Hence the size resolution covers a limited range as shown by the reduced sector in the table. Because the counter responds to single particles, the time resolution can be considered perfect as indicated by the open sector. The striated pattern in the time resolution column for the mobility analyzer shows that particle counts are integrated over an interval of minutes.

The condensation particle counter responds to all particles larger than 5 to 10 nm. Because it counts all such particles without distinguishing among them, there is no resolution with respect to size as indicated by the box containing the integral sign. The quantity measured is in principle $N_{\infty}(t)$, the total number of particles per unit volume, as a function of the time t . The response time is of the order of a few seconds so the instrument can be considered as continuous for applications to atmospheric monitoring. However, for industrial process gases, faster response times may be required in some applications.

Size distribution data obtained with the cascade impactor, the fifth device shown in the table, are lumped over size ranges corresponding to each stage as shown by the striated pattern in the size resolution column. The data are then averaged over the sampling volume or time of operation as indicated by the integrated symbol in the time resolution column.

The cascade impactor is frequently used to classify particles for chemical analysis. The quantity obtained is the concentration of various chemical species averaged over all the particles in a given size range and then averaged again with respect to time:

$$\overline{\Delta\rho_i} = \frac{M_i}{T} \int_0^T N_{\infty} \int_{v_1}^{v_2} \left[\int \dots \int g n_1 dn_2 \dots dn_i \dots dn_k \right] dv dt \quad (6.8)$$

where $\overline{\Delta\rho_i}$ is the mass of species i per unit volume of air in the size range v_1 to v_2 averaged over the time T , and M_i is the molecular weight of the i th species.

The last system shown in Table 6.3 corresponds to a filter in combination with a method of chemical analysis such as x-ray fluorescence. It provides data on the chemical composition of the entire aerosol. The particles are collected on a filter usually over a period of hours. Concentrations measured by whole sample chemical analysis can be represented by the following expression:

$$\bar{\rho}_i = \frac{M_i}{T} \int_0^T N_{\infty} \int \left[\int \dots \int g n_1 dn_2 \dots dn_i \dots dn_k \right] dv dt \quad (6.9)$$

where $\bar{\rho}_i$ is the mass of species i per unit volume of air averaged over the time T .

MONODISPERSE AEROSOL GENERATORS

Monodisperse aerosols are almost always used to calibrate the instruments described previously. They are also important for performance studies of gas-cleaning devices and in investigations of fundamental aerosol behavior such as light scattering. Aerosols composed of uniform particles can be produced by condensation processes or by atomization of liquids.

Condensation Generators

By seeding a condensable vapor with nuclei and then allowing condensation to take place under carefully controlled conditions, aerosols of nearly uniform size can be produced. The method is of great practical importance in producing test aerosols from a variety of liquids and from solid materials, such as salts, as well.

A schematic diagram of an apparatus of this type is shown in Fig. 6.13. The substance from which the aerosol is to be made, generally a high-boiling material such as dioctyl phthalate or oleic or stearic acids, is atomized and then evaporated in an electrically heated glass tube. There is usually a sufficient amount of nonvolatile impurities present in the atomized liquid to leave tiny residual particles that can serve as condensation nuclei. Because one condensation nucleus is formed from each droplet and the atomizer can be operated in a stable manner, the generator provides a steady source of nuclei and condensable vapor.

After passing through the evaporation section, condensation takes place on the residual nuclei, forming an aerosol. Even though the residual nuclei vary in size, they grow by diffusion to a final diameter nearly independent of the original size of the nucleus. The theory is discussed in Chapter 10 in the section on growth laws. The most uniform portion of the aerosol is the part flowing near the center of the tube where the temperature profile is flat. Compared with the flow near the wall, the velocity profile and hence residence time vary little with radius near the center. It is this portion of the stream that is sampled to provide an approximately monodisperse aerosol. By controlled dilution of the original material with alcohol, aerosols can be generated with diameters ranging from about 0.036 to 1.1 μm . The larger particles are more uniform than the smaller, with the geometric standard deviation increasing from 1.22 at 0.6 μm to 1.50 at 0.036 μm . Other condensation aerosol generators have been developed, and these are reviewed by Mercer (1973). Aerosol flow rates in the range 0.1 to 1 liter/min and concentrations in the range 10^4 to 10^7 particles/cm³ can be generated in this way.

Atomizing Generators

Monodisperse, spherical polystyrene latex particles in aqueous suspension are available commercially in sizes ranging from 0.088 to about 2 μm . Relative standard deviations in particle size are usually less than 10% and sometimes less than 1%. The suspensions are manufactured industrially by emulsion polymerization. Monodisperse polyvinyltoluene particles of somewhat larger diameter, up to 3.5 μm , are also available. The properties of these systems are reviewed by Mercer (1973).

Aerosols can be generated by nebulizing a suspension of these particles and mixing the droplet suspension with dry air to evaporate the solvent. Small quantities of dissolved substances, including stabilizing agents to prevent coagulation of the particles, are present in the suspension. These also appear in the aerosol after drying either coated on the latex sphere or as a very small particle when the original droplet contained no latex. Such aerosols are, therefore, composed of two types of particles: an (almost) monodisperse latex component and a secondary aerosol of much smaller particles, the dissolved solids originally present in the suspension. The secondary aerosol may cause problems in certain types of applications.

Several ingenious methods have been devised for the production of monodisperse aerosols, based on the breakup of suspensions, solutions, or pure liquids under carefully controlled conditions. In the case of the *spinning disk generator*, a liquid is fed continuously on to the center of a rotating disk, and a spray of droplets is formed. Uniform droplets result if the liquid wets the disk surface, and the flow is controlled between certain limits. Actually

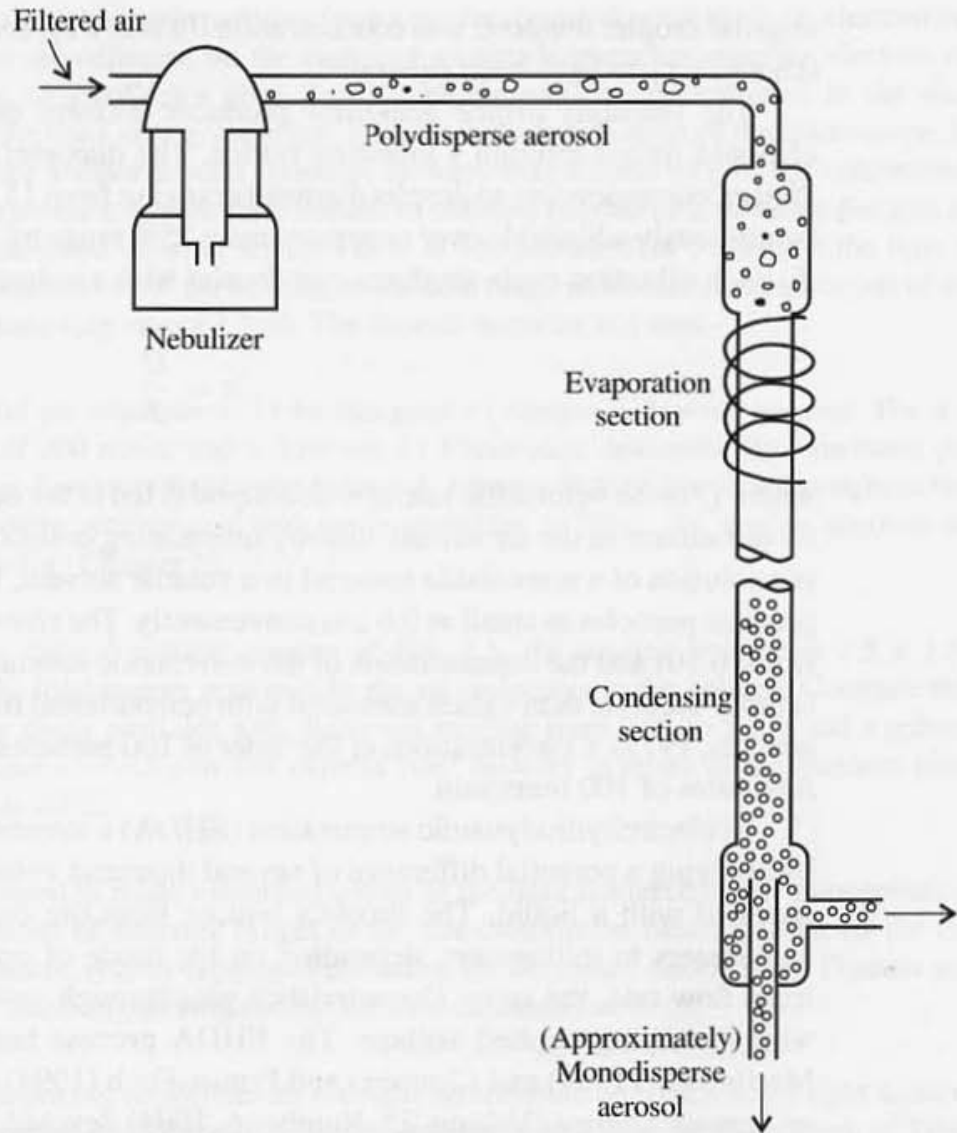


Figure 6.13 Condensation aerosol generator. The number concentrations of the polydisperse aerosol produced in the nebulizer are nearly equal to that of the monodisperse aerosol. Each evaporating droplet from the polydisperse aerosol leaves behind a residue that serves as a nucleus for the monodisperse aerosol. (After Liu et al., 1966.)

two sizes of droplets are produced. Most of the liquid goes into a set of larger droplets projected to a greater distance than the accompanying satellite droplets. The diameter of the satellite droplets is about one-fourth that of the primary droplets, and there are about four satellite droplets for each of the primary. Less than 10% of the liquid appears in the satellites for liquid flow rates below about $1 \text{ cm}^3/\text{min}$. This proportion increases with increasing liquid flow rates.

Separate large- and small-drop aerosols can be produced by taking advantage of the different stop distances of the primary and satellite droplets. Aerosols of the original pure liquids can be produced in this way with primary droplet diameters ranging from 6 to $3000 \mu\text{m}$ and liquid flow rates up to $168 \text{ cm}^3/\text{min}$. When solutions with volatile solvents are used, the solvents can be evaporated, leaving behind particles whose size depends on the

original droplet diameter and concentration. In this way, aerosols in the size range between 0.6 and 10 μm have been generated.

The *vibrating orifice generator* produces uniform droplets by the breakup of a jet of liquid forced through a vibrating orifice. The diameter of the orifice ranges from 5 to 20 μm , corresponding to droplet diameters ranging from 15 to 40 μm . Droplet diameters are continuously adjustable over an approximate 25% range by varying the vibration frequency, f . Each vibration cycle produces one droplet with a volume given by

$$v = \frac{Q}{f} \quad (6.10)$$

where Q is the volumetric rate at which liquid is fed to the orifice. The droplets are dispersed by turbulence in the air stream, thereby minimizing collision and coalescence. If the liquid is a solution of a nonvolatile material in a volatile solvent, the solvent can be evaporated to produce particles as small as 0.6 μm conveniently. The size of the particles can be calculated from (6.10) and the concentration of the nonvolatile substance. The calculated particle size is more accurate than values measured with conventional microscope techniques (Berglund and Liu, 1973). Concentrations of the order of 100 particles/ cm^3 can be produced at aerosol flow rates of 100 liters/min.

In electrohydrodynamic atomization (EHDA) a stream of charged droplets is produced by applying a potential difference of several thousand volts between a plate and a capillary supplied with a liquid. The droplets issuing from the capillary may range in size from nanometers to millimeters, depending on the mode of operation. For a given liquid at a fixed flow rate, the spray characteristics pass through several different behavioral modes with increasing applied voltage. The EHDA process has been reviewed by Grace and Marijnissen (1994) and Cloupeau and Prunet-Foch (1994) in a special issue of the *Journal of Aerosol Science* (Volume 25, Number 6, 1994) devoted to the subject.

The cone-jet mode has been the most systematically studied. In this mode, the meniscus at the capillary exit assumes the form of a cone from whose apex a liquid jet is emitted. This filament breaks up and generates an aerosol (electrospray) of droplets that may be monodisperse with a diameter comparable to that of the jet with a charge near the maximum value of the Rayleigh limit; many uncertainties remain concerning the specific operating conditions and liquid properties best suited to generate a monodisperse aerosol with a given diameter. Rosell-Llompart and de la Mora (1994) discuss the use of scaling laws based on the equations of fluid motion to correlate the experimental data.

PROBLEMS

6.1 It is proposed to filter a gas stream to obtain an aerosol sample for chemical analysis. A standard 30-mm (diameter) commercial filter is to be used, rated at 0.02% penetration for 0.3- μm particles at a face velocity of 53 cm/sec. If the velocity of the gas stream from which the sample is taken is 6 m/sec, what should be the diameter of the sampling probe for isokinetic sampling? What will be the volumetric flow rate of the sample in m^3/hr ?

6.2 It is desired to sample particles from a gas for morphological study by electron microscopy. The particles are collected on the stages of a cascade impactor using an electron micrograph grid in place of a collector plate. Let N_∞ be the particle concentration in the size range of interest that deposits on a given stage, let m be the magnification of the microscope, let d be the diameter of the aerosol deposit (assumed uniform over d), and let q be the volumetric flow rate. Derive an expression for the time needed to obtain a deposit of a particles per unit area on the electron microscope viewing screen. For $a = 100$ particles/cm², calculate the time in minutes for a concentration of 10^2 particles/cc in the size range of interest, magnification of 65,000, and volumetric sampling rate of 1 lpm. The deposit diameter is 1 mm.

6.3 A round jet impactor is to be designed to sample a flowing aerosol. For a maximum jet velocity of 200 m/sec and a flow rate of 1 liter/min, determine the minimum particle size (aerodynamic diameter) that can be collected. Assume that the pressure throughout the impactor is approximately atmospheric and the temperature is 20°C. Be sure to account for the slip correction factor (Chapter 2).

6.4 For the optical particle counter of Fig. 6.5, the sensing volume is $1.5 \times 1.5 \times 1$ mm. Determine the total energy scattered by the air molecules in the volume. Compare this with the scattering by *single* particles with diameters ranging from 0.05 to 5 μ m and a refractive index of 1.5. Assume $\lambda = 0.5$ μ m and express your answers in terms of the incident intensity. The temperature is 20°C.

6.5 It is desired to relate measured values of the light scattered by the atmospheric aerosol to the contributions of different ranges of the size distribution function. Discuss the components of a measurement system capable of providing the necessary information. Discuss assumptions that must be made in carrying out the relevant calculations.

6.6 The integrating nephelometer provides information on total aerosol light scattering. Show how the characteristics of the instrument would appear within the framework of Table 6.3.

6.7 By rotating a flat disk about an axis perpendicular to its face, an air flow can be induced in the direction of the surface. Small particles diffuse to the surface of the disk at a rate given by the expression

$$|J| = 0.62D^{2/3}v^{-1/6}\omega^{1/2}n_\infty$$

where J is the flux in particles per square centimeter per second, ω is the angular speed of the rotating disk in radians per second, and n_∞ is the particle concentration at large distances from the disk.

The particle deposition rate is independent of position on the surface as long as the boundary layer is laminar. By attaching an electron micrograph grid to the surface, a sample can be collected for examination under the electron microscope. If the atmospheric concentration is 10^5 particles/cm³, determine the sampling time necessary to have 10 particles in an area 100 μ m on a side. The speed of rotation is 20,000 rpm and the temperature is 20°C. To simplify the calculation, assume the particle size is 0.05 μ m. (For an application of this method, see Pasceri and Friedlander, 1965).

6.8 Certain metals present in the atmospheric aerosol, including Fe, Mn, and V, may serve as catalysts for the oxidation of substances such as SO₂, which is converted to H₂SO₄ in the

atmosphere. Estimate the volume of air that must be sampled to collect enough material for INAA of these metals. Refer to Table 6.2.

REFERENCES

- American Conference of Governmental Industrial Hygienists (1995) *Air Sampling Instruments*, 8th ed. ACGIH, Cincinnati, OH. This is a good, practical guide to instruments for the measurement of the physical properties of aerosols. It includes many tables and figures showing operating ranges with limited discussion of fundamental principles. It is the closest thing available to a handbook on aerosol instrumentation, with different specialists writing about each type of instrument.
- Appel, B. R. (1993) Atmospheric Sample Analysis and Sampling Artifacts, in Willeke, K., and Baron, P. A. (Eds.), *Aerosol Measurement*, Van Nostrand Reinhold, New York.
- Berglund, R. N., and Liu, B. Y. H. (1973) *Environ. Sci. Technol.*, **7**, 147.
- Butcher, S. S., and Charlson, R. J. (1972) *An Introduction to Air Chemistry*, Academic, New York.
- Cheng, Y. S. (1993) Condensation Detection and Diffusion Size Separation Techniques, in Willeke, K., and Baron, P. A. (Eds.), *Aerosol Measurement*, Van Nostrand Reinhold, New York.
- Cloupeau, M., and Prunet-Foch, B. (1994) *J. Aerosol Sci.*, **25**, 1021.
- Conner, W. D., and Hodkinson, J. R. (1967) Optical Properties and Visual Effects of Smoke-Stack Plumes, PHS Publication No. 999-AP-30, U.S. Dept. H.E.W., Cincinnati, OH.
- EPA (1996) *Air Quality Criteria for Particulate Matter*, **1**, 4-77.
- Fletcher, R. A., and Small, J. A. (1993) Analysis of Individual Collected Particles, in Willeke, K., and Baron, P. A. (Eds.), *Aerosol Measurement*, Van Nostrand Reinhold, New York.
- Gebhart, J. (1993) Optical Direct-Reading Techniques: Light Intensity Systems, in Willeke, K., and Baron, P. A. (Eds.) *Aerosol Measurement*, Van Nostrand Reinhold, New York.
- Grace, J. M., and Marijnissen, J. C. M. (1994) *J. Aerosol Sci.*, **25**, 1005.
- Grosjean, D., Williams, E. L., and Grosjean, E. (1994) *Aerosol Sci. Technol.*, **21**, 306.
- Hopke, P. D. (1985) *Receptor Modeling in Environmental Chemistry*, Wiley, New York, Chapter 2.
- Husar, R. B. (1974) Recent Developments in *in Situ* Size Spectrum Measurement of Submicron Aerosol in *Instrumentation for Monitoring Air Quality*, A.S.T.M.S.T.P. 555, American Society for Testing Materials, Philadelphia.
- Jaklevic, J. M., Loo, B. W., and Goulding, F. S. (1977) Photon-Induced X-Ray Fluorescence Analysis Using Energy-Dispersive Detector and Dichotomous Sampler, in Dzubay, T. G. (Ed.), *X-Ray Fluorescence Analysis of Environmental Samples*, Ann Arbor Science Publishers, Ann Arbor, MI.
- Liu, B. Y. H., Whitby, K. T., and Yu, H. H. S. (1966) *J. Rech. Atmos.*, **2**, 397.
- Lodge, J. P., Jr. (Ed.) (1989) *Methods of Air Sampling and Analysis*, 3rd ed., Lewis Publishers, Chelsea, MI.
- Marple, V. A., and Liu, B. Y. H. (1974), *Environ. Sci. Technol.*, **8**, 648.
- May, K. R. (1967) Physical Aspects of Sampling Airborne Microbes, in Gregory, P. H., and Monteith, J. L. (Eds.), *Airborne Microbes*, Cambridge University Press, Cambridge, UK.
- McCrone, W. C., Draftz, R. G., and Delly, J. G. (1973) *The Particle Atlas*, Ann Arbor Sciences Publishers, Ann Arbor, MI.
- Mercer, T. T. (1973) *Aerosol Technology in Hazard Evaluation*, Academic, New York. This is primarily a review of instrumentation for the measurement of the physical properties of

- aerosols. It includes more theoretical background than the ACGIH reference and much useful information on the operating characteristics of commercial instrumentation.
- Middleton, W. E. K. (1952) *Vision Through the Atmosphere*, University of Toronto Press, Toronto.
- Olmez, I. (1989) Instrumental Neutron Activation Analysis of Atmospheric Particulate Matter, in Lodge, J. P., Jr. (Ed.), *Methods of Air Sampling and Analysis*, 3rd ed., Lewis Publishers, Chelsea, MI.
- Pasceri, R. E., and Friedlander, S. K. (1965) *J. Atmos. Sci.*, **22**, 577.
- Pollak, L. W., and Metnieks, A. L. (1957) *Geofis. Pura Appl.*, **37**, 174.
- Prather, K. A., Nordneyer, T. and Salt, K. (1994) *Anal. Chem.*, **66**, 1403.
- Pui, D. Y. H., and Liu, B. Y. H. (1988) *Physica-Scripta*, **37**, 252.
- Ranz, W. E., and Wong, J. B. (1952) *Ind. Eng. Chem.*, **44**, 1371.
- Rosell-Llompart, J., and de la Mora, J. (1994) *J. Aerosol Sci.*, **25**, 1093.
- Silverman, L., Billings, C. E., and First, M. W. (1971) *Particle Size Analysis in Industrial Hygiene*, Academic, New York.
- Sinha, M. P., Giffin, C. E., Norris, D. D., Estes, T. J., Vilker, V. L., and Friedlander, S. K. (1982) *J. Colloid Interface Sci.*, **87**, 140.
- Sinha, M. P., Giffin, C. E., Norris, D. D., and Friedlander, S. K. (1983) Particle Analyzing Method and Apparatus, U.S. Patent #4,383,171.
- Sinha, M. P., Platz, R. M., Friedlander, S. K., and Vilker, V. L. (1985) *Appl. Environ. Microbiol.*, **41**, 1454.
- Spurny, K. R. (Ed.) (1986) *Physical and Chemical Characterization of Individual Airborne Particles*, Ellis Horwood, Chichester.
- Weiss, M., Verheijen, P. J. T., Marijnissen, J. C. M., and Scarlett, B. (1997) *J. Aerosol Sci.*, **28**, 159.
- Willeke, K., and Baron, P. A. (Eds.) (1993) *Aerosol Measurement*, Van Nostrand Reinhold, New York. This is a valuable state-of-the-art compilation of information on aerosol instrumentation written by specialists in the field. It includes applications in different fields such as air pollution monitoring, industrial hygiene, commercial production of particles, and clean-room monitoring.
- Zworykin, V. K., Morton, G. A., Ramberg, E. G., Hillier, J., and Vance, A. W. (1945) *Electron Optics and the Electron Microscope*, Wiley, New York.

Collision and Coagulation

Coalescing Particles

INTRODUCTION

In discussions of light scattering and deposition in previous chapters, the size distribution function, $n(v)$, was considered a given quantity. However, the deposition process itself results in the loss of particles preferentially with respect to size, thereby changing $n(v)$. In addition, processes occurring within the gas, including coagulation and gas-to-particle conversion, modify $n(v)$. This occurs in the production of titania pigment, in the evolution of the atmospheric aerosol, and at sources of combustion aerosols such as incinerators and pulverized coal combustion units. The next few chapters deal with the internal processes that modify the particle size distribution. In this chapter, we consider collisions among coalescing spherical particles, the process we define as *coagulation*.

Aerosols are unstable with respect to coagulation. The reduction in surface area that accompanies coalescence corresponds to a reduction in the Gibbs free energy under conditions of constant temperature and pressure. The prediction of aerosol coagulation rates is a two-step process. The first is the derivation of a mathematical expression that keeps count of particle collisions as a function of particle size; it incorporates a general expression for the collision frequency function. An expression for the collision frequency based on a physical model is then introduced into the equation that keeps count of collisions. The collision mechanisms include Brownian motion, laminar shear, and turbulence. There may be interacting force fields between the particles. The processes are basically nonlinear, and this leads to formidable difficulties in the mathematical theory.

In this chapter, we consider first the initial coagulation of monodisperse aerosols for which analytical solutions for the particle size distributions can easily be obtained. Results of these calculations may be sufficiently accurate for certain applications especially for short times. Then solutions approached asymptotically after long periods of time ("self-preserving" size distributions) are discussed. In the classical theory of coagulation, coalescence occurs instantaneously after two particles collide, and a new sphere is formed. The term *agglomeration* is reserved for noncoalescing collision processes. The formation of agglomerate structures composed of noncoalescing spheres is discussed in the next chapter.

Later, in Chapter 12, the theory is further generalized to take into account the factors that determine the size of the primary particles composing agglomerates. In detailed design calculations for particular geometries and flow regimes, numerical methods are necessary to solve the coagulation equations, but these are beyond the scope of the text. For discussions of numerical methods, the reader is referred to Gelbard and Seinfeld (1978), Landgrebe and Pratsinis (1990), and Williams and Loyalka (1991).

The term "aerosol conditioning" refers to modification of the size distribution through physical and/or chemical processes, usually to enhance the efficiency of gas cleaning devices. For example, considerable effort has gone into the development of acoustic coagulation as an industrial process. The goal is to grow the particles in an acoustic field and separate the enlarged particles by relatively inexpensive equipment such as a cyclone separator. While progress has been made in laboratory demonstrations, a practical industrial process has not been developed; acoustic coagulation theory is reviewed by Williams and Loyalka (1991).

COLLISION FREQUENCY FUNCTION

Particle collision and coagulation lead to a reduction in the total number of particles and an increase in the average size. An expression for the time rate of change of the particle size distribution function can be derived as follows.

Let N_{ij} be the number of collisions occurring per unit time per unit volume between the two classes of particles of volumes v_i and v_j . All particles are assumed to be spherical, which means that i and j are uniquely related to particle diameters. When two particles collide, according to this simplified model, they coalesce instantaneously to form a third whose volume is equal to the sum of the original two. In terms of the concentrations of particles n_i and n_j with volumes v_i and v_j , the collision frequency is

$$N_{ij} = \beta(v_i, v_j)n_i n_j \quad (7.1)$$

where $\beta(v_i, v_j)$, the collision frequency function, depends on the sizes of the colliding particles and on such properties of the gas as temperature and pressure and the characteristics of the flow field. The functional dependence on these variables is determined by the mechanisms by which the particles come into contact.

In the case of a discrete spectrum (Chapter 1), the rate of formation of particles of size k by collision of particles of size i and j is $\frac{1}{2} \sum_{i+j=k} N_{ij}$ where the notation $i+j=k$ indicates that the summation is over those collisions for which

$$v_i + v_j = v_k \quad (7.2)$$

A factor of 1/2 is introduced because each collision is counted twice in the summation. The rate of loss of particles of size k by collision with all other particles is $\sum_{i=1}^{\infty} N_{ik}$. Hence the net rate of generation of particles of size k is

$$\frac{dn_k}{dt} = \frac{1}{2} \sum_{i+j=k} N_{ij} - \sum_{i=1}^{\infty} N_{ik} \quad (7.3)$$

When we substitute (7.1) in (7.3), the result is

$$\frac{dn_k}{dt} = \frac{1}{2} \sum_{i+j=k} \beta(v_i, v_j) n_i n_j - n_k \sum_{i=1}^{\infty} \beta(v_i, v_k) n_i \quad (7.4)$$

which is the dynamic equation for the discrete size spectrum when coagulation alone is important. The solution to (7.4) depends on the form of $\beta(v_i, v_j)$, which is determined by the mechanism of particle collision, as discussed in the sections that follow. The theory for the discrete spectrum, including expressions for the collision frequency function for Brownian coagulation and laminar shear, is due to Smoluchowski (1917).

BROWNIAN COAGULATION

Particles smaller than about $1 \mu\text{m}$ collide as a result of their Brownian motion; most of the theoretical and experimental studies of coagulation have been concerned with this mechanism. For particles much larger than the mean free path of the gas, there is experimental evidence that the collision process is diffusion-limited. Consider a sphere of radius a_i , fixed at the origin of the coordinate system in an infinite medium containing suspended spheres of radius a_j . Particles of radius a_j are in Brownian motion and diffuse to the surface of a_i , which is a perfect sink. Hence the concentration of a_j particles vanishes at $r = a_i + a_j$. For the spherical symmetry, the equation of diffusion (Chapter 2) takes the form

$$\frac{\partial n}{\partial t} = D \frac{\partial r^2 (\partial n / \partial r)}{r^2 \partial r} \quad (7.5)$$

For this case, the initial and boundary conditions are

$$\text{at } r = a_i + a_j, \quad n = 0 \text{ for all } t \quad (7.5a)$$

$$r > a_i + a_j, \quad t = 0, \quad n = n_{\infty} \quad (7.5b)$$

Let

$$w = \left(\frac{n_{\infty} - n}{n_{\infty}} \right) \left(\frac{r}{a_i + a_j} \right) \quad (7.6)$$

and

$$x = \frac{r - (a_i + a_j)}{a_i + a_j} \quad (7.7)$$

Substitution in (7.5) gives

$$\frac{\partial w}{\partial t} = \frac{D}{(a_i + a_j)^2} \frac{\partial^2 w}{\partial x^2} \quad (7.8)$$

with the boundary conditions

$$\text{at } x = 0, \quad w = 1 \text{ for all } t$$

$$x > 0, \quad t = 0, \quad w = 0$$

Equation (7.8) with these boundary conditions corresponds to one-dimensional diffusion in a semi-infinite medium for which the solution is

$$w = 1 - \operatorname{erf} \frac{x(a_i + a_j)}{2(Dt)^{1/2}} \quad (7.9)$$

where erf denotes the error function. As $t \rightarrow \infty$, $w \rightarrow 1 - \operatorname{erf}(0) = 1$ and

$$\frac{n_\infty - n}{n_\infty} \rightarrow \frac{a_i + a_j}{r} \quad (7.10)$$

which is the steady-state solution for the concentration distribution, also obtained by setting $\partial n / \partial t = 0$ in (7.5) and solving for n .

Because the flux of a_j particles to an a_i particle is

$$-D \left(\frac{\partial n}{\partial r} \right)_{r=a_i+a_j}$$

the rate of collision of a_j particles with an a_i particle is

$$F(t) = 4\pi D \left(r^2 \frac{\partial n}{\partial r} \right)_{r=a_i+a_j} \quad (7.11)$$

Differentiating (7.9) and substituting in (7.11), we obtain

$$F(t) = 4\pi D(a_i + a_j)n_\infty \left[1 + \frac{a_i + a_j}{(\pi Dt)^{1/2}} \right] \quad (7.12)$$

This is the rate at which particles of size a_j collide with a fixed particle of size a_i (particles/s). For sufficiently long times ($t \gg (a_i + a_j)^2 / D$), particles near the j th type have coagulated or diffused, and the local rate of coagulation assumes a stationary value

$$F = 4\pi D(a_i + a_j)n_\infty \quad (7.13)$$

which is equivalent to the steady-state solution (7.10).

If the central particle is also in Brownian motion, the diffusion constant, D , should describe the relative motion of two particles. The relative displacement is given by $x_i - x_j$, where x_i and x_j are the displacements of the two particles in the x direction measured from a given reference plane. The diffusion constant for the relative motion can be obtained from the Einstein equation for the diffusion coefficient (Chapter 2):

$$D_{ij} = \frac{\overline{(x_i - x_j)^2}}{2t} \quad (7.14a)$$

$$= \frac{\overline{x_i^2}}{2t} - \frac{\overline{2x_i x_j}}{2t} + \frac{\overline{x_j^2}}{2t} \quad (7.14b)$$

$$= D_i + D_j \quad (7.14c)$$

The quantity $\overline{x_i x_j} = 0$ because the motion of the two particles is independent. The collision frequency function first derived by Smoluchowski is then obtained by substitution in (7.13):

$$\beta(v_i, v_j) = 4\pi (D_i + D_j) (a_i + a_j) \quad (7.15)$$

For particles $0.1 \mu\text{m}$ in radius, the characteristic time $(a_i + a_j)^2 / (D_i + D_j)$ is about 10^{-3} sec, and the use of the steady-state solution is justified in most cases of practical interest. When the Stokes-Einstein relation holds for the diffusion coefficient (Chapter 2) and $d_p \gg \ell$, this expression becomes

$$\beta(v_i, v_j) = \frac{2kT}{3\mu} \left(\frac{1}{v_i^{1/3}} + \frac{1}{v_j^{1/3}} \right) (v_i^{1/3} + v_j^{1/3}) \quad (7.16)$$

The derivation of (7.16) is based on the assumption that the diffusion coefficients of the colliding particles do not change as the particles approach each other. That this is not correct can be seen qualitatively from the discussion in Chapter 4 of the increased resistance experienced by a particle as it approaches a surface. The result is that the term $(D_i + D_j)$ tends to decrease as the particles approach each other. This effect is countered in the neighborhood of the surface because the continuum theory on which it is based breaks down about one mean free path ($\sim 0.1 \mu\text{m}$ at NTP) from the particle surface; in addition, van der Waals forces tend to enhance the collision rate as discussed later in this chapter. For further discussion of the theory, the reader is referred to Batchelor (1976) and Alam (1987). Experimental support for (7.16) is discussed in the next section.

For particles much smaller than the mean free path of the gas, less than about one-tenth, say, the collision frequency is obtained from the expression derived in the kinetic theory of gases for collisions among molecules that behave like rigid elastic spheres:

$$\beta(v_i, v_j) = \left(\frac{3}{4\pi} \right)^{1/6} \left(\frac{6kT}{\rho_p} \right)^{1/2} \left(\frac{1}{v_i} + \frac{1}{v_j} \right)^{1/2} (v_i^{1/3} + v_j^{1/3})^2 \quad (7.17)$$

where ρ_p is the particle density. Fuchs (1964) has proposed a general interpolation formula for β , which takes into account the transition from the free molecule regime (7.17) to the continuum range (7.16). Values of β calculated from the interpolation formula are shown in Fig. 7.1. The value of $\beta(a_1, a_2)$ is smallest for monodisperse particles ($a_1/a_2 = 1$), and the spread in value for particle size is smallest. For monodisperse particles, β passes through a maximum at a Knudsen number of 5 (Hidy and Brock, 1970).

BROWNIAN COAGULATION: DYNAMICS OF DISCRETE DISTRIBUTION FOR AN INITIALLY MONODISPERSE AEROSOL

A simple solution to the kinetic equation for Brownian coagulation can be obtained for nearly monodisperse systems. Setting $v_i = v_j$ in (7.16), the collision frequency function is given by

$$\beta(v_i = v_j) = \frac{8kT}{3\mu} = K \quad (7.18)$$

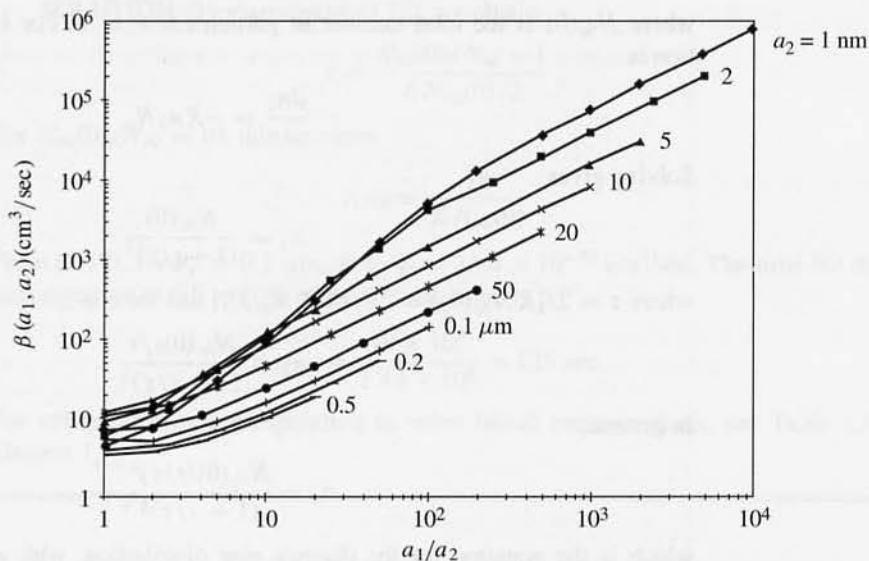


Figure 7.1 Variation of collision frequency function $\beta(a_1, a_2)$ with particle size ratio a_1/a_2 for air at 23°C and 1 atm based on Fuchs (1964, p. 294). The value of $\beta(a_1, a_2)$ is smallest for particles of equal size ($a_1/a_2 = 1$) and the spread in value with particle size is smallest. For $a_1/a_2 = 1$, β goes through a weak maximum for Knudsen number near 5. The value of $\beta(a_1, a_2)$ is highest for interacting particles of very different sizes (large a_1/a_2). The lowest curves correspond to the continuum regime.

In this special case of $\beta = K$ independent of particle size, a simple, analytical solution can be obtained for the discrete size distribution of an initially monodisperse aerosol. When we substitute in (7.4), the result is

$$\frac{dn_k}{dt} = \frac{K}{2} \sum_{i+j=k} n_i n_j - K n_k \sum_{i=1}^{\infty} n_i \tag{7.19}$$

Let $\sum_{i=1}^{\infty} n_i = N_{\infty}$ be the total number of particles per unit volume of fluid. When we sum over all values of k , the result is

$$\frac{dN_{\infty}}{dt} = \frac{K}{2} \sum_{k=1}^{\infty} \sum_{i+j=k} n_i n_j - K N_{\infty}^2 \tag{7.20}$$

It is not difficult to show by expanding the summation that the first term on the right-hand side is $(K/2)N_{\infty}^2$ so that the equation becomes

$$\frac{dN_{\infty}}{dt} = -\frac{K}{2} N_{\infty}^2 \tag{7.21}$$

Integrating once gives

$$N_{\infty} = \frac{N_{\infty}(0)}{1 + (KN_{\infty}(0)t/2)} \tag{7.22}$$

where $N_\infty(0)$ is the total number of particles at $t = 0$. For $k = 1$, the kinetic equation is

$$\frac{dn_1}{dt} = -Kn_1N_\infty \quad (7.23)$$

Solving gives

$$n_1 = \frac{N_\infty(0)}{(1 + t/\tau)^2} \quad (7.24)$$

where $\tau = 2/[KN_\infty(0)] = 3\mu/[4kTN_\infty(0)]$ and for $k = 2$

$$n_2 = \frac{N_\infty(0)t/\tau}{(1 + t/\tau)^3} \quad (7.25)$$

In general,

$$n_k = \frac{N_\infty(0)(t/\tau)^{k-1}}{(1 + t/\tau)^{k+1}} \quad (7.26)$$

which is the equation for the discrete size distribution, with an initially monodisperse aerosol and a collision frequency function independent of particle size. The variation in n_k with time is shown in Fig. 7.2. At any time, t , the discrete distribution is a monotonically decreasing function of k . Since (7.25) is based on the assumption that the collision frequency function is constant (colliding particles of equal diameter), the analysis would be expected to hold best for small values of t/τ , while the aerosol is nearly monodisperse.

The solution for the discrete distribution (7.26) can be interpreted as the size distribution for the particles in a batch system at a time t after the start of coagulation. Alternatively, it is equivalent to the distribution after a residence time t in a plug flow system where $t = x/U$, x is the distance from the entrance to the tube, and U is the average velocity.

Support for the theory of diffusion-controlled coagulation came originally from experiments with polydisperse aerosols (Whytlaw-Gray and Patterson, 1932). The measured coagulation coefficient K was shown to be approximately independent of the chemical nature of the aerosol material with a value close to that predicted theoretically. Tests of the theory have also been conducted by following the coagulation of monodisperse aerosols of dioctylphthalate generated by a condensation aerosol generator (Devir, 1963). Experimentally measured values of the coagulation coefficient were compared with values calculated from theory. Taking into account wall losses, good agreement between theory and experiment was obtained. Such experiments provide the main support for the use of the Smoluchowski kernel in coagulation theory.

Example A: Estimate the time for the concentration of a monodisperse aerosol to fall to 10% of its original value. The particle diameter is $0.1 \mu\text{m}$, and the initial concentration is 10^8 cm^{-3} . The gas is air at 20°C .

SOLUTION: By rearranging (7.22), we obtain

$$t = \frac{N_{\infty}(0)/N_{\infty} - 1}{KN_{\infty}(0)/2}$$

For $N_{\infty}(0)/N_{\infty} = 10$, this becomes

$$t_{1/10} = \frac{18}{KN_{\infty}(0)}$$

From (7.17), for $d_p = 0.1 \mu\text{m}$, $K = \beta \approx 14.4 \times 10^{-10} \text{ cm}^3/\text{sec}$. The time for the concentration to fall to 10% of its original value is

$$t_{1/10} = \frac{18 \times 10^9}{1.44 \times 10^8} = 125 \text{ sec}$$

For values of $t_{1/10}$ corresponding to other initial concentrations, see Table 1.1, Chapter 1.

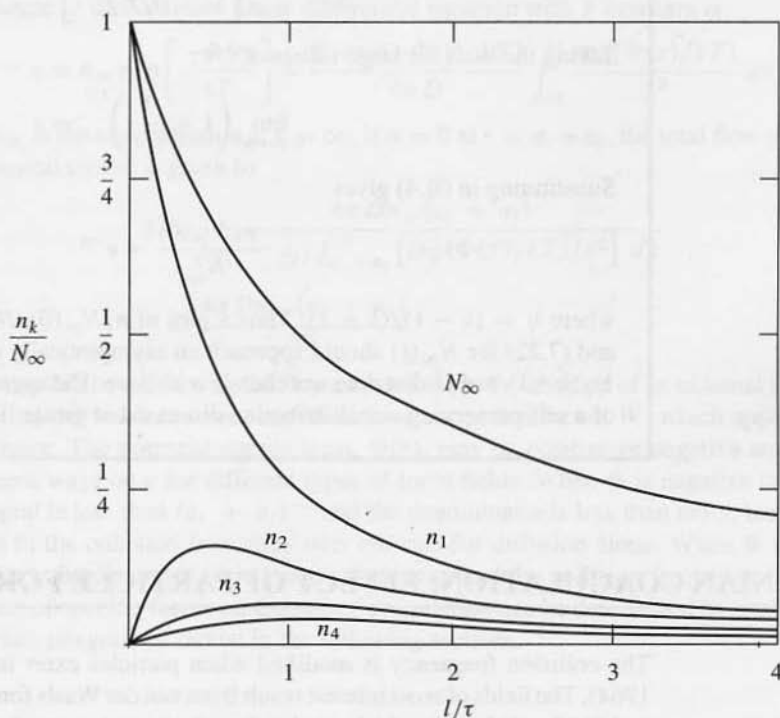


Figure 7.2 The variations in N_{∞} , n_1 , n_2 , ... with time for an initially monodisperse aerosol. The total number concentration, N_{∞} , and the concentration of n_1 both decrease monotonically with increasing time. The concentrations of n_2 ... pass through a maximum. (After Smoluchowski, 1917)

Example B: Show that for sufficiently long times we obtain $n_k \sim e^{-\eta}$, where $\eta = k/\bar{k}$ and $\bar{k}(t) = N_\infty(0)/N_\infty(t)$ is the average number of monomers in an agglomerated particle.

SOLUTION: Rearrange Smoluchowski's result (7.26) as follows:

$$\frac{n_k N_\infty(0)}{N_\infty^2} = \frac{(t/\tau)^{k-1}}{(1+t/\tau)^{k-1}} \quad (\text{B.1})$$

where we have introduced (7.22) in the form

$$N_\infty(0)/N_\infty = 1 + t/\tau$$

Rearranging (B.1) gives

$$\frac{n_k N_\infty(0)}{N_\infty^2} = \left[1 + \frac{1}{t/\tau}\right]^{-(k-1)} \quad (\text{B.2})$$

which can also be written as

$$\frac{n_k N_\infty(0)}{N_\infty^2} = \left[\left(1 + \frac{1}{t/\tau}\right)^{t/\tau}\right]^{-(k-1)\tau/t} \quad (\text{B.3})$$

Taking the limit for large values of t/τ :

$$\lim_{t/\tau \rightarrow \infty} \left(1 + \frac{1}{t/\tau}\right)^{t/\tau} = e \quad (\text{B.4})$$

Substituting in (B.4) gives

$$\frac{n_k N_\infty(0)}{N_\infty^2} = e^{-\eta}$$

where $\eta = (k-1)/(\bar{k}-1)$. Thus a plot of $n_k N_\infty(0)/N_\infty^2$ based on (7.26) for n_k and (7.22) for $N_\infty(t)$ should approach an asymptotically decaying function of $(k-1)/(\bar{k}-1) \approx k/\bar{k}$ that does not change with time. The asymptotic form is an example of a self-preserving size distribution discussed at greater length later in this chapter.

BROWNIAN COAGULATION: EFFECT OF PARTICLE FORCE FIELDS

The collision frequency is modified when particles exert forces on one another (Fuchs, 1964). The fields of most interest result from van der Waals forces, which are always present, and Coulomb forces, which result when the particles are charged. Both are considered in the following sections.

Once again we consider a particle of radius a_i to which particles of radius a_j are diffusing. In this case, however, the a_i particle exerts a force $A(r)$ per unit mass [that is, it produces an acceleration $A(r)$] on the particles of radius a_j in Brownian motion in the

surrounding fluid. Making the assumption of spherical symmetry, the diffusional flux of a_i particles to the surface of the a_i particle (Chapter 2) is given by

$$J(r) = -D \frac{\partial n}{\partial r} + \frac{A(r)}{f} n \quad (7.27)$$

In the steady state, the number of particles crossing each spherical surface concentric with the central particle is constant:

$$4\pi r^2 J = \text{const} = -F = -D4\pi r^2 \frac{\partial n}{\partial r} + \frac{4\pi r^2 A(r)n}{f} \quad (7.28)$$

where f is the friction coefficient (Chapter 2). Instead of using the force $A(r)$, it is usually more convenient to introduce the potential energy of two particles as a function of their separation distance, $\Phi(r)$:

$$A(r) = -\frac{d\Phi(r)}{dr} \quad (7.29)$$

Substituting, we obtain

$$F = 4\pi r^2 D \left(\frac{dn}{dr} + \frac{n}{kT} \frac{d\Phi}{dr} \right) \quad (7.30)$$

The solution to this ordinary linear differential equation with F constant is

$$n = n_\infty \exp\left[\frac{-\Phi(r)}{kT}\right] + \frac{F \exp[-\Phi(r)/kT]}{4\pi D} \int_\infty^r \frac{\exp[\Phi(x)/kT]}{x^2} dx \quad (7.31)$$

where n_∞ is the concentration at $r = \infty$. If $n = 0$ at $r = a_i + a_j$, the total flow of particles to the central sphere is given by

$$F = \frac{4\pi D n_\infty (a_i + a_j)}{(a_i + a_j) \int_{a_i + a_j}^\infty [\exp(\Phi(x)/kT)/x^2] dx} \quad (7.32)$$

$$= \frac{4\pi D n_\infty (a_i + a_j)}{W} \quad (7.32a)$$

Comparing this equation with the flow of particles in the absence of an external force field, we see that the result has been modified by a correction factor, W , which appears in the denominator. The potential energy term, $\Phi(r)$, may be positive or negative and depends in different ways on r for different types of force fields. When Φ is negative (attraction), the integral is less than $(a_i + a_j)^{-1}$ and the denominator is less than unity, leading to an increase in the collision frequency over the rate for diffusion alone. When Φ is positive (repulsion), the denominator is greater than unity and the collision frequency is reduced. The effect of specific forces on the rate of coagulation can be determined by evaluating the appropriate integrals as shown in the following sections.

EFFECT OF VAN DER WAALS FORCES

Attractive (van der Waals) forces between uncharged nonpolar molecules result from dipoles produced by fluctuations in the electron clouds (Chapter 2). The energy of attraction which

can be calculated from quantum theory depends on the molecular properties and the distance between the molecules (Israelachvili, 1992). The energy of attraction, Φ , between two spherical particles is found by integrating over the interactions between pairs of molecules in the separate particles.

For two spherical particles of radii a_i and a_j , Φ is given by (Hamaker, 1937; Chu 1967, p. 50 ff):

$$\Phi = -\frac{A}{6} \left[\frac{2a_i a_j}{r^2 - (a_i + a_j)^2} + \frac{2a_i a_j}{r^2 - (a_i - a_j)^2} + \ln \frac{r^2 - (a_i + a_j)^2}{r^2 - (a_i - a_j)^2} \right] \quad (7.33)$$

where r is the distance between the centers of the spheres and A is the Hamaker constant which has the dimensions of energy. Values of A for selected substances are given in Table 7.1. For two spherical particles of the same radius, a , the energy of attraction is found by setting $a_i = a_j = a$:

$$\Phi = -\frac{A}{6} \left\{ 2 \left(\frac{a}{r} \right)^2 + \frac{2a^2}{r^2 - 4a^2} + \ln \left[1 - \frac{4a^2}{r^2} \right] \right\} \quad (7.34)$$

Substituting in the correction factor, W , which appears in the denominator of (7.32a), we obtain

$$W = \int_0^1 \exp \left[-\frac{A f(x)}{6kT} \right] dx \quad (7.35)$$

where

$$x = r/a$$

and

$$f(x) = \left[\frac{x^2}{2} + \frac{x^2}{2(1-x^2)} + \ln(1-x^2) \right] \quad (7.35a)$$

Hence for colliding particles of the same diameter the effect of the van der Waals forces on collision rate does not depend on the size but only on A/kT . The integral (7.35) has been evaluated and the result is shown in Fig. 7.3. The determination of the effect of the van der Waals forces on the coagulation rate thus reduces to the evaluation of A/kT for particles of equal size.

TABLE 7.1
Hamaker Constants for Two Identical Substances
Interacting Across Vacuum (or Gas at
Low Pressure) (from Israelachvili, 1992, p. 186)

Substance	A (10^{-20} J)
Water	3.7
Cyclohexane	5.2
Benzene	5.0
Polystyrene	6.5
Fused Quartz	6.3
Alumina (Al_2O_3)	14
Iron Oxide (Fe_2O_3)	21
Rutile (TiO_2)	43
Metals (Au, Ag, Cu)	25-40

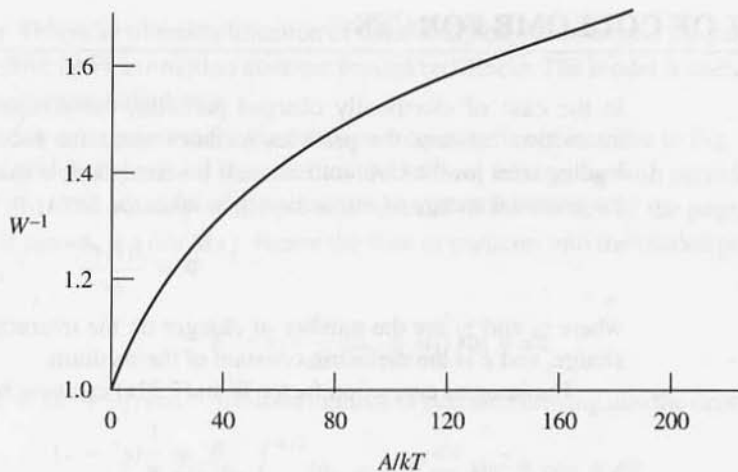


Figure 7.3 Increase in rate of collision of particles of equal diameter resulting from the action of van der Waals forces (Tikhomirov et al., 1942).

With respect to the attraction energy (7.34) there are two limiting cases of interest. When the distance between the spheres is very small compared with the particle radius.

$$\Phi \simeq -\frac{Aa}{12s} \quad (7.36)$$

where $s = r - 2a$ is the shortest distance between the surfaces of the two particles. For s approaching 0, Φ approaches infinity. It is often assumed that the gap between the particles is a few angstroms to obtain reasonable finite values of Φ for particles (almost) in contact. When the distance between particles is very large ($r \gg a$), the interaction energy is

$$\Phi \simeq -\frac{16Aa^6}{9s^6} \quad (7.37)$$

In this case, the long range interactions have a form similar to that for molecular interactions, that is, the energy varies inversely with the inverse sixth power of the distance between the particle center.

Example: Estimate the effect of the van der Waals forces on the rate of coagulation of polystyrene particles in air at 20°C.

SOLUTION: From Table 7.1, $A = 6.5 \times 10^{-20}$ J for polystyrene, hence $A/kT = 16$. According to Fig. 7.3, this corresponds to an increase in the coagulation rate of about 20%. In problems of practical interest, a factor of 20% may not be of great significance because of uncertainties resulting from convection, deposition on the walls of containment vessels and other confounding factors. Returning to Table 7.1, the maximum increase in the coagulation rate due to the van der Waals effect will only be about 50% for the wide variety of substances shown in the table.

EFFECT OF COULOMB FORCES

In the case of electrically charged particles, the complete expression for the force of interaction between the particles includes terms for induction forces, in addition to the leading term for the Coulomb force. It is often possible to neglect the induction forces, and the potential energy of interaction then takes the form

$$\Phi = \frac{z_i z_j e^2}{\epsilon r} \quad (7.38)$$

where z_i and z_j are the number of charges on the interacting particles, e is the electronic charge, and ϵ is the dielectric constant of the medium.

The integral correction factor W in (7.32a) can now be evaluated, and the result is

$$W = \frac{1}{y}(e^y - 1) \quad (7.39)$$

where the dimensionless parameter

$$y = \frac{z_i z_j e^2}{\epsilon k T (a_i + a_j)} \quad (7.39a)$$

represents the ratio of the electrostatic potential energy, to kT . In the limiting case of uncharged particles, $y = 0$, the correction factor becomes unity and (7.32a) reduces to the field-free case. When the particles are of opposite sign, y is negative and the correction factor is positive and less than unity, as can be seen by expanding the exponential. The result is that collisions occur more rapidly than in the case of uncharged particles. When the particles are of like sign, the correction factor is positive and greater than unity. The result is that the collision rate is smaller than for uncharged particles.

Depending on the charging mechanism, aerosols may be composed of particles of like charges (unipolar charging) or of unlike charges (bipolar charging), and the magnitudes of the charges may vary. For $|y| \ll 1$ the charging may be termed weak, and for $|y| \gg 1$ it may be termed strong. The atmospheric aerosol has a weak bipolar charge, with roughly equal numbers of positively and negatively charged particles. For such an aerosol, the effect on the collision frequency can be estimated by calculating separately the collision rates for particles of the same and opposite signs and then averaging the rates. For $y = 1/2$, for example, the correction factor is about 1.3, and for $y = -1/2$ it is about 0.8. Hence the average rate is but little affected by charging over the range $y = 0$ to $y \pm 1/2$. This has been confirmed experimentally (Fuchs, 1964, p. 308).

For strong bipolar aerosols ($|y| \gg 1$), this compensation does not take place. The large increase in coagulation resulting from attractive forces strongly outweighs the decrease caused by repulsion.

COLLISION FREQUENCY FOR LAMINAR SHEAR

Particles in a uniform, laminar shear flow collide because of their relative motion (Fig. 7.4a). The streamlines are assumed to be straight, and the particle motion is assumed to be

rectilinear. This is an oversimplification of what really happens because the particles affect the shear flow, and their motion does not remain rectilinear. The model is useful, however, for an approximate calculation.

To derive an expression for the collision frequency function, refer to Fig. 7.4a, which shows a single particle in the shear field with radius a_i interacting with particles of radius a_j (Fig. 7.4b). The velocity of the particles normal to the surface of the page, relative to the particle shown, is $x(du/dx)$. Hence the flow of particles into the shaded portion of the strip dx is

$$F = n_j x \frac{du}{dx} (a_i + a_j) \sin \theta dx \quad (7.40)$$

Because $x = (a_i + a_j) \cos \theta$, the total number of particles flowing into the central sphere is

$$F = 2(2)n_j \int_0^{\pi/2} (a_i + a_j)^3 \frac{du}{dx} \sin^2 \theta \cos \theta d\theta \quad (7.41)$$

where the first factor 2 takes into account the flow into the upper hemisphere from this side of the page plus the flow into the bottom hemisphere from the backside of the page. The second factor 2 is necessary because the integration from 0 to $\pi/2$ must be done twice. Carrying out the integration, we obtain

$$F = \frac{4}{3} (a_i + a_j)^3 \frac{du}{dx} n_j \quad (7.42)$$

and the collision frequency is

$$N_{ij} = \frac{4}{3} (a_i + a_j)^3 \frac{du}{dx} n_i n_j \quad (7.43)$$

The collision frequency function for coagulation by laminar shear is, therefore,

$$\beta(v_i, v_j) = \frac{4}{3} (a_i + a_j)^3 \frac{du}{dx} \quad (7.44)$$

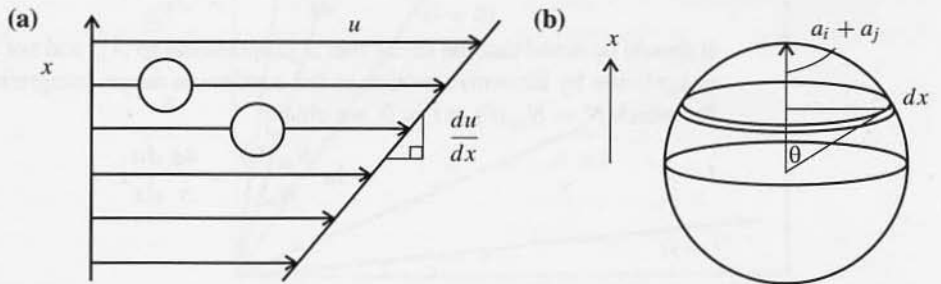


Figure 7.4 (a) Idealized model of particle collision in a shear field. The upper particle, moving at a higher velocity, overtakes and collides with the slower moving particle. (b) Geometry for coagulation in a laminar shear field. The flow is normal to the page. The particle of radius a_i has its origin at the center of the coordinate system. The velocity gradient du/dx is constant, and the velocity relative to the central sphere at x is $x(du/dx)$.

This result was first obtained by Smoluchowski. This analysis does not take into account local flows accompanying the draining of fluid from the region between the approaching particles or particle motion normal to the main flow direction. These flows would change the simple shear field assumed in the analysis and probably reduce the cross section below the result of the geometric theory. However, experimental results such as those reported below lend support to the approximate analysis. This subject is discussed further in the section on turbulent coagulation.

Substituting into (7.4), the equation of coagulation by laminar shear for the discrete spectrum becomes

$$\frac{dn_k}{dt} = \frac{1}{2} \sum_{i+j=k} \left[\frac{4}{3} (a_i + a_j)^3 \frac{du}{dx} n_i n_j \right] - \sum_{i=1}^{\infty} \frac{4}{3} (a_i + a_k)^3 \frac{du}{dx} n_i n_k \quad (7.45)$$

If the system is composed of particles that are all of nearly the same size, $a_i \approx a_j = a$, then (7.45) becomes

$$\frac{dn_k}{dt} = \frac{1}{2} \sum_{i+j=k} \left[\frac{32}{3} a^3 \frac{du}{dx} n_i n_j \right] - \sum_{i=1}^{\infty} \frac{32}{3} a^3 \frac{du}{dx} n_i n_k \quad (7.46)$$

Summing over all k , we obtain

$$\frac{dN_{\infty}}{dt} = -\frac{16}{3} \frac{du}{dx} a^3 N_{\infty}^2 \quad (7.47)$$

But

$$\frac{4}{3} \pi a^3 N_{\infty} = \phi = \text{const} \quad (7.48)$$

Hence

$$\frac{dN_{\infty}}{dt} = -\frac{4\phi}{\pi} \frac{du}{dx} N_{\infty} \quad (7.49)$$

It should be noted that the decay rate is proportional to N_{∞} and not to N_{∞}^2 , as in the case of coagulation by Brownian motion in the continuum range. Integrating from the initial state for which $N = N_{\infty}(0)$ at $t = 0$, we obtain

$$\ln \frac{N_{\infty}(0)}{N_{\infty}} = \frac{4\phi}{\pi} \frac{du}{dx} t \quad (7.50)$$

SIMULTANEOUS LAMINAR SHEAR AND BROWNIAN MOTION

Swift and Friedlander (1964) carried out experiments on the coagulation of hydrosols in the presence of simultaneous laminar shear and Brownian movement. They used a Couette-type apparatus consisting of an outside plastic cylindrical shell, an inside brass cylinder, and two

brass end plates. The outer shell and end plates were fixed and the inner cylinder was free to rotate. Suspensions of polystyrene latex particles $0.871 \mu\text{m}$ in diameter were destabilized by the addition of sodium chloride solution and allowed to coagulate in the annular space; the shear field was varied by controlling the speed of rotation of the inner cylinder.

Assuming additivity of the rates of coagulation by shear and Brownian motion, the rate of change of the total particle concentration is

$$\frac{dN_\infty}{dt} = -\frac{4\alpha_{bm} kT}{3\mu} N_\infty^2 - \frac{4G\alpha_{\ell s}\phi}{\pi} N_\infty \quad (7.51)$$

where α_{bm} is an empirical collision efficiency for Brownian motion, $\alpha_{\ell s}$ is the collision efficiency for shear flow, and $G = du/dx$. Integrating (7.51) assuming $\alpha_{\ell s} = \alpha_{bm}$, the result is

$$\ln \left[\left(\frac{N_\infty + R}{N_\infty} \right) \left(\frac{N_\infty(0)}{N_\infty(0) + R} \right) \right] = \frac{4\alpha G\phi t}{\pi} \quad (7.52)$$

where $R = 3G\phi\mu/kT$. The value of α_{bm} was found to be 0.375 in an experiment carried out in the absence of shear. Experiments were carried out with the latex dispersion subjected to shear rates of 1, 5, 20, 40, and 80 sec^{-1} , and the results were plotted in a form suggested by (7.52) as shown in Fig. 7.5. According to (7.52), the slopes of the lines of Fig. 7.5 should

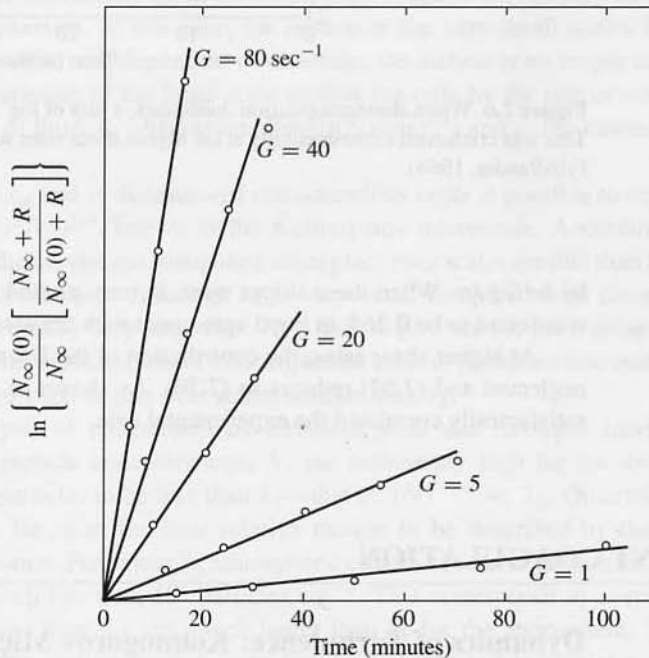


Figure 7.5 Shear coagulation of a monodisperse latex dispersion. Straight lines were obtained for differing shear rates in accordance with a simple theory assuming additivity of the effects of Brownian motion and shear. The points are experimental results (Swift and Friedlander, 1964).

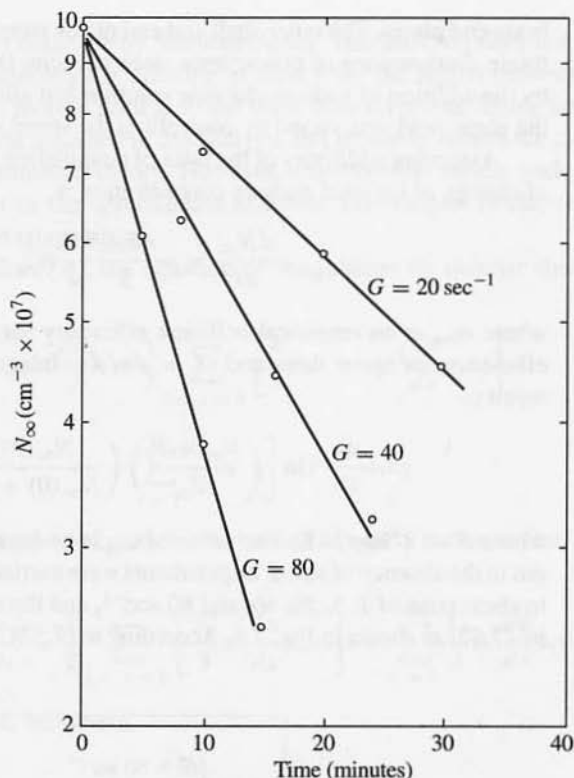


Figure 7.6 When shear coagulation dominates, a plot of $\log N_\infty$ versus t should give a straight line. This was confirmed experimentally at the higher shear rates with a monodisperse hydrosol (Swift and Friedlander, 1964).

be $4\alpha G\phi/\pi$. When these slopes were, in turn, plotted as a function of G , the value of α_{ℓ_s} was found to be 0.364, in good agreement with the assumption that $\alpha_{\ell_s} = \alpha_{bm}$.

At higher shear rates, the contribution of the Brownian motion to coagulation can be neglected and (7.52) reduces to (7.50). As shown in Fig. 7.6, this form of the equation satisfactorily correlated the experimental data.

TURBULENT COAGULATION

Dynamics of Turbulence: Kolmogorov Microscale

In practice, coagulation almost always takes place in turbulent flows. Examples are industrial aerosol reactors, combustion systems, process gas flows, and the atmosphere. Turbulent

coagulation generally becomes important for particles larger than a few microns but may be significant for submicron aerosols at very high turbulence levels. The two mechanisms that have received most attention—turbulent shear and turbulent inertial coagulation—are reviewed in this section.

The effects of turbulence on coagulation are only partially understood. There are uncertainties in the fundamental theory of turbulence and in the motion of small particles in close proximity in the turbulent flow field. As a result, theoretical predictions of turbulent coagulation rates must be considered approximate perhaps to within a factor of 10 and are likely to be on the high side.

The theoretical analysis is based on concepts that derive from the energy cascade hypothesis of turbulent flow (Batchelor, 1953, p. 109ff; Landau and Lifshitz, 1987, p. 129ff). According to this hypothesis, the turbulent field is initiated by the formation of large eddies of the scale of the dimensions of the mechanical structures generating the turbulence—for example, the diameter of the pipe through which the fluid flows or the diameter of the paddles of an impeller. Energy is transferred from the large eddies (which carry most of the kinetic energy of the turbulent flow) to smaller ones. For the motion of the large eddies, viscous effects are unimportant and there is little dissipation of energy by these structures. At the smallest scales, the directed motion of the large eddies is finally converted into the random thermal energy (temperature) of the molecules by viscous dissipation. When the Reynolds number based on the size and velocity of the large eddies is sufficiently high, the dissipation range is statistically independent of the large eddy dynamics. In this case, the motion at the very small scales is homogeneous and isotropic—that is, independent of direction; the motion is no longer influenced by the directional properties of the large-scale motion but only by the rate of energy dissipation per unit mass of fluid, ϵ_d (dimensions $(\text{length})^2(\text{time})^{-3}$) and ν , the kinematic viscosity of the fluid.

Based on ϵ_d and ν , dimensional considerations make it possible to construct a length scale $\lambda_k = (\nu^3/\epsilon_d)^{1/4}$, known as the Kolmogorov microscale. According to the energy cascade hypothesis, viscous dissipation takes place over scales smaller than λ_k at sufficiently high Reynolds numbers. Although λ_k is very small compared with the size of the large eddies, it is generally very large (8×10^{-2} to 2×10^{-1} cm for the troposphere) compared with micron-size particles. There is an important class of problems discussed in this section in which coagulation occurs over scales smaller than λ_k .

The analysis of coagulation by turbulent shear and turbulent inertial effects also requires that particle concentrations, N , are sufficiently high for the distances between the colliding particles to be less than λ_k —that is, $(N)^{-1/3} \ll \lambda_k$. Otherwise, the particles would be too far apart for their relative motion to be described by the theory for the small-scale motion. For example, atmospheric concentrations of micron and larger particles are usually much less than 10^3 particles cm^{-3} . This corresponds to average interparticle distances greater than 0.1 cm, much larger than λ_k for the atmosphere. Thus the results discussed in this section apply best to fogs and clouds and industrial aerosols in which the concentrations of particles larger than $1 \mu\text{m}$ are high enough to fall within a volume equivalent to λ_k .

Turbulent Shear Coagulation

Collisions among particles distributed randomly in a turbulent gas can occur as a result of small-scale shear flows over distances $< \lambda_k$. This process is analogous to coagulation by laminar shear flow discussed above. The form of the coagulation kernel for the case of turbulent shear can be established by dimensional analysis. The collision frequency function $\beta(v_i, v_j)$ with dimensions $(\text{length})^3(\text{time})^{-1}$ is assumed to be a function of the interaction distance $(a_i + a_j)$ and a characteristic velocity gradient. For isotropic turbulence the rms velocity gradient can be characterized by (Goldstein, 1938, p. 224)

$$\sqrt{\left(\frac{\partial u_\ell}{\partial x_m}\right)^2} = \frac{2}{15} \left(\frac{\epsilon_d}{\nu}\right)^{1/2} \quad (7.53)$$

where ℓ and m refer to orthogonal coordinates. Because the rms velocity gradient has dimensions of $(\text{time})^{-1}$, dimensional analysis requires that

$$\beta(v_i, v_j) = 1.3 \left(\frac{\epsilon_d}{\nu}\right)^{1/2} (a_i + a_j)^3 \quad (7.54)$$

where the constant 1.3 is the value calculated by Saffman and Turner (1956) based on plausible assumptions concerning the dynamics of the turbulent fluid. The result is very similar to (7.44) for laminar shear.

Turbulent Inertial Coagulation

Turbulence may also lead to coagulation as a result of inertial effects. When particles of different sizes (masses) are present in the same accelerating eddy, a relative motion is induced between the particles that may lead to collision. Again the scale of the particle motion is confined to distances $< \lambda_k$. The mean square relative velocity between the particles can be approximated using the force balance for Stokesian particles (Chapter 4):

$$m \frac{d\mathbf{u}}{dt} = -f(\mathbf{u} - \mathbf{u}_f) \quad (7.55)$$

where \mathbf{u} and \mathbf{u}_f are the particle and gas velocities, respectively. Introducing the relative velocity between the particle and gas in (7.55) and rearranging, we obtain

$$\frac{d\mathbf{u}_R}{dt} = -\beta\mathbf{u}_R - \frac{d\mathbf{u}_f}{dt} \quad \text{where } \mathbf{u}_R = \mathbf{u} - \mathbf{u}_f \quad (7.56)$$

When the characteristic time $\beta^{-1} = m/f$ is small compared with the time scale of the smallest eddies, usually the case for aerosol particles, the term $d\mathbf{u}_R/dt$ can be neglected to give

$$\mathbf{u}_R = -\frac{1}{\beta} \frac{d\mathbf{u}_f}{dt} \quad (7.57)$$

Thus the mean square relative velocity of two particles i and j of different masses is given by

$$\overline{(\mathbf{u}_i - \mathbf{u}_j)^2} = \left(\frac{1}{\beta_i} - \frac{1}{\beta_j}\right)^2 \overline{\left(\frac{d\mathbf{u}_f}{dt}\right)^2} \quad (7.58)$$

For isotropic turbulence in the high-Reynolds-number limit, the mean square acceleration of the fluctuating eddies is

$$\overline{\left(\frac{d\mathbf{u}_f}{dt}\right)^2} \sim \frac{\epsilon_d^{3/2}}{\nu^{1/2}} \quad (7.59)$$

Assuming a Gaussian form with variance given by (7.59) for the distribution of the relative velocities between the two classes of particles, the collision frequency kernel is (Saffman and Turner, 1956)

$$\beta(v_i, v_j) = 5.7(a_i + a_j)^2 \left| \frac{1}{\beta_i} - \frac{1}{\beta_j} \right| \frac{\epsilon_d^{3/4}}{\nu^{1/4}} \quad (7.60)$$

where $\pi(a_i + a_j)^2$ is the collision cross section. This analysis is limited to the case of particles confined within the Kolmogorov microscale. Collision rates for larger particles that can escape λ_k are discussed by Kruis and Kusters (1997).

Limitations on the Analysis

The models for laminar and turbulent shear coagulation and turbulent inertial coagulation are geometric in nature; they assume the particles are rigid spheres that follow the fluid motion and do not take into account local flows in the region between approaching particles. These local flows are expected to reduce the collision efficiency because of the increased resistance to the motion as the particles approach each other (Chapter 4). Thus the equations given in this section for $\beta(v_i, v_j)$ probably describe the maximum efficiency.

There is much uncertainty regarding the value of the collision efficiency needed to correct the geometric models discussed above. Some insight into this problem can be obtained from calculations for coagulation by differential sedimentation. In this process, small, slowly sedimenting particles are swept out by larger, rapidly settling particles. The collision frequency function can be written

$$\beta(v_i, v_j) = \alpha_{ds} \pi(a_i + a_j)^2 (c_{ii} - c_{ij}) \quad (7.61)$$

where α_{ds} is the collision efficiency and the rest of the expression represents a particle flow through the effective collision cross section, $\pi(a_i + a_j)^2$. The term $(c_{ii} - c_{ij})$ is the settling velocity of the large particle relative to the small one. The collision efficiency α_{ds} has been evaluated numerically taking into account the effects of particle interaction on the drag. The results of such calculations are summarized by Pruppacher and Klett (1978) and Williams and Loyalka (1991). Calculated collision frequencies for the case in which the larger of the sedimenting particles is $10 \mu\text{m}$ are usually smaller than 0.1.

There have been few experimental tests of the theoretical predictions of turbulent coagulation under controlled conditions. Delichatsios and Probstein (1975) measured rates of coagulation of 0.6-mm latex particles suspended in an aqueous solution in turbulent pipe flow. The Reynolds numbers ranged from 17,000 to 51,000 for flow through a 1-in. (I.D.) smooth-walled pipe. For the core of the pipe flow, the turbulence was approximately isotropic. The energy dissipation per unit mass was calculated from the relation

$$\epsilon_d = 4v_*^3/D_{\text{pipe}} \quad (7.62)$$

where v_* is the friction velocity and D_{pipe} is the pipe diameter. The friction velocity can be calculated from the pressure drop. The measured collision frequency function was about 70% of the theoretical value based on (7.60), much higher than the calculated efficiencies for differential sedimentation.

Thus there is a large discrepancy between the theoretical predictions of the collision efficiency for aerosol coagulation by differential sedimentation (taking into account inter-particle fluid motion) and experimental measurements for coagulation by turbulent shear in aqueous suspensions. We do not know whether this discrepancy is due to the basic difference in the coagulation mechanisms (differential sedimentation vs. turbulent shear), different phenomena operating in the different fluid media, or some other as yet unidentified effect.

Comparison of Collision Mechanisms

The various collision mechanisms are compared in Fig. 7.7 which shows the collision frequency function for 1- μm particles interacting with particles of other sizes. Under conditions corresponding to turbulence in the open atmosphere ($\epsilon_d \approx 5\text{cm}^2/\text{sec}^3$), either Brownian motion or differential sedimentation plays a dominant role. Brownian motion controls for particles smaller than 1 μm . At lower altitudes in the atmosphere and in turbulent pipe flows, shear becomes important.

EQUATION OF COAGULATION: CONTINUOUS DISTRIBUTION FUNCTION

For the continuous distribution function, the collision rate between particles in the size ranges v to $v + dv$ and \bar{v} to $\bar{v} + d\bar{v}$ is given by

$$\text{collision rate} = \beta(v, \bar{v})n(v)n(\bar{v}) dv d\bar{v} \quad (7.63)$$

where the forms of the collision frequency function discussed in previous sections are applicable. The rate of formation of particles of size v by collision of smaller particles of size $v - \bar{v}$ and \bar{v} is then given by

$$\text{formation in range } dv = \frac{1}{2} \left[\int_0^v \beta(\bar{v}, v - \bar{v})n(\bar{v})n(v - \bar{v}) d\bar{v} \right] dv \quad (7.64)$$

Here we have used the result that the Jacobian for the transformation from the coordinate system $(\bar{v}, v - \bar{v})$ to (\bar{v}, v) is unity. The factor 1/2 is introduced as in the discrete case because collisions are counted twice in the integral. The rate of loss of particles of size v by collision with all other particles (except monomer) is

$$\text{loss in range } dv = \left[\int_0^\infty \beta(v, \bar{v})n(v)n(\bar{v}) d\bar{v} \right] dv \quad (7.65)$$

The net rate of formation of particles of size v is

$$\frac{\partial(n dv)}{\partial t} = \frac{1}{2} \left[\int_0^v \beta(\bar{v}, v - \bar{v})n(\bar{v})n(v - \bar{v}) d\bar{v} \right] dv - \left[\int_0^\infty \beta(v, \bar{v})n(\bar{v})n(v) d\bar{v} \right] dv \quad (7.66)$$

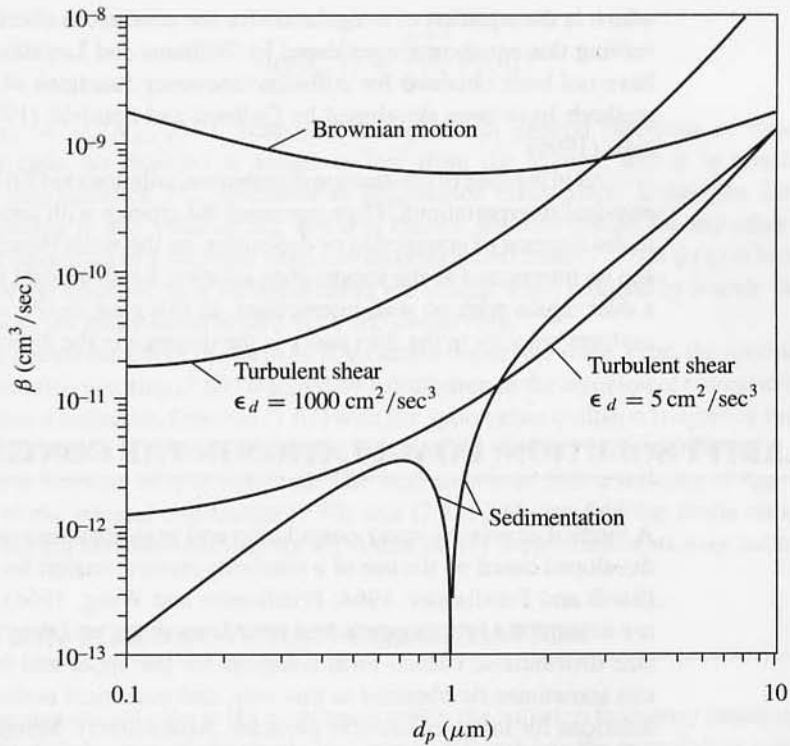


Figure 7.7 Comparison of coagulation mechanisms for particles of 1- μm diameter interacting with particles of diameter between 0.1 and 10 μm . Coagulation by shear based on $\epsilon_d = 5$ and 1000 cm^2/sec^3 . Differential sedimentation curves were obtained by an approximate calculation assuming Stokes flow around the larger of the falling spheres (Friedlander, 1964). $\epsilon_d = 5 \text{ cm}^2/\text{sec}^3$ corresponds to the open atmosphere at a height of about 100 m (Lumley and Panofsky, 1964). At a height of 1 m, $\epsilon_d \approx 1000 \text{ cm}^2/\text{sec}^3$ and shear becomes the dominant mechanism of coagulation for larger particles. For the core region of a turbulent pipe flow, the energy dissipation (based on Laufer, 1954) is given by

$$\epsilon_d = \frac{4}{d} \left(\frac{f}{2} \right)^{3/2} U^3$$

where f is the Fanning friction factor, d is the pipe diameter, and U is the gas velocity. For a smooth pipe, 10 cm in diameter, with air at 20°C and a Reynolds number of 50,000, $\epsilon_d \approx 2 \times 10^4 \text{ cm}^2/\text{sec}^3$.

Dividing through by dv , we obtain

$$\begin{aligned} \frac{\partial n}{\partial t} = & \frac{1}{2} \int_0^v \beta(\tilde{v}, v - \tilde{v}) n(\tilde{v}) n(v - \tilde{v}) d\tilde{v} \\ & - \int_0^\infty \beta(v, \tilde{v}) n(\tilde{v}) n(v) d\tilde{v} \end{aligned} \quad (7.67)$$

which is the equation of coagulation for the continuous distribution function. Methods for solving this equation are reviewed by Williams and Loyalka (1991). Analytical solutions have not been obtained for collision frequency functions of physical interest. Numerical methods have been developed by Gelbard and Seinfeld (1978) and Landgrebe and Pratsinis (1990).

As in the case of the discrete distribution, solutions to (7.67) are subject to two important physical interpretations. They represent the change with time of the aerosol in a chamber in the absence of convection or deposition on the walls (batch system). Alternatively, they can be interpreted as the steady-state solution for an aerosol in steady "plug" flow through a duct, again with no wall interactions. In this case $\partial n/\partial t = U(\partial n/\partial x)$, where U is the uniform velocity in the duct and x is the distance in the direction of flow.

SIMILARITY SOLUTION: COAGULATION IN THE CONTINUUM REGIME

A method of solving many coagulation and agglomeration problems (Chapter 8) has been developed based on the use of a similarity transformation for the size distribution function (Swift and Friedlander, 1964; Friedlander and Wang, 1966). Solutions found in this way are asymptotic forms approached after long times, and they are independent of the initial size distribution. Closed-form solutions for the upper and lower ends of the distribution can sometimes be obtained in this way, and numerical methods can be used to match the solutions for intermediate-size particles. Alternatively, Monte Carlo and discrete sectional methods have been used to find solutions.

The similarity transformation for the particle size distribution is based on the assumption that the fraction of the particles in a given size range is a function only of particle volume normalized by the average particle volume:

$$\frac{n(v, t) dv}{N_\infty} = \psi\left(\frac{v}{\bar{v}}\right) d\left(\frac{v}{\bar{v}}\right) \quad (7.68)$$

where $\bar{v} = \phi/N_\infty$ is the average particle volume, and ψ is a dimensionless function whose form does not change with time. Both sides of (7.68) are dimensionless. By rearranging, we obtain

$$n(v, t) = \frac{N_\infty^2}{\phi} \psi(\eta) \quad (7.69)$$

where $\eta = v/\bar{v} = N_\infty v/\phi$. There are also the integral relations

$$N_\infty = \int_0^\infty n dv \quad (7.70)$$

and

$$\phi = \int_0^\infty nv dv \quad (7.71)$$

where $n = n(v, t)$. It is also usually required that $n(v) \rightarrow 0$ for $v \rightarrow 0$ and $v \rightarrow \infty$. In terms of the distribution function $n_d(d_p, t)$, the similarity transformation takes the form

$$n_d(d_p, t) = \frac{N_\infty^{4/3}}{\phi^{1/3}} \psi_d(\eta_d) \quad (7.72)$$

where $\eta_d = d_p(N_\infty/\phi)^{1/3}$. Both N_∞ and ϕ are in general functions of time. In the simplest case, no material is added or lost from the system, and ϕ is constant. The number concentration N_∞ decreases as coagulation takes place. If the size distribution corresponding to any value of N_∞ and ϕ is known, the distribution for any other value of N_∞ corresponding to a different time, can be determined from (7.69) if $\psi(\eta)$ is known. The shapes of the distribution at different times are similar when reduced by a scale factor. For this reason, the distribution is said to be *self-preserving*.

The determination of the form of ψ is carried out in two steps. First, the special form of the distribution function (7.69) is tested by substitution in the equation of coagulation for the continuous distribution function (7.67) with the appropriate collision frequency function. If the transformation is consistent with the equation, an ordinary integrodifferential equation for ψ as a function of η is obtained. The next step is to find a solution of this equation subject to the integral constraints (7.70) and (7.71) and also find the limits on $n(v)$. For some collision kernels, solutions for $\psi(\eta)$ that satisfy these constraints may not exist.

SIMILARITY SOLUTION FOR BROWNIAN COAGULATION

For Brownian coagulation in the continuum range, the collision frequency function is given by (7.16). Substitution of the similarity form (7.69) reduces the coagulation equation for the continuous distribution (7.67) with (7.16) to the following form:

$$\begin{aligned} & \frac{1}{N_\infty^2} \frac{dN_\infty}{dt} \left[2\psi + \eta \frac{d\psi}{d\eta} \right] \\ &= \frac{kT}{3\mu} \int_0^\eta \psi(\tilde{\eta}) \psi(\eta - \tilde{\eta}) \left[\tilde{\eta}^{1/3} + (\eta - \tilde{\eta})^{1/3} \right] \left[\frac{1}{\tilde{\eta}^{1/3}} + \frac{1}{(\eta - \tilde{\eta})^{1/3}} \right] d\tilde{\eta} \\ & \quad - \frac{2kT}{3\mu} \psi(\eta) \int_0^\infty \psi(\tilde{\eta}) \left[\eta^{1/3} + \tilde{\eta}^{1/3} \right] \left[\frac{1}{\eta^{1/3}} + \frac{1}{\tilde{\eta}^{1/3}} \right] d\tilde{\eta} \end{aligned} \quad (7.73)$$

The change in the total number concentration with time is found by integrating over all collisions:

$$\frac{dN_\infty}{dt} = -\frac{1}{2} \int_0^\infty \int_0^\infty \beta(v, \tilde{v}) n(v) n(\tilde{v}) dv d\tilde{v} \quad (7.74)$$

The factor 1/2 is introduced because the double integral counts each collision twice. By substituting (7.69) and (7.16) in (7.74), we obtain

$$\frac{dN_\infty}{dt} = -\frac{2kT}{3\mu} (1 + ab) N_\infty^2 \quad (7.75)$$

where

$$a = \int_0^\infty \eta^{1/3} \psi d\eta \quad (7.75a)$$

and

$$b = \int_0^{\infty} \eta^{-1/3} \psi \, d\eta \quad (7.75b)$$

Equation (7.76) is of the same form as (7.21) for the decay of the total number concentration in a monodisperse system. However, the constant has a somewhat different value. Substituting (7.75) in (7.73) and consolidating terms, the result is

$$(1 + ab)\eta \frac{d\psi}{d\eta} + (2ab - b\eta^{1/3} - a\eta^{-1/3})\psi + \int_0^{\eta} \psi(\eta - \tilde{\eta})\psi(\tilde{\eta}) \left[1 + \left(\frac{\eta - \tilde{\eta}}{\tilde{\eta}} \right)^{1/3} \right] d\tilde{\eta} = 0 \quad (7.76)$$

which is an ordinary integrodifferential equation for ψ with η the independent variable. Hence the similarity transformation (7.69) represents a possible particular solution to the coagulation equation with the Brownian motion coagulation mechanism.

It is still necessary to show that a solution can be found to the transformed equation (7.76) with the integral constraints, (7.70) and (7.71). Analytical solutions to (7.76) can be found for the upper and lower ends of the distribution by making suitable approximations (Friedlander and Wang, 1966). The complete distribution can be obtained numerically by matching the distributions for the upper and lower ends, subject to the integral constraints that follow from (7.70) and (7.71):

$$\int_0^{\infty} \psi \, d\eta = 1 \quad (7.76a)$$

and

$$\int_0^{\infty} \eta \psi \, d\eta = 1 \quad (7.76b)$$

The results of the numerical calculation are shown in Fig. 7.8, where they are compared with numerical calculations carried out for the discrete spectrum starting with an initially monodisperse system. There is good agreement between the two methods of calculation. Other calculations indicate that the similarity form is an asymptotic solution independent of the initial distributions so far studied. The values of a and b were found to be 0.9046 and 1.248, respectively. By (7.75) this corresponds to a 6.5% increase in the coagulation constant compared with the value for a monodisperse aerosol (7.21). The results of more recent calculations using a discrete sectional method are shown in Table 7.2.

To predict the size distribution of a uniform aerosol coagulating in a chamber without deposition on the walls, the following procedure can be adopted: The volumetric concentration of aerosol is assumed constant and equal to its (known) initial value. The change in the number concentration with time is calculated from (7.75). The size distribution at any time can then be determined for each value of $v = \phi\eta/N_{\infty}$ from the relation $n = (N_{\infty}^2/\phi)\psi(\eta)$, using the tabulated values. The calculation is carried out for a range of values of η .

The change in the particle size distribution function with time for coagulating cigarette smoke has been measured by Keith and Derrick (1960). Smoke issuing from a cigarette was rapidly mixed with clean air, and the mixture was introduced into a 12-liter flask

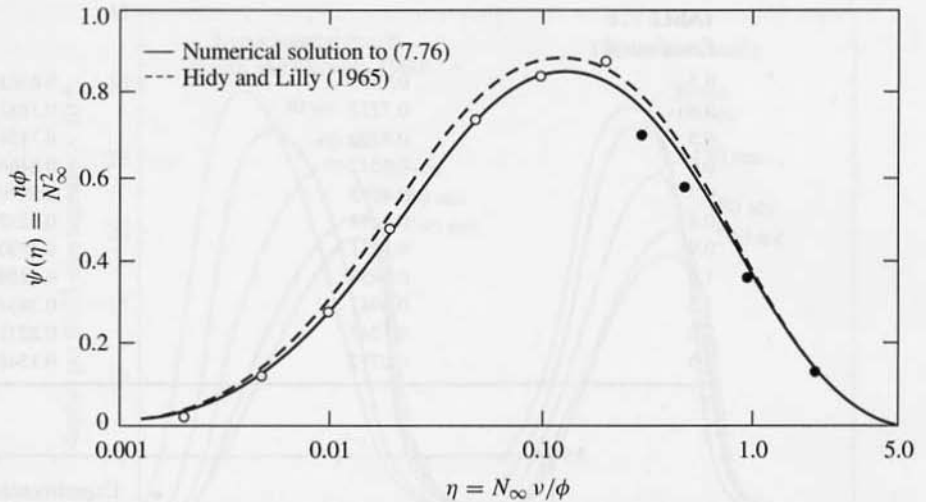


Figure 7.8 Self-preserving particle size distribution for Brownian coagulation. The form is approximately lognormal. The result obtained by solution of the ordinary integrodifferential equation for the continuous spectrum is compared with the limiting solution of Hidy and Lilly (1965) for the discrete spectrum, calculated from the discrete form of the coagulation equation. Shown also are points calculated from analytical solutions for the lower and upper ends of the distribution (Friedlander and Wang, 1966).

TABLE 7.2

Values of the Self-Preserving Size Distribution for the Continuum (ψ_c) and Free Molecule (ψ_f) Regimes Calculated by a Discrete Sectional Method (Vemury and Pratsinis, 1995)

η	ψ_f	ψ_c
0.006	0.0408	0.1218
0.007	0.0632	0.1581
0.008	0.0891	0.1933
0.009	0.1176	0.2271
0.010	0.1479	0.2592
0.015	0.3079	0.2895
0.020	0.4560	0.4170
0.025	0.5809	0.5124
0.030	0.6830	0.5852
0.035	0.7654	0.6418
0.040	0.8315	0.6868
0.045	0.8846	0.7230
0.050	0.9271	0.7525
0.060	0.9880	0.7766
0.070	1.0261	0.8132
0.080	1.0486	0.8384
0.090	1.0605	0.8559
0.1	1.0649	0.8678
0.2	0.9668	0.8755

continued

TABLE 7.2
Continued

0.3	0.8351	0.8563
0.4	0.7232	0.7883
0.5	0.6309	0.7156
0.6	0.5542	0.6466
0.7	0.4895	0.5830
0.8	0.4344	0.5252
0.9	0.3871	0.4730
1.0	0.3459	0.4259
1.5	0.2041	0.3834
2.0	0.1247	0.2271
2.5	0.0777	0.1348

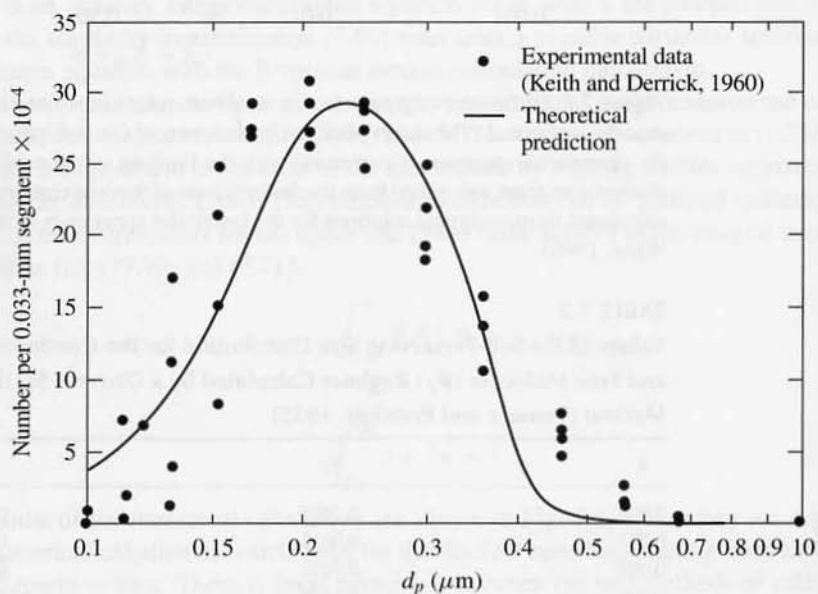


Figure 7.9 Comparison of experimental size distribution data for tobacco smoke with prediction based on self-preserving size spectrum theory. $\phi = 1.11 \times 10^{-7}$, $N_\infty = 1.59 \times 10^7 \text{ cm}^{-3}$. The peak in the number distribution measured in this way occurs at $d_p \approx 0.2 \mu\text{m}$ (Friedlander and Hidy, 1969).

where coagulation took place. The dilution ratio was 294 volumes of air to 1 volume of raw smoke.

To follow the coagulation process, samples of the smoke were taken from the flask at intervals over a period of 4 min and were passed into a centrifugal aerosol collector and classifier. Size distribution curves were measured, together with values for the total number of particles per unit volume, obtained by the graphical integration of the size distribution curves. The volume fraction of aerosol material was $\phi = 1.11 \times 10^{-7}$. Theory and experiment are compared in Figs. 7.9 and 7.10. In Fig. 7.9, the experimental points for

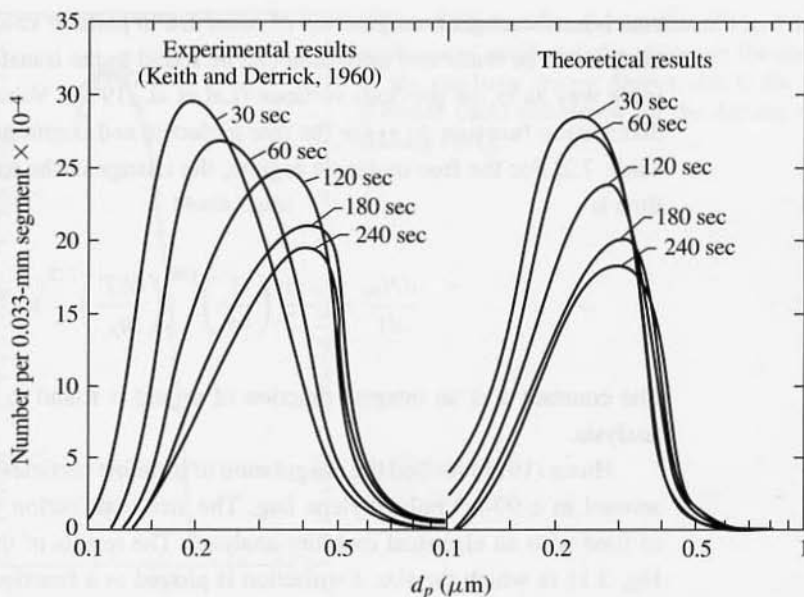


Figure 7.10 Experiment and theory compared for an aging tobacco smoke aerosol. Calculation based on $\phi = 1.11 \times 10^{-7}$ and experimental values of N_∞ (Friedlander and Hidy, 1969).

a nominal aging time of 30 sec are shown with the theoretical prediction. In Fig. 7.10, the results of measurements of the change in the distribution function with time are compared with theory. Agreement is fair; the experimental results fall significantly higher than theory at the upper end of the spectrum (large particle sizes).

SIMILARITY SOLUTION: COAGULATION IN THE FREE MOLECULE REGION

Is it possible to make the similarity transformation (7.62) for other collision mechanisms? In general, when the collision frequency $\beta(v, \tilde{v})$ is a homogeneous function of particle volume, the transformation to an ordinary integrodifferential equation can be made. The function $\beta(v, \tilde{v})$ is said to be *homogeneous* of degree λ if $\beta(\alpha v, \alpha \tilde{v}) = \alpha^\lambda \beta(v, \tilde{v})$. However, even though the transformation is possible, a solution to the transformed equation may not exist that satisfies the boundary conditions and integral constraints.

When the particles are much smaller than the mean free path, the collision frequency function is given by (7.17)

$$\beta(v, \tilde{v}) = \left(\frac{3}{4\pi}\right)^{1/6} \left(\frac{6kT}{\rho_p}\right)^{1/2} \left[\frac{1}{v} + \frac{1}{\tilde{v}}\right]^{1/2} (v^{1/3} + \tilde{v}^{1/3})^2$$

which is a homogeneous function of order 1/6 in particle volume. The similarity transformation can be made and a solution can be found to the transformed equation in much the same way as in the previous sections (Lai et al., 1972). Values of the dimensionless size distribution function $\psi(\eta)$ for the free molecule and continuum regimes are also given in Table 7.2. For the free molecule regime, the change in the total number of particles with time is

$$\frac{dN_{\infty}}{dt} = -\frac{\alpha}{2} \left(\frac{3}{4\pi} \right)^{1/6} \left(\frac{6kT}{\rho_p} \right)^{1/2} \phi^{1/6} N_{\infty}^{11/6} \quad (7.77)$$

The constant α is an integral function of ψ and is found to be about 6.67 by numerical analysis.

Husar (1971) studied the coagulation of ultrafine particles produced by a propane torch aerosol in a 90-m³ polyethylene bag. The size distribution was measured as a function of time with an electrical mobility analyzer. The results of the experiments are shown in Fig. 7.11 in which the size distribution is plotted as a function of particle diameter and in Fig. 7.12 in which ψ is shown as a function of η both based on particle radius. Numerical calculations were carried out by a Monte Carlo method, and the results of the calculation are also shown in Fig. 7.12. The agreement between experiment and the numerical calculations is quite satisfactory.

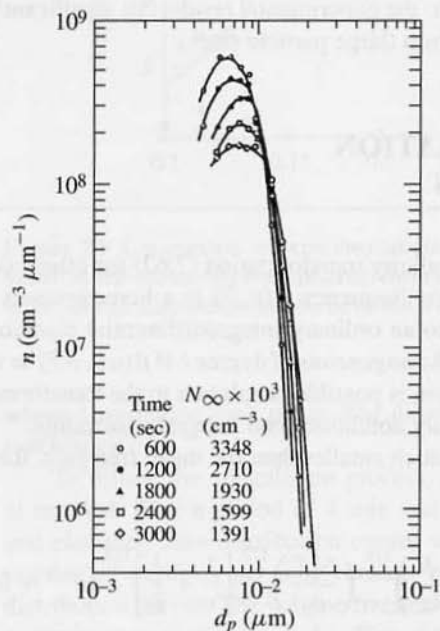


Figure 7.11 Coagulation of aerosol particles much smaller than the mean free path. Size distributions measured with the electrical mobility analyzer (Husar, 1971).

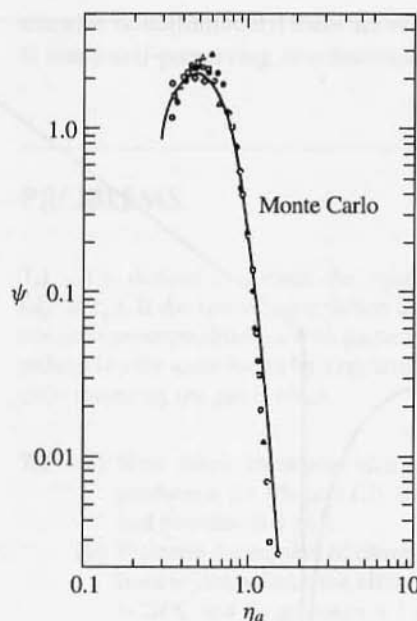


Figure 7.12 Size distribution data of Fig. 7.11 for coagulation of small particles plotted in the coordinates of the similarity theory. Shown also is the result of a Monte Carlo calculation for the discrete spectrum (Husar, 1971).

TIME TO REACH THE SELF-PRESERVING DISTRIBUTION (SPD)

The time to reach the self-preserving form depends on the shape of the initial distribution: The closer the initial distribution to the asymptotic form, the faster the approach. For initially monodisperse aerosols, Vemury et al. (1994) found that the time lag to reach the SPD was given by

$$\tau_{\text{SP}} = 5 \left\{ \left(\frac{3}{4\pi} \right)^{1/6} \left(\frac{6kT}{\rho_p} \right)^{1/2} v_0^{1/6} N_{\infty}(0) \right\}^{-1} \quad (7.78)$$

for the free molecule regime where v_0 is the initial particle volume. For the continuum regime we have

$$\tau_{\text{SP}} = 13 \left[\frac{2kTN_{\infty}(0)}{3\mu} \right]^{-1} \quad (7.79)$$

The criterion for attaining the self-preserving form was that the geometric standard deviation (σ_g) of the distribution function should be within $\pm 1\%$ of the asymptotic (self-preserving) σ_g . In this regard, it should be noted that the self-preserving distribution can be approximated by a lognormal distribution function with $\sigma_g = 1.44$ and 1.46 for the continuum and free molecule regimes, respectively.

When the initial size distribution is lognormal, the time to reach the SPD depends strongly on how far the initial σ_g is from the value for the asymptotic form. This is illustrated

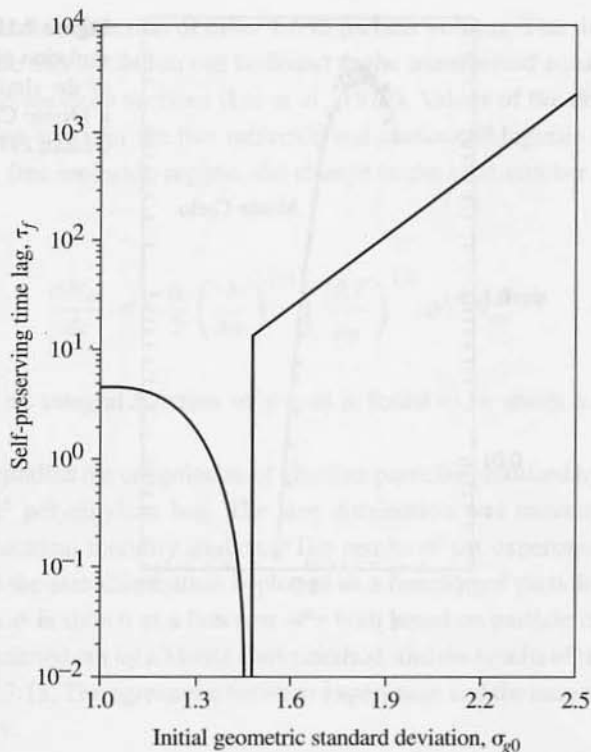


Figure 7.13 Dimensionless time to reach the SPD for initially lognormal size distributions as a function of σ_{g0} . (After Vermury et al., 1994.) The sharp minimum corresponds to the value of σ_g for an initially self-preserving free molecule aerosol.

in Fig. 7.13, which shows the dimensionless time τ_f required for initially lognormal size distributions to reach the SPD as a function of σ_{g0} :

$$t_{sp} = \tau_f \left[\left(\frac{3}{4\pi} \right)^{1/6} \left(\frac{6kT}{\rho_p} \right)^{1/2} v_0^{1/6} N_\infty(0) \right]^{-1} \quad (7.80)$$

For a monodisperse aerosol with an initial particle diameter of 1 nm and initial concentration of 10^{18} particles cm^{-3} at 1800 K, it takes 34 nsec to reach the SPD; and for an initial concentration of 10^{16} , it takes 3.4 μ sec.

In practice, each parcel of gas may have a different time/temperature history. At high particle concentrations, the size distributions in any gas parcel may be self-preserving but different from distributions in the other gas parcels. That is, the distribution may be locally self-preserving. Sampling of many gas parcels or collection of the particles in the entire gas stream will produce a composite of locally self-preserving distributions. The spread of the composite distribution will be larger than that of any individual self-preserving distribution, which represents a minimum. (See Chapter 13 for a discussion of the application of these concepts to the atmospheric aerosol.) Size distributions of mixed self-preserving aerosols

can also be multimodal if there are several significantly different residence times. Of course, if many self-preserving distributions are completely mixed and aged, a new SPD results.

PROBLEMS

7.1 It is desired to quench the coagulation of an aerosol composed of very small particles ($d_p \ll \ell_p$). If the rate of coagulation is to be reduced to 1% of its original value by isothermal, constant pressure dilution with particle-free gas, determine the dilution ratio. The rate is to be reduced by the same factor by a reversible adiabatic expansion. Determine the volume expansion ratio assuming the gas is ideal.

- 7.2** (a) How many electronic charges (opposite sign) must two $0.5\text{-}\mu\text{m}$ particles have to produce a (i) 1% and (ii) 10% increase in collision rate? The temperature is 20°C and pressure is 1 atm.
- (b) Estimate the number of charges of like sign that two $0.5\text{-}\mu\text{m}$ polystyrene particles must have to just balance the effect of van der Waals-type attractive forces. The temperature is 20°C and the pressure is 1 atm. (See Table 7.1.)

7.3 Whytlaw-Gray and his co-workers experimentally demonstrated the applicability of the theory of diffusion-controlled coagulation to aerosols. Many of their results were summarized in the book *Smoke* by Whytlaw-Gray and Patterson (1932). In later experiments (Whytlaw-Gray et al., 1936), the particle concentration was determined as a function of time by trapping a known volume of smoke from the center of a smoke chamber in a shallow box with a glass bottom. These sampling boxes were fixed to a support in the center of the smoke chamber and were withdrawn at definite intervals by means of strings passing through corks in the side of the chamber. The particles that settled on the glass plate were counted optically. In one set of experiments with a cadmium oxide smoke, the following results were obtained:

Time from start (minutes)	Number per $\text{cm}^3 \times 10^{-6}$
8	0.92
24	0.47
43	0.33
62	0.24
84	0.21

Determine the coagulation constant from these data and compare with theory for monodisperse and self-preserving aerosols.

7.4 Consider the flow of an aerosol through a 4-in. duct at a velocity of 50 ft/sec. Compare the coagulation rate by Brownian motion and laminar shear in the viscous sublayer, near the wall. Present your results by plotting the collision frequency function for particles with $d_p = 1\ \mu\text{m}$ colliding with particles of other sizes. Assume a temperature of 20°C . *Hint:* In the viscous sublayer, the velocity distribution is given by the relation

$$u = \frac{yfU^2}{2\nu}$$

where y is the distance from the wall, f is the Fanning friction factor, U is the mainstream velocity, and ν is the kinematic viscosity.

7.5 Let A be the surface area per unit volume of gas of a coagulating aerosol. Assume that at $t = 0$, both N_∞ and A are infinite. Show that for a self-preserving aerosol composed of particles much larger than the mean free path of the gas we have

$$A = \text{const } \phi^{2/3} t^{-1/3}$$

where t is the time. Find an expression for the constant.

7.6 Using the self-preserving transformation, derive an expression for the dynamics of the size distribution function when laminar shear is the controlling mechanism of coagulation. Find the corresponding expression for the change with time of the total number concentration. (Note that a solution satisfying the condition $\psi(\eta) \rightarrow 0$ as $\eta \rightarrow 0$ does not seem to exist in this case.)

REFERENCES

- Alam, M. K. (1987) *Aerosol Sci. Technol.*, **6**, 41.
- Batchelor, G. K. (1953) *The Theory of Homogeneous Turbulence*, Cambridge University Press, New York.
- Batchelor, G. K. (1976) *J. Fluid Mech.*, **74**, 1.
- Chu, B. (1967) *Molecular Forces: Based on the Baker Lectures of Peter J. W. Debye*, Wiley-Interscience, New York.
- Delichatsios, M. A., and Probst, R. F. (1975) *J. Colloid Interface Sci.*, **51**, 394.
- Devir, S. F. (1963) *J. Colloid Sci.*, **18**, 744.
- Friedlander, S. K. (1964) "The Similarity Theory of the Particle Size Distribution of the Atmospheric Aerosol" in *Proceedings of the First National Conference on Aerosols*, Publishing House of Czechoslovak Academy of Sciences.
- Friedlander, S. K., and Wang, C. S. (1966) *J. Colloid Interface Sci.*, **22**, 126.
- Friedlander, S. K., and Hidy, G. M. (1969) "New Concepts in Aerosol Size Spectrum Theory" in Podzimek, J. (Ed.) *Proceedings of the 7th International Conference on Condensation and Ice Nuclei*, Academia, Prague.
- Fuchs, N. A. (1964) *Mechanics of Aerosols*, Pergamon, New York.
- Gelbard, F. M., and Seinfeld, J. H. (1978) *J. Comput. Phys.*, **28**, 357.
- Goldstein, S. (Ed.) (1938) *Modern Developments in Fluid Dynamics*, Vol. 1, Oxford University Press, Oxford.
- Hamaker, H. C. (1937) *Physica*, **4**, 1058.
- Hidy, G. M., and Brock, J. R. (1970) *Dynamics of Aerocolloidal Systems*, Pergamon, New York, pp. 308–309.
- Hidy, G. M., and Lilly, D. K. (1965) *J. Colloid Sci.*, **20**, 867.
- Hirschfelder, J. O., Curtiss, C. F., and Bird, R. B. (1954) *Molecular Theory of Gases and Liquids*, Wiley, New York.
- Husar, R. B. (1971) Coagulation of Knudsen Aerosols, Ph.D. thesis, Department of Mechanical Engineering, University of Minnesota.

- Israelachvili, J. N. (1992) *Intermolecular and Surfaces Forces*, 2nd Ed., Academic Press, San Diego, CA.
- Keith, C. H., and Derrick, J. E. (1960) *J. Colloid Sci.*, **15**, 340.
- Kruis, F. E., and Kusters, K. A. (1997) *Chem. Eng. Comm.*, **158**, 201.
- Lai, F. S., Friedlander, S. K., Pich, J., and Hidy, G. M. (1972) *J. Colloid Interface Sci.*, **39**, 395.
- Landau, L. D., and Lifshitz, E. M. (1987) *Fluid Mechanics*, 2nd ed., Pergamon Press, Oxford, England.
- Landgrebe, J. L., and Pratsinis, S. E. (1990) *J. Colloid Interface Sci.*, **139**, 63.
- Laufer, J. (1954) NACA Report 1174.
- Lumley, J. L. and Panofsky, H. A. (1964) *The Structure of Atmospheric Turbulence*, Interscience, New York, p. 123.
- Mahan, B.N. and Person, J.C. (1964) *J. Chem. Phys.* **40**, 392
- Pruppacher, H. R., and Klett, J. D. (1978) *Microphysics of Clouds and Precipitation*, D. Reidel, Dordrecht, Holland.
- Saffman, P., and Turner, J. (1956) *J. Fluid Mech.*, **1**, 16.
- Smoluchowski, M. (1917) *Z. Physik Chem.*, **92**, 129.
- Swift, D. L., and Friedlander, S. K. (1964) *J. Colloid Sci.*, **19**, 621.
- Tikhomirov, M. V., Tunitskii, N. N., and Petrijanov, I. V. (1942) *Acta Phys.-Chim. U.R.S.S.*, **17**, 185.
- Vemury, S., and Pratsinis, S. E. (1995) *J. Aerosol Sci.*, **21**, 175.
- Vemury, S., Kusters, K. A., and Pratsinis, S. E. (1994) *J. Colloid Interface Sci.*, **165**, 53.
- Whytlaw-Gray, R., and Patterson, H. S. (1932) *Smoke: A Study of Aerial Disperse Systems*, Edward Arnold, London. In this classic monograph, the authors describe experiments on the coagulation of smokes composed of substances of many different types. The studies were carried out before the development of monodisperse aerosol generators and the electron microscope. The coagulation rate was shown to be approximately independent of the chemical nature of the aerosol material and consistent with the predictions of the diffusion limited theory of Smoluchowski. Included are many interesting photomicrographs of agglomerated particles.
- Whytlaw-Gray, R., Cawood, W., and Patterson, H. S. (1936) *Disperse Systems in Gases: Dust, Smoke and Fog*, A General Discussion of the Faraday Society, April 1936.
- Williams, M. M. R., and Loyalka, S. K. (1991) *Aerosol Science Theory and Practice: With Special Applications to the Nuclear Industry*, Pergamon Press, Oxford, England, Chapter 4 includes a detailed summary of collision kernels for many different mechanisms with methods of combining simultaneous mechanisms.

Dynamics of Agglomerate Formation and Restructuring

It was assumed in the last chapter that colliding spherical particles coalesce instantaneously to form larger spherical particles. There is, however, an important class of problems involving the formation of agglomerates composed of much smaller solid particles, known as primary particles, that usually range from a few nanometers to about $0.1 \mu\text{m}$ in diameter. The factors that control the size of the primary particles during their synthesis are discussed in Chapter 12. The primary particles generated by industrial or natural processes are almost always polydisperse; in theoretical analyses of agglomerates composed of such particles they are assumed to be monodisperse. The agglomerates may range in size from about 100 nm to several microns.

Agglomerates appear in emissions from sources such as diesel engines, smelters, and pulverized coal combustion and in the commercial production of fine particles (for example, the synthesis of silica and titania). Particulate emissions from pulverized coal combustion and incineration often have two modes in the mass distribution function. The coarse mode larger than a few microns in diameter consists of fragments of the original inorganic ash. The fine mode is often composed of agglomerates of ultrafine particles resulting from selective volatilization of certain components of the original ash. As shown in this chapter, the agglomerate size distribution is a very sensitive function of agglomerate structure and process conditions.

This chapter starts with a review of methods of characterizing agglomerate structures. Next we discuss the dynamics of agglomerate size distributions driven by collisions resulting from the Brownian motion. Little has been done on the effects of other collision mechanisms such as shear and external force fields. The dynamics of agglomerates is a relatively new field compared to the coagulation of coalescing particles discussed in the last chapter; further important developments can be expected. For example, the extension of the Smoluchowski kernels to agglomerate structures as discussed in this chapter, based on the existing literature, needs further theoretical study and experimental verification. Size distribution dynamics depend strongly on agglomerate structure, primary particle size, and aerosol volume loading. The dynamics of agglomerate behavior differs significantly from that of spherical particles, especially in the free molecular range ($d_p \ll \ell_p = \text{mean free path}$). Both the free molecule

and continuum regimes are discussed in this chapter, but the emphasis is on the free molecule range for which the effects are most important.

Agglomerates are not rigid structures. Evidence of internal restructuring of aerosol agglomerates and the flexibility of nanoparticle chains is discussed at the end of the chapter. For background reading on aggregate formation, the reader is referred to symposia edited by Family and Landau (1984) and by Stanley and Ostrowsky (1986). An early classic on agglomerate formation and properties by Whytlaw-Gray and Patterson (1932) is still worth reading.

AGGLOMERATE MORPHOLOGY: SCALING LAWS

Introduction

An electron micrograph of an alumina agglomerate is shown in Fig. 8.1. An agglomerate can be considered to be composed of N_p primary particles of radius a_{p0} . There is usually some variation in size among the primary particles but this is neglected in the theory. The factors that determine primary particle size are discussed in Chapter 12. The agglomerate structure has a characteristic radius, R , which for Fig. 8.1 is of the order of a few tenths of a micron. The value of R is defined more completely later.

It is found experimentally that in many cases of practical interest, the total number of primary particles N_p in an agglomerate is related to R through a power law expression

$$N_p \sim R^{D_f} \quad (8.1)$$

where the exponent D_f is called the fractal (or Hausdorff) dimension. This is usually true in a statistical sense after averaging over many agglomerates with the same N_p . The value of D_f depends on the details of the agglomerate formation process as explained later. For compact agglomerates we have $D_f \rightarrow 3$, while for chain-like structures we have $D_f \rightarrow 1$. In the discussion that follows, it is shown that D_f can be related to the arrangement of the primary particles within the agglomerate.

Autocorrelation Function

In experiments by Forrest and Witten (1979), tungsten wires electroplated with iron and zinc were heated by a current pulse to vaporize the plated metal into helium gas at about 0.1 atm. The hot vapor mixed with the cool helium and self-nucleated to form 7-nm primary particles. Chain-like agglomerates of primary particles formed by Brownian collision and were deposited on electron microscope grids. The agglomerates were characterized by measuring the average density of points occupied by particles at a distance r from each occupied point; this was done for all values of r . Photographs of deposited agglomerates are two-dimensional projections of three-dimensional objects. When $D_f < 2$, the two-dimensional projection has the same value of D_f as the original three-dimensional agglomerate because there is little overlap among the primary particles consistent with $D_f \leq 2$.

Based on data of this type, the density autocorrelation function between pairs of primary particles can be defined as follows: For the three-dimensional case of a suspended

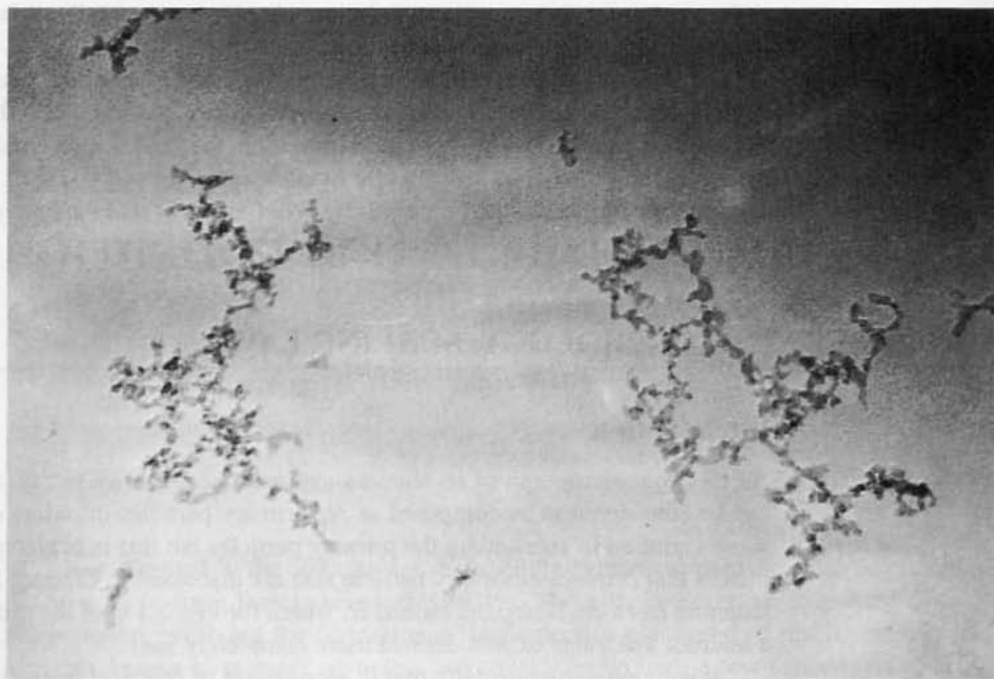


Figure 8.1 Electron micrograph of alumina agglomerates generated by the oxidation of trimethyl aluminum in a methane–air flame. The primary particles composing the agglomerate are about 3 nm in diameter. The longest dimension of the agglomerate is about 0.25 μm . (From Windeler, 1995.)

agglomerate, let $\rho(\mathbf{r}')$ be the density at a reference point vector \mathbf{r}' and let $\rho(\mathbf{r}' + \mathbf{r})$ the density at $\mathbf{r}' + \mathbf{r}$ with ρ equal to 1 if the site is occupied and 0 if it is not. The two-point autocorrelation function $c(r)$ is the average density of occupied points at a distance \mathbf{r} from any other occupied point:

$$c(r) = \frac{1}{N_p} \sum_{\mathbf{r}'} \rho(\mathbf{r}') \rho(\mathbf{r}' + \mathbf{r}) \quad (8.2)$$

where r is the magnitude of the distance between the points and N_p is the total number of pairs of particles counted. This function is assumed to depend only on the distance r separating the two points. Counting is limited to values of r much smaller than the size of the agglomerate and much larger than the primary particles. Forrest and Witten (1979) found that the pair correlation functions for the iron and zinc particles that they made and for commercially produced pyrogenic silica could be represented by an equation with a power law form:

$$c(r) \sim r^{-B} \quad (8.3)$$

where B is determined from the measurements. Figure 8.2 is a log–log plot of the two particle density autocorrelation as a function of distance between the 7-nm iron particles that composed a large agglomerate. The tendency of agglomerates to follow a power law

form when measured in this way has been confirmed by investigators who have studied the behavior of agglomerates composed of particles of other materials including soot (Samson et al., 1987; Megaridis and Dobbins, 1990) and silver (Schmidt-Ott, 1988).

When (8.3) holds, the total number of particles in a three-dimensional agglomerate of radius R is

$$N_p \sim \int_0^R 4\pi r^2 r^{-B} dr \quad (8.4)$$

After carrying out the integration, we recover (8.1)

$$N_p \sim R^{D_f} \quad (8.1)$$

or

$$R \sim N_p^{1/D_f} \quad R \gg a_{p0} \quad (8.1a)$$

where $D_f = 3 - B$. Thus from the slope of the density–density autocorrelation function, the value of D_f can be obtained. Other methods of determining D_f from photographic images of agglomerates are discussed by Forrest and Witten (1979) and Mountain et al. (1986). The value of $c(r)$ does not completely define agglomerate structure. Higher-order correlation functions would be needed for a more complete description. Thus D_f itself represents only a partial description of the morphology.

Agglomerates are fractal-like in a statistical sense. Equation (8.1) describes the average radius of many agglomerates with the same N_p and primary particle size. Agglomerates are not true fractals, because they are not infinitely scale-invariant. The lower limit on the size of an agglomerate is the primary particle ($N_p = 1$). Fractal concepts break down for

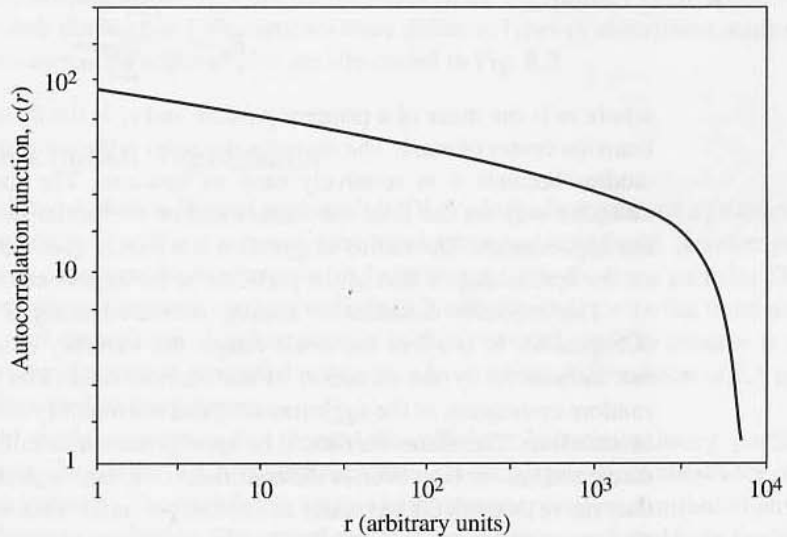


Figure 8.2 Autocorrelation function for a power-law agglomerate as a function of distance r . The fractal dimension is calculated from the straight-line portion for small values of r . The tail-off for large values of r corresponds to the edge of the agglomerate.

agglomerates composed of small numbers of primary particles; that is, the use of (8.3) requires that $R \gg a_{p0}$. For these reasons we prefer to call these power law agglomerate structures *fractal-like*.

Prefactor for the Power Law Relationship

For many practical applications, the power law relationship (8.1) requires an appropriate proportionality constant or coefficient. Consider the case of monodisperse primary particles of radius a_{p0} which form power law agglomerates according to a process whose statistical features are independent of a_{p0} . The statistical properties of the agglomerates produced by this process do not depend on the magnitude of a_{p0} . That is, if a_{p0} were multiplied by a factor of 10, the value of D_f would not be affected nor would all of the other higher-order particle correlation functions that are not considered in this analysis. This means that the system should scale as R/a_{p0} so that (8.3) becomes

$$N_p = A \left(\frac{R}{a_{p0}} \right)^{D_f} \quad (8.5)$$

The dimensionless proportionality constant A depends on how R , the characteristic radius of the agglomerate, is defined; it also depends on the process by which the agglomerate forms and on the Knudsen number. The value of A may also vary for different values of D_f . If this equation holds for $r \rightarrow a_{p0}$ ($N_p \rightarrow 1$), then A has a value of unity. However, for $D_f \neq 3$, (8.5) applies only for large values of N_p , that is, $R \gg a_{p0}$.

The characteristic agglomerate sizes most often used are the mobility diameter, defined as the diameter of a sphere with the same friction coefficient as the agglomerate under similar dynamic conditions, and the radius of gyration

$$R_g = \sqrt{\frac{\sum_i m r_i^2}{\sum_i m}} \quad (8.6)$$

where m is the mass of a primary particle and r_i is the distance of the i th primary particle from the center of mass. The mobility diameter is the value usually reported in experimental studies because it is relatively easy to measure. The mobility diameter depends in a complex way on the fluid mechanics and/or molecular interactions between the gas and the agglomerate. The radius of gyration is a purely geometric parameter that depends only on the spatial disposition of the particles in the agglomerate.

The mobility diameter is usually measured using a differential mobility analyzer (Chapter 6). In the free molecule range, the mobility diameter measured in this way is not influenced by the direction of the electric field. The Brownian motion will lead to random orientation of the agglomerates, and the mobility diameter will be averaged over all orientations. This diameter should be appropriate for calculations of rates of agglomeration discussed below. However, in the continuum regime, agglomerates may become oriented as they move through the gas under an applied potential. This will affect the measured mobility diameter and may cause error in calculations of rates of agglomeration by Brownian motion, a randomizing phenomenon.

In the free molecule range, the diameter of the sphere with the same projected area as the agglomerate is also important. The relationships among the mobility diameter, the

radius of gyration, and the projected area equivalent diameter for agglomerates have been investigated by Rogak et al. (1993).

Values of the prefactor A calculated from literature data for the free molecule and continuum regimes range from 0.95 to 1.43. Higher values were reported for the transition regime (Wu and Friedlander, 1993a). Values of A with R taken to be the radius of gyration ranged from 1.05 to 1.59 for agglomerates assembled by cluster-cluster aggregation (discussed below). These values were calculated for both the continuum and free molecule regimes. For soot agglomerates formed in a methane-air flame, Cai et al. (1995) found $A = 1.23 \pm 0.07$, in good agreement with previously reported results. In the sections that follow, we discuss the dynamics of agglomerate growth through computer simulation following certain prescribed collision processes, as well as by calculations based on the Smoluchowski equation (Chapter 7).

COMPUTER SIMULATION OF AGGLOMERATE FORMATION

In computer simulation of agglomerate formation, particles released at certain sites in space move in a specified manner until they come into contact. Assumptions are required concerning the nature of the agglomerate motion between collisions and the nature of the collision process. These assumptions may approximate the physics of real agglomerate collisions or may be highly idealized versions of the real processes. Computer simulation provides information on the structure of the agglomerates, from which the fractal dimension can be obtained, as well as information on agglomerate size distributions.

Computational algorithms have been developed to simulate the agglomeration process (Meakin, 1986). Calculations based on these algorithms produce structures whose D_f values tend to approach an asymptotic limit that depends on the algorithm. (There appears to be no proof that such limits exist.) We consider three different types of algorithms, each of which has two subcases. The six examples are illustrated in Fig. 8.3.

Diffusion-Limited Aggregation

We consider first diffusion-limited aggregation (DLA). In the first subcase, a primary particle is set at the origin of a three- or two-dimensional space and held fixed. Another particle is released from a random site in a bounded volume surrounding the fixed particle. The newly released particle undergoes a random walk until it either collides with the fixed particle or wanders out of the volume. Another particle is then released, and the process is repeated indefinitely. Agglomerates generated in this way have a fractal dimension of 2.5 and show a more or less well-defined center.

Aerosol agglomeration is not limited to collisions between primary particles and agglomerates. The second DLA example, cluster-cluster aggregation, allows for collisions among agglomerates. The calculation begins with primary particles distributed on the sites of a three-dimensional lattice. These particles execute a random walk and form agglomerates that also collide to form still larger agglomerates. The resulting structures are chain-like ($D_f = 1.80$) and lack the obvious center of the primary particle-agglomerate structures discussed above.






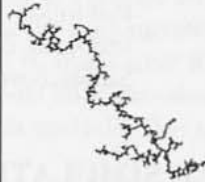
	Reaction-limited	Ballistic	Diffusion-limited
Particle-cluster	 $D_f = 3.00$	 $D_f = 3.00$	 $D_f = 2.50$
Cluster-cluster	 $D_f = 2.09$	 $D_f = 1.95$	 $D_f = 1.80$

Figure 8.3 Comparison of agglomerate structures produced by different computer simulation algorithms (Schaefer, 1988, based on results of Meakin).

Ballistic Aggregation

In ballistic collision processes, the mean free path of the colliding objects is large compared with their size; their motion can be represented by linear trajectories instead of the random walk used in DLA. Primary particles colliding with a fixed agglomerate penetrate more deeply into the interior of the agglomerate than in DLA and produce very compact structures ($D_f = 3.0$).

Ballistic aggregation in which both colliding objects are chain aggregates with linear trajectories form chain-like structures ($D_f \approx 1.95$). As in DLA, collisions between aggregates produce much lower D_f values than primary particles colliding with aggregates. Nanoparticle soot and silica are produced commercially in large quantities as rubber additives and other industrial processes in high-temperature aerosol processes. The structure of the agglomerates produced commercially look similar to the products of cluster-cluster aggregation.

Reaction-Limited Aggregation

In both the diffusion-limited and ballistic models, all collisions lead to attachment. This is usually the case when submicron aerosol particles collide, provided that they do not carry charges of the same size. For hydrosol agglomeration there may be a barrier to particle-particle adhesion resulting, for example, from the electrical double layer. The effect of barriers to adhesion can be simulated in computer calculations by extending the diffusion-limited model to require repeated collisions before sticking. This process, known as reaction-limited aggregation, leads to more compact structures than the diffusion limited or ballistic models. For the primary particle-agglomerate case, D_f approaches 3 while for cluster-cluster aggregation it is closer to 2. The asymptotic value approached by D_f depends on the number of collisions required before sticking occurs.

Coordination Number and Fractal Dimension

An agglomerate coordination number, c_N , can be defined as the average number of contacts of a particle in an agglomerate structure. The coordination number is important to understanding agglomerate mechanical and electronic properties. The value of c_N can also be related to the thermodynamics of agglomerate restructuring discussed at the end of this chapter. Formation of an agglomerate reduces the total surface free energy of a cloud of unattached primary particles by the free energy of the bonds present in the agglomerate.

Information on c_N for agglomerates is scarce compared with the extensive literature on D_f . Like D_f , c_N depends on the computational algorithm that determines the agglomeration process. However, there is not a unique relationship between c_N and D_f except for chain-like structures for which $D_f = 1$ and $c_N = 2$ (neglecting chain ends). For compact agglomerate structures, $D_f = 3$ and c_N can assume much higher values depending on the mechanism of formation and subsequent internal restructuring.

The variation of c_N with N_p was studied in computer simulations of agglomerate formation by several of the processes discussed in the previous section (Weber and Friedlander, 1997a). Using Monte Carlo simulations, agglomerates of primary particles were generated by diffusion-limited aggregation (DLA), chemically limited aggregation, and ballistic aggregation. The lattice type (cubic/hexagonal) for the random walk affected c_N but not D_f . For decreasing sticking probability, c_N and D_f increase because primary particles penetrate more deeply within the agglomerates. The coordination number is also influenced by the number of primary particles per cluster, N_p , as shown in Fig. 8.4. For $N_p < 50$, c_N shows a steep increase with N_p . At larger values of N_p , c_N approaches an asymptotic value that depends on the agglomeration mechanism; the asymptotic behavior is observed for DLA ($D_f = 2.5$) and ballistic ($D_f = 3$) agglomeration. The constant fraction of singly bonded primary particles for a growing cluster indicates that the cluster growth does not occur preferentially at the agglomerate tips.

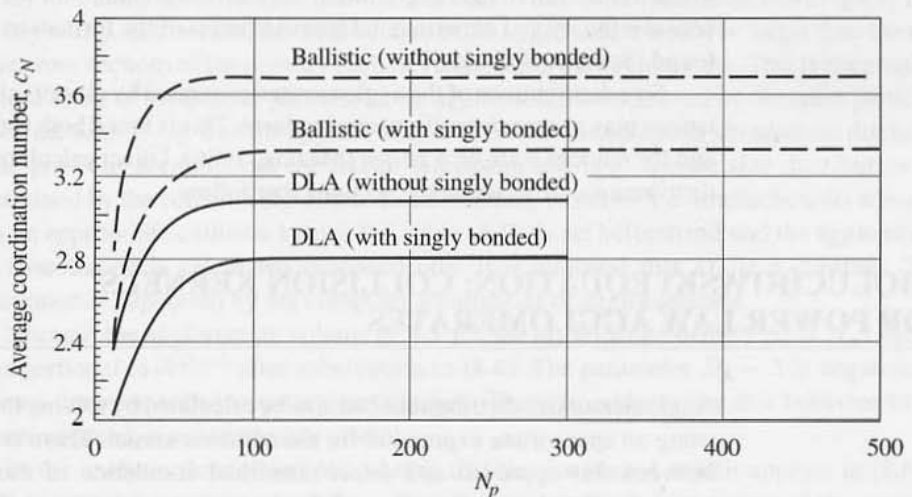


Figure 8.4 Coordination number for ballistic and diffusion-limited aggregation (particle-cluster collisions). (After Weber and Friedlander, 1997a.)

LANGEVIN SIMULATIONS OF AGGLOMERATION

In DLA simulations, the time and length scales are usually not directly linked to particle size and gas properties. A direct link was made by Mountain et al. (1986) in calculations based on the Langevin equation (Chapter 2), which introduces the gas viscosity, temperature, and primary particle diameter (Mountain et al., 1986; Samson et al., 1987). Their calculations of particle trajectories covered both the free molecule and continuum ranges. A random number generator was used to set the initial positions of the particles in a cubical region in space. Initial particle velocities were also set using a random number generator to produce normally distributed numbers such that the particles were in thermal equilibrium with the carrier gas. Periodic boundary conditions were used to eliminate the influence of the surface of the cube on agglomerate motion. The controlling parameter that appears in the Langevin analysis is the particle relaxation time, $\beta^{-1} = m/f$, where m and f are the agglomerate mass and friction coefficient, respectively. The friction coefficient of an agglomerate composed of N_p primary particles of diameter d_{p0} was assumed to be N_p times the coefficient of a single sphere, that is, $f \sim d_{p0}^2 N_p$ based on the friction coefficient for the free molecule range (Chapter 2). In making this approximation, the shielding effect of the other primary particles is neglected so this should hold best for a chain aggregate ($D_f < 2$). Both particle mass and friction coefficient are proportional to N_p so β is independent of the size (N_p) of the agglomerate.

In the free molecule range, the agglomerate moves several particle diameters before changing direction, while in the continuum regime the agglomerate diffuses only a small fraction of a particle diameter before significantly changing direction. The computation takes particle translation into account but not rotation. Studies of a two-dimensional model by other investigators have not shown a significant effect of agglomerate rotation on the fractal dimension. Value of D_f for the agglomerates were determined from a plot of R versus N_p according to (8.4) and ranged from 1.89 to 2.07 in the free molecule range. Calculations for the continuum regime gave values of D_f similar to those for the free molecule range. These values fall in the ranges found for ballistic and random walk DLA. Good agreement between theory and experimental measurements of the formation of soot agglomerates was found (Samson et al., 1987).

Size distributions of the agglomerates generated by cluster-cluster aggregation computations may approach a self-preserving form. This is found both for the Langevin simulations and for random walk on a lattice (Meakin, 1986). Direct calculations of the self-preserving distributions are made in the sections that follow.

SMOLUCHOWSKI EQUATION: COLLISION KERNELS FOR POWER LAW AGGLOMERATES

Agglomerate size distributions can also be calculated by solving the Smoluchowski equation using an appropriate expression for the collision kernel. There is a fundamental difference between this approach and direct numerical simulation of the coagulation process. In computer simulation, the value of D_f is determined by the collision algorithm; analyses based on the Smoluchowski equation require an assumption in advance of the value of

D_f that appears in the collision kernel. In the free molecule range, the basic form of the collision kernel is assumed to be the same as the kinetic theory expression for collision of rigid elastic spheres (Chapter 7)

$$\beta(v_i, v_j) = \pi(d_{pi} + d_{pj})^2 \left(\frac{kT}{2\pi}\right)^{1/2} \left(\frac{1}{m_i} + \frac{1}{m_j}\right)^{1/2} \quad (8.7)$$

where $\pi(d_{pi} + d_{pj})^2$ is the collision cross section for agglomerates of classes i and j , and $(kT/2\pi)^{1/2}[(1/m_i) + (1/m_j)]^{1/2}$ is the average relative velocity between colliding agglomerates. Hence $\beta(v_i, v_j)$ is equivalent to the volume of gas swept out per unit time by colliding agglomerates. The expression for the average relative velocity is based on the assumption that the agglomerates are in thermal equilibrium with the surrounding gas.

The collision cross section for agglomerates is based on the relationship for a power law (fractal-like) agglomerate (8.4) which can also be expressed as follows:

$$N_p = \frac{v}{v_0} = A \left(\frac{R}{a_{p0}}\right)^{D_f} \quad (8.8)$$

where a_{p0} is the radius of a primary particle, v_0 is the primary particle volume ($= 4\pi a_{p0}^3/3$), N_p is the number of primary particles in an agglomerate, and v is the volume of solids in an agglomerate. The statistically determined value for R averaged over many agglomerates of size N_p (or v) is used as the collision radius in (8.7). That is, if the fractal dimension of the agglomerates is between 2 and 3, the planar projections of the agglomerate cross sections are given by

$$\text{cross section} \sim (R_i + R_j)^2 \quad (8.9)$$

or, with (8.8),

$$\text{cross section} \sim (i^{1/D_f} + j^{1/D_f})^2 \quad (2 \leq D_f \leq 3) \quad (8.10)$$

For $D_f < 2$ and $j \gg i$, the cross section calculated from (8.10) increases more rapidly than linearly with j . In that case, the cross section of the agglomerate would be larger than the sum of the cross sections of the primary particles composing the agglomerate. This is not possible because some of the interior particles in the agglomerate are screened by the outer particles. Hence the limit $D_f \geq 2$ on the applicability of (8.10). In the computer simulations discussed in the previous section, both the fractal dimension and agglomerate size distribution are determined by the collision algorithm. In calculations based on the Smoluchowski equation with an appropriate collision kernel, the value of D_f is set beforehand and the agglomerate size distribution is calculated independently. It is assumed that D_f is a constant. This assumption is supported by the computer simulations of agglomeration.

Because the agglomerate volume is $4/3\pi R^3$, the agglomerate density $\rho_a = N_p/4/3\pi R^3$ is proportional to R^{D_f-3} after substitution in (8.4). The parameter $D_f - 3$ is negative, so ρ_a must decrease with increasing particle size. There is evidence for this behavior in the numerical simulations of Meakin (1983).

In the analysis that follows we assume that the constant A which appears in (8.8) is equal to unity to simplify calculations. This amounts to the incorporation of the constant into the prefactor of $\beta(v_i, v_j)$. This assumption is easily corrected if better information on

the value of A is available. When we substitute (8.8) and (8.10) with $A = 1$ into (8.7), the collision kernel in the free molecule regime for agglomerate particles obeying a power law relationship becomes

$$\beta(v_i, v_j) = \left(\frac{6kT}{\rho}\right)^{1/2} \left(\frac{3}{4\pi}\right)^\lambda a_{p0}^{2-6/D_f} \left(\frac{1}{v_i} + \frac{1}{v_j}\right)^{1/2} \left(v_i^{1/D_f} + v_j^{1/D_f}\right)^2 \quad (R \ll \ell_p) \quad (8.11)$$

where

$$\lambda = \frac{2}{D_f} - \frac{1}{2}$$

For coalescing spheres, $D_f = 3$ and this expression reduces to (7.17) for classical coagulation (coalescing particles).

Equation (8.11) may not be valid for collisions of a large particle with a small particle. Hagenlocher and Friedlander (1989) showed that the collision diameter for collisions between point particles and DLA clusters is a function of Kn (based on primary particle size) as well as D_f . In the present analysis it is assumed that the collision diameter scales with D_f only. Because the collision rate between large agglomerates and primary particles is high, the supply of primary particles is rapidly depleted. The effect of Kn is thus most important during the early stages of coagulation. As discussed above, (8.11) is not valid for $D_f < 2$ in the free molecule regime. Mulholland et al. (1988) and Jullien and Meakin (1989) have proposed alternative forms for the collision kernel in this range.

In the continuum regime, the collision kernel for agglomerates is based on the Smoluchowski expression derived in Chapter 7:

$$\beta(v_i, v_j) = 4\pi(d_{pi} + d_{pj})(D_i + D_j) \quad (8.12)$$

where d_{pi} is the collision diameter for power law agglomerates. For $N_p \gg 1000$, the agglomerate diffusion coefficients D_i approach the Stokes–Einstein value for a solid (impermeable) sphere with diameter equal to the collision diameter d_{pi} (Tandon and Rosner, 1995). Hence for power law agglomerates the collision kernel becomes

$$\beta(v_i, v_j) = \frac{2kT}{3\mu} \left(\frac{1}{v_i^{1/D_f}} + \frac{1}{v_j^{1/D_f}}\right) \left(v_i^{1/D_f} + v_j^{1/D_f}\right) \quad (N_p \gg 1000) \quad (8.13)$$

Example: Compare the collision frequencies of agglomerates in the free molecule range with the corresponding frequency for spherical particles of the same mass (volume).

SOLUTION: Referring to (8.11), the ratio of $\beta_{\text{agg}}/\beta_{\text{sph}}$ for $v_i = v_j = v$ is

$$\frac{\beta_{\text{agg}}}{\beta_{\text{sph}}} = a_{p0}^{2-6/D_f} v^{\frac{2}{D_f} - \frac{1}{3}}$$

where we have assumed that $A = 1$ for the agglomerates. Substituting (8.8) with $v_0 = \frac{4}{3}\pi a_{p0}^3$ into this expression gives

$$\frac{\beta_{\text{agg}}}{\beta_{\text{sph}}} = \left(\frac{4}{3}\pi\right)^{\left(\frac{2}{D_f} - \frac{2}{3}\right)} \left(\frac{R}{a_{p0}}\right)^{(2 - \frac{2}{3}D_f)}$$

For $D_f = 2$, $a_{p0} = 2$ nm and $R = 40$ nm, $\beta_{\text{agg}}/\beta_{\text{sph}} = 11.8$. That is, the agglomerate collision rate is about 12 times higher than the corresponding collision rate for compact spheres of the same mass. This illustrates the very important effect of reducing fractal dimension on agglomerate collision rate.

SELF-PRESERVING AGGLOMERATE SIZE DISTRIBUTIONS

The collision kernels for power law agglomerates, (8.11) and (8.13), are homogeneous functions of the volumes of the colliding particles:

$$\beta(\alpha v_i, \alpha v_j) = \alpha^\lambda \beta(v_i, v_j) \quad (8.14)$$

where i and j are the number of primary particles in the agglomerates, and λ is the degree of homogeneity. By (8.8) and (8.11) we obtain

$$\lambda = \frac{2}{D_f} - \frac{1}{2} \quad (8.15)$$

for the free molecule regime and by (8.13) we have $\lambda = 0$ for the continuum regime, hence independent of D_f . The homogeneity property makes it possible to use the self-preserving scaling theory (Chapter 7) to solve for the asymptotic size distribution of power law agglomerates. The results have the advantage of providing simple relationships, easy to interpret and test, for the dependence of the particle size distribution function and its moments on time, aerosol volumetric loading, temperature, primary particle size, and D_f . As noted above, the value of D_f is set independently; it cannot be derived in this calculation without making some additional assumption.

The basic self-preserving equations are derived by introducing variables similar to those used in the theory for coalescing particles:

$$n(v) = \frac{N_\infty^2}{\phi} \psi(\eta) \quad (8.16)$$

where

$$\begin{aligned} \eta &= v/\bar{v} \\ \bar{v} &= \phi/N_\infty \end{aligned}$$

and v is the *volume of solids* in the agglomerate particle. As in classical self-preserving theory, it is assumed that the volumetric concentration of solids, ϕ , is constant. This assumption can be relaxed in certain cases, such as condensation when the condensation rate follows certain special relationships.

The rate of decay of particle number density N_∞ is given by

$$\frac{dN_\infty}{dt} = -\frac{1}{2} \int_0^\infty \int_0^\infty \beta(v_i, v_j) n_i n_j dv_i dv_j \quad (8.17)$$

This expression can be evaluated for the self-preserving distribution (SPD) in the free molecule regime by substituting (8.11) for the collision kernel and (8.16) for $n(v)$ in (8.17) to give

$$\frac{dN_\infty}{dt} = -\frac{1}{2} ac\phi^\lambda N_\infty^{2-\lambda} \quad (8.18)$$

where

$$c = \left(\frac{6kT}{\rho}\right)^{1/2} \left(\frac{3}{4\pi}\right)^\lambda a_{p0}^{(2-6/D_f)} \quad (8.19)$$

and the dimensionless collision integral a is

$$a = \int_0^\infty \int_0^\infty \left(\frac{1}{\eta_i} + \frac{1}{\eta_j}\right)^{1/2} \left(\eta_i^{1/D_f} + \eta_j^{1/D_f}\right)^2 \psi_i \psi_j d\eta_i d\eta_j \quad (8.20)$$

To evaluate a it is necessary to solve for the SPD, which depends on D_f . Values of a for the free molecule regime vary little with D_f in the range 2 to 3 as shown in Table 8.1, along with the $1/D_f$ moment of the size distribution function, μ_{1/D_f} . For $D_f \neq 3$, c is a function of the size of the primary particle, a_{p0} .

The SPD for agglomerates in the free molecule range has been calculated by Wu and Friedlander (1993a) using a Monte Carlo method; it also has been calculated by Vemury and Pratsinis (1995), who used a discrete sectional method and also calculated the SPD for the continuum range. For the free molecule case (Fig. 8.5), the SPD becomes broader with decreasing D_f , while the continuum distribution narrows with decreasing D_f . Because it is assumed that D_f is constant, λ , c and a are also constant. If D_f is a slowly varying function of time, the analysis can still be carried out, approximately, provided that the time to reach the SPD is short. The calculations made previously are limited to the range $2 \leq D_f \leq 3$ for the free molecule collision kernel. As discussed above, computer simulations for cluster-cluster aggregation and experimental measurements indicate that D_f is usually somewhat less than 2.

Time to Reach the Self-Preserving Form

The time required for an initially monodisperse aerosol to reach the self-preserving distribution is shown in Fig. 8.6 as a function of D_f for the free molecule and continuum

TABLE 8.1
Moments of the Self-Preserving Size Distributions (Wu and Friedlander, 1993b)

	D_f				
	2.0	2.2	2.5	2.8	3.0
μ_{1/D_f}	0.827	0.843	0.867	0.886	0.896
a	7.037	6.748	6.607	6.560	6.552

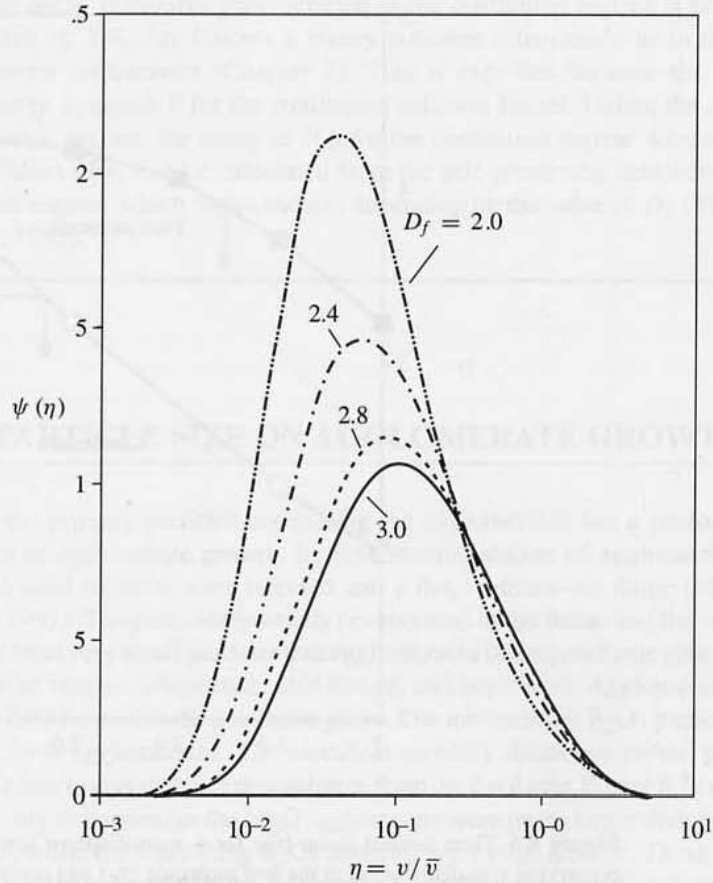


Figure 8.5 Self-preserving size distributions of agglomerates of various D_f in the free molecule regime. Values of ψ_η and η are tabulated in the original reference. (After Vemury and Pratsinis, 1995.)

ranges. The criterion for attaining the SPD is that the geometric standard deviation (GSD) of the distribution should be 99% of the GSD for the SPD. In the free molecule regime the time is

$$\tau_f = \frac{1}{N_\infty(0)} \left(\frac{4\pi}{3} \right)^{1/6} \left(\frac{\rho}{6kT a_{p0}} \right)^{1/2} \quad (8.21)$$

and in the continuum regime it is

$$\tau_c = \frac{3\mu}{2kTN_\infty(0)} \quad (8.22)$$

where $N_\infty(0)$ refers to the initial number concentration. In the free molecule range, τ_f decreases from 4.31 for $D_f = 3$ to 3.24 for $D_f = 2$; in the continuum regime, τ_c decreases from 12.68 for $D_f = 3$ to 5.8 for $D_f = 2$. Thus in both cases, agglomerates reach the self-preserving distribution faster than the equivalent spherical particles.

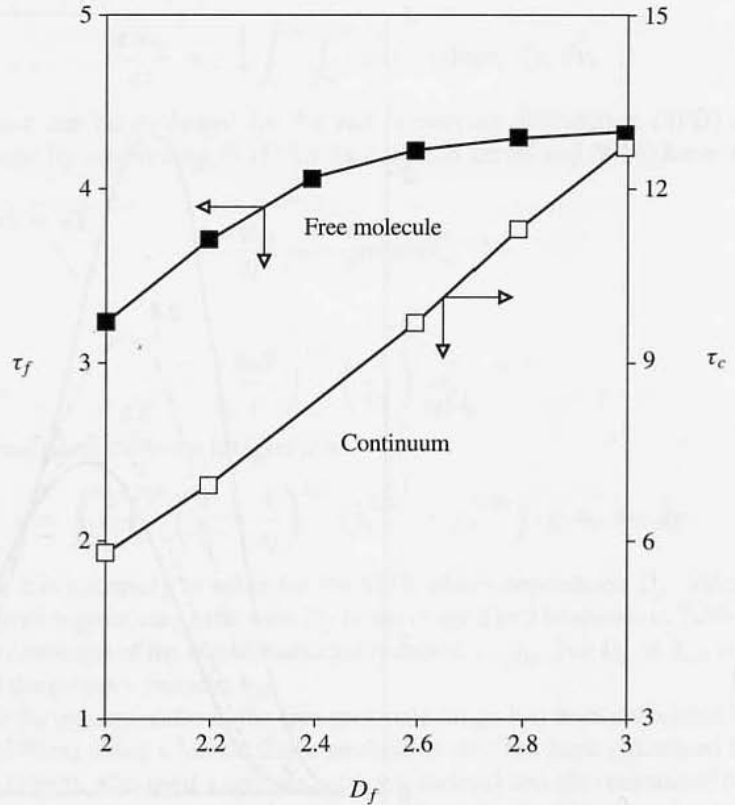


Figure 8.6 Time needed (time lag) for a monodisperse aerosol to reach the corresponding self-preserving size distribution in the free molecule (τ_f) and continuum (τ_c) regimes as a function of its fractal dimension, D_f . (After Vemury and Pratsinis, 1995.)

Example: Derive an expression for the change in the number density with time for the self-preserving distribution in the continuum regime.

SOLUTION: Substituting the continuum collision kernel (8.13) in (8.17) gives

$$\frac{dN_\infty}{dt} = -\frac{kT}{3\mu} \int_0^\infty \int_0^\infty \left(\frac{1}{v^{1/D_f}} + \frac{1}{\bar{v}^{1/D_f}} \right) (v^{1/D_f} + \bar{v}^{1/D_f}) n(v)n(\bar{v}) dv d\bar{v}$$

Introducing the self-preserving variables (8.16), we obtain

$$\frac{dN_\infty}{dt} = -\frac{kT a_1}{3\mu} N_\infty^2$$

where the collision integral a_1 is

$$a_1 = \int_0^\infty \int_0^\infty \left(\frac{1}{\eta^{1/D_f}} + \frac{1}{\bar{\eta}^{1/D_f}} \right) (\eta^{1/D_f} + \bar{\eta}^{1/D_f}) \psi(\eta)\psi(\bar{\eta}) d\eta d\bar{\eta}$$

Hence the decay in number concentration in the continuum regime is proportional to N_∞^2 ; that is, dN_∞/dt follows a binary collision relationship as in the case of instantaneous coalescence (Chapter 7). This is expected because the degree of homogeneity, λ , equals 0 for the continuum collision kernel. Unlike the case of the free molecule regime, the decay in N_∞ for the continuum regime does not depend on a_{p0} . Values of a_1 can be calculated from the self-preserving distribution for the continuum regime, which varies in form depending on the value of D_f (Vemury and Pratsinis, 1995).

EFFECT OF PRIMARY PARTICLE SIZE ON AGGLOMERATE GROWTH

The size of the primary particles composing the agglomerates has a profound effect on the dynamics of agglomerate growth. In experimental studies of agglomerate formation, micron-sized solid particles were injected into a flat, methane-air flame (Matsoukas and Friedlander, 1991). The particles (partially) evaporated in the flame and the vapors reacted (oxidized) to form very small particles that agglomerated in the postflame gases. The aerosol precursors were magnesium acetate, zinc nitrate, and boric acid. Agglomerates composed of MgO and ZnO formed in the postflame gases. The low-melting B_2O_3 particles coalesced and did not form agglomerates. The electrical mobility diameters of the particles were measured as a function of distance downstream from the flat flame. Figure 8.7a shows that the average mobility diameters for the MgO agglomerate were much larger than that of the ZnO agglomerates, while the coalescing B_2O_3 particles were even smaller. These experimental results can be explained qualitatively by an analysis of the dynamics of agglomeration based on the results of the self-preserving theory derived in the previous section.

The analysis is limited to the free molecule range. Substituting (8.8) and (8.16) into (8.18) and integrating, the increase in the number average volume $\bar{v} = \phi/N_\infty$ with time is

$$\bar{v} = \left[v_0^{1-\lambda} + \frac{1-\lambda}{2} ac\phi t \right]^{1/(1-\lambda)} \quad (8.23)$$

The corresponding value for the average radius is

$$\bar{R} = \left[a_{p0}^{1/z} + \frac{1-\lambda}{2} \left(\frac{6kT}{\rho} \right)^{1/2} \left(\frac{3}{4\pi} \right) a_{p0}^{(3D_f-9)/2} a\phi t \right]^z \quad (8.24)$$

where the exponent z is

$$z = \frac{1}{D_f(1-\lambda)}$$

The expressions (8.23) and (8.24) for \bar{v} and \bar{R} cannot hold for short times when the agglomerates are composed of few primary particles, before the power law structure is established. However, these expressions can be used to examine qualitatively the transition from small to large agglomerates as shown in Fig. 8.7b. The results indicate that there is a

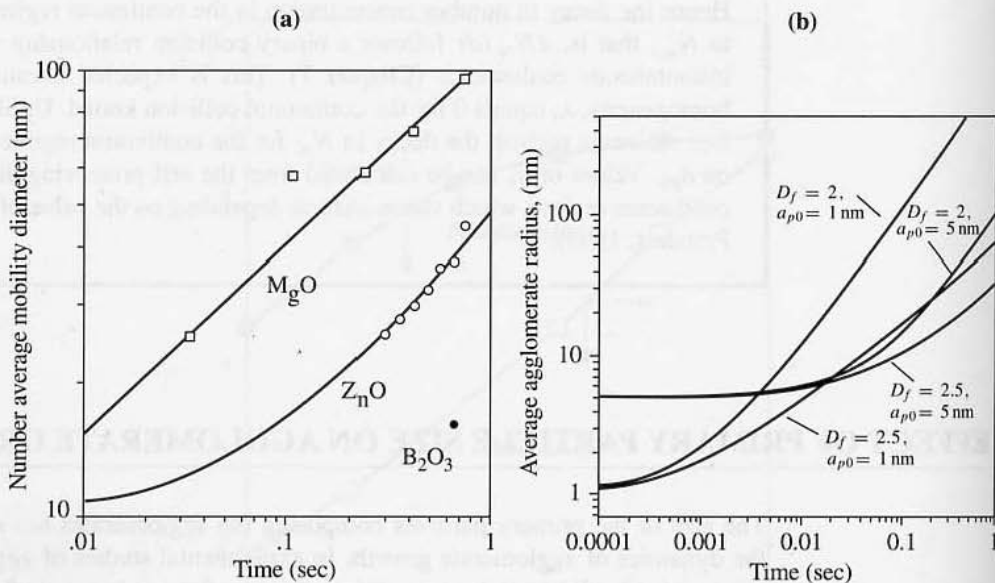


Figure 8.7 (a) Time evolution of the number average electrical mobility diameter for several inorganic oxide aerosols. The MgO agglomerates were larger than ZnO agglomerates but were composed of smaller primary particles. Only one data point was obtained for low-melting boric oxide particles that coalesce to form small spherical particles instead of agglomerates. (After Matsoukas and Friedlander, 1991.) (b) Calculations based on (8.24) show that agglomerates composed of small primary particles (radius = a_{p0}) grow much more rapidly than agglomerates of larger a_{p0} for the same ϕ , D_f , and T . This results in a crossover of the two growth curves. Results apply to the free molecule regime. The analysis breaks down as the number of particles in the agglomerate approaches unity ($\bar{R} \rightarrow a_{p0}$). The crossover takes place in the first two time decades not accessible in the experiments shown in part (a).

crossover point for the curves for different initial particle sizes. Agglomerates of very small primary particles (1-nm radius) grow much more rapidly than larger (5-nm radius) particles of the same fractal dimension. These results hold for the free molecule range.

For long times ($R \gg a_{p0}$), the rate of growth of the number average volume can be approximated by

$$\bar{v} \sim a_{p0}^{4q/3} (T^{1/2} \phi t)^{1/(1-\lambda)} \quad (8.25)$$

based on (8.23), and the average agglomerate radius can be approximated by

$$\bar{R} \sim a_{p0}^q (T^{1/2} \phi t)^z \quad (\bar{R} \gg a_{p0}) \quad (8.26)$$

based on (8.24) with

$$q = \frac{D_f - 3}{D_f - 4/3} \quad (8.26a)$$

When $D_f = 3$, the exponent q is zero, and the agglomerate size is independent of the

primary particle size. This is the case for coalescing particles discussed in Chapter 7. When $D_f < 3$, q is negative (Fig. 8.9). For the same values of T , ϕ , D_f , and t , larger agglomerates are formed from smaller primary particles. The effect of primary particle size becomes more important with decreasing D_f because the magnitude of q increases. When $D_f = 2$, $q = -3/2$ and the primary particle size has a major influence on the growth of agglomerates.

The experiments with MgO and ZnO agglomerates (Fig. 8.7a) lend qualitative support to this analysis. A transmission electron photomicrograph of the MgO aerosol showed large agglomerates composed of small primary particles about 5 nm in diameter. The appearance of the ZnO aerosol was quite different. The ZnO agglomerates were much smaller than the MgO particles but were composed of larger primary particles about 10 nm in diameter. Similar effects have been observed for the agglomerates produced by industrial aerosol reactors (Ulrich, 1984).

In the continuum regime the effect of the primary particle size on agglomerate growth is not as strong as in the free molecule regime. From a similar analysis for the continuum collision kernel (8.13), $q = 1 - 3/D_f$. The exponent is still negative but a weaker function of D_f (Fig. 8.8). In the continuum regime, the enhancement resulting from the increased radius of capture is balanced by the smaller mobility of the cluster. The average volume \bar{v} grows linearly with time and is independent of the fractal dimension or the primary particle size. The average agglomerate radius \bar{R} , however, is related to D_f and a_{p0} through (8.8).

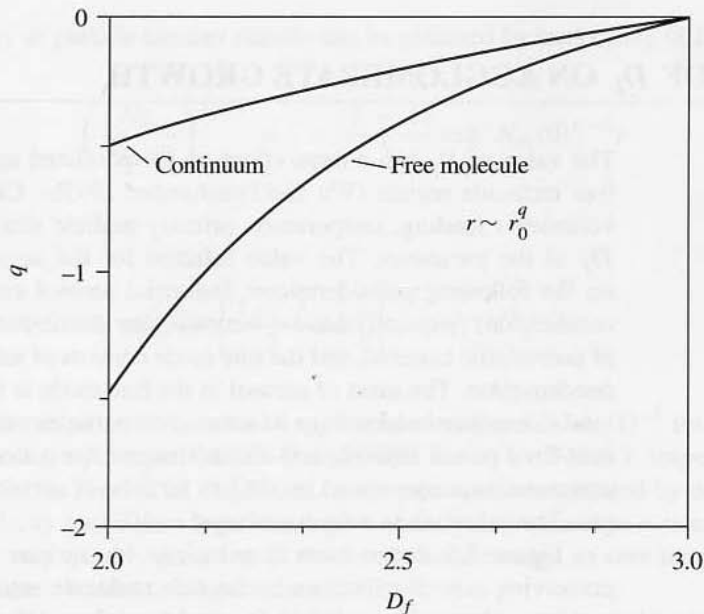


Fig. 8.8 The dependence of the exponent q on D_f for agglomeration in the free molecule regime is much more sensitive than in the continuum regime. (After Matsoukas and Friedlander, 1991.)

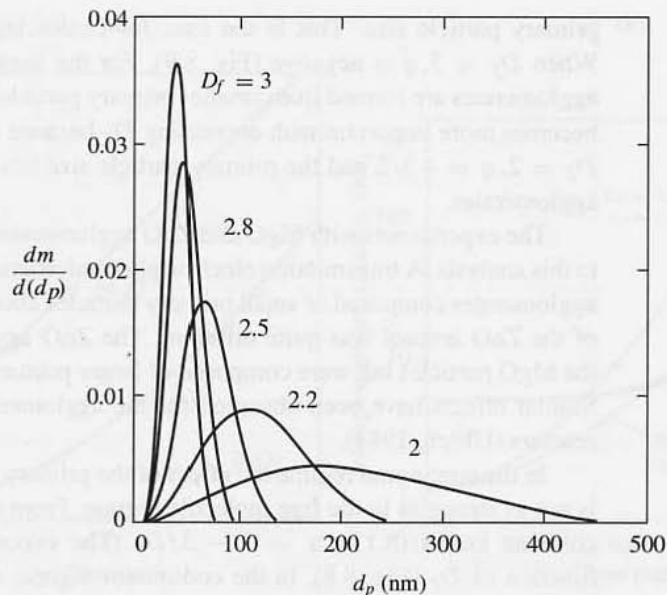


Figure 8.9 The size distribution for $D_f = 3$ is narrow, while that for $D_f = 2$ is much broader and includes a high proportion of larger particles. (Results calculated for $a_{p0} = 5$ nm, $\phi = 10^{-8}$, $T = 1500$ K, $\rho_p = 2$ g/cm³, $t = 0.5$ sec.) (After Wu and Friedlander, 1993b.)

EFFECT OF D_f ON AGGLOMERATE GROWTH

The value of D_f has a large effect on the predicted agglomerate size distribution in the free molecule regime (Wu and Friedlander, 1993b). Calculations were made for a given volumetric loading, temperature, primary particle size, and time of agglomeration with D_f as the parameter. The value selected for the aerosol volume loading ϕ was based on the following considerations: Industrial aerosol emissions, such as those from coal combustion, frequently have a bimodal size distribution. The coarse mode is composed of nonvolatile material, and the fine mode consists of submicron particles formed by vapor condensation. The mass of aerosol in the fine mode is typically on the order of 1% of the total mass. Aerosol loadings of submicron particles range between 1 and 400 mg/m³ for coal-fired power stations, and about 7 mg/m³ for a steel plant. On a volume basis, these concentrations correspond to 10^{-9} to 10^{-7} cc of aerosol material per cubic centimeter of gas. The calculations were based on $\phi = 10^{-8}$.

Figure 8.9 shows mass distributions for various values of D_f , based on the self-preserving size distributions in the free molecule regime. For the same conditions and residence time, a low value of D_f produces a broad distribution with a high proportion of mass at large particle sizes. The growth in the mass median diameters with time are shown in Fig. 8.10 with D_f as the parameter.

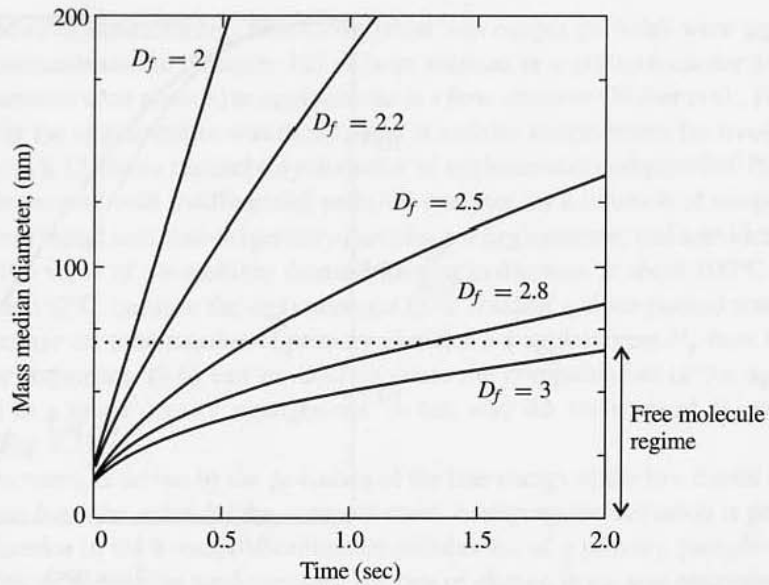


Figure 8.10 The growth rate of the mass median diameter is much greater for low values of D_f , due to the increased collision cross section (results are for $a_{p0} = 5$ nm, $\phi = 10^{-8}$, $T = 1500$ K, $\rho_p = 2$ g/cm³). (After Wu and Friedlander, 1993b.)

The decay of particle number density can be obtained by integrating (8.18):

$$\left(\frac{N_\infty}{N_\infty(0)}\right)^{\lambda-1} = 1 + \frac{(1-\lambda)}{2} ac\phi^\lambda N_\infty(0)^{1-\lambda} t \quad (8.27)$$

For $t \rightarrow \infty$

$$N_\infty \rightarrow \left[\frac{1-\lambda}{2} ac\phi^\lambda\right]^{1/(\lambda-1)} t^{1/(\lambda-1)} \quad (8.27a)$$

Thus a logarithmic plot of N_∞ versus t approaches a slope of $(\lambda - 1)^{-1}$ for large t . This corresponds to asymptotic values of -2 and $-6/5$ for $D_f = 2$ and 3 , respectively, after 0.3 sec (Fig. 8.11). The fractal dimension can in principle be estimated by measuring the slope of the decay curve on a logarithmic plot of the particle number concentration. The agglomerates very quickly grow out of the free molecule range so care must be taken in extrapolating these results to longer times.

In these analyses, it has been assumed that the power law exponent (fractal dimension) is constant during the agglomeration process. This is not necessarily the case as the experimental observations discussed in the next section show.

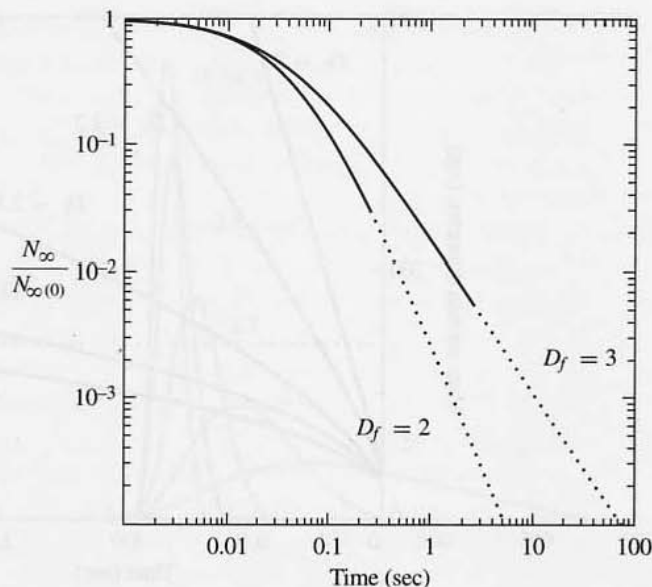


Figure 8.11 The decay of particle number density rapidly approaches the asymptotic slope of -2 and $-6/5$ for $D_f = 2$ and $D_f = 3$, respectively. The solid portion of the curves represent the free molecule regime (results are for $a_{p0} = 5$ nm, $\phi = 10^{-8}$, $T = 1500$ K, $\rho_p = 2$ g/cm³). (After Wu and Friedlander, 1993b.)

AGGLOMERATE RESTRUCTURING

Agglomerates formed by the processes discussed in this chapter do not have rigid structures. Their form may change due to (a) condensation and evaporation of vapor, (b) heating, and (c) mechanical stresses. The ability of aggregates to change their shape has important implications for aggregate transport and light scattering, as well as for the use of nanoparticles in the fabrication of new materials. In this section, we discuss thermal restructuring and rearrangement under tension.

Thermal Restructuring

When nanoparticle agglomerates are heated *in situ* (i.e., while suspended in the gas), there are two limiting types of behavior. On one hand, agglomerates of strongly bonded particles may retain their general structure (expressed by the fractal dimension) during heating. In this case, the size of the agglomerates decreases while the mean size of the subunits (e.g., thickness of the dendrites or primary particle size) increases as a result of melting of smaller particles (Sempéré et al., 1993). On the other hand, agglomerates of weakly bonded primary particles tend to restructure and become more compact (higher D_f) when heated (Schmidt-Ott, 1988).

In studies of restructuring, nanometer silver and copper particles were produced by evaporation/condensation (Chapter 12) or laser ablation in a nitrogen carrier gas, and the primary particles were allowed to agglomerate in a flow chamber (Weber et al., 1997b). The gas carrying the agglomerates was then heated at various temperatures for fixed residence times. Figure 8.12 shows the mobility diameter of agglomerates composed of 16-nm silver particles, measured with a differential mobility analyzer, as a function of temperature for four different initial size classes (primary particles per agglomerate) and a residence time of 3.12 sec. The value of the mobility diameter begins to decrease at about 100°C and levels off at about 350°C, because the agglomerates have reached a close-packed state with D_f near 3. Because the total number of primary particles per agglomerate N_p does not change during rearrangement, (8.6) can be used to relate the compact state of the agglomerate ($D_f = 3$) to a lower density arrangement. In this way the variation of D_f with T was obtained (Fig. 8.13).

Restructuring is driven by the deviation of the free energy of the low fractal dimension agglomerate from the value for the compact state. Assuming the deviation is proportional to the difference in the average coordination number c_N of a primary particle in the low and high fractal dimension agglomerates, the rate of change in c_N was estimated from the change in D_f . This is shown in Fig. 8.14 as a function of $1/T$ for silver agglomerates. The results indicate that restructuring is an activated process, and the activation energy for restructuring was calculated from the slope of the curve. The activation energy was independent of the number of primary particles per agglomerate, which ranged from 19 to 270.

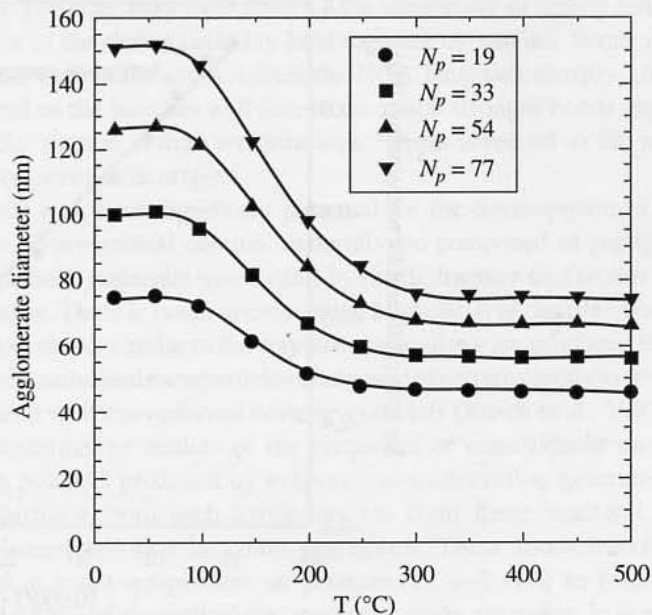


Figure 8.12 Mobility diameter of agglomerates composed of 16-nm silver particles decreases as a result of *in situ* heating at constant temperature. (After Weber and Friedlander, 1997b.)

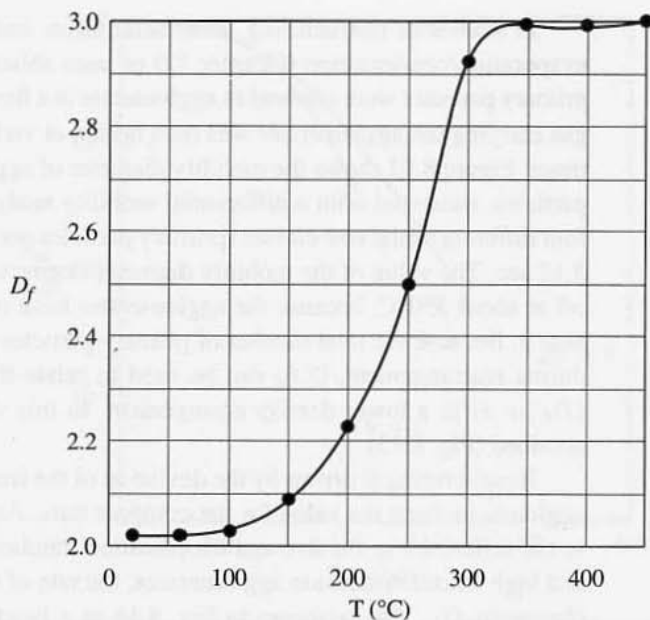


Figure 8.13 Variation of D_f with temperature for agglomerates heated at a given temperature and a residence time of 3.12 sec. (After Weber and Friedlander, 1997b.)

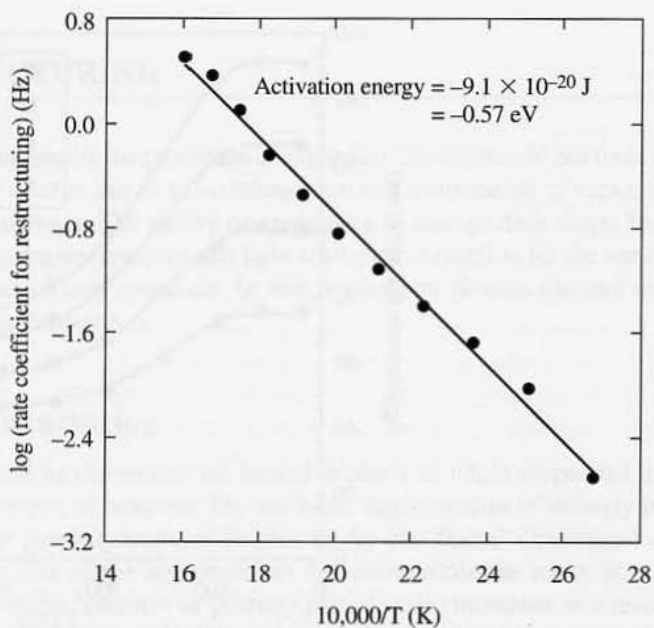


Figure 8.14 Rate of restructuring of silver particles follows an Arrhenius form with a characteristic energy of restructuring. (After Weber and Friedlander, 1997b.)

The activation energies for silver and copper were, respectively, about the same and an order of magnitude lower than the bond energies calculated from the bulk Hamaker constants and an assumed spacing between primary particles. This suggests that restructuring probably occurs when agglomerate branches rotate around the weakest bonds, and not from single primary particles detaching and relocating. Branch rotation may be lubricated by enhanced rates of solid state diffusion in the high-surface-energy regions near the necks connecting the particles. This effect is promoted by increasing temperature because solid-state diffusion is an activated process (Chapter 12).

Restructuring under Tension: Elastic Properties of Chain Aggregates

Nanoparticle chain aggregates (NCAs) of titania stretch under tension and contract when the tension is relaxed (Friedlander et al., 1998). Titania NCAs were generated by thermal decomposition of titanium tetraisopropoxide vapor in a nitrogen stream at 800°C. The chain aggregate fractal dimension was about 2.3 and the individual (primary) particle size about 7 nm. Chain aggregates a few hundred nanometers long were deposited on an electron micrograph grid and were observed in the electron microscope. By focusing on an individual NCA, a hole was produced in the carbon film on the grid due to localized evaporation. The NCA stretched across the expanding hole in the film. After stretching up to 90%, the NCA broke loose at one end and contracted to a tightly folded chain on the other side of the hole (Fig. 8.15). The stretching took place by the unraveling of tightly bunched clumps of primary particles in the chains probably held together by van der Waals forces. Once the chain straightens, the tensile stress within the NCA increases sharply, shifting from van der Waals control as the bunches pull out, to the much stronger bonds expressed through the particle necks formed at high temperatures. Forces involved in the strong bonds are probably ionic or covalent in origin.

These results may have significant potential for the development of ductile or even elastic ceramics. Conventional ceramic materials are composed of particles much larger than 1 to 10 μm . Such materials usually fail by brittle fracture that occurs with little or no plastic deformation. There is much interest in the fabrication of ductile ceramics that can be formed to near net shape, similar to the way that metal alloys are produced in industry. There is evidence that consolidated nanoparticles composed of certain metal oxides show enhanced ductility compared with conventional ceramic materials (Karch et al., 1987; Siegel, 1994). Many of the experimental studies of the properties of consolidated nanoparticles have been made with powders produced by evaporation/condensation generators (Chapter 12). Typically the particles from such generators (as from flame reactors) are low fractal dimension agglomerates—that is, chain aggregates. These loose fractal structures can be consolidated at room temperature at pressures of 1–2 GPa to form compacts with densities 75% to 85% of theoretical for inorganic oxide ceramics. It is reported that the voids can be removed at high pressures and temperatures with little increase in primary particle size.

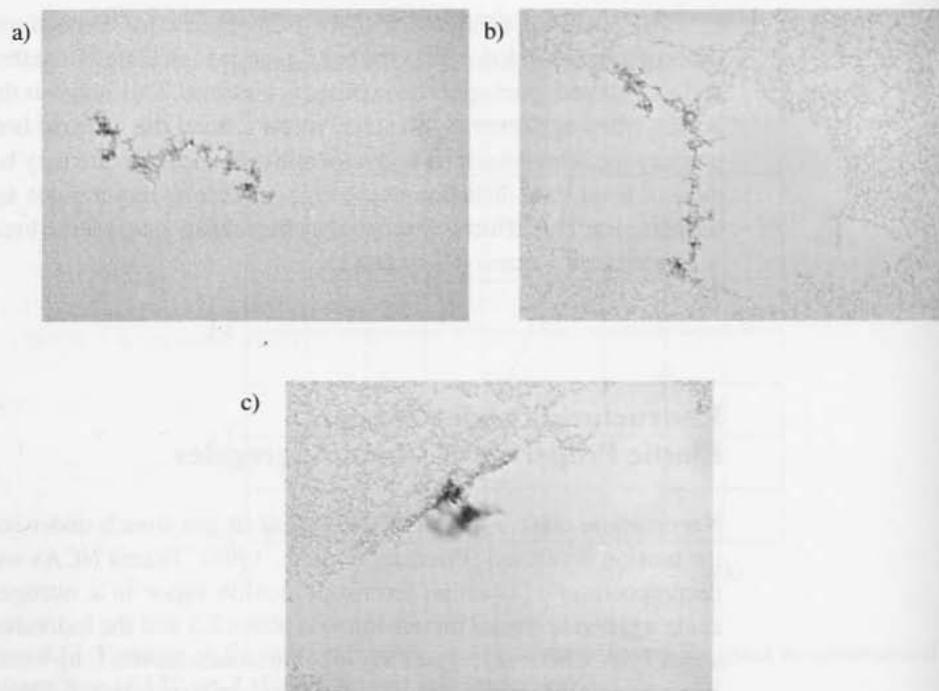


Figure 8.15 (a) Initial shape of a titania NCA deposited on the carbon film. (b) Stretched NCA connecting the sides of the carbon film in which a hole with receding edges has developed. (c) Contracted NCA that is vibrating (seen as a blur) at one side of the carbon film after disconnecting from the other side. A portion of the NCA embedded in the film remains in focus. Parts (a), (b), and (c) show the same NCA. The exposure time was about 4 sec (Friedlander et al., 1998).

PROBLEMS

8.1 A power law (fractal-like) agglomerate grows according to an algorithm that generates a structure with $D_f = 2$. The radius of gyration of the agglomerate, R_g , equals $1 \mu\text{m}$; the primary particle size, d_{p0} , equals 5 nm ; and the prefactor, A , equals 1.23 .

- What is the total number of primary particles in the agglomerate?
- The agglomerate is heated and coalesces to form a spherical particle. What is the radius of the particle?
- If d_{p0} is doubled what is the new value of R_g ? Assume the same growth algorithm for large and small primary particles; the number of particles remains the same.
- An agglomerate with $R_g = 0.5 \mu\text{m}$ composed of the same primary particles ($d_{p0} = 5 \text{ nm}$) with the same D_f collides and sticks to the original $R_g = 1 \mu\text{m}$ agglomerate. What is the new value of R_g , assuming that D_f is preserved?

8.2 The density of an agglomerate is the ratio of the mass of the primary particles that compose the agglomerate to the volume of the agglomerate. The agglomerate volume can be related to the

radius R that appears in the power law expression, by a suitable definition of the volume. The agglomeration process corresponds to an increase in N_p with time. Show how the agglomerate density changes as N_p increases.

8.3 Derive an expression for the change in total particle concentration dN_∞/dt for a cloud of monodisperse agglomerates in the free molecule regime.

8.4 According to the analysis in this chapter, for given values of T , ϕ , D_f and t , larger agglomerates are formed from smaller primary particles. This means that curves that show the size of the agglomerate \bar{R} as a function of time for two different values of a_{p0} must cross. Show this phenomenon by plotting \bar{R} as a function of t for $a_{p0} = 3$ and 30 nm, taking $\phi = 10^{-8}$, $T = 1500$ K, and $\rho_p = 2$ g/cm³.

8.5 Plot agglomerate radius as a function of primary particle radius in the long time limit ($\bar{R} \gg a_{p0}$), over the range 5 nm $< a_{p0} < 50$ nm. Take $\phi = 10^{-8}$, $D_f = 2$, $\rho_p = 2$ g/cm³, and $T = 1500$ K.

REFERENCES

- Cai, J., Lu, N., and Sorensen, C. M. (1995) *J. Colloid Interface Sci.*, **171**, 470.
- Family, F., and Landau, D. (Eds.) (1984) *Kinetics of Aggregation and Gelation*, North Holland, Amsterdam.
- Forrest, S. R., and Witten, T. A., Jr. (1979) *J. Phys. A: Math. Gen.* **12**, L109.
- Friedlander, S. K., Jang, H. D., and Ryu, D. H. (1998) *Appl. Phys. Lett.*, **72**, 173.
- Hagenlocher, R., and Friedlander, S. K. (1989) *J. Colloid Interface Sci.* **133**, 185.
- Jullien, R., and Meakin, P. (1989) *J. Colloid Interface Sci.* **127**, 265.
- Karch, J., Birringer, R., and Gleiter, H. (1987) *Nature (London)* **330**, 556.
- Kolb, M., Botet, R., Jullien, R., and Herrmann, H. J. (1986) in Stanley, H. E., and Ostrowsky, N. (Eds.), *On Growth and Form*, Martinus Nijhoff, Dordrecht, The Netherlands.
- Matsoukas, T., and Friedlander, S. K. (1991) *J. Colloid Interface Sci.* **146**, 495.
- Meakin, P. (1983) *Phys. Rev. Lett.*, **51**, 1119.
- Meakin, P. (1986) in Stanley, H. E. and Ostrowsky, N. (Eds.) *On Growth and Form*, Martinus Nijhoff, Dordrecht, The Netherlands.
- Megaridis, C. M., and Dobbins, R. A. (1990) *Combust. Sci. Technol.* **71**, 95.
- Mountain, R. D., Mulholland, G. W., and Baum, H. (1986) *J. Colloid Interface Sci.*, **114**, 67.
- Mulholland, G. W., Samson, R. J., Mountain, R. D., and Ernst, M. H. (1988) *Energy & Fuels* **2**, 481.
- Rogak, S. N., Flagan, R. C., and Nguyen, H. V. (1993) *Aerosol Sci. Technol.*, **18**, 25.
- Samson, R. J., Mulholland, G. W., and Gentry, J. W. (1987) *Langmuir* **3**, 272.
- Schaefer, D. W. (1988) *MRS Bull.* **13**, No. 2, 22.
- Schmidt-Ott A. (1988) *Appl. Phys. Lett.* **52**, 954.
- Sempéré, R., Bourret, D., Woignier, T., Phalippou, J., and Jullien, R. (1993) *Phys. Rev. Lett.*, **71**, 3307.
- Siegel, R. W. (1994) *Nanophase Materials: Synthesis, Structure and Properties*, in Fujita, F. E. (Ed.), *Physics of New Materials*, Springer-Verlag, Berlin.
- Stanley, H. E., and Ostrowsky, N. (Eds.) (1986) *On Growth and Form*, Martinus Nijhoff, Dordrecht, The Netherlands.

- Tandom, P., and Rosner, D. E. (1995) *Ind. Eng. Chem. Res.*, **34**, 3625.
- Ulrich, G. D. (1984) *Chem. Eng. News*, Aug. 6, p. 22.
- Vemury, S., and Pratsinis, S. E. (1995) *J. Aerosol Sci.*, **26**, 175.
- Weber, A. P., and Friedlander, S. K. (1997a) *J. Aerosol Sci.*, **28**, Suppl. 1, S765.
- Weber, A. P., and Friedlander, S. K. (1997b) *J. Aerosol Sci.*, **28**, 179.
- Whytlaw-Gray, R., and Patterson, H. S. (1932) *Smoke: A Study of Aerial Disperse Systems*, Edward Arnold, London.
- Windeler, R. S. (1995) *Production of Nanometer-Sized Metal Oxide Particles by Gas Phase Reaction in a Free Jet*, PhD Thesis in Chemical Engineering, UCLA.
- Witten, T. A., and Sander, M. (1984) *Phys. Rev. Lett.*, **52**, 1433.
- Wu, M. K., and Friedlander, S. K. (1993a), *J. Colloid Interface Sci.* **159**, 246.
- Wu, M. K., and Friedlander, S. K. (1993b), *J. Aerosol Sci.* **24**, 273.

Thermodynamic Properties

Aerosols are, by their nature, multiphase, and equilibrium thermodynamics provides constraints and limiting conditions on particle interaction with the surrounding gas. Thermodynamic factors play a major role in atmospheric nucleation processes including fog and cloud formation. They are also important in the synthesis of small solid particles, affecting particle size and crystalline properties.

The ability of small particles to serve as condensation nuclei depends in a complex way on the thermodynamic path of the gas (pressure and temperature as a function of time), the vapor pressure curve, and the particle properties. Examples are given in this chapter of two common processes whose paths can lead to a supersaturated state, namely, isentropic expansion and the mixing of hot vapors with cold gases. The vapor pressure of a substance normally cited in the literature is the value in equilibrium with a planar surface of the material. However, a small particle suspended in the vapor may equilibrate with a vapor at a pressure that is larger or smaller than the planar equivalent value, depending on the particle surface tension, charge, and/or chemical composition. How these factors affect the equilibrium vapor pressure is reviewed in this chapter. The same factors that influence the particle equilibrium vapor pressure also reduce the melting temperature of small solid particles and affect the composition of a reacting gas mixture in equilibrium with small particles.

The thermodynamics of interacting clouds of molecular clusters is discussed at the end of this chapter. The equilibrium size distribution of the clusters always present in an unsaturated condensable vapor is the basis of the classical theory of homogeneous nucleation discussed in the next chapter.

THE VAPOR PRESSURE CURVE AND THE SUPERSATURATED STATE

Saturation Ratio

For a single-component, two-phase system such as a liquid and vapor of the same substance, the relationship between the vapor pressure p_s and temperature is usually of the form shown in Fig. 9.1. The region to the right of the curve represents unsaturated vapor, whereas the region to the left represents liquid under pressure. Along the curve, vapor and liquid coexist in equilibrium. Similar considerations apply to solid–vapor equilibria.

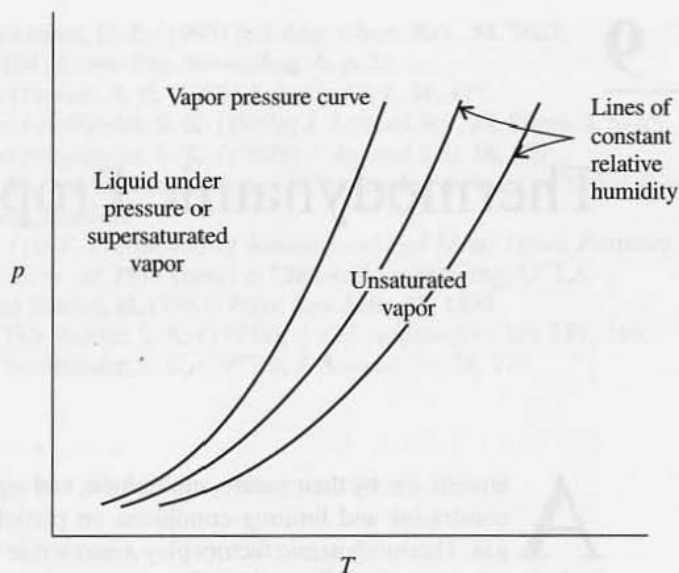


Figure 9.1 Typical form of the vapor pressure curve with lines of constant relative humidity.

An expression for the slope of the vapor pressure curve can be derived from fundamental thermodynamic considerations (Denbigh, 1971):

$$\frac{dp_s}{dT} = \frac{\Delta H}{T \Delta v} \quad (9.1)$$

where ΔH is the molar heat of vaporization and Δv is the volume change per mole accompanying vaporization of the condensed phase. Away from the critical point, which is represented by the end point of the vapor pressure curve in Fig. 9.1, the molar volume of the gas is much larger than that of the liquid. If the gas is ideal, the slope of the vapor pressure curve is

$$\frac{dp_s}{dT} = \frac{\Delta H p_s}{RT^2} \quad (9.2)$$

which is known as the Clapeyron equation. Because the heat of vaporization is approximately constant over a wide range of temperatures, the vapor pressure can be represented approximately by the expression

$$\ln p_s \approx -\frac{\Delta H}{RT} + \text{const} \quad (9.3)$$

These results hold to a close approximation even in the presence of an inert gas, such as air, when the system behaves like an ideal gas mixture.

How does an initially unsaturated vapor, represented by a point to the right of the vapor pressure curve, reach conditions under which condensation can occur? Any number of paths on the (p, T) diagram are imaginable, but two are of particular interest: reversible adiabatic expansion and mixing with cooler air at a lower concentration. Both processes may lead to the formation of an aerosol composed of small liquid droplets. The paths followed

through the unsaturated state up to the equilibrium curve can be followed approximately from theoretical considerations in both cases as shown in this section.

If insufficient condensation nuclei and/or surface are available, condensation is delayed and the system passes into a metastable state, even though it is on the liquid side of the equilibrium curve. The ratio of the actual pressure of the vapor to the equilibrium vapor pressure at the temperature in question is the *saturation ratio* (or *relative humidity*):

$$S = \frac{p}{p_s(T)} \quad (9.4)$$

The saturation ratio is greater than unity when p and T correspond to a vapor state on the liquid side of the vapor-liquid equilibrium curve. For $S > 1$, the system is said to be supersaturated. The supersaturation is given by $(p - p_s)/p_s$.

Once the system passes over into a metastable state ($S > 1$), it becomes unstable with respect to a planar surface of the condensed phase. The planar surface is in equilibrium with the vapor pressure p_s . However, a whole range of equilibrium states exist between particles in different energy states and vapor for which $S \neq 1$ —that is, vapor pressures either larger or smaller than p_s . Equilibria between particles in different energy states and the vapor are the subject of this chapter. In the rest of this section, the passage of the vapor into a metastable state is discussed for two common processes, namely, adiabatic expansion and vapor mixing.

Condensation by Adiabatic Expansion

Adiabatic expansion may be carried out as a batch process in a cloud chamber or as a steady-flow process in the diverging section of the nozzle of a steam turbine or supersonic wind tunnel. If the process is carried out reversibly (this is often a good approximation), the conditions along the path for an ideal gas are related by the expression

$$\frac{p_2}{p_1} = \left(\frac{T_2}{T_1} \right)^{\gamma/(\gamma-1)} \quad (9.5)$$

where p_1 , p_2 and T_1 , T_2 are the total pressures and temperatures before and after the expansion, and γ is the ratio of the specific heat at constant pressure to the specific heat at constant volume. Because $\gamma > 1$, reversible adiabatic expansion leads to a decrease in both temperature and pressure of an initially unsaturated gas up to the point of condensation. In the absence of condensation, the partial pressure is proportional to the total pressure so (9.5) also represents the partial pressure ratio. The path of the expansion process is shown in Fig. 9.2 with the vapor pressure curve.

The cloud chamber experiments of Wilson (summarized in his 1927 Nobel Lecture) qualitatively demonstrated two nucleation mechanisms: (1) condensation on ions at relatively low saturation ratios and (2) condensation on uncharged molecular clusters at much higher saturation ratios. Wilson's studies of condensation on ions are discussed briefly in this chapter. His results on nucleation by molecular clusters which served as a starting point for development of the theory of homogeneous nucleation are discussed in the next chapter. Wilson's principal interest was in condensation on ions and its application to the measurement of high-energy nuclear particles.

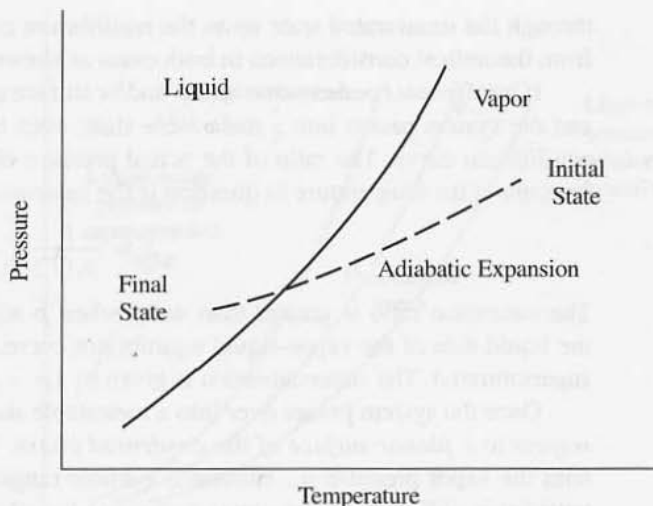


Figure 9.2 Reversible, adiabatic expansion from an initially unsaturated state carries the vapor across the saturation curve into a region where the stable state is a liquid.

There are important examples of adiabatic expansion in nature and industry. Clouds form in the atmosphere by adiabatic expansion when warm, humid air masses rise and cool by nearly adiabatic expansion. As the air mass becomes supersaturated, water vapor condenses on atmospheric aerosol particles. This relieves the supersaturation that reaches a maximum value usually less than about 1%. Vapor condensation occurs in steady adiabatic expansion in turbine nozzles, leading to the formation of droplets that can cause the erosion of turbine blades. A similar process occurs in wind tunnels designed for the study of supersonic flows, and this leads to undesired effects on the Mach number and pressure distribution. Condensation in converging–diverging nozzles has been studied to investigate nucleation kinetics (Wegener and Pouring, 1964).

Condensation by Mixing

Condensation can result when a hot gas carrying a condensable vapor is mixed with a cool gas. This process occurs in stack gases as they mix with ambient air or with exhaled air that is saturated at body temperature when it comes from the lungs. What determines whether condensation occurs in such systems?

As mixing between the two streams takes place, the temperature drops, thereby favoring condensation, but dilution tends to discourage condensation. Unlike reversible adiabatic expansion, mixing is an irreversible process. Whether saturation conditions are reached during mixing depends on the relative rates of cooling and dilution during the mixing process. The situation can be analyzed as follows (Hidy and Friedlander, 1964):

In the absence of condensation, the concentration distribution in the gas is determined by the equation of convective diffusion for a binary gas mixture:

$$\rho \frac{\partial c}{\partial t} + \rho \mathbf{v} \cdot \nabla c = \nabla \cdot \rho D \nabla c \quad (9.6)$$

where ρ is the mass density of the gas (g/cm^3), c is the mass fraction of the diffusing species (g/g gas), and D is the diffusion coefficient of the condensing species. The temperature distribution is determined by the energy equation

$$\rho C_p \frac{\partial T}{\partial t} + \rho C_p \mathbf{v} \cdot \nabla T = \nabla \cdot \kappa \nabla T \tag{9.7}$$

where C_p is the heat capacity at constant pressure and κ is the thermal conductivity.

The mixing system that has received the most careful experimental study is the hot jet of a condensable vapor–air mixture, which is mixed with air at a lower temperature. The boundary conditions for the jet geometry can be written

$$\begin{aligned} c &= c_0, T = T_0 \text{ at the orifice of the jet} \\ c &= c_\infty, T = T_\infty \text{ in the ambient air} \end{aligned} \tag{9.8}$$

When C_p is constant, the equations for the concentration and temperature fields and the boundary conditions are satisfied by the relation

$$\frac{c - c_\infty}{c_0 - c_\infty} = \frac{T - T_\infty}{T_0 - T_\infty} \tag{9.9}$$

provided $\kappa/C_p = \rho D$ or $\kappa/\rho C_p D = 1$. The dimensionless group $\kappa/\rho C_p D$ known as the Lewis number, is usually of order unity for gas mixtures. Table 9.1 shows values of $\kappa/\rho C_p D$ for air and water vapor as a function of temperature.

For $\kappa/\rho C_p D = 1$, the relation between concentration and temperature, (9.9), is independent of the nature of the flow, either laminar or turbulent. It applies to both the instantaneous and time-averaged concentration and temperature fields, but only in regions in which condensation has not yet occurred. When the equations of transport for the jet flow are reduced to the form used in turbulent flow, the molecular diffusivity and thermal diffusivity are usually neglected in comparison with the turbulent diffusivities. This is acceptable for studies of gross transport and the time-averaged composition and temperature. However, this frequently made assumption is not correct for molecular scale processes like nucleation and condensation, which depend locally on the molecular transport properties.

According to (9.9), the path of the condensing system on a diagram of mass fraction versus temperature is a straight line determined by the conditions at the orifice and in the ambient atmosphere. For $c \ll 1$, the partial pressure is approximately proportional

TABLE 9.1
Lewis Number for Trace Amounts of Water Vapor in Air

$T(K)$	Schmidt Number, v/D	Prandtl Number, $C_p \mu / \kappa$	Lewis Number, $\kappa / \rho C_p D$
300	0.604	0.708	0.854
400	0.650	0.689	0.945
500	0.594	0.680	0.873
600	0.559	0.680	0.822
700	0.533	0.684	0.780

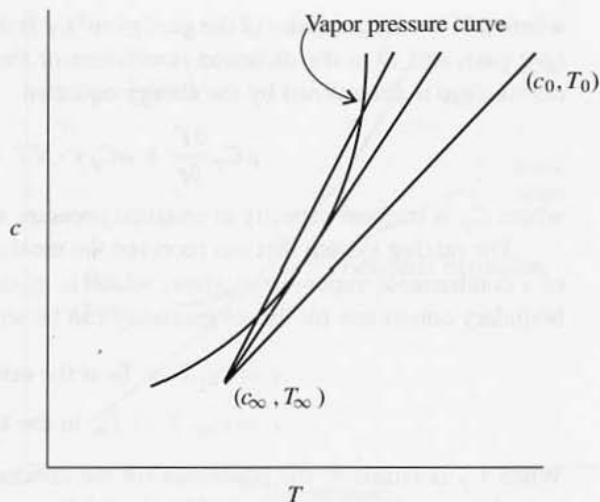


Figure 9.3 Air–vapor mixtures at three different source conditions (c_0, T_0) mixing with air of the same ambient conditions (c_∞, T_∞) . No condensation occurs for the source on the right, while condensation can occur (depending on availability of nuclei and mixing rates) for the one on the left. The middle line shows a limiting situation. Case of the Lewis number $= \kappa/\rho C_p D = 1$.

to the mass fraction. The path is shown in Fig. 9.3 with the vapor pressure curve. From this relationship, it is possible to place limits on the concentrations and temperatures that must exist at the jet orifice for condensation to occur. The mixing line must be at least tangent to the vapor pressure curve for condensation to occur on particles already present in the gas. However, in the case of tangency the supersaturation will not be high enough for homogeneous nucleation to occur (Chapter 10). For nuclei to form in the gas, it will be necessary for the mixing line to pass through a region equivalent to a much higher supersaturation. For $\kappa/\rho C_p \neq 1$, the relationship between c and T will not follow a straight line but will in general depend on the flow field. Homogeneous nucleation by mixing in a turbulent jet is discussed in greater detail at the end of Chapter 10.

EFFECT OF SOLUTES ON VAPOR PRESSURE

The presence of a nonvolatile solute in an aqueous solution tends to reduce its water vapor pressure to an extent that depends on the nature and concentration of the solute. On a purely geometric basis, there are fewer solvent molecules in the surface layer than in the case of a pure solvent drop. This would lead to a vapor pressure reduction proportional to concentration, and this is observed for *ideal solutions*. Specific chemical effects of an attractive nature between solute and solvent may lead to a further reduction in vapor pressure. The reduction of vapor pressure makes it possible for aerosol particles to incorporate significant amounts of aqueous solution in equilibrium with air whose relative humidity is much less than 100%. The water associated with aerosol particles strongly affects light

scattering and may contribute to the delivery of dissolved chemical components by particle deposition to surfaces such as the lung.

An important example related to the atmospheric aerosol is the droplet containing dissolved sulfates that form as a result of the oxidation of SO_2 in solution. The sulfates may be present as sulfuric acid or in a partially neutralized form as ammonium salts or metallic salts from sources such as flyash. The droplet size distribution and chemical composition are determined by a combination of thermodynamic and rate processes. In this section, we consider only equilibrium thermodynamics as it affects the vapor pressure of the drop.

For dilute solutions, the relationship between partial pressure and composition can be determined from theory; over wider concentration ranges, it is in general necessary to determine the relationship by experiment. This has been done for solutions of certain salts and acids; data for the equilibrium vapor pressure of water over solutions of sulfuric acid at 25°C are shown in Table 9.2. As the concentration of sulfuric acid increases, the vapor pressure of water over the solution drops sharply.

For a binary solution at constant composition, an expression of the form (9.1) is found for the slope of the vapor pressure curve as a function of temperature in which the latent heat of vaporization is the value for the solution. Solution vapor pressure curves can be represented as a set of parametric curves at constant composition on the vapor pressure diagram.

For binary solutions such as sulfuric acid and water, droplets may be distributed with respect to size, but at equilibrium all have the same composition unless the Kelvin effect is important as discussed in a later section. For ternary mixtures, the situation is more complicated; the same droplet size may result from different chemical compositions in equilibrium at a given relative humidity.

When equilibrium between the bulk of the gas and the droplet phase does not exist for a chemical species, it is usually assumed that there is local equilibrium between the phases at the interface. From the transport rates in the gas and droplet phases and the equilibrium boundary condition, the droplet growth or evaporation rate can be calculated as shown in the next chapter.

TABLE 9.2
Water Vapor Pressure over Sulfuric Acid Solutions
at 25°C (Perry, 1950)

Wt %	Density (g/cm^3)	Vapor Pressure (mmHg)
0	0.997	23.8
10	1.064	22.4
20	1.137	20.8
30	1.215	17.8
40	1.299	13.5
50	1.391	8.45
60	1.494	3.97
70	1.606	1.03
80	1.722	0.124
90	1.809	0.00765

VAPOR PRESSURE OF A SMALL PARTICLE

If a small spherical particle, liquid or solid, is in equilibrium with its vapor, the pressure of the vapor must be greater than that in equilibrium with a planar surface of the same material as the particle. The vapor may be one component in an ideal gas mixture. An expression for the vapor pressure increase can be derived from classical thermodynamics, taking surface phenomena into account as follows.

The Kelvin Relation

If the particle is not too small (see later in this section), the surface free energy of the particle is given by $4\pi r^2\sigma$, where r is the particle radius and σ is the surface tension of the bulk material corresponding to a planar surface. The Gibbs free energy for the system composed of the vapor and the particle is given by (Frenkel, 1946)

$$G = n_A\mu_A(p, T) + n_B\mu_B(p, T) + 4\pi r^2\sigma \quad (9.10)$$

where n_A and n_B are the number of moles in the vapor and particle phases, respectively, and $\mu_A(p, T)$ and $\mu_B(p, T)$ are the corresponding chemical potentials (per mole) at the temperature T and external pressure p in the vapor phase. As shown in the next subsection, the pressure inside the particle may be substantially higher than the external pressure.

Now consider a variation in the free energy due to the transfer of $dn_B = -dn_A$ moles from the vapor to the particle. The condition for equilibrium, $\delta G = 0$, results in the expression

$$\mu_B - \mu_A + 4\pi\sigma \frac{dr^2}{dn_B} = 0 \quad (9.11)$$

If the molar volume in the liquid is \bar{v}_B , then $n_B = 4\pi r^3/3\bar{v}_B$ and substitution in (9.11) gives

$$\mu_B - \mu_A + \frac{2\sigma\bar{v}_B}{r} = 0 \quad (9.12)$$

For $r \rightarrow \infty$, corresponding to a planar surface, this expression reduces to the usual equilibrium condition, $\mu_A = \mu_B$. Differentiating (9.12) at constant T and using the thermodynamic relations, we obtain

$$d\mu_A = \bar{v}_A dp \quad (9.13a)$$

and

$$d\mu_B = \bar{v}_B dp \quad (9.13b)$$

$$(\bar{v}_A - \bar{v}_B) dp = 2\sigma\bar{v}_B d\left(\frac{1}{r}\right) \quad (9.13)$$

The volume per mole in the liquid is much smaller than that in the gas. For a perfect gas mixture we obtain

$$\bar{v}_A = \frac{RT}{p} \quad (9.15)$$

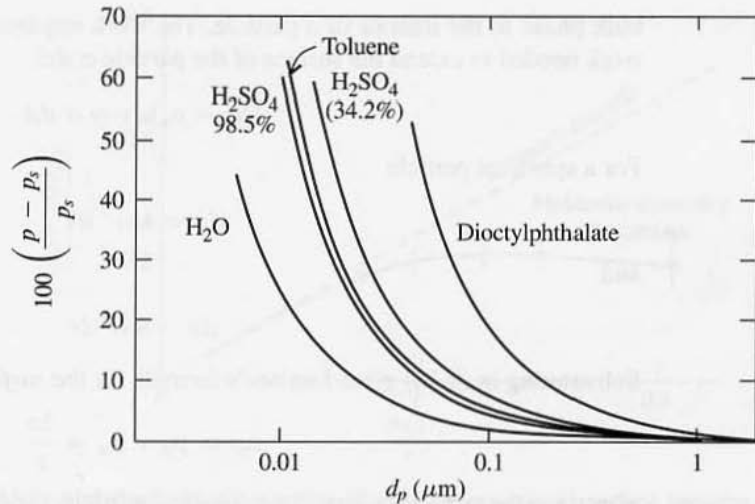


Figure 9.4 Percentage increase in vapor pressure resulting from the Kelvin effect for various liquids. Sulfuric acid at a concentration of 34.2% has a water vapor pressure p_s corresponding to a relative humidity of 75%. Water shows the smallest effect over the size range shown because of the small value of $\sigma \bar{v}_B$.

Substituting in (9.14), we obtain

$$RT \frac{dp}{p} = 2\sigma \bar{v}_B d \left(\frac{1}{r} \right) \quad (9.16)$$

Integrating from $p = p_s$ at $r = \infty$ to $p(r)$ gives the Kelvin relation

$$\ln \frac{p}{p_s} = \frac{2\sigma \bar{v}_B}{rRT} \quad (9.17)$$

This is one of the most important results in the thermodynamics of aerosols. It shows the increase in vapor pressure of small drops compared with the planar surface of the bulk material. Although the Kelvin effect appears often in the field of aerosol formation and growth, direct experimental verification is difficult and few such tests have been made (LaMer and Gruen, 1952).

The percentage increase in vapor pressure as a function of particle size calculated from (9.17) is shown in Fig. 9.4 for several liquids. The vapor pressure increases indefinitely as particle size decreases, and this reduces the ability of small particles to serve as condensation nuclei. In the atmosphere, the water vapor supersaturation rarely exceeds a few percent. Figure 9.7 shows that particles smaller than $0.2 \mu\text{m}$ will not be activated if the supersaturation is less than 1%. For condensing organic vapors, still larger particles must be activated at the same supersaturation.

Particle Internal Pressure: Laplace's Formula

It is easy to show that the pressure inside a small particle or drop p_β is higher than that in the external gas phase, p_α . Consider the transfer of a small volume of material dv from a

bulk phase to the interior of a particle. The work required, $(p_\beta - p_\alpha)dv$, must equal the work needed to extend the surface of the particle σda :

$$(p_\beta - p_\alpha)dv = \sigma da \quad (9.18)$$

For a spherical particle

$$dv = 4\pi r^2 dr \quad (9.19a)$$

and

$$da = 8\pi r dr \quad (9.19b)$$

Substituting in (9.18) gives Laplace's formula for the *surface pressure*:

$$\Delta p = p_\beta - p_\alpha = \frac{2\sigma}{r} \quad (9.20)$$

where r is the particle radius. For a spherical particle, the pressure is uniform in each phase (particle and gas) up to the interface and the pressure jump is constant over the surface of separation. The effect is most significant for substances with large surface tensions. The effect is most significant for substances with large surface tensions such as liquid metals. For the air-mercury interface $\sigma = 547 \text{ erg/cm}^2$ at 175°C and for air and liquid platinum $\sigma = 1820$ at 2000°C , corresponding to a surface pressure of about 10^3 atmospheres for a 20-nm platinum droplet. The effect is also significant for crystalline solids as discussed later in the chapter; small crystals may assume irregular nonequilibrium shapes determined by transport processes in the gas and particle phases. The behavior of irregular solid particles is much more complex than spherical liquid droplets.

Equation (9.20) can be generalized for nonspherical liquid surfaces as follows: For a curved surface separating two continuous media, at equilibrium, a pressure difference exists between the concave and convex sides of the surface; the excess pressure on the concave side over the convex side is given by

$$p_\beta - p_\alpha = \sigma \left(\frac{1}{r_1} + \frac{1}{r_2} \right) \quad (9.21)$$

where r_1 and r_2 are the principal radii of curvature, taken positive when they lie in the β phase.

Limit of Applicability of Kelvin Relation

The interface between the droplet and the gas is not discontinuous; the average molecular density decreases over a narrow region from the liquid side to the vapor. When the size of the droplet becomes sufficiently small compared with the thickness of the transition layer, the use of classical thermodynamics and the bulk surface tension become inaccurate; the Kelvin relation and Laplace formula no longer apply. This effect has been studied by molecular dynamics calculations of the behavior of liquid droplets composed of 41 to 2004 molecules that interact through a Lennard-Jones (LJ) intermolecular potential (Thompson et al., 1984). The results of this analysis are shown in Fig. 9.5, in which the nondimensional pressure difference between the drop interior and the surrounding vapor $(p_d - p)\sigma_{\text{LJ}}^3/\epsilon_{\text{LJ}}$ is

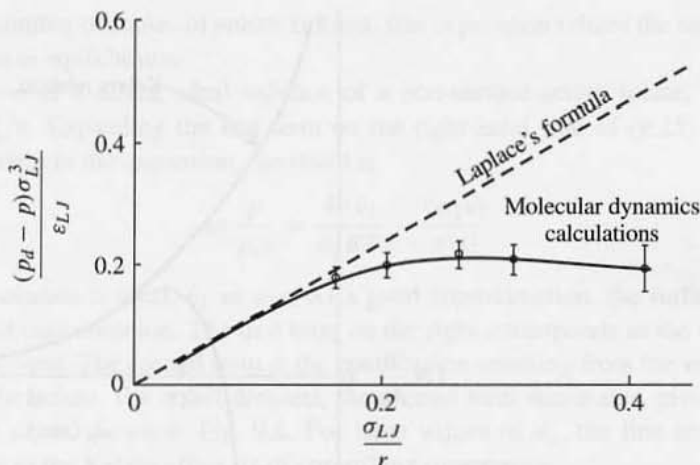


Figure 9.5 Molecular dynamics calculations of the nondimensional surface pressure (difference between pressure inside a drop and the gas) for a Lennard-Jones intermolecular potential. Classical liquid drop theory begins to break down for droplet radii smaller than about 10 times the Lennard-Jones diameter σ_{LJ} . Calculations for $kT/\epsilon_{LJ} = 0.71$ and $\sigma_{LJ}^2/\epsilon_{LJ} = 0.58$. (After Thompson et al., 1984.)

plotted against σ_{LJ}/r , where σ_{LJ} is the LJ characteristic molecular diameter and ϵ_{LJ} is the characteristic LJ energy potential.

Comparison of the molecular dynamics calculations with the predictions of classical thermodynamics indicates that the Laplace formula is accurate for droplet diameters of $20 \sigma_{LJ}$ (about 3400 molecules) or larger and predicts a Δp value within 3% of the molecular dynamics calculations for droplet diameters of $15 \sigma_{LJ}$ (about 1400 molecules). Interestingly, vapor pressures calculated from the molecular dynamics simulations suggested that the Kelvin equation is not consistent with the Laplace formula for small droplets. Possible explanations are the additional assumptions on which the Kelvin relation is based including ideal vapor, incompressible liquid, and bulk-like liquid phase in the droplet.

HYGROSCOPIC PARTICLE–VAPOR EQUILIBRIUM

As a good approximation, the vapor pressure of the solvent over a drop containing a nonvolatile solute is given by an expression of the same form as the Kelvin relationship (9.17) (Defay and Prigogine, 1966). The partial molar volume, \bar{v} , is that of the solvent, and p_s is the vapor pressure of the solvent over a solution with a planar surface.

The equilibrium vapor pressure of a solution droplet containing a fixed mass of solute varies with droplet size in a way very different from that of a droplet of the pure solvent (Fig. 9.6). A droplet of pure solvent is always unstable at vapor pressures below saturation; a solution droplet may be stable because of the vapor pressure lowering of the solute. The vapor pressure of the solvent can be expressed by the relation

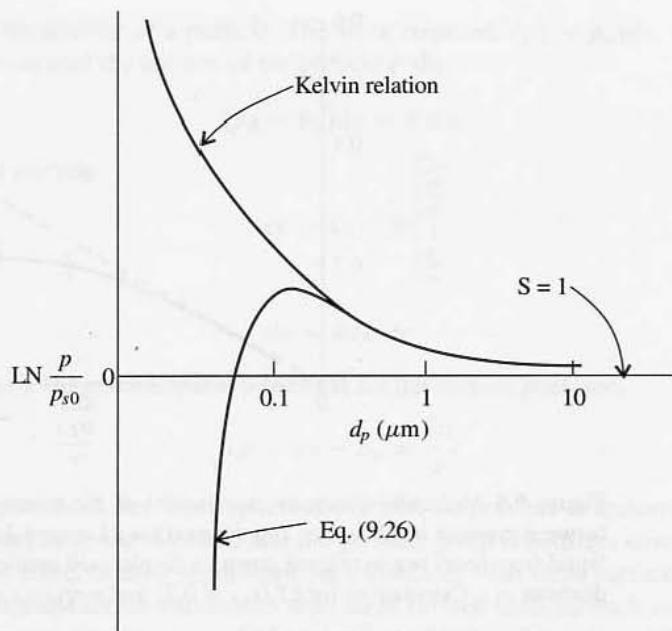


Figure 9.6 Equilibrium vapor pressure curves for droplets composed of solvent alone (Kelvin relation) and of a solvent with a fixed mass of nonvolatile solute.

$$p_s = \gamma x p_{s0} \quad (9.22)$$

where γ is the activity coefficient, x is the mole fraction of the solvent, and p_{s0} the vapor pressure of the pure solvent at the temperature of the system. There are thus two competing effects. The Kelvin effect tends to increase the vapor pressure, whereas the solute tends to reduce it. Consider a droplet containing a fixed amount of nonvolatile solute. The volume of the droplet can be expressed in terms of the partial molar volumes of the solvent and solute:

$$\frac{\pi d_p^3}{6} = n_1 \bar{v}_1 + n_2 \bar{v}_2 \quad (9.23)$$

where n_1 and n_2 represent the number of moles of solvent and solute, respectively. Rearranging (9.23) in terms of the mole fraction of solvent, we obtain

$$\frac{1}{x_1} = 1 + \frac{n_2}{n_1} = 1 + \frac{n_2 \bar{v}_1}{\pi d_p^3/6 - n_2 \bar{v}_2} \quad (9.24)$$

When we substitute (9.22) and (9.24) in (9.17), the result is

$$\ln \frac{p}{p_{s0}} = \frac{4\sigma \bar{v}_1}{d_p RT} + \ln \gamma_1 - \ln \left[1 + \frac{n_2 \bar{v}_1}{\pi d_p^3/6 - n_2 \bar{v}_2} \right] \quad (9.25)$$

Because the number of moles of solute is fixed, this expression relates the saturation ratio to particle size at equilibrium.

In the case of a dilute, ideal solution of a non-surface-active solute, $\gamma_1 = 1$ and $n_2 \bar{v}_2 \ll \pi d_p^3/6$. Expanding the last term on the right-hand side of (9.25) and keeping only the first term in the expansion, the result is

$$\ln \frac{p}{p_{s0}} = \frac{4\sigma \bar{v}_1}{d_p RT} - \frac{6n_2 \bar{v}_1}{\pi d_p^3} \quad (9.26)$$

Because the solution is ideal, $\bar{v}_1 = v_{10}$. As a good approximation, the surface tension is independent of concentration. The first term on the right corresponds to the Kelvin effect for the pure solvent. The second term is the contribution resulting from the vapor pressure lowering of the solute. For small droplets, the second term dominates, giving the lower branch of the curve shown in Fig. 9.6. For large values of d_p , the first term of (9.26), corresponding to the Kelvin effect, is of controlling importance.

This analysis can be applied to a small dry salt particle exposed to increasing relative humidity. The particle remains solid until, if it is hygroscopic, a characteristic relative humidity less than 100% at which it absorbs water and dissolves, forming a saturated solution. The relative humidities at which this occurs for saturated solutions of various salts are shown in Table 9.3. These values will vary with crystal size because of the Kelvin effect. For sodium chloride, solution takes place at a relative humidity of 75% at which the diameter about doubles. With increasing relative humidity, the equilibrium relationship between drop size and vapor pressure is determined by the interaction of the Kelvin effect and vapor pressure lowering.

As humidity is *decreased* in the range below 100%, the sodium chloride droplet shrinks following the path, in reverse, of increasing humidity. However, instead of crystallizing at 75%, the droplet evaporates while remaining as a supersaturated solution until a humidity of about 40% at which crystallization does take place. Droplet diameter changes relatively little. The failure to crystallize probably results from a lack of crystallization nuclei in the solution. Hence there is a hysteresis effect for small salt crystals exposed to varying relative humidities as shown in Fig. 9.7.

The size of the droplet formed when a salt crystal dissolves depends on the concentration of the saturated solution—that is, the solubility. Salts that absorb much water form dilute solutions and relatively large droplets. This is the case for sodium chloride (and other sodium

TABLE 9.3
Relative Humidity and Concentration for Saturated Solutions at 20°C

Salt	Relative* Humidity (%)	Solubility† (g 100 g H ₂ O)
(NH ₄) ₂ SO ₄	81	76.7
NaCl	75	36.2
NH ₄ NO ₃	62	215.9
CaCl ₂ •6H ₂ O	29	87.4

*Wexler (1995), pp. 15–25

†Perry (1984), pp. 3–97ff

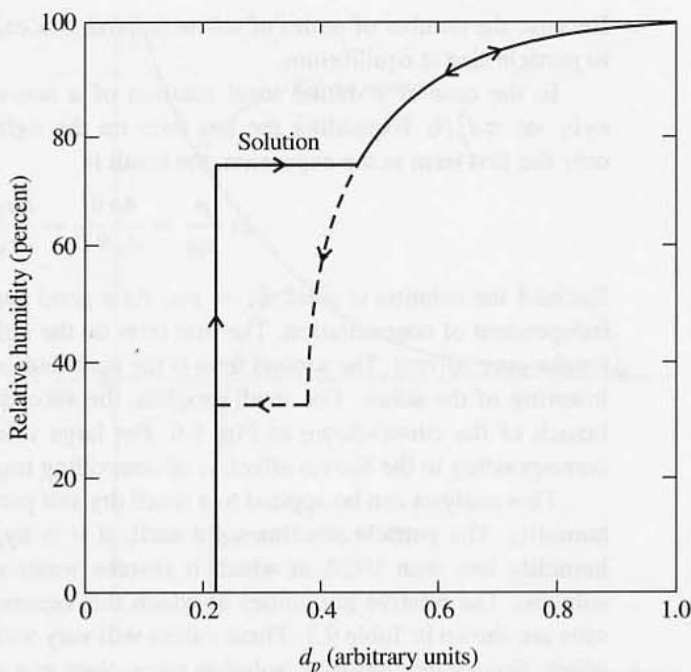


Figure 9.7 Variation in particle (droplet) size with relative humidity. The solid curve shows the effect of *increasing* humidity on a salt crystal. At a relative humidity of about 75%, the crystal absorbs water and goes into solution; the droplet then continues to grow with increasing humidity. As humidity *decreases* below 100%, the evaporation curve initially follows the condensation curve. As shown by the dashed curve, however, the droplet does not crystallize at a relative humidity of 75% but remains supersaturated until a much lower humidity (hysteresis effect) (Junge, 1963).

salts) as shown in Table 9.3. Ammonium salts tend to form more concentrated solutions corresponding to smaller droplets for the same mass concentration.

Example: Taking the Kelvin effect into account, determine the percentage increase in the sulfuric acid concentration of a $0.05\text{-}\mu\text{m}$ -diameter aqueous solution droplet compared with a solution with a planar surface. The temperature is 25°C and the relative humidity is 40%. Assume that the sulfuric acid is nonvolatile. This particle size falls within the size range of sulfuric acid droplets emitted by automobiles equipped with catalytic converters. Other data:

$$\sigma = 72 \text{ ergs/cm}^2$$

$$R = 8.3 \times 10^7 \text{ ergs/mole K}$$

$$\bar{v} = 18 \text{ cm}^3/\text{mole}$$

$$\text{M.W. of H}_2\text{SO}_4 = 98$$

SOLUTION: From Table 9.2, the vapor pressure of water, p_{s0} , is 23.8 mmHg. At a relative humidity of 40%, $p = 0.4(23.8) = 9.52$ mm. By linear interpolation in the table, this corresponds to a 47.9% solution of sulfuric acid with infinite radius of curvature (planar surface). By (9.17)

$$p_s = p \exp\left(-\frac{4\sigma\bar{v}}{d_p RT}\right)$$

where p_s is the vapor pressure over a planar surface of the same composition as a droplet with vapor pressure p . Now $p = 9.52$ mm and substituting the data given previously, $p_s = 9.52(0.96) = 9.14$ mm. By interpolation in Table 9.2, this corresponds to a droplet with a composition of 48.6% sulfuric acid. Thus the percentage increase in composition is $[(48.6 - 47.9)/47.9]100 \approx 1.5\%$.

CHARGED PARTICLE–VAPOR EQUILIBRIA

Condensation can take place on ions as well as on aerosol particles. In his classic cloud chamber studies, Wilson (1927) found that a rain of relatively large droplets at low concentration formed at a saturation ratio of about 4.2 compared with a dense fog of smaller droplets at saturation ratios above 7.9. Wilson hypothesized that ions continuously generated in the air by natural processes served as nuclei at the lower saturation ratio; he verified this hypothesis using ions produced by an x-ray source. In later experiments he showed that condensation took place on negative ions at saturation ratios near 4 at about -6°C and on positive ions at a saturation ratio near 6 at a slightly lower temperature. Similar results were obtained by later investigators.

An approximate thermodynamic theory of ion–vapor equilibrium was developed over a century ago by J. J. Thomson; modified versions of this theory can be used to explain qualitatively the results of Wilson and other investigators. The theory is based on a generalization of (9.10) for the Gibbs free energy of the single-droplet–vapor system to include the electrical energy of the droplet. According to classical electrostatics, the electrical energy of a drop of radius r with charge q uniformly distributed over its surface is $(1/2)q^2/r$. However, in many cases the ions carry only one charge and it appears that a more realistic model consists of a charged ion surrounded by two or three layers of molecules of condensed vapor. For this model the electrical energy is given by

$$W_{\text{el}} = \frac{q^2}{2} \left(\frac{1}{\epsilon_0} - \frac{1}{\epsilon} \right) \left(\frac{1}{r} - \frac{1}{r_0} \right) \quad (9.27)$$

where q is the charge on the droplet, ϵ_0 and ϵ are the dielectric constants of the vapor and droplet substance, respectively, and r and r_0 are the radii of the droplet and ion, respectively. Thus the Gibbs free energy of the droplet–vapor system is given by

$$G = n_A \mu_A + n_B \mu_B + 4\pi r^2 \sigma + \frac{q^2}{2} \left(\frac{1}{\epsilon_0} - \frac{1}{\epsilon} \right) \left(\frac{1}{r} - \frac{1}{r_0} \right) \quad (9.28)$$

The equilibrium condition for this system is determined by setting $\delta G = 0$ for a variation $dn_B = -dn_A$. Taking $\epsilon_0 = 1$ (a good assumption), the resulting equilibrium saturation ratio is given by

$$\ln \frac{p}{p_s} = \frac{2\sigma \bar{v}_B}{RT r} - \frac{q^2 \bar{v}_B}{8\pi RT r^4} \left(1 - \frac{1}{\epsilon}\right) \quad (9.29)$$

Figure 9.8 shows that the equilibrium saturation ratio for droplets with unit electronic charge is always less than that of an uncharged droplet. The value of S passes through a maximum as droplet size decreases. For very small particles, the second (charge-dependent) term on the right-hand side of (9.29) dominates; the first term that corresponds to the Kelvin relation controls for larger particles. Charged particles can serve as condensation nuclei at lower saturation ratios than uncharged particles of the same size; this explains Wilson's experimental observations of condensation on the ions present in the tracks of high-energy nuclear particles passing through a gas.

Figure 9.8 is similar in appearance to Fig. 9.6, which shows the effect of the presence of solute on the saturation ratio; this is somewhat deceiving because the particle size range

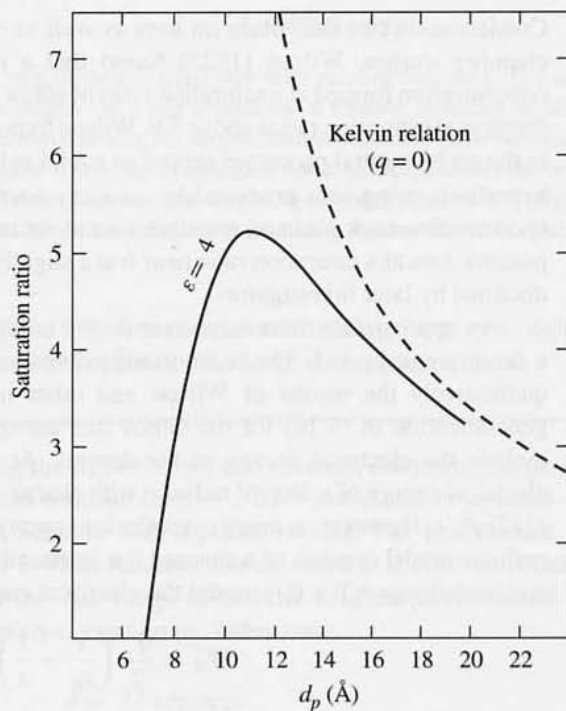


Figure 9.8 Equilibrium saturation ratio for water droplets with unit electronic charge for a dielectric constant $\epsilon = 4$ at 0°C . To obtain qualitative agreement with experimental data, it is necessary to use values of ϵ much smaller than the bulk value (about 80); in the strong field near the ion, ϵ is likely to be much smaller than the bulk value. (After Byers, 1965.)

of Fig. 9.8 (ion nucleation) is two orders of magnitude smaller than Fig. 9.6. As a result, stochastic processes of the type discussed in Chapter 10 best describe the rate of nucleation of supersaturated gases by ions.

A major weakness of the theory is that (9.29) does not explain the observed difference in behavior of positive and negative ions for water vapor condensation observed by Wilson and other investigators. This difference is usually attributed to the polar character of water molecules. Highly polar water molecules form an oriented surface layer that is probably modified depending on the magnitude and polarity of the ionic charge(s) on the droplet. We also note that as shown by the molecular dynamics calculations, theories based on bulk material properties such as the dielectric constant are likely to break down for very small droplets.

The particle size corresponding to the maximum in p/p_s does not in general correspond to a critical size at which nucleation takes place. Development of a more complete theory of nucleation by ions will require the use of fluctuation theory, introduced at the end of this chapter for equilibrium systems and in Chapter 10 for homogeneous nucleation in supersaturated vapors.

It is difficult to test theories such as the Thomson relationship using ions generated by exposing gas mixtures (air and water vapor, for example) to radiation. The resulting ions are mixtures of clusters of differing molecular weight and composition, which are hard to characterize. To generate well-defined ions of single chemical components, Seto et al. (1997) have used the electrospray method. They report encouraging results in preliminary tests of the Thomson theory.

SOLID-PARTICLE-VAPOR EQUILIBRIUM

Vapor and Surface Pressures of Crystalline Particles

The surface free energies of different crystal faces differ. For small particles, there is an equilibrium shape that depends on the variation of the surface free energies with direction of the crystal face. To determine the equilibrium crystal shape, it is necessary to minimize the total surface free energy for a given crystal volume. The shape is determined by drawing a set of vectors from a common origin of length r_i proportional to the surface free energy σ_i of each face with a direction normal to the crystal plane (Wulff construction). This is equivalent to the requirement that for all crystal faces

$$\frac{\sigma_i}{r_i} = \text{constant} \quad (9.30)$$

It can also be shown (see Dunning, 1969, for references) that the Kelvin relation applies to the equilibrium crystal in the form

$$\ln \frac{p}{p_s} = \frac{2\sigma_i \bar{v}_B}{RT r_i} \quad (9.31)$$

and presumably Laplace's formula for the difference in pressure between the interior of the small crystal and the external vapor pressure

$$\Delta p = \frac{2\sigma_i}{r_i} \quad (9.32)$$

The surface pressures for small crystals are in general much larger than the equivalent pressures for liquid droplets because the surface tensions of crystalline solids are usually much greater than those of liquids. As an example, consider an NaCl nanocrystal with $r_i = 5$ nm for the (100) face for which $\sigma_i = 415$ dyne cm^{-1} (Tasker, 1979). The surface pressure $\Delta p = 2(415)/(5)(10)^{-7}$ dynes/ cm^2 or 1660 bars. Thus the internal pressures of nanometer-size solid particles in equilibrium with atmospheric pressure vapors may reach thousands of bars. However, small crystals formed under dynamic gas-phase conditions in which their shape is controlled by heat and mass transfer may not have time to attain the equilibrium shape, so the use of (9.31) and (9.32) may not be quantitatively correct in practical applications.

Melting Point Reduction of Small Solid Particles

Solid particles smaller than about 100 nm melt at temperatures significantly lower than the bulk melting point of the solid. This has been confirmed for a wide variety of materials ranging from metals to semiconductors to insulators (Peppiatt and Sambles, 1975; Goldstein et al., 1992). Several thermodynamic analyses have been made relating the melting point reduction to the solid-liquid interfacial tension, and these have been compared with experimental results by Peppiatt and Sambles (1975). The analysis that agreed best with their experimental results is based on the assumption that melting begins by the formation of a thin liquid skin over the surface of the particle. The "skin melting temperature," T_{sk} , and bulk melting point, T_0 , are related by the expression

$$T_0 - T_{\text{sk}} = \frac{2T_0}{\Delta H_f \rho_s r} \left[\sigma_{s\ell} + \left(1 - \frac{\rho_s}{\rho_\ell} \right) \sigma_\ell \right] \quad (9.33)$$

where ΔH_f is the latent heat of fusion, ρ_s and ρ_ℓ are the densities of the solid and liquid, respectively, r is the particle radius, $\sigma_{s\ell}$ is the solid-liquid interfacial energy and σ_ℓ is the surface energy of the liquid. It is assumed that the liquid skin, once formed, progresses through the solid crystallite. Because ρ_s and ρ_ℓ are usually not too different, the term in brackets is dominated by $\sigma_{s\ell}$. The liquid skin (if it exists) may play a role in the formation of the necks present in agglomerate structures (Chapter 12). Particle size can also affect the crystal structures through solid-phase transitions. The effect of particle size on the melting of CdS nanocrystals is shown in Fig. 9.9.

EFFECT OF PARTICLE SIZE ON THE EQUILIBRIUM OF A HETEROGENEOUS CHEMICAL REACTION

Particle size has a major effect on the equilibrium of a chemical reaction between a component of a gas and small solid particles. We consider the case of small solid particles with negligible vapor pressure in chemical reaction equilibrium with a gas. One component of the gas reacts at the surface of the particle to form gaseous products:

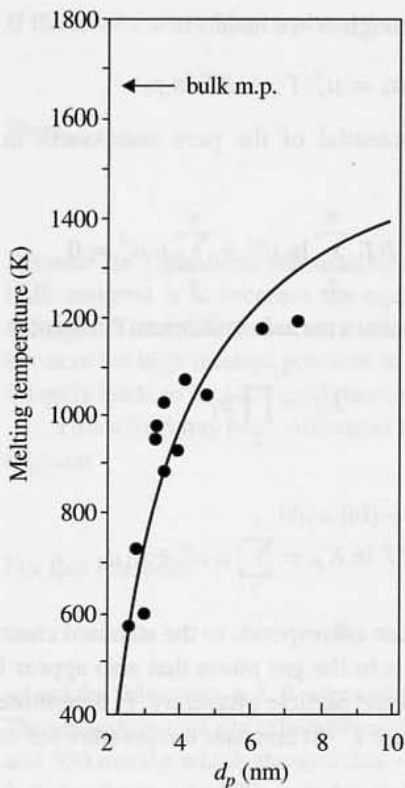
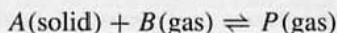


Figure 9.9 Effect of particle size on the melting temperature of CdS nanocrystals determined by observing the disappearance of diffraction patterns on the hot stage of an electron microscope (after Goldstein et al., 1992).



We wish to know how the equilibrium composition of the gas mixture depends on particle size. The total gas pressure p and temperature T are held constant.

The problem of a heterogeneous chemical reaction can be treated as follows (Denbigh, 1971, p. 159ff): A chemical reaction can be represented in a general way by the expression

$$\sum_{i=1}^N v_i M_i = 0 \quad (9.34)$$

where M_i is a chemical component and v_i is the stoichiometric coefficient appearing in the reaction involving N species. The condition for chemical equilibrium is

$$\sum_{i=1}^N v_i \mu_i = 0 \quad (9.35)$$

and this holds for a multiphase system. Assume that $i = 1$ corresponds to the component in the particle; the components 2 through N are present in the ideal gas mixture in which the particles are suspended. The condition for equilibrium can then be written

$$v_1 \mu_1 + \sum_{i=2}^N v_i \mu_i = 0 \quad (9.36)$$

For the gaseous components 2 through N we have

$$\mu_i = \mu_i^0(T) + RT \ln p_i \quad (9.37)$$

where $\mu_i^0(T)$ is the chemical potential of the pure component in the standard state. Substituting in (9.36) gives

$$v_i \mu_i + RT \sum_2^N \ln p_i^{v_i} + \sum_2^N v_i \mu_i^0 = 0 \quad (9.38)$$

For the components in the gas phase, a partial equilibrium constant is defined by

$$K_p = \prod_2^N p_i^{v_i} \quad (9.39)$$

Hence (9.38) becomes

$$-RT \ln K_p = \sum_2^N v_i \mu_i^0 + v_1 \mu_1 \quad (9.40)$$

The first term on the right-hand side corresponds to the standard chemical potentials at the temperature T for the components in the gas phase that also appear in K_p . The chemical potential of pure component 1 in the particle phase, μ_1 , is determined by the pressure in the particle, p_s , and the temperature T . At constant temperature for component 1

$$d\mu_1 = \bar{v}_1 dp_s \quad (9.41)$$

Integrating between unit pressure (standard state) and the internal pressure of the particle

$$\mu_1 = \mu_1^0(T, 1) + \bar{v}_1 \Delta p \quad (9.42)$$

where \bar{v}_1 the volume per mole of the solid is assumed to be independent of the pressure. The difference in pressure between the interior of the particle and the pressure in the exterior gas (assumed to be unit pressure) is given by the Laplace formula $\Delta p = 2\sigma/r$. Substituting in (9.42) gives

$$-RT \ln K_p = \sum_{i=1}^N v_i \mu_i^0 + \frac{2v_1 \bar{v}_1 \sigma}{r} \quad (9.43)$$

The first term on the right-hand side is the free energy change for the reaction with all components in their standard state at unit pressure and the temperature T :

$$\Delta G_T^0 = \sum_{i=1}^N v_i \mu_i^0 \quad (9.44)$$

Hence

$$-RT \ln K_p = \Delta G_T^0 + \frac{2v_1 \bar{v}_1 \sigma}{r} \quad (9.45)$$

If the solid material has a planar surface (bulk form), then $r = \infty$ and

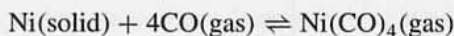
$$-RT \ln K_{p0} = \Delta G_T^0 \quad (9.46)$$

Thus

$$-RT \ln \frac{K_p}{K_{p0}} = \frac{2v_1 \bar{v}_1 \sigma}{r} \quad (9.47)$$

Because the right-hand side is always positive, the effect of using fine particles instead of bulk material is to increase the equilibrium constant—that is, to shift the equilibrium to the right. The smaller the particles, the larger will be the effect. This phenomenon occurs because the high internal pressure in the particles which can be calculated from the Laplace formula leads to an increased thermodynamic activity of the particle substance.

This effect has been discussed by Defay and Prigogine (1966) for the heterogeneous reaction



For this reaction

$$K_p = \frac{p_3}{(p_2)^4} = \frac{1}{p^3} \cdot \frac{x_3}{(1+x_3)^4} \quad (9.48)$$

where the subscripts 1, 2, 3 refer to Ni, CO, Ni(CO)₄, respectively, and x is the mole fraction. The importance of the effect of particle size is illustrated by experimental studies at 70°C and 400 mmHg which showed that x_3 increased from 0.06 in the presence of bulk nickel to 0.27 for the powder. The exact particle size was not known, but rough calculations based on independent determinations of the surface tension indicated that particle diameters ranged from 10 to 20 nm.

MOLECULAR CLUSTERS

Introduction

Even in a thermodynamically stable system, such as an unsaturated vapor, collisions between the molecules lead to the formation of molecular clusters whose lifetime depends on the strength of the bonds holding the clusters together. There is convincing experimental evidence for the existence of such clusters in vapors. For example, Miller and Kusch (1956) determined the concentrations of dimers and trimers in the vapors of ten alkali halides (CsCl, CsBr, RbCl, KCl, KI, NaF, NaCl, NaI, LiCl, and LiBr) at temperatures ranging from about 800 to 1100 K. For this purpose they measured the velocity distribution of the molecules in the beam issuing through a small slit in a copper oven source. The resulting molecular velocity distribution is a superposition of the individual molecular components. They were able to deconvolute the velocity distribution to determine the relative abundance of the clusters. They found significant concentrations of dimers in all cases except for cesium salts and, found observable concentrations of trimers for NaF, LiCl, and LiBr. Figure 9.10 shows the vapor pressure of NaCl and

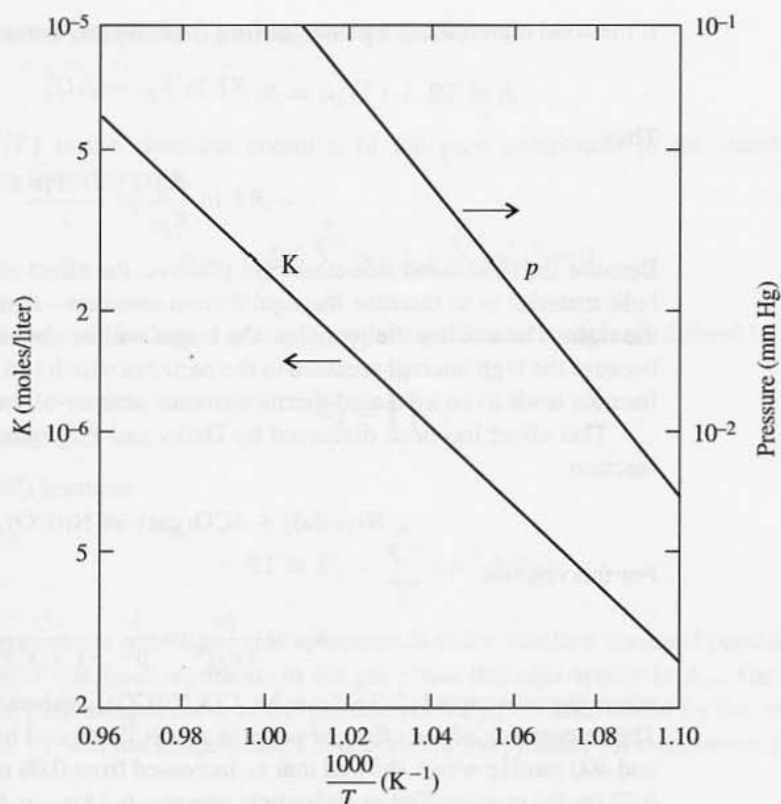
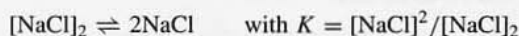


Figure 9.10 The vapor pressure of NaCl and the equilibrium constant K for the reaction



Over this temperature range, 931 to 1037 K, between 25% and 35% of the total NaCl was present as dimer, $[\text{NaCl}]_2$. The data are those of Miller and Kusch (1956).

the equilibrium constant for the reaction between the dimer $[\text{NaCl}]_2$ and the individual molecules of NaCl.

Other such studies are reviewed by Andres (1969). In the absence of foreign nuclei, such as smoke and dust particles, these molecular clusters serve as the nuclei on which condensation takes place in supersaturated gases (Chapter 10). An approximate theory for the equilibrium size distribution ($S < 1$) is discussed in the next section.

Equilibrium Size Distribution

The discussions in the previous sections of this chapter have focused on the thermodynamics of single particles. However, there is an important class of problems involving the statistical properties of interacting clouds of particles in the molecular cluster size range. The size distribution of these particles can be calculated using a simple spherical particle model as follows.

Consider a gas composed of single molecules of a condensable vapor (monomers), clusters of molecules of a condensable vapor distributed in size, and an inert carrier gas such as air. When the saturation ratio is less than unity, no net growth occurs, and the rates of formation and decay of clusters of any size are equal. This statement can be written using the formalism for a chemical reaction:



where A_g is a cluster containing g molecules and A_1 is a monomer molecule. The rate of formation of A_g by condensation of monomer on A_{g-1} is equal to the rate of loss of A_g by evaporation. The equilibrium relationship can also be written as follows:

$$\beta s_{g-1} n_{g-1} = \alpha_g s_g n_g \quad (9.50)$$

where n_g is the concentration of clusters containing g molecules. The flux of monomers (molecules per unit time per unit area) condensing on clusters of class $g - 1$ is β , and s_{g-1} is the effective area for condensation of the clusters of this class. The evaporative flux from class g is α_g , and the effective area for evaporation is s_g . As an approximation, it can be assumed that $s_{g-1} \approx s_g$. The flux of condensing monomers (molecules/cm² sec) is assumed to be given by an expression derived from the kinetic theory of gases:

$$\beta = \frac{p_1}{(2\pi mkT)^{1/2}} \quad (9.51)$$

where p_1 is the monomer partial pressure and m is the molecular mass. It is assumed that all molecules that strike the surface of the nucleus stick. There is an evaporative flux, however, which is assumed to be given by the Kelvin relation for the vapor pressure above a curved surface:

$$\alpha_s = \frac{p_s}{(2\pi mkT)^{1/2}} \exp \left[\frac{4\sigma v_m}{d_p kT} \right] \quad (9.52)$$

where p_s is the vapor pressure above a plane surface of the liquid, σ is the surface tension, and v_m is the molecular volume of the liquid. Substituting in (9.50), we obtain

$$\frac{n_{g-1}}{n_g} = \frac{1}{S} \exp \left[\frac{2\sigma v_m \left(\frac{4}{3}\pi/v_m \right)^{1/3}}{g^{1/3} kT} \right] \quad (9.53)$$

where the saturation ratio S has been set equal to p_1/p_s . When we multiply equations of this form for successively smaller values of g down to $g = 2$, the result is

$$\frac{n_1 n_2 \dots n_{g-2} n_{g-1}}{n_2 n_3 \dots n_{g-1} n_g} = \frac{n_1}{n_g} = \frac{1}{S^{g-1}} \exp \left[\frac{2\sigma v_m \left(\frac{4}{3}\pi/v_m \right)^{1/3}}{kT} \sum_{g=2}^g g^{-1/3} \right]$$

For sufficiently large values of g , we have

$$\sum_{g=2}^g g^{-1/3} = \int_0^g \frac{dg}{g^{1/3}} = \frac{3}{2} g^{2/3} \quad (9.54)$$

Hence the equilibrium distribution of nuclei (discrete spectrum) is given by

$$n_g = n_s S^g \exp \left[\frac{-3\sigma v_m \left(\frac{4}{3}\pi/v_m\right)^{1/3} g^{2/3}}{kT} \right] \quad (9.55)$$

where $S = p_1/p_s$ and $n_s = p_s/kT$. This is one of the few cases in which an analytical solution can be obtained for the size distribution of a particulate system. For small g , the approximation (9.54) leads to considerable error in the value of n_g . If the gas is unsaturated, $S < 1$ and n_g is a monotonically decreasing function of g because the exponential always decreases with g . For $S > 1$, n_g passes through a minimum at a cluster diameter:

$$d_p^* = \frac{4\sigma v_m}{kT \ln S} \quad (9.56)$$

determined by differentiating (9.55) with respect to g and setting the derivative equal to zero. This value of d_p is designated the critical nucleus size. Smaller nuclei tend to evaporate while larger ones grow (refer to the discussion of the Kelvin effect). The number of nuclei of critical size is

$$n_g^* = n_1 \exp \left[\frac{-16\pi\sigma^3 v_m^2}{3(kT)^3 (\ln S)^2} \right] \quad (9.57)$$

The shapes of the equilibrium distributions are sketched in Fig. 9.11 for unsaturated and supersaturated cases. Equilibrium over the entire distribution is unattainable in supersaturated cases. Such a state would require an infinite amount of condensable vapor.

However, the equilibrium distribution plays a very important role in the growth of a dispersed phase from a continuous phase when foreign nuclei such as smoke or dust particles are not present in sufficient quantity. Their concentration and size distribution can be estimated by modifying the equilibrium theory for $S > 1$ as described in the next chapter.

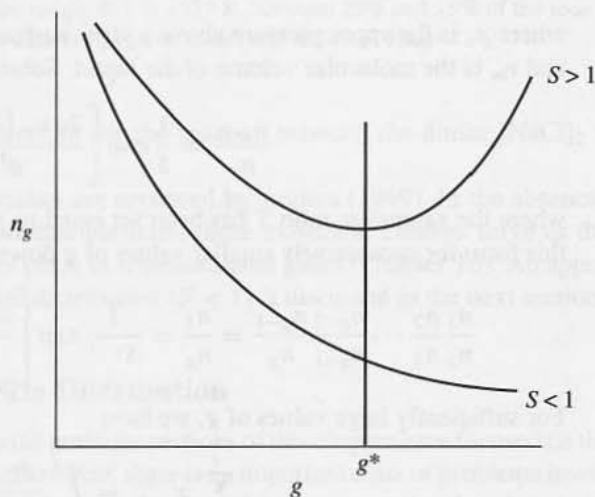


Figure 9.11 Discrete size distribution at equilibrium for clusters formed by homogeneous nucleation. For $S > 1$, an infinite mass of material must be present in the cluster phase at equilibrium.

An important limitation on the analysis is the use of the bulk surface tension that is not applicable to very small clusters as discussed in the section on the Kelvin relation.

When aerosol particles in the size range larger than 10 nm are present, the size distribution is composed of these particles and the equilibrium cluster size distribution. The mass concentration of foreign particles is normally many times greater than that of the clusters.

PROBLEMS

9.1 Estimate the humidity (% saturation) of the ambient air at which you would expect your breath to condense for ambient air temperatures of 10°C and 20°C.

9.2 A gas is discharged from a stack at a temperature of 200°F and a relative humidity of 90%. In the ambient atmosphere, the temperature is 60°F and the relative humidity is 80%.

- Estimate the maximum possible mass concentration of condensed water in the plume. Express your answer in micrograms per cubic meter.
- To what temperature would the stack gases have to be heated to prevent possible condensation in the plume?

9.3 In the special case of a Lewis number, $Le = \kappa / \rho C_p D = 1$, the path describing mixing on a concentration versus temperature diagram is a straight line. For real gases, the Lewis number is less than unity. Show on the c versus T diagram how the path for a real binary gas mixture deviates from the ideal path ($Le = 1$), starting at a given unsaturated initial state.

9.4 Consider a solution droplet that contains a fixed quantity of nonvolatile solute, and allow the amount of solvent in the droplet to vary. For a droplet that contains a large amount of solvent, the equilibrium solvent vapor pressure approaches the vapor pressure of the solvent above a planar surface. As the amount of solvent is reduced, the equilibrium vapor pressure of the solvent passes through a maximum due to the Kelvin effect and then decreases below the planar surface value of the solvent as a result of the high concentration of dissolved solute.

- Show that the vapor pressure maximum occurs when $dp = (9n_2RT/2\pi\sigma)^{1/2}$ for an ideal solution. In this expression n_2 is the (fixed) number of moles of solute dissolved in the droplet.
- A small aqueous solution droplet of sulfuric acid is in equilibrium with water vapor in air at 25°C. The mass of sulfuric acid in the droplet is 10^{-6} grams. Prepare a figure that shows $\log p/p_{so}$ as a function of droplet diameter where p = equilibrium droplet vapor pressure and p_{so} = equilibrium vapor pressure above a planar surface of the solvent. Diagrams of this type are called Koehler curves (Koehler, 1936).

9.5 Calculate the mass concentration of water in the vapor phase present as equilibrium clusters ($g > 2$) at a relative humidity of 50% and a temperature of 20°C. Express your answer as nanograms/m³. Calculate the fraction of the total mass of water vapor present in the form of equilibrium clusters under these conditions.

9.6 (a) Plot the equilibrium cluster size distribution n_g as a function of g for $1 < g < 10$ for an inert gas at 1 atm and 931 K saturated with NaCl vapor. Use the Kelvin relationship model.

The vapor pressure of solid NaCl at 931 K is 6.32×10^{-3} mmHg (Miller and Kusch, 1956). The surface tension of NaCl is 415 dyne cm^{-1} for the (100) surface and 256 dyne cm^{-1} for the (110) surface (Tasker, 1979).

- (b) Calculate the equilibrium constant $K = [\text{NaCl}]^2/[\text{NaCl}]_2$ in moles liter $^{-1}$ and compare with Fig. 9.10.
- (c) Discuss the major uncertainties inherent in the calculation.

REFERENCES

- Andres, R. P. (1969) Homogeneous Nucleation in a Vapor, in Zettlemoyer, A. C. (Ed.), *Nucleation*, Dekker, New York.
- Byers, H. R. (1965) *Elements of Cloud Physics*, University of Chicago Press, Chicago.
- Defay, R., and Prigogine, I. (1966) *Surface Tension and Adsorption*, Wiley, New York.
- Denbigh, K. G. (1971) *The Principles of Chemical Equilibrium*, 3rd ed., Cambridge University Press, Cambridge.
- Dunning, W. J. (1969) General and Theoretical Introduction, in Zettlemoyer, A. C. (Ed.), *Nucleation*, Dekker, New York.
- Frenkel, J. (1946) *Kinetic Theory of Liquids*, Oxford University Press, Oxford, UK (Dover Edition, 1955).
- Goldstein, A. N., Echer, C. M., and Alivisatos, A. P. (1992) *Science*, **256**, 1425
- Hidy, G. M., and Friedlander, S. K. (1964) *AIChE J.*, **10**, 115.
- Junge, C. E. (1963) *Air Chemistry and Radioactivity*, Academic, New York, p. 133.
- Koehler, H. (1936) trans. *Faraday Soc.* **32**, 1152.
- LaMer, V. K., and Gruen, R. (1952) *Trans. Faraday Soc.* **48**, 410.
- Miller, R. C., and Kusch, P. (1956) *J. Chem. Phys.*, **11**, 860.
- Peppiatt, S. J., and Sambles, J. R. (1975) *Proc. R. Soc.*, **345**, 387.
- Perry, J. H. (Ed.) (1950) *Chemical Engineers' Handbook*, McGraw-Hill, New York.
- Perry, J. H. (1984) *Perry's Chemical Engineers' Handbook*, 6th Ed., McGraw-Hill, New York.
- Seto, T., Okuyama, K., DeJuan, L., and de la Mora, J.F. (1997) *J. Chem. Phys.*, **107**, 1576.
- Stokes, R. H., and Robinson, R. A. (1949) *Ind. Eng. Chem.*, **41**, 2013.
- Tasker, P. W. (1979) *Philos. Mag. A*, **39**, 119.
- Thompson, S. M., Gubbins, K. E., Walton, J. P. R. B., Chantry, R. A. R., and Rowlinson, J. S. (1984) *J. Chem. Phys.*, **81**, 530.
- Wegener, P. P., and Pouring, A. A. (1964) *Physics of Fluids*, **7**, 352.
- Wexler, A. (1994) in Constant Humidity Solutions, Lide, D. P. (Ed.) *CRC Handbook of Chemistry and Physics 75th Edition*, Boca Raton, FL.
- Wilson, C. T. R. (1927) On the Cloud Method of Making Visible Ions and the Tracks of Ionizing Particles, in *Nobel Lecture Physics*, Elsevier, New York, published in 1965.

Gas-to-Particle Conversion

Although coagulation (Chapter 7) modifies the size distribution of an aerosol, it causes no change in the mass concentration. The other important *internal* process within a gas that shapes the size distribution, gas-to-particle conversion, results in an increase in the aerosol mass concentration. In studying this process we are interested in the mechanisms by which gases are converted to particles, the rates at which conversion takes place, and the distributions of the condensed matter with respect to particle size.

Gas-to-particle conversion may result from homogeneous gas-phase processes, or it may be controlled by processes in the particulate phase. Gas-phase processes, either physical or chemical, can produce a supersaturated state which then collapses by aerosol formation. Physical processes producing supersaturation include adiabatic expansion or mixing with cool air—discussed in the last chapter—or radiative or conductive cooling. Gas-phase chemical reactions such as the oxidation of SO_2 to sulfuric acid in the atmosphere or the oxidation of SiCl_4 to SiO_2 in industry also generate condensable products.

Once a condensable species has been formed in the gas phase, the system is in a nonequilibrium state. It may pass toward equilibrium by the generation of new particles (homogeneous nucleation) or by condensation on existing particles (heterogeneous condensation). If all collisions among condensable molecules are effective, the process resembles aerosol coagulation (Chapter 7). However, in certain important cases, small molecular clusters are unstable; an energy barrier must be surmounted before stable nuclei can form as discussed in this chapter. Heterogeneous condensation may be limited by gas-phase transport processes or by chemical reactions in the aerosol particles. Table 10.1 summarizes the gas-to-particle conversion processes discussed in this chapter. Measurements of the change in the size distribution function with time can be used to determine the form of particle growth laws. Inferences can then be drawn concerning the mechanism of growth. Homogeneous and heterogeneous condensation can occur in the same parcel of gas either sequentially or simultaneously. In flow systems, this can lead to sustained oscillations in particle number density. The result of experimental studies of this phenomenon are described and theoretical explanations are discussed. Finally the effects of turbulence on homogeneous nucleation are discussed for certain limiting cases.

TABLE 10.1
Examples of Gas-to-Particle Conversion Mechanisms

I. Homogeneous nucleation
A. Physical processes producing supersaturation
1. Adiabatic expansion
2. Mixing
3. Conductive cooling
4. Radiative cooling
B. Gas-phase chemical reaction
1. Single condensable species (classical theory)
2. Multicomponent condensation (heteromolecular theory)
II. Heterogeneous condensation
A. Transport limited
1. Diffusion, $d_p \gg l$
2. Molecular bombardment, $d_p \ll l$
B. Surface-controlled chemical reaction
C. Particulate phase-controlled chemical reaction

CONDENSATION BY ADIABATIC EXPANSION: THE EXPERIMENTS OF C. T. R. WILSON

Cloud chamber experiments of the type carried out by Wilson at the end of the nineteenth century (summarized in his Nobel Lecture, 1927) demonstrate the nature of the condensation process at various saturation ratios with and without foreign particles. The air in a chamber is first saturated with water vapor. By rapid expansion of the chamber contents, both pressure and temperature fall, carrying the system into a supersaturated state. At first, condensation takes place on small particles initially present in the air. Concentrations of such particles in urban atmospheres range from 10^4 to 10^5 cm^{-3} . By repeatedly expanding the chamber contents and allowing the drops to settle, the vapor-air mixture can be cleared of these particles.

With the clean system, no aerosol forms unless the expansion exceeds a limit corresponding to a saturation ratio of about four. At this critical value, a shower of drops forms and falls. The number of drops in the shower remains about the same no matter how often the expansion process is repeated, indicating that these condensation nuclei are regenerated.

Further experiments show a second critical expansion ratio corresponding to a saturation ratio of about eight. At higher saturation ratios, dense clouds of fine drops form, the number increasing with the supersaturation. The number of drops produced between the two critical values of the saturation ratio is small compared with the number produced above the second limit.

Wilson interpreted these results in the following way: The nuclei that act between the critical saturation limits are air ions normally present in a concentration of about $1000/\text{cm}^3$. We know now that these result largely from cosmic rays and the decay of radioactive gases emitted by the soil. Wilson supported this interpretation by inducing condensation

at saturation ratios between the saturation limits by exposing the chamber to x rays that produced large numbers of air ions. Wilson proposed that the vapor molecules themselves serve as condensation nuclei when the second limit is exceeded, leading to the formation of very high concentrations of very small particles. The original experiments were carried out with water vapor. Similar results were found with other condensable vapors, but the value of the critical saturation ratio changed with the nature of the vapor.

Wilson used the droplet tracks generated in the cloud chamber at the lower condensation limit to determine the energy of atomic and subatomic species. Other workers subsequently became interested in the phenomena occurring at the upper condensation limit when the molecules themselves serve as condensation nuclei.

KINETICS OF HOMOGENEOUS NUCLEATION

According to the Kelvin relation (Chapter 9), the higher the saturation ratio, the smaller the radius of the droplet that can serve as a stable nucleus for condensation. However, calculations based on the observations of Wilson and subsequent measurements by many other experimenters indicate values of d_p^* many times greater than the diameter of a single water molecule, about 2.8 \AA . How, then, does condensation take place in systems that have been freed from condensation nuclei?

As shown in the previous chapter, molecular clusters are always present even in an unsaturated gas. When a system becomes supersaturated, these clusters increase in concentration and pass through the critical size d_p^* by attachment of single molecules. The formation of stable nuclei relieves the supersaturation in the gas. Because condensation nuclei are generated by the vapor itself, the process is known as *homogeneous nucleation* or *self-nucleation*.

When condensation occurs, the equilibrium relation $A_{g-1} + A_1 \rightleftharpoons A_g$ no longer holds. With the nonequilibrium cluster distribution function now given by n_g , the difference

$$I_g = n_{g-1}s_{g-1}\beta - n_g s_g \alpha_g \quad (10.1)$$

is equal to the excess rate at which nuclei pass from the size $g - 1$ to g by condensation over the rate of passage from g to $g - 1$ by evaporation. The quantity I_g , known as the *droplet current*, has cgs dimensions of $\text{cm}^{-3} \text{ sec}^{-1}$.

Eliminating α_g by substituting [Eq. (9.50)] for the equilibrium distribution n_g^e , we obtain

$$I_g = n_{g-1}^e s_{g-1} \beta \left[\frac{n_{g-1}}{n_{g-1}^e} - \frac{n_g}{n_g^e} \right] \quad (10.2)$$

The rate of change of the number of clusters in a given class is given by

$$\frac{\partial n_g}{\partial t} = \underbrace{\text{in from}}_{g-1 \text{ condensation}} + \underbrace{\text{in from}}_{g+1 \text{ evaporation}} - \underbrace{\text{out}}_{\text{from } g \text{ condensation}} - \underbrace{\text{out}}_{\text{from } g \text{ evaporation}} = I_g - I_{g+1} \quad (10.3)$$

For sufficiently large values of g ($g > 10$ say) we can treat the variables appearing in these equations as continuous functions of g , and replace the difference equations by differential equations that are easier to handle analytically. In this way, (10.2) becomes

$$I(g) = -\beta n^e s \frac{\partial(n/n^e)}{\partial g} \quad (10.4a)$$

$$= -\beta s \frac{\partial n}{\partial g} + \beta s n \frac{\partial n^e}{n^e \partial g} \quad (10.4b)$$

Substituting the equilibrium distribution n^e in (10.4b) gives

$$I(g) = -\beta s \frac{\partial n}{\partial g} - \frac{\beta s n}{kT} \frac{\partial \Delta \Phi}{\partial g} \quad (10.5)$$

where $\Delta \Phi/kT = (36\pi)^{1/3} \sigma v_m^{2/3} g^{2/3}/kT - g \ln S$. The first term of the right-hand side of (10.5) is proportional to the concentration gradient in g space. It can be interpreted as a diffusion of clusters through g (or v) space with βs playing the part of a spatially dependent diffusion coefficient. The second term represents the transport of droplets through g space under the influence of an external force field corresponding to a potential energy $\Delta \Phi$. The migration velocity is given by $-(\beta s/kT)(\partial \Delta \Phi/\partial g)$.

The kinetic equation (10.3) for the continuous distribution function becomes

$$\frac{\partial n}{\partial t} = -\frac{\partial I}{\partial g} \quad (10.6)$$

where $I_g - I_{g+1}$ has been replaced by $-\partial I/\partial g$. This expression represents a continuity (or Liouville) relation for particle transport through the g space.

An approximate solution to (10.6) with (10.5) can be obtained by making the following assumptions:

1. For $g \rightarrow 0$, the nonequilibrium distribution function approaches the equilibrium distribution; that is,

$$\frac{n}{n^e} \rightarrow 1 \quad \text{as } g \rightarrow 0$$

This is equivalent to the assumption that the time for the lower end of the spectrum to reach the equilibrium distribution is much shorter than that for the upper end.

2. For very large values of g , $n/n^e \rightarrow 0$ because the nuclei concentration for the nonequilibrium distribution is much smaller than that for the equilibrium distribution.
3. A quasi-steady state exists such that as many nuclei enter a size range as leave. This means that the droplet current is independent of the size; that is,

$$\frac{\partial I}{\partial g} = -\frac{\partial n}{\partial t} \approx 0 \quad (10.7)$$

Hence

$$I(g) = \text{const} = I \quad (10.8)$$

Integrating (10.4a) between limits with these assumptions, the result is

$$\int_I^0 d\left(\frac{n}{n^e}\right) = \frac{-I}{\beta} \int_0^\infty \frac{dg}{n^e s} \quad (10.9a)$$

or

$$I = \beta / \int_0^\infty \frac{dg}{n^e s} \quad (10.9b)$$

To calculate I , the droplet current, it is necessary to evaluate the integral in the denominator. The equilibrium distribution can be written in the form

$$\frac{1}{n^e} = \frac{1}{n_1} \exp\left[-\frac{\Delta\Phi}{kT}\right] \quad (10.10)$$

Now $1/n^e$ has a sharp maximum $1/n^{e*}$ when $g = g^*$ so in this region, we can replace $\Delta\Phi$ by its expansion about $g = g^*$:

$$\Delta\Phi \approx \Delta\Phi_{\max} + \frac{1}{2} \left(\frac{\partial^2 \Delta\Phi}{\partial g^2} \right)_{g=g^*} (g - g^*)^2 \quad (10.11a)$$

$$= \Delta\Phi_{\max} - \frac{\pi}{9g^{*2}} \sigma d_p^{*2} (g - g^*)^2 \quad (10.11b)$$

Substituting in (10.10), we obtain

$$\frac{1}{n^e} = \frac{1}{n_1} \exp\left[\frac{\Delta\Phi_{\max}}{kT}\right] \exp\left[-\frac{\pi\sigma d_p^{*2}}{9kTg^{*2}} (g - g^*)^2\right] \quad (10.12)$$

Substituting (10.12) in the integral in (10.9b) gives

$$\int_{g \rightarrow 0}^\infty \frac{dg}{n^e s} = \frac{1}{s^* n^*} \int_{g \rightarrow 0}^\infty \exp\left[-\frac{\gamma}{2} (g - g^*)^2\right] dg \quad (10.13)$$

where

$$\gamma = \frac{2\pi\sigma d_p^{*2}}{9kTg^{*2}}$$

and

$$n^* = n_1 \exp\left[-\frac{\Delta\Phi_{\max}}{kT}\right]$$

As a good approximation, the lower limit can be changed to $-\infty$ to give

$$\int_{-\infty}^\infty \exp\left[-\frac{\gamma}{2} (g - g^*)^2\right] dg = \int_{-\infty}^\infty \exp\left(-\frac{\gamma}{2} z^2\right) dz = \left[\frac{2\pi}{\gamma}\right]^{1/2} \quad (10.14)$$

Then the droplet current is

$$I = \beta / \int_0^\infty \frac{dg}{n^e s} = \frac{p_1 \pi d_p^{*2} n_1 \exp(-\Delta\Phi_{\max}/kT)}{(2\pi mkT)^{1/2} [2\pi/\gamma]^{1/2}} \quad (10.15)$$

$$= 2 \left[\frac{p_1}{(2\pi mkT)^{1/2}} \right] (n_1 v_m^{2/3}) \left[\frac{\sigma v_m^{2/3}}{kT} \right]^{1/2} \exp\left[-\frac{16\pi\sigma^3 v_m^2}{3(kT)^3 (\ln S)^2}\right] \quad (10.16)$$

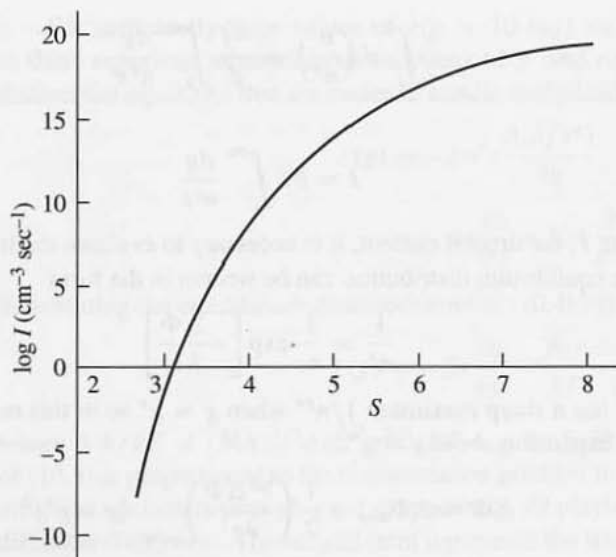


Figure 10.1 The droplet current (nucleation rate) for supersaturated water vapor at $T = 300$ K calculated from (10.16). The critical saturation ratio, corresponding to $I = 1$ $\text{cm}^{-3} \text{sec}^{-1}$, is about 3.1.

The first term in brackets is the monomer flux (molecules per unit area per unit time), and the second is proportional to the monomer surface area per unit volume of gas. Their product has the same dimensions as I , the number per unit volume per unit time. The group $\sigma v_m^{2/3} / kT$ is dimensionless. The droplet current calculated from (10.16) is shown in Fig. 10.1 for water vapor at a temperature of 300 K. Order of magnitude changes in I result from small changes in S , primarily because of the dependence on $\ln S$ in the argument of the exponential function. *Although a supersaturated vapor is always unstable*, the rate of generation of stable nuclei is negligible for small values of S . When $I = 1$ particle/ cm^3 sec, particle formation can be conveniently observed experimentally. The corresponding value of S is called the critical saturation ratio, S_{crit} . Values of S_{crit} , the size of the corresponding stable nucleus, and the number of molecules in the nucleus are shown in Table 10.2 for water and a number of organic vapors. The stable nuclei sizes range from about 2 to 3 nm for all of the substances. The number of molecules in the stable nuclei ranges from 32 to 128.

For condensable materials with very low vapor pressures, essentially all collisions are effective and the critical nucleus is a single molecule. This case is discussed in the next two chapters.

EXPERIMENTAL TEST OF NUCLEATION THEORY

It is difficult to carry out experimental studies to verify the theory. Measurements of the nuclei size distribution would constitute a sensitive check, but fast response instruments capable of measurement in the 10- to 100-Å size range have not been available. Most experimental tests have involved measurements of the saturation ratio at which condensation

TABLE 10.2
Characteristics of Stable Nuclei at Critical Supersaturation for Various Substances
 (from Hirth and Pound, 1963)

Vapor	T (K)	S_{crit}	Diameter of Critical Nucleus (nm)	Number of Molecules in Stable Nucleus
Water	275.2	4.2	1.78	80
Methanol	270.0	1.8	1.58	32
Ethanol	273.0	2.3	2.84	128
<i>n</i> -Propanol	270.0	3.2	3.0	115
<i>n</i> -Butanol	270.0	4.5	2.72	72
Ethyl acetate	242.0	10.4	2.28	40

occurs using an expansion (Wilson) cloud chamber. Data collected with the chamber are difficult to interpret because of the unsteady nature of the expansion process. These investigations are reviewed by Mason (1971). Reversible adiabatic expansion can be carried out as a steady process (Chapter 9), and such systems have been used to study nucleation (Wegener and Pouring, 1964).

The diffusion cloud chamber has been widely used in the study of nucleation kinetics; it is compact and produces a well-defined, steady supersaturation field. The chamber is cylindrical in shape, perhaps 30 cm in diameter and 4 cm high. A heated pool of liquid at the bottom of the chamber evaporates into a stationary carrier gas, usually hydrogen or helium. The vapor diffuses to the top of the chamber, where it cools, condenses, and drains back into the pool at the bottom. Because the vapor is denser than the carrier gas, the gas density is greatest at the bottom of the chamber, and the system is stable with respect to convection. Both diffusion and heat transfer are one-dimensional, with transport occurring from the bottom to the top of the chamber. At some position in the chamber, the temperature and vapor concentrations reach levels corresponding to supersaturation. The variation in the properties of the system are calculated by a computer solution of the one-dimensional equations for heat conduction and mass diffusion (Fig. 10.2). The saturation ratio is calculated from the computed local partial pressure and vapor pressure.

The goal of an experiment is to set up a "critical" chamber state—that is, a state that just produces nucleation at some height in the chamber where the vapor is critically supersaturated and droplets are visible. This occurs when the temperature difference across the chamber has been increased to the point where a rain of drops forms at an approximately constant height. Drop formation in this way must be distinguished from condensation on ions generated by cosmic rays passing through the chamber. An electrical field is applied to sweep out such ions which appear as a trail of drops.

For each critical chamber state, the distribution of the saturation ratio and temperature can be calculated as shown in Fig. 10.2. The set of curves for the critical chamber states based on measurements with toluene is shown in Fig. 10.3. The experimental saturation ratio passes through a maximum with respect to temperature in the chamber. Condensation occurs not at the peak supersaturation but at a value on the high-temperature side because the critical supersaturation decreases with increasing temperature. Hence the family of

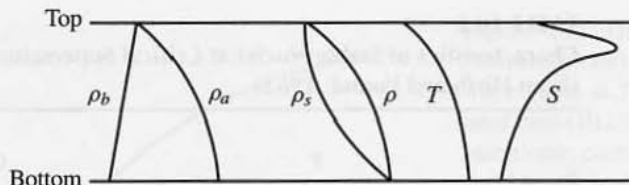


Figure 10.2 Variation with height of the properties of a mixture in the diffusion cloud chamber. Shown are the mass densities of the carrier gas, ρ_b , and the vapor, ρ_a , the equilibrium vapor pressure, p_s , the partial pressure of the vapor, p , the temperature, T_i , and the saturation ratio, S . The highest temperature, vapor pressure, and gas density are at the chamber bottom, above the heated pool. The distributions with respect to chamber height are calculated by integrating expressions for the steady-state fluxes of heat and mass through the chamber.

experimental curves should be tangent to the theoretical curve. Good agreement between theory and experiment has been obtained in this way for toluene (Fig. 10.3) and other organic compounds. For water, agreement is poorer (Heist and Reiss, 1973).

In these experiments the supersaturated state was produced physically for a single condensable substance. Gas-phase chemical reactions may also lead to the formation of condensable species, and several may be present simultaneously. This occurs in air pollution and in the commercial synthesis of fine particles.

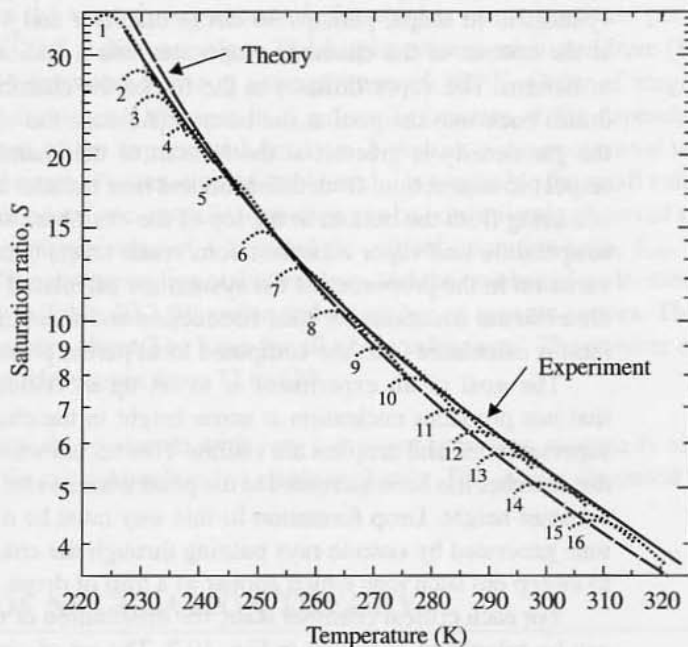


Figure 10.3 Comparison of theoretical and experimental critical saturation ratios for toluene. The dashed line is the theoretical prediction (10.16) with $I = 1 \text{ cm}^{-3} \text{ sec}^{-1}$, and the solid line is the experimental result, the envelope to the numbered individual chamber state curves. (After Katz et al., 1975; data for many other *n*-alkyl benzenes are given in this reference.)

When two or more condensable species present simultaneously in the gas are strongly interacting, nucleation can take place at partial pressures much lower than those required for the nucleation of the pure vapors. A well-known example is the water vapor–sulfuric acid vapor system. The details of this process, known as *heteromolecular* nucleation, are beyond the scope of this text (Reiss, 1950).

HETEROGENEOUS CONDENSATION

When high concentrations of particles are present and the supersaturation is low, condensation takes place on the existing particles without formation of new nuclei. We call this process *heterogeneous condensation*. Cloud droplet formation in the atmosphere takes place in this way because supersaturations are usually less than a few percent and particle concentrations are high. Aerosol formation in the atmosphere or in industrial process gases may take place by homogeneous or heterogeneous mechanisms.

The rate of heterogeneous condensation depends on the exchange of matter and heat between a particle and the continuous phase. The extreme cases of a particle much larger or much smaller than the mean free path of the suspending gas are easy to analyze. In the continuum range ($d_p \gg \ell_p$), diffusion theory can be used to calculate the transport rate. For a single sphere in an infinite medium, the steady-state equation of diffusion in spherical coordinates takes the form

$$\frac{\partial c}{\partial t} = \frac{D \partial r^2 (\partial c / \partial r)}{r^2 \partial r} = 0 \quad (10.17)$$

where c is the molecular concentration of the condensing species and D is its coefficient of diffusion. The solution that satisfies the boundary conditions— $c = c_d$, the concentration in equilibrium with the surface at $r = d_p/2$, and $c = c_1$ at $r = \infty$ —is

$$\frac{c - c_d}{c_1 - c_d} = 1 - \frac{d_p}{2r} \quad (10.18)$$

The rate of diffusional condensation is given by

$$F = D \left(\frac{\partial c}{\partial r} \right)_{r=d_p/2} \pi d_p^2 = 2\pi d_p D (c_1 - c_d) = \frac{2\pi d_p D (p_1 - p_d)}{kT} \quad (10.19)$$

where F is the flow of molecules (number per unit time) to the surface of the particle. The surface concentration, c_d , is determined by the surface temperature and curvature. It is assumed that the condensation rate is sufficiently slow for the latent heat of condensation to be dissipated without changing droplet temperature.

For particles much smaller than the mean free path of the gas, the rate of condensation can be calculated from kinetic theory: The net flow of molecules (sec^{-1}) at a surface of area πd_p^2 is given by

$$F = \frac{\alpha (p_1 - p_d) \pi d_p^2}{(2\pi mkT)^{1/2}} \quad (10.20)$$

Separate accommodation coefficients, α , are often introduced for the condensation, $p_1/(2\pi mkT)^{1/2}$, and evaporation, $p_d/(2\pi mkT)^{1/2}$, fluxes, but the values are assumed

equal in (10.20). In general, these coefficients must be determined experimentally. An approximate interpolation formula for the entire Knudsen number range has been proposed by Fuchs and Sutugin (1971):

$$F = 2\pi D d_p (c_1 - c_d) \left\{ \frac{1 + \text{Kn}}{1 + 1.71 \text{Kn} + 1.333 \text{Kn}^2} \right\} \quad (10.21)$$

where the Knudsen number is equal to ℓ_p/a_p and ℓ_p is the mean free path for collision of the condensing species. When $\text{Kn} \ll 1$, (10.21) reduces to (10.19) for the continuum range. When $\text{Kn} \gg 1$, (10.21) is about 1.2 times (10.20), with $\alpha = 1$ for rigid elastic spheres.

If the Kelvin effect is important, the partial pressure driving force for condensation takes the form

$$(p_1 - p_d) = p_1 - p_s \exp \left[\frac{4\sigma v_m}{d_p kT} \right] = p_1 - p_s \exp \left[\frac{d_p^* \ln S}{d_d} \right] \quad (10.22)$$

where p_s is the vapor pressure over a flat surface or pool of liquid and d_p^* is the critical droplet diameter. It has been assumed that the nucleus behaves like a pure drop of the condensing species. If the surface of the particle is composed of a material different from that of the condensing vapor, this result must be modified to account for surface wetting effects.

Expanding the exponential of (10.22), we obtain

$$\Delta p = p_s \left[S - 1 - \frac{d_p^*}{d_p} \right] \ln S - \frac{1}{2} \left(\frac{d_p^*}{d_p} \ln S \right)^2 - \dots$$

where $S = p_1/p_s$. For small values of $S - 1$, this takes the approximate form:

$$\Delta p = \frac{p_s}{d_p} (S - 1)(d_p - d_p^*) \quad (10.23)$$

As an example, this result can be substituted in (10.19) for growth by diffusion in the continuum range:

$$F = \left(\frac{2\pi D}{kT} \right) p_s (S - 1)(d_p - d_p^*) \quad (S - 1 \ll 1) \quad (10.24)$$

The rate of condensation is proportional to the difference between the particle diameter and the critical particle diameter.

GROWTH LAWS

Aerosol growth laws are expressions for the rate of change in particle size as a function of particle size and the appropriate chemical and physical properties of the system. Such expressions are necessary for the calculation of changes in the size distribution function with time as shown in this and the next chapter. In this section, transport-limited growth laws based on the previous section are discussed first followed by growth laws determined by aerosol phase chemical reactions.

Transport-Limited Growth

When growth is limited by gas-phase transport, the rate can be determined from the expressions derived in the previous section. For the continuum range, the growth law based on (10.19) is

$$\frac{dv}{dt} = \frac{2\pi D d_p v_m}{kT} (p_1 - p_d) \quad (10.25)$$

where v_m is the molecular volume of the condensing species. The effect of the moving boundary of the growing particle is neglected. For nuclei smaller than the mean free path of the gas, the growth law, based on (10.20), is

$$\frac{dv}{dt} = \frac{\pi d_p^2 v_m (p_1 - p_d)}{(2\pi m k T)^{1/2}} \quad (10.26)$$

where the accommodation coefficient α has been set equal to unity. An interpolation formula for the growth rate that covers the entire range of the mean free path is given by (10.21). Chemical reactions at particle surfaces may also lead to particle growth. Such reactions are likely to be important near aerosol sources where the particle surfaces are fresh and their catalytic activity high. (In the atmosphere, however, contamination probably destroys the specific catalytic activity of aerosol surfaces.) Particles will grow if the products of reaction accumulate at the surface. When reaction rates are fast compared with transport, growth laws are of the same form as the transport-limited laws. When reaction rates are slow compared with transport, the concentration of the reactive species in the gas near the surface is practically the same as in the bulk of the gas, and the rate of conversion is

$$\frac{dv}{dt} = \frac{\alpha p_1 \pi d_p^2 v_m}{(2\pi m k T)^{1/2}} \quad (10.27)$$

where α , the fraction of effective collisions with the surface, is usually much less than unity.

Example: Derive an expression for the variation of particle diameter with time for a particle growing by diffusion from the gas phase for the case $d_p \ll \ell_p$. Neglect the Kelvin effect.

SOLUTION: The rate of growth is given by (10.26). When we substitute $v = \pi d_p^3/6$ and rearrange, the result for $p_d = p_s$ is

$$d(d_p) = \frac{2v_m(p_1 - p_s) dt}{(2\pi m k T)^{1/2}}$$

Integrating from the initial condition $d_p = d_{p0}$ at $t = 0$,

$$d_p = d_{p0} + \int_0^t \frac{2v_m(p_1 - p_s)}{(2\pi m k T)^{1/2}} dt'$$

The partial pressure driving force for growth, $p_1 - p_s$, is a function of time determined by the conditions of the system. For example, in the condensation aerosol generator (Chapter 6), it is determined by the cooling rate in the chimney. None of the quantities

in the second term on the right is a function of drop radius. If $d_p \gg d_{p0}$ for all values of d_{p0} , the drops will all be roughly of the same size provided that the variation of $p_1 - p_s$ with time is the same for all particles. Hence the condensation generator produces almost monodisperse aerosols even though the original nuclei are nonuniform in size. The same holds true for the condensation particle counter, which makes it possible to convert total light scattering to particle number concentration (Chapter 6). Moreover, for sufficiently long times, the final particle diameter is nearly independent of the initial size. In the atmosphere or in process gases, the temperature-time histories of the various gas parcels vary. As a result, $(p_1 - p_s)$ varies and the resulting size distributions are polydisperse.

Aerosol Phase, Reaction-Limited Growth

Many important chemical reactions take place in the aqueous component of the atmospheric aerosol or in fog droplets. An example is the solution-phase oxidation of SO_2 to SO_4^{2-} . Such reactions may drive the diffusional transport of reactants from the gas to the particles followed by absorption and chemical reaction. If the chemical reactions are slow compared with the gas- and aerosol-phase transport rates, the dissolved reactive species will be nearly in equilibrium between the gas and particles.

A general growth law for conversion controlled by droplet phase reaction can be derived as follows: Consider an aerosol composed of small droplets all of the same composition but distributed with respect to size. The same chemical reactions take place in all droplets, leading to the conversion of molecules from gas to particle phases. The process is limited by the droplet-phase reactions. As fast as material is consumed by reaction in the droplet phase, it is replenished by transport from the gas. In many cases it can be assumed that the gas-phase concentrations remain nearly constant because the reservoir of reactive molecules in the gas is much larger than that in the aerosol phase. Under these circumstances the fractional rate of growth of all droplets *must be the same* provided that the Kelvin effect does not intervene. The rate of chemical conversion *per unit volume of droplet* is independent of size. That this must be true becomes clear if it is considered that the rate of conversion per unit volume is the same whether the solution is present as a large volume in a beaker or dispersed as an aerosol.

The result can be expressed mathematically. The change in mass of a droplet is given by

$$\frac{dm}{dt} = \sum_i \frac{dm_i}{dt} \quad (10.28)$$

where m_i is the mass of species i absorbed by the droplet. If the rate of uptake is equal to the rate of conversion by chemical reaction (quasi-stationary state), then

$$\frac{dm_i}{dt} = M_i \frac{dn_i}{dt} = v_i M_i v \left(\frac{1}{v_i v} \frac{dn_i}{dt} \right) = v_i M_i v r \quad (10.29)$$

where n_i is the number of moles of species i , M_i is the molecular weight, and v_i is the stoichiometric coefficient for species i in the reaction. The reaction rate

$$r = \frac{1}{v_i v} \frac{dn_i}{dt} \quad (10.30)$$

is the same for all chemical species and can often be expressed by the power law forms of chemical kinetics (Denbigh, 1971). The droplet growth law is obtained by combining (10.28) through (10.30):

$$\frac{dm}{dt} = \rho_p \frac{dv}{dt} = v \left(\sum_i M_i v_i \right) r \quad (10.31)$$

where the density of the droplet ρ_p has been assumed constant. Because the composition is the same in all droplets, the rate of reaction per unit volume, r , is independent of droplet size. If also the chemical composition of all the droplets stays constant, the reaction rate r remains constant and by (10.31) the growth rate is proportional to droplet volume. While the derivation was carried out for a single chemical reaction, the result can easily be generalized to the case of a multireaction system.

Example: Derive an expression for the variation of particle diameter growing at a rate determined by the rate of chemical reaction in the particles.

SOLUTION: The rate of particle growth is given by (10.31) rearranged as follows

$$\frac{dv}{dt} = \left\{ \frac{(\sum_i M_i v_i) r}{\rho_p} \right\} v$$

or

$$\frac{d(d_p)}{dt} = k_v d_p \quad \text{where } k_v = \frac{(\sum_i M_i v_i) r}{3\rho_p}$$

Integrating from $d_p = d_{p0}$ at $t = 0$,

$$\frac{d_p}{d_{p0}} = e^{k_v t}$$

Thus for particle volume-controlled growth, the final particle diameter is proportional to the initial diameter. For volume-controlled growth, the initial polydispersity is carried through to the final size distribution. This result is quite different from that of diffusion in the free molecule regime for which the final particle diameter is independent of the initial diameter.

It may seem strange that the droplet growth law is so different in form from the transport-limited law. After all, the gas-phase species must be transported to the droplets. Actually, both laws are obeyed. The explanation is that the reactive species are *nearly* in equilibrium in the gas and droplet phases. Their small displacement from equilibrium differs, however, *depending on droplet size*, but not sufficiently to affect the rate of reaction in solution.

Examples of growth laws including those limited by chemical reaction in the aerosol phase are summarized in Table 10.3. The growth rate dv/dt is proportional to d_p for diffusion in the continuum range and to d_p^3 for droplet phase chemical reaction. Different

TABLE 10.3
Limiting Growth Laws for Gas-to-Particle Conversion

Mechanism	Growth Law, dv/dt	Equation
Diffusion ($d_p \gg l$)	$\frac{2\pi D d_p v_m (p_1 - p_d)}{kT}$	(10.25)
Molecular bombardment ($d_p \ll l$)	$\frac{\alpha \pi d_p^2 v_m (p_1 - p_d)}{(2\pi mkT)^{1/2}}$	(10.26)
Surface reaction (all sizes)	$\frac{\alpha \pi d_p^2 v_m p_1}{(2\pi mkT)^{1/2}} \quad (\alpha \ll 1)$	(10.27)
Droplet-phase reaction	$\frac{\pi d_p^3}{6\rho_p} \left(\sum M_i v_i \right) r$	(10.31)

forms for the growth lead to markedly different changes in the size distribution function with time and to the distribution of chemical species with respect to size.

DYNAMICS OF GROWTH: CONTINUITY RELATION IN v SPACE

We consider a polydisperse aerosol growing by gas-to-particle conversion. The system is spatially uniform in composition—a growing aerosol in a box. As growth occurs, the size distribution function changes with time; we wish to derive an expression for $\partial n/\partial t$. Let $I(v, t)$ be the particle current or number of particles per unit time per unit volume of gas passing the point v . The rate at which particles enter the small element of length δv in v space (Fig. 10.4) is given by

$$I - \frac{\partial I}{\partial v} \frac{\delta v}{2}$$

The rate at which particles leave δv is

$$I + \frac{\partial I}{\partial v} \frac{\delta v}{2}$$

The net rate of change in particle number in δv is given by

$$\frac{\partial [n\delta v]}{\partial t} = I - \frac{\partial I}{\partial v} \frac{\delta v}{2} - \left[I + \frac{\partial I}{\partial v} \frac{\delta v}{2} \right] \quad (10.32)$$

$$= \frac{\partial I}{\partial v} \delta v \quad (10.32a)$$

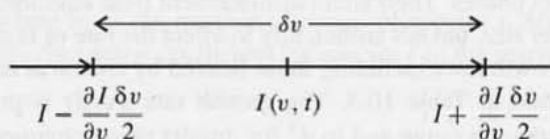


Figure 10.4 The flow of particles through v space as a result of a growth process.

When we divide both sides by δv , the result is

$$\frac{\partial n}{\partial t} = -\frac{\partial I}{\partial v} \quad (10.33)$$

which is the continuity relation for the v space equivalent to (10.6) for the nuclei distribution. Multiplying both sides of (10.33) by v and integrating over the range between v_1 and v_2 , we obtain

$$\int_{v_1}^{v_2} v \frac{\partial n}{\partial t} dv = \frac{\partial \int_{v_1}^{v_2} nv dv}{\partial t} = - \int_{v_1}^{v_2} v \frac{\partial I}{\partial v} dv \quad (10.34)$$

The last term can also be written as

$$- \int_{v_1}^{v_2} v \frac{\partial I}{\partial v} dv = - \int_{v_1}^{v_2} \frac{\partial Iv}{\partial v} dv + \int_{v_1}^{v_2} I dv \quad (10.35)$$

Integrating the first term on the right-hand side and combining (10.34) with (10.35), we obtain

$$\frac{\partial \int_{v_1}^{v_2} nv dv}{\partial t} = [Iv]_1 - [Iv]_2 + \int_{v_1}^{v_2} I dv \quad (10.36)$$

The term on the left-hand side represents the rate of change in the volume in the size range bounded by v_1 and v_2 . The first and second terms on the right are the flow of volume into and out of the range between v_1 and v_2 . Hence by difference, the third term on the right represents the flow from the gas phase into the range. This leads to an alternative interpretation of I . The particle current also represents the volume of material converted from the gas phase per unit v space in unit volume of gas and unit time.

In general, the particle current can be expressed as the sum of two terms, one representing diffusion and the other representing migration in v space (10.5). Diffusion leads to a spread in v space of a group of particles initially of the same size. The diffusion term is proportional to $\partial n/\partial v$ (or $\partial n/\partial g$), which is very important for homogeneous nucleation. For the growth of larger particles, diffusion can be neglected in comparison with migration because $\partial n/\partial v$ is relatively small. The particle current is then given by the relation

$$I(v, t) \approx n \frac{dv}{dt} \quad (10.37)$$

where dv/dt is the growth law (Table 10.3). According to (10.37), all particles of the same initial size grow to the same final size. By substitution of (10.33) with the appropriate growth law, (10.33) can be solved for $n(v, t)$.

Example: We consider the case of a growth law

$$\frac{dv}{dt} = F(t)v$$

which would hold for reaction in a droplet phase. Derive an expression for $n(v, t)$.

SOLUTION: Substitution in (10.33) gives

$$\frac{\partial n}{\partial t} = -F(t) \frac{\partial nv}{\partial v}$$

which can be written

$$\frac{\partial nv}{\partial \tau} + \frac{\partial nv}{\partial \ln v} = 0 \quad (\text{i})$$

where $\tau = \int_0^t F(t') dt'$. The solution to this equation, obtained by the method of characteristics, is

$$nv = f(\ln v - \tau) \quad (\text{ii})$$

where f represents a functional relationship that is determined by the known distribution at any time. The result (ii) can be checked by substitution in (i). If at $t = 0$, which corresponds to $\tau = 0$, the distribution function is given by a power law

$$n(v, 0) = \text{const } v^p$$

then the functional form f , which satisfies (ii), is

$$nv = \text{const } e^{(p+1)(\ln v - \tau)}$$

or

$$n = \text{const } v^p e^{-(p+1)\tau}$$

Thus if the distribution begins as a power law form, it will retain the same dependence on particle size as growth continues if $dv/dt \sim v$ (Brock, 1971).

The distribution with respect to size of a chemical species converted from the gas phase depends on the mechanism of conversion. In general, species that form by gas-phase reaction and then diffuse to the particle surface are found in the smaller size range; species that form in a droplet phase tend to accumulate in the larger size range.

MEASUREMENT OF GROWTH RATES: HOMOGENEOUS GAS-PHASE REACTIONS

The growth law for a polydisperse aerosol can be determined by measuring the change in the size distribution function with time. In experiments by Heisler and Friedlander (1977), small quantities of organic vapors that served as aerosol precursors were added to a sample of the normal atmospheric aerosol contained in an 80-m³ bag exposed to solar radiation. The bag was made of a polymer film almost transparent to solar radiation in the UV range and relatively unreactive with ozone and other species. Chemical reaction led to the formation

of condensable species and to aerosol growth. The change with time of the size distribution function was measured with a single particle optical counter.

The number of particles per unit volume larger than a given particle size d_p , $\int_{d_p}^{\infty} n_d(\tilde{d}_p) d(\tilde{d}_p)$ is shown in Fig. 10.5 for an experiment with cyclohexene. Consider a horizontal line on the figure corresponding to constant values of this integral. In the absence of homogeneous nucleation, each such line corresponds to the growth with time of a particle of size given initially by the curve for $t = 0$. No particle can move across such a line because the total number larger is conserved.

The growth rate, $d(d_p)/dt \approx \Delta d_p/\Delta t$, can be obtained from adjacent distributions in Fig. 10.5 as a function of d_p and of the time. The data were then plotted with dv/dt as a function of particle diameter as shown in Fig. 10.6. For this set of data, an approximately linear relationship was found with an intercept on the positive d_p axis.

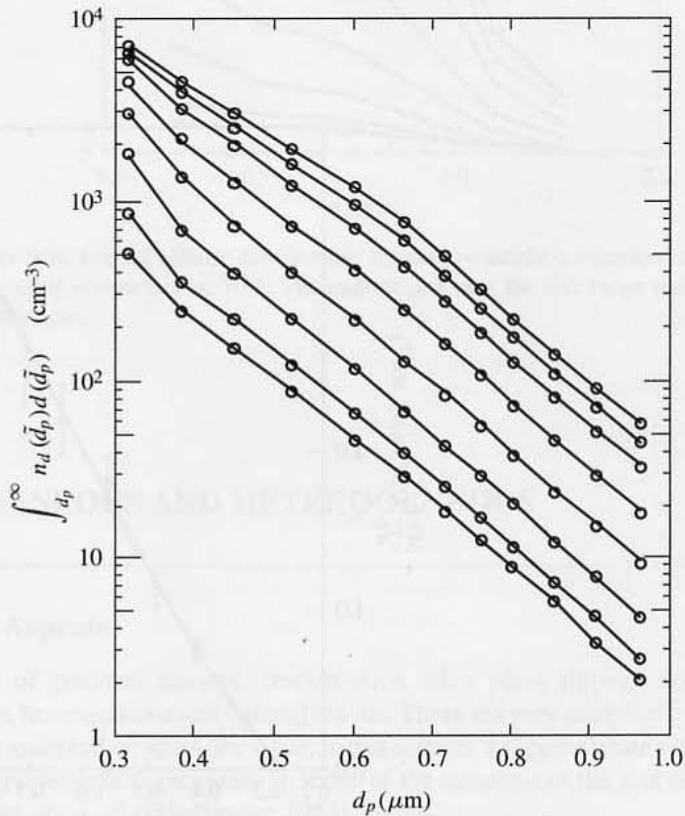


Figure 10.5 Number concentrations of particles larger than a given diameter, d_p , at various times in a smog chamber experiment. Initial concentrations were 2.02 ppm cyclohexene, 0.34 ppm NO, and 0.17 ppm NO_2 . The time between measurements was about 3 to 4 min. The first measurement shown was made 12 min after the addition of the reactants (Heisler and Friedlander, 1977).

To explain these results, it was assumed that a single condensable species, or a small group of species with similar thermodynamic properties, formed in the gas as a result of chemical reaction. Molecules of these reaction products then diffused to the surfaces of existing aerosol particles. The data were correlated by a diffusion-controlled growth law modified by the Kelvin effect in the small saturation ratio approximation (10.20) as shown in Fig. 10.6. The cutoff particle diameter probably results from the Kelvin effect. For the run shown, the critical diameter was about $0.28 \mu\text{m}$. The line is the result of a least-squares fit using (10.21) combined with (10.23) in calculating the growth law. The curvature in the line results from the form of the interpolation formula (10.21). Aerosol volume distributions calculated from the data are shown in Fig 10.7. Material accumulates in the size range near $0.6 \mu\text{m}$, which is particularly efficient for light scattering. Small particles grow little because of the Kelvin effect.

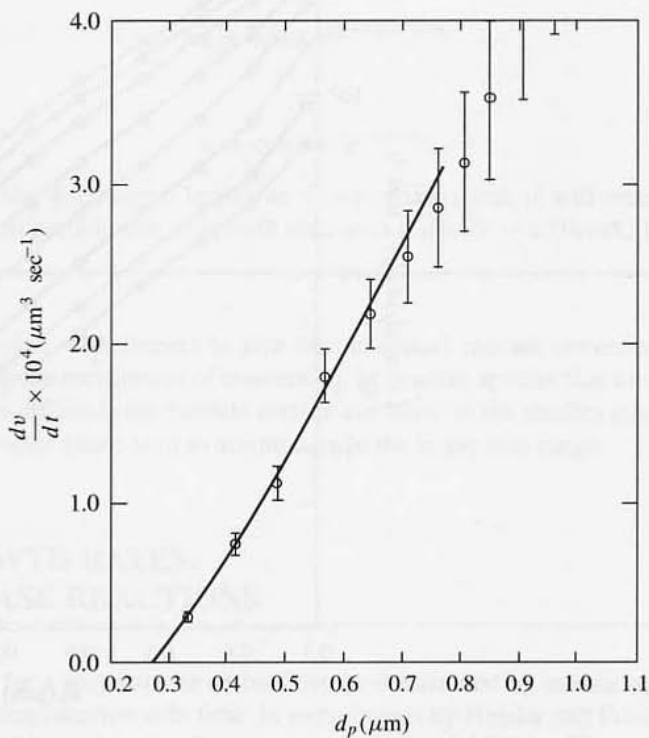


Figure 10.6 Particle growth rates between the fourth and fifth size distribution measurements for the data of Fig. 10.5. The solid line is a least-square best fit of the diffusional growth law, modified to include mean free path effects (10.21) and the Kelvin effect (10.24). The intercept on the size axis is the average critical size, d_p^* .

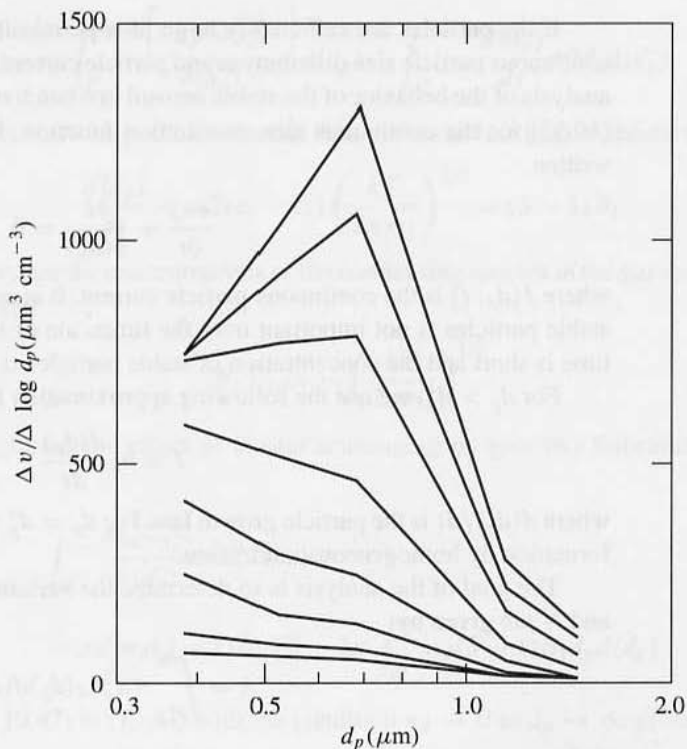


Figure 10.7 Growth in aerosol volume distributions by gas-to-particle conversion calculated from the growth relationship shown in Fig. 10.6. The peak occurs near the size range most efficient for scattering of visible light.

SIMULTANEOUS HOMOGENEOUS AND HETEROGENEOUS CONDENSATION

Theoretical Aspects

In many cases of practical interest, condensation takes place through both pathways discussed above, homogeneous and heterogeneous. These are very complex systems that in general must be analyzed on an *ad hoc* basis. In this section, an approximate set of equations is derived incorporating both processes in terms of the moments of the size distribution of the stable aerosol, $d_p > d_p^*$ (Friedlander, 1983).

The behavior of the stable aerosol is linked to the subcritical particle size range in several ways: (1) Stable particles originate from the subcritical size range by nucleation. (2) The growth of stable particles takes place primarily by condensation of the monomer, but also by the scavenging of subcritical clusters. (3) Monomer molecules evaporating from the stable aerosol may return to the total monomer pool.

If the particles are sufficiently large, it is permissible to pass from the discrete to the continuous particle size distribution and particle current. The basic starting equation for the analysis of the behavior of the stable aerosol in a batch reactor is the continuity relationship (10.33) for the continuous size distribution function. In terms of n_d and d_p , this can be written

$$\frac{\partial n_d}{\partial t} + \frac{\partial I}{\partial (d_p)} = 0 \quad (10.38)$$

where $I(d_p, t)$ is the continuous particle current. It is assumed that coagulation among the stable particles is not important over the timescale of interest. This can be justified if the time is short and the concentration of stable particles is low.

For $d_p > d_p^*$, we use the following approximation for the particle current,

$$I = n_d \frac{d(d_p)}{dt} \quad (10.39)$$

where $d(d_p)/dt$ is the particle growth law. For $d_p = d_p^*$ we have $I = I^*$, the rate of particle formation by homogeneous nucleation.

The goal of the analysis is to determine the variation of A and N with time, where A and N are given by

$$A = \int_{d_p^*}^{\infty} \pi d_p^2 n_d(d_p) d(d_p) \quad (10.40)$$

and

$$N = \int_{d_p^*}^{\infty} n_d(d_p) d(d_p) \quad (10.41)$$

By Leibnitz's rule, the change in the area of the stable aerosol with time is

$$\frac{dA}{dt} = \frac{d \int_{d_p^*}^{\infty} \pi d_p^2 n_d(d_p) d(d_p)}{dt} = \int_{d_p^*}^{\infty} \pi d_p^2 \frac{\partial n_d}{\partial t} d(d_p) - \pi d_p^{*2} n_d^* \frac{d(d_p^*)}{dt} \quad (10.42)$$

To find the first term on the right-hand side, multiply (10.38) by πd_p^2 and integrate:

$$\int_{d_p^*}^{\infty} \pi d_p^2 \frac{\partial n_d}{\partial t} d(d_p) + \int_{d_p^*}^{\infty} \frac{\partial n_d}{\partial (d_p)} \frac{d(d_p)}{dt} \pi d_p^2 d(d_p) = 0 \quad (10.43)$$

Substituting (10.43) in (10.42), we obtain

$$\frac{dA}{dt} = -\pi d_p^{*2} n_d^* \frac{d(d_p^*)}{dt} - \int_{d_p^*}^{\infty} \frac{\partial n_d}{\partial (d_p)} \frac{d(d_p)}{dt} \pi d_p^2 d(d_p) \quad (10.44)$$

Here $d(d_p^*)/dt$ represents the change in the critical particle size with time due to the variation of the saturation ratio with time.

The integral on the right-hand side of (10.44) is

$$\int_{d_p^*}^{\infty} \frac{\partial n_d}{\partial (d_p)} \frac{d(d_p)}{dt} \pi d_p^2 d(d_p)$$

$$= \int_{d_p^*}^{\infty} \frac{\partial \left[\pi d_p^2 n_d \frac{d(d_p)}{dt} \right]}{\partial (d_p)} d(d_p) - \int_{d_p^*}^{\infty} n_d \frac{d(d_p)}{dt} \pi 2d_p d(d_p) \quad (10.45)$$

The growth law for particles smaller than the mean free path of the carrier gas is

$$\frac{d(d_p)}{dt} = v_1 2(c_1 - c_s) \left(\frac{kT}{2\pi m_1} \right)^{1/2} = (S - 1)B_1 \quad (10.46)$$

where c_1 and c_s are the concentrations of the condensing species in the gas and at saturation, respectively, and

$$B_1 = 2n_s v_1 \left(\frac{kT}{2\pi m_1} \right)^{1/2}$$

(We have neglected the effect of cluster scavenging on growth.) Substituting (10.46) in (10.45) gives

$$\begin{aligned} & \int_{d_p^*}^{\infty} \frac{\partial n_d \frac{d(d_p)}{dt}}{\partial (d_p)} \pi d_p^2 d(d_p) \\ &= \pi d_p^{*2} n_d (S - 1) B_1 \Big|_{d_p^*}^{\infty} - 2\pi \int_{d_p^*}^{\infty} n_d (S - 1) B_1 d_p d(d_p) \end{aligned} \quad (10.47)$$

Substituting (10.47) in (10.44) with the condition $n_d \rightarrow 0$ as $d_p \rightarrow \infty$ gives

$$\frac{dA}{dt} = -\pi d_p^{*2} n_d^* \frac{d(d_p^*)}{dt} + Ik^{*2/3} S_1 + 2\pi B_1 (S - 1) M_1 \quad (10.48)$$

where $M_1 = \int_{d_p^*}^{\infty} n_d d_p d(d_p)$ and s_1 is the monomer surface area. The first term on the right-hand side represents the change in stable area, A , due to the moving boundary d_p^* that separates the stable from the unstable aerosol. To simplify the analysis, we consider cases in which this term can be neglected. This assumption can be tested after the calculation is completed. Hence, as an approximation we have

$$\frac{dA}{dt} = Ik^{*2/3} s_1 + 2B_1 (S - 1) M_1 \quad (10.49)$$

The first term on the right-hand side is the increase in area due to the formation of stable particles; the second term is the growth of existing stable particles. As noted above, we have neglected the moving boundary condition term in $d(d_p^*)/dt$. The moment, M_1 , is obtained by multiplying both sides of (10.47) by d_p and integrating by parts:

$$\begin{aligned} \frac{dM_1}{dt} &= \frac{d \int_{d_p^*}^{\infty} n_d d_p d(d_p)}{dt} = - \int_{d_p^*}^{\infty} \frac{\partial \left[d_p n_d \frac{d(d_p)}{dt} \right]}{\partial d_p} d(d_p) \\ &+ \int_{d_p^*}^{\infty} n_d \frac{d(d_p)}{dt} d(d_p) \end{aligned} \quad (10.50)$$

Carrying out the integrations on the right-hand side using (10.46) and neglecting the term in $d(d_p^*)/dt$, as before, we obtain

$$\frac{dM_1}{dt} = Id_p^* + (S-1)B_1N \quad (10.51)$$

Also, a monomer balance gives

$$\frac{dc_1}{dt} = R - Ik^* - c_s(S-1) \left(\frac{kT}{2\pi m_1} \right)^{1/2} A \quad (10.52)$$

or dividing by the saturation concentration c_s

$$\frac{dS}{dt} = \frac{R}{c_s} - \frac{Ik^*}{c_s} - (S-1) \frac{B_1A}{2v_1c_s} \quad (10.53)$$

Differentiating (10.41), integrating the continuity relation, (10.38), and neglecting the term in $d(d_p^*)/dt$, as before, we get

$$\frac{dN}{dt} = I \quad (10.54)$$

Thus, we have the following set of differential equations, which are applicable to the behavior of the stable particles in a uniform batch reactor:

$$\begin{aligned} \frac{dA}{dt} &= Ik^{*2/3}s_1 + 2\pi B_1(S-1)M_1 \\ \frac{dM_1}{dt} &= Id_p^* + (S-1)B_1N \\ \frac{dS}{dt} &= \frac{R}{n_s} - \frac{Ik^*}{n_s} - (S-1) \frac{B_1A}{2v_1n_s} \end{aligned}$$

and

$$\frac{dN}{dt} = I$$

The dependence of I on S is known from homogeneous nucleation theory discussed earlier in this chapter. Thus, there are four differential equations in five unknowns, A , M_1 , S , N , and I , with a relationship between I and S . The set of equations for the dynamics of the stable aerosol is remarkable because the calculation of the important moments, A and N , does not require the determination of the size distribution of the stable particles.

Oscillating Aerosol Reactors: An Experimental Study

Badger and Dryden (1939) studied aerosol formation in batch and flow reactors. They were interested in the aerosol that forms in coal gas which also contains trace amounts of nitric oxide. The nitric oxide reacts with diolefins in the coal gas, such as butadiene and cyclopentadiene, to form products of low vapor pressure. These condense and produce a sticky aerosol present at concentrations usually less than 0.5 mg m^{-3} which may foul the gas transfer system.

The experiments were made in a 10-ft^3 gas holder. In the flow reactor studies, a mixture of NO in nitrogen was added at a constant rate to a stream of coal gas entering the holder. Aerosol samples were withdrawn from the center of the gas holder, and the particles were

observed by using ultramicroscopy and by thermal precipitation with optical microscopy. At certain values of the controllable parameters of the system, sustained oscillations of the aerosol number density with time were observed that continued as long as the system was observed. The period of the oscillation was about 1 hr and the residence time was 2 hr (Fig. 10.8).

The experimental results can be explained as follows. At the start, in the absence of particles in the entering reactant stream, the concentration of monomer formed by reaction between NO and the coal gas components mounts, increasing more rapidly than the depletion by flow from the reactor. Homogeneous nucleation then takes place, and the particle concentration rapidly increases. Condensation on the growing particles then depletes the monomer concentration to the point that nucleation ceases. Meanwhile, the particle concentration starts to fall because of the flow of the gas through the holder and, to a lesser extent, because of sedimentation and coagulation. As the aerosol is depleted, the monomer concentration increases until nucleation again generates high concentrations of new particles and the process repeats itself.

Thus, at any instant, the gas should contain several different generations of particles, each of a characteristic size. Microscopic observations of aerosol samples deposited by thermal precipitation indicate that this is the case.

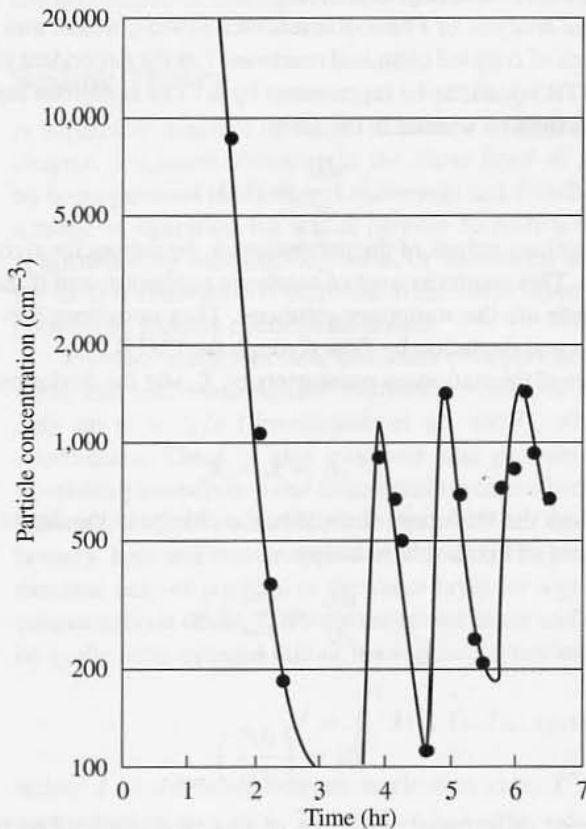


Figure 10.8 Oscillatory behavior of particle number density ($d_p > 0.3 \mu\text{m}$) in a flow reactor study of coal gas containing NO at a concentration of 11.6 ppm. Measurements of deposited particles were made with an optical counter. It is likely that many more particles were present in the ultrafine range ($d_p < 0.1 \mu\text{m}$) and not counted. (After Badger and Dryden, 1939.)

The number density shown in Fig. 10.8 is for particles larger than $0.3 \mu\text{m}$ measured by optical microscopy. The measured number density is almost certainly much smaller (perhaps by orders of magnitude) than the true number density of stable particles, most of which are ultrafine ($d_p < 0.1 \mu\text{m}$). The variations shown in Fig. 10.8 are probably more closely related to particle surface area A than to the total number density; most of the stable surface area is associated with particles larger than $0.1 \mu\text{m}$ during much of the cycle. However, the same explanations for oscillations in A apply as for N .

This qualitative explanation for the oscillatory behavior of the particle number density is supported by theory. Assume the system can be modeled as a continuous steady-state stirred tank reactor (CSTR); that is, reactants enter and products leave from a perfectly mixed tank with composition equal to that of the products. The set of equations derived in the previous section applies, but a new term must be subtracted from the right-hand side in each case to account for the loss of particles from the CSTR by the flow process. Equation (10.49) for the change in aerosol surface area with time becomes

$$\frac{dA}{dt} = Ik^{*2/3}s_1 + 2B_1(S-1)M_1 - \frac{A}{\tau} \quad (10.55)$$

where the residence time, τ , is equal to the chamber volume divided by the volumetric flow rate. Corresponding terms, M_1/τ , S/τ , and N/τ , are subtracted from (10.51), (10.53), and (10.54). The result is a set of four nonlinear first-order ordinary differential equations containing both positive and negative terms.

We follow the analysis of Frank-Kamenetskii (1955), which was originally applied to the behavior of sets of coupled chemical reactions. Let the dependent parameters, A , M_1 , S , and N , of the CSTR equations be represented by x_i . The equations for the dynamics of the stable aerosol can then be written in the form

$$\frac{dx_i}{dt} = F_i(x_k) \quad (10.56)$$

We may seek stationary values of the parameters x_i by setting the right-hand sides of these equations to zero. This results in a set of algebraic equations; and if there are finite positive real solutions, these are the stationary solutions. They correspond to the balance between aerosol formation and depletion by flow through the CSTR.

Let the values of the stationary parameters be X_i and the deviations from the stationary values be ε_i

$$\varepsilon_i = x_i - X_i \quad (10.57)$$

If the system is near the stationary state, then the change in the deviation with time can be represented by a set of linear relationships

$$\frac{d\varepsilon_i}{dt} = \sum_k f_{ik}\varepsilon_k \quad (10.58)$$

where

$$f_{ik} = \left(\frac{\partial F_i}{\partial x_k} \right)_{x=X} \quad (10.59)$$

Systems of coupled differential equations of this type can lead to periodic behavior for

certain values of the characteristic parameters. The values of x_i should either tend to the stationary solutions or oscillate around them, as in the experiments of Badger and Dryden (Fig. 10.8). Based on an analysis of this kind, Pratsinis et al. (1986) determined the conditions for instabilities in these equations and for the existence of oscillating number densities. However, a detailed comparison of theory with the experiments of Badger and Dryden was not possible because of the unknown properties of the aerosol material.

EFFECTS OF TURBULENCE ON HOMOGENEOUS NUCLEATION

In practical applications, homogeneous nucleation often occurs in turbulent flows; examples include vehicular and aircraft emissions, fugitive and accidental releases from industrial sources, and mixing in industrial aerosol reactors. The complexity of turbulent flow fields, coupled with uncertainties in nucleation theory, preclude exact analysis of homogeneous nucleation in turbulent flows. The effects of turbulent fluctuations are usually neglected, and calculations are based on mean velocity, temperature, and concentration profiles. However, such calculations can lead to serious error because of the highly nonlinear dependence of the nucleation rate on concentration and temperature (10.16). The discussion in this section is limited to particle formation in free turbulent jets that have been well-characterized with respect to heat, mass and momentum transfer, and are of practical interest. Emphasis is on the application of scaling concepts rather than on detailed calculations.

Scaling Theory

A schematic diagram of the jet structure is shown in Fig. 10.9. As discussed in the last chapter, processes occurring in the shear layer of a jet strongly affect particle formation by homogeneous nucleation. Lesniewski and Friedlander (1998) hypothesized that there is a range of operation for which particle formation occurs in the shear layer of the jet but is quenched by dilution, depletion, or nucleation suppression as the particles move down the axis. If nucleation is confined to the shear layer, useful scaling laws can be derived for correlating particle concentration data.

Previous studies of heat and mass transport in turbulent shear layers have shown that mean and root-mean-square fluctuation values of temperature and concentration depend only on $\eta = y/z$ (Sreenivasan et al., 1977), where y and z are the radial and axial coordinates. There is also evidence that probability density functions (PDFs) for the fluctuating temperature and concentration depend only on η and not on the Reynolds number (Konrad, 1977; Broadwell and Mungal, 1991). If the Lewis number of the binary gas mixture is unity, heat and matter spread at the same rate and the local average nucleation rate is a function only of position in the shear layer for a given set of gas stream temperatures and concentrations. If the PDFs for the temperature and concentration fluctuations depend only on η , the local average rate of homogeneous nucleation in a turbulent flow is given by

$$\bar{I} = \int_0^1 I(\theta, T_0, T_\infty, c_0, c_\infty) \cdot P(\theta) d\theta \quad (10.60)$$

where I is the instantaneous nucleation rate, T and c are the temperature and vapor concentration, $\theta = (T - T_\infty)/(T_0 - T_\infty) = (c - c_\infty)/(c_0 - c_\infty)$, and $P(\theta)$ is the PDF for

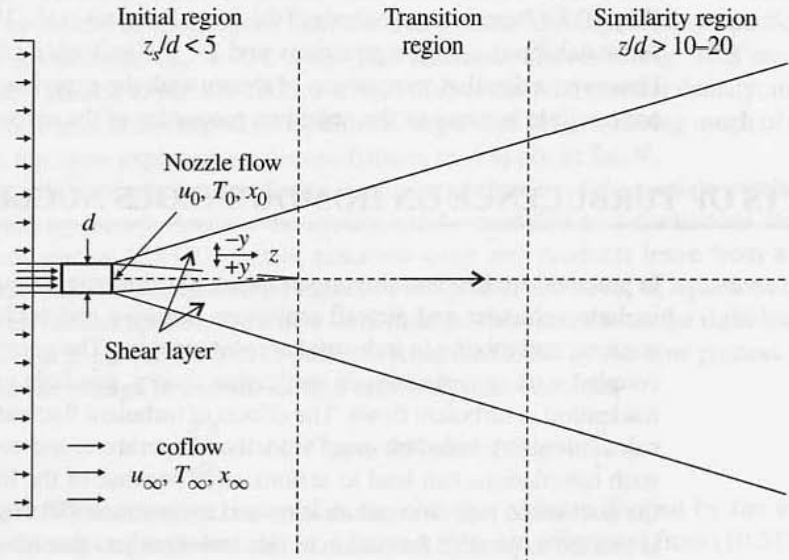


Figure 10.9 The axisymmetric free turbulent jet. The initial region of the axisymmetric jet, extending to 5–10 nozzle diameters, consists of an undisturbed cone of nozzle fluid surrounded by the shear layer. For nucleation-controlled growth, particle formation is confined to the shear layer.

the turbulent flow. Both the instantaneous nucleation rate and the PDF can be taken from theory or experimental data; scaling laws can be derived without assuming a detailed form for either.

The total rate of particle formation—that is, the number of particles formed over the entire shear layer per unit time—is of interest in many applications. In the limit of negligible coagulation and vapor depletion, the total rate of particle formation in an axisymmetric shear layer is

$$\bar{Y} = \frac{2\pi z^3}{3} \int_{\eta_1}^{\eta_2} \bar{I} \eta d\eta \quad (10.61)$$

where η_1 and η_2 define the edges of the shear layer. Because the PDFs are independent of Reynolds number, the particle formation rate is a function only of z and the nucleation rate, which depends on the gas stream temperatures, vapor concentrations, and material properties of the condensate.

In a free turbulent jet, the length of the shear layer is 5 to 10 times the nozzle diameter, d . If nucleation is confined to the shear layer, according to (10.61) the particle formation rate is proportional to d^3 and is independent of the initial jet velocity u_0 . Because the volumetric flowrate of a turbulent jet (Q) is proportional to $u_0 d^2$ and \bar{Y} to $\bar{N}_s Q$, the particle concentration in the gas exiting the initial region (\bar{N}_s) is proportional to d/u_0 . Moreover, because the particle concentration downstream of the shear layer changes only by dilution, $\bar{N} \sim \bar{N}_s d/z$, and the group $\bar{N} u_0 z/d^2$ should be constant at any point on the jet axis for a given initial temperature and vapor concentration conditions.

Experimental Tests of Scaling Theory

In experiments designed to test the scaling laws, size distributions and number concentrations of dibutyl phthalate (DBP) aerosol were measured for different jet velocities, vapor concentrations, nozzle diameters, and sampling positions in a bench-scale condensing jet. Two different nozzle diameters were used, 0.235 and 0.375 cm, and jet Reynolds numbers were greater than 3000.

Particle size distributions were measured 20 nozzle diameters downstream of the nozzle exit, on the jet centerline (Fig. 10.10). At low DBP vapor concentrations, the size distributions were unimodal with count mean diameters of 0.4 to 0.5 μm and mass mean diameters of about 3 μm . As the vapor mole fraction increased, the count mean diameter

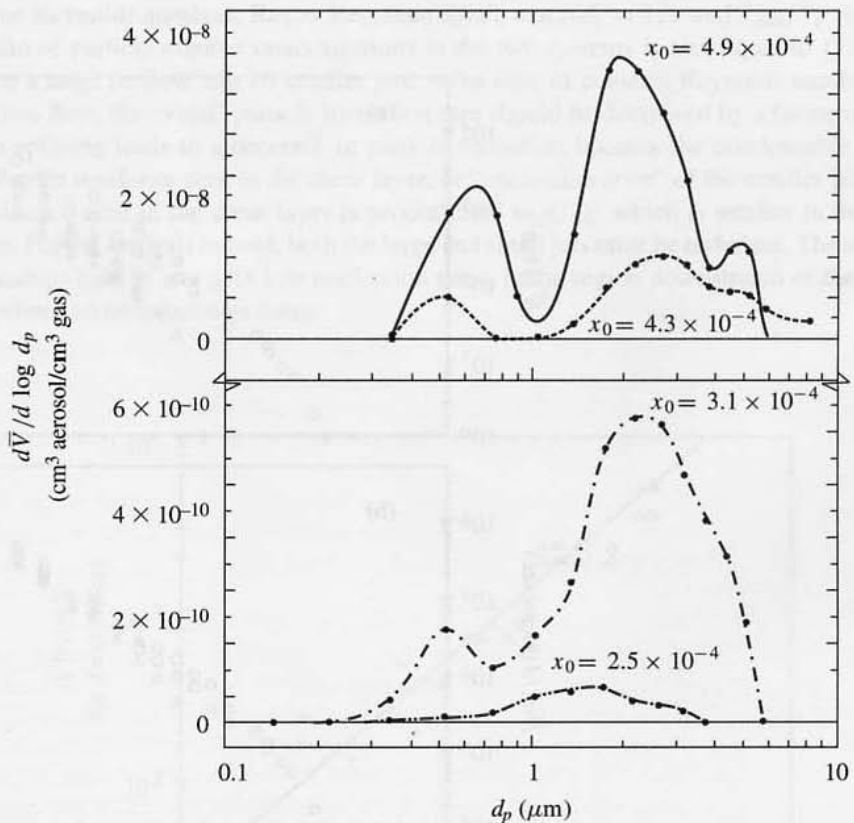


Figure 10.10 Evolution of the size distribution as the nozzle concentration of DBP, x_0 increased. Lines are fits to data measured with an electrostatic classifier and an optical particle counter on the jet centerline at 20 nozzle diameters. The area under each curve is proportional to the total particle volume per volume of gas. At low vapor concentrations ($x_0 = 2.5 \times 10^{-4}$), most of the aerosol mass is in 1- to 3- μm particles, which form by nucleation in the shear layer and grown by condensation from the gas. At slightly higher vapor concentrations ($x_0 = 3.1 \times 10^{-4}$), a submicron mode breaks out, the sign of the onset of particle formation downstream from the shear layer. At intermediate vapor concentrations ($x_0 = 4.3 \times 10^{-4}$), the smaller mode grows. At the highest vapor concentrations ($x_0 = 4.9 \times 10^{-4}$), a third mode of larger particles appears due to coagulation of the other modes.

increased. At a certain concentration, in the DBP experiments $3.5(10)^{-4}$, a second submicron mode developed in the size distribution, suggesting that nucleation occurred outside the shear layer. Eventually, coagulation became significant; a third mode appeared at $5 \mu\text{m}$, and the two smaller modes grew together. At very high vapor concentrations, coagulation would dominate particle growth.

In Fig. 10.11, data taken at an axial distance of 20 nozzle diameters are shown as a function of DBP vapor concentration for different jet velocities and nozzle diameters. At a given value of x_0 , the measured particle concentration decreased as the nozzle diameter decreased and the initial velocity increased. The data collapsed onto a single curve when plotted as $\bar{N}u_0/d$ versus the vapor concentration, consistent with scaling predictions. Axial particle concentration profiles showed similar trends.

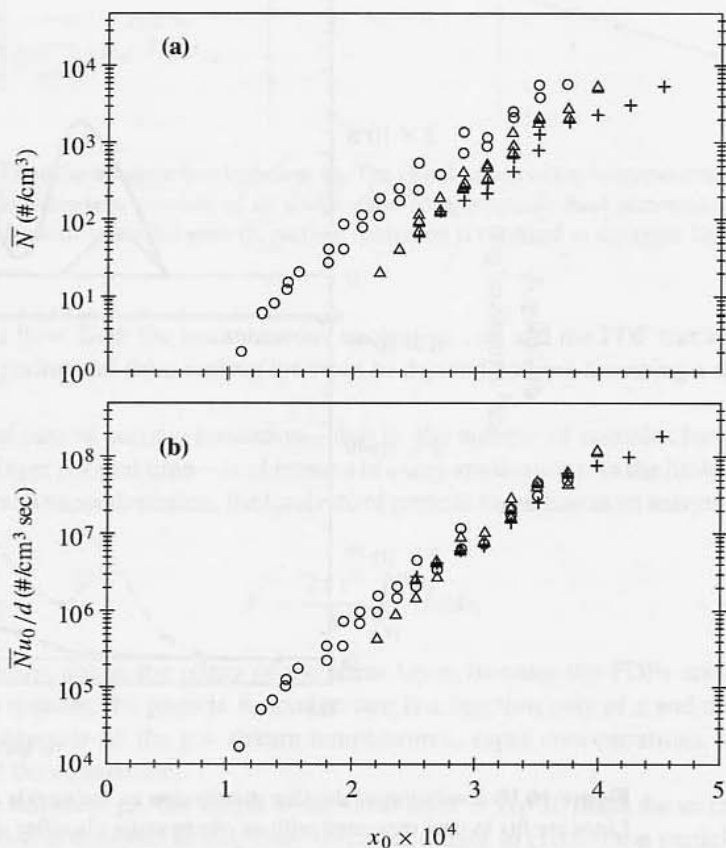


Figure 10.11 Scaling of particle number concentration in a turbulent jet. (a) Aerosol number density measured at 20 nozzle diameters on the jet centerline. (○) $d = 0.375$ cm, $Re = 4700$; (△) $d = 0.235$ cm, $Re = 4700$; (+) $d = 0.235$ cm, $Re = 7100$. For a given value of x_0 , \bar{N} increased with d and u_0 . (b) Data of (a) replotted as $\bar{N}u_0/d$ versus x_0 ; the data collapse to a single curve. The data demonstrate the effects of varying both nozzle diameter and velocity.

Effect of Splitting the Flow into Multiple Streams

The scaling relationships can be exploited to decrease the overall particle formation rate by splitting a large nozzle flow into multiple smaller streams. Consider a large stream (“1”) split into n smaller, noninteracting jets with equal diameters. The temperatures and vapor concentrations are the same in both systems. Two additional relations are needed to compare their particle formation rates. The first is that the total mass flow for the multiple jets is equal to the single jet flow $\dot{m} = n \cdot \dot{m}_n$. The ratio of total particle formation rates in the two systems, $\bar{Y}_{\text{tot}} = n \cdot \bar{Y}_n$ and \bar{Y}_1 , is then

$$\frac{\bar{Y}_{\text{tot}}}{\bar{Y}_1} = \frac{nd_n^3}{d_1^3} = \frac{1}{n^2} \frac{\text{Re}_1}{\text{Re}_n} \quad (10.62)$$

If the system is operated such that the main flow and the individual small jet flows have the same Reynolds numbers, $\text{Re}_1 = \text{Re}_n$, then $d_n/d_1 = u_n/d_1 = 1/n$ and $\bar{Y}_{\text{tot}}/\bar{Y}_1 = 1/n^2$. The ratio of particle number concentrations in the two systems is also equal to $1/n^2$. By splitting a large jet flow into 10 smaller jets, in the case of constant Reynolds number and total mass flow, the overall particle formation rate should be decreased by a factor of 100. Stream splitting leads to a decrease in particle formation because the condensable vapor has a shorter residence time in the shear layer, or “nucleation zone” of the smaller jets, and the residence time in the shear layer is proportional to d/u_0 , which is smaller in the split streams. For the analysis to hold, both the large and small jets must be turbulent. The scaling relationships hold in jets with low nucleation rates, in the region downstream of the shear layer, where no new particles form.

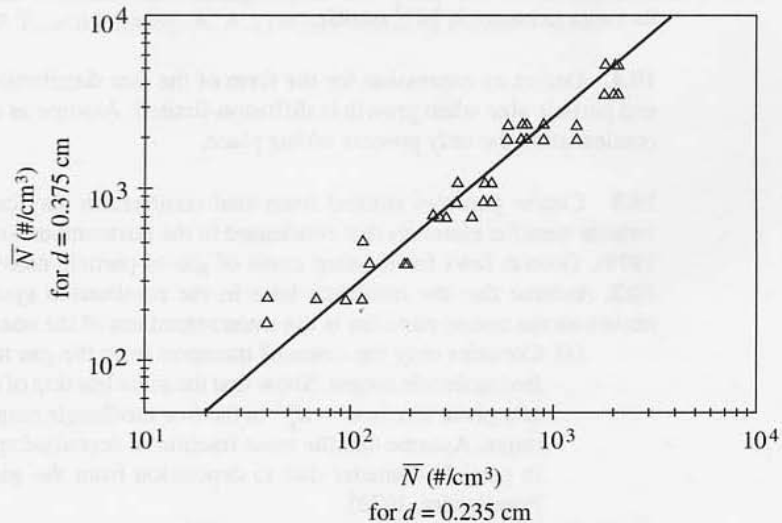


Figure 10.12 Particle number concentration in jet with 0.375-cm-diameter nozzle versus particle concentration in jet with 0.235-cm nozzle. In agreement with the stream splitting prediction (solid line), $\bar{N}_{d=0.375\text{cm}}/\bar{N}_{d=0.235\text{cm}} = (0.375/0.235)^2 = 2.6$. Data were measured at 20 nozzle diameters on jet centerline with $\text{Re} = 4700$.

The stream splitting concept was tested experimentally by measuring the particle concentration in jets with two different nozzle diameters and the same Reynolds number. The results are shown in Fig. 10.12. For a given axial position and vapor concentration, the aerosol concentration measured on the jet centerline was proportional to the nozzle diameter. For example, at 20 nozzle diameters, for $Re = 4700$, the concentration in the jet with $d = 0.375$ cm was $5400/\text{cm}^3$, and the one with $d = 0.235$ cm was $2100/\text{cm}^3$. The ratio of the two measured particle concentrations was close to the theoretically predicted value $(0.375/0.235)^2 = 2.6$. The stream splitting correlation held for the entire range of vapor concentrations tested in the experiments.

PROBLEMS

10.1 Estimate the time it takes for an $0.1\text{-}\mu\text{m}$ water droplet at a temperature of 25°C to evaporate completely. Take into account the Kelvin effect and assume it applies to particles of vanishing diameter. Assume also that the vapor pressure of the water in the bulk of the gas far from the surface of the particle is zero. Neglect the heat of evaporation in your calculation.

10.2. Determine the size of the smallest stable drop at the critical saturation ratio for toluene at 300 K. Of how many molecules are these drops composed?

10.3 The total surface area of the Los Angeles smog aerosol is of the order of $1000 \mu\text{m}^2/\text{cm}^3$. Estimate the maximum rate of formation of a condensable species by chemical reaction that can be sustained *without* homogeneous nucleation taking place. Express your answer in $\mu\text{g}/\text{m}^3 \text{ hr}$ as a function of the saturation ratio. The molecular weight of the condensable species is 100 and its vapor pressure is 10^{-7} mmHg.

10.4 Derive an expression for the form of the size distribution function as a function of time and particle size when growth is diffusion-limited. Assume as a model an aerosol in a box with condensation the only process taking place.

10.5 Coarse particles emitted from coal combustion may carry small amounts of relatively volatile metallic elements that condensed in the postcombustion gases (Flagan and Friedlander, 1978). Growth laws for limiting cases of gas-to-particle conversion are summarized in Table 10.3. Assume that the residence time in the combustion system during which condensation occurs on the coarse particles is the same regardless of the coarse particle diameter.

(a) Consider only the cases of transport from the gas to particles in the continuum and free molecule ranges. Show that the mass fraction of deposited species x_i for a particle of a given size is $x_i \sim d_p^{-1}$ in the free molecule range and $x_i \sim d_p^{-2}$ in the continuum range. Assume that the mass fraction of deposited species is so small that the change in particle diameter due to deposition from the gas can be neglected (Flagan and Friedlander, 1978).

(b) Data on trace element concentrations in the coarse ($d_p > 1\mu\text{m}$) fraction of aerosols emitted in coal combustion are given in Table 1.2. Plot the mass fractions in $\mu\text{g}/\text{g}$ for As, Ni, Se, and Cd as a function of particle diameter (log-log) and compare the resulting slopes with the theoretical relationships derived in part (a).

REFERENCES

- Badger, E. H. M., and Dryden, I. G. C. (1939) *Trans. Faraday Soc.*, **35**, 607.
- Broadwell, J. E., and Mungal, M. G. (1991) *Phys. Fluids*, **A3**, 1193.
- Brock, J. R. (1971) *Atmos. Environ.*, **5**, 833.
- Denbigh, K. G. (1971) *The Principles of Chemical Equilibrium*, 2nd ed., Cambridge University Press, Cambridge, UK.
- Flagan, R. C. and Friedlander, S.K. (1978) Particle Formation in Pulverized Coal Combustion—A Review in Shaw, D.T. (ed) *Recent Developments in Aerosol Science* pp. 47–50.
- Frank-Kamenetskii, D. A. (1955) *Diffusion and Heat Exchange in Chemical Kinetics*, Princeton University Press, Princeton, NJ, Chapter X.
- Friedlander, S. K. (1983) *Annals of the New York Academy of Sciences*, **44**, 354.
- Fuchs, N. A., and Sutugin, A. G. (1971) High-Dispersed Aerosols, in Hidy, G. M., and Brock, J. R. (Eds.), *Topics in Current Aerosol Research*, Pergamon, New York.
- Heisler, S. L., and Friedlander, S. K. (1977) *Atmos. Environ.*, **11**, 157.
- Heist, R. H., and Reiss, H. (1973) *J. Chem. Phys.*, **59**, 665.
- Hirth, J. P., and Pound, G. M. (1963) *Condensation and Evaporation: Nucleation and Growth Kinetics*, Macmillan, New York.
- Katz, J. L., Scoppa, C. J., Kumar, N. G., and Mirabel, P. (1975) *J. Chem Phys.*, **62**, 448.
- Konrad, J. H. (1977) An Experimental Investigation of Mixing in Two-Dimensional Turbulent Shear Flows with Applications to Diffusion-Limited Chemical Reactions, SQUID Technical Report, CIT-8-PU.
- Lesniewski, T. K., and Friedlander, S. K. (1998) *Proc. R. Soc.*, **454**, 2477.
- Mason, B. J. (1971) *The Physics of Clouds*, Clarendon Press, Oxford.
- Pratsinis, S. E., Friedlander, S. K., and Pearlstein, A. J. (1986) *AIChE J.*, **32**, 177.
- Reiss, H. (1950) *J. Chem. Phys.*, **18**, 840.
- Sreenivasan, K. A., Antonia, R. A., and Stephenson, S. E. (1977) Conditional Measurements in a Heated Axisymmetric Mixing Layer, University of Newcastle, Australia, T.N.F.M.5.
- Wegener, P. P., and Pouring, A. A. (1964) *Physics of Fluids*, **7**, 352.

Chapter 11

The General Dynamic Equation for the Particle Size Distribution Function

Gas-to-particle conversion, coagulation and particle transport have been discussed in previous chapters. These processes determine the change in the size distribution function with time and position. A general dynamic equation (GDE) for $n(\mathbf{r}, v, t)$ that includes all of these processes is set up in this chapter. This equation is sometimes referred to as a population balance equation. By solving the equation for different initial and boundary conditions, the size distribution function can be calculated for geometries and flow conditions of practical interest. The GDE is of fundamental importance to understanding and modeling industrial and atmospheric processes.

At the beginning of the chapter it is shown that the usual models for coagulation and nucleation presented in Chapters 7 and 10 are special cases of a more general theory for very small particles. An approximate criterion is given for determining whether nucleation or coagulation is rate-controlling at the molecular level. The continuous form of the GDE is then used to derive balance equations for several moments of the size distribution function.

Because the GDE is a nonlinear, partial integrodifferential equation, numerical solutions are usually required. Simple analytical solutions, some approximate, are given for several cases in which two or more processes that modify the size distribution are occurring at the same time. As examples, we consider simultaneous condensation and coagulation, turbulent diffusion and growth, and coagulation with transport to surfaces. Various terms that appear in the GDE such as the collision frequency function and migration velocities depend on the gas temperature and pressure. Hence it is necessary to have independent information on the gas properties as a function of time and position. This can be obtained either through experimental measurements or through calculations based on the energy equation and the equations of fluid motion.

Advances in instrumentation and analytical methods have made it easier to follow the dynamics of aerosols experimentally. This has stimulated development of numerical methods for solving the GDE which have been reviewed by Williams and Loyalka (1991, Chapter 5). Further development of numerical methods can be expected especially for

turbulent systems that are of great practical importance both in the atmosphere and in process gases.

GENERAL DYNAMIC EQUATION FOR THE DISCRETE DISTRIBUTION FUNCTION

The Smoluchowski equation for the discrete size distribution (Chapter 7) can be generalized to take into account evaporation from the particles using the evaporative flux terms that appear in nucleation theory

$$\frac{\partial n_k}{\partial t} = \frac{1}{2} \sum_{i+j=1}^{\infty} \beta(i, j)n_i n_j - \sum_{i=1}^{\infty} \beta(i, k)n_i n_k + \alpha_{k+1}s_{k+1}n_{k-1} - \alpha_k s_k n_k \quad (11.1)$$

In this expression, k refers to the number of molecules in each particle. Equation (11.1) represents not only a generalization of the Smoluchowski equation but also the kinetic equation that appears in the classical theory of homogeneous nucleation (Chapter 10):

$$\frac{\partial n_k}{\partial t} = I_k - I_{k+1} \quad (11.2)$$

This is shown by grouping collisions among clusters ($i, j \neq 1$) in (11.1) as follows:

$$\begin{aligned} \frac{\partial n_k}{\partial t} = & \frac{1}{2} \sum_{\substack{i+j=k \\ i, j \neq 1}} \beta(i, j)n_i n_j - \sum_{i=2}^{\infty} \beta(i, k)n_i n_k \\ & + \beta(i, k-1)n_1 n_{k-1} - \beta(1, k)n_1 n_k - \alpha_k s_k n_k + \alpha_{k+1} s_{k+1} n_{k+1} \end{aligned} \quad (11.3)$$

The first two terms on the right-hand side represent collisions between particles larger than a single molecule. The last four terms are equal to $I_k - I_{k+1}$. Summarizing, (11.1) represents the change in n_k due to the *internal* processes taking place within an elemental volume, namely coagulation and gas-to-particle conversion. The elemental volume is fixed in space. The value of n_k in the elemental volume may also change as a result of *external* processes that lead to particle transport across the boundaries of the volume. These processes include diffusion and external force fields such as gravity, electrical potential gradients, and thermophoresis (Chapter 2).

The change in the discrete distribution function with time and position is obtained by generalizing the equation of convective diffusion (Chapter 3) to include terms for particle growth and coagulation:

$$\frac{\partial n_k}{\partial t} + \nabla \cdot n_k \mathbf{v} = \nabla \cdot D \nabla n_k + \left[\frac{\partial n_k}{\partial t} \right]_{\text{growth}} + \left[\frac{\partial n_k}{\partial t} \right]_{\text{coag}} - \nabla \cdot \mathbf{c} n_k \quad (11.4)$$

where the diffusion coefficient D is a function of particle size and \mathbf{c} is the particle velocity resulting from the external force field. The summation of the growth and coagulation terms is given by (11.1). Equation (11.4) is the general dynamic equation for the discrete distribution function where k refers to the number of molecules in the particle. This result is most useful

for particles containing a relatively small number of molecules, say less than a few thousand. This corresponds to particles smaller than about 50 nm.

COAGULATION AND NUCLEATION AS LIMITING PROCESSES IN GAS-TO-PARTICLE CONVERSION

When a fast chemical reaction or a rapid quench leads to the formation of a high density of condensable molecules, particle formation may take place either by homogeneous nucleation, an activated process, or by molecular "coagulation" a process in which nearly all collisions are successful. What determines which of these processes controls? In principle, this problem can be analyzed by solving the GDE for the discrete distribution discussed in the previous section. An approximate criterion proposed by Ulrich (1971) for determining whether nucleation or coagulation is the dominant process is based on the critical particle diameter d_p^* that appears in the theory of homogeneous nucleation (Chapter 9)

$$d_p^* = \frac{\sigma v_m}{kT \ln p/p_s} \quad (11.5)$$

where p/p_s is the ratio of the partial pressure of the condensable vapor to the saturation vapor pressure at the local temperature, T , σ is the surface tension, and v_m is the molecular volume of the material composing the particle. This relationship holds best for particles composed of a large number of molecules, say more than 50 or 100, but is used for an order of magnitude estimate down to molecular dimensions in this analysis. The value of d_p^* can be compared with the molecular diameter of the condensing species:

$$d_{pm} = \left[\frac{6v_m}{\pi} \right]^{1/3} \quad (11.6)$$

When the partial pressure of the condensing vapor is very high (compared with the vapor pressure), d_p^* approaches molecular dimensions. Equating (11.5) and (11.6) and rearranging gives

$$\ln \frac{p}{p_s} = \left(\frac{\pi}{6} \right)^{1/3} \frac{\sigma v_m^{2/3}}{kT} \quad (11.7)$$

For partial pressures higher than the value corresponding to (11.7), individual molecules can serve as stable nuclei, and the problem reduces to the case of the coagulation of coalescing spheres (Chapter 7). Calculations of this type made for the commercial synthesis of fumed silica showed that the size of the critical SiO_2 nucleus was indeed smaller than the molecular diameter (Ulrich, 1971). This indicates that classical coagulation theory holds at least approximately from the beginning of the particle formation process, immediately following the chemical reactions that generate condensable molecules. In this case, nucleation theory does not enter into the dynamics.

There is another limitation on the applicability of this analysis. It holds when particle collision leads to coalescence and not to the formation of solid primary particles and their aggregates. The assumption of coalescing particles usually holds best during the early stages of particle formation. In the later stages, for highly refractory (low vapor pressure)

substances, coalescence slows and solid primary particles form. Prediction of the diameter of the primary particles and the time of formation of their agglomerates requires extension of the GDE to include particle coalescence rates in addition to collision rates. These phenomena are discussed in the next chapter.

GENERAL DYNAMIC EQUATION FOR THE CONTINUOUS DISTRIBUTION FUNCTION

As particle size increases ($v \gg v_m$), it becomes convenient to pass from the discrete distribution to the continuous distribution to carry out calculations. The transition to the continuous distribution function requires care. For the growth term, this was shown to be (Chapter 9)

$$\left[\frac{\partial n}{\partial t} \right]_{\text{growth}} = -\frac{\partial I}{\partial v} \quad (v \gg v_m) \quad (11.8)$$

The particle current, I , can be expressed as the sum of diffusion and migration terms in v space (Chapter 9):

$$I = -D_v \frac{\partial n}{\partial v} + nq \quad (11.9)$$

where $q = dv/dt$ is the migration velocity through v space. Similarly, the coagulation terms become

$$\begin{aligned} \left[\frac{\partial n}{\partial t} \right]_{\text{coag}} &= \frac{1}{2} \int_0^v \beta(\tilde{v}, v - \tilde{v}) n(\tilde{v}) n(v - \tilde{v}) d\tilde{v} \\ &\quad - \int_0^\infty \beta(v, \tilde{v}) n(v) n(\tilde{v}) d\tilde{v} \quad (v \gg v_m) \end{aligned} \quad (11.10)$$

Substituting (11.8) and (11.10) for growth and coagulation, respectively, in (11.4), we obtain the GDE for the continuous distribution function:

$$\begin{aligned} \frac{\partial n}{\partial t} + \nabla \cdot n\mathbf{v} + \frac{\partial I}{\partial v} &= \nabla \cdot D\nabla n + \frac{1}{2} \int_0^v \beta(\tilde{v}, v - \tilde{v}) n(\tilde{v}) n(v - \tilde{v}) d\tilde{v} \\ &\quad - \int_0^\infty \beta(v, \tilde{v}) n(v) n(\tilde{v}) d\tilde{v} - \nabla \cdot \mathbf{c}n \quad (v \gg v_m) \end{aligned} \quad (11.11)$$

Collisions with single molecules are excluded from the coagulation terms in this expression. For the usual case of an incompressible flow, the second term on the left-hand side takes the form

$$\nabla \cdot n\mathbf{v} = \mathbf{v} \cdot \nabla n$$

An equation of similar form was derived by Hulburt and Katz (1964) in a different way. Relationships among the terms appearing in (11.11) have been discussed by Dunning (1973).

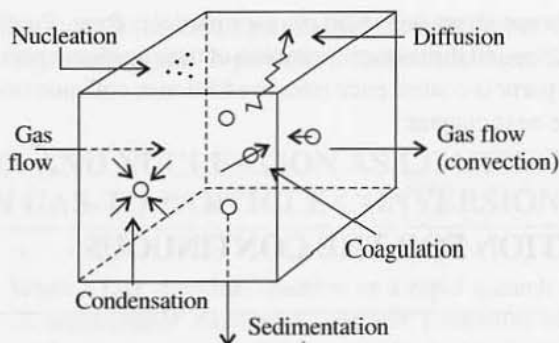


Figure 11.1 Processes taking place in an elemental volume included in the general dynamic equation. Gas flows produce particle transport across the element boundaries. In addition to gravitation, other force fields that drive fluxes (not shown) are electrical potential and temperature gradients.

Processes affecting the size distribution function are summarized in Fig. 11.1. To solve the GDE, expressions are needed for I and $\beta(v, \tilde{v})$ as shown later in this chapter. However, it is possible to derive useful expressions for the dynamics of the number and volume concentrations without assuming forms for these parameters.

THE DYNAMIC EQUATION FOR THE NUMBER CONCENTRATION N_∞

The dynamics of the total number concentration, N_∞ , and volume fraction of aerosol material, ϕ , are moments of special interest. There is a problem in defining the total number concentration, N_∞ , in all experimentally meaningful way. This parameter is usually measured with a condensation particle counter (CPC) (Chapter 6). The CPC detects particles larger than some minimum size that depends to some extent on their chemical nature and shape. Let v_d be the minimum detectable particle volume. Then

$$N_\infty = \int_{v_d}^{\infty} n(v) dv \quad (11.12)$$

and assume $v_d > v^*$ the critical particle volume for homogeneous nucleation.

The dynamic equation for the total number concentration is obtained by integrating the GDE with respect to v over all values of $v > v_d$:

$$\begin{aligned} \frac{\partial N_\infty}{\partial t} + \mathbf{v} \cdot \nabla N_\infty + \int_{v_d}^{\infty} \frac{\partial I}{\partial v} dv &= \nabla^2 \int_{v_d}^{\infty} Dn dv \\ &+ \frac{1}{2} \int_{v_d}^{\infty} \left[\int_0^v \beta(\tilde{v}, v - \tilde{v}) n(\tilde{v}) n(v - \tilde{v}) d\tilde{v} \right] dv \\ &- \int_{v_d}^{\infty} \left[\int_0^\infty \beta(v, \tilde{v}) n(v) n(\tilde{v}) d\tilde{v} \right] dv \\ &- \frac{\partial \int_{v_d}^{\infty} c_s n dv}{\partial z} \end{aligned} \quad (11.13)$$

The growth term is evaluated as follows:

$$\int_{v_d}^{\infty} \frac{\partial I}{\partial v} dv = I_{\infty} - I_d \quad (11.14)$$

On physical grounds, $I_{\infty} = 0$ because there is no loss of particles by growth from the upper end of the distribution. The term I_d is the particle current flowing into the lower end of the spectrum. When homogeneous nucleation takes place, this term is important. For $v_d = v^*$, the critical particle size, I_d , is the particle current of homogeneous nucleation theory. Hence the dynamic equation for the number concentration is

$$\begin{aligned} \frac{\partial N_{\infty}}{\partial t} + \mathbf{v} \cdot \nabla N_{\infty} &= I_d + \nabla^2 \int_{v_d}^{\infty} Dn dv \\ &+ \frac{1}{2} \int_{v_d}^{\infty} \left[\int_0^v \beta(\tilde{v}, v - \tilde{v}) n(\tilde{v}) n(v - \tilde{v}) d\tilde{v} \right] dv \\ &- \int_{v_d}^{\infty} \left[\int_0^{\infty} \beta(v, \tilde{v}) n(v) n(\tilde{v}) d\tilde{v} \right] dv - \frac{\partial \int_{v_d}^{\infty} c_s n dv}{\partial z} \end{aligned} \quad (11.15)$$

Experiments are often carried out with the aerosol contained in a large chamber. If the surface-to-volume ratio is sufficiently small to neglect deposition on the walls by diffusion and sedimentation, (11.15) becomes

$$\frac{\partial N_{\infty}}{\partial t} = I_d + \left[\frac{\partial N_{\infty}}{\partial t} \right]_{\text{coag}} \quad (11.16)$$

where $[\partial N_{\infty}/\partial t]_{\text{coag}}$ represents the coagulation terms in (11.16). The change in N_{∞} results from the competing effects of formation by homogeneous nucleation and loss by coagulation.

THE DYNAMIC EQUATION FOR THE VOLUME FRACTION

The aerosol volume fraction, ϕ , is closely related to the mass concentration, which is usually determined by filtration. We assume the filter is ideal, removing all particles larger than single molecules. Then

$$\phi = \int_0^{\infty} nv dv$$

The change in the volume fraction, ϕ , with time is obtained by multiplying the GDE by v and integrating with respect to v :

$$\begin{aligned} \frac{\partial \phi}{\partial t} + \mathbf{v} \cdot \nabla \phi + \left[\frac{\partial \phi}{\partial t} \right]_{\text{growth}} &= \nabla^2 \int_0^{\infty} Dvn dv \\ &+ \left[\frac{\partial \phi}{\partial t} \right]_{\text{coag}} - \frac{\partial \int_0^{\infty} c_s vn dv}{\partial z} \end{aligned} \quad (11.17)$$

The change in ϕ resulting from gas-to-particle conversion can be written as follows:

$$\left[\frac{\partial \phi}{\partial t} \right]_{\text{growth}} = \frac{\partial \int_0^{\infty} n v \, dv}{\partial t} = - \int_0^{\infty} v \frac{\partial I}{\partial v} \, dv$$

If homogeneous nucleation is taking place, we can write $[\partial \phi / \partial t]_{\text{growth}}$ as the sum of two terms:

$$\left[\frac{\partial \phi}{\partial t} \right]_{\text{growth}} = \frac{\partial \int_0^{v^*} n v \, dv}{\partial t} + \frac{\partial \int_{v^*}^{\infty} n v \, dv}{\partial t} \quad (11.18)$$

where v^* is the critical particle volume.

The term $(\partial \int_0^{v^*} n v \, dv) / \partial t$ represents the accumulation of material in the cluster size range below the critical particle size range v^* . In homogeneous nucleation theory (Chapter 10), this term vanishes; there is a steady state for this portion of the distribution in which material is removed as fast as it is supplied. (This is actually true only as a quasi-steady approximation.) The second term on the right-hand side of (11.18) can be written as follows:

$$\frac{\partial \int_{v^*}^{\infty} n v \, dv}{\partial t} = - \int_{v^*}^{\infty} v \frac{\partial I}{\partial v} \, dv = - \int_{v^*}^{\infty} \frac{\partial I v}{\partial v} \, dv + \int_{v^*}^{\infty} I \, dv \quad (11.19)$$

but

$$\int_{v^*}^{\infty} \frac{\partial I v}{\partial v} \, dv = [I v]_{\infty} - [I v]_{v^*} \quad (11.20)$$

The term $\int_{v^*}^{\infty} I \, dv$ represents the growth of stable particles ($v > v^*$) by gas-to-particle conversion. On physical grounds, this is clear because the particle current represents the volume of material converted per unit of v space in unit volume of gas and unit time.

Because there is no loss of material by growth to the upper end of the distribution, we obtain

$$[I v]_{\infty} = 0$$

The term $[I v]_{v^*}$ is the volumetric rate at which material is delivered by homogeneous nucleation to the stable part of the size distribution.

The contribution of the coagulation term $[\partial \phi / \partial t]_{\text{coag}}$ vanishes identically no matter what the form of the collision frequency function. The coagulation mechanism only shifts matter up the distribution function from small to large sizes and does not change the local volumetric concentration of aerosol.

The balance on ϕ (11.17) then takes the form

$$\frac{\partial \phi}{\partial t} + \mathbf{v} \cdot \nabla \phi = \underbrace{\int_{v^*}^{\infty} I \, dv}_{\substack{\text{growth} \\ \text{of stable} \\ \text{particles}}} + \underbrace{[I v]_{v^*}}_{\substack{\text{formation by} \\ \text{homogeneous} \\ \text{nucleation}} + \nabla^2 \int_0^{\infty} D v n \, dv}_{\text{diffusion}} - \underbrace{\frac{\partial \int_0^{\infty} c_s v \, dv}{\partial z}}_{\text{sedimentation}} \quad (11.21)$$

For $D \sim d_p^{-2}$ (free molecule region), the integral $\int_0^{\infty} D v n \, dv$ is proportional to the average particle diameter (Chapter 1). Hence this term represents the diffusion of a quantity proportional to the average particle diameter.

SIMULTANEOUS COAGULATION AND DIFFUSIONAL GROWTH: SIMILARITY SOLUTION FOR CONTINUUM REGIME

Suppose the aerosol contained in a large chamber is composed of particles larger than the mean free path of the gas. The surface-to-volume ratio of the chamber is sufficiently small to neglect deposition on the walls, and the composition of the system is uniform. Coagulation takes place, and at the same time the particles grow as a result of diffusion-controlled condensation but sedimentation can be neglected. Homogeneous nucleation does not occur and the system is isothermal. A system of this type has been used to model aerosol formation in photochemical air pollution.

For growth and coagulation alone, the GDE can be written as follows:

$$\frac{\partial n}{\partial t} + \frac{\partial I}{\partial v} = \frac{1}{2} \int_0^v \beta(v - \bar{v}, \bar{v}) n(v - \bar{v}) n(\bar{v}) d\bar{v} - \int_0^\infty \beta(v, \bar{v}) n(v) n(\bar{v}) d\bar{v} \quad (11.22)$$

with the collision frequency function for the continuum range given by

$$\beta = \frac{2kT}{3\mu} \left(\frac{1}{v^{1/3}} + \frac{1}{\bar{v}^{1/3}} \right) (v^{1/3} + \bar{v}^{1/3}) \quad (11.23)$$

The particle current is assumed to be given by (Chapter 10)

$$I = n \frac{dv}{dt} \quad (11.24)$$

The diffusional growth law (Chapter 10) can be written in the form:

$$\frac{dv}{dt} = 3^{1/3} (4\pi)^{2/3} \frac{Dp_s v_m}{kT} (S - 1) v^{1/3} = B(S - 1) v^{1/3} \quad (11.25)$$

where S is the saturation ratio, p_s is the saturation vapor pressure, v_m is the molecular volume in the condensed phase, and B is a constant defined by this expression. Latent heat effects in condensation are neglected, as is the Kelvin effect.

The similarity transformation, $n = (N_\infty^2/\phi)\psi(\eta)$ (Chapter 7), is still applicable in this case (Pich et al., 1970), but the volumetric concentration is no longer constant because of the condensation of material from the gas phase. Substituting the self-preserving form in (11.22) with (11.23) through (11.25), it is found that similarity is preserved provided that the saturation ratio changes with time in a special way and that the dimensionless group,

$$C = \frac{3\mu}{4kT} \left[\frac{2}{\phi^{2/3} N_\infty^{1/3}} \right] B(S - 1) \quad (11.26)$$

is constant. This group is a measure of the relative rates of condensation and coagulation. When C is small, condensation proceeds slowly compared with coagulation. The time rate of change of the total number of particles is given by an expression of the same form for coagulation without condensation (Chapter 7):

$$\frac{dN_\infty}{dt} = -\frac{2kT}{3\mu} (1 + ab) N_\infty^2 \quad (11.27)$$

but the values of the moments a and b are different. The volumetric concentration increases as a result of condensation at a rate given by

$$\phi = \phi_0 \left[1 + \frac{2kT}{3\mu} (1 + ab) N_\infty(0) t \right]^{aC/(1+ab)} \quad (11.28)$$

where ϕ_0 and $N_\infty(0)$ are the values at $t = 0$. In the important special case of constant saturation ratio, it is found that the total surface area of the system is constant. The decrease of surface area by coagulation is, in this case, balanced by the formation of new surface as a result of vapor condensation. The value of ab is 1.05 while the exponent in (11.28), $aC/(1+ab)$, equals 1/2. Calculated values of $N_\infty/N_\infty(0)$ and ϕ/ϕ_0 are shown in Fig. 11.2.

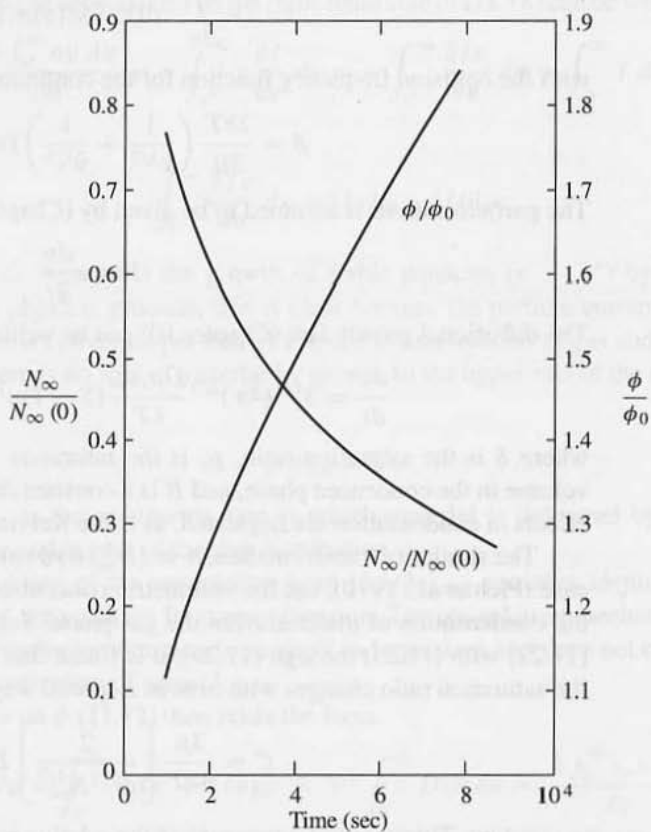


Figure 11.2 Variations of number and volume concentration with time for a self-preserving aerosol with constant saturation ratio and constant surface area. The value of ab is 1.05 for this case. $N_\infty(0) = 10^6 \text{ cm}^{-3}$ and $T = 20^\circ\text{C}$. The number concentration decreases as a result of coagulation, and the volume concentration increases because of condensation.

If the size distribution reaches a self-preserving form, a special relationship exists among the number, surface area, and volume concentrations. The surface area per unit volume of gas is

$$A = \int_0^{\infty} \pi d_p^2 n(v) dv = (36\pi)^{1/3} \int_0^{\infty} v^{2/3} n dv \quad (11.29)$$

Substituting the self-preserving transformation (Chapter 7), we obtain

$$A = (36\pi)^{1/3} N_{\infty}^{1/3} \phi^{2/3} \int_0^{\infty} \eta^{2/3} \psi d\eta \quad (11.30)$$

In the special case of constant A (and saturation ratio) the integral is equal to 0.951 (Pich et al., 1970) so that in this case

$$\frac{A}{N_{\infty}^{1/3} \phi^{2/3}} = 4.60 \quad (11.31)$$

SIMULTANEOUS COAGULATION AND GROWTH: EXPERIMENTAL RESULTS

Experiments on simultaneous coagulation and growth were made by Husar and Whitby (1973). A 90-m³ polyethylene bag was filled with laboratory air from which particulate matter had been removed by filtration. Solar radiation penetrating the bag induced photochemical reactions among gaseous pollutants, probably SO₂ and organics, but the chemical composition was not determined. The reactions led to the formation of condensable species and photochemical aerosols. Size distributions were measured in 20-min intervals using an electrical mobility analyzer. The results of one set of experiments for three different times are shown in Fig. 11.3.

The number, surface, and volume concentrations were calculated from the size distribution function and are shown in Fig. 11.4. The variation with time of the number concentration is interpreted as follows: In the absence of foreign nuclei, particles are formed initially by homogeneous nucleation. As concentrations mount, coagulation takes place, and growth occurs on nuclei already generated. The number concentration reaches a maximum and then decays. The maximum concentration is reached when the rate of formation by self-nucleation and rate of coagulation are equal. The maximum concentration is determined by setting $\partial N_{\infty} / \partial t = 0$ in (11.16):

$$I_d = - \left[\frac{\partial N_{\infty}}{\partial t} \right]_{\text{coag}} \quad (11.32)$$

As growth continues, the aerosol surface area becomes sufficiently large to accommodate the products of gas-to-particle conversion. The saturation ratio decreases, leading to a reduction in the particle formation rate. The decay in the number concentration for $t > 80$ min in Fig. 11.4 is probably due to coagulation; calculations for free molecule aerosols support this hypothesis.

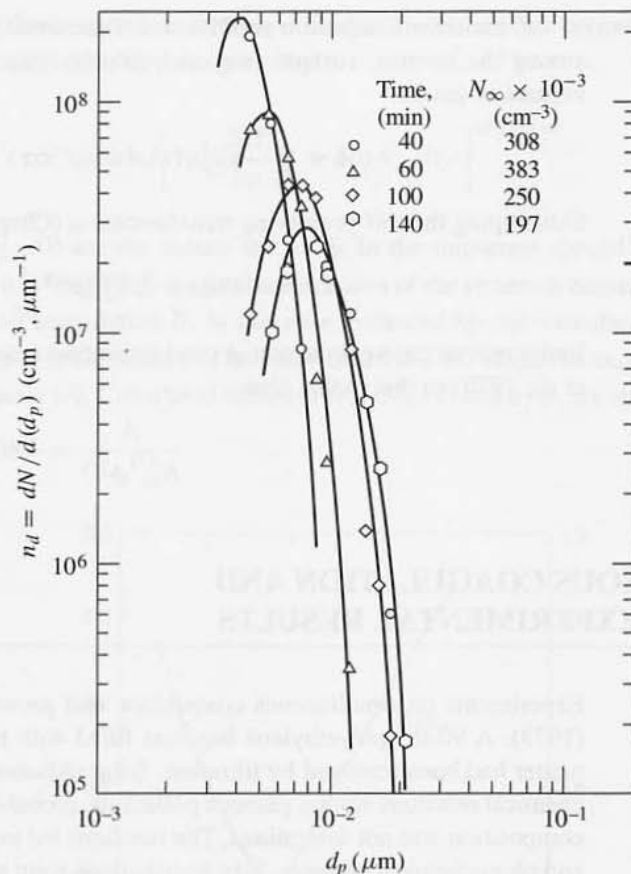


Figure 11.3 Size distributions of an aging free molecule aerosol generated by exposing filtered laboratory air in a 90-m^3 polyethylene bag to solar radiation. Change in the distribution function results from the combined effects of coagulation and growth (Husar and Whitby, 1973).

Unlike the case of coagulation without growth, the volume fraction of dispersed material increases with time as a result of gas-to-particle conversion. The total surface area, on the other hand, tends to an approximately constant value. Coagulation tends to reduce surface area, whereas growth tends to increase it, and the two effects in this case almost balanced each other.

The ratio $A/N_{\infty}^{1/3}\phi^{2/3}$ reaches a constant value after about 1 hr, indicating that the asymptotic, self-preserving stage has been reached. The relationship (11.24) holds for both the continuum and free-molecule ranges, but the value of the integral would be expected to vary somewhat. As shown in Fig. 11.4, however, the value of the ratio falls very close to 4.60, the value for the continuum range with constant A (11.31).

In Fig. 11.5, the data of Fig. 11.3 have been replotted in the self-preserving form. As a good approximation, all the data fall on a single curve. The theory for the continuum range

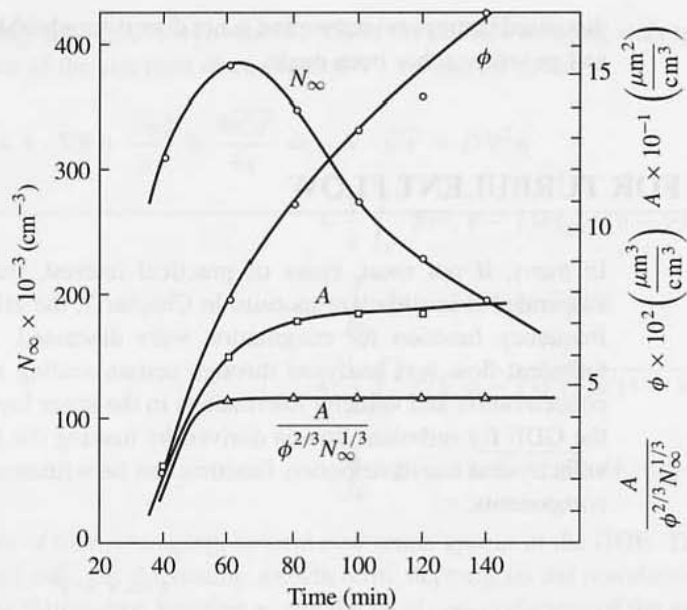


Figure 11.4 Evolution of the moments of the size distribution function for the aerosols shown in Fig. 11.3. The peak in the number distribution probably results when formation by homogeneous nucleation is balanced by coagulation. Total aerosol volume increases with time as gas-to-particle conversion takes place. Total surface area, A , increases at first and then approaches an approximately constant value, due probably to a balance between growth and coagulation (Husar and Whitby, 1973). The results should be compared with Fig. 11.2.

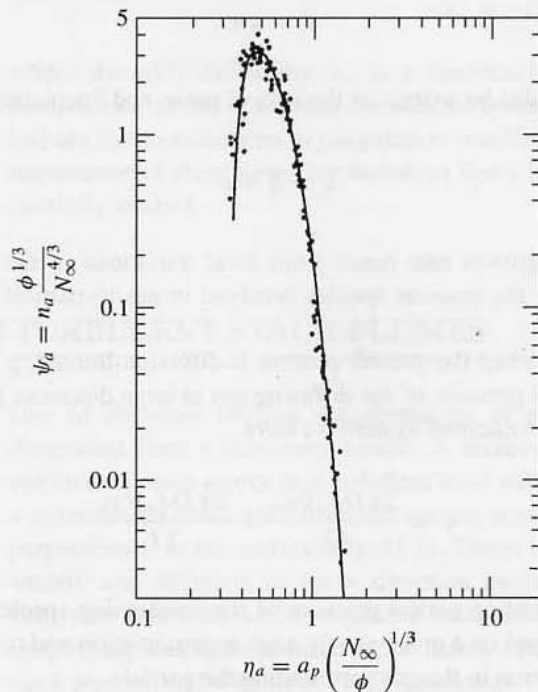


Figure 11.5 Size distributions of Fig. 11.3 plotted in the self-preserving form (Husar and Whitby, 1973). The curve is based on the data. The self-preserving distribution for simultaneous coagulation and growth in the free-molecule range has not been calculated from theory, so no comparison is made.

discussed in the previous section is not directly applicable, so no comparison between theory and experiment has been made.

THE GDE FOR TURBULENT FLOW

In many, if not most, cases of practical interest, the fluid in which the particles are suspended is in turbulent motion. In Chapter 7, the effects of turbulence on the collision frequency function for coagulation were discussed. In the last chapter, nucleation in turbulent flow was analyzed through certain scaling relations based on the form of the concentration and velocity fluctuations in the shear layer of a turbulent jet. In this section the GDE for turbulent flow is derived by making the Reynolds assumption that the fluid velocity and size distribution function can be written as the sum of mean and fluctuating components:

$$\mathbf{v} = \bar{\mathbf{v}} + \mathbf{v}' \quad (11.33)$$

$$n = \bar{n} + n' \quad (11.34)$$

It is assumed that homogeneous nucleation does not take place and that the particle current is proportional to the concentration through the growth law:

$$I = qn \quad (11.35)$$

The growth law can also be written as the sum of mean and fluctuating terms:

$$q = \bar{q} + q' \quad (11.36)$$

The fluctuations in growth rate result from local variations in the temperature and in the concentrations of the gaseous species involved in gas-to-particle transformation processes.

As an example, when the growth process is diffusion-limited, $q = 2\pi Dd_p p v_m / kT$, where p is the partial pressure of the diffusing gas at large distances from the surface and $p_s = 0$. Then for an isothermal system we have

$$q = \frac{2\pi Dd_p \bar{p} v_m}{kT} + \frac{2\pi Dd_p p' v_m}{kT} \quad (11.37)$$

where p' is the fluctuating partial pressure of the condensing species. This form for the diffusional flux is based on a quasi-steady-state approximation and may not hold for rapid changes in concentration in the gas surrounding the particle.

Substituting (11.33), (11.34), and (11.35) in the GDE, averaging with respect to time, and making use of the equation of continuity, $\nabla \cdot \mathbf{v} = 0$, we obtain

$$\begin{aligned} \frac{\partial \bar{n}}{\partial t} + \mathbf{v} \cdot \nabla \bar{n} + \frac{\partial \bar{n} \bar{q}}{\partial v} + \frac{\partial \overline{n'q'}}{\partial v} = & -\nabla \cdot \overline{n'\mathbf{v}'} + D \nabla^2 \bar{n} \\ & + \frac{1}{2} \int_0^v \beta(\bar{v}, v - \bar{v}) \bar{n}(\bar{v}) \bar{n}(v - \bar{v}) d\bar{v} \\ & - \int_0^\infty \beta(v, \bar{v}) \bar{n}(v) \bar{n}(\bar{v}) d\bar{v} \\ & + \frac{1}{2} \int_0^v \beta(\bar{v}, v - \bar{v}) \overline{n'(\bar{v})n'(v - \bar{v})} d\bar{v} \\ & - \int_0^\infty \beta(v, \bar{v}) \overline{n'(v)n'(\bar{v})} d\bar{v} - c_s \frac{\partial \bar{n}}{\partial z} \end{aligned} \quad (11.38)$$

As a result of time averaging, several new terms appear in the GDE. The fourth term on the left-hand side, the fluctuating growth term, depends on the correlation between the fluctuating size distribution function n' and the local concentrations of the gaseous species converted to aerosol. It results in a tendency for spread to occur in the particle size range—a turbulent diffusion through v space (Levin and Sedunov, 1968).

The first term on the right-hand side is a well-known form that represents the change in \bar{n} resulting from turbulent diffusion. The separate components of the vector flux $n'\mathbf{v}'$ are usually assumed to follow an equation of the form

$$\overline{n'v'_i} = -\varepsilon_i \frac{\partial \bar{n}}{\partial x_i} \quad (11.39)$$

where the eddy diffusivity, ε_i , is a function of position and $i = 1, 2, 3$ refers to the components of the Cartesian coordinate system. The second and third terms from the last are the contributions to coagulation resulting from the fluctuating concentrations. The importance of these terms for turbulent flows in ducts or in the atmosphere has not been carefully studied.

THE GDE FOR TURBULENT STACK PLUMES

One of the most obvious manifestations of air pollution is the visible plume formed downwind from a stationary source. A relatively simple model for such systems is the continuous point source in a turbulent fluid with a mean velocity, $\bar{u}(x, z)$. The coordinate x is measured downwind from the source, parallel to the ground, and z is the coordinate perpendicular to the surface (Fig. 11.6). The velocity components in the y and z directions vanish, and diffusion in the x direction can be neglected compared with convection. Brownian diffusion is also neglected compared with eddy diffusion. These are the usual simplifying assumptions made in the theory of diffusion of molecular species in turbulent stack plumes, and with them (11.38) becomes

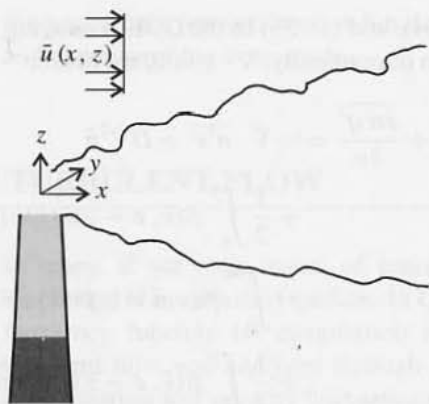


Figure 11.6 Schematic diagram of turbulent stack plume with coordinate system employed in the text.

$$\begin{aligned}
 \bar{u} \frac{\partial \bar{n}}{\partial x} + \frac{\partial \bar{n} \bar{q}}{\partial v} + \frac{\partial \bar{n}' \bar{q}'}{\partial v} &= \frac{\partial \varepsilon_y (\partial \bar{n} / \partial y)}{\partial y} + \frac{\partial \varepsilon_z (\partial \bar{n} / \partial z)}{\partial z} \\
 &+ \frac{1}{2} \int_0^v \beta(\bar{v}, v - \bar{v}) \bar{n}(\bar{v}) \bar{n}(v - \bar{v}) d\bar{v} \\
 &- \int_0^\infty \beta(v, \bar{v}) \bar{n}(v) \bar{n}(\bar{v}) d\bar{v} \\
 &+ \frac{1}{2} \int_0^v \beta(\bar{v}, v - \bar{v}) \overline{n'(\bar{v}) n'(v - \bar{v})} d\bar{v} \\
 &- \int_0^\infty \beta(v, \bar{v}) \overline{n'(v) n'(\bar{v})} d\bar{v} - c_s \frac{\partial \bar{n}}{\partial z}
 \end{aligned} \quad (11.40)$$

Away from the immediate neighborhood of the source when concentrations have decreased sufficiently as a result of coagulation and dilution, additional coagulation can often be neglected. When we restrict attention to particles smaller than a few micrometers for which sedimentation is not important, as well as neglect the turbulent growth term in the absence of further information, (11.40) takes the following form:

$$\bar{U} \frac{\partial \bar{n}}{\partial x} + \frac{\partial \bar{n} \bar{q}}{\partial v} = \frac{\partial \varepsilon_y (\partial \bar{n} / \partial y)}{\partial y} + \frac{\partial \varepsilon_z (\partial \bar{n} / \partial z)}{\partial z} \quad (11.41)$$

for a constant mean velocity, \bar{U} .

We wish to know how the size distribution function changes with position downwind from the stack for a given form of the growth law, \bar{q} . This problem has a surprisingly simple solution for a growth law of the form

$$q = V(v)X(x) \quad (11.42)$$

where V and X are arbitrary functions of v and x , respectively.

Only x and v appear as independent variables on the left-hand side, while y and z appear on the right-hand side. Hence we try as a solution

$$\bar{n} = \frac{1}{V} g(s) \bar{N}_\infty(x, y, z) \quad (11.43)$$

where g is an arbitrary function of $s = [\int_0^\infty X dx/\bar{U} - \int_0^\infty dv/V]$ and $\bar{N}_\infty(x, y, z)$ is the distribution in space of the number concentration of particles:

$$\bar{N}_\infty(x, y, z) = \int_0^\infty \bar{n}(v, x, y, z) dv \quad (11.44)$$

Substituting (11.43) in (11.41), we obtain

$$X\bar{N}_\infty \frac{dg}{ds} + \bar{U}g \frac{\partial \bar{N}_\infty}{\partial x} - X\bar{N}_\infty \frac{dg}{ds} = g \frac{\partial \varepsilon_y (\partial \bar{N}_\infty / \partial y)}{\partial y} + g \frac{\partial \varepsilon_z (\partial \bar{N}_\infty / \partial z)}{\partial z} \quad (11.45)$$

Rearranging terms, we have

$$\bar{U} \frac{\partial \bar{N}_\infty}{\partial x} = \frac{\partial \varepsilon_y (\partial \bar{N}_\infty / \partial y)}{\partial y} + \frac{\partial \varepsilon_z (\partial \bar{N}_\infty / \partial z)}{\partial z} \quad (11.46)$$

This is the equation for the distribution in space of the number concentration of particles that can be derived independently from (11.41) by integrating over all values of v . Hence the form (11.43) is indeed a solution to (11.41) with the growth law (11.42).

A particularly simple solution is obtained in the case of a growth law of the form $q = vX$ corresponding to a droplet-phase reaction (Chapter 10). If the initial size distribution is of a power law form, $\bar{n} = bv^p \bar{N}_\infty$, substitution in (11.43) results in the following expression:

$$\bar{n} = bv^p \bar{N}_\infty \exp \left[-(p+1) \int \frac{X dx}{\bar{U}} \right] \quad (11.47)$$

The power law form cannot hold over the entire size range because singularities develop in certain integral functions. As a result, integrals of the type (11.44) must be truncated at the upper or lower ranges or both.

The growth law is, in general, a function of the local concentrations of the reactive gas-phase species:

$$q = V(v)F(c_1, c_2, \dots, c_i) \quad (11.48)$$

where the function $V(v)$ depends on the conversion mechanism (Chapter 10), and the c_i are the concentrations of the reactive gases. Because the concentrations are in general functions of x, y, z , it is clear that the form (11.42) is an approximation. A complete solution to the problem would require simultaneous solution of the GDE and the equations of conservation of the gaseous components that participate in the reaction, including the chemical kinetics. This general problem is beyond the scope of this text.

COAGULATION AND STIRRED SETTLING

Suppose a chamber is filled with an aerosol that is kept well-mixed. The particles are coagulating and at the same time settling and diffusing to the walls. This type of model has been used to analyze the behavior of radioactive particles generated in a nuclear reactor accident and then collected in a vessel specially designed for the purpose. The contents of the containment structure are mixed as a result of natural convection induced by temperature gradients present under postaccident conditions. The effectiveness of the

vessel in containing the products depends on the severity of the accident, with core meltdown representing a very severe test. Both theoretical and experimental models of such systems have been studied. The goal of the analysis is to predict the decay rate of the cloud in the vessel and the size of the particles, based on certain assumptions concerning the amount of material in the aerosol phase. Assumptions are also made concerning the leak rate from the containment vessel.

We consider only the one-dimensional problem in which the chamber is replaced by two parallel, horizontal plates a distance h apart, and sedimentation occurs in the z direction. All three components of the mean velocity vanish. The equation for the mean concentration (11.40) takes the following form:

$$\frac{\partial \bar{n}}{\partial t} = \frac{\partial(D + \varepsilon)(\partial \bar{n} / \partial z)}{\partial z} + \frac{1}{2} \int_0^v \beta(v - \bar{v}, \bar{v}) \bar{n}(v - \bar{v}) \bar{n}(\bar{v}) d\bar{v} - \int_0^\infty \beta(v, \bar{v}) \bar{n}(v) \bar{n}(\bar{v}) d\bar{v} - c_s \frac{\partial \bar{n}}{\partial z} \quad (11.49)$$

The fluctuating coagulation terms can be neglected because the concentration is approximately uniform away from the walls. Moreover, because the system is well-stirred, the concentration through the bulk is approximately uniform up to a small distance, δ , from the bottom of the chamber corresponding to the region where the eddy diffusion goes from its value in the bulk of the fluid to zero (at the wall). To a certain extent, this distance is arbitrary and need not be defined exactly for this analysis.

The average concentration in the chamber is defined by

$$[\bar{n}] = \frac{1}{h} \int_0^h \bar{n} dz \quad (11.50)$$

The concentration in the bulk of the fluid is approximately equal to $[\bar{n}]$, because the volume of fluid bounded by δ and the wall is small. Outside region δ , the particle flux toward the bottom of the chamber is given by $[\bar{n}]c_s$, because the concentration gradients and, therefore, diffusion are negligible.

Assuming a quasi-stationary state, the flux of particles to the bottom of the chamber will also be $[\bar{n}]c_s$; that is,

$$\left[-(D + \varepsilon) \frac{\partial \bar{n}}{\partial z} + \bar{n} c_s \right]_{z=0} = [\bar{n}] c_s \quad (11.51)$$

When we integrate (11.49) term by term with respect to z over the height of the chamber with this boundary condition, the following results are obtained: The unsteady term takes the form

$$\int_0^h \frac{\partial \bar{n}}{\partial t} dz = \frac{\partial \int_0^h \bar{n} dz}{\partial t} = h \frac{\partial [\bar{n}]}{\partial t} \quad (11.52)$$

The combined diffusion and sedimentation terms can be integrated as follows:

$$\int_0^h \frac{\partial [(D + \varepsilon)(\partial \bar{n} / \partial z) - c_s \bar{n}]}{\partial z} dz = 0 - [\bar{n}] c_s \quad (11.53)$$

Deposition on the roof of the chamber has been neglected, and (11.51) has been introduced for the floor of the chamber. For the coagulation term, we have

$$\begin{aligned} & \int_0^h \int_0^v \beta(v - \tilde{v}, \tilde{v}) \bar{n}(v - \tilde{v}) \bar{n}(\tilde{v}) d\tilde{v} dz \\ &= \int_0^v \beta(v - \tilde{v}, \tilde{v}) \left[\int_0^h \bar{n}(v - \tilde{v}) \bar{n}(\tilde{v}) dz \right] d\tilde{v} \end{aligned} \quad (11.54)$$

Except for a small region near the wall, \bar{n} is almost independent of z at any time. Hence

$$\int_0^h \bar{n}(v - \tilde{v}) \bar{n}(\tilde{v}) dz = [\bar{n}(v - \tilde{v})][\bar{n}(\tilde{v})]h \quad (11.55)$$

with an analogous result for the other coagulation term. Thus the result of integrating (11.49) with respect to z is

$$\begin{aligned} \frac{\partial[\bar{n}]}{\partial t} &= \frac{1}{2} \int_0^v \beta(v - \tilde{v}, \tilde{v}) [\bar{n}(v - \tilde{v})][\bar{n}(\tilde{v})] d\tilde{v} \\ &\quad - \int_0^\infty \beta(v, \tilde{v}) [\bar{n}(v)][\bar{n}(\tilde{v})] d\tilde{v} - \frac{c_s[\bar{n}]}{h} \end{aligned} \quad (11.56)$$

This is the equation that is usually solved in calculating simultaneous coagulation and settling in a well-mixed chamber. Numerical solutions for special values of the collision frequency function have been obtained by Lindauer and Castleman (1971). They report results for the decay in the mass concentration as a function of chamber height and time.

In the coagulation process, small particles from the low end of the size distribution are transferred to the large particle size range. The large particles formed in this way settle to the floor of the chamber. A quasi-steady state may develop for the upper end of the distribution in which the rate of formation in a given size range by coagulation is equal to the rate of loss by sedimentation. This is equivalent to equating the first and last terms on the right-hand side of (11.56), which for coagulation in the continuum regime, gives

$$\frac{kT}{3\mu} \int_0^v \left[1 + \left(\frac{v - \tilde{v}}{\tilde{v}} \right)^{1/3} \right] n(\tilde{v}) n(v - \tilde{v}) d\tilde{v} = \frac{c_s n}{h} \quad (11.57)$$

where $n = [\bar{n}]$. A particular solution that satisfies (11.57) and the requirement that the total aerosol volume per unit volume of gas is finite is

$$n = A_1 v^{-1/3} e^{-A_2 v} \quad (11.58)$$

where A_1 and A_2 are constants (Fig. 11.7). This can be tested by substitution in (11.57), which also shows that

$$A_1 = \left(\frac{\pi}{6} \right)^{1/3} \frac{\rho_p g}{\pi k T h [3 + B(2/3, 2/3)]} \quad (11.59)$$

where B is the beta function. The constant A_1 has dimensions L^{-5} . The total aerosol volume concentration is

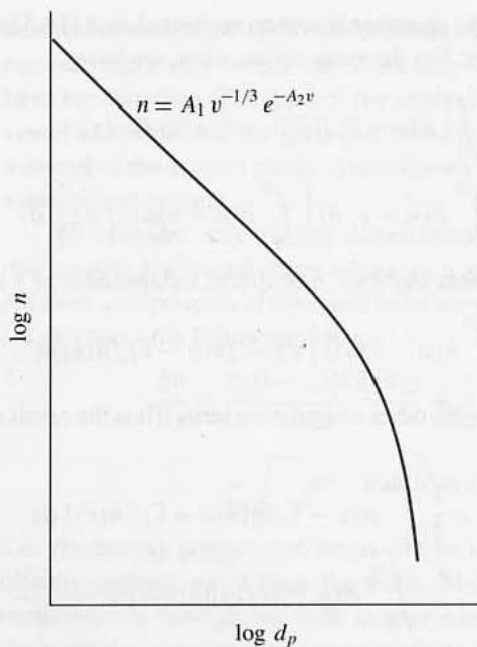


Figure 11.7 Upper end of the size distribution for the steady state between coagulation and sedimentation. The solution breaks down for small values of the particle diameter because the second term on the right hand side of (11.56)—representing loss by coagulation—has been neglected in (11.57).

$$\phi = A_1 \int_0^{\infty} v^{2/3} e^{-A_2 v} dv \quad (11.60)$$

The integral can be expressed in terms of a gamma function, and A_2 can be evaluated in this way:

$$A_2 = \frac{[A_1 \Gamma(5/3)]^{3/5}}{\phi^{3/5}} \quad (11.61)$$

The rate of particle deposition (volume of particulate matter per unit surface per unit time) has the dimensions of velocity and is given by

$$\text{sedimentation flux} = \int_0^{\infty} c_s v n(v) dv \quad (11.62)$$

$$= \left(\frac{6}{\pi}\right)^{2/3} \frac{\rho_p g}{18\mu} A_1 \int_0^{\infty} v^{4/3} e^{-A_2 v} dv \quad (11.62a)$$

$$= \left(\frac{6}{\pi}\right)^{2/3} \frac{\Gamma(7/3)}{18[\Gamma(5/3)]^{7/5}} \frac{\rho_p g}{\mu A_1^{2/5}} \phi^{7/5} \quad (11.62b)$$

Hence the sedimentation flux is proportional to $\phi^{7/5}$ for the steady state. The analysis

is approximate because the second coagulation term on the right-hand side of (11.56) is neglected.

In a quasi-steady-state situation, the concentration of suspended material changes slowly with time. The sedimentation flux then represents the rate of loss of material from the volume of the chamber above unit area of floor. The results of the calculation of the volumetric concentration compare well with the numerical computations of Lindauer and Castleman (1971) for long times.

COAGULATION AND DEPOSITION BY CONVECTIVE DIFFUSION

The combustion of fuels in vehicular engines is a major source of submicron particles in urban atmospheres. An earlier example in the United States was the emission of lead containing particles from the combustion of gasoline containing lead tetraethyl. Another is the emission of soot from diesel engines. In these systems small submicron particles form by homogeneous nucleation. These particles coagulate, and some deposit on the walls of the tailpipe by combined Brownian diffusion and thermophoresis because the walls are usually cooler than the exhaust gases. In principle, (11.40) must be solved with an additional term for transport by thermophoresis—a formidable task. An approximate calculation can be made by adopting the following simplified model: A gas carrying many particles smaller than the mean free path flows through a straight pipe with smooth walls at constant temperature. Particles deposit by diffusion on the walls that behave as a perfect sink ($n = 0$).

If the rate of coagulation is rapid compared with the rate of loss to the walls of the pipe, the two processes—coagulation and surface deposition—can be treated separately. For the purposes of the calculation, the flow can be broken into two parts: In the turbulent core, coagulation controls the shape of the size distribution, which is then determined by the solution to the equation for coagulation under steady flow conditions.

Near the surface, the flux of particulate matter to the wall is

$$\bar{J} = -(D + \varepsilon) \frac{\partial \bar{n}}{\partial z} \quad (11.63)$$

when diffusion alone controls transport, The bars that denote time average quantities are omitted in the rest of this section to simplify the notation. If thermal gradients are present, these must also be included in the driving forces for surface deposition. Equation (11.63) can be integrated for different forms of the eddy diffusion coefficient $\varepsilon(z)$ in the viscous sublayer. The result using the generally accepted dependence $\varepsilon \sim y^3$ is discussed in Chapter 3. However, to simplify the forms of the expressions derived in the rest of the discussion, it is convenient to use $\varepsilon \sim y^4$, which gives (Deissler, 1955)

$$J = kn = 0.079 U n f^{1/2} S c^{-3/4} \quad (11.64)$$

The total local flux of particle volume (proportional to mass) to the walls of the pipe is

$$\int_0^\infty J v \, dv = 0.079 \frac{U f^{1/2}}{v^{3/4}} \int_0^\infty n D^{3/4} v \, dv \quad (11.65)$$

For spherical particles much smaller than the mean free path of the surrounding gas molecules, the diffusion coefficient is given by (2.17) and (2.19), with $\alpha = 0$:

$$D = \frac{kT}{f} = \frac{3kT}{2\rho d_p^2} \left[\frac{kT}{2\pi m} \right]^{1/2} \quad (11.66)$$

where m is the molecular mass of the gas molecules and mp/kT has been substituted for ρ . For gas molecules that behave as rigid elastic spheres, this expression can also be written as

$$D \approx \frac{4D_{11}}{\sqrt{2}} \left(\frac{v_m}{v} \right)^{2/3} \quad (11.67)$$

where D_{11} is the coefficient of self-diffusion for the gas and v_m is the molecular volume of the gas molecules. Substituting in (11.65), the result is

$$\int_0^\infty Jv \, dv = \frac{0.17Uf^{1/2}v_m^{1/2}}{(v/D_{11})^{3/4}} \int_0^\infty nv^{1/2} \, dv \quad (11.68)$$

The calculation is easily carried out when the size distribution is self-preserving. Substituting $n = (N_\infty^2/\phi)\psi(\eta)$ (where ϕ and N_∞ are time-averaged quantities in keeping with the turbulent nature of the flow) in (11.68) and taking $v/D_{11} = 0.7$, the value for air, we obtain

$$\int_0^\infty Jv \, dv = 0.23Uf^{1/2}v_m^{1/2}\phi^{1/2}N_\infty^{1/2} \int_0^\infty \psi\eta^{1/2} \, d\eta \quad (11.69)$$

The integral $\int_0^\infty \psi\eta^{1/2} \, d\eta$ equals 0.89 when evaluated from the self-preserving distribution for the free molecule range. The heaviest mass deposition occurs upstream where N_∞ and ϕ are largest.

The change in ϕ with x is given by a mass balance on a small element of the pipe wall (Fig. 11.8):

$$\left(\frac{\pi d_{\text{pipe}}^2}{4} \right) U \, d\phi = -\pi d_{\text{pipe}} \left[\int_0^\infty Jv \, dv \right] dx \quad (11.70)$$

Substituting (11.69), we obtain

$$-\frac{d_{\text{pipe}}}{4} d\phi = 0.20f^{1/2}v_m^{1/2}\phi^{1/2}N_\infty^{1/2} dx \quad (11.71)$$

The variation of N_∞ with distance is obtained from Chapter 7, the expression for free molecule coagulation:

$$U \frac{dN_\infty}{dx} = -0.334 \left(\frac{3}{4\pi} \right)^{1/6} \left(\frac{6kT}{\rho_p} \right)^{1/2} \phi^{1/6} N_\infty^{11/6} \quad (11.72)$$

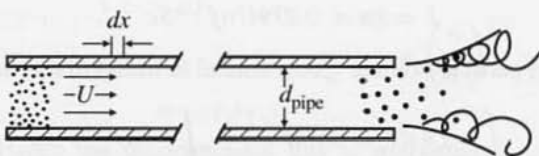


Figure 11.8 Coagulation and deposition to the wall in a turbulent pipe flow. Initially high particle concentrations decrease due to coagulation and deposition. Processes occur in vehicular tailpipes.

When we combine (11.72) with (11.71), the result is

$$\frac{d\phi}{\phi^{1/3}} = \frac{0.25 f^{1/2} v_m^{1/2} U}{d_{\text{pipe}} (3/4\pi)^{1/6} (6kT/\rho_p)^{1/2}} \frac{dN_\infty}{N_\infty^{4/3}} \quad (11.73)$$

Integrating with the initial condition $\phi = \phi_0$ at $N_\infty = \infty$, we obtain

$$(\phi_0^{2/3} - \phi^{2/3}) = \frac{2B}{N_\infty^{1/3}} \quad (11.74)$$

where B is the constant coefficient on the right hand side of (11.73).

When we substitute (11.74) in (11.72), a differential equation is obtained for the variation of particle volume along the pipe:

$$-\frac{[\phi_0^{2/3} - \phi^{2/3}]^{3/2} d\phi}{\phi^{1/2}} = \frac{0.82}{d_{\text{pipe}}} f^{1/2} v_m^{1/2} (2B)^{3/2} dx \quad (11.75)$$

The deposition up to any point in the pipe can be obtained by numerical integration of this expression.

In practice, the surfaces over which the gas flows become roughened as a result of particle deposition, corrosion, and scaling. Hence the deposition rates are probably significantly greater than those calculated from (11.75) based on (11.64) for mass transfer in smooth pipes. In addition, the tailpipe flow is unsteady because of the usual patterns of driving in traffic. These factors contribute to the reentrainment of agglomerates formed on the surface and the appearance of large mass fractions of coarse particles ($> 10 \mu\text{m}$) in the exhaust gases (Habibi, 1973). The actual size distribution of particles leaving the tailpipe is then considerably broader than the self-preserving distribution because of both reentrainment and the variation in residence times across the pipe.

CONTINUOUSLY STIRRED TANK REACTOR

An aerosol flows steadily into and out of a chamber that is kept well-stirred (Fig. 11.9). In the chamber, processes that modify the size distribution take the place of the type represented by the terms in the GDE. If the flow is maintained for a sufficiently long time—about five times the mean residence time—the chamber contents tend to approach a steady state. The steady-state distribution is determined by the size distribution of the input, the flow rate, and the growth, coagulation, and deposition processes taking place within the tank. Such a system is analogous to the continuously stirred tank reactor (CSTR) often employed in modeling chemical reactors in industry or the laboratory. A basic assumption is that the concentration in the reactor is everywhere uniform and equal to the concentration at the exit. Such aerosol systems have not been carefully studied experimentally. They are of interest because of their potential use as aerosol generators. Because they represent a simple model of a chemical reactor, they may be useful in the design of processes for minimum or at least controllable pollution production.

The CSTR for aerosols is in some respects simpler to analyze than the unsteady or spatially varying systems considered previously. We consider a reactor of volume B with

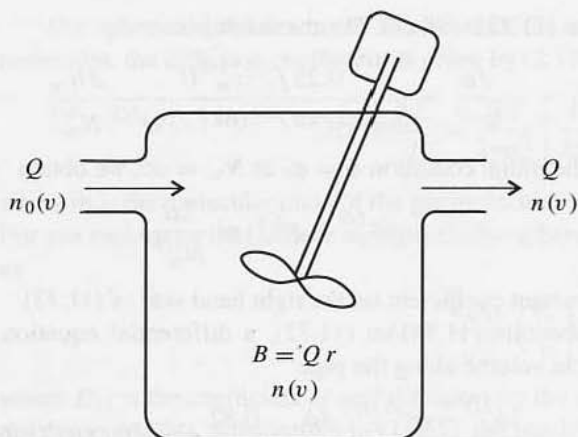


Figure 11.9 Stirred tank reactor of volume B . The distribution at the inlet is $n_0(v)$. The distribution in the reactor and in the exit stream is $n(v)$.

an aerosol entering of size distribution $n_0(v)$. In the steady state, for a volumetric flow of gas Q , a balance on the number of particles in the size range v to $v + dv$ gives

$$Qn(v) = Qn_0(v) + B \left(\begin{array}{c} \text{net rate of formation} \\ \text{per unit volume} \end{array} \right) - B \left(\begin{array}{c} \text{rate of deposition} \\ \text{per unit volume} \end{array} \right)$$

We consider the following simple problem that can be solved analytically: An aerosol with size distribution $n_0(v)$ enters the reactor continuously. Chemical or physical processes within the reactor produce condensable species that deposit on the aerosol particles. In the steady state, the balance on particles in the size range v to $v + dv$ becomes

$$\frac{n_0}{\tau} = \frac{n}{\tau} + \frac{d(nq)}{dv} \quad (11.76)$$

where the mean residence time τ equals B/Q . Particle deposition on the walls has been neglected. Equation (11.76) is an ordinary linear equation. Taking nq as the dependent variable, the integrating factor is $\exp(\int dv/q\tau)$ and the solution to (11.76) with $n = 0$ at $v = 0$ is

$$n = \frac{1}{q} \exp\left(-\int \frac{dv}{q\tau}\right) \int_0^v \exp\left(\int \frac{dv}{q\tau}\right) \frac{n_0}{\tau} dv \quad (11.77)$$

If the growth rate is diffusion controlled, $q = Av^{1/3}$, where A is a constant. Now suppose the aerosol entering the chamber is monodisperse; that is, $n_0 = N_0\delta(v-v_0)$, where $\delta(v-v_0)$ represents the Dirac delta function and N_0 is the number of particles per unit volume of size v_0 . Then the integral on the right-hand side of (11.77) becomes $(\exp((3/2)Av_0^{2/3}/\tau))N_0/\tau$ and the size distribution of the aerosol leaving the chamber is

$$n(v) = \frac{1}{Av^{1/3}} \left\{ \exp\left[\frac{3}{2} \frac{(v_0^{2/3} - v^{2/3})}{A\tau}\right] \right\} \frac{N_0}{\tau} \quad (v > v_0) \quad (11.78)$$

Thus the result of particle growth in the chamber is to convert a monodisperse aerosol into a polydisperse aerosol. This is the reverse of what occurs in a condensation aerosol generator (Chapter 10).

Why does this spread in the distribution occur? The reason is that there is a distribution of residence times for the particles in the CSTR. Some particles stay for times longer than τ and others for times shorter so that the growth period varies among the particles leaving the reactor at any time.

In practice, deposition on the walls of the chamber must be taken into account. Small particles will be preferentially removed by diffusion, and large particles will be removed by turbulent deposition and sedimentation. Quantitative estimates of such deposition rates are usually difficult to make. The particle size distribution in the effluent from a CSTR has been discussed by Bransom et al. (1949) for the case of homogeneous nucleation in the reactor.

PROBLEMS

11.1 According to Ulrich (1971), process conditions typical of pyrogenic silica aerosol reactors are: silica mole fraction in vapor phase = 0.07, pressure = 1 atm, $T = 1800$ to 2100 K.

(a) Calculate the diameter of the critical silica nucleus under these conditions, taking $T = 2080$ K.

(b) Compare this value with the diameter of the silica molecule. The following data on the material properties of silica are provided (Kingery, 1959):

Silica density = 2.2 g cm^{-3}

Silica vapor pressure at $2080 \text{ K} = 1 \text{ Pa}$

Silica surface tension at $2080 \text{ K} = 300 \text{ dyne cm}^{-1}$

11.2 Derive a general expression, based on the GDE, for the change in the total surface area of an aerosol with time and position.

11.3 An aerosol issuing from a point source is dispersed in a steady turbulent plume in the atmosphere. Derive an expression for the variation of the extinction coefficient, b (Chapter 5), with position in the plume assuming that (a) the only mechanism affecting the light-scattering portion of the size distribution is turbulent diffusion and (b) the only mechanisms are turbulent diffusion and growth.

11.4 An aerosol is injected at a point into a turbulent gas over a very short time period (an instantaneous point source). Set up the equation describing the dynamics of the size distribution. Assume that the mean flow is uniform so that the cloud, once released, spreads only radially with respect to the mean flow. Settling is not important.

11.5 A well-stirred vessel contains a coagulating, sedimenting aerosol. Assume that the upper end of the size distribution has reached a steady or quasi-steady state such that the rate of loss by sedimentation is equal to the rate of formation by coagulation. Consider two cases: The mass (or volumetric) concentration of aerosol in one is double that of the other. In both cases, the steady state has been attained. What are the relative rates of loss of matter by sedimentation?

11.6 As an idealized model for the automobile exhaust aerosol, assume that the distribution is self-preserving with a very high initial number concentration, and that deposition to the tailpipe

walls occurs by diffusion. The aerosol mass loading 10 ft upstream from the exit is 1 mg/ft³ (STP), and the average temperature is 400°F. The density of the aerosol material is 2 g/cm³, and the gas velocity is 90 ft/sec. Estimate the fraction of the aerosol that deposits on the walls by diffusion before leaving the tailpipe. As a first approximation, assume that the tailpipe wall is smooth.

11.7 A monodisperse aerosol enters a CSTR in which growth occurs only by diffusion. Show by integration of (11.78) that the total number concentration is conserved.

11.8 The general dynamic equation discussed in this chapter does not include terms for the inertial transport of particles. Discuss possible methods of incorporating particle transport by the inertial mechanism in the GDE.

REFERENCES

- Bransom, S. H., Dunning, W. J., and Millard, B. (1949) *Faraday Soc. Discussions*, No. 5, 83.
Deissler, R. G. (1955) NACA Report 1210.
Dunning, W. J. (1973) in *Faraday Symposia of the Chemical Society No. 7, Fogs and Smokes*, Faraday Division, Chemical Society London.
Habibi, K. (1973) *Environ. Sci. Technol.*, 7, 223.
Hulburt, H. M., and Katz, S. (1964) *Chem. Eng. Sci.*, 19, 555.
Husar, R. B., and Whitby, K. T. (1973) *Environ. Sci. Technol.*, 7, 241.
Kingery, W. D. (1959) *J. Am. Ceram. Soc.*, 42, 5.
Levin, L. M., and Sedunov, Y. S. (1968) *Pure Appl. Geophys.*, 69, 320.
Lindauer, G. C., and Castleman, A. W., Jr. (1971) *Aerosol Sci.*, 2, 85.
Note: There is an extensive literature in the field of containment vessel design, composed of unclassified reports issued by the Atomic Energy Commissions of various countries and their contractors. See also: International Atomic Energy Agency (IAEA) (1968) *Treatment of Airborne Radioactive Wastes*, IAEA, Vienna.
Pich, J., Friedlander, S. K., and Lai, F. S. (1970) *Aerosol Sci.*, 1, 115.
Ulrich, G. D. (1971) *Comb. Sci. Technol.*, 4, 47.
Williams, M. M. R., and Loyalka, S. K. (1991) *Aerosol Science Theory and Practice*, Pergamon Press, Oxford, UK.

Synthesis of Submicron Solid Particles: Aerosol Reactors

Solid submicron particles may form from condensable molecules generated in a gas by chemical or physical processes. This method is used routinely for the commercial production of fine particles and materials fabricated from them, as well as for pilot and laboratory scale production. Similar processes occur in fine particle formation in many other cases ranging from coal combustion to meteor burn-up on entering Earth's atmosphere. The smallest individual particles composing such aerosols (*primary particles*) range from less than 10 nm to about 1 μm , depending on the application.

Aerosol reactors are technological systems used in the synthesis of particles of desired properties; *aerosol reaction engineering* refers to the design principles and methods. Key factors are aerosol precursor properties and reactor process conditions. The most important process conditions are usually the aerosol volume concentration (volume of particles per unit volume of gas) and the time-temperature history of the system. The basic principles of aerosol reaction engineering are still under development (Ulrich, 1984; Gurav et al., 1993; Marijnissen and Pratsinis, 1993; Pratsinis and Kodas, 1993; Wu et al., 1993; Siegel, 1994), and the field can be expected to change rapidly over the next few years. This chapter discusses elements of aerosol dynamics relevant to reactor design for one-component system. Applications to multicomponent cases such as coal combustion and meteor burn-up are not covered.

Table 12.1 gives examples of aerosol reactors that have been used for fine-particle production. The most important full-scale commercial systems are (a) flame reactors for production of pigments and powdered materials and in the manufacture of optical fibers, and (b) pyrolysis reactors for carbon black manufacture. Primary particles produced by these systems range from a few nanometers to a few tenths of a micron in size. Large pilot aerosol reactors are operated for the conversion of SO_x and NO_x to $(\text{NH}_4)_2\text{SO}_4$ and NH_4NO_3 aerosols using high-energy electron beams to irradiate flue gases from fossil fuel combustion. The goal is to convert the pollutant gases to a particulate fertilizer product. Nanometer metal particles are produced in large pilot-scale evaporation-condensation (EC) generators operated at low pressures, usually a few torr. Examples of commercial and pilot scale reactors are discussed in the next section.

Aerosol product properties of interest include primary particle size (and/or size distribution) and substructure (grain boundary, pore size, and defect concentrations and crystalline

TABLE 12.1
Comparison of Aerosol Processes for Powder Production (from Pratsinis and Kodas, 1993)

	Flame	Evaporation/ Condensation Reaction	Laser	Plasma	Hot Wall	Spray Pyrolysis
Max size (μm)	1	0.1–10	1	1	10	0.10–100
Spread	Broad	Narrow	Narrow	Broad	Narrow	Broad
Morphology	Solid, agglomerates	Solid	Solid	Agglomerates, solid	Spherical, solid	Spherical, solid, porous, hollow
Max T (K)	2500	<2000	2000	25,000	2000	1600
Material	Oxides	Metals, oxides	Nonoxides, oxides	Nonoxides, oxides, semi-conductors	Nonoxides, oxides, semi-conductors	Nonoxides, oxides
Complexity	Low	Low	Medium	High	Low	Low

state). Also important are the properties of the aggregates including fractal dimension and particle bond energies (Chapter 8). Methods have been developed for relating particle properties to process conditions and the properties of the solid material composing the particles, usually the solid-state diffusion coefficient, surface energy, and particle density. Commercial processes for the manufacture of fine particles were for the most part designed with limited recourse to the principles of particle formation and growth. Requirements for product properties for existing commercial applications are not exceptionally demanding, compared with anticipated needs for advanced materials. Commercially produced particles are polydisperse, but the size range can be controlled. The individual particles may be polycrystalline with internal grain boundaries and significant necking between particles. It should be possible to exploit the available theory (and foreseeable advances) to permit significant improvements in product properties, while retaining the high throughputs of commercial production methods, without excessive cost increments.

The collision-coalescence mechanism of particle growth discussed in this chapter is thought to control primary particle size in flame reactors. The emphasis is on the synthesis of transition metal oxide particles, which are important in the manufacture of pigments, additives, and ceramic powders. Also discussed are the factors that determine the formation of necks between particles and particle crystallinity. As demands on product quality become more stringent, more research will be needed on particle size, uniformity, crystallinity, and aggregate formation.

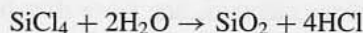
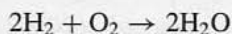
AEROSOL REACTORS: COMMERCIAL AND PILOT SCALE

Flame Reactors

The flame reactor is the one most widely used for the commercial production of inorganic oxide particles by aerosol processes. The aerosol precursor in the form of a vapor is

mixed with oxygen, fed into a reaction chamber and burned. Inert gases and fuels such as hydrogen or methane may also be present. An important commercial product made this way is pyrogenic silica with silicon tetrachloride vapor as the aerosol precursor (Fig. 12.1). Pyrogenic silica is used as a filler in silicone rubber and in natural and synthetic rubber and to modify the rheological properties of paints, resins, and inks. Annual worldwide silica production (1991) was an estimated 10^5 tons.

The stoichiometry of the reaction (but not the true chemical reaction steps) can be represented by the equations



Because the reaction occurs with water vapor, the process is called flame hydrolysis. The gas leaving the furnace, which contains silica particles, gaseous hydrochloric acid, hydrogen, and a small amount of chlorine, is passed through a series of tubes to provide residence time for agglomeration. The agglomerates are collected in cyclone separators that may be followed by a bag filter. Flame temperature is varied over the range 1850°F to 2000°F by varying air, hydrogen, and silicon tetrachloride concentrations. At the lower end of the temperature range, the product particle size is smaller and the surface area is higher. Nominal particle sizes for the various grades range from 7 to 27 nm, and surface areas range from 100 to 380 m²/g. The particles form as a result of the collision-coalescence mechanism discussed later.

The flame process is also used in the production of nanoparticles from other aerosol precursors. Examples are alumina and titania, commercial products produced from the vapors of AlCl₃ and TiCl₄, respectively. Mixed oxides are produced from a vapor precursor mixture—for example, 99% SiCl₄ and 1% TiCl₄. Zirconium oxide is also produced on a pilot scale.

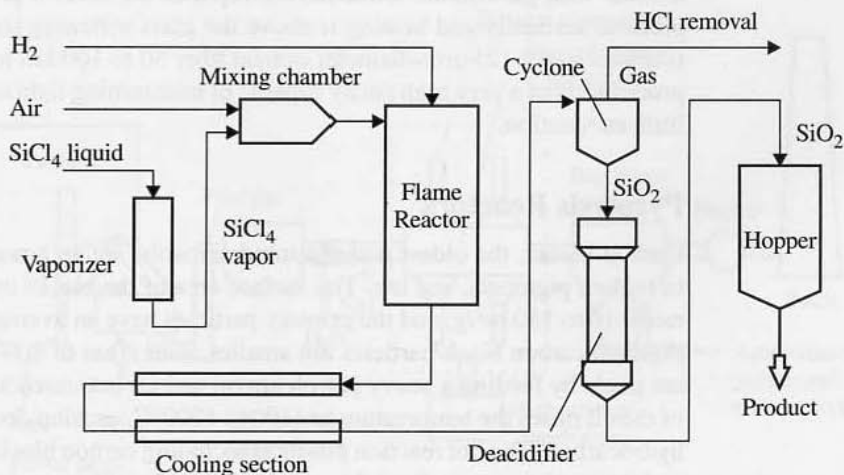


Figure 12.1 Schematic diagram of the process for the manufacture of pyrogenic silica. (After Michael and Ferch, 1993.)

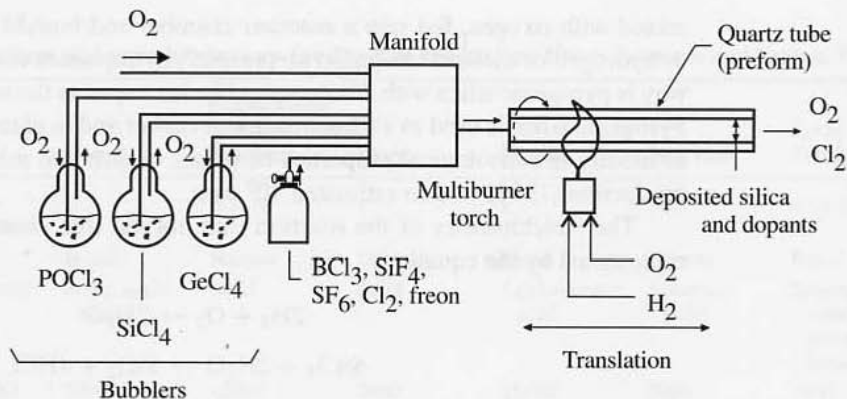


Figure 12.2 Schematic diagram of process for the fabrication of optical fibers. (After Nagel et al., 1985.)

In the fabrication of optical fibers, a silica aerosol generated by the oxidation of silicon tetrachloride vapor in argon or helium passes into a quartz tube preform about a meter long with 25 mm o.d. and 19 mm i.d. (Fig. 12.2). The silica aerosol deposits on the walls of the tube by thermophoresis. Detailed information on the particle size distribution of the aerosol that forms has not been published, but the size range is said to be 20 to 100 nm. Because the particle size is in the free molecule range, the thermophoretic velocity is almost independent of the diameter. The rotating tube is heated by a traversing oxyhydrogen torch that sinters the deposited silica aerosol to form a surface layer without deforming the substrate tube. In this way, the core or cladding is built up layer by layer. The composition of the individual layers can be varied between torch traverses to produce the desired refractive index gradient in the fiber.

The principal dopant added to the silica for control of the refractive index is germanium dioxide with germanium tetrachloride vapor as the aerosol precursor. After mounting the preform vertically and heating it above the glass softening temperature, the 1-m preform is drawn into a 125- μm -diameter optical fiber 50 to 100 km long. This product of aerosol processes is of a very high purity capable of transmitting light over long distances with very little attenuation.

Pyrolysis Reactors

Carbon blacks, the oldest manufactured aerosols, are an amorphous form of carbon used in rubber, pigments, and ink. The surface area of the blacks used in rubber goods is in the range 10 to 150 m^2/g , and the primary particles have an average diameter of 20 to 300 nm. Pigment carbon black particles are smaller, with areas of 300 to 500 m^2/g . Carbon blacks are made by feeding a heavy petroleum oil and air into a reactor where partial combustion of the oil raises the temperature to 1100 to 1700°C, causing decomposition of the unburned hydrocarbon. The hot reaction products including carbon black are cooled by a water spray, and the particles are collected by cyclones and bag filters.

Reactors designed to produce higher surface-area grades are operated at high gas velocities, temperatures, and turbulence. The reactors have three zones: a mixing zone

in which the feedstock is introduced as a spray into a gas–air mixture, a cylindrical reactor where carbon is generated by the chemical reactions and particle formation occurs, and a third zone consisting of a water quench. The mechanisms of particle formation are not well understood, but appear to be a combination of nucleation and growth followed by particle collision and coalescence, similar to inorganic oxide particle formation.

Electron-Beam Dry Scrubbing

In electron-beam dry scrubbing (EBDS), flue gases from the combustion of medium- to high-sulfur fuels are injected with water and ammonia vapor, and exposed to high-energy electron beams (Ratafia-Brown et al., 1995). The SO_2 and NO_x react to form ammonium sulfate and nitrate, and the aerosol product is collected for sale as a fertilizer. Several existing installations are operated on a large pilot scale, about 1% of plant-scale gas flow rates.

The EBDS process is shown schematically in Fig. 12.3. An electrostatic precipitator is used to remove flyash from the flue gases before they pass to the treatment system to prevent contamination of the fertilizer byproduct. The flue gas is then cooled from about 200°C to $60\text{--}80^\circ\text{C}$ in a water spray cooler, and ammonia is added. The conditioned flue gas enters the irradiation chamber (reactor), where high-energy electrons generate hydroxyl (OH) and hydroperoxyl (HO_2) radicals by collision with the water molecules. These radicals play the major role in the formation of sulfuric and nitric acids that react with ammonia to form the sulfate and nitrate.

High levels of SO_2 removal ($>98\%$) with up to 80% NO_x removal have been reported for inlet concentrations of 3000 and 500 ppm of SO_2 and NO_x , respectively. The mass median diameter of the aerosol product falls in the size range 0.6 to $1.0\ \mu\text{m}$. The particles tend to be sticky because of their hygroscopicity and the high relative humidity, and particle collection is difficult. Recent efforts at commercialization have focused on the use of a pulse power

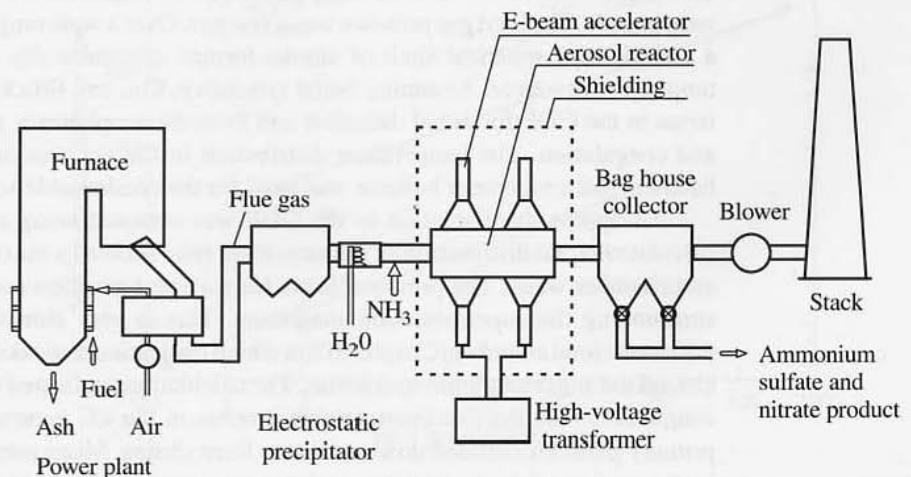


Figure 12.3 Schematic diagram of electron-beam dry scrubbing system. (After Ratafia-Brown et al., 1995.)

electron beam, developed in the United States for simulation of nuclear weapons effects. The economic competitiveness of the process depends strongly on the market value of the fertilizer product, which fluctuates widely.

Evaporation–Condensation Generators

In the evaporation–condensation (EC) generator, a solid material, usually a metal, is evaporated into an inert gas; as the hot vapor mixes with the cool gas, aerosol formation takes place. Granqvist and Buhrman (1976) made a systematic study of aerosol properties using a chamber consisting of a glass cylinder, 0.34 m in diameter and 0.45 m high, fitted with water-cooled stainless steel endplates (Fig. 12.4). Samples of different metals including Al, Mg, Zn, and Sn were placed in an alumina crucible mounted in the chamber and heated by radiation from a graphite heater element. An inert gas, usually argon at 0.5 to 4 torr, was introduced into the chamber, and the crucible was heated at constant temperature and inert gas pressure. Hot metal vapor from the crucible mixed with cool surrounding inert gas to nucleate and form particles ranging from about 3 to 100 nm. Particles were collected by thermophoretic deposition on a cold plate above the crucible. This system was capable of producing a few milligrams of powdered material over a reasonable period of operation; it has served as a prototype for similar systems operated at higher production rates.

The effect of metal vapor pressure on median particle diameter for magnesium and zinc particles was studied at argon pressures of 2.5 and 3.5 torr. The median particle diameter was roughly proportional to the vapor pressure, for a given inert gas pressure. Increasing the inert gas pressure or atomic weight significantly increased particle size (Fig. 12.5). Electron diffraction showed that in all cases, the particles were crystalline. Size distributions were correlated by lognormal size distribution functions.

Based on earlier measurements and their own experimental data, Kim and Brock (1986) proposed a theory for particle formation in EC generators. Particles were generated in their experiments by passing a current through a tungsten wire that held the sample material. The source was held at a fixed temperature, and the chamber walls were held at a lower temperature. The inert gas pressure was a few torr. Over a wide range of operating conditions, a well-defined spherical shell of smoke formed concentrically at some distance from a tungsten wire source. Assuming radial symmetry, Kim and Brock incorporated appropriate terms in the GDE for radial diffusion and flow, thermophoresis, nucleation, condensation, and coagulation. The temperature distribution in the gas was calculated from an energy balance, and a monomer balance was used for the condensable vapor molecules.

An approximate solution to the GDE was obtained using a moments method. The calculated radial distribution of the saturation ratio showed a maximum between the source and chamber walls. The principal locus for particle formation and growth was a thin shell surrounding the supersaturation maximum. This is very similar to the behavior of the diffusion cloud chamber (Chapter 10) in which nucleation also takes place in a narrow region around the supersaturation maximum. The calculations indicated that condensation and not coagulation was the dominant growth process in the EC generator. After formation, the primary particles collided downstream to form chains. Mean particle diameters calculated in the region of high particle concentration increased with inert gas pressure, source temperature, and atomic weight of the carrier gas in qualitative agreement with the data shown in Fig. 12.5.

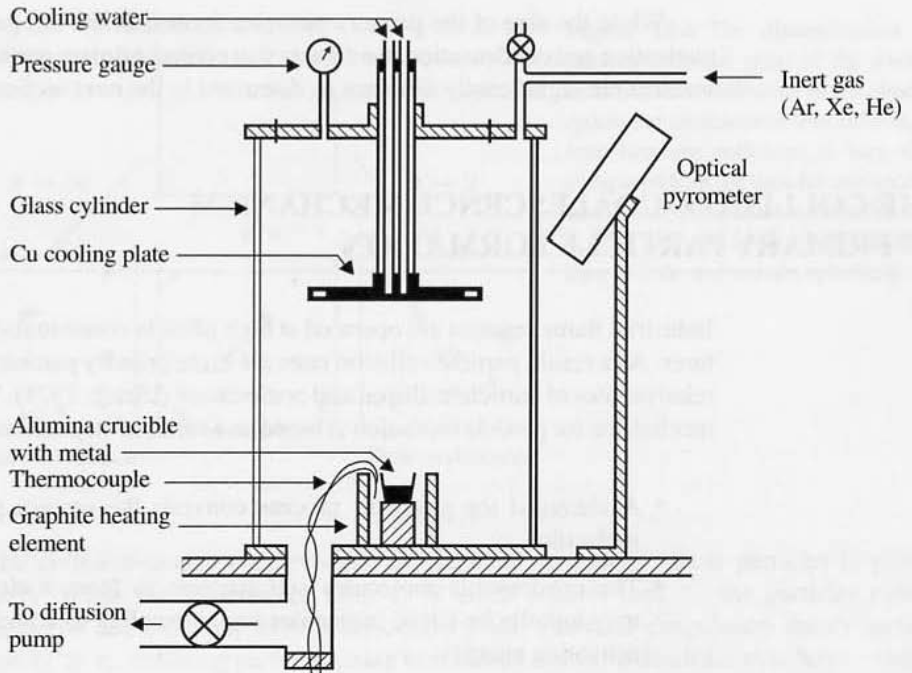


Figure 12.4 Evaporation-condensation generator for the synthesis of ultrafine metal particles. The cylindrical glass chamber was 0.34 m in diameter and 0.45 m in height. Metal vapor from the alumina crucible mixes with the inert gas. The vapor nucleates; particles grow by condensation and deposit on the cooled copper plate by thermophoresis. (After Granqvist and Buhman, 1976.)

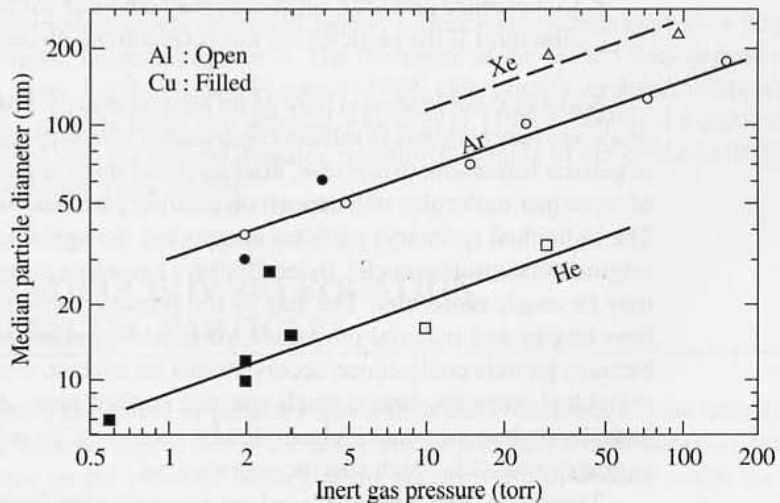


Figure 12.5 Sizes of Al and Cu particles produced in an evaporation–condensation generator. Median particle diameter increased with increasing inert gas pressure and atomic weight. (After Granqvist and Buhman, 1976.)

While the size of the primary particles formed in the EC generator is determined by nucleation and condensation, the factors that control primary particle size in industrial flame reactors are significantly different as discussed in the next section.

THE COLLISION-COALESCENCE MECHANISM OF PRIMARY PARTICLE FORMATION

Industrial flame reactors are operated at high particle concentrations and high gas temperatures. As a result, particle collision rates are high; primary particle size is determined by the relative rates of particle collision and coalescence (Ulrich, 1971). The collision/coalescence mechanism for particle formation is based on a series of steps assumed to proceed as follows:

- A chemical (or physical) process converts the aerosol precursor to condensable molecules.
- The condensable molecules self-nucleate to form a cloud of stable nuclei that may initially be single molecules (corresponding to a nucleation process with zero activation energy).
- Stable nuclei collide and, initially, coalesce to form larger particles. The particles may be liquid or solid during the coalescence period.
- Coalescence ceases or slows significantly as particle size increases and/or the gases cool.
- Fractal-like agglomerate structures form as coalescence ceases.
- Coalescence and neck formation may continue for particles within the agglomerate structures if the particles are not cooled and collected.

Some of these processes may go on simultaneously. For example, chemical or physical processes may continue to release condensable monomer molecules throughout the process of particle formation. In this case, after an initial surge of particle formation, further releases of monomer molecules will deposit on existing particles without generating new particles. The individual (primary) particles composing the agglomerates are much larger than the original condensation nuclei. Indeed for very low vapor pressure materials the original nuclei may be single molecules. The size of the primary particles depends on the temperature-time history and material properties. At high temperatures, the individual particles grow because particle coalescence occurs almost on contact, resulting in agglomerates of large individual particles, hence small specific surface area. At low temperatures, however, particle coalescence takes place slowly compared to collisions, producing fractal-like agglomerates with a high specific surface area.

These concepts can be placed on a quantitative basis by introducing characteristic times for collision and coalescence, defined as the average time between binary particle collisions, τ_c , and the time for two particles to coalesce after making contact, τ_f , respectively. Figure 12.6 illustrates the effect of the characteristic times on the type of particles produced

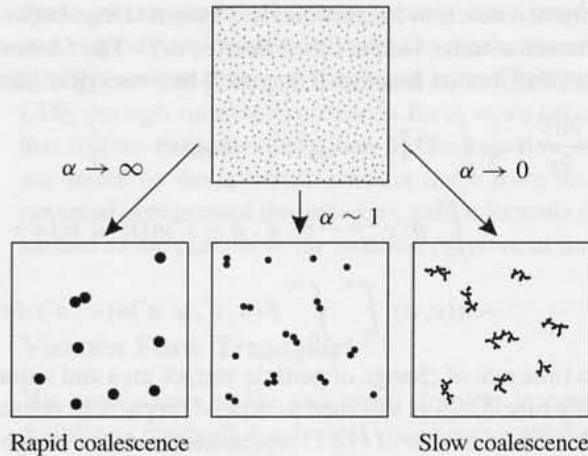


Figure 12.6 The dimensionless parameter α is the ratio of the average time between collisions to the time required for coalescence. For $\alpha \rightarrow 0$, the time between collisions is very short compared with the time for coalescence and fractal-like particles form. For $\alpha \rightarrow \infty$, the particles coalesce as fast as they collide and remain spherical.

by the collision–coalescence process: A cloud of very small stable particles is present initially. When the coalescence time τ_f is much smaller than τ_c , the particles rapidly coalesce on collision and form spherical particles. Classical coagulation theory applies. When $\tau_f \gg \tau_c$, colliding particles cease to coalesce and form dendritic structures—that is, fractal-like agglomerates. There is a continuum of states between these two limiting cases that can be analyzed by allowing for a finite rate of coalescence once two particles have collided. In the sections that follow, the collision and coalescence processes are incorporated in a single theory by extending the Smoluchowski equation (Chapters 7 and 8) to include a finite rate of coalescence. Expressions are derived for τ_c and τ_f in terms of material properties and process conditions from the collision–coalescence theory. The results have direct application to flame reactors and may also apply to the EBDS system.

In the simplest cases, discussed below, a chemical reaction releases a large number of condensable molecules at $t = 0$. The dynamics of the system then depend on aerosol processes alone. Landgrebe and Pratsinis (1989) gave criteria for determining when chemical kinetics must be taken into account. Floess et al. (1997) combined a detailed chemical kinetic model with the general dynamic equation in a study of the synthesis of fumed silica in a hydrogen–air flame reactor.

EXTENSION OF THE SMOLUCHOWSKI EQUATION TO COLLIDING, COALESCING PARTICLES

For an aerosol composed of particles that collide and coalesce at a finite rate, the particles in a given volume range v to $v + dv$ at any instant will have a distribution of surface areas that depends on the previous history of the particles in the volume range. As a limiting case, the aerosol cloud can be characterized by a distribution function that depends *only* on particle volume and surface area and no other morphological details. The analysis does not take into account the fractal nature of the agglomerates, and it holds best in the early stages of agglomerate formation.

Let the distribution function for particles in a volume range between v and $v + dv$, and the area range between a and $a + da$ at time t be $n(v, a, t)$. The Smoluchowski equation for the continuous size distribution function (Chapter 7) becomes (Koch and Friedlander, 1990)

$$\begin{aligned} \frac{\partial n}{\partial t} + \frac{\partial n \dot{a}}{\partial a} + \frac{\partial n \dot{v}}{\partial v} = & \frac{1}{2} \int_0^v \Theta [a - a_{\text{sph}}(v') - a_{\text{sph}}(v - v')] \\ & \times \int_0^a \beta(v', v - v', a', a - a') n(v', a') n(v - v', a - a') da' dv' \\ & - n(v, a) \int_0^\infty \int_0^\infty \beta(v, v', a, a') n(v', a') da' dv' \end{aligned} \quad (12.1)$$

where \dot{a} and \dot{v} are time rate of change of particle surface area and volume, respectively. The collision frequency function β is assumed to depend on particle volume and area only. The second term on the left-hand side of (12.1) represents the drift through particle surface area space caused by particle coalescence. The third term represents the drift through volume-space due to molecular condensation from the gas phase. This term would contribute if a chemical reaction that forms condensable molecules continues during the collision and coalescence processes.

The right-hand side of (12.1) is the change in $n(v, a, t)$ due to collision. The step function Θ is introduced because the surface area of a particle produced by collision must be greater than the sum of the minimum surface areas ($a_{\text{sph}}(v)$) of the two original colliding particles. The total surface area of particles per unit mass of gas contained within the volume range v to $v + dv$ is

$$A_v = \int_a n(v, a', t) a' dv' \quad (12.2)$$

Multiplying (12.1) by a and integrating with respect to a gives

$$\frac{dA_v}{dt} - \int_a n(v, a', t) \frac{da'}{dt} da' = \Delta_{\text{coll}} \quad (12.3)$$

where condensation has been neglected, that is, $\dot{v} = 0$. The second term of (12.3) represents the surface area reduction of particles in the volume range v to $v + dv$ resulting from coalescence. The term Δ_{coll} is the net change in surface in the range v to $v + dv$ resulting from collisions. Both area and volume are conserved at the instant of collision. However, the area begins to relax toward the equilibrium shape (spherical for a liquid) at a rate that depends on the coalescence law da/dt discussed in the next section.

RATE EQUATION FOR PARTICLE COALESCENCE

General Considerations

There is an extensive literature on the rate at which spherical particles in contact coalesce as a result of various mechanisms for molecular transport in the contact region. This literature, developed largely for application to sintering in the ceramics field, has been summarized by Kingery et al. (1976, Chapter 10); and Brinker and Scherer (1990, Chapter 11). For liquids,

the mechanism of coalescence usually considered is viscous flow. For solids, diffusion and evaporation–condensation are the mechanisms usually cited. Diffusion can take place through various routes as discussed later. These mechanisms can be incorporated in the GDE through suitable expressions for $\dot{a} = da/dt$ as shown in (12.1) and the expressions that follow. Examples are given for viscous flow and diffusion. Both transport processes are driven by deviations in particle shape from the spherical. The effect on the chemical potential is expressed through the Laplace formula that relates the local normal stress at the surface of the particle to the external pressure in the gas.

Viscous Flow Transport

The coalescence of the two small droplets in contact is driven by the tendency for the doublet to approach a spherical shape corresponding to minimum surface free energy for the doublet volume. For liquid particles including glassy materials like silica, coalescence takes place by viscous flow. For a Newtonian liquid, during the initial stages of coalescence of two liquid spheres of equal diameter, a neck forms at the contact point with a radius that grows as $t^{1/2}$ (Frenkel, 1945). After a short initial period in which coalescence is very rapid, the rate of decrease in the surface area becomes linear in the deviation of the doublet surface area from the sphere of the same volume as the doublet (Koch and Friedlander, 1990):

$$\frac{da}{dt} = -\frac{1}{\tau_f}(a - a_{\text{sph}}) \quad (12.4)$$

where

a = surface area of doublet

a_{sph} = surface area of sphere of same volume

τ_f = characteristic time independent of surface area but dependent on the mechanism of coalescence

For the viscous flow mechanism, Frenkel (1945) found that

$$\tau_f = \frac{\pi \mu d_p}{\sigma} \quad (12.5)$$

where μ is the viscosity of the particle material and σ is the surface tension.

Transport by Diffusion

The coalescence of crystallites in contact is much more complex than the coalescence of a Newtonian liquid. For coalescing liquids, the equilibrium shape is a sphere. For crystallites in contact, the equilibrium form is presumably determined by a Wulff construction; exact calculations for such complex configurations have not been made. To estimate τ_f for crystallites, it is customary to assume a simple geometry—for example, two spheres in contact as in the case of liquid droplets in contact. The particle properties are assumed to be isotropic.

For short times, the radius of the neck between two solid particles grows as $t^{1/5}$ when lattice diffusion dominates (Kingery and Berg, 1955). After a short initial period the rate of decrease in the surface area for coalescing solid particles approaches the linear rate law (12.4) with τ_f given by (Friedlander and Wu, 1994)

$$\tau_f = \frac{3}{64\pi} \frac{kTv}{D\sigma v_m} \quad (12.6)$$

where T is the absolute temperature, v is the particle volume, D is the solid-state diffusion coefficient, σ is the surface tension, and v_m is the molecular volume. The value of D corresponds to the dominant transport route—for example, lattice, grain boundary, or surface diffusion—discussed in the next section.

Molecular Dynamic Simulations: Solid–Liquid Transition

Molecular dynamics (MD) computations of coalescence have been made for silicon nanoparticles ranging in size from 30 to 480 atoms, corresponding to a maximum diameter smaller than 3 nm (Zachariah and Carrier, 1999). The computations were based on an interatomic potential developed for silicon atoms with covalent bonding. The particle structure was assumed to be amorphous. The MD simulations indicate that the transition between solid- and liquid-state behavior occurs over a wide temperature range significantly lower than the melting point of bulk silicon (1740 K), a well-known effect for nanoparticles (Chapter 9). The broadest transition occurred for the smallest particles studied (30 atoms), probably because the surface atoms make up a large fraction of the particle mass.

Figure 12.7 shows values of τ_f calculated in two different ways as a function of temperature for particles of different size. One set of curves (solid lines) was calculated from the phenomenological relationships (12.5) and (12.6). For the solid particles (low temperature), MD simulations were used to obtain the diffusion coefficient and surface tension that appear in (12.6). For the liquid-like particles (high temperature), data for the viscosity and surface tension that appear in (12.5) were obtained from experimental results reported in the literature. The dashed lines in Fig. 12.7 were calculated directly from MD simulations of the decrease in the moment of inertia of two coalescing spheres.

The figure shows good agreement between the MD calculations of τ_f based on the moment of inertia and values calculated from the phenomenological theory. (The phenomenological theory for the liquid was corrected by a factor of 10 to improve agreement on the grounds that the viscosity data for bulk silicon is not accurate for very small particles.) At the higher temperatures ($T \geq 1200$ K) when the particles tend to be most liquid-like, the dependence of τ_f on particle size and temperature is relatively weak. At the lowest temperatures, far below the bulk melting point, the dependence on size and temperature is strong.

MD simulations shed light on the solid–liquid transition that determines primary particle size and the onset of aggregate (agglomerate) formation discussed later in the chapter. MD calculations also provide a test of the validity of the phenomenological theories. However, the simulations shown in Fig. 12.7 are limited to very small particles and very short coalescence times ($\tau_f < 10^{-8}$ sec). For larger values of τ_f and larger particles, the computations became intractable. Calculations such as these and improvements on them will be vital to further advances in the theory of nanoparticle formation.

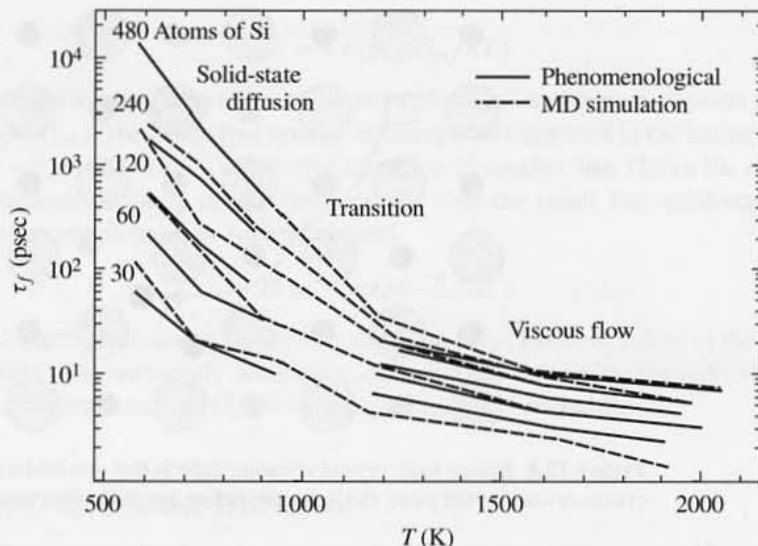


Figure 12.7 Computer simulations of coalescence times for particles composed of varying numbers of silicon atoms. The dotted lines connect the molecular dynamic computations based on the approach of the moment of inertia of two coalescing particles in contact to the value for the sphere of the same volume. The solid lines show calculations based on the phenomenological theories, (12.5) and (12.6). Values calculated from (12.6) (for the liquid) were multiplied by a factor of 10 on the grounds that viscosity values for bulk silicon are too small for nanoparticles. (After Zachariah and Carrier, 1999.)

The tests of the phenomenological theory were based on diffusion coefficients (determined from the MD simulations) that fell in a range that corresponded to surface diffusion. This is to be expected because of the very small particle size for which the MD simulations were made. As particle size is increased, bulk diffusion processes are likely to become more important. More is known about diffusion mechanisms for this process than for surface diffusion. The factors that determine bulk diffusion are reviewed in the next section.

SOLID-STATE DIFFUSION COEFFICIENT

Temperature Dependence

According to the analysis in the previous sections, the primary particle size in flame reactors is determined by the relative rates of particle collision and coalescence. For highly refractory materials, the characteristic coalescence time (12.6) depends on the solid-state diffusion coefficient, which is a very sensitive function of the temperature. The mechanisms of solid-state diffusion depend in a complex way on the structure of the solid. For example, a perfect cubic crystal of the substance AB consists of alternating ions A and B . Normally there are many defects in the lattice structure even in a chemically pure single crystal; defect types are shown schematically in Fig. 12.8. The mechanism of diffusion in crystalline solids depends on the nature of the lattice defects. Three mechanisms predominate in ionic

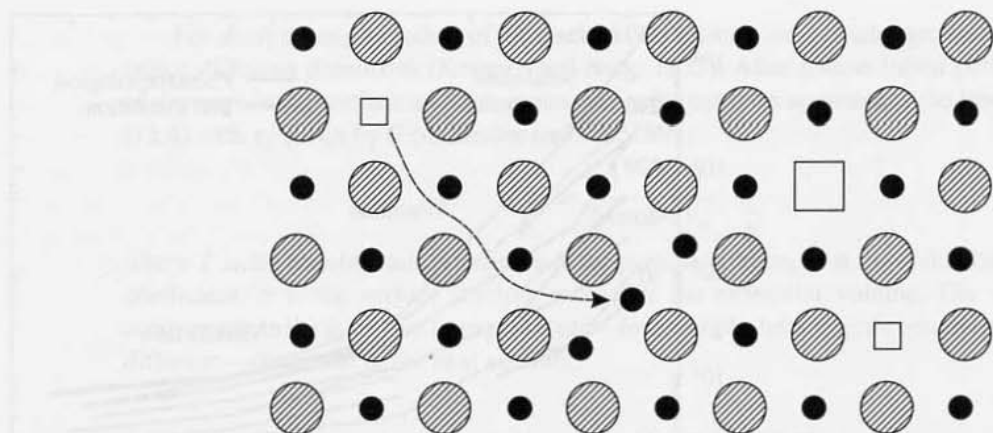


Figure 12.8 Binary ionic crystal showing defects that can lead to lattice diffusion. (a) Frenkel defect (vacancy–interstitial pair), (b) Schottky defect (anion–cation vacancy). (After Kingery et al., 1976.)

solids. If the diffusing species is transported by jumping from its initial lattice site to a vacant adjacent site, the diffusion process is said to occur by a *vacancy mechanism*. This mechanism depends on the presence of Schottky defects—that is, equal numbers of anion and cation vacancies. If the diffusing species occupies an interstitial lattice position and moves directly from one interstitial site to another, the process is an *interstitial mechanism*. This corresponds to Frenkel defects—that is, equal numbers of interstitial ions and vacancies in the corresponding sublattice. Finally, if transport occurs by the interstitial atom moving into a normally occupied lattice site, forcing the original resident into an interstitial site, the process is called an *interstitialcy mechanism*. The situation is further complicated by the presence of impurities that will not be discussed here.

According to the vacancy mechanism for lattice diffusion,

$$D = \frac{1}{6} \sqrt{r^2} Z w n f \quad (12.7)$$

where $\sqrt{r^2}$ is the jump distance, Z is the number of nearest neighbor sites, w is the atomic jump frequency, n is the fraction of atomic defects, and f is a correlation function. Both the jump frequency and fraction of atomic defects are activated functions of the temperature, so the solid state diffusion coefficient typically has an Arrhenius form. For cubic crystals, one value of D is sufficient to characterize the material because the structure is isotropic. For other crystal structures, several diffusion coefficients may be necessary, depending on the direction of diffusion. This level of complexity has so far not been considered in studies of particle coalescence.

At thermal equilibrium, the defect fraction, n , in a perfect crystal is given by a Boltzmann relationship:

$$n = \exp(-G_f/kT) \quad (12.8)$$

where G_f is the free energy of formation of the defect. For metals, n is typically a few parts in 10^4 at the melting point. The jump frequency w is a thermally activated process which can be expressed in a similar form

$$w = \nu \exp(-G_m/kT) \quad (12.9)$$

where ν is the vibration frequency of an atom about its equilibrium position in the jump direction and G_m is the Gibbs free energy difference between ions in the lattice site and the maximum value needed for a successful transition to another site. Hence the new product in (12.7) depends strongly on the temperature, with the result that solid-state diffusion coefficients generally have an Arrhenius form

$$D = D_0 \exp(-E/RT) \quad (12.10)$$

where E , the activation energy, is the sum of G_f and G_m . Because values of the parameters in (12.8) and (12.9) are usually not known, diffusion coefficients for the individual ions are measured and correlated by (12.10) for extrapolation or interpolation.

Values of D for Lattice Diffusion

Values of D range over many orders of magnitude for different substances. Here we consider only metals (briefly) and metal oxides. Metallic diffusion has been especially well-studied because of its industrial importance and the relatively simple transport mechanisms. Most metals have face-centered cubic, body-centered cubic, or hexagonal close-packed structures. Each atom is related geometrically to its neighbors in a similar manner so only one kind of lattice site need be considered in analyzing transport. Extensive data sets are available on self-diffusion in solid elements including metals, carbon, silicon, and phosphorus as well as in homogeneous alloys (Brandes and Brook, 1998).

There are many more mechanisms of diffusion for ionic crystals, than for simple metals. Limiting the discussion to binary compounds, there are two sublattices, one for cations and the other for anions. Thus there are a variety of combinations of vacancy and interstitial defects that can serve as diffusion paths. In addition, ionic compounds often possess nonstoichiometric vacancies resulting from multiple oxidation states of crystal components, usually the cation. Diffusion coefficients for cations and oxygen have been measured for many oxides in tracer studies (Kingery et al., 1976; Kofstad, 1972). Both cation and oxygen diffusion coefficients vary with the partial pressure of oxygen in the surrounding gas.

In the case of coalescence/sintering, diffusion is driven by the chemical potential gradient in the solid that results from the surface deformation (deviation from the equilibrium crystal shape usually assumed to be a sphere). In general, tracer diffusion coefficients for the anion and cation differ. There is a coupling between the diffusion fluxes of anions and cations due to the constraints of local electroneutrality and absence of current flow. An analysis leads to an equation for the effective diffusion coefficient of the ion pair that is of the same form as the Nernst equation for ion diffusion in solution:

$$D = \frac{|z_1| + |z_2|}{|z_2|/D_1 + |z_1|/D_2} \quad (12.11)$$

where $|z|$ is the magnitude of the ionic charge and 1 and 2 refer to the ions. This result holds in the ideal solution limit. It is easy to see that the rate of diffusion is controlled by the slower moving component when the diffusion coefficients are markedly different; that is, $D \approx [D_1(|z_1| + |z_2|)]/[|z_2|]$ when $D_1 \ll D_2$.

High Diffusivity Paths

In most crystalline materials, there are also much larger scale structural imperfections than the point defects at the atomic or ionic scales that lead to lattice diffusion. Certain large-scale imperfections called *dislocations* can be well-characterized mathematically (Read, 1953); imperfections in polycrystalline materials, composed of many small grains (crystals) of different particle size and orientation, are more difficult to characterize. The regions separating the individual crystals are called grain boundaries. Transport of ions and atoms along grain boundaries and dislocations is much faster than through the crystal lattice itself at low temperatures. At high temperatures, diffusion through the solid lattice becomes dominant. All of these mechanisms may contribute to diffusion in coalescing particles.

An interpolation formula often used for the effective diffusion coefficient that includes both lattice and grain boundary (or other) diffusion processes is

$$D_{\text{eff}} = (1 - f)D_V + fD_B \quad (12.12)$$

where D_V is the perfect crystal or lattice value of the diffusion coefficient, D_B is the average value in the structurally flawed material, and f is the average fraction of the time the diffusing species spends in the flawed material (dislocations and grain boundaries). The effective diffusion coefficient, D_{eff} , is assumed to be the value for the rate-controlling diffusing species, usually the ion that moves more slowly through the particles. The relative influences of grain boundary and lattice diffusion depend on the ratio D_B/D_V and f . If lattice diffusion is the dominant mechanism, $f \rightarrow 0$ and $D_{\text{eff}} \approx D_V$. If D_B/D_V and f are large, which is likely in polycrystalline particles, grain boundary diffusion tends to dominate and $D_{\text{eff}} \approx D_B f$. Grain boundary diffusion is also an activated process, but the activation energy is usually smaller than that for lattice diffusion.

Applying basic concepts of solid-state diffusion to transport across the boundaries of coalescing submicron particles is difficult. Information is lacking on the crystalline state and the nature of the structural imperfections in the colliding particles. However, values of the solid-state diffusion coefficient can provide qualitative guidance in estimating the effects of material properties on primary particle size as discussed in a later section.

Nanosized particles have high ratios of surface area to volume, and it is expected that surface diffusion is of importance. The driving force for surface diffusion is the gradient of the chemical potential along the surface. The form of the diffusion coefficient for surface diffusion is similar to that for grain boundary diffusion, except that the grain boundary width b is replaced by the width of the surface layer. Because of the similarity between the forms of the diffusion coefficient, surface diffusion can sometimes be treated in a manner equivalent to grain boundary diffusion.

ESTIMATION OF AVERAGE PRIMARY PARTICLE SIZE: METHOD OF CHARACTERISTIC TIMES

When we introduce a suitable coalescence rate law, the extended Smoluchowski equation (12.1) can, in principle, be solved numerically for $n(v, a, t)$ with the appropriate initial conditions. Using the linear rate law (12.4) for solid-state diffusion, Xiong and Pratsinis

(1993) obtained numerical solutions for the distributions of particle surface area and volume. The analysis in this chapter is limited to the estimation of the average primary particle size, determined by the interaction between collision and coalescence.

Returning to (12.3) and substituting the linear form of the coalescence law (12.4), we obtain

$$\frac{dA_v}{dt} + \frac{(A_v - A_{v,\text{sph}})}{\tau_f} = \Delta_{\text{coll}} \quad (12.13)$$

where $A_{v,\text{sph}}$ is the minimum possible surface area in the size range v to $v + dv$. Multiplying (12.13) by v and integrating over v , the collision term on the right-hand side vanishes because there is no net change in surface area by collision processes alone. Coalescence drives the reduction in surface area, and the integral of the first term on the left-hand side becomes

$$\frac{d \int_0^\infty A_v dv}{dt} = \frac{dA_m}{dt} \quad (12.14)$$

where A_m is the total surface area per unit mass of gas. The integral of the second term on the left-hand side of (12.13) can be written as

$$\int_0^\infty \frac{(A_v - A_{v,\text{sph}})v dv}{\tau_f(v)} = \frac{1}{\tau_f(\bar{v})} (A_m - A_{\text{sph}}) \quad (12.15)$$

where \bar{v} is an average particle volume defined by the relation

$$\int_0^\infty \frac{A_v}{\tau_f(v)} dv = \frac{1}{\tau_f(\bar{v})} A_m \quad (12.15a)$$

The term A_{sph} is defined by

$$A_{\text{sph}} = \tau_f(\bar{v}) \int_0^\infty \frac{A_{v,\text{sph}}}{\tau_f(v)} dv \quad (12.16)$$

The evaluation of A_{sph} presents a closure problem because the term $A_{v,\text{sph}}$, which is a function of time, is not known over the path of the system. However, A_{sph} is closely related to the minimum surface area of the aerosol—that is, the surface area that would be attained if each individual agglomerate particle became spherical. Indeed, the two would be equal if the aerosol were monodisperse with size \bar{v} . When the rate of coalescence is fast compared with the collision rate, the minimum surface area can be approximated by the self-preserving size distribution for coalescing spheres (Chapter 7).

Substituting (12.14)–(12.16) in (12.13) gives

$$\frac{dA_m}{dt} = -\frac{1}{\tau_f(\bar{v})} (A_m - A_{\text{sph}}) \quad (12.17)$$

This expression is the starting point for estimating the average primary particle size. Initially, for a hot gas containing many small particles that coalesce almost instantaneously, $\tau_f \rightarrow 0$ and $A_m \approx A_{\text{sph}}$. As the gas cools, τ_f starts to increase; that is, coalescence is not quite instantaneous. This is seen from (12.6) and the strong (Arrhenius) dependence of D on T . Next we assume that $\bar{v} = \phi_m/N_m$, and we take the minimum surface area, in which each particle has relaxed to the spherical shape, as an approximation for A_{sph} . (This would be exact if the aerosol were monodisperse.) Here ϕ_m is the total volume and N_m the total

number of the aerosol particles per unit mass of gas. It is convenient to introduce a new variable, which represents the fractional deviation of the aerosol surface area from the state in which each particle has relaxed to the spherical shape:

$$\theta = \frac{A_m - A_{\text{sph}}}{A_{\text{sph}}} \quad (12.18)$$

Combining (12.18) and (12.17) gives

$$\frac{d\theta}{dt} + \left[\frac{1}{\tau_f(\bar{v})} - \frac{1}{\tau_c(\bar{v})} \right] \theta = \frac{1}{\tau_c(\bar{v})} \quad (12.19)$$

where τ_c is the characteristic collision time, defined by

$$\frac{1}{\tau_c} = -\frac{1}{A_{\text{sph}}} \frac{dA_{\text{sph}}}{dt} = \frac{1}{3\bar{v}} \frac{d\bar{v}}{dt} \quad (12.20)$$

As shown by (12.19) the behavior of the system depends on the relative values of the collision and coalescence times which are determined by the process conditions and material properties. If the size distribution remains nearly self-preserving throughout the time of interest, the fractional change in average particle volume with time in the free molecule regime (Chapter 7), is

$$\frac{3}{\tau_c} = \frac{1}{\bar{v}} \frac{d\bar{v}}{dt} = \frac{1}{2} \alpha \left(\frac{6kT}{\rho_p} \right)^{1/2} \left(\frac{3}{4\pi} \right)^{1/6} \phi \bar{v}^{-5/6} \quad (12.21)$$

Thus when the average particle size \bar{v} is very small, τ_c is very small. Equation (12.21) holds also when dilution takes place by turbulent mixing, for example, along the center line of a turbulent jet (Lehtinen et al., 1996). Substituting (12.21) into (12.19) gives

$$\frac{3d\theta}{d \ln \bar{v}} = 1 - \left[\frac{\tau_c}{\tau_f} - 1 \right] \theta \quad (12.22)$$

with $\theta = 0$ at the start of the process. Equation (12.22) shows the importance of the ratio of the collision to coalesce times in the particle formation process.

Consider the case of a hot gas that contains a high concentration of very small aerosol particles that collide and coalesce. Initially, $\tau_f \ll \tau_c$ and the particles coalesce as fast as they collide. The value of θ remains very near zero, and the classical theory of coagulation for coalescing particles holds (Chapter 7). As coagulation proceeds and the gas cools, τ_f increases rapidly. This can be seen by inspection of (12.6), which shows the dependence of τ_f on particle volume and the diffusion coefficient. The diffusion coefficient, in particular, is a very sensitive function of temperature through an Arrhenius relationship as discussed in the previous section.

As shown by (12.21), the value of τ_c also tends to increase as the temperature decreases and the average particle size increases. At some point τ_f becomes larger than τ_c and the term in brackets on the right-hand side of (12.22) changes sign. The value of $d\theta/d \ln \bar{v}$ increases rapidly after the point where $\tau_f = \tau_c$. Physically this corresponds to the range where collisions take place more rapidly than coalescence. As a result, fractal-like structures begin to develop. The detailed behavior of the system depends on the time-temperature history of the gas.

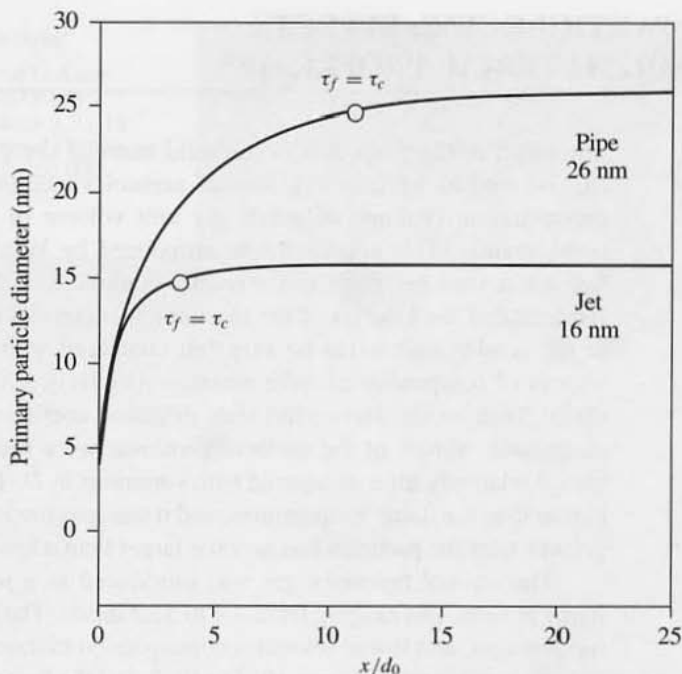


Figure 12.9 Primary diameter \bar{d}_p for TiO_2 particles as a function of distance for a plug flow of a gas being cooled. The initial gas temperature $T_0 = 2000$ K, the temperature of the pipe wall is 1000 K, the gas velocity is 100 msec^{-1} , and the aerosol volumetric concentration is 10^{-5} . The point at which τ_c equals τ_f is shown (Lehtinen et al., 1996).

Calculations based on these equations have been made for the formation of TiO_2 particles in a uniform (plug) flow through a pipe and for the center line of a free jet (Lehtinen et al., 1996). Of special interest is the particle size shown in Fig. 12.9 as a function of axial distance from the point where the aerosol is introduced. For both the pipe and jet flows, the calculated particle size levels off rapidly after the point at which $\tau_f = \tau_c$. At this point, agglomerate structures begin to form. *If the system were frozen at this point, the final primary particle size would be determined.* However, if the temperature remains high, the primary particles composing the agglomerates continue to grow in size as a result of coalescence.

Very small particles melt at temperatures less than the bulk melting point (Chapter 9). The calculated melting point reduction for spherical TiO_2 particles was greatest during the earliest stages of particle formation but was less important for particles larger than about 5 nm. The reduction in melting point means that in the earliest stages, the characteristic coalescence time has been overestimated in these calculations. This, however, has little effect on the results, because at the early stages solid-state diffusion is fast enough for complete coalescence of two particles before further collisions.

Finally, the reader is reminded that the analysis is based on the use of the linear approximation (12.4) for the decay with time of the area of a doublet. The characteristic collision time used in the calculations was based on the free molecule regime.

PRIMARY PARTICLE SIZE: EFFECTS OF AEROSOL MATERIAL PROPERTIES

The effect of the properties of the solid material composing the particles on particle size can be studied by injecting various aerosol vapor precursors at fixed particle volume concentration (volume of solids per unit volume of gas) into a given aerosol reactor configuration. This approach was introduced by Windeler et al. (1997a,b), who used a free jet aerosol generator as the reactor configuration. In its simplest form, this approach requires that the kinetics of the reactions that convert the metal compound in vapor form to the condensable oxide be very fast compared with the aerosol processes that follow. Vapors of compounds of three metals— $\text{Al}(\text{CH}_3)_3$, TiCl_4 , and Nb_2F_5 —were selected for study. Their oxides have solid-state diffusion coefficients ranging over several orders of magnitude. Values of the molecular volume were nearly the same and surface tensions varied relatively little, compared with variations in D . The oxides had melting points much higher than the flame temperatures, and it was assumed that solid-state processes controlled growth after the particles had become larger than a few nanometers.

The aerosol precursor gas was introduced as a jet into a low-velocity methane–air flame at velocities ranging from 4.8 to 53.2 m/sec. The highest flow rate corresponded to a turbulent jet, and lower velocities corresponded to transitional and laminar flows. Aerosol volume loading ranged from 10^{-7} to 10^{-6} , and the flame was operated under stoichiometric conditions at flow rates of 8.8 and 33 liters/min to obtain different jet temperature profiles. Vapor concentrations were adjusted so that aerosol volume loadings were the same for each set of flame conditions (temperature profiles and gas flow regimes). After an initial period of heating during which the aerosol precursor gases reacted in the flame, the entire gas flow cooled as surrounding room temperature air was entrained into the flame. Maximum temperatures in the aerosol precursor jet ranged from 1050 to 1920 K. The jet orifice was 1.2 mm in diameter, and the aerosol mass production rate ranged from 0.05 to 1.0 g/hr. Aerosol samples were collected for electron microscopy for varying volume loading, axial distance along the jet, exit velocity, and jet temperature.

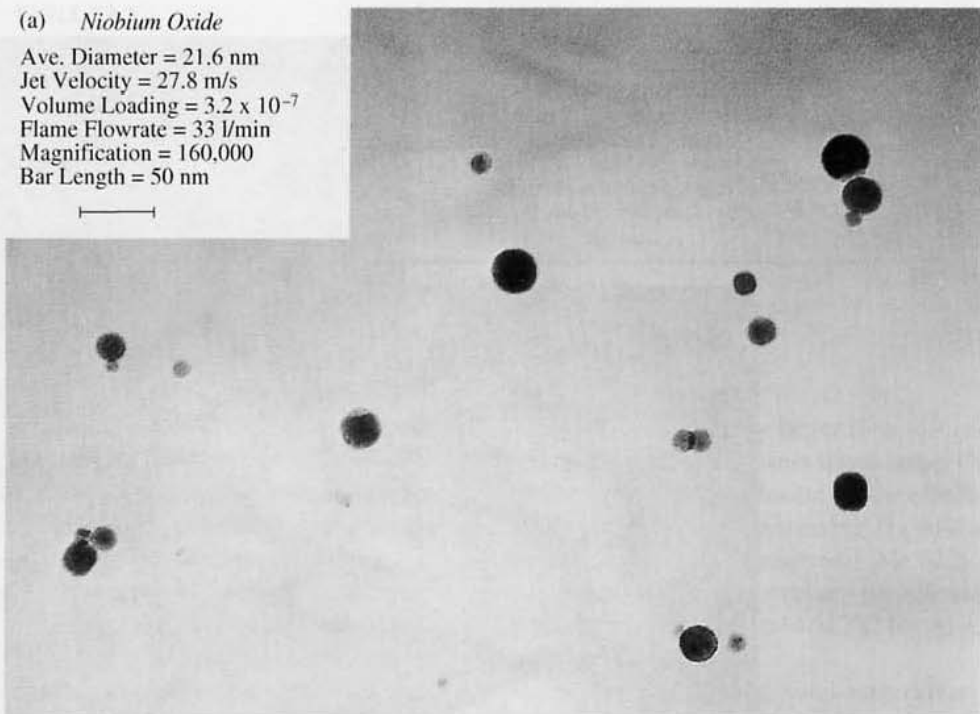
Particle formation is thought to have proceeded as follows: Metal oxide molecules formed as the aerosol vapor precursor reacted near the jet orifice. The oxide molecules collided to form particles that grow by the collision–coalescence mechanism until the temperature fell to the point where coalescence was quenched. Particle coalescence was probably driven by solid-state diffusion and, perhaps, surface diffusion. Metal oxides with higher diffusion coefficients would be expected to form larger primary particles because they continue to coalesce at lower temperatures during the cooling period.

Electron micrographs of samples of the three different metal oxide particles are shown in Fig. 12.10. The process parameters including flame conditions, jet velocity, and aerosol volumetric loading were the same for the three materials. The alumina particles were smallest ($\bar{d}_p = 4.1$ nm) and formed large agglomerate structures. Titania particles were larger ($\bar{d}_p = 11.6$ nm) and tended to be more spherical. Largest and most spherical were the niobia particles with $\bar{d}_p = 22$ nm.

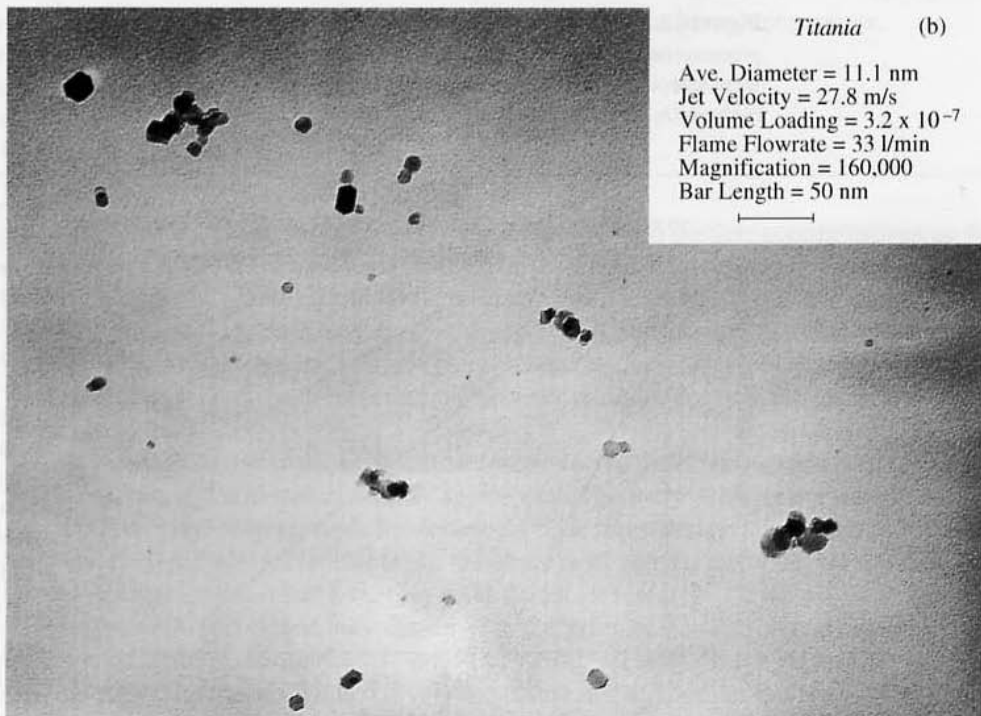
Values of D have been reported for self-diffusion of Al and O in Al_2O_3 with $D_{\text{O}} < D_{\text{Al}}$, as well as for self-diffusion of Ti and O in TiO_2 with $D_{\text{O}} < D_{\text{Ti}}$. Diffusion coefficients for TiO_2 were much larger than for Al_2O_3 (Fig. 12.11). Hence, the particle size of alumina would be expected to be smaller than for titania, in agreement with experiment. For niobia,

(a) *Niobium Oxide*

Ave. Diameter = 21.6 nm
Jet Velocity = 27.8 m/s
Volume Loading = 3.2×10^{-7}
Flame Flowrate = 33 l/min
Magnification = 160,000
Bar Length = 50 nm

*Titania* (b)

Ave. Diameter = 11.1 nm
Jet Velocity = 27.8 m/s
Volume Loading = 3.2×10^{-7}
Flame Flowrate = 33 l/min
Magnification = 160,000
Bar Length = 50 nm



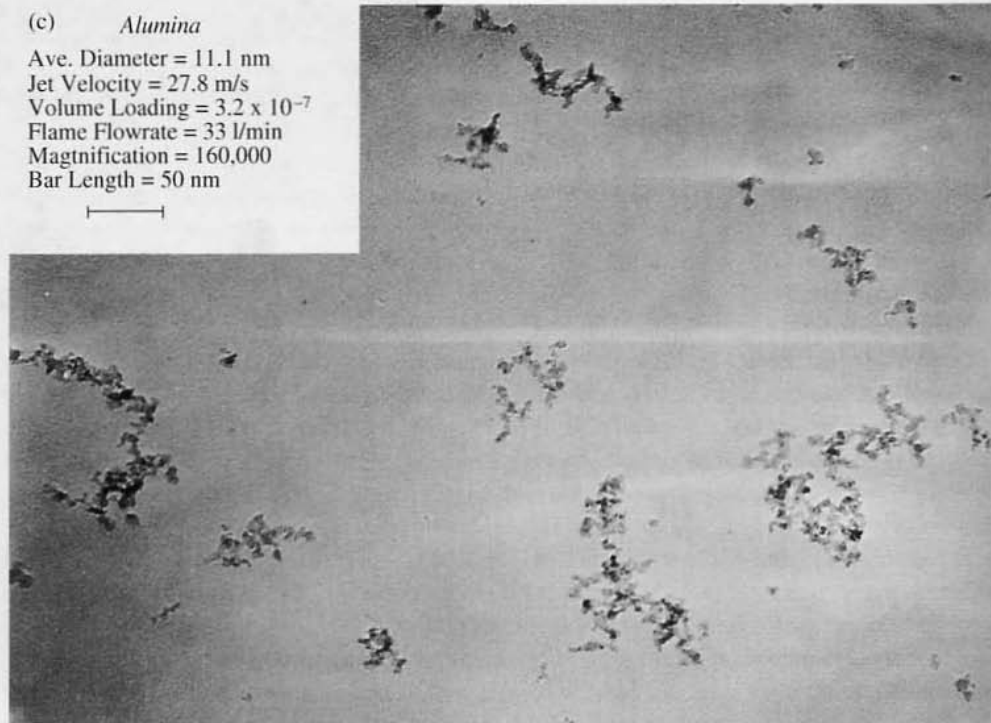


Figure 12.10 Electron micrographs of particles of different metal oxides generated under the same process conditions (precursor jet velocity and volumetric loading) (Windeler et al., 1997b). Substances were selected for widely differing values of D_0 (assumed to be rate-limiting ionic species). (a) Nb_2O_5 highest D_0 . (b) TiO_2 medium D_0 . (c) Al_2O_3 smallest D_0 . Compare with Fig. 12.11.

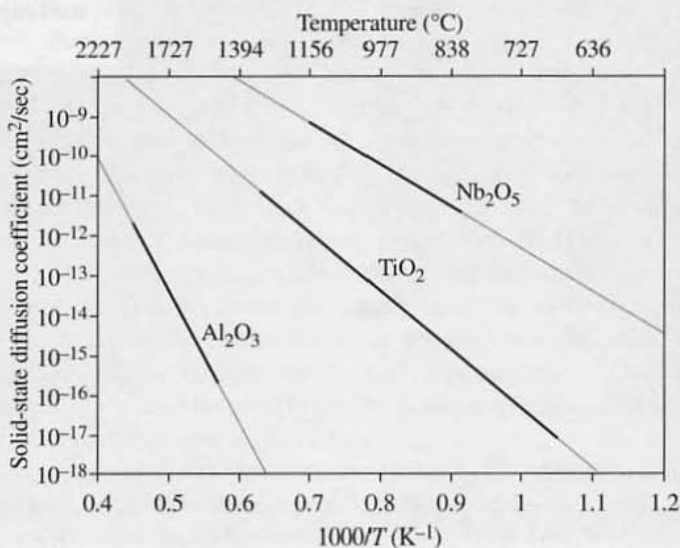


Figure 12.11 Solid-state diffusion coefficients for oxygen in the oxides studied by Windeler et al. (1997a). For both alumina and titania, oxygen diffusion coefficients were smaller (presumably rate-limiting) than the cation values. The value of the metal ion diffusion coefficient for niobia is not known. Data on which the figure is based are cited in Table 12.2.

TABLE 12.2
Oxygen Diffusion in Inorganic Oxides (Fig. 12.11)

Material	Activation Energy (kcal/mol)	D_0 (cm ² /sec)
Nb ₂ O ₅ ^a	48.5	1.85×10^{-2}
TiO ₂ ^b	67.5	2.40×10^{-2}
Al ₂ O ₃ ^c	152	1.9×10^3

^aMassiani, Y., Crousier, J. P., and Streiff, R. (1978) *J. Solid State Chem.*, **24**, 92.

^bDerry, D. J., Lees, D. G., and Calvert, J. M. (1981) *J. Phys. Chem. Solids*, **42**, 57.

^cOishi, Y., and Kingery, W. D. (1960) *J. Chem. Phys.*, **33**, 484.

only values of D_0 have been reported, and these were significantly larger than diffusion coefficients for titania or alumina (Fig. 12.10). Niobia particle sizes were much larger than titania or alumina (Fig. 12.9). However, lacking data on niobium diffusion (or the effective diffusion of niobia), the hypothesis that particle size increases with increasing D could not be verified in this case. Oxide properties relevant to this study are shown in Table 12.2.

It is interesting to note that for the three substances studied, the primary particle sizes increased with decreasing oxide melting points: 2054°C, 1843°C, and 1512°C for Al₂O₃, TiO₂, and Nb₂O₅, respectively.

In general, primary particle size increased with volume loading, solid-state diffusion coefficient, and maximum temperature. Larger particles were also obtained by decreasing the jet velocity. The number of particles per agglomerate increased with volume loading and decreased with solid-state diffusion coefficient and maximum temperature.

PARTICLE NECK FORMATION

Industrial aerosol processes are usually carried out at high particle concentrations so that collision and coalescence have a major effect on the morphological properties of the product. Individual isolated primary particles occur rarely, and the product is composed of groups of adhering particles ranging from loosely linked particles, sometimes termed *agglomerates*, to strongly necked particles, called *aggregates* or *hard agglomerates*. For strongly aggregated particles, it may be difficult to define the primary particles because the necks connecting them are so thick.

In commercial applications of submicron powdered materials as additives, fillers, and pigments, nonagglomerated or weakly agglomerated primary particles are usually desired. Quantitative, predictive methods for describing neck formation and the nature of the bonds between particles are not available. In the absence of proven methods, we discuss some guidelines that may serve as a starting point for future research.

In previous sections it was shown that the primary particle size is approximately determined by the condition that $\tau_f = \tau_c$. The theoretical analysis that led to this conclusion can be extended to explain qualitatively the nature and strength of the bonds between the primary particles. During the time period before $\tau_f \approx \tau_c$, coalescence is rapid and the

particles are nearly spherical. As τ_f and τ_c approach each other, two limiting types of neck formation processes occur. Figure 12.12 shows that when $d\tau_f/dt \gg d\tau_c/dt$ during the time that $\tau_f \approx \tau_c$, the sharp increase in τ_f freezes the particles almost between collisions. Subsequent collisions do not produce further coalescence but lead to agglomerates held together by weak forces (van der Waals, for example). On the other hand, if τ_f increases only a little faster than τ_c as the two characteristic times intersect, the particles have time to coalesce partially before being quenched (Fig. 12.12b). The resulting agglomerates are probably held together by necks comprised of strong chemical forces (ionic/covalent bonds).

Studies of the stretching of nanoparticle chain aggregates (Chapter 8) (Friedlander et al., 1998) provide insight on the energies that hold particles together. Chain aggregate

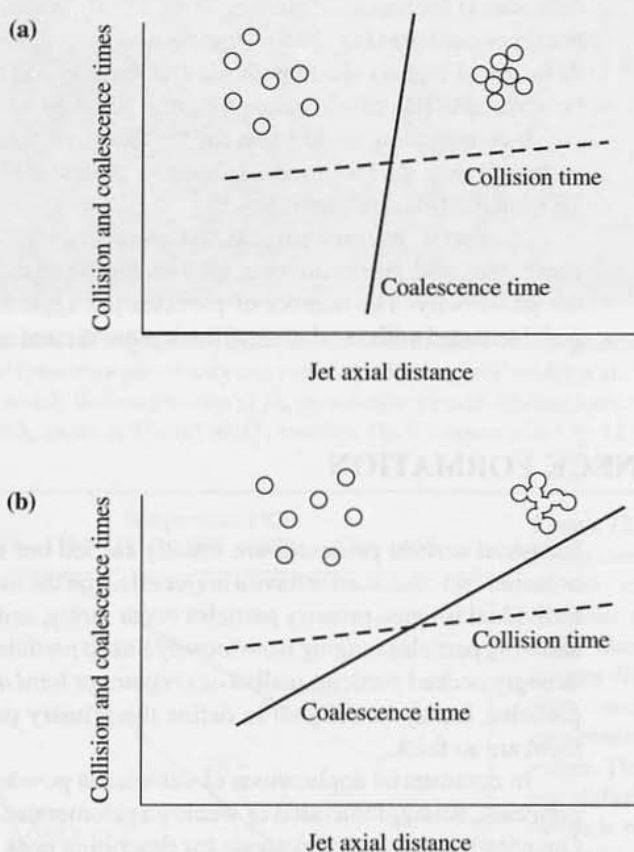


Figure 12.12 Effect of variation of collision and coalescence rates on the formation of necks between primary particles. (a) The coalescence time increases sharply while the time between collisions changes little. This results in agglomerates composed of weakly bonded primary particles. (b) The coalescence and collision processes proceed at similar rates producing strong necks between the primary particles.

stretching appears to involve two phenomena: (i) grain boundary sliding between adjacent necked particles that form the backbone of the chain and (ii) separation and straightening of folded particle chains held together by relatively weak (perhaps van der Waals) forces.

If the gases in which agglomerates are suspended continue to be heated, the agglomerates become more compact (higher fractal dimension) and eventually coalesce. The resulting particles have a much smaller collision diameter than the original agglomerates and a smaller standard deviation. As an example, Kruis et al. (1998) prepared compact PbS particles in the 10-nm size range by heating PbS agglomerates produced in an EC generator. The resulting aerosol was passed through an electrical aerosol classifier to produce monodisperse PbS particles of interest in studies of quantum confinement effects.

PARTICLE CRYSTAL STRUCTURE

Basic Concepts

The factors that determine the crystal structure of particles formed in aerosol reactors have not been studied systematically. In this section, we identify key theoretical concepts and review relevant experimental observations. Consideration is limited to single-component systems. Particle crystal structure depends on a combination of thermodynamic (equilibrium) factors and rate processes. The equilibrium shape of a particle is determined by the surface energies of its crystal faces according to the Wulff construction (Chapter 8). Another factor that may enter into the process is the excess pressure inside small particles according to the Laplace formula (Chapter 9). Thus the equilibrium form may vary with particle size depending on the phase diagram.

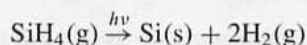
Because particle formation is a dynamic process, kinetic factors including rates of collision, coalescence, and annealing limit attainment of equilibrium behavior. For example, the collision-coalescence mechanism discussed in previous sections may lead to the formation of particles incorporating smaller particles in various stages of coalescence. This results in grain boundaries and other defects in the particles. The extent to which these defects are removed by annealing probably depends on the melting point reduction of fine particles (Chapter 9). A comprehensive analysis incorporating the rate of annealing into the dynamics of particle formation has not been made. There is a body of experimental observations that provide some guidelines for further conceptual developments.

Experimental Observations

Information is available on the crystal structure of commercial nanoparticle powders produced in flame reactors (Ettlinger, 1993). The most common industrial product, nanoparticle silica, is amorphous. Alumina occurs primarily in two forms, the thermodynamically stable α form (hexagonal) and the unstable λ form (cubic). The α form results when alumina is heated above 1200°C; commercial nanoparticle alumina has been reported to be in the δ

group of the λ form. Nanoparticle titania (~ 20 nm) is an important component of cosmetic and medical preparations used as a protection against sunlight ("sun block") because it absorbs in the UV range. The anatase form absorbs radiation of wavelengths less than 385 nm while rutile absorbs wavelengths less than 415 nm. Anatase and rutile are both tetragonal forms of titania, but anatase usually occurs in near-rectangular octahedra while rutile forms prismatic crystals that are frequently twinned. Commercial nanoparticle titania is reported to be 70% anatase and 30% rutile, the thermodynamically more stable form. The rutile proportion increases significantly as the temperature of manufacture increases above 700°C. For zirconia, the monoclinic is the predominant form, with the remainder tetragonal. At about 1100°C the monoclinic form is converted to the tetragonal.

The crystalline properties of silicon, silicon nitride, and silicon carbide nanoparticles produced in a laboratory aerosol reactor were measured by Cannon et al. (1982). Particles were produced using a CO₂ laser to irradiate aerosol precursor gases. For example, silane (SiH₄) used to produce silicon particles could be heated adiabatically to the reaction temperature as long as the gas pressure was maintained above 0.05 atm. At lower pressures, heat conduction to the cell walls balanced the heat absorbed by the gases. Silicon particles were generated at about 1000°C by silane decomposition:



Particles produced at low laser intensities ($< 280\text{W}/\text{cm}^2$) were amorphous, while x-ray analysis of powders produced at higher intensities showed evidence of the cubic form of Si. For crystalline Si powders, the particle to crystallite diameter ratio was 3 to 5. Mechanisms proposed for the polycrystalline structure included (i) crystallization from an amorphous solid, (ii) the coalescence of agglomerates of primary particles, and (iii) crystallization from the liquid phase. The last mechanism was regarded as unlikely because the measured temperatures in the reaction zone were below the melting point of Si. Silicon nitride particles produced by the reaction between silane and ammonia in the size range 10 to 25 nm were amorphous. However, when heated in nitrogen between 1300 and 1400°C, the amorphous powders crystallized. Crystalline silicon carbide particles were produced by the reaction of silane and methane in argon.

BET studies of both the commercial and laboratory scale particles discussed above indicate that there is little internal area accessible to BET adsorbate molecules. This holds for both amorphous and polycrystalline particles. If the individual particles are composed of multiple crystalline substructures, internal defects capable of adsorption would be expected. However, the BET measurements show that internal pores, if they are present, are not accessible to adsorbate gases. A possible explanation is that annealing by solid-state diffusion occurs sufficiently rapidly at the temperatures of formation to block access of the external gas to dislocations and grain boundaries. However, the origins of the crystallites within the particles and the mechanisms of crystallization are not understood at present.

PROBLEMS

- 12.1 (a) Prepare a figure that shows the number of TiO₂ molecules as a function of particle size for particles ranging from molecular dimensions to 20 nm.

- (b) Plot the fraction of the total number of molecules present on the particle surface as a function of particle size over the same size range as part (a). The density of TiO₂ (rutile) is 4.26 g/cm³.

12.2 The atoms composing very small particles move around by self-diffusion and sample other sites in the particle. Plot the time it would take for atoms originally at the center of a spherical 5-nm silver particle to reach the surface as a function of temperature over the temperature range from 300 K to the melting point, 1235 K. For this purpose define a characteristic time based on a solution to the diffusion equation in spherical coordinates for atoms moving from the particle center to its periphery. Neglect the effect of melting point reduction on the behavior of the system. The diffusion coefficient of crystalline (fcc) silver is given by

$$D = D_0 \exp(-E/RT)$$

where

$$D_0 = 0.67 \text{ cm}^2/\text{sec}$$

$$E = 45.2 \text{ kcal/mole}$$

12.3 A cloud of TiO₂ molecules is generated in a gas at $t = 0$ by a very fast chemical reaction. The molecules collide to form particles that grow by coagulation at a constant gas temperature of 1000°C. The volumetric concentration of aerosol material is 10⁻⁶ cc solids/cc gas. The aerosol can be assumed to be in uniform constant velocity ("plug flow reactor"). When the average particle size has reached 10 nm, the gas is suddenly quenched; that is, the temperature is reduced to the point where the coalescence time is equal to the collision time.

- (a) Calculate the time necessary for the volume average particle size to reach 10 nm, assuming perfect coalescence.
 (b) Calculate the temperature to which the gas must be reduced such that $\tau_c = \tau_f$.

REFERENCES

- Brandes, E. A., and Brook, G. B. (1998) *Smithells Metals Reference Book*, 7th ed., Butterworth-Heinemann, Oxford, UK.
- Brinker, C. J., and Scherer, G. W. (1990) *Sol-Gel Science*, Academic Press, San Diego, CA.
- Cannon, W. R., Danforth, S. C., Flint, J. H., Haggerty, J. S., and Marra, R. A. (1982) *J. Am. Ceram. Soc.*, **65**, Parts I and II, 324 and 330.
- Ettlinger, M. (1993) Highly Dispersed Metallic Oxides Produced by the AEROSIL Process, *Tech. Bull.*, Degussa, Frankfurt, Germany.
- Floess, J. K., Kiefer, J. H., Kumaran, S. S., and Fotou, G. P. (1997) A Kinetic Model for Fumed Silica Formation in a Flame Reactor, paper presented at the AIChE Meeting, Los Angeles, CA, November 1997.
- Frenkel, J. (1945) *J. Phys.*, **9**, 385.
- Friedlander, S. K., and Wu, M. K. (1994) *Phys. Rev. B*, **49**, 3622.
- Friedlander, S. K., Jang, H. D., and Ryu, D. H. (1998) *Appl. Phys. Lett.*, **72**, 173.
- Granqvist, C. G., and Buhman R. A. (1976) *J. Appl. Phys.*, **47**, 2200.
- Gurav, A., Kodas, T., Pluym, T., and Xiong, Y. (1993) *Aerosol Sci. Technol.*, **19**, 411.
- Kim, S. G., and Brock, J. R. (1986) *J. Appl. Phys.*, **60**, 509.
- Kingery, W. D., and Berg, M. (1955) *J. Appl. Phys.*, **26**, 1206.

- Kingery, W. D., Bowen, H. K., and Uhlmann, D. R. (1976) *Introduction to Ceramics*, 2nd ed., Wiley, New York.
- Koch, W., Friedlander, S. K. (1990), *J. Colloid Interface Sci.*, **140**, 419.
- Kofstad, P. (1972) *Nonstoichiometry, Diffusion and Electrical Conductivity in Binary Metal Oxides*, Wiley-Interscience, New York.
- Kruis, F. E., Nielsen, K., Fissan, H., Rellinghaus, B., and Wassermann, E. F. *Appl. Phys. Lett.*, **73**, 547.
- Landgrebe, J. D., and Pratsinis, S. E. (1989) *IEC Res.*, **28**, 1474.
- Lehtinen, K. E. J., Windeler, R. K., and Friedlander, S. K. (1996) *J. Aerosol Sci.*, **27**, 883.
- Marijnissen, J. C. M., and Pratsinis, S. (Eds.) (1993) *Synthesis and Measurement of Ultrafine Particles*, Delft University Press, Delft.
- Michael, G., and Ferch, H. (1993) Basic Characteristics and Applications of AEROSIL, *Tech. Bull.*, No. 11, Degussa Frankfurt, Germany.
- Nagel, S. R., MacChesney, J. B., and Walker, K. L. (1985) Modified Chemical Vapor Deposition, in Tingye Li (Ed.), *Optical Fiber Communications*, Academic Press, New York.
- Pratsinis, S. E., and Kodas, T. T. (1993) Manufacturing of Materials by Aerosol Processes, in Willeke, K., and Baron, P. A. (Eds.), *Aerosol Measurement*, Van Nostrand Reinhold, New York.
- Ratafia-Brown, J. A., Briggs, D., Paur, H. R., and Matzing, H. (1995) Advanced Electron Beam Dry Scrubbing for High-Sulfur Coal-Fired Power Plant Applications—Process Engineering Study Results for Phase 1 of the e⁻ Scrub Project, paper presented at 1995 Summer National Meeting, July 30–Aug. 2.
- Read, W. T., Jr. (1953) *Dislocations in Crystals*, McGraw-Hill, New York.
- Siegel, R. W. (1994) Nanophase Materials: Synthesis, Structure and Properties, in Fujita, F. E. (Ed.), *Physics of New Materials*, Springer-Verlag, Berlin.
- Ulrich, G. D. (1971) *Comb. Sci. Tech.*, **4**, 47.
- Ulrich, G. D. (1984) Flame Synthesis of Fine Particles, *Chem. Eng. News*, **62**, 22.
- Windeler, R. S., Friedlander, S. K., and Lehtinen, K. E. J. (1997a) *Aerosol Sci. Technol.*, **27**, 174.
- Windeler, R. S., Lehtinen, K. E. J., and Friedlander, S. K. (1997b) *Aerosol Sci. Technol.*, **27**, 191.
- Wu, M. K., Windeler, R. S., Steiner, C. K. R., Bors, T., and Friedlander, S. K. (1993) *Aerosol Sci. Technol.*, **19**, 527.
- Xiong, Y., and Pratsinis, S. E. (1993) *J. Aerosol Sci.*, **24**, 283.
- Zachariah, M. R., and Carrier, M. J. (1999) *J. Aerosol Sci.*, **30**, 1139.

Atmospheric Aerosol Dynamics

The atmospheric aerosol has profound effects on the nature of the air environment. Effects on human health have led to the establishment of ambient air quality standards by the United States and other industrial nations. The optical properties of the aerosol affect local and regional visibility and Earth's radiation balance, hence global climate. There is evidence that reactions that take place on the surface of the stratospheric aerosol play a major role in the destruction of the stratospheric ozone layer. Particularly complex (and poorly understood) are the indirect effects of the aerosol serving as condensation nuclei for the formation of clouds which in turn affect the radiation balance. For an extensive review of the properties of the atmospheric aerosol and its effects, especially health related, the reader is referred to the document prepared by the U.S. EPA (1996) for use in setting the ambient air quality standard for particulate matter. Atmospheric aerosol properties and dynamics are reviewed in detail by Seinfeld and Pandis (1998).

The effects of the atmospheric aerosol are largely determined by the size and chemical composition of the individual particles and their morphology (shape and/or fractal character). For many applications, the aerosol can be characterized sufficiently by measuring the particle size distribution function and the average distribution of chemical components with respect to particle size. Particle-to-particle variations in chemical composition and particle structure are less often measured, although they may have significant effects on biochemical and nucleation phenomena. In this chapter we focus on certain important generalizations concerning size and chemical composition distributions and their interpretation through the principles of aerosol dynamics. Particle morphology is discussed briefly. Emphasis is on the submicron aerosol, which plays a key role in many of the effects mentioned above.

How can the atmospheric aerosol present at any measurement point be related to its sources, natural and man-made? *Receptor modeling* makes use of the aerosol chemical composition at a sampling site to resolve source contributions, and the relationship of receptor modeling to aerosol dynamics is discussed. The large chemical databases that have been collected for source apportionment make it possible to study the statistical variations in aerosol chemical composition. These show surprising regularities that permit inferences concerning the causes of the variations.

Dry deposition is discussed briefly as it relates to atmospheric residence times. Wet deposition is beyond the scope of this text; basic mechanisms are reviewed by Pruppacher and Klett (1997) and by Seinfeld and Pandis (1998).

Our understanding of the atmospheric aerosol has been strongly influenced by the many field studies conducted in California. An example is the Aerosol Characterization Experiment (ACHEX), the first large-scale study of the atmospheric aerosol involving a multidisciplinary group of investigators (Hidy et al., 1980). The California aerosol is closely linked to photochemical smog processes and to vehicular emissions, so caution is necessary in extrapolating the results of that study and later ones in California to aerosols in colder, more humid regions with different types of emission sources.

ATMOSPHERIC AEROSOL SIZE DISTRIBUTION

General Features

The size distribution of the atmospheric aerosol results from the action of the dynamic processes discussed in this book, on particles and gases introduced into the atmosphere from natural and man-made sources. Measurements of atmospheric size distributions at various California locations are shown in Fig. 13.1 as $dV/d \log d_p$ versus $\log d_p$. Plotted in this form, the aerosol mass in any size range is proportional to the area under the curve between the size range limits, assuming that particle density does not vary with particle size. Figure 13.1 shows that there are usually two modes in the mass distribution: the *coarse mode* corresponding to particles larger than 2 to 3 μm in diameter and the *accumulation mode* between about 0.1 and 2.5 μm . Distributions of this form have been observed at many different geographical locations. This important generalization, due to K. T. Whitby, has had a profound effect on our understanding of the atmospheric aerosol. Particles smaller than about 0.1 μm , the *ultrafine range*, sometimes appear in the form of an additional mode if freshly formed or emitted. Usually, however, the ultrafine mass distribution decreases monotonically with decreasing particle size. Aerosol number and volume concentrations in each size range can be grouped according to the type of atmospheric region. Approximate values for these integral parameters are given in Table 13.1.

Atmospheric aerosol distribution functions may also be plotted in the form $\log(dN/d \log d_p)$ versus $\log d_p$ (Fig. 13.2), but the area under the curve does not have a direct physical interpretation. However, the slope of the curve on the log-log plot is often approximately constant over one or two decades in the particle diameter, and the size distribution function can be represented by a power law:

$$n_d(d_p) \sim d_p^p$$

A value of $p = -4$ ("Junge" distribution) provides a useful approximation for many continental aerosol distributions over the size range $0.2 < d_p < 10 \mu\text{m}$. The power law form also simplifies Mie theory calculations of light scattering (Chapter 5). Small deviations from the power law in the range around 1 to 3 μm lead to the bimodal volume distributions of Fig. 13.1.

In this section, basic concepts from aerosol dynamics and the general dynamic equation (GDE) are employed to explain important features of atmospheric size distribution functions. The goal is to provide physical insight into these features. For the application of numerical methods to modeling atmospheric aerosol dynamics, the reader is referred to Wexler et al. (1994) and Jacobson (1997).

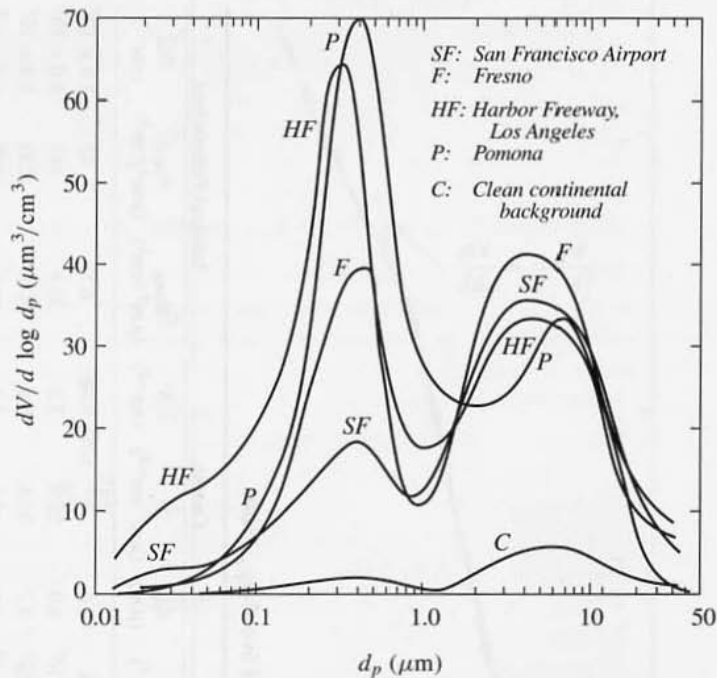


Figure 13.1 Atmospheric aerosol size distributions measured at various locations in California by Whitby and Sverdrup (1980) as part of a statewide aerosol study (Aerosol Characterization Experiment). The bimodal distributions include a coarse mode ($d_p > 2.5 \mu\text{m}$) composed of wind-raised dust and other large particles, and they also include the accumulation mode ($0.1 \leq d_p < 2.5 \mu\text{m}$) resulting largely from gas-to-particle conversion.

Coarse Mode ($d_p > 2.5 \mu\text{m}$)

The coarse mode is largely composed of primary particles generated by mechanical processes such as soil dust raised by the wind and/or vehicular traffic and construction activities. Coarse particles are also emitted in gases from industrial sources such as coal combustion and smelting. The coarse mode often peaks at about $10 \mu\text{m}$. The chemical composition of the coarse mode is for the most part the sum of the chemical components of the primary aerosol emissions. However, there may be some contributions from gas-to-particle conversion, such as ammonium nitrate, as discussed below.

The atmospheric residence time of the coarse particles depends on the interaction between *sedimentation*, which leads to deposition, and *turbulent mixing*, which maintains particles in suspension. Because turbulent mixing is a stochastic process, there is a distribution of residence times for particles of a given size originally present at a given location in the atmosphere. The rate of coarse particle deposition can be estimated by solving the equation of turbulent diffusion with simultaneous settling for the atmospheric conditions of interest (Pasquill and Smith, 1983). An approximate estimate of residence times can be made as follows: In the lower troposphere near the surface there is sufficient mixing to keep aerosol particles smaller than about $50 \mu\text{m}$ approximately uniform with height. For a

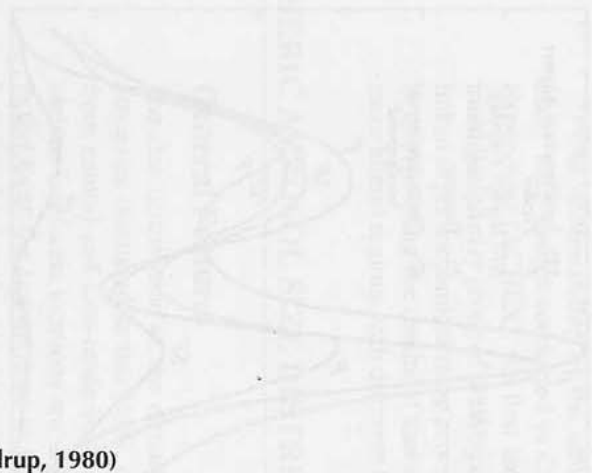


TABLE 13.1
Modal and Integral Parameters for Various Types of Aerosols (from Whitby and Sverdrup, 1980)

Aerosol Type	Ultrafine (Nuclei)			Accumulation			Coarse			Integral Parameters		
	d_{pg} (μm)	ϕ ($\mu\text{m}^3 \text{cm}^{-3}$)	N (cm^{-3})	d_{pg} (μm)	ϕ ($\mu\text{m}^3 \text{cm}^{-3}$)	N (cm^{-3})	d_{pg} (μm)	ϕ ($\mu\text{m}^3 \text{cm}^{-3}$)	N (cm^{-3})	ϕ_{total} ($\mu\text{m}^3/\text{cm}^3$)	S_{total} ($\mu\text{m}^2/\text{cm}^3$)	N_{∞} (cm^{-3})
Clean continental background	0.03	6×10^{-3}	10^3	0.35	1.5	800	6.0	5	0.72	6.5	42	1.8×10^3
Average background	0.034	3.7×10^{-2}	6.4×10^3	0.32	4.5	2.3×10^3	6.0	25.9	3.2	30.4	148	8.6×10^3
Urban average	0.038	0.63	1.1×10^5	0.32	38.4	32×10^3	5.7	30.8	5.4	69.8	1130	1.4×10^5
Urban and freeway	0.032	9.2	2.1×10^6	0.25	37.5	37×10^3	6.0	42.7	4.9	89.4	3200	2.2×10^6

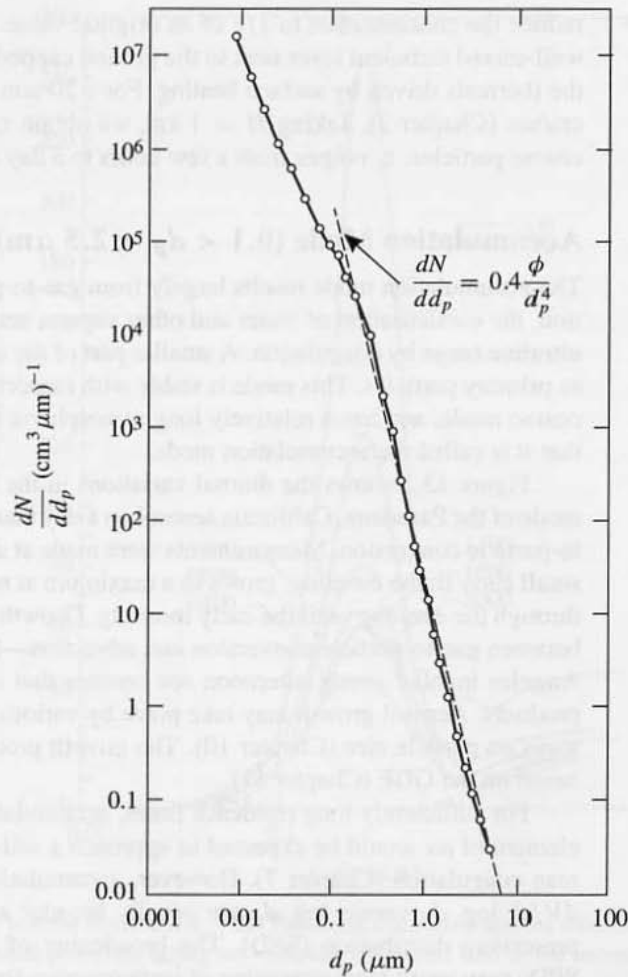


Figure 13.2 Atmospheric aerosol number distributions measured during August and September 1969 in Los Angeles. Such data can frequently be correlated over two particle size decades $0.1 < d_p < 10 \mu\text{m}$ by a power law relationship. However, data of this type can often be satisfactorily correlated by bimodal volume distributions (Fig. 13.1) because of small but highly significant deviations from the power law form. (After Whitby et al., 1972.)

uniformly mixed layer of height H , the rate of loss of particles of terminal settling velocity, c_s , in the absence of coagulation is given by [Chapter 11, Eq. (11.56)]

$$-\frac{dn}{dt} = \frac{c_s}{H}n \quad (13.1)$$

and

$$\tau_c^{-1} = -\frac{1}{n} \frac{dn}{dt} = \frac{c_s}{H} \quad (13.2)$$

where n is the average concentration in the mixed layer and τ_c is the time necessary to

reduce the concentration to $1/e$ of its original value. During the day, there is frequently a well-mixed turbulent layer next to the ground capped by an inversion at about 1 km above the thermals driven by surface heating. For a 20- μm particle with $\rho_p = 2 \text{ g/cc}$, $c_s = 2.44 \text{ cm/sec}$ (Chapter 2). Taking $H = 1 \text{ km}$, we obtain $\tau_c = 4.1 \times 10^4 \text{ sec} \approx 11 \text{ hr}$. Thus for coarse particles, τ_c ranges from a few hours to a day or two.

Accumulation Mode ($0.1 < d_p < 2.5 \mu\text{m}$)

The accumulation mode results largely from gas-to-particle conversion by chemical reaction, the condensation of water and other vapors, and the attachment of particles from the ultrafine range by coagulation. A smaller part of the accumulation mode is directly emitted as primary particles. This mode is stable with respect to deposition, interacts little with the coarse mode, and has a relatively long atmospheric residence time. It is for these reasons that it is called the accumulation mode.

Figure 13.3 shows the diurnal variations in the size distribution of the accumulation mode of the Pasadena, California aerosol on a day that photochemical processes caused gas-to-particle conversion. Measurements were made at a fixed site. The accumulation mode is small early in the morning, grows to a maximum at noon, and then decreases continuously through the evening until the early morning. Growth and decay result from the interaction between gas-to-particle conversion and advection—that is, the air movements that in Los Angeles involve strong afternoon sea breezes that sweep out aerosol and other reaction products. Aerosol growth may take place by various mechanisms that depend in different ways on particle size (Chapter 10). The growth process can be simulated by calculations based on the GDE (Chapter 11).

For sufficiently long residence times, accumulation mode aerosols in a given volume element of air would be expected to approach a self-preserving form as a result of Brownian coagulation (Chapter 7). However, accumulation mode size distributions plotted as $dV/d \log d_p$ versus $\log d_p$ are usually broader and have a lower peak than the self-preserving distribution (SPD). The broadening of the distribution (compared with the SPD) may result from averaging of instantaneous size distributions over the measurement time of the instrument. If the instantaneous size distributions are locally self-preserving, averaging over many distributions will lead to a broadening. For example, the electrical mobility analyzer may require several minutes to determine a distribution, which leads to contributions from many different air parcels. Moreover, reported accumulation mode distributions are often averaged over measurements made on many different days, adding to the spread. A test of the applicability of self-preserving size distribution theory to the accumulation mode would require making measurements with instruments that have a very short time of resolution.

Example: Derive an expression for the volume distribution $dV/d \log d_p$ over the particle size range where the power law distribution holds with $p = -4$.

SOLUTION: The volume of particles in the size range d_p to $d_p + d(d_p)$ is given by

$$dV = \frac{\pi d_p^3}{6} n_d(d_p) d(d_p)$$

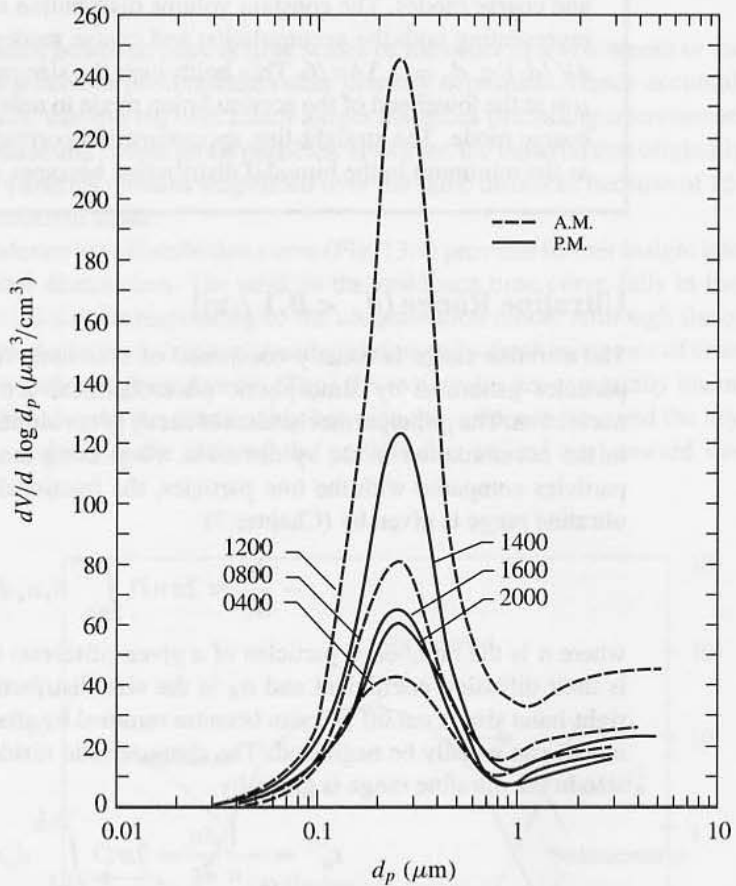


Figure 13.3 The volume distribution of the Pasadena, California aerosol measured on September 3, 1969. Photochemical processes acting on vehicular emissions lead to the increase in accumulation mode particles from 4 A.M. to noon. Advection of cleaner air clears out the aerosol products in the afternoon. (After Whitby et al., 1972.)

Dividing by $d \log d_p$, we obtain

$$\frac{dV}{d \log d_p} = \frac{2.3\pi d_p^4}{6} n_d$$

Substituting the power law form $n_d = Ad_p^{-4}$ gives

$$\frac{dV}{d \log d_p} = \frac{2.3A\pi}{6}$$

Thus the volume distribution function is constant over the particle size range where the power law exponent $p = -4$. Can the constant volume distribution for $p = -4$ be compatible with the bimodal volume distribution that covers much the same particle size range? The power law and bimodal volume distributions are equivalent only as a very rough approximation. Most of the aerosol volume is present in the accumulation

and coarse modes. The constant volume distribution approximation is equivalent to representing both the accumulation and coarse modes by the same horizontal line, $dV/d \log d_p = 2.3A\pi/6$. This holds over the size range extending from about $0.2 \mu\text{m}$ at the lower end of the accumulation mode to near $10 \mu\text{m}$ at the upper end of the coarse mode. The straight-line approximation corresponding to $p = -4$ improves as the minimum in the bimodal distribution becomes shallower.

Ultrafine Range ($d_p < 0.1 \mu\text{m}$)

The ultrafine range is usually composed of emissions from local combustion sources or particles generated by atmospheric photochemical activity that leads to homogeneous nucleation. The principal mechanism of decay of the ultrafine range is attachment to particles in the accumulation mode by diffusion. Neglecting the Brownian motion of the coarse particles compared with the fine particles, the fractional rate of decay of particles in the ultrafine range is given by (Chapter 7)

$$-\frac{dn}{dt} \approx 2\pi n D \int_{0.1}^{1.0} d_p n_d d(d_p) \quad (13.3)$$

where n is the number of particles of a given (discrete) size in the ultrafine size range, D is their diffusion coefficient and n_d is the size distribution function. The integral on the right-hand side is cut off at $1 \mu\text{m}$ because removal by attachment to larger particles (coarse mode) can usually be neglected. The characteristic residence time for particles of a given size in the ultrafine range is given by

$$\tau_u^{-1} = -\frac{1}{n} \frac{dn}{dt} = 2\pi D \int_{0.1}^{1.0} d_p n_d d(d_p) \quad (13.4)$$

or

$$\tau_u^{-1} = 2\pi D \bar{d}_{pa} N_{ac} \quad (13.5)$$

where \bar{d}_{pa} is the average particle diameter of the accumulation mode and N_{ac} is the number density of that mode. We can estimate the residence time for the removal of 10 nm ($0.01 \mu\text{m}$) particles in an urban atmosphere using the values in Table 13.1. For $N_{ac} = 3.2 \times 10^4 \text{ cm}^{-3}$, $\bar{d}_{pa} = 0.32 \mu\text{m}$ and $D = 5.24 \times 10^{-4} \text{ cm}^2/\text{sec}$, $\tau_u \approx 6 \text{ min}$. For average background air ($N_{ac} \approx 2.3 \times 10^3 \text{ cm}^{-3}$), the residence time for $0.01\text{-}\mu\text{m}$ particles would be about 80 mins.

Residence Time and Dry Deposition

The variation of the atmospheric residence time with particle size is illustrated in Fig. 13.4, which shows the limiting behavior for ultrafine and coarse particles. In the ultrafine range, $\tau_u \sim D^{-1}$. Because $D \sim d_p^{-2}$ in the free molecule range ($d_p < 0.07 \mu\text{m}$), $\tau_u \sim d_p^2$. For the coarse particles according to (13.2), $\tau_c \sim d_p^{-2}$ based on the dependence of the terminal settling velocity on d_p . For both coarse and very fine particles, the residence time is of the order of minutes to hours (depending on other factors discussed above). Accumulation mode

residence times, however, peak at time scales of the order of a few weeks or more because wet removal processes predominate rather than dry deposition. Hence accumulation mode aerosols can be transported over much longer distances (including intercontinental scales) than the ultrafine and coarse mode particles. However, the material that originally composed the ultrafine particles remains suspended over the same distances because of its attachment to the accumulation mode.

The residence time distribution curve (Fig. 13.4) provides further insight into the origins of the bimodal distribution. The peak in the residence time curve falls in the size range $0.1 < d_p < 1.0 \mu\text{m}$ corresponding to the accumulation mode. Although the coarse mode has a short residence time, it is continually reinforced by fresh injections of crustal material and, perhaps, anthropogenic sources. Thus the two modes are essentially uncoupled.

Finally, we discuss the relationship between the residence time and the dry deposition velocity, v_d , defined as the ratio of the particle flux ($\#/\text{cm}^2 \text{ sec}$) toward the surface to

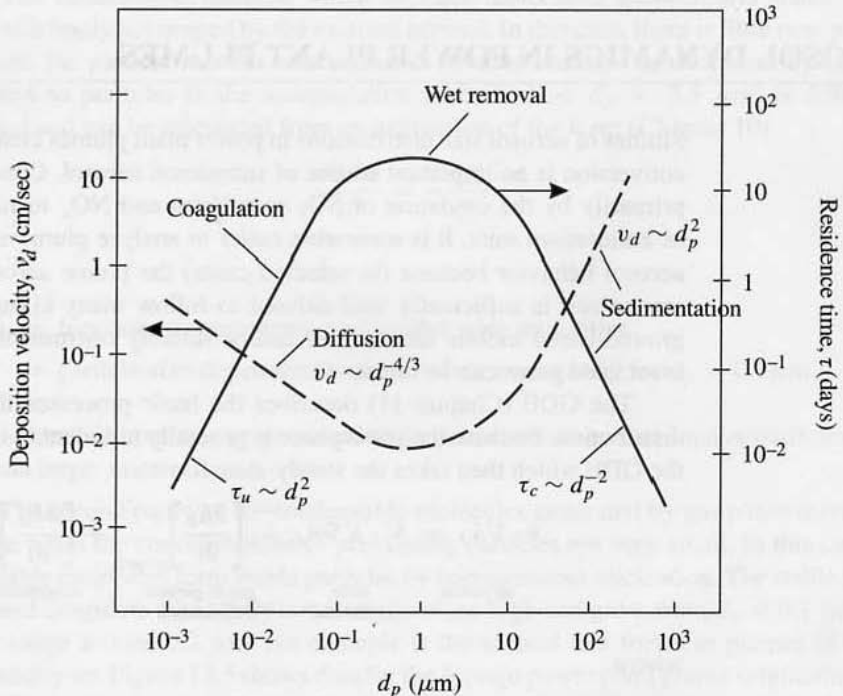


Figure 13.4 The atmospheric aerosol residence time goes through a maximum in the size range corresponding to the accumulation mode $0.1 < d_p < 2.5 \mu\text{m}$. Smaller (ultrafine) particles rapidly attach to the accumulation mode by Brownian motion. Larger particles are lost by sedimentation. The estimated residence times are for a continental aerosol with $N_\infty = 1.5 \times 10^4 \text{ cm}^{-3}$ and height of the mixed layer 1.5 km (After Jaenicke, 1980.) Also shown is a dry deposition velocity curve with a characteristic minimum in the accumulation mode size range. The deposition velocity approaches the settling velocity for large particles, and settling controls their residence time. Diffusion and interception dominate deposition for submicron particles (Chapter 3) but do not usually have a significant effect on their residence times as explained in the text.

the particle concentration at a reference height about 10 m above the ground. The basic mechanisms that underlie dry deposition were discussed in Chapters 3 and 4. For a turbulent boundary layer over a rough surface, particles are transported by eddy diffusion to the roughness elements on which they deposit by diffusion, interception, impaction, and sedimentation. For submicron particles, diffusion and interception dominate; the smallest particles are removed by diffusion, which is most effective as particle size decreases. As particle size increases, deposition by interception may contribute. With further increases in particle size, sedimentation and, perhaps, impaction take over; when sedimentation dominates, we have $v_d \sim d_p^2$. The form of the deposition velocity curve is shown in Fig. 13.4 with the residence time. There are actually a family of v_d curves depending on the surface roughness and the wind field. These curves typically show a minimum in the size range $0.1 < d_p < 1 \mu\text{m}$. As discussed above, dry deposition plays a determining role for both the residence time and the particle size distribution of coarse mode particles. For submicron particles, however, dry deposition has a minor effect on residence time and size distribution.

AEROSOL DYNAMICS IN POWER PLANT PLUMES

Studies of aerosol size distributions in power plant plumes clearly show that gas-to-particle conversion is an important source of submicron aerosol. Condensable material is formed primarily by the oxidation of SO_2 to sulfates and NO_x to nitrates, both usually present as ammonium salts. It is somewhat easier to analyze plume aerosol dynamics than urban aerosol behavior because (in selected cases) the plume aerosol originates from a single source and is sufficiently well-defined to follow many kilometers downwind. By using ground-based mobile laboratories and/or suitably instrumented aircraft, the aerosol and associated gases can be measured.

The GDE (Chapter 11) describes the basic processes that modify the particle size distribution. Because the atmosphere is generally turbulent, it is appropriate to time smooth the GDE which then takes the steady-state form:

$$\underbrace{\bar{\mathbf{v}} \cdot \nabla \bar{n}_d}_{\text{advection}} = \underbrace{\nabla \cdot K \nabla \bar{n}_d}_{\text{eddy diffusion}} + \underbrace{\left[\frac{\partial \bar{n}_d}{\partial t} \right]_{\text{growth}}}_{\text{gas-to-particle conversion}} + \underbrace{\left[\frac{\partial \bar{n}_d}{\partial t} \right]_{\text{coag}}}_{\text{coagulation}} - \underbrace{c_s \frac{\partial \bar{n}_d}{\partial z}}_{\text{sedimentation}} \quad (13.6)$$

where

\bar{n}_d = time-averaged size distribution function

$\bar{\mathbf{v}}$ = mean wind field

K = eddy diffusion coefficient

c_s = terminal settling velocity

Most of the terms that appear in this equation can be evaluated fairly easily, at least approximately. For example, there is an extensive literature on the wind field and the eddy diffusion coefficients for the dispersion of passive (nonreactive) air pollutants in plumes

with sedimentation (Pasquill and Smith, 1983). Time-averaged coagulation calculations can be made based on mean concentrations. Estimating the fluctuating coagulation terms is more difficult and the processes are not well understood. However, they are expected to be smaller than the mean terms. Much less is known about the particle growth rate, the second term on the right-hand side of (13.6). This term includes gas-to-particle conversion processes that play a major role in shaping atmospheric aerosol size distributions as discussed in the rest of this section.

Gas-phase molecules in the atmosphere can be converted to the aerosol phase by homogeneous (gas phase) or heterogeneous (aerosol phase) reactions. Both mechanisms may be operative over different particle size ranges. Information on the dominant growth mechanisms can be inferred by an analysis of aerosol dynamics in power plant plumes (McMurry et al., 1981; Wilson and McMurry, 1981). When homogeneous gas-phase reactions are controlling, there are two possible pathways for the reaction products to enter the size distribution function:

1. The condensable material which includes molecules, clusters, and stable nuclei may be efficiently scavenged by the existing aerosol. In this case, there is little new particle formation; the particle number concentration remains constant or decreases by mixing. Deposition to particles in the accumulation mode ($0.1 < d_p < 2.5 \mu\text{m}$) is diffusion-controlled and can be calculated from an expression of the form (Chapter 10)

$$\frac{d(d_p)}{dt} = \frac{F_1(t)C}{d_p} \quad (13.7)$$

where

$F_1(t)$ = function of concentration of condensable molecules

C = particle-size-dependent correction factor near unity for $d_p > 0.1 \mu\text{m}$

The growth rate is inversely proportional to particle diameter so that smaller particles grow faster than larger ones.

2. The second pathway for condensable molecules generated by gas phase reaction is operative when the concentrations of preexisting particles are very small. In this case the condensable molecules form stable particles by homogeneous nucleation. The stable nuclei collide and coagulate when their concentrations are high and grow from $d_p < 0.1 \mu\text{m}$ into the size range around $0.2 \mu\text{m}$. An example is the aerosol that forms in plumes in clean, low-humidity air. Figure 13.5 shows data for the Navajo power plant plume originating near Page, Arizona. The increase in aerosol volume concentration in the plume was accompanied by sharp increases in number concentration; the existing aerosol was unable to collect sufficient condensable material to prevent new particle formation. Plume measurements provide a convincing case study of atmospheric homogeneous nucleation.

When the rate of conversion of gas-phase molecules is controlled by aerosol phase processes such as the reaction of SO_2 in accumulation mode microdroplets, a volume-based growth law (Chapter 10) holds which can be expressed as follows:

$$\frac{d(d_p)}{dt} = F_2(t)d_p$$

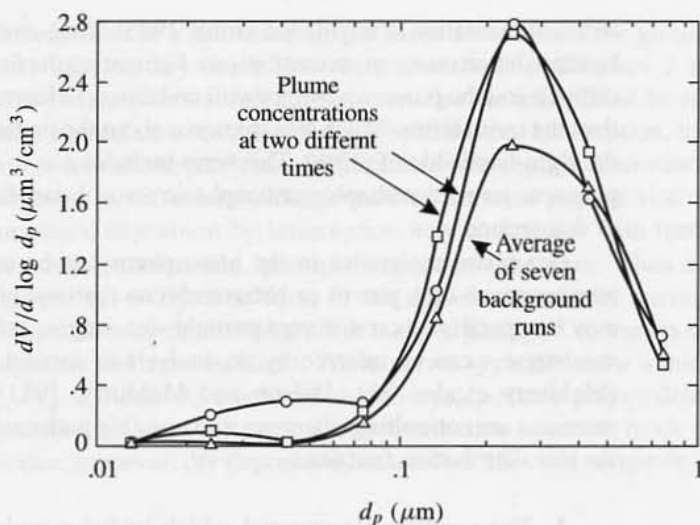


Figure 13.5 Aerosol volume distributions for the Navajo (Page, AZ) power plant plume on 7/10/79. This is an example of a low-humidity (5 to 20% RH) high-solar-radiation environment. The aerosol volume excess over background is associated primarily with particles smaller than $0.3 \mu\text{m}$. This is best explained by homogeneous gas-phase reactions that form a condensable product and not by aerosol-phase reactions. (After Wilson and McMurry, 1981.)

This form is quite different from the diffusional growth expression (13.7) in its dependence on particle size; in this case, larger particles grow faster than smaller ones. McMurry et al. (1981) analyzed data for several power plant plumes (Fig. 13.6a). They found that both diffusion to the particles and droplet phase reaction contributed to plume aerosol growth (Fig. 13.6b). However, the droplet-phase reactions accounted for less than 20% of total aerosol volume growth.

CHEMICAL COMPOSITION OF URBAN AEROSOLS

Introduction

There have been many measurements of the elemental composition of urban aerosols stimulated by the need for large databases in aerosol source apportionment (discussed in a later section). Table 13.2 compares concentrations in the fine and coarse fractions for various U.S. cities. The results show remarkable similarities in the order of magnitude of the concentrations from city to city for each element. Soil dust is a major component of the coarse fraction as indicated by the strong enrichment in aluminum and silicon in every city. The coarse fraction is much less active chemically both with respect to its mechanisms of formation and as a site for reaction, compared to the fine fraction discussed next.

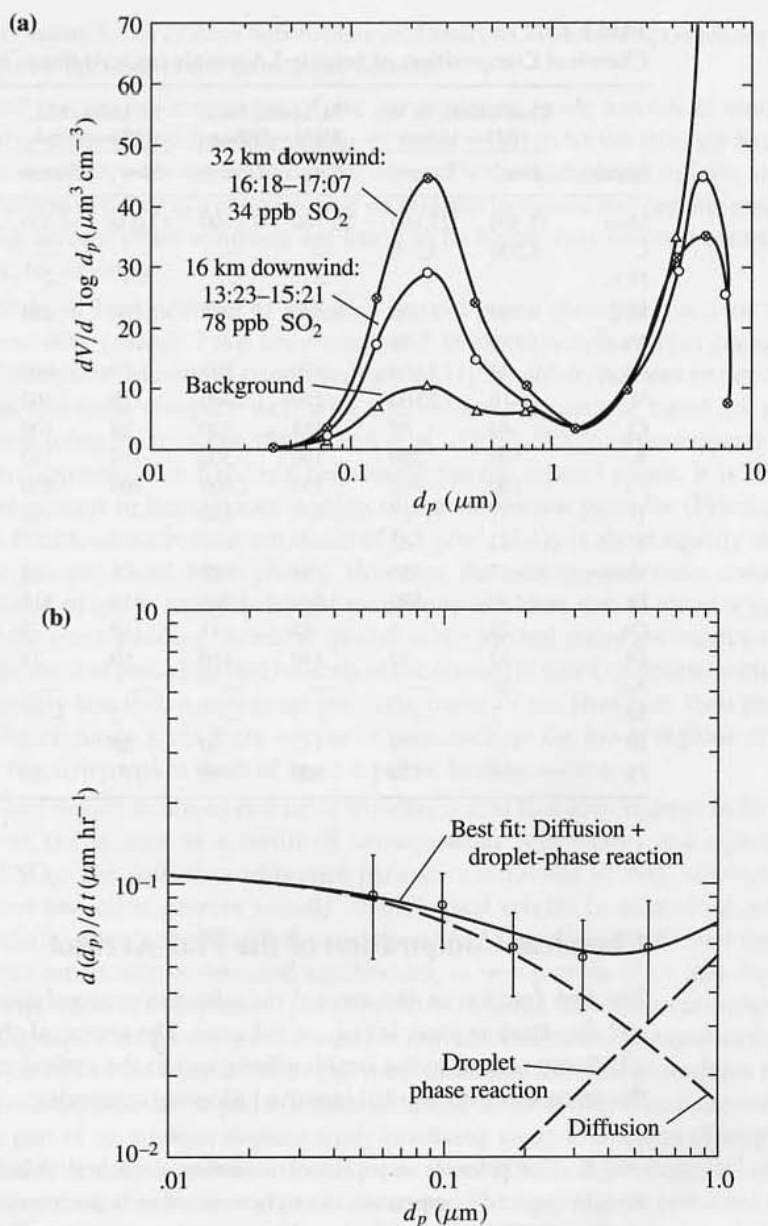


Figure 13.6 (a) Volume distributions for the Cumberland power plant (Clarksville, TN) measured at various locations in the plume downwind from the plant on 8/10/79. Secondary aerosol accumulated in all particles up to 1 μm —in contrast with the Navajo plant aerosol (Fig. 13.5) which was limited to $d_p < 0.3 \mu\text{m}$. (b) Particle diameter growth rates calculated from data shown in part (a) with a best-fit curve based on an interpolation formula that reduces to the diffusion mechanism for the smaller particles (13.7) and droplet phase reaction for the larger particles (13.8). (After McMurtry et al., 1981.)

TABLE 13.2
Chemical Composition of Selected Aerosols (ng/m³) (from NRC, 1979)

Species	Charleston, W. Va. 1976—Urban		St. Louis, Mo. 1976—Urban		St. Louis, Mo. 1976—Rural		Portland, Oreg. 1977/78—Urban		Portland, Oreg. 1977/78—Rural	
	Fine	Coarse	Fine	Coarse	Fine	Coarse	Fine	Coarse	Fine	Coarse
Mass	33,400	27,100	23,100	23,100	17,000	16,200	25,000	39,000	14,300	16,300
C	5,200	3,200	—	—	—	—	6,800	6,900	4,100	3,000
NO ₃ ⁻	—	—	—	—	—	—	350	360	250	240
SO ₄ ²⁻	9,900	1,020	8,500	980	7,400	450	2,500	1,300	1,830	710
Na	190	34	—	—	—	—	280	750	250	400
Al	74	1,100	170	980	70	600	190	1,900	110	690
Si	410	2,800	250	3,400	170	2,400	200	6,000	180	2,200
Cl	40	80	165	320	20	100	840	810	390	320
K	100	290	180	300	110	240	150	320	120	155
Ca	100	960	130	2,600	100	1,800	120	1,270	65	410
Ti	11	77	—	190	—	55	9	160	4	48
V	<2	<2	—	—	—	—	12	12	4	3
Mn	7	10	24	27	5	14	32	55	8	16
Fe	150	590	240	1,000	110	515	200	1,800	60	430
Cu	20	4	45	11	10	3	26	58	17	52
Zn	32	10	140	110	60	24	62	70	19	12
As	26	—	—	—	—	—	4	1	3	—
Se	7	—	3	—	2	—	2	1	1	—
Br	150	39	145	30	25	5	240	95	38	—
Pb	660	120	630	190	170	30	645	410	100	40

Chemical Composition of the Fine Aerosol

The fine fraction of the aerosol includes the accumulation mode ($0.1 < d_p < 2.5 \mu\text{m}$) and the ultrafine particles ($d_p < 0.1 \mu\text{m}$). The chemical characteristics of the fine fraction which are central to the health effects and to the optical and nucleating characteristics of the aerosol can be divided into the following categories:

1. The primary component includes elemental (black) carbon and high-molecular-weight organic compounds directly emitted into the atmosphere by combustion processes such as the burning of fuel and biomass burning including forest fires. Other sources of submicron primary particles include metallic compounds from high-temperature processes (smelting, welding, etc.). There may also be contributions from the smaller particles present in wind-raised dust and the marine aerosol near coastal sites.

2. The secondary component results from atmospheric chemical reactions that produce inorganic ionic species of which the most important are NH_4^+ , SO_4^{2-} and NO_3^- . Organic vapors also react in the atmosphere to form condensable products. For example, cyclic olefins react with ozone to form less volatile dicarboxylic acids. The secondary chemical species normally reported in studies of atmospheric aerosol composition are relatively stable reaction products; they have usually survived in the atmosphere and on filter or impactor

substrates for many hours or days before chemical analysis. These compounds are often the largest single component of the submicron aerosol.

3. Water is a major component of the accumulation mode aerosol in amounts that depend on the relative humidity. The uptake of water is driven by the strongly hygroscopic nature of the secondary aerosol components, especially the ammonium sulfates and nitrate. The water content depends in a complex way on both the inorganic and organic components. The resulting aerosol phase solutions are likely to be highly concentrated compared with fog droplets, for example.

4. Short-lived intermediates of gas- and aerosol-phase chemical reactions including peroxides and free radicals have been measured in the atmosphere (gas phase) and in clouds and rainwater. Measured concentrations of H_2O_2 , aldehydes and organic acids in Los Angeles rainwater compare well with equilibrium calculations based on gas-phase concentrations using Henry's law (Sakugawa et al., 1993). While measurements of short-lived reactive intermediates have not been made for the aerosol phase, it is very likely that they are present in the aqueous portion of the submicron particles (Friedlander and Yeh, 1998). For cloud water concentrations of 0.5 g/m^3 , H_2O_2 is about equally distributed between the gas and cloud water phases. However, the total aerosol water concentration per unit volume of gas is many orders of magnitude less than that in cloud water, so the fractions of the corresponding chemical species in the aerosol phase are much smaller.

The total mass of peroxides and radicals in the aerosol is small compared with the other species, probably less than a nanogram per cubic meter of air. However, their presence in the accumulation mode gives them access to sites, such as the lower regions of the lung where their reactivity makes them of special public health concern.

5. Aerosol acidity is linked primarily to sulfuric acid that accumulates in the aqueous component of the aerosol as a result of homogeneous (gas-phase) and aqueous-phase reactions of SO_2 . The sulfuric acid is then partially neutralized by NH_3 originating from animal wastes and other sources usually of biological origin. In measuring acidity, the aerosol is usually sampled by filtration over a period of several hours. Even if the gas and aerosol phases are locally in chemical equilibrium, as new parcels of air pass through the filter, the composition of both phases (gas and aerosol) change. This can lead to chemical reactions among deposited aerosol particles and/or reaction and exchange between the aerosol deposit and parcels of air with different gas concentrations. Intricate procedures involving denuder trains have been developed to reduce sampling artifacts from data on aerosol acidity collected as part of an epidemiological study involving many U.S. cities (Spengler et al., 1996). The mass median concentration of H^+ was about 20 nanoequivalents/ m^3 equivalent to a few micrograms of sulfuric acid per cubic meter. The lung may be protected from this acidity by the neutralizing presence of ammonia, a metabolic product in the exhaled gases. Much effort has gone into the measurement of aerosol acidity, but the evidence linking health effects to acid aerosols is not strong.

DISTRIBUTIONS OF CHEMICAL SPECIES WITH PARTICLE SIZE

Distributions of chemical species with particle size determine (a) the rate of deposition of chemical components from the atmosphere and in the lung and (b) their affect on

visibility degradation. The theory of chemical component distributions is based on the GDE and equations of conservation for molecular species (such as SO₂ and NO₂) that are converted from gas to aerosol. Quantitative predictions generally require numerical modeling. Measurements of chemical component distributions are almost always made using cascade impactors for size segregation followed by chemical analysis of the collected material to determine the average composition on each stage (Chapter 6). Certain general features that have been observed for chemical component size distributions are discussed in this section. Three examples are considered: (i) products of gas-to-particle conversion, specifically sulfates and nitrates, (ii) primary aerosols emitted with a narrow size distribution, and (iii) water.

Sulfates and Nitrates

Sulfates and nitrates are products of gas-to-particle conversion. They frequently have multimodal distributions with respect to particle size, but for reasons different from those that produce the bimodal mass or volume distributions discussed above.

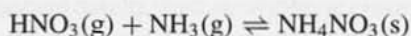
Sulfate ion is the chemical component usually present in highest concentration in the submicron atmospheric aerosol. Almost all of the sulfate results from the atmospheric oxidation of SO₂ either by homogeneous gas-phase reactions or by aerosol- or droplet-phase reactions. Reaction with the hydroxyl radical OH• is thought to be the major gas-phase mechanism. Many solution-phase processes are possible, including reaction with dissolved H₂O₂ and reactions with O₂ catalyzed by dissolved metals such as Fe and Mn (Seinfeld and Pandis, 1998).

Two types of sulfur size distributions have been observed in the Los Angeles aerosol as shown in Fig. 13.7. The first and more common type with mass median diameter (mmd) of 0.46 to 0.65 μm was observed on days of high mass loadings (above 10 μg/m³ SO₄). The second type with mmd 0.17 to 0.22 μm was observed on drier days, with fairly high oxidant (0.2 ppm) levels but lower sulfate loadings. Calculations indicate that sulfates in the larger particle sizes are formed from aerosol- and droplet-phase reactions, while the finer sulfates probably result from homogeneous gas-phase reactions. The predominance of the larger particle sulfate distribution, particularly on days of heavy loadings, points to the importance of droplet-phase reactions. The droplet mode (0.46 to 0.65 μm) sulfate peak occurs in the optimum light-scattering range (Chapter 5), which explains why sulfates contribute so heavily to visibility degradation.

Nitric acid forms in the atmosphere as a result of the reaction between hydroxyl radicals and NO₂:



A significant portion of the nitric acid reacts with ammonia to form ammonium nitrate according to the reversible reaction



The ammonium nitrate product is present only in the aerosol phase either as a solid or in solution depending on the relative humidity. The author was the first to point out that HNO₃ and NH₃ in the gas phase may be present in equilibrium with aerosol phase concentrations of

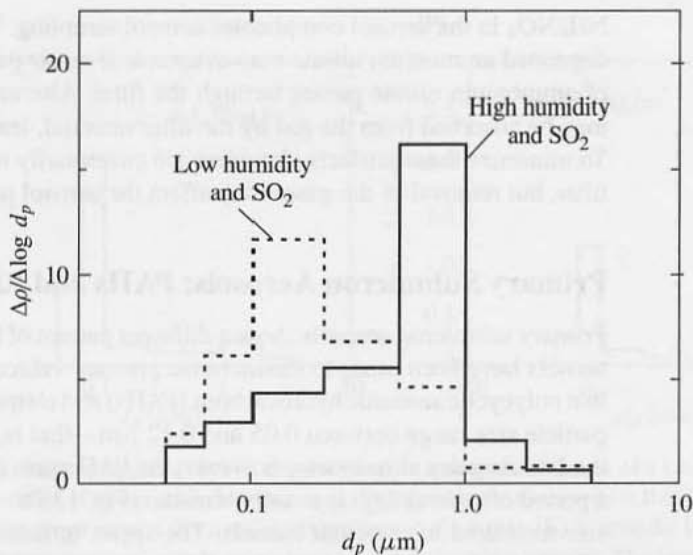


Figure 13.7 Normalized sulfate size distributions measured in Los Angeles. The smaller mode ($d_p \approx 0.2 \mu\text{m}$) was observed during periods of low relative humidity, in the absence of morning fog. The larger mode ($d_p \approx 0.5 \mu\text{m}$) occurred on high-humidity days and was observed more frequently. (After Hering and Friedlander, 1982.)

similar order of magnitude in cases of practical interest (Stelson et al., 1979). Because there is a significant temperature effect, material easily shifts back and forth between the aerosol and gas phases. In field studies designed to test the presence of the nitrate equilibrium in the Southern California atmosphere, Hildemann et al. (1984) found that the measured $[\text{NH}_3][\text{HNO}_3]$ product was generally less than or equal to the calculated product. Agreement was better at inland sites than in coastal areas, where it appeared that some nitrate is bound in large particles by the reaction of HNO_3 with sea salt or soil dust.

Ammonium nitrate appears in the aerosol accumulation and coarse modes (Fig. 13.8). The existence of a near-equilibrium relationship between NH_3 and HNO_3 in the gas and

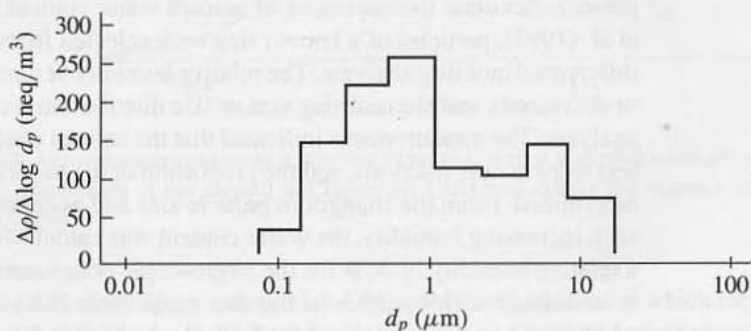


Figure 13.8 Size distribution for ammonium nitrate in the Claremont, California aerosol, 13 July 1987 (0600–0930) (John et al., 1990). Strong nitrate peaks are frequently observed in the coarse mode. This is not usually the case for sulfates (Fig. 13.7).

NH_4NO_3 in the aerosol complicates aerosol sampling. When filters are used for sampling, deposited ammonium nitrate may evaporate if an air parcel containing low concentrations of ammonium nitrate passes through the filter. Alternatively, ammonia and/or nitric acid may be adsorbed from the gas by the filter material, leading to high nitrate measurements. To minimize these artifacts, denuders are customarily used to remove the gases before the filter, but removal of the gases may affect the aerosol particles suspended in the gas.

Primary Submicron Aerosols: PAHs and Elemental Carbon

Primary submicron aerosols show a different pattern of behavior. Studies of the air in traffic tunnels have been made to characterize primary vehicular emissions. The results indicate that polycyclic aromatic hydrocarbons (PAHs) and elemental carbon are emitted in a narrow-particle size range between 0.05 and 0.12 μm —that is, the ultrafine range (Fig. 13.9a). In the Los Angeles atmosphere, however, the PAH mass distribution function measured over a period of several days is usually bimodal (Fig. 13.9b). The lower mode corresponds to the size measured in vehicular tunnels. The upper, broader mode peaks in the 0.5- to 1.0- μm range corresponding to the usual peak in the accumulation mode. The bimodality is probably due to two effects: (i) Freshly emitted ultrafine particles attach by diffusion to (coagulate with) accumulation mode particles, and (ii) particles emitted by motor vehicles serve as nuclei for the condensable products of atmospheric gas-phase reactions, including sulfates. The atmospheric aerosol averaged over a period of days includes contributions directly emitted from vehicles that have relatively short residence times. This is the lower mode of the bimodal distribution. The upper PAH mode results from attachment and condensation. The more reactive PAHs are depleted to a greater extent in the 0.5- to 1.0- μm range, which is evidence for aerosol aging. Similar behavior was observed for elemental carbon measured in a traffic tunnel and in an urban atmosphere.

Water

Most of the aerosol water is associated with the accumulation mode in which hygroscopic inorganic salts including sulfates and nitrates and some polar organic compounds are present. Accurate measurement of aerosol water content is difficult. In studies by Zhang et al. (1993), particles of a known size were selected from the atmospheric aerosol using a differential mobility analyzer. The relative humidity of the air was adjusted (either increased or decreased), and the resulting size or size distribution was measured by a second mobility analyzer. The measurements indicated that the aerosol could often be divided into more and less hygroscopic fractions, and the proportion of the particles associated with each type was determined. From the changes in particle size and assumptions concerning particle growth with increasing humidity, the water content was calculated as a function of particle size at a relative humidity of 46% for the hygroscopic component (Fig. 13.10). Most of the water is associated with particles in the size range from 0.5 to 2.0 μm . At relative humidities of 80%, the water was about 50% of the dry mass; the water and dry mass were about equal at a humidity of 87%. Substances dissolved in the aqueous portion of the aerosol that are in equilibrium with their vapor in the gas phase will have the same normalized mass distribution with respect to particle size as the water. The distribution should be normalized

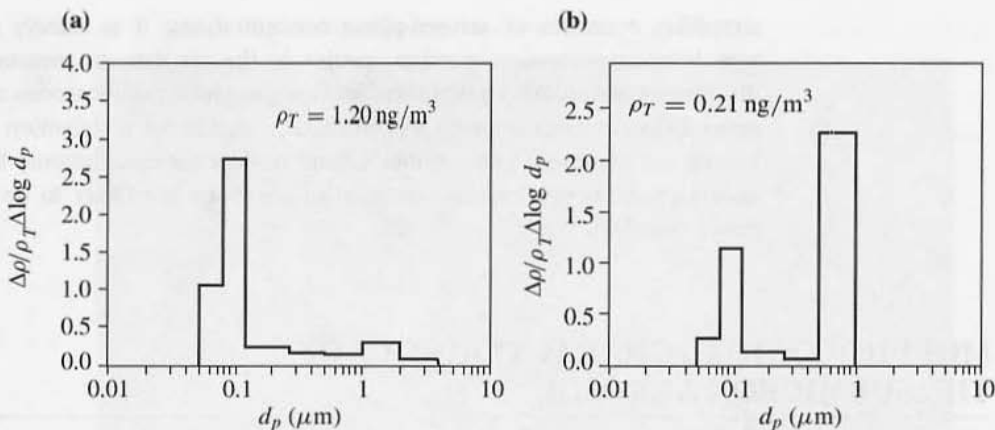


Figure 13.9 (a) Benzo(a)pyrene (BAP) size distribution measured in the air of a Los Angeles traffic tunnel representative of direct vehicular emissions. Sharp peaks are observed for BAP (and many other PAHs) in the size range around $0.1 \mu\text{m}$ (Venkataraman et al., 1994). (b) A bimodal BAP distribution is observed for measurements made away from strong (vehicular) sources. The large-particle mode probably originates from growth of the original $0.1\text{-}\mu\text{m}$ emissions by condensation of secondary aerosol components, especially sulfates and nitrates. (After Venkataraman and Friedlander, 1994.)

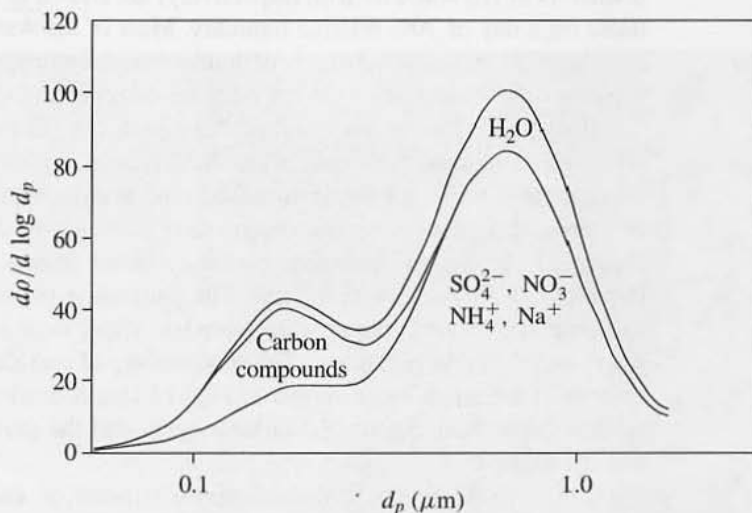


Figure 13.10 Aerosol water content as a function of particle size at a relative humidity of 46% for the hygroscopic component of the aerosol at Claremont, California during the summer of 1987. (After Zhang et al., 1993.)

by the total mass of the dissolved species. Examples of substances for which the equilibrium assumption may hold are peroxides, aldehydes, organic acids, and ammonium nitrate.

An important feature of the aqueous component of the aerosol is its role as a carrier of dissolved chemical species, including short-lived reactive intermediates. The assumption of equilibrium between the aerosol and gas phases, when applicable, considerably

simplifies estimates of aerosol-phase concentrations; it is usually much easier to measure low concentration reactive species in the air than to measure the corresponding dissolved species. At equilibrium, data on gas-phase compositions can be converted into aerosol distributions with respect to particle size if the distribution function for water is known (or assumed) and reliable solubility data (or calculations) are available. Care is necessary, however, because the aerosol solutions are likely to be highly concentrated, hence nonideal.

MORPHOLOGICAL CHARACTERISTICS OF THE SUBMICRON AEROSOL

There are marked differences between the morphological characteristics of accumulation mode and ultrafine particles. This is illustrated by studies of size segregated samples of the atmospheric aerosol collected in Los Angeles using an eight-stage Hering low-pressure impactor. The particles were deposited on electron micrograph grids. Sampling times of three minutes resulted in an optimum loading of particles on the grid for electron microscopic study. Images of the particles on the fourth and eighth stage (50% cutoff diameters of 0.5 and 0.05 μm , respectively) are shown in Fig. 13.11. These samples were taken on a day of 70% relative humidity. Most of the water associated with the particles evaporates in the sample chamber of the electron microscope, which operates under vacuum. However, the impaction of the wet particles onto the grid leaves a water halo (Fig. 13.11a). Small agglomerates of very fine primary particles (diameter less than 20 nm) are also observed associated with each water halo. These agglomerates may have served as the condensation nuclei for the accumulation mode particles or may have been scavenged by Brownian diffusion to accumulation mode particles as discussed earlier in the chapter. Figure 13.11b shows particulate matter collected from the eighth stage of the impactor (50% cutoff diameter of 0.05 μm). The particulate matter in this size range consists of agglomerates of very fine primary particles. Water does not appear to be associated with the material in this size range. The morphology of these agglomerates is similar to those present in the water halos shown in Fig. 13.11a. It is likely that the accumulation mode particles shown in Figure 13.11a have aged, and the particles shown in Fig. 13.11b are freshly emitted.

These two samples, collected within minutes of each other at the same sampling location, illustrate the complex nature of the submicron aerosol. The two morphologies result in quite different aerosol behavior both physicochemically and biochemically. For example, biologically active species such as peroxides, originally in the gas phase, may be dissolved in the aqueous component of the aerosol as discussed above. This is in contrast with the ultrafine particles that are probably freshly formed and have not had time to accumulate condensed material or be scavenged by the accumulation mode. In this regard, very small (30-nm primary particles) freshly formed perfluoropolymer fume particles cause acute pulmonary toxicity in rats (Warheit et al., 1990). This has encouraged the hypothesis that ultrafine atmospheric particles are responsible for the adverse health effects observed in epidemiological studies (Pope et al., 1995).

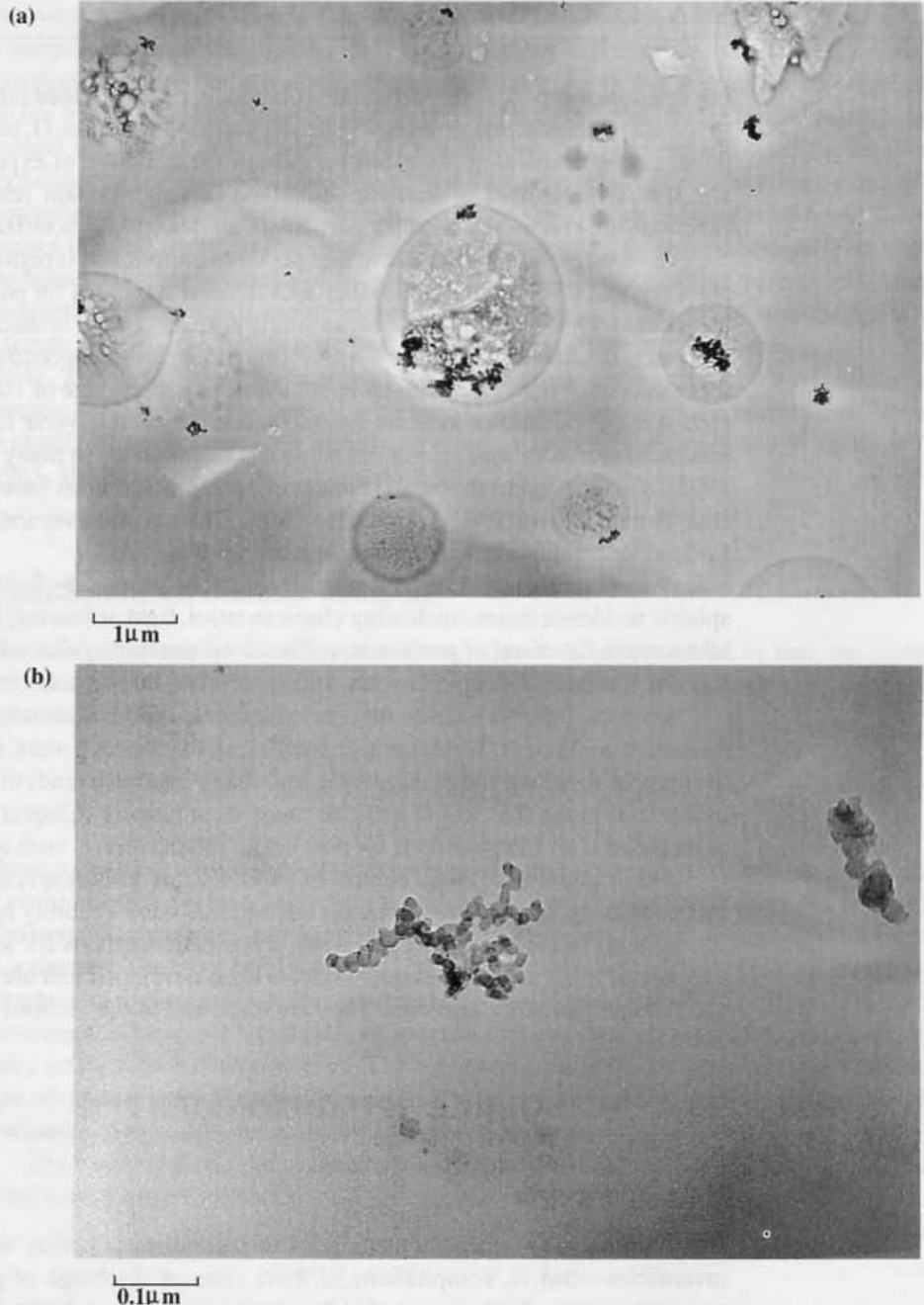


Figure 13.11 (a) Electron micrograph of accumulation mode particles collected on a cascade impactor from air outside an engineering laboratory at UCLA. Halos surround residues of what are probably inorganic salts and polar organic compounds. Soot-like particles are also present. (b) Aggregates of very fine particles collected on the eighth stage of a low-pressure impactor. These are probably soot particles emitted from diesel engine sources such as buses. More volatile particles may have evaporated in the electron microscope.

COMMON MEASURES OF AIR QUALITY FOR PARTICULATE MATTER: FEDERAL STANDARDS

For scientific purposes, the particulate component can be defined fairly completely in terms of the size–composition probability density function (Chapter 1), but this quantity is not of direct use in practical applications because of the difficulty of experimental measurement and the large number of variables involved. Instead, certain relatively simple integral functions are commonly used for particulate air quality characterization.

The total mass of particulate matter per unit volume of air is perhaps the simplest integral property, and it is on this quantity that U.S. federal standards for particulate pollution have been based. Until recently there was a single primary (health related) standard of $50 \mu\text{g}/\text{m}^3$ (annual geometric mean) and $150 \mu\text{g}/\text{m}^3$ (maximum 24-hr concentration not to be exceeded more than once per year), with an upper cutoff in particle size of $10 \mu\text{m}$ (PM_{10}). However, epidemiological studies indicate an association between adverse health effects, including enhanced mortality, and submicron aerosol concentrations in many U.S. cities (Pope et al., 1995). This has led to the establishment of an additional mass based standard for particles smaller than $2.5 \mu\text{m}$ ($\text{PM}_{2.5}$) (U.S. EPA, 1996). There is also a separate health-based standard for lead, one component of the atmospheric aerosol.

Particulate mass is only a limited measure of air quality for several reasons. Atmospheric residence times, nucleating characteristics, light scattering, and lung deposition are all sensitive functions of particle size. The cloud nucleating characteristics of one $0.05 \mu\text{m}$ and one thousand $0.5\text{-}\mu\text{m}$ particles, which are of equal mass, are entirely different.

Another important air-quality parameter, visibility, is closely related to the aerosol extinction coefficient. The extinction coefficient, like the total mass, is an integral function of the particle size distribution. However, for urban pollution it tends to weight the contribution of material in the 0.1- to $1.0\text{-}\mu\text{m}$ size range most heavily (Chapter 5). There is a separate mass based U.S. EPA standard for non-health related effects such as visibility.

A central problem in the control of particulate air pollution is source apportionment—that is, relating air-quality parameters such as mass and visibility reduction to the separate components of the atmospheric aerosol. Systematic methods for source apportionment of the aerosol mass and light extinction have been developed and are used routinely by state and federal regulatory agencies. They are discussed in the sections that follow.

RECEPTOR MODELING: SOURCE APPORTIONMENT

Basic Concepts

Early estimates of source contributions to particulate pollution were based on emission inventories—that is, compilations of mass rates of discharge of particulate matter from various sources. Such inventories by themselves are of limited value in determining quantitatively contributions to the aerosol concentration at a given point, such as an air monitoring station. Emission inventories make no provision for natural background, or particle deposition between the source and the point of measurement. They also do not account for products of gas-to-particle conversion, which contribute significantly to the

total mass of aerosols and affect visibility and health. An alternative approach, *receptor modeling*, makes use of chemical composition measurements at a sampling (“receptor”) site in conjunction with information on the chemical signatures of sources to estimate source contributions. A major advantage of receptor modeling is that it requires no information on the wind field. The first receptor model to be developed, the *chemical mass balance method* (Hidy and Friedlander, 1971; Friedlander, 1973), is widely used for regulatory applications. The method makes use of two data sets: (i) the chemical composition of the atmospheric aerosol at a given measurement site and (ii) the chemical composition of the aerosol emitted from the principal sources in the region, presumed known. The method has been well-summarized by Watson et al. (1991) and is discussed in this section. Another frequently used approach, multivariate receptor modeling, makes use of atmospheric data to estimate not only the source contributions but compositions of the sources as well (Henry, 1991). This is achieved by searching for correlations among the measured atmospheric species; species from the same source tend to be correlated and the correlations are used to identify the sources. Good reviews of receptor modeling methods are given by Hopke (1985, 1991).

Chemical Mass Balance Method

The basic idea behind the chemical mass balance (CMB) method is that the material collected on a filter or impactor stage at a given sampling site is composed of a set of contributions from various sources:

$$\rho = \sum_j^p m_j \quad (j = 1, 2, \dots, p) \quad (13.9)$$

where ρ , the local mass concentration in mass of species per unit volume of air, is a function of position and is averaged over the sampling time. The source contribution, m_j , is the mass of material from source j per unit volume of air at the *point of measurement*. There are a total of p sources. The right-hand side of (13.9) represents the sum of the source contributions to the total mass, assuming that the sources can be considered discrete. In practice, it is usually convenient to lump certain classes of sources, automobiles, power plants, and so on, such that j refers to each class of source. The source contributions, m_j , are exact quantities; each type of source makes a well-defined contribution to the aerosol measured at a point. The evaluation of m_j is the main goal of receptor modeling.

The concentration ρ_i of a chemical component i in the aerosol at a given point is related to the source contributions by

$$\rho_i = \sum_j^p c_{ij} m_j \quad (i = 1, 2, \dots, n) \quad (13.10)$$

where c_{ij} , the mass fraction of component i in m_j , is the source concentration matrix. There are a total of n chemical components.

When samples are obtained in discrete size fractions as with the cascade impactor, relations similar to (13.9) and (13.10) hold for the discrete fractions:

$$\Delta\rho = \sum_j^p \Delta m_j \quad (13.11)$$

and

$$\Delta\rho_i = \sum_j^p c_{ij} \Delta m_j \quad (13.12)$$

where the symbol Δ denotes the material in the discrete size range between d_{p1} and d_{p2} .

The dependence of the air-quality parameters on the properties of the emission sources is thus reduced to the two quantities Δm_j , the mass contributed by source j per unit volume of air to the size range Δd_p , and the source concentration matrix c_{ij} , the mass of chemical species i in unit mass of material from source j .

The chemical mass balance (CMB) method depends on the inversion of (13.11) or (13.12) to obtain the source contributions m_j or Δm_j . Values of ρ_i are measured at a given sampling site. The matrix c_{ij} should also correspond to the point of measurement. Usually, however, it is assumed that the value of c_{ij} is equal to the value at the source, and fractionation by exchange with the gas phase or by sedimentation is neglected. Hence in carrying out the chemical element balance, it is necessary to choose elements for which fractionation is not important.

In applications to field data, the systems of equations (13.11) and (13.12) are usually overdetermined because there are more chemical components measured than sources. That is, there are more equations than unknowns. At least two approaches can be used to solve for the source contributions, m_j : One can choose a set of chemical components equal in number to the number of unknown sources. The chemical components chosen for this purpose are the ones with minimum uncertainty in the experimentally measured values and which are present in high concentrations in the aerosol. The quality of the fit with the rest of the data is measured by the mean square deviation between the measured and calculated chemical component concentrations.

In the second method, a least squares analysis is performed making use of all chemical components; the contributions of the sources are varied, and the mean square difference between the measured and calculated concentrations of each species is calculated. These must be weighted, for example, with respect to the experimental error in each component. Otherwise, the components present in highest concentration will dominate the calculation. Weighting with respect to the error increases the importance of the components with the smallest error. In this way the set of mass concentrations leading to the minimum weighted least square is determined. This approach can be further generalized by including uncertainties in the compositions of the sources (Watson et al., 1991). An early application of the method to the design of a regional air pollution control program in Portland, Oregon is discussed next.

Portland Aerosol Characterization Study

In the 1970s, Portland experienced persistent violations of the Federal Ambient Air Quality Standard for particulate matter. The principal sources of the ambient aerosol were uncertain; the importance of industrial sources was especially controversial. The existing emission

inventory, based on emission factors and industrial source testing, was used as a basis for the installation of new controls. This resulted in an additional reduction of 60,000 tons per year in regional industrial emissions. There was an improvement in air quality, but violations of the particulate standard continued; modeling studies were unable to account for more than half the particulate mass. After a technical review of alternative methodologies, the CMB approach was adopted as a basis for a source resolution study.

Measurements were made of emissions from 37 industry sources. During the same period, samples of the atmospheric aerosol were taken and 27 chemical species were measured. Samples of the ambient aerosol were collected for total suspended particulate (TSP) matter and for particles with aerodynamic diameter less than $2.5 \mu\text{m}$. Figure 13.12

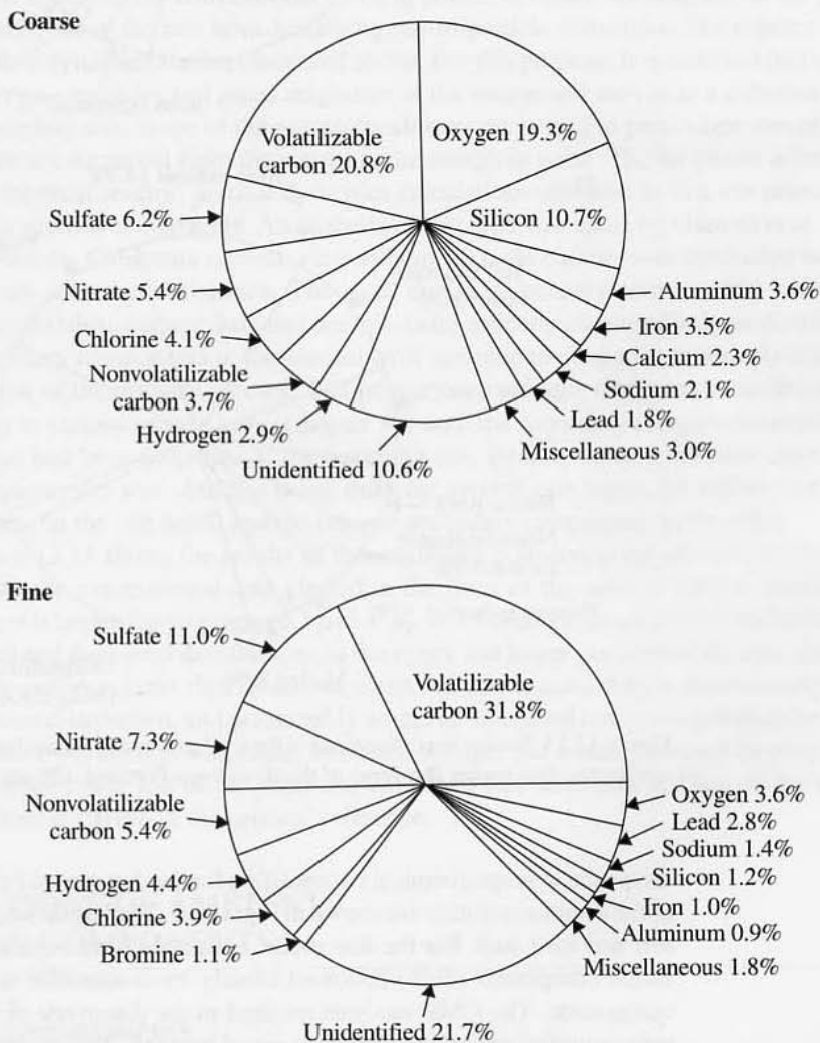


Figure 13.12 Average chemical composition of the total suspended particulate matter (**top**) and the fine ($d_p < 2.5 \mu\text{m}$) particulate matter (**bottom**) of the downtown Portland, Oregon aerosol. (From Core et al., 1982.)

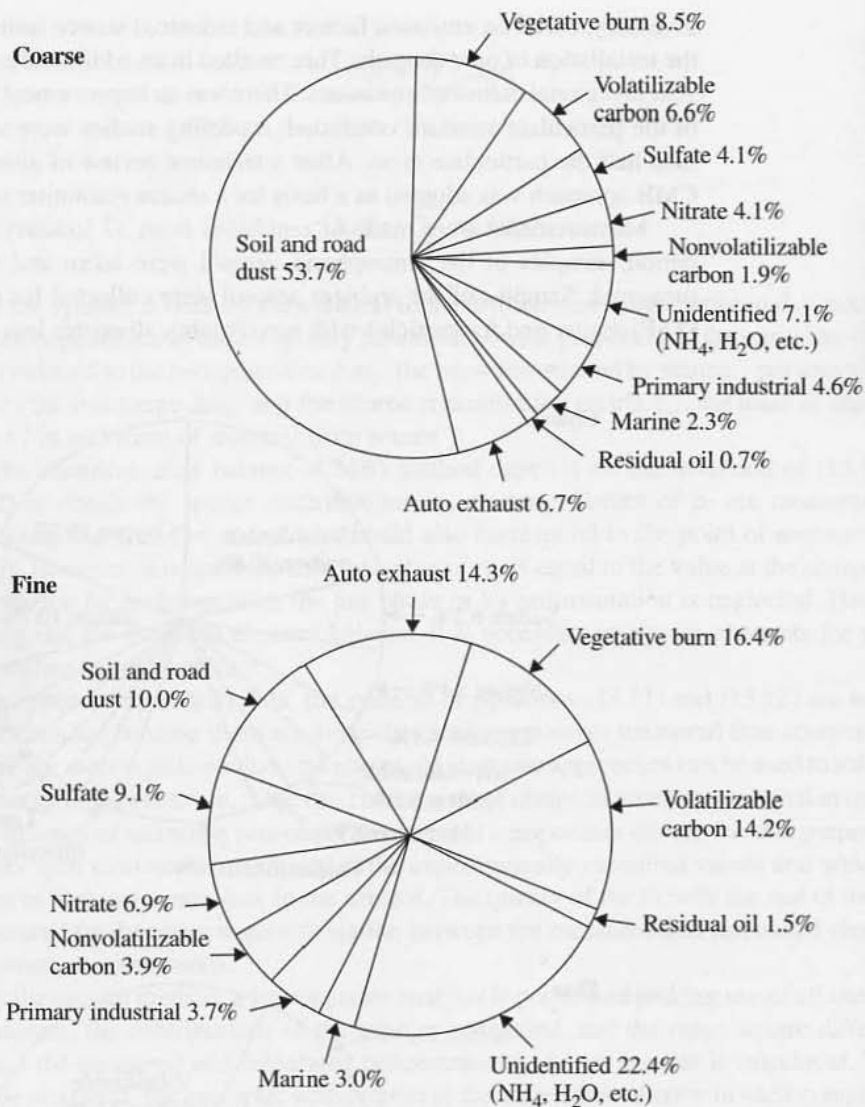


Figure 13.13 Source apportionment of the total suspended particulate matter (**top**) and fine ($d_p < 2.5 \mu\text{m}$) particulate matter (**bottom**) of the downtown Portland, OR aerosol. (From Core et al., 1981.)

shows the average chemical composition for the downtown Portland aerosol, and the results of the source resolution are shown in Fig. 13.13. The largest single component of the TSP was soil and road dust. For the fine mode, emissions from vegetative burning were the largest single component (16%) followed closely by automobile emissions and volatile carbon compounds. The CMB analysis resulted in the discovery of 6500 tons/year of previously uninventoried emissions including wood burning. The presence of high concentrations of potassium in the fine mode aerosol is an indicator of smoke from the burning of wood which is enriched in potassium. Primary industrial emissions accounted for only about 5% of the

total Portland aerosol mass. These findings led to a rethinking of the strategy needed to meet air pollution standards including major efforts to reduce residential wood burning.

Visibility is reduced by particulate matter and in some cases by light-absorbing gases, especially NO_2 . Analogous to the chemical mass balance discussed in the previous section, it is possible to prepare an extinction budget to estimate the contributions of the various aerosol components to the extinction coefficient and visibility reduction (Groblicki et al., 1981; Sloane, 1983,1984).

Relating the CMB to Aerosol Dynamics

Conventional receptor modeling gives no information on atmospheric aerosol dynamics. It is possible to extend the conventional CMB approach to obtain information on the particle size dependence of the rate laws describing gas-to-particle conversion in a manner similar to the plume dynamics studies discussed above. For this purpose, it is assumed that a parcel of air carrying particles and gases originates at the source and moves as a coherent packet to the sampling site. Some of the gas molecules are converted to particulate matter during passage of the air parcel from the source to the sampling point. The air parcel is treated as a small chemical reactor; aerosol dynamics calculations are used to link the primary and secondary aerosol components. An analysis of this type was made by Gartrell et al. (1980) for the Pomona, California aerosol. First a chemical mass balance was conducted to obtain the primary source contributions. The most important primary sources were automobile emissions, soil dust, cement dust, and sea salt. Independently measured volume distributions for the primary components of the aerosol were summed to obtain the (nominal) initial size distribution of the primary aerosol. The primary aerosol was then grown mathematically according to various growth laws (Chapter 10) until the secondary components reached the values that had been measured at the sampling site. Best agreement between calculations and measurements was obtained using different growth rate forms for sulfate and nitrate conversion, on the one hand, and the organic secondary component on the other.

Figure 13.14 shows the results of the secondary conversion calculations for Pomona, along with the experimental data plotted in the form of the aerosol volume distribution. Agreement is best in the size range $0.1 \mu\text{m} < d_p < 1.0 \mu\text{m}$. There are deviations between the calculated and measured distributions in the upper and lower portions of the size spectrum. The spike in the volume distribution at about $1.1 \mu\text{m}$ is caused by a discontinuity in the primary size distribution, and presumably would be smoothed out by coagulation for a well-aged aerosol. No attempt was made, however, to “age” the primary aerosol by coagulation except for the lower end of the vehicular emissions size distribution. Data on the number distributions are given in the original reference.

STATISTICAL VARIATIONS OF AMBIENT AEROSOL CHEMICAL COMPONENTS

Field Measurements

Further insight into atmospheric aerosol dynamics can be obtained by analyzing variations in aerosol chemical composition with time at a given sampling site. Many long-time

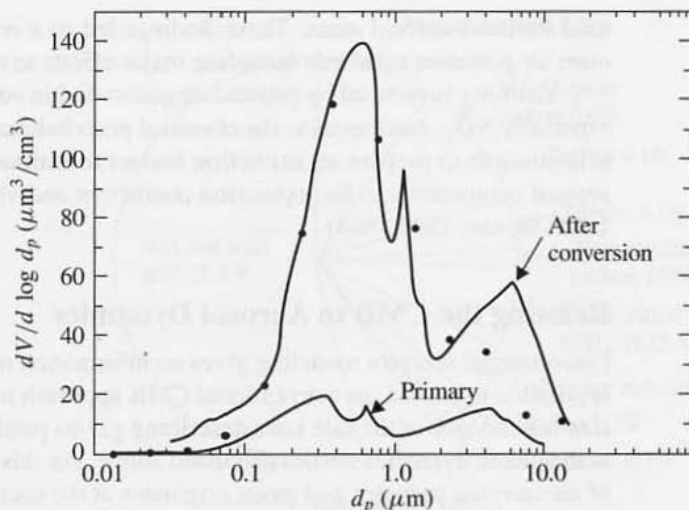


Figure 13.14 Distribution of primary component of the aerosol measured in Pomona, California on 10/24/72 based on a chemical mass balance. The calculated final distribution is based on assumed forms for the growth mechanisms for the secondary components. The points show the experimental data. (After Gartrell et al., 1980.)

data sets for aerosol chemical composition and mass have been gathered, often for the purpose of source apportionment. The dimensionless geometric standard deviation σ_{gi} for each chemical component represents the spread in the data around the geometric mean. The magnitude of σ_{gi} is a measure of the effects of various random processes including (i) variations in source strengths, natural and anthropogenic, that affect both the primary and secondary components of the aerosol, (ii) variations in wind speed and direction, eddy diffusion, and inversion height, and (iii) variations in chemical reaction rates (gas-to-particle conversion) driven by changes in temperature, solar radiation, and humidity.

Values of σ_{gi} for various aerosol chemical components in the size range $d_p < 3.5 \mu\text{m}$ were calculated by Kao and Friedlander (1994, 1995) from a data set that consisted of eight-hour (12 to 8 P.M.) samples collected from June 1987 to June 1988 at Duarte, California, a residential area located about 20 miles east of downtown Los Angeles. Their calculations were based on the definition of σ_{gi} (without assuming a lognormal frequency distribution):

$$\ln \sigma_{gi} = \sqrt{\frac{\sum_{i=1}^N (\ln x_i - \ln x_{gi})^2}{N - 1}} \quad (13.13)$$

where N is the total number of data points, x_i is the concentration corresponding to a given measurement, and x_{gi} is the geometric mean concentration.

Figure 13.15 shows σ_{gi} for various aerosol chemical components. Elements present in the primary emissions include the metals, silicon, and black carbon (BC). Among the primary aerosol emission sources are automotive emissions and tire wear, residual fuel oil combustion, crustal materials, and the marine aerosol. Despite the variety of primary emission sources, values of σ_{gi} fell within a narrow band, 1.85 ± 0.14 . Similar results were obtained for data sets at other Los Angeles sites. Thus variations in the ambient

concentrations of the primary components are probably due to meteorological factors, and not to variations in source emissions which would be expected to vary in different ways, leading to different values of σ_{gi} .

Values of σ_g for the secondary aerosol components were larger than those of the primary species (2.05 for SO_4^{2-} , 3.45 for NO_3^- , and 2.66 for NH_4^+). In the Los Angeles area, the secondary components are generated locally and depend on a larger set of random variables than the primary components. These additional variables include temperature, humidity, and solar radiation, which affect the rates of the chemical processes that produce the secondary aerosol. Thus differences in σ_g may help distinguish between primary and secondary components of the aerosol when the secondary components are formed near the point of measurement, and their concentrations are not dominated by long-range transport. Referring to Fig. 13.15, all of the carbon-containing components including black carbon (BC), volatile carbon (VC), and organic carbon (OC) had values of σ_g characteristic of the primary components of the aerosol. This is somewhat surprising for the volatile carbon component.

Values of σ_g for the total mass concentration consistently showed a lower variability than values for the individual components of the aerosol. This probably resulted from seasonal variations that are opposite in sign for some of the major chemical components of the fine aerosol especially the sulfate and total carbon (TC). Levels of TC in the aerosol tend to be high during the winter and low in the summer, whereas sulfate concentrations are high during the summer and low in the winter. These summer maxima accompany higher solar radiation intensity, relative humidities, and temperatures. TC levels, which are related to vehicular sources, are probably highest in the winter because of low inversion heights and reduced atmospheric mixing. Further insight into the causes of the variations

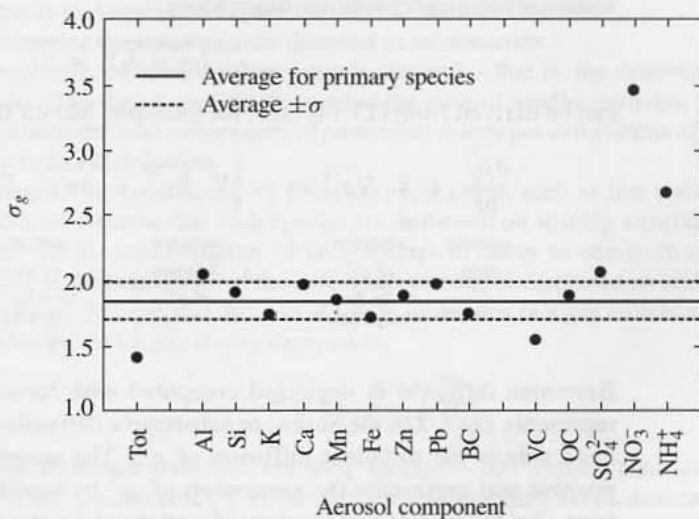


Figure 13.15 Geometric standard deviations (σ_g) of fine-particle chemical components: trace elements Al to Pb; VC \equiv (volatile carbon), OC (organic carbon), BC (black carbon), SO_4^{2-} , NO_3^- , and NH_4^+ in Duarte, California. Values of σ_g for the primary components (Al to BC) are approximately constant at 1.85 ± 0.14 (Kao and Friedlander, 1995).

is obtained from the theory of atmospheric concentration fluctuations discussed in the next section.

Relation to Aerosol Dynamics

Variations in atmospheric aerosol compositions can be linked to aerosol dynamics through the equations of conservation of species for the chemical components in the submicron aerosol:

$$\frac{\partial \rho_i}{\partial t} + \mathbf{v} \cdot \nabla \rho_i = \left[\frac{\partial \rho_i}{\partial t} \right]_{\text{Brownian Diffusion}} + R_i \quad (13.14)$$

where

ρ_i = instantaneous total mass concentration of component i in the aerosol

\mathbf{v} = instantaneous air velocity

$\left[\frac{\partial \rho_i}{\partial t} \right]_{\text{Brownian Diffusion}}$ = change in ρ_i due to Brownian diffusion of the aerosol integrated over all particle sizes

R_i = rate of formation of aerosol component i by gas-to-particle conversion at any instant

$R_i = 0$ for primary chemical components. Coagulation is included in (13.14), which can easily be shown to be a form of the GDE integrated over particle mass. Sedimentation is neglected for the submicron range. A time-smoothed conservation equation for the mean square aerosol concentration fluctuations

$$\overline{(\rho_i - \bar{\rho}_i)^2} = \overline{\rho_i'^2} \quad (13.15)$$

can be derived from (13.14) (see, for example, Monin and Yaglom, 1971, p. 387).

$$\frac{\partial \overline{\rho_i'^2}}{\partial t} + \bar{\mathbf{v}} \cdot \nabla \overline{\rho_i'^2} = - \left[\nabla \cdot \bar{\mathbf{v}} \overline{\rho_i'^2} + 2 \bar{\mathbf{v}}' \rho_i' \cdot \nabla \bar{\rho}_i \right] + 2 \overline{\rho_i' R_i'} - 2 \bar{N} \quad (13.16)$$

unsteady	advection	turbulent	gain of $\overline{\rho_i'^2}$	formation	dissipation
term	of $\overline{\rho_i'^2}$	diffusion	by transfer	by	
	by the	of $\overline{\rho_i'^2}$	from the mean	gas-to	
	mean flow		flow (with	particle	
			negative sign)	conversion	

Brownian diffusion is neglected compared with turbulent transport. The left-hand side represents $D\overline{\rho_i'^2}/Dt$, the Stokes or substantive derivative of $\overline{\rho_i'^2}$. The first term on the right-hand side is the turbulent diffusion of $\overline{\rho_i'^2}$. The second term $-2\bar{\mathbf{v}}' \rho_i' \cdot \nabla \bar{\rho}_i$ is generally positive and represents the generation of $\overline{\rho_i'^2}$ by transfer from the mean flow. The third term, $2\overline{\rho_i' R_i'}$, is the contribution of variations in the rate of gas-to-particle conversion by chemical reaction to the rate of production of $\overline{\rho_i'^2}$. The last term is the decrease of mean square fluctuations $\overline{\rho_i'^2}$ due to the action of small scale diffusion (dissipation). Thus three types of terms appear on the right-hand side of (13.16), the balance equation for $\overline{\rho_i'^2}$: (i) turbulent diffusion of $\overline{\rho_i'^2}$ and transfer from the mean flow to $\overline{\rho_i'^2}$, which affect

variations in both primary and secondary components, (ii) chemical reaction that affects only the variation of the secondary component, and (iii) dissipation by molecular diffusion. Hence as observed in the field studies, secondary aerosol components would be expected to show larger statistical variations than primary components in regions where the secondary components are generated. If the secondary components at a downwind site are the result of long-range transport, their statistical variations would be expected to be damped compared with local primary sources.

It is known that time means of the temperature and wind velocity at a given point in the atmosphere depend strongly on the length of the averaging time interval. Moreover, for a given averaging time the mean values tend to drift, thereby complicating efforts to characterize the statistical properties (Monin and Yaglom, 1971, pp. 420–421). However, by limiting observations to a given season, time of day, and synoptic conditions (weather type) and averaging over a long enough time, the mean values are relatively stable. Thus averaging over periods of 10 to 20 minutes results in relatively stable values of the means.

If the averaging period is increased to several hours as in the case of the Duarte data discussed above, or to even longer times, the mean values change significantly and may show very low stability. These considerations suggest that more attention should be paid to the selection of sampling time intervals in future studies of the statistics of aerosol chemical compositions.

PROBLEMS

13.1 The size distribution function $n_d(d_p) \approx \Delta N / \Delta d_p$ for the Pasadena aerosol averaged over the measurements in August and September 1969 is shown in the table.

- Determine the mean particle diameter in micrometers.
- Determine the mass median particle diameter—that is, the diameter for which the mass of the larger particles is equal to the mass of smaller particles.
- Estimate the total surface area of particulate matter per unit volume of air corresponding to this distribution.
- Many of the constituents of photochemical smog, such as free radicals, are highly reactive. Assume that such species are destroyed on striking a surface. Estimate the time for the concentration of such species to decay to one-tenth of their original value in the atmosphere if they are destroyed and not replaced on striking the aerosol surfaces. Assume that the rate at which molecules in a gas collide with a surface is given by the kinetic theory expression,

$$\beta = c \left(\frac{RT}{2\pi M} \right)^{1/2}$$

where M is the molecular weight of colliding species = 100 g/mole (assumed), R is the gas constant (8.3×10^7 ergs/K mole), T is the absolute temperature (300 K, assumed), and c is the concentration of reactive species.

- Show that the power law form of the size distribution function holds approximately for the data, and evaluate the constant of proportionality and its dimensions.
- Compare the self-preserving size distribution for coalescing spheres with the data for the accumulation mode. For this purpose, plot $dV/d \log d_p$ versus $\log d_p$ for the data

Particle Size Distribution Functions Averaged Over
Measurements Made in Pasadena, August to September
1969 (Whitby, et al., 1972)

d_p (μm)	$\Delta N/\Delta d_p$ (No./ $\text{cm}^3 \mu\text{m}$)	$\Delta V/\Delta \log d_p$ ($\mu\text{m}^3/\text{cm}^3$)
0.00875	1.57×10^7	0.110
0.0125	5.78×10^6	0.168
0.0175	2.58×10^6	0.289
0.0250	1.15×10^6	0.536
0.0350	6.01×10^5	1.08
0.0500	2.87×10^5	2.14
0.0700	1.39×10^5	3.99
0.0900	8.90×10^4	7.01
0.112	7.02×10^4	13.5
0.137	4.03×10^4	17.3
0.175	2.57×10^4	28.9
0.250	9.61×10^3	44.7
0.350	2.15×10^3	38.6
0.440	9.33×10^2	42.0
0.550	2.66×10^2	29.2
0.660	1.08×10^2	24.7
0.770	5.17×10^1	21.9
0.880	2.80×10^1	16.1
1.05	1.36×10^1	22.7
1.27	5.82	18.6
1.48	2.88	13.6
1.82	1.25	19.7
2.22	4.80×10^{-1}	13.4
2.75	2.17×10^{-1}	15.2
3.30	1.18×10^{-1}	13.7
4.12	6.27×10^{-2}	25.3
5.22	3.03×10^{-2}	26.9

Total number of particles = $1.14 \times 10^5/\text{cm}^3$.

Total volume of particles = $58.1 \mu\text{m}^3/\text{cm}^3$.

given in this problem and compare with values calculated from Table 7.2, Chapter 7. Use values of N_∞ and ϕ corresponding to $0.09 < d_p < 2.22 \mu\text{m}$.

- 13.2** (a) Estimate the atmospheric residence time for 10-nm particles in air from various locations (Table 13.1): continental background, average background, and urban average. Base your estimate on Brownian coagulation with accumulation mode particles.
- (b) Also calculate the residence time when dry deposition is the controlling mechanism of particle removal. Assume that the dry deposition velocity is 0.1 cm/sec and that the height of the mixed layer is 1 km [refer to Eq. (13.2)]. Compare with the results of the Brownian coagulation mechanism. Discuss your conclusions.

13.3 Prepare a source concentration matrix for the stratospheric aerosol. Take into account as sources the tropospheric aerosol, emissions from volcanoes, meteoritic material, and high-flying aircraft.

13.4 It is planned to use a cascade impactor to sample the atmospheric aerosol for chemical analysis. The size distribution, measured by a single particle optical counter and an electrical mobility analyzer, is given in Problem 13.1. The impactor is to have four stages followed by a 100% efficient afterfilter. The impactor stages can be characterized by the size corresponding to an efficiency of 50%. If the first stage collects all particles larger than 5 μm , determine the characteristic particle size for the other three stages that will provide equal mass on each stage and the afterfilter. Assume particle density is constant. Explain why one might wish to design for equal mass on each stage.

REFERENCES

- Core, J. E., Hanrahan, P. L., and Cooper, J. A. (1981) Air Pollution Control Strategy Development: A New Approach Using Chemical Mass Balance Methods in Atmospheric Aerosol: Source/Air Quality Relations, in Macias, E. S., and Hopke, D. (Eds.), *Symposium Series No. 167*, American Chemical Society, Washington, D.C., p. 107.
- Friedlander, S. K. (1973) *Environ. Sci. Technol.*, **7**, 235.
- Friedlander, S. K., and Yeh, E. K., (1998) *Applied Occupational and Environmental Hygiene*, **13**, 416.
- Gartrell, G., Jr., Heisler, S. L., and Friedlander, S. K. (1980) in Hidy, G. M., Mueller, P. K., Grosjean, D., Appel, B. R., Wesolowski, J. J. (Eds.), *The Character and Origins of Smog Aerosols: A Digest of Results from the California Aerosol Characterization Experiment (ACHEX)*. Wiley, New York, pp. 477–517 (*Adv. Environ. Sci. Technol.*, **9**).
- Groblicki, P. J., Wolff, G. T., and Countess, R. J. (1981) *Atmos. Environ.*, **15**, 2473.
- Henry, R. C. (1991) Multivariate Receptor Models, in Hopke, P. K. (Ed.), *Receptor Modelling for Air Quality Management*, Elsevier, Amsterdam.
- Hering, S. V., and Friedlander, S. K. (1982) *Atmos. Environ.*, **16**, 2647.
- Hidy, G. M., and Friedlander, S. K. (1971) in *Proceedings of the 2nd International Clean Air Congress* (Englund, H. M., and Berry, W. T., Eds.), Academic Press, New York.
- Hidy, G. M., Mueller, P. K., Grosjean, D., Appel, B. R., and Wesolowski, J. J. (Eds.) (1980) *The Character and Origins of Smog Aerosols: A Digest of Results from the California Aerosol Characterization Experiment (ACHEX)*.
- Hildemann, L. M., Russell, A. G., and Cass, G. R. (1984) *Atmos. Environ.*, **18**, 1737.
- Hopke, P. K. (1985) *Receptor Modeling in Environmental Chemistry*, Wiley-Interscience, New York.
- Hopke, P. K. (Ed.) (1991) *Receptor Modeling for Air Quality Management*, Elsevier, Amsterdam.
- Jacobson, M. Z. (1997) *Atmos. Environ.*, **31**, 131.
- Jaenicke, R. (1980) Natural Aerosols, in Kneip, T. J., and Liroy, P. J. (Eds), *Aerosols: Anthropogenic and Natural, Sources and Transport*, *Ann. NY Acad. Sci.*, **338**, 317.
- John, W., Wall, S. M., Ondo, J. L., and Winkylmayr, W. (1990) *Atmos. Environ.*, **24A**, 2349.
- Kao, A. S., and Friedlander, S. K. (1994) *Aerosol Sci. Technol.*, **21**, 283.
- Kao, A. S., and Friedlander, S. K. (1995) *Environ. Sci. Technol.*, **29**, 19.
- McMurry, P. H., Rader, D. J., and Stith, J. L. (1981) *Atmos. Environ.*, **15**, 2315.
- Monin, A. S., and Yaglom, A. M. (1971) *Statistical Fluid Mechanics: Mechanics of Turbulence*, Vol. 1, MIT Press, Cambridge, MA.

- NRC Committee on Particulate Control Technology (1979) *Controlling Airborne Particles*, NAS, Washington, D.C.
- Pasquill, F., and Smith, F. B. (1983) *Atmospheric Diffusion*, 3rd ed., Ellis Horwood, Chichester, England. The diffusion of sedimenting particles is discussed on pp. 158–165 and pp. 246–251.
- Pope, C. A. III, Thun, M. J., Namboodiri, M. M., Dockery, D. W., Evans, J. S., Speizer, F. E., and Heath, C. W. (1995) *Am. J. Respir. Crit. Care Med.*, **151**, 669.
- Pruppacher, H. R., and Klett, J. D. (1997) *Microphysics of Clouds and Precipitation*, 2nd ed., Kluwer Academic, Dordrecht, Holland.
- Sakugawa, H., Kaplan, I. R., and Shepard, L. S. (1993) *Atmos. Environ.*, **27B**, 203.
- Seinfeld, J. H., and Pandis, S. N. (1998) *Atmospheric Chemistry and Physics*, Wiley, New York.
- Sloane, C. S. (1983) *Atmos. Environ.*, **17**, 409.
- Sloane, C. S. (1984) *Atmos. Environ.*, **18**, 871.
- Spengler, J. D., Koutrakis, P., Dockery, D. W., Raizenne, M., and Speizer, F. E. (1996) *Environ. Health Perspect.*, **104**, 492.
- Stelson, A. W., Friedlander, S. K., and Seinfeld, J. H. (1979) *Atmos. Environ.*, **13**, 369.
- U.S. EPA (1996) *Air Quality Criteria for Particulate Matter*, v. I, US EPA, Research Triangle Park, NC. An extensive review of the properties of the atmospheric aerosol, prepared as a basis for setting the ambient air quality standard.
- Venkataraman, C., Lyons, J. M., and Friedlander, S. K. (1994) *Environ. Sci. Technol.* **28**, 555.
- Venkataraman, C., and Friedlander, S. K. (1994) *Environ. Sci. Technol.* **28**, 563.
- Warheit, D. B., Seidel, W. C., Carakostas, M. C., and Hartsy, M. A. (1990) *Exp. Mol. Pathol.*, **52**, 309.
- Watson, J. G., Chow, J. C., and Pace, T. G. (1991) Chemical Mass Balance, in Hopke, P. K. (Ed.), *Receptor Modeling for Air Quality Management*, Elsevier, Amsterdam.
- Wexler, A. S., Lurmann, F. W., and Seinfeld, J. H. (1994) *Atmos. Environ.*, **28A**, 531.
- Whitby, K. T., Husar, R. B., and Liu, B. Y. H. (1972) The Aerosol Size Distribution of Los Angeles Smog, in Hidy, G. M. (Ed.), *Aerosols and Atmospheric Chemistry*, Academic Press, New York.
- Whitby, K. T., and Sverdrup, G. M. (1980), in Hidy, G. M., Mueller, P. K., Grosjean, D., Appel, B. R., Wesolowski, J. J., (Eds.), *The Character and Origins of Smog Aerosols: A Digest of Results from the California Aerosol Characterization Experiment (ACHEX)*. Wiley, New York, pp. 477–517 (*Adv. Environ. Sci. Technol.*, **9**).
- Wilson, J. C., and McMurry, P. H. (1981) *Atmos. Environ.*, **15**, 2329.
- Zhang, X. Q., McMurry, P. H., Hering, S. V., and Casuccio, G. S. (1993) *Atmos. Environ.*, **27A**, 1593.

COMMON SYMBOLS

The equation in which the symbol is first used or best defined is given in parenthesis. Not all symbols appearing in the text are included.

LATIN ALPHABET

a_p	particle radius
A	aerosol surface area per unit volume of gas (1.18) or Hamaker constant (2.58)
b	extinction coefficient (5.16)
c	mass fraction, dimensionless (1.38)
e	migration velocity in the presence of an external force field (2.27)
e_e	electrical migration velocity (2.35)
c_s	terminal settling velocity (1.21), (2.29)
c_t	thermophoretic velocity (2.56)
C	slip correction, dimensionless (2.21)
d_p	particle diameter
D	diffusion coefficient (2.24)
D_f	fractal dimension (2.23)
e	electronic charge
E	electric field intensity (2.34)
f	friction coefficient (2.9)
g	size-composition probability density function, dimensionless (1.13)
G	velocity gradient in laminar shear (7.51)
I	intensity of light (5.2)
I_λ	intensity distribution function (5.20)
J	diffusion flux in one direction, or light source function (5.45)
J_x, J_y, J_z	diffusion flux components (2.1)
k	mass transfer coefficient (3.7)
k_g, k_p	thermal conductivities of gas and particle in thermophoresis (2.56)
K	coagulation coefficient or collision frequency for monodisperse particles in continuum range (7.18)

l_p	mean free path (1.1)
m	mass of particle or molecule
M	molecular weight
M_p	moments of particle size distribution function (1.15)
n	concentration
n_∞	concentration at large distances from a surface
n_l	n/n_∞ , dimensionless concentration (3.2) or monomer concentration
$n(v)$	distribution function with particle volume the distributed variable (1.5)
$n_a(a)$	distribution function with particle area the distributed variable (Problem 1.3)
$n_d(d_p)$	distribution function with particle diameter the distributed variable (1.4)
N_p	number of primary particles in an agglomerate
N_∞	total particle number concentration
p	pressure
p_d	equilibrium vapor pressure above a drop of diameter d_p
p_s	equilibrium vapor pressure above a planar surface
Q_{abs}	light absorption efficiency, dimensionless (5.6)
Q_{ext}	light extinction efficiency, dimensionless (5.6)
Q_{sca}	light scattering efficiency, dimensionless (5.5)
s	particle stop distance (Chap. 2, Example)
s^*	visual range (5.58)
S	saturation ratio, dimensionless (9.4)
t	time
T	absolute temperature
u, v, w	velocity components in x, y, z directions, respectively
u_f, v_f, w_f	gas velocity components in equations in which the particle velocity appears
U, U_∞	free stream or average velocity
v	particle volume
v_m	molecular volume, $M/N_{\text{av}}\rho_p$ for particle component (9.52)
x, y, z	Cartesian coordinates
Z	electrical mobility (2.36)

GREEK ALPHABET

α	accommodation coefficient, dimensionless (2.19)
β	collision frequency function (7.1)
ϵ	eddy diffusivity
ϵ_d	rate of turbulent energy dissipation per unit mass of gas (7.53)
ϵ_p	dielectric constant of particle
η	dimensionless particle volume (1.32a)
η_R	single cylinder (fiber) removal efficiency, dimensionless (3.30)
θ	dimensionless time

κ	thermal conductivity of gas
λ	wavelength of light
μ	viscosity or chemical potential (Chap. 9)
ν	kinematic viscosity
Π	ratio of particle diameter to concentration boundary layer thickness, dimensionless (3.34) and (3.58)
ρ	gas density or aerosol mass per unit volume of gas (1.37)
ρ_p	particle density
σ	molecular diameter (1.1), surface tension (Chap. 9), standard deviation (1.26)
σ_g	geometric standard deviation (1.27)
ϕ	aerosol volumetric concentration, dimensionless (1.19) or electrostatic potential (2.39)
Φ	potential energy (2.3)
ψ	self-preserving size distribution function, dimensionless (7.69) or stream function (Chap. 3)

DIMENSIONLESS NUMBERS

Number	Symbol	Definition*
Knudsen	Kn	$2l_p/d_p$
Lewis	Le	$\kappa\rho C_p/D$
Peclet	Pe	LU/D
Interception	R	d_p/L
Reynolds	Re	LU/ν
Schmidt	Sc	ν/D
Sherwood	Sh	kL/D
Stokes	Stk	$\rho_p d_p^2 U / 18\mu L$

*L = characteristic length

PHYSICAL CONSTANTS

Constant	Symbol	CGS Value
Electronic charge	e	4.803×10^{-10} esu
Gravitational acceleration	g	980 cm/sec ² (New York)
Boltzmann's constant	k	1.381×10^{-16} erg/K
Avogadro's number	N_{av}	6.022×10^{23} mol ⁻¹
Gas constant	R	8.314×10^7 erg/K mol
Atomic mass unit	amu	1.661×10^{-24} g

INDEX

A

- Absorption, in light-particle interaction, 126
- Accommodation coefficients
in condensation, heterogeneous, 283–284
free molecule and friction coefficient, 33
- Accumulation mode, 3
in atmospheric aerosol, 360, 364–366
- ACHEX. *See* Aerosol Characterization Experiment
- Acidity, in atmospheric aerosol, 373
- Acoustic coagulation, 189
- Adiabatic expansion, condensation by, 251–252, 276–277
- Aerodynamic diameter, 5, 173–174
- Aerodynamic focusing, 118–120
beam expansion angle *vs.* source pressure, 119
and particle trajectory, 119–120
- Aerosol
definition of, 1
as a generic term, 1
- Aerosol characterization, relation aerosol dynamics, 23–24
- Aerosol Characterization Experiment (ACHEX), *xiii*, 360
- Aerosol conditioning, definition of, 189
- Aerosol dynamics, advances in, *xiii–xiv*
relation to characterization, 23–24.
See also General Dynamic Equation
Aerosol reaction engineering, 331
- Aerosol reactors and synthesis of submicron solid particles
collision-coalescence mechanism of primary particle formation.
See Collision—Coalescence Mechanism
commercial and pilot scale reactors, 332–338
overview, 331–332
particle crystal structure in
basic concepts, 355
experimental observations, 355–356
particle neck formation in, 353–355
primary particle size
effects of aerosol material properties on, 350–352
estimation of, 346–349
- Aerosol science, applications, 1
- Agglomerate(s)
definition of, 353
power law, fractal-like, 226
structure of, 5
- Agglomerate diffusion coefficients, 35–36
- Agglomerate formation
computer simulation of, 227–229
ballistic aggregation, 228
diffusion-limited aggregation, 227
fractal dimension in, 229
reaction-limited aggregation, 228
and coordination number, in computer simulations, 229
and fractal dimension, 223, 230, 240–241
Langevin simulations of, 230
morphology, 223–227
overview, 222–223
primary particle size and, 237–238
scaling laws in
autocorrelation function, 223–226
and power law relationship, prefactor for, 226–227
self-preserving agglomerate size distributions, 233–237
time to reach, 234–235
and Smoluchowski equation, 230–232
- Agglomerate restructuring, 242–245
and chain aggregates, elastic properties of, 245
under tension, 245
thermal, 242–244
- Aggregate(s), definition of, 353
- Aggregation
ballistic, computer simulation of, 228
diffusion-limited, computer simulation of, 227
reaction-limited, computer simulation of, 228
- Air light, and visibility, 149–150
- Air pollution, stack plumes and, 319–321
- Air Quality Criteria for Particulate Matter* (EPA), 157, 359, 380
- Air quality measures, common, 380
- Alkali halides, vapors of, dimers and trimers in, 269–270
- Alumina
commercial synthesis, 333
forms of, 355–356
primary particle size in synthesis of, 350–352

- Anatase, structure and applications of, 356
- Angular scattering of light, by single particles of intermediate size, 133-134
- Anti-Stokes emission, 151-152
- Atmospheric aerosol
- air quality measures, common, 380
 - chemical composition of, 370-373
 - particle size and, 373-378
 - for PAH and elemental carbon, 376
 - for sulfates and nitrates, 374-375
 - for water, 376-378
 - statistical variations in aerosol dynamics and, 388-389
 - field measurement of, 385-388
 - dry deposition velocity of, 76-78, 367-368
 - dynamics, in power plant plumes, 368-370
 - optical properties of, 145-151, 359
 - overview, 359
 - primary component, 372
 - properties and effects of, 359
 - residence time distribution curve for, 366-367
 - secondary component, 372
 - size distribution
 - accumulation mode, 360, 364-366
 - coarse mode, 360, 361-364
 - overview, 360
 - ultrafine range, 360, 366
 - source apportionment in
 - basic concepts, 380-381
 - chemical mass balance (CMB) method, 381-382
 - aerosol dynamics and, 385
 - Portland aerosol characterization study, 382-385
 - sources of, 359
 - submicron aerosol, morphological characteristics of, 378
- Atomizing generators, 182-184
- Attenuation coefficient, 136-137
- Autocorrelation function, in agglomerate formation, 223-226
- Averaging of particle size distribution functions, 14
- Avogadro's number, 33
- B**
- Ballistic aggregation, computer simulation of, 228
- Beams, aerosol, 118-120
- beam expansion angle vs. source pressure, 119
 - and mass spectrometry, 177
 - and particle trajectory, 119-120
- Bipolar charging, 46-49
- Boltzmann equation and, 42
 - definition of, 41
- Boltzmann equation, and bipolar charging, 42
- Brownian coagulation, 190-192
- collision frequency function in, 189-192
 - and Coulomb forces, 200
 - for initially monodisperse aerosol, 192-196
 - for laminar shear, 200-202
 - and simultaneous Brownian motion, 202-203
 - and particle force fields, 196-197
 - and van der Waals forces, 197-199
 - similarity solution for, 211-215
- Brownian motion
- and diffusion, 30-32, 58
 - deposition, 90
 - from pipe flow
 - laminar, 79
 - turbulent, 80-82
 - with laminar shear, coagulation in, 202-203
 - and quasi-elastic light scattering, 143-144
- Brownian particles, path length of, 37-38
- Bubbles, rising, deposition from, 82-84
- C**
- Carbon, in atmospheric aerosol, 372
- and particle size, 375-376
- Carbon blacks, fabrication of, 334-335
- Carbon spheres
- refractive index for, 132
- Cascade impactors, 21-22, 171-174, 181
- Chain aggregates, elastic properties of, 245
- Characterization of particles, and dynamics, 23-24
- Charged particle-vapor equilibrium, 263-265
- effect of solutes on, 259-262
- Charging of particles
- causes of, 41
 - unipolar vs. bipolar, 41
- Chemical analysis of particles, 157, 174-178
- measurement instruments, characteristics of, 178-181
 - multielement analysis, for source resolution, 175-176
 - overview, 174-175
 - Raman spectroscopy and, 152
 - single-particle, by mass spectrometry, 177-178
- Chemical composition, 19-21
- applications of, 2-3
 - of atmospheric aerosol, 370-373
 - particle size and, 373-378
 - for PAH and elemental carbon, 376
 - for sulfates and nitrates, 374-375
 - for water, 376-378
 - statistical variations in aerosol dynamics and, 388-389
 - field measurement of, 385-388
 - and average chemical composition, 20
 - chemical species distribution, determination of, 171-174
 - internally vs. externally mixed, 19
 - vs. particle size, 21
 - and size-composition probability density function, 19-20
- Chemical mass balance (CMB) method, 381-382
- aerosol dynamics and, 385
- Chemical reaction, heterogeneous, effect of particle size on, 266-269
- Cigarette smoke, particle size distribution, 221-223
- Clapeyron equation, 250
- Clean rooms
- deposition and thermophoresis in, 89
 - modeling of, 142
 - particle concentrations in, 7
- Cloud chamber
- diffusion, 281-282
 - Wilson (expansion), 276-277

- CMB. *See* Chemical mass balance (CMB) method
- Coagulation.
- as limiting process in gas-to-particle conversion, general dynamic equation (GDE) and, 308–309
 - overview, 188–189
 - and particle concentrations, 8
 - and self-preserving distribution, time to reach, 217–218
 - similarity solution for
 - in Brownian coagulation, 211–213
 - in continuum regime, 210–211
 - in free molecule region, 213–215
 - and simultaneous diffusional growth
 - general dynamic equation and, 313–314
 - experimental results, 315–316
 - and stirred settling, general dynamic equation in, 321–325
 - turbulent
 - comparison of collision mechanisms, 208
 - dynamics of, 204–205
 - inertial, 206–207
 - limitations on analysis, 207–208
 - shear, 206
- Coalescence.
- collision-coalescence mechanism of primary particle formation, in aerosol reactors. *See* Collision-coalescence mechanism of primary particle formation
 - extension of Smoluchowski equation to, 339–340
 - molecular dynamics (MD)
 - computations of, 342–343
- Coal gas, aerosol formation in, 296
- Coarse mode particles, in atmospheric aerosol, 360, 361–364
- Coefficient(s)
- of accommodation, in condensation, heterogeneous, 283–284
 - in free molecule friction coefficient, 33
 - of attenuation, 136–137
 - of diffusion, 30–33
 - agglomerate, 35–36
 - for nonspherical particles, 34–35
 - Stokes-Einstein, 33
 - and Taylor theory of diffusion by
 - continuous movements, 37
 - of extinction
 - in experimental methods, 165–166
 - light scattering by aerosol clouds, and optical thickness, 136–138
 - of friction, 31, 33–35
 - Knudsen number and, 33
 - for nonspherical particles, 35
 - Reynolds number and, 33
 - of particle eddy diffusion, 113–115
 - in deposition from rotating flow, 113–115
 - for Stokesian particles, 113–115
 - of restitution, in particle-surface interactions, rebounding, 99
 - of solid-state diffusion
 - in synthesis of submicron solid particles, 343–346
 - high-diffusivity paths and, 346
 - for lattice diffusion, 345
 - temperature dependence of, 343–345
- Collection methods for aerosol analysis, 158
- Collision-coalescence mechanism of primary particle formation, in synthesis of submicron solid particles, 338–339
- extension of Smoluchowski equation to, 339–340
- rate equation for, 340–343
 - by solid-state diffusion, 341–342
 - in solid-liquid transition, 342–343
 - by viscous flow, 341
- solid-state diffusion coefficient in, 343–346
 - high diffusivity paths and, 346
 - for lattice diffusion, 345
 - temperature dependence, 343–345
- Collision frequency function, 189–190
- for Brownian coagulation, 189–192
 - and Coulomb forces, 200
 - for initially monodisperse aerosol, 192–196
 - in collision-coalescence theory, 340
 - for laminar shear, 200–202
 - and simultaneous Brownian motion, 202–203
 - and particle force fields, 196–197
 - for turbulent coagulation, 204–208
 - and van der Waals forces, 197–199
- Collision kernels, for power law agglomerates, and Smoluchowski equation, 230–233
- Computer simulation of agglomerate formation, 227–229
 - ballistic aggregation, 228
 - coordination number in, 229
 - diffusion-limited aggregation, 227
 - fractal dimension in, 229
 - reaction-limited aggregation, 228
- Concentration boundary layer. *See* Convective diffusion
- Concentrations of particles, 6–10. *See also* Mass concentration
 - in clean rooms, 7
 - and coagulation, calculation of, 8
 - number concentration, calculation of, 6–8
 - total, 15
 - in urban atmosphere, 7
 - volumetric concentrations, calculation of, 7–8
- Condensation
 - by adiabatic expansion, 251–252, 276–277
 - heterogeneous, 283–284
 - in gas-to-particle conversion, 283–284
 - on ions, 263
 - by mixing, 252–254
- Condensation generators, 181–182
- Condensation nuclei counters, 181
- Condensation particle counters (CPC), 163–165
- Conditioning of aerosols, definition of, 189
- Continuity relations in v space, in gas-to-particle conversion, 288–290
- Continuous distribution function
 - coagulation equation for, 208–210
 - general dynamic equation for, 309–310
- Continuous size distribution, definition of, 10
- Continuum range
 - coagulation in, similarity solution for, 210–211
 - in agglomerates, 234
- Convective diffusion

- concentration boundary layer and
 low Reynolds numbers, 63–73
 high Reynolds numbers, 73–78
 and deposition to rough surfaces,
 76–78
 equation for, 59
 and external force fields,
 electrical precipitation, 84–87
 thermophoresis, 87–90
 and filtration theory, 69–73
 laminar pipe flow, 78–80
 overview of, 58
 from rising bubbles, 82–84
 similitude law, 66–69
 and simultaneous coagulation,
 325–327
 turbulent pipe flow, 80–82
 Coordination number, in agglomerate
 formation, 229
 Coulomb forces, Brownian coagulation
 and, 200
 Coarse particles, definition of, 3
 CPC. *See* Condensation particle
 counters
 Critical expansion ratio, saturation
 ratio and, 276
 Critical saturation ratio. *See* Saturation
 ratio, critical
 Critical Stokes number for impaction,
 105–107
 Crystalline particles, vapor and
 surface pressures of, and solid-
 particle-vapor equilibrium,
 265–266
 Crystal structure, in synthesis of
 submicron solid particles
 basic concepts, 355
 experimental observations, 355–356
 Cyclone separators
 and deposition from rotating flow,
 111–113
 and inertial deposition, 94
- D**
- DBP. *See* Dibutyl phthalate
 Deposition
 by diffusion
 Brownian, 90
 and convective diffusion equation,
 59–60
 general dynamic equation and,
 325–327
 to Earth's surface, dry, 73, 76–78,
 366–368
 inertial
 overview of, 94
 in transition to diffusion range,
 121–122
 and Reynolds number
 high, to rough surfaces, 76–78
 low, theory vs. experiment, 69–71
 from rising bubbles, 82–84
 from rotating flow, 111–113
 particle eddy diffusion coefficient,
 113–115
 in sampling, 160
 in transition from diffusion to
 inertial ranges, 121–122
 turbulent, 115–118
 Deposition velocity, 61
 Differential mobility analyzer,
 168–170
 Diffusion
 boundary conditions for, 53–54
 and Brownian motion, 53–54
 convective
 and concentration (diffusion)
 boundary layer, 61–62
 and concentration (diffusion)
 boundary layer equation
 for low Reynolds numbers,
 63–64
 diffusion vs. convection in, 62
 diffusion vs. interception in,
 73–76
 in external force field, 84–87
 from laminar pipe flow, 78–80
 and Reynolds number
 high
 deposition, 76–78
 interception at, 73–76
 and point particles, 66
 low
 and concentration boundary
 layer equation, 63–64
 deposition, 69–71
 and point particles, 64–66
 similitude law in, for particles of
 finite diameter, 66–69
 in transition to inertial range,
 121–122
 from turbulent pipe flow, 80–82,
 325–327
 equation of
 basic, 28–30
 in cylindrical coordinates, 63
 with gas velocity distribution,
 59–60
 growth by
 and simultaneous coagulation,
 general dynamic equation
 and, 313–314
 experimental results, 315–316
 and migration, in external force
 field, 39
 rate equation for, in synthesis of
 submicron solid particles,
 341–342
 similitude and, 60–61
 Diffusion battery, 170
 design of, 79–80
 Diffusion (concentration) boundary
 layer. *See* Convective diffusion
 layer. *See* Convective diffusion
 layer. *See* Convective diffusion
 layer. *See* Convective diffusion
 layer.
 Diffusion charging, unipolar
 continuum range, 43–45
 free molecule range, 42–43
 stochastic theory, 46
 Diffusion cloud chamber, in nucleation
 kinetics, 281–282
 Diffusion coefficients, 30–33
 agglomerate, 35
 for nonspherical particles, 34–35
 solid-state, 343–346
 Stokes-Einstein expression of, 33
 Diffusion-limited aggregation (DLA),
 computer simulation of, 227
 Dimers and trimers, in vapors of alkali
 halides, 269–270
 Direct interception. *See* Interception
 Discrete distribution, definition of, 10
 Discrete distribution function, general
 dynamic equation for, 307–308
 Dislocations, in solid-state diffusion,
 346
 DLA. *See* Diffusion-limited
 aggregation
 Doppler shift, in light scattering, 143
 Drag of gas on particle, 5
 Droplet current, in homogeneous
 nucleation, 277–278
 Dry deposition velocity, for
 atmospheric aerosol, 73,
 76–78, 367–368
 Dust free space, 87–90
 Dynamic light scattering. *See*
 Quasi-elastic light scattering

- E**
- EBDS. *See* Electron-beam dry scrubbing
 - EC generators. *See* Evaporation-condensation (EC) generators
 - Eddy diffusion coefficient
 - for gases, 80–82
 - for Stokesian particles, 113–115
 - Electrical migration, 40–49
 - bipolar charging, 46–50
 - field charging, 41
 - unipolar diffusion charging
 - continuum range, 43–45
 - free molecule range, 42–43
 - stochastic theory, 46
 - Electrical particle counters, 168–170
 - Electrical precipitation, 84–87
 - Electric mobility analyzer, characteristics of, 180
 - Electrohydrodynamic atomization (EHDA), 184
 - Electron-beam dry scrubbing (EBDS), 335–336
 - Electrostatic classifier, 168–179
 - Environmental Protection Agency (EPA) Criteria Document and atmospheric aerosol, properties and effects of, 359
 - and measures of air quality, 359
 - Equivalent particle diameter, for nonspherical solid particles, 5–6
 - Eulerian time scale, *vs.* Lagrangian, and particle eddy diffusion, 115
 - Evaporation-condensation (EC) generators, 181–182, 331, 336–337
 - Expansion ratio, critical, saturation ratio and, 276
 - Experimental methods
 - aerosol measurement instruments, summary of, 178–181
 - applications of, 157
 - calibration of equipment in, 181
 - cascade impactors, 171–174
 - chemical analysis, 157, 174–178
 - multielement analysis, for source resolution, 175–176
 - on-line, 177
 - single-particle, by mass spectrometry, 177–178
 - collection methods, 158
 - condensation particle counters (CPC), 163–165
 - electrostatic classifier, 168–179
 - extinction coefficients, 165–166
 - filtration, 162–163
 - mass and chemical species distribution, determination of, 171–174
 - mass concentration, 162–163
 - microscopy, 160–162
 - monodisperse aerosol generators, atomizing, 182–184
 - condensation, 181–182
 - overview, 157–158
 - sampling, 158–160
 - for size distribution function, 166–170
 - differential mobility analyzer, 168–170
 - diffusion battery, 170
 - single-particle optical counter, 166–168
 - total light scattering, 165–166
 - total number concentration, 163–165
 - External flow, definition of, 60
 - Externally mixed aerosols, definition of, 19
 - Extinction coefficient
 - experimental methods for, 165–166
 - in light scattering by aerosol clouds, 136–138
 - and optical thickness, 136–138
 - as measure of air quality, 380
 - Extinction paradox, 130

F

 - Federal Ambient Air Quality Standard, 380, 382
 - Fick's second law of diffusion, 30
 - Field charging, 41
 - Filters and filtration, 162–163
 - efficiency minimum of, 2
 - fibrous, 62, 63, 69–71, 162
 - model of, 104
 - thickness of, 71
 - and inertial deposition, 94
 - mesh, 73
 - pipes and rods, 62
 - porous membrane, 162
 - quartz-fiber, 162, 163
 - single-fiber, collection efficiency, by diffusion, low Reynolds number flows, 63–73
 - in transition from diffusion to inertial ranges, 121–122
 - teflon membrane, 162–163
 - types available, 162
 - Flame hydrolysis, 333
 - Flame reactors, 331, 332–334
 - Flux
 - definition of, 27
 - in external force field, 39
 - of particles sedimenting from stationary fluid, 16
 - Flyash
 - removal of, cyclone separators, 111
 - Force field, external
 - convective diffusion in, 84–87
 - particle migration in, 38–40
 - Fractal dimension (D_f)
 - agglomerate formation and, 223, 230, 240–241
 - in computer simulation, 229
 - and agglomerate structure, 5
 - Fractal-like power law agglomerates, 226
 - Free-molecule region, 4
 - agglomerates, self-preserving distribution for, 234
 - coagulation in, similarity solution, 213–215
 - Free radicals, in atmospheric aerosol, 373
 - Frenkel defects, in solid state diffusion, 344
 - Friction coefficient, 31, 34–35
 - Knudsen number and, 32
 - for nonspherical particles, 35
 - Reynolds number and, 109

G

 - Gas cleaning devices, and aerosol conditioning, 189
 - Gas-to-particle conversion
 - growth dynamics in
 - continuity relations in v space, 288–290
 - measurement of, in homogeneous gas-phase reaction, 290–292
 - with heterogeneous condensation, 293–296
 - experimental study, 296–299
 - growth laws in, 284–288
 - in reaction-limited growth, 286–288
 - in transport-limited growth, 285
 - Kelvin effect in, 292

- limiting processes in, general
 - dynamic equation (GDE) and, 308–309
 - mechanisms of, 275
 - overview, 275
 - in power plant plumes, 368–370
 - Gaussian distribution, 16–17
 - GDE. *See* General dynamic equation
 - General dynamic equation (GDE)
 - and aerosol characterization, 23–24
 - and atmospheric aerosol dynamics, 388–389
 - and atmospheric aerosol dynamics, in power plant plumes, 368–369
 - in coagulation and diffusional growth, 313–314
 - experimental results, 315–316
 - and coagulation and nucleation as limiting processes in gas-to-particle conversion, 308–309
 - in coagulation and stirred settling, 321–325
 - for continuous distribution function, 309–310
 - for continuous stirred tank reactor, 327–329
 - and deposition by convective diffusion, 325–327
 - for discrete distribution function, 307–308
 - for number concentration, 310–311
 - overview, 306–307
 - and similarity solution for continuum regime, 313–314
 - experimental results, 315–316
 - for turbulent flow, 318–319
 - for turbulent stack plumes, 319–321, 368–369
 - for volume fraction, 311–312
 - Generators of aerosols, monodisperse
 - atomizing, 182–184
 - condensation, 181–182
 - electrohydrodynamic atomization (EHDA), 184
 - spinning disk, 182–184
 - vibrating orifice, 184
 - Gibbs free energy, for vapor-particle system, 256
 - Graetz problem, 79
 - Grashof number, in thermophoresis, 88
 - Gravitational field, particle migration in, 38–39
 - Growth dynamics
 - in gas-to-particle conversion
 - continuity relations in v space, 288–290
 - measurement of, in homogeneous gas-phase reactions, 290–292
 - with heterogeneous condensation, 293–296
 - experimental study, 296–299
 - Growth laws
 - in gas-to-particle conversion, 284–288
 - in reaction-limited growth, 286–288
 - in transport-limited growth, 285
 - Growth rates, in gas-to-particle conversion, measurement of, in homogeneous gas-phase reactions, 290–292
- H**
- Hamaker constant
 - and coagulation, 197–199
 - London-van der Waals forces and, 52
 - Hard agglomerates, definition of, 353
 - Health effects of particle pollutants, 372–374, 378
 - and measures of air quality, 380
 - Heterodisperse aerosols, definition of, 10
 - Homogeneous aerosols, definition of, 10
 - Homogeneous function, degree of, definition of, 215
 - Homogeneous nucleation. *See* Nucleation, Homogeneous
 - Hygroscopic particle-vapor equilibrium, 259–262
- I**
- ICP. *See* Inductively coupled plasma (ICP) method
 - Ideal solutions, vapor pressure of, and solutes, 254
 - Impaction
 - of non-Stokesian particles, 108–111
 - similitude law for, and Stokesian particles, 102–104
 - of Stokesian particles
 - on cylinders and spheres, 104–108
 - critical Stokes number for inviscid flows, 105–107
 - experiment vs. theory, 107–108
 - INAA. *See* Instrument neutron activation analysis
 - Independent scattering, 135–136
 - Inductively coupled plasma (ICP) method, 176
 - Inertial transport. *See also* Deposition; Impaction
 - and aerodynamic focusing, 118–120
 - beam expansion angle vs. source pressure, 119
 - and homogeneous nucleation, 299–304
 - and particle trajectory, 119–120
 - overview, 94
 - and particle acceleration, at low Reynolds numbers, stop distance and, 100–102
 - and particle-surface interactions at low speeds, 95–97
 - rebound and, 98–100
 - Instrument neutron activation analysis (INAA), 175–176
 - Integrating nephelometer, 165
 - Interception
 - and convective diffusion, 61
 - at high Reynolds numbers, 73–76
 - at low Reynolds numbers, 66–68
 - and impaction, 102–104
 - Interception number, and inertial deposition, 104
 - Internal flow, definition of, 60
 - Internally mixed aerosols, definition of, 19
 - Interstitialcy mechanism, in solid state diffusion, 344
 - Interstitial mechanism, in solid state diffusion, 344
 - Ions, concentrations in air, 46
 - Isokinetic sampling, 159
 - Isotropic, definition of, 29
- J**
- Joint distribution functions, example of, 19–20
 - Junge distribution, 18
- K**
- Kelvin effect

- in condensation, heterogeneous, 284
 - in gas-to-particle conversion, 292
 - Kelvin relation, 256–257
 - limit of applicability, 258–259
 - solutes and, 260
 - Knudsen number
 - accommodation coefficients and, 284
 - and friction coefficient, 33–34
 - and particle behavior, 3
 - and thermophoretic velocity, 51
 - and transport properties, 28
 - Kolmogorov microscale, 204–205, 207
- L**
- Lagrangian time scale, vs. Eulerian, and particle eddy diffusion, 115
 - Langevin simulation, of agglomerate formation, 230
 - Laplace formula
 - for particle internal pressure, for small particles, 257–258
 - limit of applicability, 258–259
 - Lennard-Jones (LJ) intermolecular potential, and particle surface pressure, 258
 - Lewis number, for water vapor in air, trace amounts, 253
 - Light scattering, 5, 16
 - by aerosol clouds, 134–136
 - extinction coefficient for, and optical thickness, 136–138
 - aerosol contributions by volume, 138–139
 - characterization of scattered light, 126–128
 - definition of, 126
 - Doppler shift in, 143
 - Extinction paradox, 130
 - independent scattering, 135–136
 - inelastic, Raman effect, 151–154
 - intensity of scattered wave, 126
 - Mie scattering, power law distributions, 141–143
 - overview, 125–126
 - quasi-electric (QELS), 143–145
 - Rayleigh scattering, 139–141
 - by single particles
 - of intermediate size, 130–132
 - angular scattering, 133–134
 - large, 130
 - overview, 126–128
 - small, 128–130
 - specific intensity of
 - and radiative transfer equation, 145–146
 - formal solution of, 146–147
 - Light transfer through atmosphere, 148–150
 - Lognormal distribution functions, 17–18
 - London-van der Waals forces
 - in attraction between two plates, 96
 - and particle migration, 52–54
- M**
- Magnification of microscopes, maximum useful, 161
 - Mass and chemical species distribution, determination of, 171–174
 - Mass concentration. *See also* Concentrations of particles
 - for atmospheric air, 7
 - calculation of, 8
 - experimental methods for determining, 162–163
 - Mass spectrometry, and single-particle analysis, 177–178
 - MD. *See* Molecular dynamics
 - Mean free path of gas molecules, 3–4
 - of particles, 37–38
 - Measurement of aerosol properties. *See* Experimental methods
 - Melting point reduction of small solid particles, and solid-particle-vapor equilibrium, 266
 - Meteorology
 - and power law distributions, 18
 - and size distribution data, 12
 - Microcontamination, and power law distributions, 18
 - Microscopy, 160–162
 - magnification, maximum useful, 161
 - resolving power of, 160–161
 - Mie theory, 16, 130–132
 - angular scattering, 133–134
 - power law distributions, 141–143
 - Migration velocity
 - and diffusion, in external force field, 39
 - in electrical field, 40–49
 - bipolar charging, 46–49
 - field charging, 41
 - unipolar diffusion charging
 - continuum range, 43–45
 - free molecule range, 42–43
 - stochastic theory, 46
 - in external force field, 38–40
 - London-van der Waals forces and, 52–54
 - in thermophoresis, 50–51
 - and industrial applications, 50
 - Mobility diameter
 - in agglomerates, 226
 - definition of, 5
 - Molecular clusters, thermodynamic properties, 269–273
 - equilibrium size distribution in, 270–273
 - Molecular density, and mean free path of gas molecules, 3–4
 - Molecular dynamics (MD) simulations
 - of coalescence, 342–343
 - Moments of particle size distribution functions, 14–16, 293–296, 313–317
 - Monodisperse aerosol generators, 181–189
 - Monodisperse aerosols, definition of, 10
 - Morphology
 - agglomerates, 223–227
 - atmospheric aerosol, 378
- N**
- Nanoparticle chain aggregates (NCAs)
 - of titania, tension and, 245
 - NCAs. *See* Nanoparticle chain aggregates
 - Neck formation, in synthesis of submicron solid particles, 353–355
 - Nephelometer, integrating, 165
 - Niobia, primary particle size in synthesis of, 350–352
 - Nitrates, in atmospheric aerosol, particle size, 374–375
 - Nonspherical solid particles, equivalent particle diameter for, 5–6
 - Non-Stokesian particles, impact of, 108–111
 - Normal size distribution functions, 16–17
 - Nozzle flows. *See also* Beams, aerosol and aerosol beams, 119
 - and condensation, 252
 - and nucleation in turbulent, 299–304

- Nuclear reactor accidents, behavior of radioactive particles in, 321–325
- Nucleation
 homogeneous
 critical saturation ratios in, 280, 281
 for two origin of more condensable species, 283
 droplet current in, 277–278
 experimental test of, 280–283
 in gas-to-particle conversion turbulence and, 299–304
 scaling theory in, 299–300, 301–302
 splitting flow into multiple streams, effect of, 303–304
 kinetics of, 277–280
 in zero activation energy limit, 308–309
 thermodynamics and, 249, 251
- Number concentration
 at a point, 6–8
 and first moment, 15
 general dynamic equation for, 310–311
- O**
- Optical fibers, fabrication of, 334
- Optical particle counters, 166–168, 180
- Optical properties of aerosols
 atmospheric, 359
 and light scattering, 5
 parameters determining, 2
- Optical thickness, and extinction coefficient, in light scattering, by aerosol clouds, 136–138
- Organic compounds, in atmospheric aerosol, 372
- Oscillating aerosol reactors, in gas-to-particle conversion, measurement of growth rates, 296–299
- Ozone layer, destruction of, 359
- P**
- Packed beds, removal by impaction in, 107
- PAHs (polycyclic aromatic hydrocarbons), in atmospheric aerosol, chemical composition and particle size, 376
- PAMS. *See* Particle analysis by mass spectrometry
- Particle analysis by mass spectrometry (PAMS), 177–178, 179–180
- Particle beam apparatus, 99
- Particle collection. *See* Filters and filtration
- Particle counters, types of, 166
- Particle-surface interaction
 complete model of, 100
 in inertial transport
 at low-speeds, 95–97
 rebounds, 98–100
- Particulate mass, as measure of air quality, 380
- Particulate systems, common names for, 1
- Path length of Brownian particles, 37–38
- Péclet number for mass transfer, and convective diffusion, 61, 62
- Peroxides, in atmospheric aerosol, 373
- Photon correlation spectroscopy. *See* Quasi-elastic light scattering
- Pipe flow
 convective diffusion from
 laminar, 78–80
 turbulent, 80–82
 turbulent deposition, 115–118
- Poisson's equation, and unipolar diffusion charging, 42
- Pollack counter, 163
- Polycyclic aromatic hydrocarbons. *See* PAHs (polycyclic aromatic hydrocarbons)
- Polydisperse aerosols
 definition of, 10
 size distribution function and, 10–14
 continuous vs. discrete size distributions, 10
- Population balance equation, 306
- Portland aerosol characterization study, 382–385
- Power law agglomerates
 agglomerate size distributions for, and Smoluchowski equation, 230–233
 fractal-like, 226
- Power law distributions
 in clean rooms, 18
 in meteorology, 18, 360
 in Mie scattering, 141–143
- Precipitation, electrical, 84–87
- Primary particles
 definition of, 5
 in agglomerates, 222
 and agglomerate morphology, 223–227
 in atmospheric aerosols, 378–379
 and collision-coalescence
 mechanism of formation, 338–343
 estimating particle size
 effects of aerosol material properties, 350–352
 method of characteristic times, 346–349
 neck formation, 353–355
 synthesis of submicron solid particles, overview, 331
- Primary component, atmospheric aerosol, 372, 376, 385–386
- Pyrolysis reactors, 331, 334–335
- Q**
- Quasi-elastic light scattering (QELS), 143–145
- R**
- Radiative transfer equation, 145–146
 formal solution of, 146–147
 and visibility, 148–151
- Radioactive particles, behavior of, in nuclear reactor accident, 321–325
- Radius of gyration, in agglomerates, 226
- Raman effect, 151–154
 and particle chemical analysis, 177
- Raman spectroscopy, 152
- Rayleigh scattering, 16
 and self-similar size distributions, 139–141
- Reaction-limited aggregation, computer simulation of, 228
- Reactors. *See* Aerosol reactors, Nuclear reactor accidents
- Receptor modeling, for atmospheric aerosol, 359, 380–385
- Residence time distribution, for atmospheric aerosol, 366–367

- Resolving power of microscopes, 160–161
- Rotating flow. *See* Cyclone separations
- Rutile
structure and applications of, 356
- S**
- Sampling, 158–160
collection methods for, 158
and velocity ratio, stream to sample, 159
- Saturation ratio
critical, 280
and expansion ratio, 276
in nucleation, homogeneous, 280, 281
for two or more condensable species, 283
and critical expansion ratio, 276
in thermodynamics, 249–251
definition of, 251
supersaturation
by adiabatic expansion, 251–252
causes of, 249, 250
by mixing, 252–254
- Scaling laws, in agglomerate formation
autocorrelation function, 223–226
and power law relationship, prefactor for, 226–227
- Scaling theory, for homogeneous nucleation in turbulent jets, 299–300, 301–302
- Scattering cross section, 127
- Scattering diagrams, 126
- Scattering efficiency, 127–128
- Schmidt number
and concentration boundary layer equation, 63
and convective diffusion, 58
from laminar pipe flow, 79
- Schottky defects, in solid-state diffusion, 344
- Scrubbers, and inertial deposition, 94
- Secondary component, atmospheric aerosol, 372–373, 385–387
- Sedimentation
and coagulation, 321–325
of coarse mode particles, in atmospheric aerosol, 361
and fifth moment, size distribution function, 16
- Self-nucleation, 277
- Self-preserving distribution (SPD)
for agglomerates, 233–234
time to reach, 234–235
definition of, 211
for coalescing particles, 210–217
time to reach, 217–218
- Self-similar size distribution functions, 18–19
- Self-similar size distributions, and Rayleigh scattering, 139–141
average particle size, 140
- Settling velocity
terminal, 39
- Sherwood number, 61
- Silica, pyrogenic, manufacture of, 332–333
particle size distribution, 7
- Silicon, crystalline properties of, 356
- Similarity solution
for coagulation
Brownian, 211–213
in continuum regime, 210–211
in free molecule region, 213–215
for continuum regime coagulation and differential growth, 313–316
- Similitude
in convective diffusion, for particles of finite diameter, 66–69
for impaction, and Stokesian particles, 102–104
- Simultaneous distribution functions, example of, 20
- Single-element particle capture, by diffusion and interception, at high Reynolds numbers, 73–76
- Single fiber collection efficiency, 71
- Single-particle counteranalyzer (SPCA), 179
- Single-particle optical counter, 166–168
- Size, of particles, 3–6
vs. chemical composition, 21
distribution, and power law, 141–143
effect on equilibrium of heterogeneous chemical reaction, 266–269
and light scattering performance of unit volume, 139
measurement of, 3
range of, 3
terminology of, 3
- Size-composition probability density function, 19–20
and average chemical composition, 20
- Size distribution
in atmospheric aerosol
accumulation mode, 360, 364–366
coarse mode, 360, 361–364
overview, 360
ultrafine range, 360, 366
processes affecting, 23
- Size distribution function, 10–14.
See also Gas-to-particle conversion, growth laws in averaging of, 14
dimensions of, 11
graphing of, 12
for particle diameter, 10–11
relation to particle volume equation, 11–12
for particle volume, relation to particle diameter equation, 11–12
relationships among, 11–12
experimental methods for, 166–170
differential mobility analyzer, 168–170
diffusion battery, 170
single-particle optical counter, 166–168
for mixed aerosols, 19–20
moments of, 14–16
normal distributions, 16–17
power law distributions, 18
rate of change in, for coagulation, 189–190
self-similar distribution functions, 18–19
standard deviations in, 17, 18
- Skylight, and visibility, 149–150
- Smoluchowski equation
in agglomerate formation, 230–232
extension to colliding, coalescing particles, 339–340
generalization of, 307
- Solid-liquid transition, in collision-coalescence mechanism of primary particle formation, 342–343
- Solid-particle-vapor equilibrium
melting point of small solid particles, 266
vapor and surface pressures of crystalline particles, 263–265, 265–266

- Solid-state diffusion coefficient, in synthesis of submicron solid particles, 343–346
 high-diffusivity paths and, 346
 for lattice diffusion, 345
 temperature dependence of, 343–345
- Solutes
 effect on vapor pressure, 254–255
 and hygroscopic particle-vapor equilibrium, 259–262
 for small particles, Kelvin relation and, 258–259
 solutes and, 260
- Source apportionment, in air quality analysis
 basic concepts, 380–381
 chemical mass balance (CMB) method, 381–382
 aerosol dynamics and, 385
 multielement analysis for, 175–176
 Portland aerosol characterization study, 382–385
- SPCA. *See* Single-particle counteranalyzer
- SPD. *See* Self-preserving distribution
- Stagnation point, and Stokesian particle motion, 106
- Stirred settling, coagulation and, general dynamic equation in, 321–325
- Stirred tank reactor, with particle growth, 327–329
- Stokes-Einstein coefficient of diffusion, 33
- Stokes emission, 151–152
- Stokes form of Navier-Stokes equations, 35, 100–101
- Stokesian particles
 definition of, 103
 deposition from rotating flow, 111–113
 particle eddy diffusion coefficient, 113–115
 impaction of
 on cylinders and spheres, 104–108
 experiment vs. theory, 107–108
 and similitude law for impaction, 102–104
- Stokes law
 and Brownian motion, 35
 correction for motion perpendicular to fault plane, 97
 and friction coefficient, 31, 33
 and particle motion at stagnation point, in inertial transport, 106
- Stokes number, 102
 and convective diffusion, 71
 for impaction on cylinders and spheres, theoretical limits of, 105–107
 and inertial deposition, 104
- Stop distance
 and acceleration of particles at low Reynolds numbers, 100–102
 and turbulent deposition, 115–118
- Submicron aerosols, primary, in atmospheric aerosol, particle size, 376
- Submicron solid particles, synthesis of collision-coalescence mechanism of primary particle formation in, 338–339
 commercial and pilot scale, 332–337
 extension of Smoluchowski equation to, 339–340
 overview, 331–332
 particle crystal structure in, 355–356
 particle neck formation in, 353–355
 primary particle size
 effects of aerosol material properties on, 350–352
 estimation of, 346–349
 rate equation for, 340–343
 in diffusion, 341–342
 in solid-liquid transition, 342–343
 in viscous flow transport, 341
 solid-state diffusion coefficient, 343–346
 high-diffusivity paths and, 346
 for lattice diffusion, 345
 temperature dependence of, 343–345
- Sulfates, in atmospheric aerosol, particle size, 374–375
- Supersaturation
 in thermodynamics
 by adiabatic expansion, 251–252
 causes of, 249, 250
 by mixing, 252–254
- Surface area of particles, and particle size distribution functions, 15
- Surface pressure
 crystalline particles, 265–266
 Laplace's formula, 258
 liquids, 258
 molecular dynamics calculations, 258–259
- T**
- Terminal settling velocity, 39
- Thermodynamic properties of aerosols
 charged particle-vapor equilibrium, 263–265
 and molecular clusters, 269–273
 equilibrium size distribution in, 270–273
 overview of, 249
 particle size, effect on equilibrium of heterogeneous chemical reaction, 266–269
 particle-vapor equilibrium
 hygroscopic, 259–262
 saturation ratio in, 249–251
 solid-particle-vapor equilibrium
 melting point reduction of small solid particles, 266
 vapor and surface pressures
 of crystalline particles, 265–266
- supersaturation
 by adiabatic expansion, 251–252
 causes of, 249, 250
 definition of, 251
 by mixing, 252–254
 and vapor pressure
 Kelvin relation, 256–257
 limit of applicability, 258–259
 solutes and, 260
 particle internal pressure, 257–258
- and vapor pressure curve, 249–251
 effect of solutes on, 254–255
 hygroscopic particle-vapor equilibrium, 259–262
 solid-particle-vapor equilibrium
 melting point reduction of small solid particles, 266
 vapor and surface pressures
 of crystalline particles, 265–266
- Thermophoresis, 50–51
 dust-free space caused by
 in stagnation flow, 89–90
 on vertical plate, 88–89
 in industrial applications, 50
 in optical fiber fabrication, 334
- Thermophoretic velocity, 50
 slip-corrected, 50
- Time average of particle size distribution functions, 14
- Titania

- commercial synthesis, 333
 hiding power, 2
 nanoparticle chain aggregates (NCAs) of, 245
 primary particle size in synthesis of, 350–352
 structure and applications of, 356
Total number concentration, experimental measurement, 163–165
Transmissometers, 165
Transport properties
 equation of diffusion, 28–30
 and Knudsen numbers, large vs. small, 28
 overview, 27
Trimers and dimers, in vapors of alkali halides, 269–270
Turbidity, 136–137
Turbulence
 and coagulation. *See* Coagulation, turbulent
 energy cascade hypothesis of, 204
 and general dynamic equation, 317–319
 and nucleation, homogeneous
 in gas-to-particle conversion, 299–304
 scaling theory in, 299–300
 experimental tests of, 301–302
 splitting nozzle flow into multiple streams, effect of, 303–304
Turbulent stack plumes, 319–321
Turbulent deposition, 115–118
 and aerosol sampling, 160
Turbulent mixing, of coarse mode particles, in atmospheric aerosol, 361
- U**
- Ultrafine particles**
 in atmospheric aerosol, 360, 366
 definition of, 3
Unipolar charging, definition of, 41
- Urban aerosol**
 atmospheric aerosol
 air quality measures, common, 380
 and average chemical composition, 20
 chemical composition of, 370–373
 particle size and, 373–378
 for PAH and elemental carbon, 376
 for sulfates and nitrates, 374–375
 for water, 376–378
 particle concentrations in, 7, 16
 small particles in, 276
 submicron aerosol, morphological characteristics of, 378
- V**
- Vacancy mechanism**, in diffusion solid-state, 344
van der Waals forces
 and boundary condition for particle diffusion, 53–54
 Brownian coagulation and, 197–199
 origin, 52–53
Vapor pressure
 of crystalline particles, and solid-particle-vapor equilibrium, 265–266
 effect of solutes on, 254–255
 of small particle, 256–259
 Kelvin relation, 256–257, 258–259
 limit of applicability, 258–259
 solutes and, 260
 particle internal pressure, 257–258
Vapor pressure curve, 249–251
 and charged particle-vapor equilibrium, 263–265
 effect of solutes on, 254–255
 and hygroscopic particle-vapor equilibrium, 259–262
 and solid-particle-vapor equilibrium
 melting point reduction of small solid particles, 266
 vapor and surface pressures of crystalline particles, 265–266
Vibrating orifice generator, 184
Viscosity, and volumetric concentration, 7–8
Viscous flow, rate equation for, in synthesis of submicron solid particles, 341
Visibility, 131, 148–150, 165–166
 as measure of air quality, 380
Visual range. *See* Visibility
Volume average of particle size distribution functions, 14
Volume fraction, general dynamic equation for, 311–312
Volume of particles per gas volume, and particle size distribution functions, 15
Volumetric concentrations, calculation of, 7–8
- W**
- Water**
 angular scattering from droplets, 133
 in atmospheric aerosol, 373
 and particle size, 376
 saturation ratios for, 282
 trace amounts in air, Lewis, Schmidt, and Prandtl numbers for, 253
- X**
- X-ray fluorescence (XRF)**, 175, 181
 XRF. *See* X-ray fluorescence
- Z**
- Zirconia**, forms of, 356

Ideal for courses in aerosol science or particle technology, *Smoke, Dust, and Haze: Fundamentals of Aerosol Dynamics, 2/e*, is the only modern text that focuses on aerosol dynamics—the study of the factors that determine changes in the distribution of aerosol properties with respect to particle size. It covers fundamental concepts, experimental methods, and a wide variety of applications. Using the aerosol dynamics approach, the author integrates a broad range of topics including stochastic processes, aerosol transport theory, coagulation, formation of agglomerates, classical nucleation theory, and the synthesis of ultrafine solid particles. The book makes extensive use of scaling concepts and dimensional analysis and emphasizes physical and physicochemical interpretations. Basic concepts are illustrated by applications to many fields including air pollution control, the atmospheric sciences, microcontamination in the semiconductor industry, and the industrial manufacture of powders, pigments, additives, and nanoparticles.

Revised and expanded, this second edition features new chapters on the kinetics of agglomeration of noncoalescing particles and the fundamentals of aerosol reactor design. It covers the effects of turbulence on coagulation and gas-to-particle conversion and also discusses the formation of primary particles by the collision-coalescence mechanism. The chapter on the atmospheric aerosol has been completely rewritten within the aerosol dynamics framework. Its basic approach and topicality make *Smoke, Dust, and Haze: Fundamentals of Aerosol Dynamics, 2/e*, an essential guide for both students and researchers.

ABOUT THE AUTHOR

Sheldon K. Friedlander is Parsons Professor of Chemical Engineering and Director of the Air Quality/Aerosol Technology Laboratory at UCLA. He is a member of the National Academy of Engineering and received the 1990 Fuchs Memorial Award from the International Committee representing the American Association for Aerosol Research, Gesellschaft Für Aerosolforschung, and the Japan Association for Aerosol Science and Technology. In 1984-85 he received a Senior U.S. Scientist Award (Humboldt Award) from the West German Government and is a past president of the American Association for Aerosol Research. During his career he has received a Fulbright Scholarship; a Guggenheim Fellowship; the Colburn, Alpha Chi Sigma, and Walker Awards from the American Institute of Chemical Engineers (AIChE); and a certificate of recognition from NASA. He received the 1995 Lawrence K. Cecil Award in Environmental Chemical Engineering from AIChE.

PRAISE FOR THE PREVIOUS EDITION

“The reader of this excellent senior- or first-year-graduate-level text will recognize the catholic nature of the material treated. Sheldon Friedlander... is probably America’s pre-eminent investigator of aerosols, by virtue of his theoretical and experimental work conducted in a variety of areas since the 1950’s.... *Smoke, Dust, and Haze* is the first published book on aerosols written primarily for classroom use. It was written explicitly for chemical- and environmental-engineering first-year-graduate students but it could serve excellently as a physics course to introduce students to the nature of applied science.”

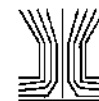
—*Physics Today*

COVER DESIGN BY ED ATKINSON/BERG DESIGN

OXFORD
UNIVERSITY PRESS
www.oup.com



ISBN 0-19-512999-7



The Aerosol Community Mourns the Loss of a Giant Sheldon K. Friedlander 1927–2007

**Cliff I. Davidson,¹ Daniel P. Y. Chang,² Adam Dalis,³ Sheryl H. Ehrman,⁴
Steven L. Heisler,⁵ George M. Hidy,⁶ Anshuman A. Lall,⁷ Thomas Lesniewski,⁸
Peter H. McMurry,⁹ Sotiris E. Pratsinis,¹⁰ Daryl L. Roberts,¹¹ Paul T. Roberts,¹²
Weizhi Rong,¹³ Patrick Sisljan,¹⁴ Chandra Venkataraman,¹⁵ Chiu-Sen Wang,¹⁶
Robert S. Windeler,¹⁷ and Cheng Xiong¹⁸**

¹*Department of Civil & Environmental Engineering and Engineering & Public Policy, Carnegie Mellon University, Pittsburgh, Pennsylvania, USA*

²*Department of Civil & Environmental Engineering, University of California—Davis, Davis, California, USA*

³*Intel Corporation, Portland Technology Department, Hillsboro, Oregon, USA*

⁴*Department of Chemical and Biomolecular Engineering, University of Maryland, College Park, Maryland, USA*

⁵*ENSR Corporation, Camarillo, California, USA*

⁶*Envair/Aerochem, Placitas, New Mexico, USA*

⁷*Department of Mechanical Engineering, University of Maryland, College Park, Maryland, USA*

⁸*Northrup Grumman Corporation, San Diego, California, USA*

⁹*Department of Mechanical Engineering, University of Minnesota, Minneapolis, Minnesota, USA*

¹⁰*Particle Technology Laboratory, Swiss Federal Institute of Technology, Zurich, Switzerland*

¹¹*MSP Corporation, Shoreview, Minnesota, USA*

¹²*Sonoma Technology, Inc., Petaluma, California, USA*

¹³*UCLA BH5531, Los Angeles, California, USA*

¹⁴*Department of Chemical and Biomolecular Engineering, University of California—Los Angeles, Los Angeles, California, USA*

¹⁵*Department of Chemical Engineering, India Institute of Technology—Bombay, Powai, Mumbai, India*

¹⁶*124 Idaho Avenue, Unit 304, Santa Monica, CA, USA*

¹⁷*OFS Laboratories, Murray Hill, New Jersey, USA*

¹⁸*Intel Corporation, DC1 Lithography, RA2, Hillsboro, Oregon, USA*

On February 9, 2007, the aerosol community lost one of its most respected members. Sheldon K. Friedlander died at age 79 of complications from pulmonary fibrosis at his home in Pacific Palisades. He was the Parsons Professor of Chemical Engineering at University of California, Los Angeles (UCLA).

Sheldon's remarkable career, which spanned six decades, began with a B.S. from Columbia University and a Masters degree from MIT, both in Chemical Engineering. He also worked at the Harvard School of Public Health on an Atomic Energy Commission project regarding control of radioactive aerosols. His time at Harvard catalyzed an interest in aerosols, which he pursued through subsequent Ph.D. research in Chemical Engineering at the University of Illinois at Urbana-Champaign. He then served as a faculty member at Columbia University (1954–1957), John

Hopkins University (1957–1964), California Institute of Technology (1964–1978), and UCLA (1978–2007).

Sheldon started his Ph.D. studies at a time when the field of aerosol science was in its early stages of development. Working with H.F. Johnstone, he focused on how particles in turbulent airflow are deposited on the walls of pipes and ducts. Sheldon made important contributions right from the start: he introduced the notion of a “stopping distance” of a particle injected into stagnant air, and then used this concept to predict particle motion through the viscous boundary layer to the surface. His thesis work laid the foundation for much of the later work on deposition of particles in industrial systems as well as dry deposition from the ambient atmosphere, where turbulent eddies impart velocities normal to the mean flow and enable particles to reach the surface.



Sheldon K. Friedlander

As a natural extension of this early work, Sheldon then considered the transport of particles to collectors of various geometries, such as cylindrical fibers and spheres. He developed expressions for the deposition of particles of different sizes to these obstacles which became valuable for predicting the efficiencies of fiber filters and collection of airborne particles by cloud droplets.

His work also involved studies of aerosol dynamics in the human respiratory system, including transport through the upper airways down into the lung. These studies informed research by others on both detrimental and therapeutic aspects of aerosols. For example, his early work on aerosol deposition in the lung led to the later development by others of methods to deliver therapeutic drugs directly to the lung.

But Sheldon went far beyond investigations of particle deposition. In what is often acclaimed as one of his most valuable scientific contributions, he theorized that regardless of the initial size distribution, a collection of particles in certain size ranges tends to grow, coagulate, and settle as it ages to form a "self-preserving" size distribution. In other words, the distribution of well-aged particles tends toward a predictable spectrum when expressed in dimensionless form regardless of the initial conditions. The theory of the self-preserving size distribution is based on selected solutions to the General Dynamic Equation (GDE), essentially a mass balance for aerosols that incorporates major mechanisms affecting aerosol formation, growth, transport, and ultimately loss. Since its development, many researchers

have used the self-preserving distribution for such applications as the design of controlled aerosol reactor experiments and industrial-scale manufacturing of chemical commodities. The theory greatly simplifies analysis of the motion and transformations of particle clouds, since it is no longer necessary to account for the initial distribution. The theory also permits back-of-the-envelope calculations of concentrations and size distributions, thus avoiding the need for numerical solutions to the GDE.

By the early 1970s, the Clean Air Act established by the newly founded Environmental Protection Agency had focused attention on identifying the sources of particles in the ambient atmosphere. Once again, Sheldon made pioneering contributions to the field. He reasoned that different categories of particle sources such as coal-fired power plants, automobiles, and soil resuspension have different characteristic chemical compositions. The atmospheric aerosol includes mixtures of particles from these and other sources. By measuring the composition of ambient particles and knowing the composition of particles emitted from different sources, it was thus possible to estimate the relative contribution of each source type influencing the measurement site. This "chemical element balance" was the forerunner of Source-Receptor Modeling that has become a major subdiscipline in its own right. The numerous software packages commercially available to conduct this type of modeling demonstrate the power and importance of the method.

When equipment became available to measure number concentrations of very small particles, Sheldon began to study yet another topic within aerosol science: the formation and growth of particles from molecular clusters. Using large Teflon bags on the laboratory roof at Caltech, he and his students studied the oxidation of SO_2 to form sulfate aerosol. He identified two different regimes of oxidation: a low humidity process which forms very small particles without photochemistry, and a high humidity mechanism in which SO_2 is absorbed into existing particles and oxidized in the presence of liquid water. This work was followed by major studies around the world on the formation of atmospheric aerosol from precursor gases.

Sheldon was a strong believer in the collection of ambient data as a means of understanding aerosols. In this vein, he was co-Principal Investigator of one of the first major urban field campaigns, the California Aerosol Characterization Experiment (ACHEX) in the early 1970s. Many noteworthy accomplishments came out of ACHEX. As one example, Sheldon and his group assembled an inventory of carbon emissions in Los Angeles and used it to apportion sources for the measured carbon aerosol; this resulted in the first carbon balance for an urban airshed. His group also compared particle size distributions measured during ACHEX across the Basin to demonstrate aerosol growth by photochemistry. This work promoted widespread interest in elemental and organic carbon during the 1990s, which included chemical speciation of organic compounds in aerosols.

Later in his career, Sheldon devoted considerable attention to the creation of synthetic aerosols. He explored the potential of aerosols to make useful products, and looked into the

development of aerosol reactors to generate particles with carefully controlled characteristics. Sheldon also studied the properties of nanoparticles, and postulated a revolutionary relationship on how agglomerates sinter to become compact particles. His work greatly simplified the description of non-spherical particle dynamics at high temperatures, placing the design and safe operation of aerosol reactors on a firm scientific basis. Sheldon also discovered the elastic, rubber-like behavior of micrometer-long chains of ceramic nanoparticles 10 nm in diameter. Such characteristics of nanoparticles can affect their useful properties and also their impacts on human health.

These examples are but a small sample of Sheldon's original scientific contributions during his productive career. He published many seminal archival papers. In addition, he wrote the influential book *Smoke, Dust, and Haze*, which was published in 1977 by John Wiley and Sons and later published in a modified second edition in 2000 by the Oxford University Press. This book is widely used by aerosol scientists and educators around the world.

Although his technical contributions have had a major effect on the field of aerosol science, perhaps his most significant accomplishment was training and inspiring others. His brilliant insights motivated those working with him, and his fascination with aerosols was contagious. He supervised numerous Ph.D. students, postdoctoral fellows, and visiting scientists during his career, as well as a large number of undergraduates and MS students. He also worked with several dozen aerosol scientists at his own and other institutions.

Sheldon's vision went beyond the training of other individuals to continue research in the field. He recognized the importance of establishing a community that could not only advance the understanding of aerosol science but also provide credibility for advocates of the discipline to be of service to society. He envisioned a world where aerosol scientists offered their expertise to solve a myriad of problems and improve people's lives in many ways.

With this vision in mind, Sheldon was one of the original founders of the American Association for Aerosol Research (AAAR). From its humble beginning as a small group in Santa Monica in 1982, the Association has grown to nearly 1000 members. Along with the European Aerosol Association, the AAAR has become a flagship of a network of aerosol associations worldwide. Sheldon served as President of AAAR during 1984–1986, and remained active in the association until the time of his death.

Sheldon also believed in the importance of linking science to public policy. He served on the advisory committee to the National Institutes of Health that shaped the first agenda for the National Institute of Environmental Health Sciences in 1969. He also served as the first chair of the EPA Clean Air Science

Advisory Committee in 1978–1982, and was a member of the EPA Science Advisory Board Executive Committee during this period. He was chair of the National Research Council (NRC) Panel on Abatement of Particulate Emissions from Stationary Sources, and chair of the NRC Subcommittee on Photochemical Oxidants and Ozone. In addition, he spent time at other Universities; for example, he was a Fulbright Scholar in 1960 and a Guggenheim Fellow in 1969, both at the University of Paris.

As a result of his contributions and leadership in aerosol science, Sheldon received many honors throughout his career. For example, he received five awards from the American Institute of Chemical Engineers: the Colburn Award in 1959, the Alpha Chi Sigma Award in 1974, the Walker Award in 1979, the Cecil Award in 1995, and the Lifetime Achievement Award of the AIChE Particle Technology Forum in 2001. He also received the Humboldt Senior Scientist Award from the West German Government in 1984–1985. He presented several invited lectures around the world, and more recently he was the first recipient of the Christian Junge Award of the European Aerosol Association in 2000 and the Aurel Stodola Medal of ETH in Zurich in 2004.

Two more awards, however, deserve special comment. Sheldon was elected to the National Academy of Engineering in 1975, "in recognition of his contributions to the understanding of the origin and control of pollution by particulate matter." In addition, Sheldon was the first individual to receive the Fuchs Memorial Award in 1990, which is the highest honor that can be bestowed on an aerosol scientist, presented by the AAAR, Gesellschaft für Aerosolforschung, and the Japan Association for Aerosol Science and Technology. The Fuchs Award is presented only once every four years. In the mid-1990s, the AAAR recognized Sheldon's impact in the field by creating the Sheldon K. Friedlander Award for an outstanding Ph.D. dissertation "in any discipline in the physical, biomedical, or engineering sciences in a field of aerosol science and technology."

The world community of aerosol researchers is indebted to Sheldon Friedlander, outstanding researcher, educator, mentor, and role model who was one of the giants in aerosol science. His contributions to the field will be long remembered, and his wisdom will remain with us in his scientific papers. Most important, his inspiration will continue through his many students and colleagues, as we attempt to emulate the character of a great scientist and a great human being.

Sheldon Friedlander's doctoral students were invited to contribute to this obituary and be co-authors, and those who were successfully contacted and who accepted this invitation are included in the author list. Many other individuals consider Sheldon as one of their primary mentors, although their names are not included as co-authors to keep the list manageable.